

Load history effects in fibre-reinforced polymer composite materials

Thèse N° 9384

Présentée le 28 juin 2019

à la Faculté de l'environnement naturel, architectural et construit
Laboratoire de construction en composites
Programme doctoral en science et génie des matériaux

pour l'obtention du grade de Docteur ès Sciences

par

Abdolvahid MOVAHEDIRAD

Acceptée sur proposition du jury

Prof. P. Bowen, président du jury
Dr. A. Vassilopoulos, Prof. T. Keller, directeurs de thèse
Prof. G. Pinter, rapporteur
Dr R. Alderliesten, rapporteur
Prof. V. Michaud, rapporteuse

2019



*To my unforgettable father
my lovely mother
Zeinab
Saeed & Arefeh
&
Mohamad Ali*

Preface



The comparative advantages of composite materials, allowed the development of all fiber reinforced polymer (FRP) structures in several engineering domains. The technological challenge of designing such structures against extreme loading conditions for an operational life exceeding several decades with minimal maintenance and, without the development of critical damage is exciting. Usually able to sustain the ultimate extreme loading conditions, these structures fail mainly due to time dependent and fatigue related phenomena.

Nevertheless, profound information regarding the fatigue and fracture performance of engineering structures made of polymeric materials under realistic loading patterns is soundly missing. Most of the research works performed in the field are usually following standardized experimental methods and specific protocols, e.g. the S-N curves' derivation for composite laminates by performing continuous constant amplitude loading, for the establishment of fatigue design allowables. As a result, the behavior of composite laminates under loading patterns that are frequently seen during operation of engineering structures, involving combined creep/fatigue/recovery conditions is practically not investigated.

A rigorous experimental campaign has been conducted in this Thesis in order to comprehend the behavior of angle ply composite laminates that are usually implemented in engineering structures. A pioneering fatigue database emerged from this research including information regarding damage development and failure under continuous and interrupted failure loading profiles.

This Thesis proved that there is still a lot of “mystery” and hidden information regarding the material response to random, realistic, loading profiles, and could serve as a basis for the development of more laborious and thorough investigations on the fatigue damage assessment and fatigue life prediction of composite materials and structures.

The Swiss National Science Foundation under the grant No. 200021_156647 has financially supported this Thesis; this support is highly appreciated.

Lausanne 15/03/2019

Dr. Anastasios P. Vassilopoulos

Senior Scientist (MER)

EPFL

Acknowledgements



A PhD is like a journey, and reaching the destination during these four years was not possible without the help of many people. First, I would like to express my deepest appreciation to my supervisors Dr. Anastasios Vassilopoulos and Prof. Thomas Keller. Indeed without their guidance, support, availability, willingness to discuss, and good nature, I would never have been able to pursue my PhD. In addition, I would like to express my greatest gratitude to my thesis defense juries for the time devoted to evaluating my thesis and their feedback; Prof. Michaud Véronique (EPFL), Prof. Pinter Gerald (Kunststoff Technik Leoben), Dr. Alderliesten Rene (Delft University of Technology), and Prof. Paul Bowen (President of the jury, EPFL).

A large part of my PhD project was experimental, which was done in the EPFL Structural Laboratory. I had to deal with many different devices and machines and each had many specific points to consider, and sometimes it learning new software and tools was necessary. Carrying out all these activities rapidly and correctly would not have been possible without the technicians' support and patience. First of all, I would like to acknowledge Sylvain Demierre for his great sense of leadership and availability who taught me how to work with the Intsrn machine and diligently helped me progress with my project. I would like to thank Gilles Guignet for his great assistance in the experimental design part, software-related issues, and designing the frame for the pure creep experiments. I also cannot forget Serge Despont for cutting the specimens with a very high quality as well as Armin Krkic who fabricated the frame for pure creep experiments.

The Composite Construction Laboratory (CCLab) was my nest during my PhD, a great place to be with great scientists and friends (CCLabians), and indeed they made my life colorful and more pleasant. Among them I would like to start with my dear friend and colleague, Aida, for always being so open to listen to my words, being motivated to have scientific talks, and being very supportive during all these four years of PhD. Secondly, I would like to mention my first officemate and my great friend Kyriaki for her sincere friendship and always being receptive. I would like also to mention Haifeng for his very kind friendship and his patience in listening to me, and indeed he was my example for learning new languages. During my PhD, I had the great opportunity to be a teaching assistant for the 'Structures et Matériaux I et II' course and work closely with Dr. Julia de Castro who was always a great friend and helped me to improve my teaching skills. In addition, I thank all my other officemates, Zhengwen, Polina, and Francesco, for making our office (BP 2123) a very pleasant place to work. I would like to thank all CCLabians, Sonia, Myrsini, Maria, Alireza, Chao, Xing, João, Mário, Wei, Behzad, Moslem, Lingfeng, and Luca, also my kind Iranian friends Ghazaleh and

Niloufar. Also, I would like to express my greatest gratitude to the laboratory secretary Saira Mohamed for always being so willing to help me and very skillful in administrative issues. Many thanks also to Margaret for patiently revising the English text of my thesis.

There were many more people whose contributions on my life were undeniable. I would like to start with my Swiss family, the Mühlbergs especially Anne-Claude, the Bingueli family especially Philippe, Mother Antonia and Sister Maria in the Monastery of Saint Mary in Les Sciernes, Zainab Mohamed, Ali Mohamed, Nassima Nasri and Nicolas Chobaut, Zisti Haghparast, Bahar Khalilian, Sigurd Rogne Myklebost, and Damien Sommer.

My life with my Iranian friends became very enjoyable, who always gave me the feeling of being in my country; Reza Ghanaatian, Ali Pahlevan, Farzaneh Jahanbakhshi, Peyman Karami, Majid Yousef Sani, Fatemeh Qaderi, Morteza Hassani, Mohammadmahdi Kiaee, Ali Tehranchi, Farnood Salehi, Seyed Mohsen Moosavi, Seyyed Mohammad Hashemi, Amir Shaikhha and Elmira Shahrabi. Special thanks to Ebrahim Farmand and Azadeh Khoushabi for helping me a lot during all the important steps of my life before applying for the PhD at EPFL, during my PhD, and also in finding my future path after graduation.

I express my deepest gratitude to my beloved family; my unforgettable father who is always with me and I feel his presence, my lovely mother, Zeinab, Saeed and Arefeh, and Mohamad Ali. Also, I would like to express my great thankfulness to my grandmothers, Uncle Ismael, Aunt Tayebbeh, and Aunt Raziye for their words and kind wishes for me.

Vahid

05.03.2019

Abstract



Today, it is widely accepted that fatigue is one of the most common failure mechanisms in structural components, and pure static failure is rarely observed. Engineering structures are subjected to complex mechanical fatigue loading histories, which cause damage that eventually leads to functional and structural deterioration. One reason for this complexity is that the cyclic loading is accompanied by time-dependent deformations including creep and recovery. Fiber-reinforced polymer (FRP) composite materials are susceptible to time-dependent deformation, due to the viscoelastic nature of their matrix. Therefore, fatigue-creep-recovery interactions can play a role in the overall deformation behavior of FRP composite materials. The limited experimental investigations of FRP composite materials showed considerable effects of time-dependent phenomena on the fatigue behavior. However, no systematic analysis to clearly determine the effect of creep and recovery on developed damage mechanisms of FRP composites has yet been conducted. The aim of this research is to understand the fatigue behavior of glass fiber-reinforced composite (GFRP) materials and establish a reliable methodology to analytically/numerically model the fatigue behavior of FRP composite materials.

The fatigue behavior of $(\pm 45)_{2S}$ angle-ply glass/epoxy laminated composite at different stress levels has been investigated in this thesis. It was observed that cyclic-dependent parameters (cyclic creep, fatigue stiffness, and hysteresis loop area) as well as damage development were a function of applied stress levels. In tension-tension continuous fatigue, by decreasing the stress ratio, the damage became more severe, fatigue stiffness exhibited greater changes, the hysteresis loop area became larger and a higher and more uneven self-generated temperature was recorded.

The effect of loading interruption on fatigue behavior was studied by subjecting the specimens to tension-tension constant amplitude fatigue loading interrupted at σ_{\max} by creep intervals. At high stress levels, the fatigue life was improved when hold time was short as a result of the fiber realignment caused by the creep strain, while longer hold time caused considerable creep damage and therefore premature fatigue failure of the specimens.

The cyclic loading was also interrupted at zero stress level. The stiffness degradation rates and hysteresis loop area decreased during the cyclic loading phase, while specimen recovery occurred after each stress removal. It was observed that specimens loaded under interrupted fatigue exhibited longer fatigue lives than those continuously loaded at high stress levels as a result of partial fatigue stiffness restoration and crack blunting. It was concluded that fatigue design allowables based on continuous fatigue could be conservative.

A model based on the theory of viscoelasticity was developed to simulate specimen recovery in viscoelastic materials and predict their cyclic-dependent mechanical properties. The developed model predicted the cyclic-dependent parameters well - the fatigue stiffness, hysteresis loop area, cyclic creep, storage and loss moduli as well as $Tan(\delta)$.

Keywords: fatigue; fiber-reinforced composite (FRP); damage, stress ratio; cyclic creep; fatigue stiffness; hysteresis loop area; self-generated temperature; pure creep; interrupted loading; creep-fatigue interaction; recovery; modeling; viscoelasticity

Résumé



De nos jours, la fatigue est largement considérée comme l'un des mécanismes de rupture les plus courants dans les composants structurels, une rupture purement statique étant rarement observée. Les structures d'ingénierie sont soumises à des historiques de chargement mécanique complexes, qui provoquent des dommages pouvant conduire à une détérioration fonctionnelle et structurelle. Une raison de cette complexité est que le chargement cyclique est accompagné de déformations liées au temps, comme le fluage et le recouvrement. Les matériaux composites polymères renforcés de fibres (FRP) sont susceptibles de déformations dépendantes du temps, en raison de la nature viscoélastique de leur matrice. Par conséquent, les interactions fatigue-fluage-recouvrement peuvent jouer un rôle dans le comportement de la déformation globale des composites en PRF. Le nombre limité d'études expérimentales sur les matériaux composites en PRF ont montré des effets considérables des phénomènes liés au temps sur le comportement en fatigue. Cependant, aucune analyse systématique visant à clairement déterminer l'effet du fluage et du recouvrement sur les mécanismes d'endommagement développés dans des composites en PRF n'a été menée jusque-là. Le but de cette recherche est de comprendre le comportement en fatigue des matériaux composites renforcés de fibres de verre (GFRP) et d'établir une méthodologie fiable permettant de modéliser analytiquement et numériquement leur comportement en fatigue.

Le comportement en fatigue de stratifiés $(\pm 45)_{2s}$ en composites fibre de verre / époxy sous différents niveaux de contrainte a été étudié dans cette thèse. Il a été observé que les paramètres dépendant du cycle (fluage cyclique, raideur de fatigue et surface de la boucle d'hystérésis) ainsi que le développement des dommages sont fonction des niveaux de contrainte appliqués. Sous un chargement cyclique de traction axiale, la diminution du rapport des contraintes a entraîné des endommagements plus sévères, de grands changements de la raideur de fatigue, une plus grande surface de la boucle d'hystérésis et une température auto-générée plus élevée et inégale.

L'effet de l'interruption de la charge sur le comportement en fatigue a été étudié en soumettant les échantillons à des essais de fatigue en traction à amplitude constante, interrompus à la contrainte maximale σ_{max} par des intervalles de fluage. Sous des niveaux de contraintes élevés, la durée de vie à la fatigue a augmenté lorsque le temps de maintien est court, en raison du réalignement des fibres provoqué par la déformation de fluage, tandis qu'un temps de maintien plus long a provoqué un endommagement par fluage considérable et donc une rupture de fatigue prématurée des échantillons.

La charge cyclique a également été interrompue au niveau de la contrainte nulle. La vitesse de dégradation de la raideur de fatigue et la surface de la boucle d'hystérésis ont diminué pendant la phase de chargement cyclique, tandis que le recouvrement de l'échantillon a eu lieu après chaque déchargement. Les échantillons chargés en fatigue interrompue ont présenté une durée de vie en fatigue supérieure à ceux chargés de manière continue à des niveaux de contrainte élevés en raison du rétablissement partiel de la raideur en fatigue et du crack blunting. En conclusion, les tolérances de conception en fatigue basée sur une fatigue continue pourraient être conservatrices.

Un modèle basé sur la théorie de la viscoélasticité a été développé pour simuler le recouvrement des échantillons en matériaux viscoélastiques et prévoir leurs propriétés mécaniques en fonction des cycles. Le modèle développé a permis de prévoir les paramètres dépendant du cycle - la raideur de fatigue, la surface de boucle d'hystérésis, le fluage cyclique, les modules de conservation et de perte ainsi que $Tan(\delta)$.

Mots clés: fatigue; composite renforcé de fibres (PRF); dommage ; le rapport de contrainte; fluage cyclique; la raideur de fatigue ; surface de boucle d'hystérésis; température auto-générée; fluage pur; chargement interrompu; interaction de fluage-fatigue; recouvrement.; modélisation; viscoélasticité

Zusammenfassung



Es ist heutzutage allgemein akzeptiert, dass Ermüdung eine der häufigsten Versagensmechanismen in strukturellen Komponenten ist und rein statisches Versagen selten beobachtet wird. Ingenieur-Tragwerke unterliegen komplexen mechanischen Ermüdungsbeanspruchungen, welche Schäden verursachen, die schließlich zu funktionalen und strukturellen Beeinträchtigungen führen. Ein Grund für diese Komplexität ist, dass die zyklische Beanspruchung von zeitabhängigen Verformungen begleitet wird wie Kriechen und Erholung. Faserverbundwerkstoffe (FRP) sind empfindlich auf zeitabhängige Verformungen aufgrund der viskoelastischen Natur ihrer Matrix. Daher kann die Interaktion von Ermüdung, Kriechen und Erholung im gesamten Verformungsverhalten von FRP-Verbundwerkstoffen von Bedeutung sein. Die wenigen experimentellen Arbeiten über FRP-Verbundwerkstoffe zeigten einen erheblichen Einfluss von zeitabhängigen Phänomenen auf das Ermüdungsverhalten. Es wurde jedoch noch keine systematische Analyse durchgeführt, um die Wirkung von Kriechen und Erholung auf die sich einstellenden Schädigungsmechanismen von FRP-Verbundwerkstoffen eindeutig zu bestimmen. Das Ziel dieser Arbeit ist, das Ermüdungsverhalten von Glasfaser-Verbundwerkstoffen (GFRP) zu verstehen und eine zuverlässige Methode zu etablieren, um dieses analytisch und numerisch zu modellieren.

In dieser Arbeit wurde das Ermüdungsverhalten von winkelschichtigen (± 45)_{2s} Glas-Epoxy Laminaten unter verschiedenen Stressniveaus untersucht. Es wurde beobachtet, dass zyklisch abhängige Parameter (zyklisches Kriechen, Ermüdungssteifigkeit und Hysterese-Schleifenfläche) und die Schadensentwicklung eine Funktion des aufgetragenen Belastungsniveaus sind. Unter Zug-Zug kontinuierlicher Ermüdung, bei Abnahme des Spannungsverhältnisses, wurde die Schädigung schwerwiegender, die Ermüdungssteifigkeit zeigte größere Veränderungen, die Hysterese-Schleifenfläche wurde größer und die selbst-erzeugte Temperatur höher und ungleichmäßiger.

Die Wirkung von Belastungsunterbrüchen auf das Ermüdungsverhalten wurde untersucht. Die Proben wurden einer Zug-Zug kontinuierlichen Ermüdungsbelastung ausgesetzt, die bei σ_{\max} durch Kriechintervalle unterbrochen wurde. Bei hohem Spannungsniveau wurde die Ermüdungslebensdauer bei kurzer Haltezeit länger, weil die Fasern sich durch Kriechdehnung neu ausrichteten. Längere Haltezeiten hingegen führten zu einer Kriechschädigung, die ein vorzeitiges Ermüdungsversagen der Proben verursachte.

Die zyklische Belastung wurde auch bei Nullspannungsniveau unterbrochen. Die Steifigkeitsabnahmeraten und die Hysterese-Schleifenfläche nahmen während der zyklischen Belastungsphase ab, während eine Erholung der Proben nach jedem Spannungsunterbruch erfolgte. Es

wurde beobachtet, dass - infolge partieller Erholung der Ermüdungssteifigkeit und Crack blunting - Proben bei unterbrochener Ermüdung eine längere Lebensdauer aufwiesen als diejenigen, die kontinuierlich durch hohe Spannungen belastet wurden. Eine auf kontinuierlicher Ermüdung basierende Ermüdungsdimensionierung kann deshalb konservativ sein.

Ein Modell basierend auf der Theorie der Viskoelastizität wurde entwickelt, um die Erholung in viskoelastischen Materialien zu simulieren und deren zyklisch-abhängigen mechanischen Eigenschaften vorherzusagen. Das entwickelte Modell hat die zyklisch-abhängigen Parameter gut vorhergesagt – das heisst Ermüdungssteifigkeit, Hysterese-Schleifenfläche, zyklisches Kriechen, Speicher- und Verlustmodul sowie $\tan(\delta)$.

Schlüsselwörter: Ermüdung; Faserverbundwerkstoffe (FRP); Schädigung; Spannungsverhältnis; Zyklisches Kriechen; Ermüdungssteifigkeit; Hysterese-schleifenfläche; Selbsterzeugte Temperatur; Reines Kriechen; Unterbrochene Belastung; Interaktion zwischen Kriechen und Ermüdung; Erholung; Modellieren; Viskoelastizität



امروزه به صورت گسترده پذیرفته شده است که خستگی یکی از رایج ترین مکانیزم های تخریب در اجزای سازه ای است و به ندرت تخریب تنها بصورت کششی مشاهده می شود. سازه های مهندسی تحت تاثیر بارهای خستگی مکانیکی پیچیده قرار می گیرند که باعث آسیب و در نهایت سبب تخریب عملکردی و ساختاری می شود. یک دلیل برای این پیچیدگی، همراهی بارگذاری سیکلی با تغییر شکل های وابسته به زمان شامل خزش و بازیابی است. کامپوزیت پلیمری تقویت شده با الیاف (FRP) به دلیل طبیعت ویسکوالاستیک ماده ی زمینه مستعد تغییر شکل وابسته به زمان هستند. بنابراین، اندرکنش بین خستگی، خزش، و بازیابی می تواند در رفتار کلی تغییر شکل کامپوزیت های FRP نقش ایفا کند. پژوهش های تجربی محدود نشان دهنده ی تاثیر قابل ملاحظه پدیده های وابسته به زمان بر رفتار خستگی کامپوزیت های FRP است. اگرچه هنوز هیچ آنالیز سیستماتیکی برای تعیین دقیق اثر خزش و بازیابی بر توسعه ی مکانیزم های آسیب دیده گی در کامپوزیت های FRP انجام نشده است. هدف از این پژوهش، بررسی رفتار خستگی کامپوزیت های پلیمری تقویت شده با الیاف شیشه (GFRP) و ارایه یک روش قابل اعتماد برای مدل کردن تحلیلی/عددی رفتار خستگی کامپوزیت های FRP است.

رفتار خستگی لمینیت های کامپوزیتی $2s$ angle-ply (± 45) شیشه/اپکسی در سطوح تنشی متفاوت در این پایان نامه مطالعه شده است. بررسی های انجام شده نشان می دهد که پارامترهای وابسته به الگوی بارگذاری سیکلی (خزش سیکلی، سفتی خستگی و مساحت حلقه ی هیستریزیس) و همچنین گسترش آسیب دیدگی خستگی تابعی از سطح تنش اعمالی است. در خستگی پیوسته کشش-کشش، با کاهش نسبت تنش، آسیب دیدگی شدیدتر شده و سفتی خستگی تغییرات بیشتری را نشان داد. همچنین، مساحت حلقه ی هیستریزیس بزرگ تر و دمای خود تولید بالاتر و غیر یکنواخت تری اندازه گیری شد.

اثر وقفه در بارگذاری بر رفتار خستگی با توقف تنش خستگی کشش-کشش با دامنه ی ثابت در σ_{max} (فواصل خزشی) مطالعه شد. در سطوح تنشی بالا با زمان نگهداری کوتاه، عمر خستگی به دلیل جهت گیری الیاف در نتیجه ی کرنش خزشی افزایش پیدا کرد، در حالی که زمان نگهداری بلند سبب آسیب دیدگی خزشی قابل توجه، و در نتیجه تخریب خستگی زودرس نمونه ها شد.

تنش سیکلی همچنین در سطح تنش صفر متوقف شد. نرخ کاهش سفتی و مساحت حلقه ی هیستریزیس در حین فاز بارگذاری سیکلی کاهش پیدا کرد، در حالیکه بازیابی نمونه بعد از هر حذف بارگذاری رخ داد. مشاهده شد که نمونه هایی که تحت بار گذاری منقطع نسبت به نمونه هایی که بصورت پیوسته بارگذاری می شوند، به دلیل ترمیم بخشی از سفتی خستگی و crack blunting، عمر خستگی بلندتری دارند. بنابراین نتیجه گیری شد که معیارهای طراحی برای خستگی براساس بارگذاری خستگی بصورت پیوسته می تواند محافظه کارانه باشد.

یک مدل مبتنی بر تئوری ویسکوالاستیسیته برای شبیه سازی بازیابی نمونه در مواد ویسکوالاستیک و پیش بینی خواص مکانیکی وابسته به سیکل طراحی شد. مدل ارایه شده خواص مکانیکی وابسته به بارگذاری سیکلی - سفتی خستگی، مساحت حلقه ی هیستریزیس، خزش سیکلی، مدول ذخیره، مدول اتلاف، و $\tan(\delta)$ را به خوبی پیش بینی کرد.

کلمه های کلیدی: خستگی، کامپوزیت پلیمری تقویت شده با الیاف (FRP)، آسیب دیدگی، نسبت تنش، خزش سیکلی، سفتی خستگی، مساحت حلقه ی هیستریزیس، دمای خود تولید، خزش، بارگذاری منقطع، اندرکنش خزش - خستگی، بازیابی، شبیه سازی، ویسکوالاستیسیته

Table of Contents



Preface	v
Acknowledgement	vii
Abstract	ix
Résumé	xi
Zusammenfassung	xiii
چکیده	xv
Table of Contents	xvii
List of Figures	xxi
List of Tables	xxvii
Chapter 1 Introduction	1
1.1 Context and motivation	1
1.2 Objectives	4
1.3 Methodology	5
1.4 Thesis organization	6
1.5 List of publications	8
References	9
Chapter 2 Continuous fatigue behavior	13
2.1 Introduction	13
2.2 Experimental procedure	16
2.2.1 Material and specimen preparation	16
2.2.2 Experimental set-up and instrumentation	17
2.2.3 DMA experiment	19
2.3 Experimental results	20
2.3.1 Quasi-static behavior	20
2.3.2 Fatigue behavior	21
2.3.2.1 Fatigue life	21
2.3.2.2 Stress-strain loops, dissipated energy and stiffness degradation	22
2.3.2.3 Self-generated temperature evolution	26
2.3.2.4 Fatigue damage growth	28
2.3.2.5 Fatigue failure mode	30
2.4 Discussion	31
2.5 Conclusions	32

References	33
Chapter 3 Stress ratio effect on fatigue behavior	39
3.1 Introduction	39
3.2 Experimental procedure	41
3.2.1 Material and specimen preparation	41
3.2.2 Experimental set-up and instrumentation	41
3.3 Experimental results and discussion	43
3.3.1 Fatigue life	43
3.3.2 Specimen translucency and self-generated temperature	44
3.3.3 Stress-strain loops and fatigue stiffness	47
3.4 Effect of stress ratio	51
3.5 Conclusions	55
References	56
Chapter 4 Creep-fatigue behavior	63
4.1 Introduction	63
4.2 Experimental procedure	66
4.2.1 Material and specimen preparation	66
4.2.2 Experimental set-up and instrumentation	66
4.2.2.1 Pure creep	66
4.2.2.2 Creep-fatigue	67
4.3 Experimental results and discussion	69
4.3.1 Pure creep experiments	69
4.3.2 Creep-fatigue experiments	72
4.3.2.1 Fatigue life	72
4.3.2.2 Creep strain, hysteresis loops, and stiffness degradation	72
4.3.2.3 Damage evolution and self-generated temperature evolution	78
4.3.3 Fracture surfaces and failure mode	81
4.4 Conclusions	83
References	84
Chapter 5 Interrupted fatigue behavior	89
5.1 Introduction	89
5.2 Experimental procedure	91
5.2.1 Material and specimen preparation	91
5.2.2 Experimental set-up and instrumentation	91
5.3 Experimental results and discussion	94
5.3.1 Effect of stress level	94
5.3.2 Effect of interruption	101
5.4 Comparison to continuous fatigue	104
5.4.1 Accumulated damage and distribution	104
5.4.2 Damage retardation and distribution mechanisms	108
5.4.3 Reliability analysis	109
5.4 Conclusions	110
References	111
Chapter 6 Modeling of fatigue behavior	115
6.1 Introduction	115
6.2 General constitutive equation	117
6.3 Recovery solution and application	118

6.3.1	Experimental investigation and recovery results	118
6.3.2	Recovery solution	121
6.3.3	Estimation of viscoelastic parameters	122
6.4	Fatigue solution, application and validation	124
6.4.1	Material Fatigue solution	124
6.4.2	Validation of implemented solutions	125
6.5	Conclusions	129
	References	130
	Annex I	133
	Annex II	135
Chapter 7	Conclusions and future work	139
7.1	Conclusions	139
7.2	Original contributions	142
7.3	Recommendations for future work	142
7.3.1	Study the effect of loading pattern on other types of composite	142
7.3.2	Study the effect of loading pattern in compressive-compressive fatigue loading	143
7.3.3	Study the temperature and moisture effect on the sensitivity of laminated composites to the applied loading pattern	143
7.3.4	Finite element analysis of the crack tip in viscoelastic materials	143
7.3.5	Study the effect of loading pattern on repeatability of fatigue results	144
7.3.6	Study the evolution of inter-lamina stress during cyclic loading	144
	References	145
Annex A	Continuous-fatigue at R=0.1	149
Annex B	Continuous-fatigue at R=0.5	173
Annex C	Creep-fatigue	193
Annex D	Interrupted-fatigue	249
Annex E	DSC results	275
Annex F	Localized measurements of strain in creep-fatigue experiments	277
Annex G	Study the effect of damage on viscoelasticity using DMA	279
Annex H	Experimental study of crack blunting effect in viscoelastic media	283
Curriculum Vitae		285

List of Figures



Chapter 1 | Introduction

Fig. 1.1	Relative importance of material development through history.	2
Fig. 1.2	Examples of application of composite materials in different industries; (a) Skin stringer panel made of PETI-5/IM7 composite in commercial passenger airplane, (b) Spaceship constructed of carbon fiber composites, (c) Lexus LFA sports car incorporates carbon fiber parts, (d) Spare wheel recess molded with 60% glass-reinforced Durethan PA6 from Lanxess, (e) 7.5 MW Enercon E126 wind turbine, (Photo by jfz, licensed under a Creative Commons Attribution 3.0), (f) Pontresina bridge.	3
Fig. 1.3	Thesis structure.	9

Chapter 2 | Continuous fatigue behavior

Fig. 2.1	Schematic representation of hysteresis loops and definitions.	15
Fig. 2.2	Experimental set-up.	19
Fig. 2.3	Evolution of storage modulus as function of temperature.	20
Fig. 2.4	Quasi-static stress-strain curves and typical hysteresis loops at different stress levels.	20
Fig. 2.5	Experimental fatigue data and S-N curve.	21
Fig. 2.6	Failure strain under different loading conditions.	22
Fig. 2.7	Variation of hysteresis loops under cyclic loading at (a) $\sigma_{\max} = 68$ MPa (Conf-0.1-68-a) and at (b) $\sigma_{\max} = 47$ MPa (CF-0.1-47-c).	22
Fig. 2.8	Hysteresis area per cycle versus normalized number of cycles at different stress levels.	23
Fig. 2.9	Variation of TDE versus maximum fatigue stress.	23
Fig. 2.10	Variation of TDE versus fatigue life in double-logarithmic representation.	24
Fig. 2.11	Variation of normalized fatigue stiffness versus normalized number of cycles at different stress levels.	25
Fig. 2.12	Normalized fatigue stiffness versus number of cycles at early age.	25
Fig. 2.13	Average cyclic strain versus normalized number of cycles at different stress levels.	25
Fig. 2.14	Pairwise representation of light transmittance and self-generated temperature in different percentages of fatigue life at (a) $\sigma_{\max} = 68$ MPa (Conf-0.1-68-c), and (b) $\sigma_{\max} = 47$ MPa (Conf-0.1-47-c).	26
Fig. 2.15	Variation of average self-generated temperature.	27
Fig. 2.16	Variation of maximum self-generated temperature.	27
Fig. 2.17	UV-Vis-NIR spectra at different distances from fracture surface (see Fig. 2.19) at $\sigma_{\max} = 58$ MPa (dashed lines/Conf-0.1-58-b), $\sigma_{\max} = 49$ MPa (solid lines/Conf-0.1-49-b).	29
Fig. 2.18	Positions of optical measurements on failed specimen with corresponding reflectance values for wavelength of 510 nm at $\sigma_{\max} = 58$ MPa (Conf-0.1-58-b), and $\sigma_{\max} = 49$ MPa (Conf-0.1-49-b).	29
Fig. 2.19	Fatigue fracture surface, (a) $\sigma_{\max} = 68$ MPa (Conf-0.1-68-c), (b) $\sigma_{\max} = 58$ MPa (Conf-0.1-58-c), (c) $\sigma_{\max} = 53$ MPa (Conf-0.1-53-c), and (d) $\sigma_{\max} = 49$ MPa (Conf-0.1-49-a).	30

Fig. 2.20	Lateral depiction of fracture surface, (a) $\sigma_{\max} = 68$ MPa (Conf-0.1-68-c), (b) $\sigma_{\max} = 58$ MPa (Conf-0.1-58-c), (c) $\sigma_{\max} = 53$ MPa (Conf-0.1-53-c), and (d) $\sigma_{\max} = 49$ MPa (Conf-0.1-49-a).	30
-----------	--	----

Chapter 3 | Stress ratio effect on fatigue behavior

Fig. 3.1	Experimental fatigue data and S-N curve.	43
Fig. 3.2	Light transmittance at different percentages of fatigue life, at (a) $\sigma_{\max}=78$ MPa (Conf-0.5-78-b), and (b) $\sigma_{\max}=58$ MPa (Conf-0.5-58-d).	45
Fig. 3.3	Self-generated temperature at different percentages of fatigue life, at (a) $\sigma_{\max}=78$ MPa (Conf-0.5-78-d), and (b) $\sigma_{\max}=64$ MPa (Conf-0.5-64-d).	46
Fig. 3.4	Variation of (a) maximum, and (b) average self-generated temperature versus normalized number of cycles at different stress levels.	47
Fig. 3.5	Variation of hysteresis loops under cyclic loading at (a) $\sigma_{\max}= 78$ Mpa (Conf-0.5-78-a) and at (b) $\sigma_{\max}= 58$ Mpa (Conf-0.5-58-a).	48
Fig. 3.6	Cyclic strain versus normalized number of cycles at different stress levels.	48
Fig. 3.7	Realignment of glass fiber bundles;(a) 0%, (b) 25%, (c) 60%, and (d) 99% of fatigue life (Conf-0.5-78-b).	49
Fig. 3.8	Schematic representation of realignment angle.	49
Fig. 3.9	Average realignment of fibers at different percentages of fatigue life.	49
Fig. 3.10	Variation of normalized fatigue stiffness versus normalized number of cycles at different stress levels.	51
Fig. 3.11	Hysteresis area per cycle versus normalized number of cycles at different stress levels.	51
Fig. 3.12	Cyclic creep versus normalized number of cycles loaded under different stress ratios and at different stress levels.	53
Fig. 3.13	Failure strain at different stress ratios and stress levels.	53
Fig. 3.14	Normalized fatigue stiffness versus normalized number of cycles loaded under different stress ratios and at different stress levels.	54
Fig. 3.15	Hysteresis loop area versus normalized number of cycles loaded under different stress ratios and at different stress levels.	54

Chapter 3 | Creep-fatigue behavior

Fig. 4.1	Creep experimental set-up.	67
Fig. 4.2	Schematic representation of loading pattern in interrupted fatigue experiments.	69
Fig. 4.3	(a) Creep curves at different stress levels, (b) isochrone stress-strain curves at different loading blocks.	71
Fig. 4.4	Creep curve at $\sigma_{\max} = 70$ MPa with corresponding representation of light transmittance for different percentages of creep life; (Creep-70).	71
Fig. 4.5	Experimental fatigue data and S-N curves.	73
Fig. 4.6	Average cyclic strain versus normalized number of cycles at different loading patterns at two stress levels of (a) $\sigma_{\max} = 68$ MPa, and (b) $\sigma_{\max} = 47$ MPa.	74
Fig. 4.7	Transition of stress from cyclic loading to constant stress level and corresponding strain response (Cref-0.1-70-2-b).	75
Fig. 4.8	Creep curves at different loading patterns at two different stress levels.	75
Fig. 4.9	Reorientation of glass fibers at different percentages of fatigue life (Cref-0.1-70-2-d).	76

Fig. 4.10	Normalized fatigue stiffness versus number of cycles loaded under different loading patterns at two stress levels (a) $\sigma_{\max} = 68$ MPa, and (b) $\sigma_{\max} = 47$ MPa.	76
Fig. 4.11	Hysteresis area per cycle versus number of cycles at different stress levels.	77
Fig. 4.12	Pairwise representation of light transmittance and self-generated temperature for different percentages of fatigue life at $\sigma_{\max} = 70$ MPa (a) $t_{\text{creep}} = 2\text{h}$ (Cref-0.1-70-2-c) and (b) $t_{\text{creep}} = 48\text{h}$ (Cref-0.1-70-48-b).	78
Fig. 4.13	Pairwise representation of light transmittance and self-generated temperature for different percentages of fatigue life at $\sigma_{\max} = 47$ MPa (a) $t_{\text{creep}} = 2\text{h}$ (Cref-0.1-47-2-d) and (b) $t_{\text{creep}} = 48\text{h}$ (Cref-0.1-47-48-b).	79
Fig. 4.14	Pairwise representation of light transmittance and self-generated temperature for different percentages of fatigue life at $\sigma_{\max} = 47$ MPa (a) $t_{\text{creep}} = 2\text{h}$ (Cref-0.1-47-2-d) and (b) $t_{\text{creep}} = 48\text{h}$ (Cref-0.1-47-48-b).	80
Fig. 4.15	Fracture surfaces under different loading patterns and stress levels, (a) Creep-70, (b) Creep-64, (c) Creep-58, and (d) Creep-53, (e) Cref-0.1-70-2-d, (f) Cref-0.1-64-2-c, (g) Cref-0.1-58-2-c, (h) Cref-0.1-49-2-a, (i) Cref-0.1-70-48-a, (j) Cref-0.1-64-48-a, (k) Cref-0.1-58-48-a, (l) Cref-0.1-49-48-a.	81
Fig. 4.16	Pairwise representation of light transmittance and self-generated temperature for different percentages of fatigue life at $\sigma_{\max} = 47$ MPa (a) $t_{\text{creep}} = 2\text{h}$ (Cref-0.1-47-2-d) and (b) $t_{\text{creep}} = 48\text{h}$ (Cref-0.1-47-48-b).	82
Fig. 4.17	Pairwise representation of light transmittance and self-generated temperature for different percentages of fatigue life at $\sigma_{\max} = 47$ MPa (a) $t_{\text{creep}} = 2\text{h}$ (Cref-0.1-47-2-d) and (b) $t_{\text{creep}} = 48\text{h}$ (Cref-0.1-47-48-b).	83

Chapter 5 | Interrupted fatigue behavior

Fig. 5.1	Dimensions (in [mm]) and geometry of fatigue specimen.	91
Fig. 5.2	Schematic representation of loading pattern in interrupted fatigue experiments.	92
Fig. 5.3	Experimental fatigue data and S-N curves.	95
Fig. 5.4	Variation of hysteresis loops under cyclic loading at (a) $\sigma_{\max} = 64$ MPa (Intf-0.1-64-b) and (b) $\sigma_{\max} = 49$ MPa (Intf-0.1-49-b).	96
Fig. 5.5	Total dissipated energy (TDE) versus maximum cyclic stress.	96
Fig. 5.6	Normalized fatigue stiffness versus normalized number of cycles.	97
Fig. 5.7	Normalized fatigue stiffness versus number of cycles at different stress levels.	97
Fig. 5.8	Hysteresis area per cycle versus normalized number of cycles at different stress levels.	98
Fig. 5.9	Pairwise representation of light transmittance and self-generated temperature for different percentages of fatigue life in (a) interrupted (Intf-0.1-68-d) and (b) continuous fatigue loading (Conf-0.1-68-c) patterns at $\sigma_{\max} = 68$ MPa.	99
Fig. 5.10	Pairwise representation of light transmittance and self-generated temperature for different percentages of fatigue life in (a) interrupted (Conf-0.1-47-a) and (b) continuous loading patterns (Conf-0.1-47-c) at $\sigma_{\max} = 47$ MPa.	100
Fig. 5.11	Temperature versus normalized number of cycles at different stress levels, (a) average and (b) maximum temperature.	100
Fig. 5.12	Average cyclic strain versus normalized number of cycles at different stress levels.	101

Fig. 5.13	Fatigue fracture surfaces under different loading patterns and stress levels, (a) Intf-0.1-68-a, (b) Intf-0.1-58-a, (c) Intf-0.1-53-c, and (d) Intf-0.1-49-c, (e) Conf-0.1-68-c, (f) Conf-0.1-58-c, (g) Conf-0.1-53-c, and (h) Conf-0.1-49-a.	102
Fig. 5.14	Transition of (a) stress and (b) strain from cyclic loading to interruption at zero stress level in third loading block and passing into fourth loading block (Intf-0.1-58-a).	103
Fig. 5.15	Back-shift of hysteresis loop from last loop before interruption (solid line) to first loop (dashed line) of subsequent reloading (Intf-0.1-64-b).	104
Fig. 5.16	Strain reduction versus normalized number of cycles at different stress levels.	104
Fig. 5.17	Maximum cyclic stress versus ratio of interrupted-to-continuous fatigue life.	105
Fig. 5.18	Average normalized fatigue stiffness versus number of cycles loaded under interrupted fatigue (Intf) and continuous fatigue (Conf) at $\sigma_{\max}=68$ MPa.	106
Fig. 5.19	Average normalized fatigue stiffness versus number of cycles loaded under interrupted fatigue (Intf) and continuous fatigue (Conf) at $\sigma_{\max}=49$ MPa.	106
Fig. 5.20	Average hysteresis area per cycle versus number of cycles loaded under interrupted fatigue (Intf) and continuous fatigue (Conf) at $\sigma_{\max}=68$ MPa.	107
Fig. 5.21	Average hysteresis area per cycle versus number of cycles loaded under interrupted fatigue (Intf) and continuous fatigue (Conf) at $\sigma_{\max}=49$ MPa.	107
Fig. 5.22	Maximum self-generated temperature versus number of cycles loaded under interrupted fatigue (Intf) and continuous fatigue (Conf) at $\sigma_{\max}=68$ MPa.	109
Fig. 5.23	Probability density function versus fatigue life and corresponding Weibull distribution for specimens loaded under interrupted fatigue (Intf), and continuous fatigue (Conf) at $\sigma_{\max}=53$ MPa.	110

Chapter 6 | Modeling of fatigue behavior

Fig. 6.1	Basis of constitutive equation to describe behavior of viscoelastic materials.	119
Fig. 6.2	Flowchart of implementation of constitutive equation.	119
Fig. 6.3	Schematic representation of loading pattern in interrupted fatigue experiments.	120
Fig. 6.4	Elastic, three-stage viscoelastic recovery, and remaining strains of specimen Intf-0.1-58-a after third loading block.	121
Fig. 6.5	Experimental and modeled recovery curves for different loading blocks and stress levels, (a) Intf-0.1-58-a, and (b) Intf-0.1-49-a.	122
Fig. 6.6	Variation of viscoelastic parameters (a) E , (b) E_1 , (c) η_1 , (d) E_2 , (e) η_2 , (f) E_3 , (g) η_3 , and (h) η versus normalized number of cycles at different stress levels.	123
Fig. 6.7	Applied sinusoidal stress and strain response in viscoelastic material.	125
Fig. 6.8	Experimental (dots) and predicted fatigue (solid line) hysteresis loops at different number of cycles (N) at two stress levels, (a) Intf-0.1-64-b, and (b) Intf-0.1-49-a.	126
Fig. 6.9	Hysteresis loop area versus normalized number of cycles at different stress levels (a) Intf-0.1-64-b, and (b) Intf-0.1-49-a.	126
Fig. 6.10	Fatigue stiffness versus normalized number of cycles at different stress levels (a) Intf-0.1-64-b, and (b) Intf-0.1-49-a.	127

Fig. 6.11 Evolution of average cyclic, elastic, viscoelastic, and remaining strain at different stress levels (a) Intf-0.1-64-c, and (b) Intf-0.1-49-a. 128

Fig. 6.12 Variation of storage modulus, loss modulus, and $\tan(\delta)$ during fatigue loading at different stress levels (a) Intf-0.1-64-b, and (b) Intf-0.1-49-a. 129

Chapter 7 | Conclusions and future work

Fig. 7.1 Distribution of F_{zx} interlaminar stress in $(\pm 45)_{2s}$. 144

Fig. 7.2 Fatigue fracture surface of glass/epoxy composite with $(\pm 45)_{2s}$ layout. 145

List of Tables



Chapter 2 | Continuous fatigue behavior

Table 2.1	Fatigue experimental results	18
Table 2.2	Quasi-static tensile properties under different loading conditions	21
Table 2.3	Fatigue parameters for different $\pm 45^\circ$ glass/epoxy and carbon/epoxy laminates	31

Chapter 3 | Stress ratio effect on fatigue behavior

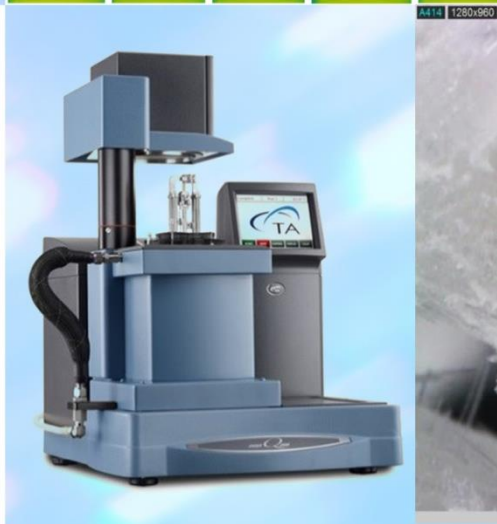
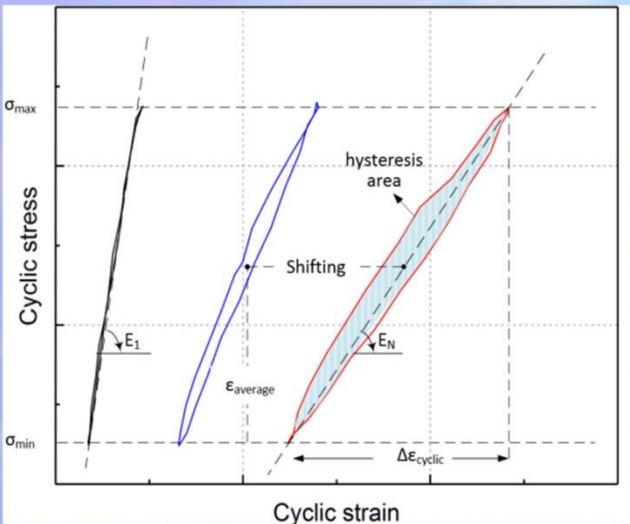
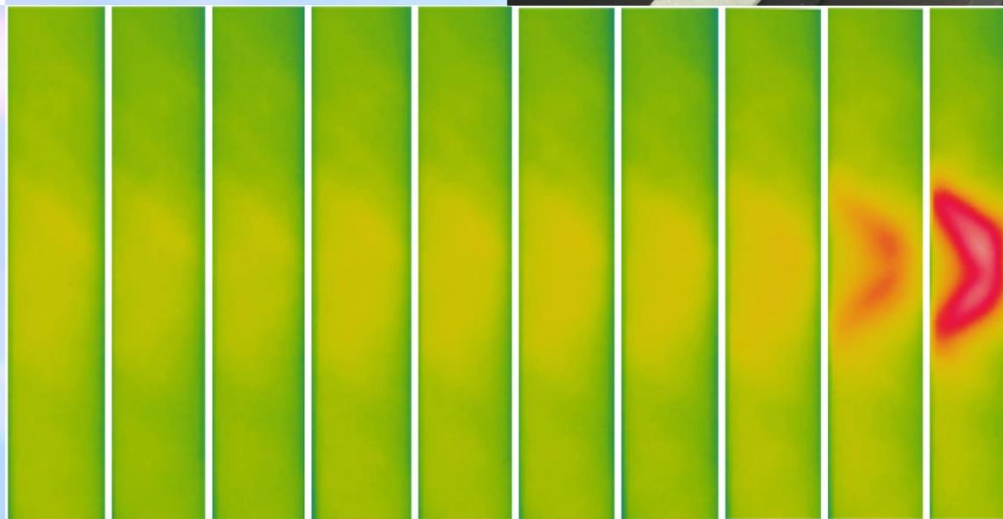
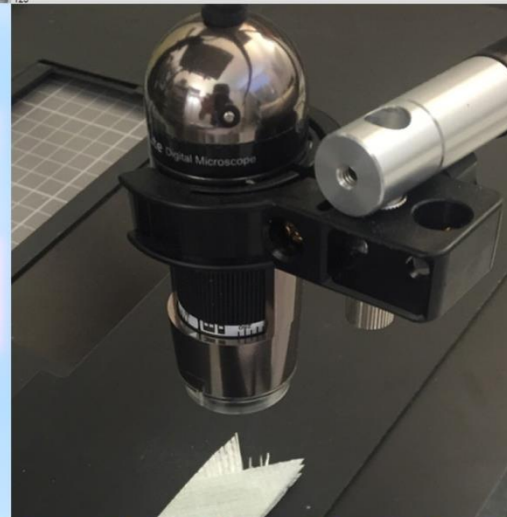
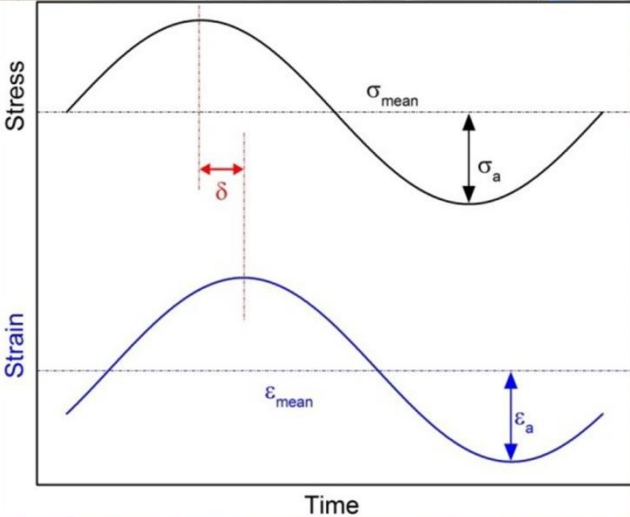
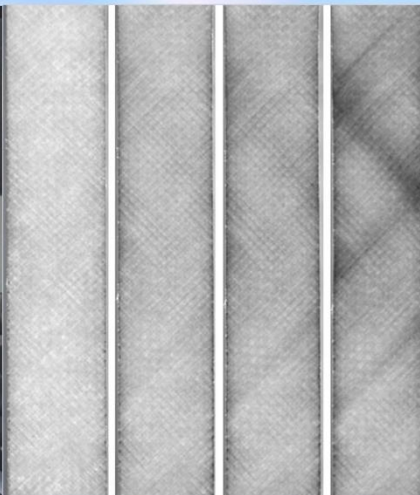
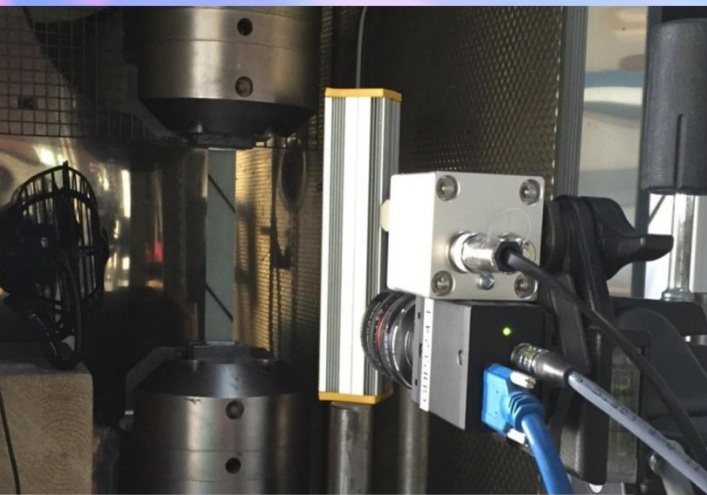
Table 3.1	Fatigue experimental results	42
Table 3.2	Fatigue parameters for continuous loading patterns at two stress ratios of 0.1 and 0.5	43

Chapter 4 | Creep-fatigue behavior

Table 4.1	Overview of creep experiments and results	67
Table 4.2	Overview of interrupted fatigue experiments and main results	70
Table 4.3	Fatigue parameters for continuous and interrupted loading patterns	73

Chapter 5 | Interrupted fatigue behavior

Table 5.1	Overview of interrupted fatigue experiments and main results	93
Table 5.2	Overview of continuous and interrupted fatigue experiments at $\sigma_{\max} = 53.4$ MPa	93
Table 5.3	Fatigue parameters for continuous and interrupted loading patterns	95
Table 5.4	Scale and shape parameters of Weibull distribution at $\sigma_{\max} = 53.4$ MPa	110



Chapter 1



Introduction

1.1 Context and motivation

The structural materials most commonly used in engineering designs can be categorized in four primary groups: metals, polymers, ceramics, and composites. Of these, composite is a material that contains two or more distinct constituents (metals, polymers, or ceramics) with significantly different macroscopic behavior and a distinct interface between each constituent ^[1].

Ashby ^[2] presents a chronological variation of the relative importance of each group from 10,000 B.C. and extrapolates their importance through the year 2020. The information contained in Ashby's article has been partially reproduced in [Fig. 1.1](#). Composite materials have been in existence for many centuries. No record exists as to when people first started using composites. Some of the earliest records of their use date back to the Mesopotamians and Egyptians, who are credited with the introduction of plywood, papier-mâché, and the use of straw in mud for strengthening bricks ^[2]. Bible also described people who mixed straw with mud to fabricate bricks. In the mid 2nd millennium BC in Persia, bows formed of horn and wood laminated together using animal resin were employed. In Greek mythology, the shields of Achilles and Ajax Telamonius are presented as laminated structures consisting of successive layers of different metals, and metal and leather layers respectively.

From the 19th century, the revolution in chemical science changed composite technology by developing cross-linked polymers. The importance of material development through history including

composite materials after the Second World War started growing and continued to increase over the next several decades with the advent of glass fiber-reinforced composite (GFRP), carbon fiber-reinforced composite (CFRP), metal matrix composite (MMC), and recently nanocomposites.

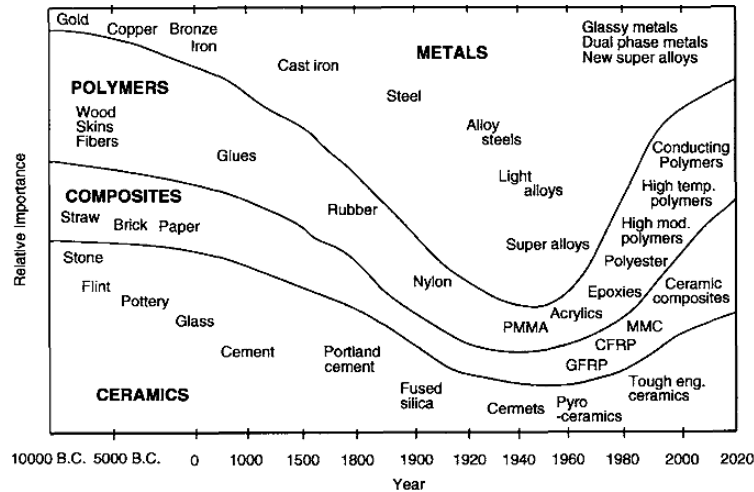


Fig. 1.1. Relative importance of material development through history [2].

The composites generally used in structural applications are classified as high-performance materials, which have high strength-to-weight ratios, and require controlled manufacturing environments for optimum performance. These materials offer numerous advantages compared to conventional engineering materials such as high tensile strength, good stiffness-to-weight ratio, high resistance to corrosion, low thermal expansion coefficient, and multi-functionality and diverse thermal insulation properties [3,4]. Fig. 1.2 shows some common applications of FRP composites.

FRP composites have revolutionized the transportation industries by virtue of their multifunctional, multi-directional and tailorable properties. These materials have been used for the manufacturing of different parts of commercial passenger airplanes since the early 1990s [6]. Composite materials are also potential candidates for use in space applications and have dominated the space industry [6,7,8]. High modulus unidirectional (UD) carbon fiber composites are used in strap elements, housing, antennas, and solar panels of satellites and space ships [9].

Another application target for laminated composites is in automotive structures. A strong incentive to apply FRPs to automotive structures comes essentially from regulations aimed at reducing CO₂ emission per unit distance [10,11]. Therefore, car manufacturers have been very seriously undertaking the development of new technologies for CO₂ emission reduction, which can be done by reducing the weight of vehicles in order to enhance their fuel efficiency [12].

FRP composite materials are also used in the wind energy industry, which, thanks to the superior specific mechanical properties they offer grew so rapidly during the last quarter of the twentieth century and is still growing by using hybrid tailor-made materials in order to meet the requirements for today's huge wind turbine rotor blades ^[13].

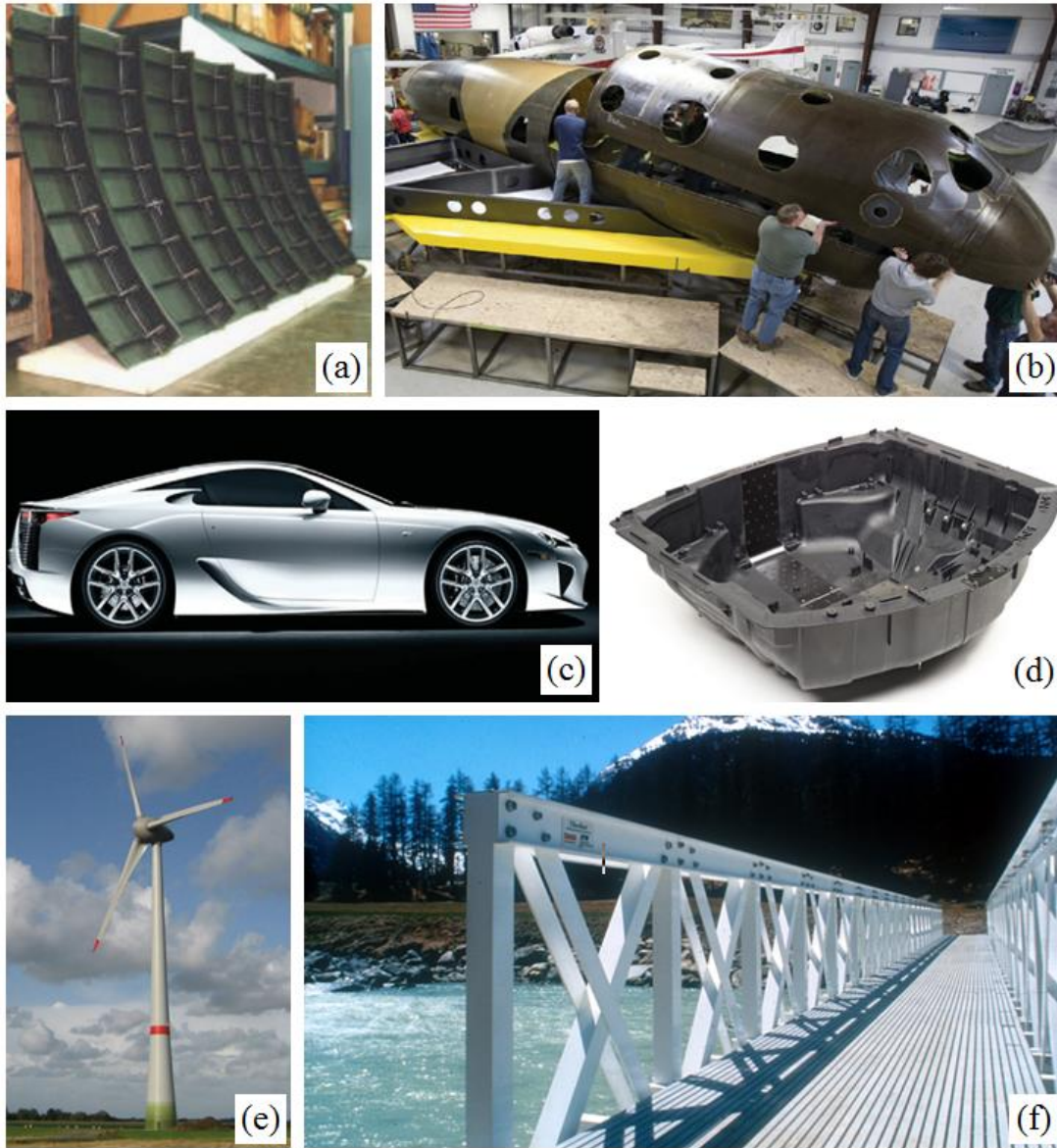


Fig. 1.2. Examples of application of composite materials in different industries; (a) Skin stringer panel made of PETI-5/IM7 composite in commercial passenger airplane ^[5], (b) Spaceship constructed of carbon fiber composites ^[10], (c) Lexus LFA sports car incorporates carbon fiber parts ^[10], (d) Spare wheel recess molded with 60% glass-reinforced Durethan PA6 from Lanxess ^[11], (e) 7.5 MW Enercon E126 wind turbine, (Photo by jfz, licensed under a Creative Commons Attribution 3.0), (f) Pontresina bridge ^[14].

Civil engineering projects relating to new constructions and the rehabilitation of bridge and building structures are demanding construction methods that can contribute to accelerating construction processes ^[15]. The Pontresina bridge (Fig. 1.2f) is a temporary lightweight pedestrian bridge, installed each year in the autumn and removed in the spring. Two truss girder spans, with adhesively-bonded pultruded glass fiber-reinforced polymer (GFRP) profiles in one span (fully load-bearing) and bolted joints in the other span, were used and additional structural safety was provided by a redundant truss and joint configuration ^[15].

Today, it is widely accepted that fatigue is one of the most common failure mechanisms in structural components, and pure static failure is rarely observed ^[13,16,17,18,19]. FRP composites used in open-air applications are subjected to different irregular loading profiles, in most cases including interrupted loading at high or low stress levels. The complex mechanical fatigue loading histories cause damage that eventually leads to functional and structural deterioration ^[17,18,20,21]. Compared to metallic materials, fatigue damage mechanisms in FRP composite materials are considerably more complex since they usually involve various combinations of damage modes, including delamination, matrix cracking, debonding, ply failure, and fiber breakage ^[22]. In addition, FRP composites are susceptible to time-dependent deformation including creep and recovery, due to the viscoelastic nature of their matrix.

In most of the existing works, solely cyclic-dependent mechanical properties have been considered for determining the behavior of materials, while time-dependent mechanical properties as well as their interactions also affect their fatigue behavior ^[23,24,25,26,27,28,29]. The limited experimental investigations of FRP composite materials showed considerable effects of time-dependent phenomena on fatigue behavior. However, no systematic analysis to clearly determine the effect of creep and recovery on developed damage mechanisms of FRP composites has yet been conducted and further research is therefore required.

1.2 Objectives

The aim of this PhD thesis is to explore the effect of different loading patterns on the fatigue behavior of glass fiber-reinforced composites (GFRPs), investigate their micromechanics, and develop an analytical model to link cyclic- and time-dependent mechanical properties. The following objectives were thus defined:

1. Experimental investigation of GFRP composite behavior under different loading patterns:
 - 1-1. Continuous loading fatigue at stress ratio ($R=\sigma_{\min}/\sigma_{\max}$) of 0.1, characterization of fatigue behavior at different stress levels

- 1-2. Continuous loading fatigue at stress ratio of 0.5, characterization of the stress ratio effect on fatigue behavior at different stress levels
- 1-3. Interrupted loading pattern at σ_{\max} stress level, characterization of creep-fatigue interactions at different stress levels and hold times
- 1-4. Pure creep, characterization of creep behavior at different stress levels
- 1-5. Interrupted loading pattern at zero stress level, characterization of recovery-fatigue interaction at different stress levels
- 2. Micromechanical investigations
 - 2-1. Identify the damage mechanisms developed under different loading patterns
- 3. Develop an analytical model:
 - 3-1. To describe interactions between the time- and cyclic-dependent mechanical properties based on the theory of viscoelasticity
 - 3-2. To predict fatigue behavior at different stress levels

1.3 Methodology

In order to achieve these objectives, the following methodology has been defined:

1: Characterization of continuous fatigue behavior

- a. Establishment of an experimental design
- b. Characterization of fatigue behavior at different stress levels at $R=0.1$
- c. Provision of reference data to compare with other loading patterns

2: Stress ratio effect on fatigue behavior

- a. Characterization of fatigue behavior at different stress levels at $R=0.5$
- b. Investigation of the stress ratio effect on fatigue behavior of GRFP composites by comparing the results obtained at $R=0.5$ with $R=0.1$

3: Characterization of pure creep behavior

- a. Characterization of pure creep behavior at different stress levels
- b. Provision of the required information for comparison with creep behavior after applying cyclic loading (section 4)

4: Characterization of creep effect on fatigue behavior

- a. Identification of the effect of interruption at σ_{\max} stress level on sustainability and fatigue behavior of GRFP composites at different stress levels and hold times
- b. Investigation of the effect of fatigue damage on creep behavior of GRFP composites

5: Characterization of interrupted fatigue behavior

- a. Identification of the effect of interruption at zero stress level on sustainability and fatigue behavior of GRFP composites at different stress levels
- b. Investigation of the effect of fatigue damage on recovery behavior of GRFP composites
- c. Provision of the required information for the theoretical part (Chapter 6)

6: Develop a model to describe recovery-fatigue behavior

- a. Use of the theory of viscoelasticity, to link the time- and cyclic-dependent mechanical properties.
- b. The experimental recovery data from Task 2 is used as input data to model the recovery behavior of GFRP composites and then predict their fatigue behavior.
- c. Different components of cyclic strain are simulated and studied.

1.4 Thesis organization

The research presented in this thesis is divided into five main chapters, Chapter 2 to Chapter 6, which address the objectives defined in Section 1.2, and an additional chapter presenting the main conclusions of the research. The structure of the thesis is presented in [Fig. 1.3](#).

Chapter 2: Continuous fatigue behavior at the stress ratio of 0.1

The fatigue behavior of $(\pm 45)_{2S}$ angle-ply glass/epoxy composite laminates is investigated. Rectangular specimens are subjected to constant amplitude fatigue loading at different stress levels, with stress ratio of 0.1 until failure. A video-extensometer and an infrared thermal camera are employed respectively to measure the evolution of strain and the self-generated temperature during the fatigue experiments. The evolution of cyclic creep, fatigue stiffness, and hysteresis loop area are recorded in each experiment and the effect of the applied stress level is evaluated. Using a digital camera and microscope, the progression of damage at the different locations and the fracture surfaces are also studied at different stress levels.

Chapter 3: Stress ratio effect on fatigue behavior

The fatigue behavior of $(\pm 45)_{2S}$ angle-ply glass/epoxy composite laminates at the stress ratio of 0.5 is investigated. The specimens' behavior and damage status are continuously monitored during the experiments; strains are measured by a video extensometer, the self-generated temperature on the specimens' surface is recorded by an infrared camera, while a digital camera was used to capture damage development in the translucent specimens throughout the experiments. To investigate the

stress ratio effect on fatigue behavior, the results were compared with previous fatigue results at the stress ratio of 0.1.

Chapter 4: Creep-fatigue behavior

Angle-ply (± 45)_{2S} glass/epoxy composite specimens are subjected to pure creep and tension-tension constant amplitude fatigue loading interrupted at σ_{\max} by creep intervals lasting for two or 48 hours in order to examine the effects of creep loading on the fatigue response and vice versa. The experimental set-up and instrumentation are the same to those used for continuous fatigue (Chapter 2). The evolution of fatigue behavior is recorded at different stress levels and holding times. To determine the effect of creep on fatigue behavior, the obtained results are compared with those for continuous fatigue at the same stress level. In addition, the effect of fatigue damage on creep behavior is studied by comparing with pure creep at the same stress level.

Chapter 5: Interrupted fatigue behavior

The effect of load interruptions on the tension-tension fatigue behavior of angle-ply (± 45)_{2S} glass/epoxy composite laminates is investigated. The cyclic loading is interrupted for two hours at regular cycle intervals, corresponding to 20% of the fatigue life under continuous loading at the same maximum cyclic stress level. The experimental set-up and instrumentation are the same to those used for continuous fatigue (Chapter 2). To evaluate the effect of loading interruption on fatigue behavior, the obtained results are compared with those for continuous fatigue at the same stress level. In addition, the recovery behavior at different stress levels and loading blocks are studied and the effect of fatigue damage on recovery behavior is investigated.

Chapter 6: Modeling of fatigue behavior using viscoelastic theory

A model based on the viscoelastic theory is developed to simulate specimen recovery in viscoelastic materials and predict their cyclic-dependent mechanical properties. This model is based on a general constitutive equation that is separately solved for load control sinusoidal cyclic loading and specimen recovery after removal of the cyclic loading. To implement and evaluate the modeling results, the tensile-tensile interrupted fatigue experiments on angle-ply glass/epoxy composite laminates at different stress levels were conducted (Chapter 5). The recovery model parameters at different percentages of lifetime are calibrated by using the recovery experimental results, and subsequently used to predict the fatigue stiffness, hysteresis loop area, cyclic creep, storage and loss moduli as well as $\tan(\delta)$, of the examined material system under cyclic loading.

Chapter 7: Conclusion and future works

The main conclusions of the conducted research are summarized in this chapter and some suggestions for future works are mentioned.

Chapter 8: Annexes

Supplementary information concerning the main chapters of the thesis is provided in eight annexes:

Annex A: Continuous-fatigue at $R=0.1$

Annex B: Continuous-fatigue at $R=0.5$

Annex C: Creep-fatigue

Annex D: Interrupted-fatigue

Annex E: DSC results

Annex F: Localized measurements of strain in creep-fatigue experiments

Annex G: Study the effect of damage on viscoelasticity using DMA

Annex H: Experimental study of crack-blunting effect in viscoelastic media

1.5 List of publications

The results of this thesis have been presented in five journal papers. Each paper corresponds to one of the main chapters of the thesis:

Paper 1. A. Vahid Movahedi-Rad, Thomas Keller, Anastasios P. Vassilopoulos, Fatigue damage in angle-ply GFRP laminates under tension-tension fatigue, *International Journal of Fatigue*, 109 (2018) 60-69.

Paper 2. A. Vahid Movahedi-Rad, Thomas Keller, Anastasios P. Vassilopoulos, Stress ratio effect on fatigue behavior of angle-ply GFRP laminates, *submitted*.

Paper 3. A. Vahid Movahedi-Rad, Thomas Keller, Anastasios P. Vassilopoulos, Creep effects on the tension-tension fatigue behavior of angle-ply GFRP composite laminates, *International Journal of Fatigue*, 123 (2019) 144-156.

Paper 4. A. Vahid Movahedi-Rad, Thomas Keller, Anastasios P. Vassilopoulos, Interrupted tension-tension fatigue behavior of angle-ply GFRP composite laminates, *International Journal of Fatigue*, 113 (2018) 337-388.

Paper 5. A. Vahid Movahedi-Rad, Thomas Keller, Anastasios P. Vassilopoulos, Modeling of fatigue behavior using viscoelastic theory, *submitted*.

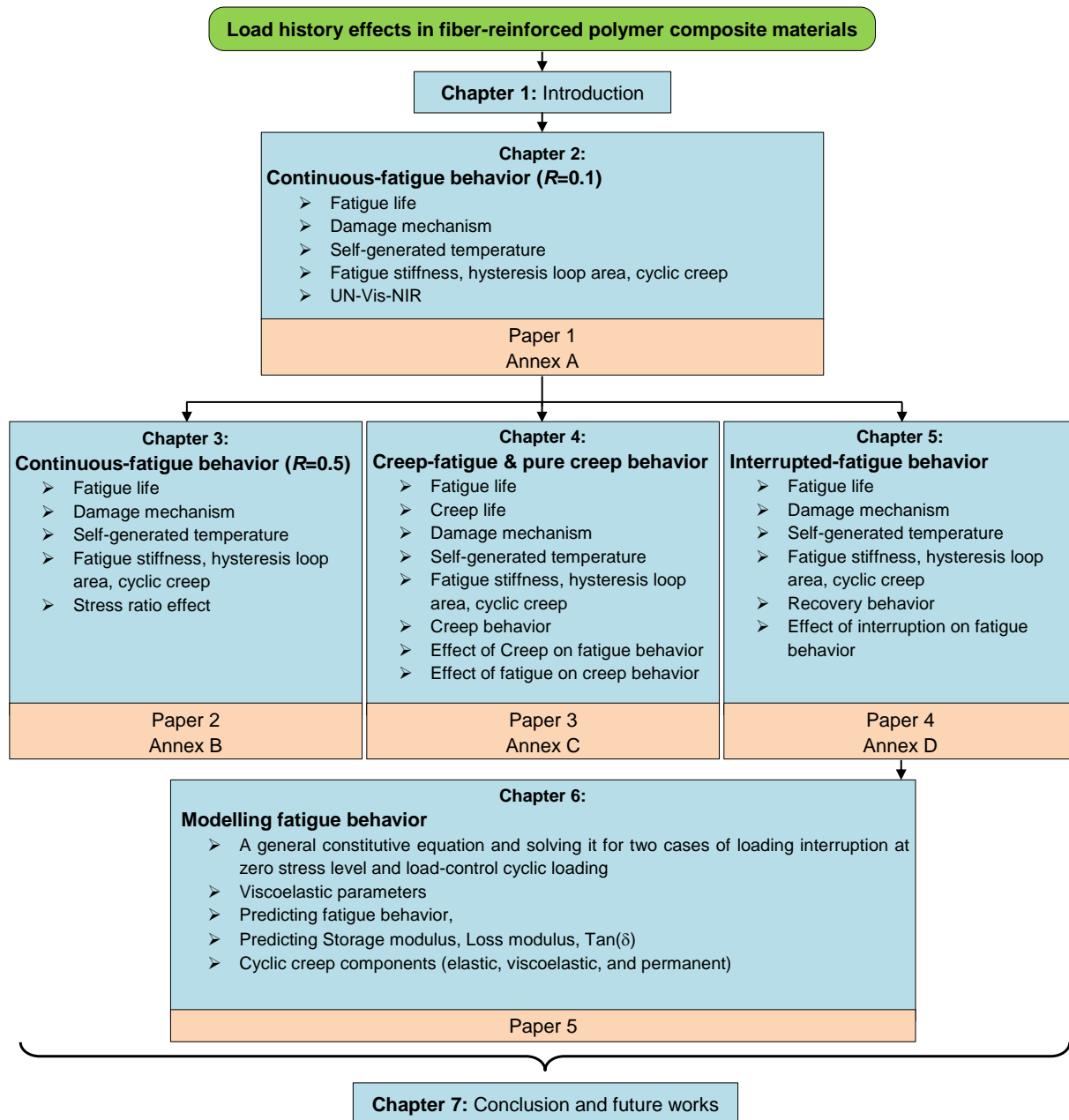


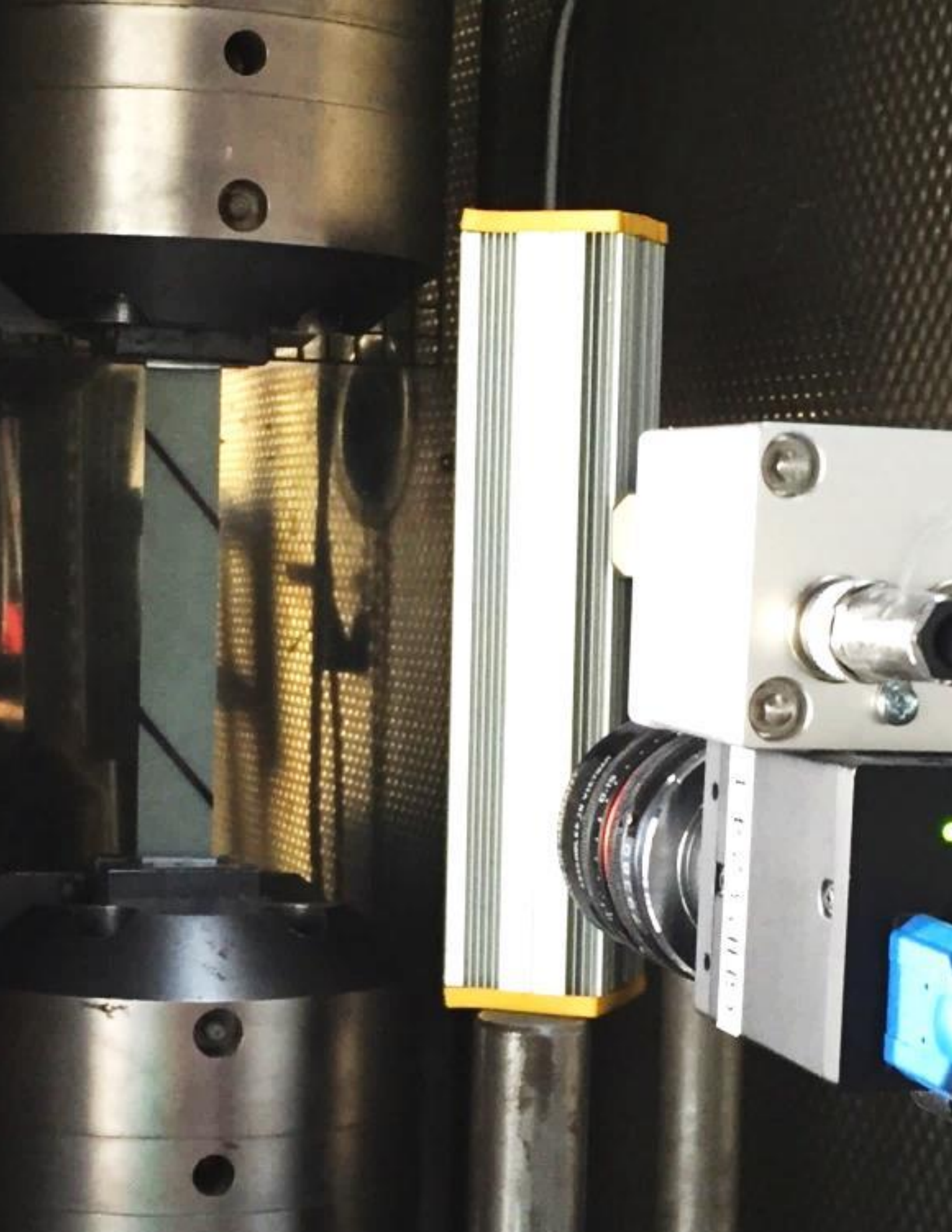
Fig. 1.3. Thesis structure.

References

- [1] George, H. S. (1999). Laminar composites. In *Library of Congress Cataloging-in-Publication Data* (Vol. 40).
- [2] Ashby, M. F. (1987). Technology of the 1990s: advanced materials and predictive design. *Phil. Trans. R. Soc. Lond. A*, 322(1567), 393-407.
- [3] Adam, H. (1997). Carbon fibre in automotive applications. *Materials & design*, 18(4-6), 349-355.

- [4] Brøndsted, P., Lilholt, H., & Lystrup, A. (2005). Composite materials for wind power turbine blades. *Annu. Rev. Mater. Res.*, 35, 505-538.
- [5] Pater, R. H., & Curto, P. A. (2007). Advanced materials for space applications. *Acta Astronautica*, 61(11-12), 1121-1129.
- [6] Tenney, D. R., Sykes, G. F., & Bowles, D. E. (1985). Composite materials for space structures.
- [7] Rawal, S. P., Misra, M. S., & Wendt, R. G. (1990). Composite materials for space applications.
- [8] Zweben, C. (2006). High-performance Thermal Management Materials Crucial for Future Packaging New, high-performance materials solve key packaging problems. *Advanced packaging*, 15(2), 20.
- [9] Schedler, A. R. M. I. N. (1988). Fibre composites in satellites. *Cryogenics*, 28(4), 220-223.
- [10] Stewart, R. (2010). Carbon fibre producers optimistic in downturn. *Reinforced Plastics*, 54(1), 18-24.
- [11] Stewart, R. (2011). Rebounding automotive industry welcome news for FRP. *Reinforced Plastics*, 55(1), 38-44.
- [12] Ishikawa, T., Amaoka, K., Masubuchi, Y., Yamamoto, T., Yamanaka, A., Arai, M., & Takahashi, J. (2018). Overview of automotive structural composites technology developments in Japan. *Composites Science and Technology*, 155, 221-246.
- [13] Vassilopoulos, A. P., & Keller, T. (2011). *Fatigue of fiber-reinforced composites*. Springer Science & Business Media.
- [14] Keller, T., Theodorou, N. A., Vassilopoulos, A. P., & De Castro, J. (2015). Effect of Natural Weathering on Durability of Pultruded Glass Fiber-Reinforced Bridge and Building Structures. *Journal of Composites for Construction*, 20(1), 04015025.
- [15] Osei-Antwi, M., De Castro, J., Vassilopoulos, A. P., & Keller, T. (2014). Structural limits of FRP-balsa sandwich decks in bridge construction. *Composites Part B: Engineering*, 63, 77-84.
- [16] Demers, C. E. (1998). Tension-tension axial fatigue of E-glass fiber-reinforced polymeric composites: tensile fatigue modulus. *Construction and Building Materials*, 12(1), 51-58.
- [17] Sarfaraz, R., Vassilopoulos, A. P., & Keller, T. (2012). Experimental investigation and modeling of mean load effect on fatigue behavior of adhesively-bonded pultruded GFRP joints. *International Journal of Fatigue*, 44, 245-252.
- [18] Shahverdi, M., Vassilopoulos, A. P., & Keller, T. (2012). A total fatigue life model for the prediction of the R-ratio effects on fatigue crack growth of adhesively-bonded pultruded GFRP DCB joints. *Composites Part A: Applied Science and Manufacturing*, 43(10), 1783-1790.

- [19] Samborsky, D., Mandell, J. F., & Miller, D. A. (2014). Creep/fatigue response of resin infused biaxial (Double bias) glass fabric laminates in reversed loading. In *32nd ASME Wind Energy Symposium*.
- [20] Varvani-Farahani, A., & Shirazi, A. (2007). A fatigue damage model for (0/90) FRP composites based on stiffness degradation of 0 and 90 composite plies. *Journal of Reinforced Plastics and Composites*, 26(13), 1319-1336.
- [21] Guedes, R. M. (Ed.). (2010). *Creep and fatigue in polymer matrix composites*. Elsevier.
- [22] Whitworth, H. A. (1997). A stiffness degradation model for composite laminates under fatigue loading. *Composite structures*, 40(2), 95-101.
- [23] Miyano, Y., Nakada, M., McMurray, M. K., & Muki, R. (1997). Prediction of flexural fatigue strength of CRFP composites under arbitrary frequency, stress ratio and temperature. *Journal of Composite Materials*, 31(6), 619-638.
- [24] Petermann, J., & Schulte, K. (2002). The effects of creep and fatigue stress ratio on the long-term behaviour of angle-ply CFRP. *Composite Structures*, 57(1-4), 205-210.
- [25] A.P. Vassilopoulos, T.P. Philippidis, Effect of interrupted cyclic loading on fatigue life of composites, Comp 03, 5th international symposium on advanced composites, Advances in composite technology, Corfu imperial Hotel, Corfu, Greece, 5-7 May 2003.
- [26] Mallick, P. K., & Zhou, Y. (2004). Effect of mean stress on the stress-controlled fatigue of a short E-glass fiber reinforced polyamide-6, 6. *International journal of fatigue*, 26(9), 941-946.
- [27] Guedes, R. M. (2007). Durability of polymer matrix composites: Viscoelastic effect on static and fatigue loading. *Composites Science and Technology*, 67(11-12), 2574-2583.
- [28] Vieille, B., Albouy, W., & Taleb, L. (2014). About the creep-fatigue interaction on the fatigue behaviour of off-axis woven-ply thermoplastic laminates at temperatures higher than T_g. *Composites Part B: Engineering*, 58, 478-486.
- [29] Sayyidmousavi, A., Bougherara, H., & Fawaz, Z. (2015). The role of viscoelasticity on the fatigue of angle-ply polymer matrix composites at high and room temperatures-a micromechanical approach. *Applied Composite Materials*, 22(3), 307-321.



Chapter 2



Continuous fatigue behavior

2.1. Introduction

Damage accumulates in the volume of composite materials during fatigue loading and eventually leads to failure. Several damage mechanisms, including fiber breakage and matrix cracking, debonding, transverse-ply cracking, and delamination, are activated either independently or synergistically during fatigue loading; the predominance of one or the other is strongly affected by both material variables and the sequence and duration of the damage events ^[1, 2]. The presence of these damage mechanisms results in the degradation of the materials properties under service loading conditions. The type of the individual damage mechanisms and sequence of their occurrence are usually dependent on, among other things, the loading pattern, material type, laminate architecture, and environmental conditions ^[2,3,4,5,6,7]. Despite the complexity and multitude of the damage mechanisms, a common failure process for unidirectional, cross-ply, and angle-ply laminates has been identified ^[3,4,5,8,9,10]. This resembles the three-stage damage progression process, starting with the damage formation in the matrix with multiple crack development, followed by the initiation of matrix cracks reaching the vicinity of the fibers and matrix/fiber debonding and delaminations, and ending with fiber breakage when damage accumulated during the previous stages becomes saturated ^[8,9,10].

In addition to fatigue loading, the creep phenomena play an important role in the reliability and durability of composite structures ^[11]. The susceptibility to creep in laminated composites, even at room temperature, originates from the viscoelastic nature of their polymeric matrices. It has been shown that laminated composites cyclically creep under fatigue mean stress ^[11]. Therefore, structural changes in polymer-based composite materials, depending on loading conditions and material type, can be due to damage growth and cyclic creep ^[11,12].

The main composite components of engineering structures are manufactured from materials whose performance may be matrix-dominated. Typical examples are shear webs and the aerodynamic parts of wind turbine rotor blades that consist mainly of biaxial composite laminates. These structural components may undergo severe stiffness degradation early in their lifetime due to fatigue loading, resulting in a decrease in their ability to bear extreme loads, which may lead to failure due to elastic instability. When angle-ply laminates are considered, multiaxial stress states develop in the principal material system, even under uniaxial loading ^[13]. The extent of the effect of each stress component on the development of the damage mechanisms mainly depends on the laminate lay-up ^[13].

The evolution of structural changes affects the mechanical behavior ^[3,14,15,16,17,18], thermal behavior ^[19,20,21,22,23,24], acoustic properties ^[25], and optical properties ^[26,27,28,29] of polymer matrix composites. In terms of mechanical behavior, the evolution of structural changes with the number of cycles decreases the fatigue stiffness and residual strength due to the damage growth, and increases the average fatigue strain owing to cyclic creep ^[11,14,15]. The fatigue damage also increases self-generated temperature ^[19,20] and changes the heat capacity and thermal conductivity of the material ^[21]. The distribution and magnitude of the self-generated temperature are related to the distribution of fatigue damage in the material ^[22], and, therefore, the variation and distribution of self-generated heating during the cyclic loading can be used to characterize the structural performance of the examined composite materials ^[23]. Moreover, it has been shown that the formation of damage during cyclic loading changes the optical properties ^[26,27,28,29] of polymer matrix composites. One of the optical properties is reflectance, which has mainly been used for characterization of the chemical composition of materials; however, it has also been successfully employed for the identification of damage accumulation ^[27].

Cyclic dissipated energy is another parameter that is affected by structural changes during the fatigue process. Measurement of the cyclic stress and strain allows the derivation of the stress-strain hysteresis loops ^[11,30]. For materials with a purely elastic behavior, the elastic energy per loading cycle is equal to the total energy and no dissipation energy is measured. However, for the majority of materials, energy is dissipated at each load cycle. The hysteresis area is a measure of the total dissipated energy per cycle; the slope of each stress-strain hysteresis loop corresponds to the fatigue stiffness. During a load-controlled fatigue experiment, the hysteresis loops can shift, indicating the presence of creep, and the

evolution of the average strain per cycle can be monitored to describe creep behavior ^[11,19,31,32,33,34]. Typical definitions regarding the hysteresis loops and relevant measurements are summarized in Fig. 2.1.

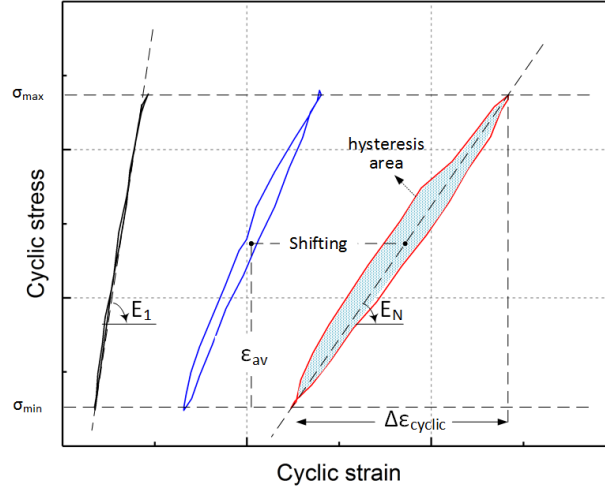


Fig 2.1. Schematic representation of hysteresis loops and definitions.

The sources of energy dissipation in laminated composites are damage formation and growth, the viscoelasticity of the material and the self-generated hysteretic heating ^[35]. The presence of damage causes the dissipation of energy due to the following mechanisms: fiber bridging, broken fibers, crack tip plasticity, and friction of unbounded regions in the matrix and fiber/matrix interface ^[35]. As a result of the viscoelastic nature of the polymeric matrix, the secondary bonds create more frictional forces between the polymeric chains, which results in more energy dissipation ^[36]. In addition, due to internal friction, the temperature of the specimen increases and causes thermal energy dissipation ^[25]. Internal friction is a process in which heat is generated as a result of the resisting frictional force between the two sides of cracks in a solid material while it undergoes deformation ^[37]. The evolution of the hysteresis area per cycle has been studied by researchers ^[11,30], however, the total capacity of materials to dissipate energy and the effect of stress level on that capacity have not yet been discussed.

The effects of fatigue stress level on the fatigue behavior of angle-ply laminated composites have been investigated, mainly by studying the stiffness fluctuations during the lifetime at different loading levels and stress ratios ^[30,38]. However, the effect of the stress level on other aspects of the fatigue process like damage evolution, cyclic creep, evolution of dissipated energy, and failure mode, and their correlations to describe the fatigue behavior of angle-ply laminates have not yet been discussed. Although the three-stage fatigue damage process is common in composite materials, a fatigue failure with fiber pull-out (without Stage III) has also been observed in angle-ply carbon/epoxy and

glass/epoxy laminates ^[8,39,40]. Therefore, a complete study of fracture behavior at different stress levels is required in order to elucidate under which loading conditions the specimen fails by fiber pull-out.

The objective of the present paper is to identify the fatigue behavior of angle-ply composite laminates at different stress levels by monitoring the evolution of the mechanical, thermal, and optical properties of the material as well as the failure modes based on a multitude of experimental evidence obtained by using different techniques to measure the damage development occurring fatigue loading. The dependence of fatigue damage on the applied cyclic load level and the variation of the material's capability to dissipate energy are thoroughly investigated.

To achieve this objective, the behavior of $\pm 45^\circ$ angle-ply GFRP composite laminates has been experimentally investigated at different stress levels under load control mode in order to determine the evolution of damage growth, cyclic creep, energy dissipation per cycle, and failure mode. This is carried out by performing a multitude of measurements to monitor the load and displacement, strain variations, stiffness development, as well as fluctuations of the specimen's surface temperature. Post-mortem analysis comprises microscopic photos of failure surfaces, as well as optical measurements of virgin and damaged specimens in order to measure the changes in light transmittance.

2.2. Experimental procedure

2.2.1 Material and specimen preparation

In this work, glass/epoxy composites with a stacking sequence of $(\pm 45)_{2s}$ were used in all experiments. Rectangular specimens with average dimensions of $250 \times 24.96 \times 2.30 \text{ mm}^3$ (length \times width \times thickness) were prepared, according to ASTM D3039 ^[41] and ASTM D7791-12 ^[42]. To fabricate the specimens, unidirectional E-glass fiber fabrics (EC 9-68) with an area density of 425 gr/m^2 and layer thickness of 0.45 mm were used. These fabrics have a finish bonding agent, which provides better adhesion to the matrix. The low-viscosity resin, Biresin® CR83 mixed with the hardener Sika CH83-2 in a ratio of 3:1 was used for impregnation of the fabrics. Laminates of $500 \times 500 \times 2.25 \text{ mm}^3$ and stacking sequence of $(\pm 45)_{2s}$ were fabricated by vacuum-assisted hand-lay-up, using a vacuum pump with a pressure of 0.9 bar. The laminate was kept in vacuum for 24 hours under laboratory conditions ($22 \pm 2^\circ \text{C}$, $40 \pm 10\% \text{ RH}$) and subsequently placed in an oven at 70°C for eight hours to complete the curing process. The achieved fiber content was 62% as determined according to the burn-off tests described in ASTM D 3171-99 ^[43]. Specimens were then cut from the laminates by a water-jet cutting machine and four aluminum tabs with dimensions of $45 \times 25 \times 4 \text{ mm}^3$ were glued to the grip parts.

2.2.2 Experimental set-up and instrumentation

Fatigue experiments were performed by applying a sinusoidal cyclic loading pattern with maximum cyclic stresses of between 47.4 and 68.0 MPa under load control to cover a wide range of fatigue lives from ca. 500 to around 10^6 cycles. At least three specimens were examined at each one of the six selected stress levels. The stress ratio, $R=\sigma_{\min}/\sigma_{\max}$, was kept constant at 0.1 in order to apply tensile cyclic loads to the specimens. All fatigue experiments were performed in a chamber at a constant temperature of 20°C and two fans were used to circulate the air inside the chamber and cool the specimen. The same loading rate, \dot{F} , of 30.5 kN/s was used for all tests. This loading rate was derived after preliminary experiments to avoid excessive temperature increases during the fatigue loading. Accordingly, different frequencies were selected to keep the loading rate constant for all stress levels. The frequency, f , of each load level with cyclic load amplitude, F_a , was calculated by solving the following equation:

$$\dot{F} = 4F_a f \quad (2.1)$$

The details of the fatigue experiments including the different frequencies are summarized in [Table 2.1](#). The specimen denomination is in the following form: the first term is Conf, which denotes the continuous fatigue, the second term shows the magnitude of the stress ratio, the third term the maximum fatigue stress, and the last term is the specimen number with the same parameter combination. Quasi-static tensile experiments were also carried out under displacement control at a rate of 1 mm/min, and under load control at the same rate of 30.5 kN/s as the rate applied to the fatigue loading. The tensile properties of the material were determined based on the measurements of three specimens per loading rate. All experiments were performed on an Instron 8800 hydraulic universal testing rig of 100-kN capacity with an accuracy of 0.2 kN.

Different instrumentations were used to monitor the mechanical, thermal, and optical changes in the material during and after the fatigue process. During the fatigue experiments, the machine's displacement, load and number of cycles were recorded. The variation of the longitudinal strains was measured by a high-resolution video-extensometer (camera Point Grey - Grasshopper3 with a resolution of 1936×1216 Mpixels and Fujinon HF35SA-1 35mm F/1.4 lens) with a frequency of acquisition of 160 images/s. The video-extensometer measured the relative position of two lines marked on the specimen's surface and calculated the corresponding strain values. Approximately twenty-five load and displacement measurements were recorded per cycle to estimate the strain fluctuations and hysteresis loops throughout the fatigue life of all the examined specimens. An infrared (IR) thermal camera with an accuracy of 0.1°C optical resolution of 160×120 pixels was also

employed during the fatigue experiments to record the evolution of the specimen's surface temperature, starting from 1 cm away from each grip. To detect the damage development in the translucent specimens at a macro- scale level, photographs were taken at regular intervals (depending on the life expectancy) with a digital camera with a maximum aperture f/2.8 and focal length range of 24–70mm zoom range during loading. A bright white light source was positioned behind the specimens to assist this procedure. The experimental set-up is shown in [Fig. 2.2](#).

After failure, the failure surfaces were examined using a digital handheld Dino-Lite microscope, AD7013MZT, with a magnification of 20x and resolution of 2592×1944 pixels, and photographs were taken for all examined specimens. The delamination in the specimens at failure was observed by taking side-view microscopy photographs of the fracture region.

Table 2.1. Fatigue experimental results

No.	Code	σ_{\max} (MPa)		Frequency (Hz)	N_f
		Nominal	Actual		
1	Conf-0.1-68-a	68.0	67.94	4.35	1969
2	Conf -0.1-68-b	68.0	67.97	4.35	1007
3	Conf -0.1-68-c	68.0	67.18	4.35	591
4	Conf -0.1-68-d	68.0	67.55	4.35	3689
5	Conf -0.1-64-a	64.2	64.37	4.68	2593
6	Conf -0.1-64-b	64.2	64.32	4.68	2304
7	Conf -0.1-64-c	64.2	64.39	4.68	1161
8	Conf -0.1-64-d	64.2	64.28	4.68	4112
9	Conf -0.1-58-a	58.2	59.53	5.06	6785
10	Conf -0.1-58-b	58.2	59.26	5.06	22321
11	Conf -0.1-58-c	58.2	59.05	5.06	18028
12	Conf -0.1-58-d	58.2	59.05	5.06	15063
13	Conf -0.1-53-a	53.4	54.56	5.53	49151
14	Conf -0.1-53-b	53.4	54.11	5.53	29832
15	Conf -0.1-53-c	53.4	53.97	5.53	22583
16	Conf -0.1-53-d	53.4	54.80	5.53	79623
17	Conf -0.1-49-a	48.6	49.46	6.10	289050
18	Conf -0.1-49-b	48.6	49.45	6.10	194115
19	Conf -0.1-49-c	48.6	49.08	6.10	460664
20	Conf -0.1-49-d	48.6	49.45	6.10	277227
21	Conf -0.1-47-a	47.4	48.04	6.33	533634
22	Conf -0.1-47-b	47.4	48.02	6.33	1198627
23	Conf -0.1-47-c	47.4	47.94	6.33	430211
24	Conf -0.1-47-d	47.4	47.94	6.33	545689

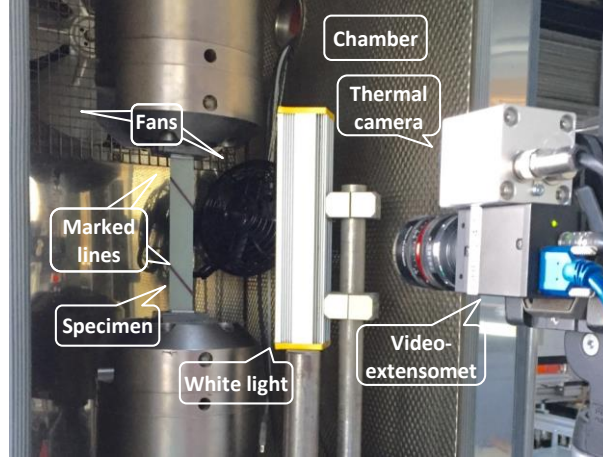


Fig. 2.2. Experimental set-up.

The Ultraviolet Visible Near-Infrared (UV-Vis-NIR) spectroscopy technique was also used to measure the reflectance of the reference specimen, not subjected to any loading, and the failed specimens along their length. The reflectance of an undamaged specimen is caused by surface reflection and internal reflection due to the different reflectance indices of the matrix, fiber, and manufacturing imperfections, which cause the reflection at the boundary of two different media. Changes in the reflectance measurements for the same material indicate new interfaces in the path of the penetrated light that can be attributed to damage in the material volume ^[44]. However, the detection of small damage and crack surfaces parallel to the beam of light cannot be captured by this method. In this study, a UV-vis-NIR spectrophotometer Perkin-Elmer Lambda 950 was used and spectra were collected from 250 to 1250 nm with an incident beam size of $15 \times 5 \text{ mm}^2$.

2.2.3 DMA experiment

Dynamic Mechanical Analyses (DMA) were performed to verify that the self-generated temperatures did not exceed the $T_{g,onset}$ of the material ^[45]. A TA Instruments Q800 dynamic mechanical analyzer in single cantilever configuration was used to perform the experiment. A specimen of $35.0 \times 10.0 \times 2.3 \text{ mm}^3$ (length \times width \times thickness) was cut with the same glass fiber layout as in the fatigue experiments. Three experiments were carried out on three different specimens in the temperature range of 15-160°C with a heating rate of 5°C/min in an air atmosphere, and the same maximum loading rate at the top and bottom specimen edges as in the fatigue experiments. Fig. 2.3 shows the variation of storage modulus versus temperature. It can be seen that the storage modulus in the glassy region up to 50°C was almost constant and then started rapidly decreasing.

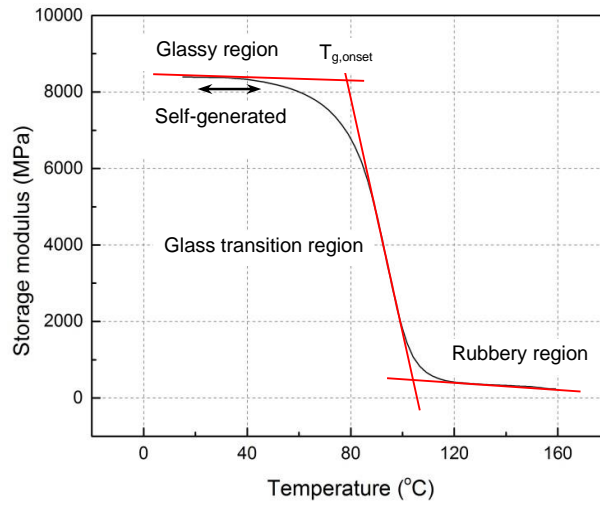


Fig. 2.3. Evolution of storage modulus as function of temperature.

2.3. Experimental results

2.3.1 Quasi-static behavior

Typical stress-strain curves of the examined laminates under the two different loading conditions are shown in Fig. 2.4. The specimens exhibited a rate-dependent, non-linear, stress-strain response. When the loading rate was increased, the value of yield stress (YS) and ultimate tensile stress (UTS) increased, although the strain to failure slightly decreased. The rate-dependent behavior was attributed to the viscoelastic behavior of the polymeric matrix. The tensile properties of the material per loading rate are presented in Table 2.2.

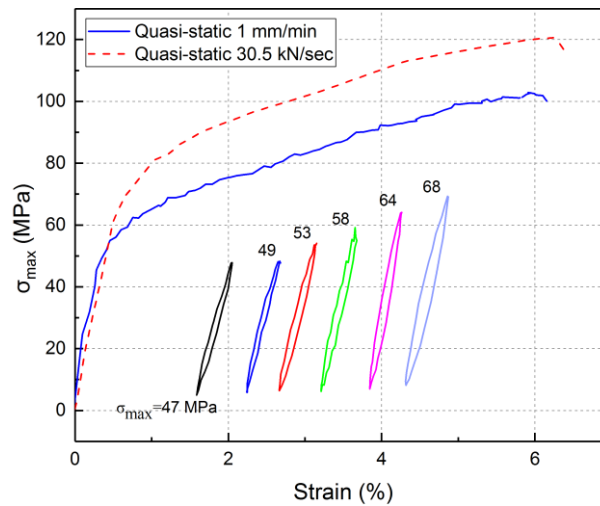


Fig. 2.4. Quasi-static stress-strain curves and typical hysteresis loops at different stress levels.

Table 2.2. Quasi-static tensile properties under different loading conditions

Type of tensile experiment	YS (MPa)	UTS (MPa)	Strain at failure (%)
Displacement control (1mm/min)	46 ± 1.9	97 ± 6.7	5.8 ± 0.7
Load control (30.5 KN/s)	78 ± 1.4	122 ± 1.4	5.0 ± 1.2

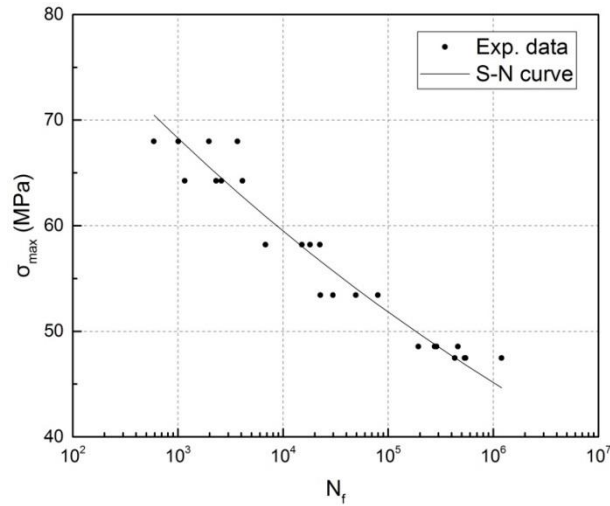
2.3.2 Fatigue behavior

2.3.2.1 Fatigue life

The variation of the fatigue maximum stress level, σ_{\max} , versus fatigue life, N_f , on a semi-logarithmic scale is shown in Fig. 2.5. The complete experimental matrix is presented in Table 2.1. The derived fatigue data exhibited the typical response for this kind of material; a classical power law relationship can be used for the simulation of the fatigue behavior:

$$\sigma_{\max} = \sigma_0 N_f^{\frac{1}{k}} \quad (2.2)$$

in which σ_0 , $1/k$ are model parameters derived by linear regression analysis, after fitting Eq. 2.2 to the available experimental fatigue data, which are 102.09 and -0.0596, respectively.

**Fig. 2.5.** Experimental fatigue data and S-N curve.

2.3.2.2 Stress-strain loops, dissipated energy and stiffness degradation

The applied fatigue loading patterns induced cyclic stresses in the linear region of the quasi-static stress- strain curves derived by applying the same loading rate, as shown in Fig. 2.4. The strains reached at failure due to fatigue loading increased with increasing stress level; however, they remained well below the strains to failure under quasi-static loading at any strain rate, as shown in Fig. 2.6.

Typical hysteresis loops up to failure are presented in Fig. 2.7 for high (68 MPa) and low (47 MPa) nominal maximum cyclic stresses. The hysteresis area as well as the fatigue stiffness and cyclic creep exhibited measureable changes with fatigue cycles for both high and low cyclic stresses. The behavior of all other specimens, at any stress level, was similar.

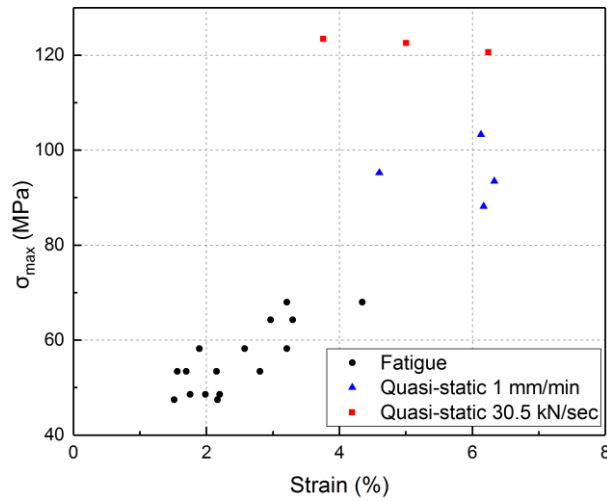


Fig. 2.6. Failure strain under different loading conditions.

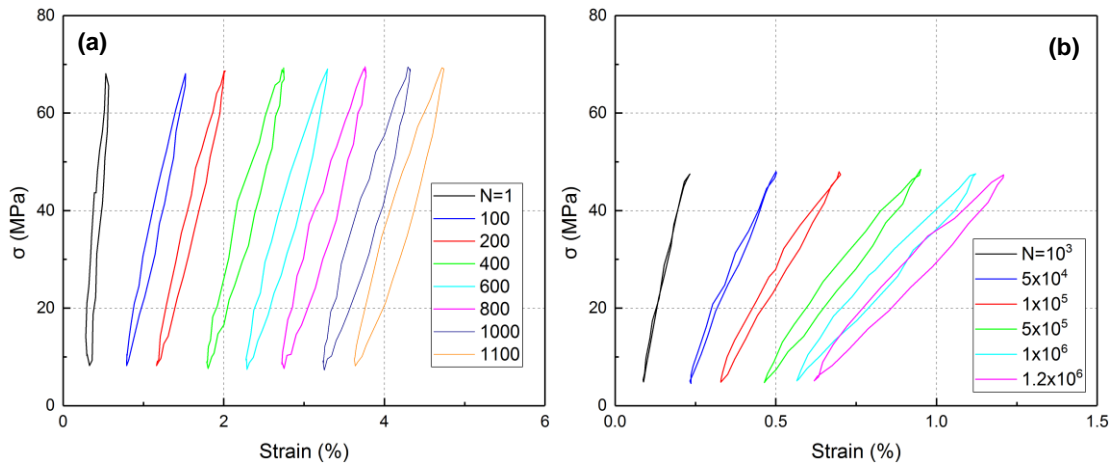


Fig. 2.7. Variation of hysteresis loops under cyclic loading at (a) $\sigma_{max} = 68$ MPa (Conf-0.1-68-a) and at (b) $\sigma_{max} = 47$ MPa (CF-0.1-47-c).

When the number of cycles and applied cyclic loads was increased, more energy was dissipated per cycle, as demonstrated in Fig. 2.8, where the hysteresis area per cycle, as a function of the normalized number of cycles, is presented for all specimens and a fitted line is added per stress level in the same color as the corresponding specimens. The total dissipated energy (TDE) for each specimen is calculated as the integral of all the individual stress strain hysteresis areas throughout the lifetime of the specimen. Fig. 2.9 shows the variation of maximum fatigue stress versus TDE in semi-logarithmic representation. As the specimens at lower cyclic stresses underwent significantly larger numbers of fatigue cycles, they dissipated more energy during their lifetime. A nearly linear relationship between the number of cycles and the TDE could be established in a double-logarithmic representation, as shown in Fig. 2.10.

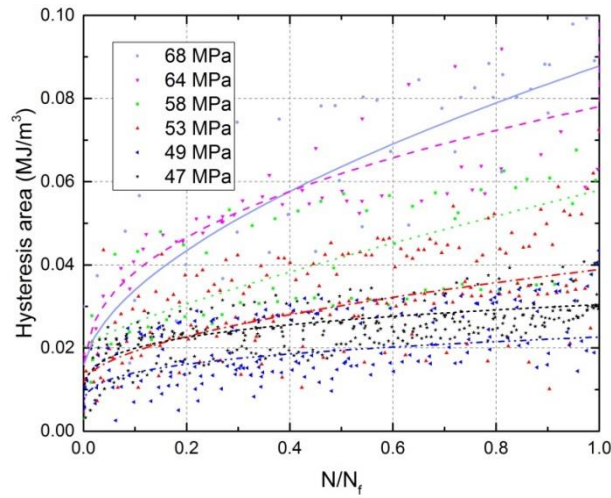


Fig. 2.8. Hysteresis area per cycle versus normalized number of cycles at different stress levels.

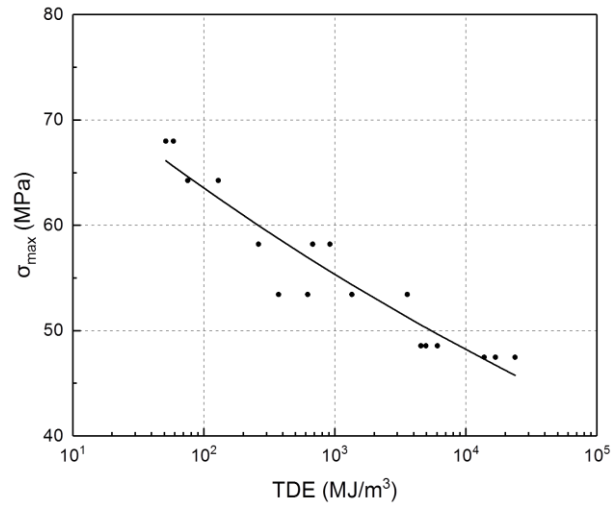


Fig. 2.9. Variation of TDE versus maximum fatigue stress.

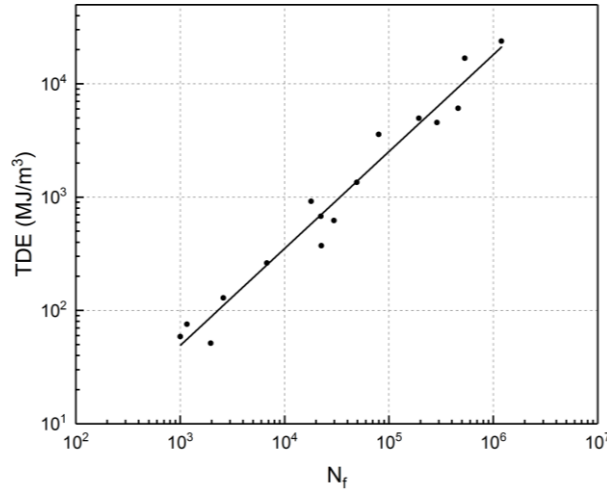


Fig. 2.10. Variation of TDE versus fatigue life in double-logarithmic representation.

In Fig. 2.11, the fatigue stiffness, E_N , normalized by the stiffness of the first cycle, E_I , is plotted against the normalized fatigue life for all specimens and a fitted line is added per stress level in the same color as the corresponding specimens. Stiffness degradation, irrespective of stress level, followed the same pattern. An initial steep decrease during the first 10-15% of the lifetime was followed by a steady state stiffness decreasing trend up to the failure of all specimens. This behavior was partly different from that exhibited by similar composite materials, see e.g. [8,15,16,17,18], where a third segment of steep drop before failure was observed. Nevertheless, similar observations have also been reported in other experimental works, see e.g. [38] for $[\pm 45]_{2s}$ angle-ply carbon-epoxy specimens at a stress ratio of 0.1. A certain, although not very consistent, trend was further observed in Fig. 2.11 - as cyclic stresses decreased, fatigue stiffness and failure stiffness decreased further, i.e., more damage was accumulated during the lifetime, as was also reported elsewhere [14,16,17,18]. If the comparison is performed at the early age however, see Fig. 2.12, more stiffness degradation was clearly observed at higher fatigue stress levels, attributed to greater damage formation and growth in the early age.

The average cyclic strain versus normalized number of cycles is shown in Fig. 2.13 for selected representative specimens from each stress level. Again, as was observed for the stiffness, all curves followed a similar pattern independent of stress level, and in this case, a consistent behavior was detected in the case of specimens loaded at higher fatigue stress exhibiting larger cyclic creep, which accelerated during cyclic loading.

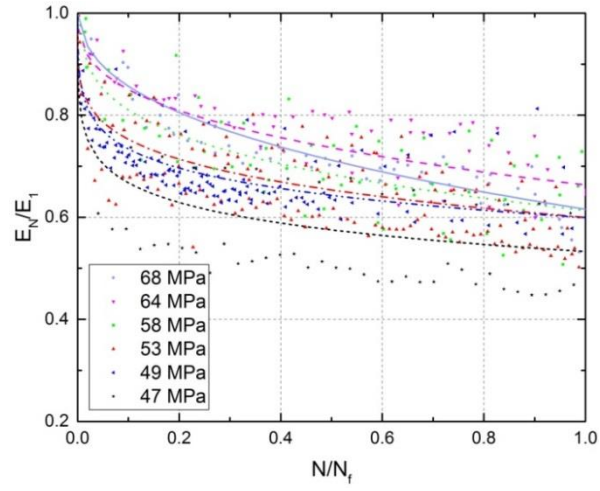


Fig. 2.11. Variation of normalized fatigue stiffness versus normalized number of cycles at different stress levels.

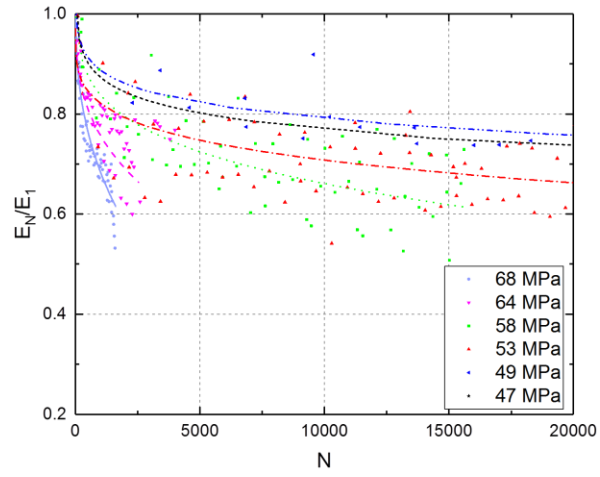


Fig. 2.12. Normalized fatigue stiffness versus number of cycles at early age.

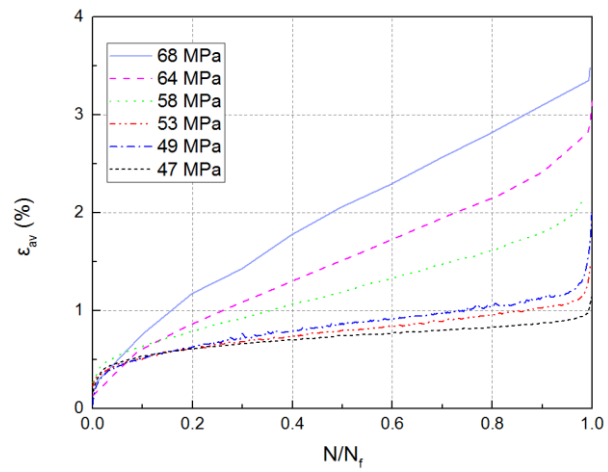


Fig. 2.13. Average cyclic strain versus normalized number of cycles at different stress levels.

2.3.2.3 Self-generated temperature evolution

During fatigue loading the temperature of the specimens increased due to the self-generated heating as a result of internal friction. The magnitude and distribution of surface temperature across selected specimens, with σ_{max} of 68.0 MPa and 53.4 MPa, at different percentages of specimen life, are shown in Fig. 2.14a and 2.14b respectively. Due to the formation of hotspots as failure was approached, the temperature distribution remained non-uniform throughout the lifetime. In all cases, failure occurred at, or close to, the location where hotspots were detected on the specimen surface. The self-generated temperature pattern was more uniform for lower stress levels, see Fig. 2.14b, while more obvious hotspots were detected at higher stress levels, as shown in Fig. 2.14a. In addition, hotspots were observed earlier in the lifetime when the specimen was subjected to higher stress levels.

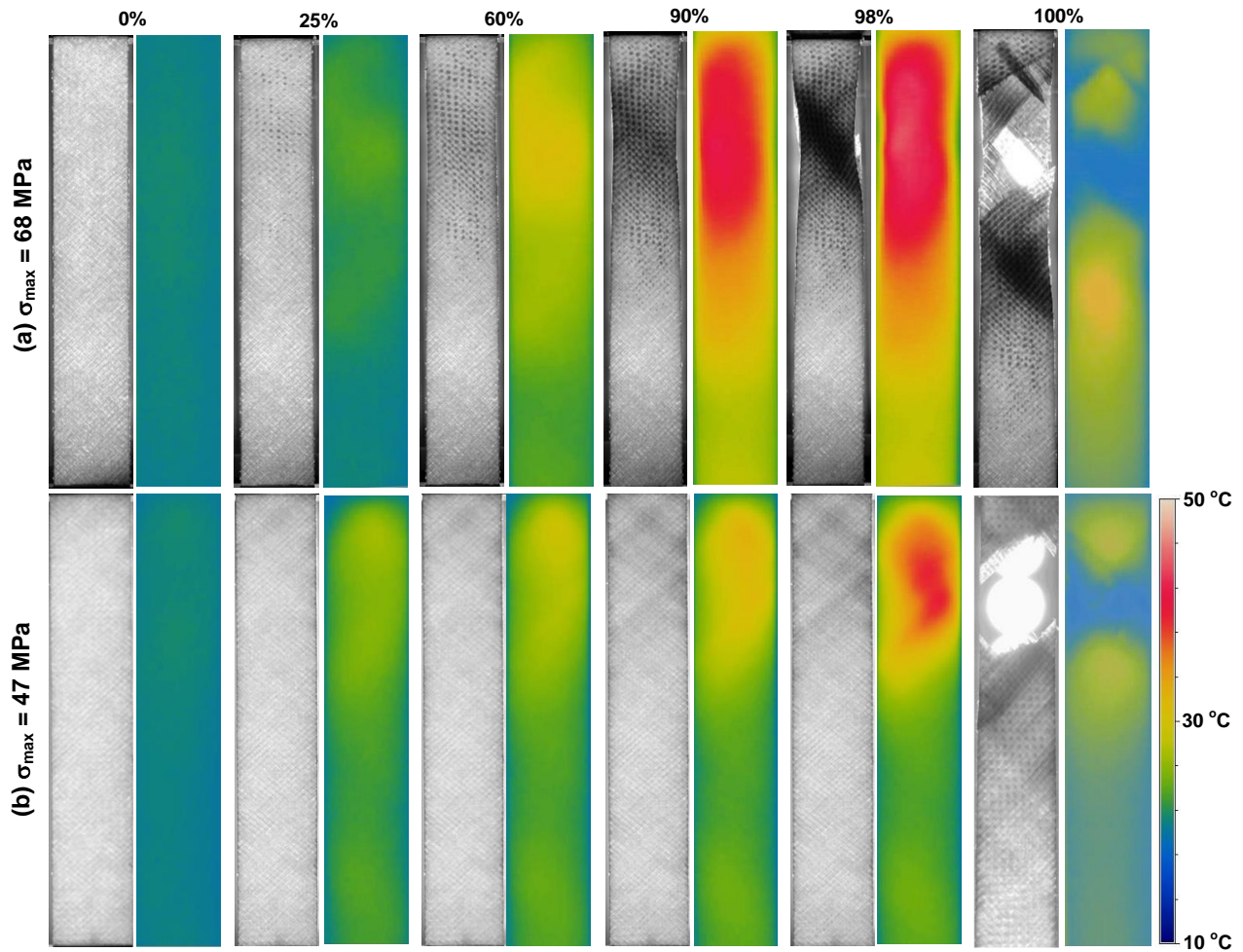


Fig. 2.14. Pairwise representation of light transmittance and self-generated temperature in different percentages of fatigue life at (a) $\sigma_{max}=68$ MPa (Conf-0.1-68-c), and (b) $\sigma_{max}=47$ MPa (Conf-0.1-47-c).

Fig. 2.15 shows the evolution of the average surface temperature of selected specimens from each stress level, while Fig. 2.16 shows the evolution of the maximum measured temperature (hotspot) of the same specimens.

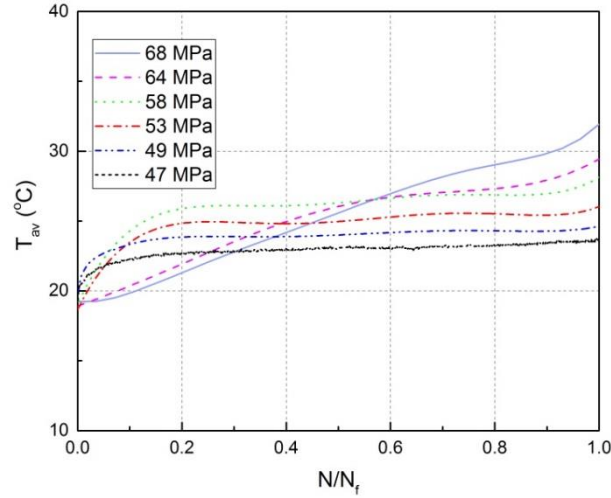


Fig. 2.15. Variation of average self-generated temperature.

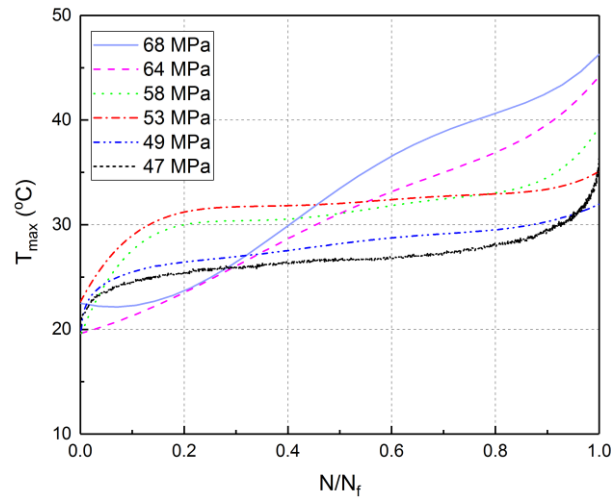


Fig. 2.16. Variation of maximum self-generated temperature.

The specimen temperature, both average and maximum, for all specimens, except those at high stress levels, increased rapidly at the beginning of the experiments, reached a steady state for most of the lifetime, then increased rapidly at the end of life. However, at the high stress levels of σ_{\max} of 68.0 MPa and 64.2 MPa, the ternary form of the curves had changed because of the rapid increase of

temperature. At low and intermediate stress levels, a maximum temperature of ca. 30°C was measured, while for higher loading a higher maximum temperature of ca. 45°C was observed before failure, which was localized however. Nonetheless, according to the DMA experiment (Fig. 2.2), the temperatures remained within the indicated range of the glassy region in which the storage modulus value is almost independent of temperature.

2.3.2.4 Fatigue damage growth

The formation of cracks in the matrix and fiber-matrix debonding during loading caused light scattering and changed the specimen transparency. The darker color in the photographs corresponded to decreased light transmittance due to the more damaged specimen areas. As shown for both cases, damage is observed along the fibers, at 45° with respect to the specimen longitudinal axis. Damage is more concentrated in the specimen loaded at higher cyclic loads (Fig 2.14a) while it is more evenly distributed over the specimen volume for lower stress levels. Failure occurs in the region where significant damage is observed. In some rare cases two such regions were detected, with one being more critical and specimen failure occurred at that point.

The reflectance results of the UV-Vis-NIR spectroscopy in the range between 250-2000 nm wavelengths for the reference specimen are shown in Fig. 2.17 by the black solid line. Higher reflectance values were measured in the visible range (400-700 nm) with the maximum reflectance at ca. 510 nm. Measurements were taken at different positions on the failed specimens, as defined in Fig. 2.18. The reflectance values, at these different positions, i.e. distances from the failure area, are compared to those of the undamaged specimen in Fig. 2.18. The reflectance of the damaged specimen increased when the measurement was taken at regions closer to the failure location, indicating the accumulation of more damage in this region, with new interfaces and fatigue cracks. A comparison of the measured reflectance between low (48 MPa) and higher stress levels (58 MPa) is also shown in Fig. 2.17. In order to obtain a better view, the corresponding values of reflectance at the indicated areas were further plotted along the failed specimen in Fig 2.18 at the 510 nm wavelength. In specimens subjected to higher stress levels, the reflectance and damage across the specimen length increased.

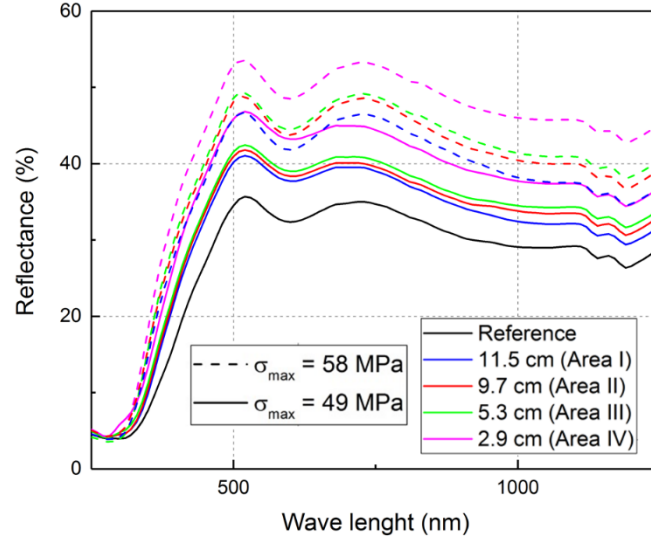


Fig. 2.17. UV-Vis-NIR spectra at different distances from fracture surface (see Fig. 2.19) at $\sigma_{\max}=58$ MPa (dashed lines/Conf-0.1-58-b), $\sigma_{\max}=49$ MPa (solid lines/Conf-0.1-49-b).

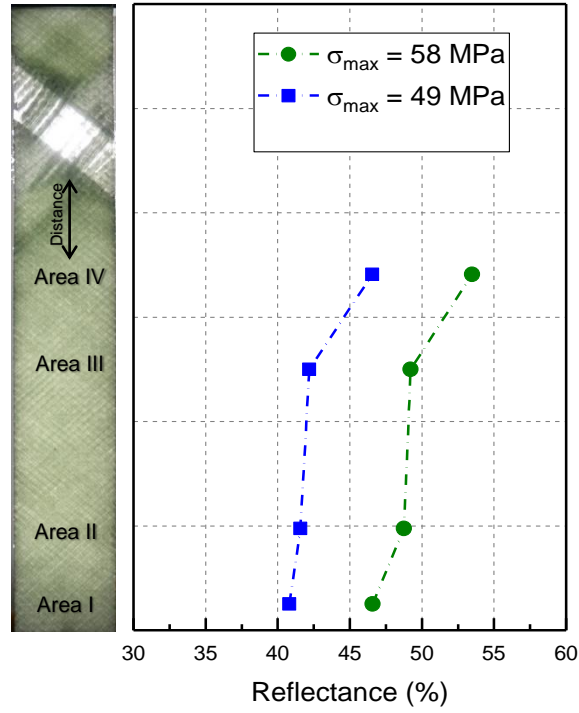


Fig. 2.18. Positions of optical measurements on failed specimen with corresponding reflectance values for wavelength of 510 nm at $\sigma_{\max}=58$ MPa (Conf-0.1-58-b), and $\sigma_{\max}=49$ MPa (Conf-0.1-49-b).

2.3.2.5 Fatigue failure mode

The fatigue fracture surfaces at different stress levels are shown in Fig. 2.19 (top view) and Fig. 2.20 (side view). All fracture surfaces exhibited a diagonal damage pattern, similar to the pattern observed for other composite laminates with lay-up of $(\pm 45)_{2s}$ e.g. [8,39,40]. Fatigue failure at high stress levels (see Fig. 2.19a) occurred through fiber pull-out. In contrast to specimens loaded at intermediate and low stress levels, a significant necking was observed in the failure zone (see also Fig. 2.14). At intermediate fatigue loads, as shown in Fig. 2.19b and 2.19c the failure is characterized by mixed fiber pull-out and fiber breakage (partially fiber breakage and partially fiber pull-out), and at low stress level with extensive fiber breakage, as shown in Fig. 2.19d. All specimens independent of stress level exhibited delamination, as shown in Fig. 2.20. Delamination occurred in the resin-rich regions between the plies as a result of damage accumulation (cracks) in the matrix. Fig. 2.20 shows that the delamination size is longer for specimens examined at higher stress levels, i.e. exhibiting fiber pull-out.

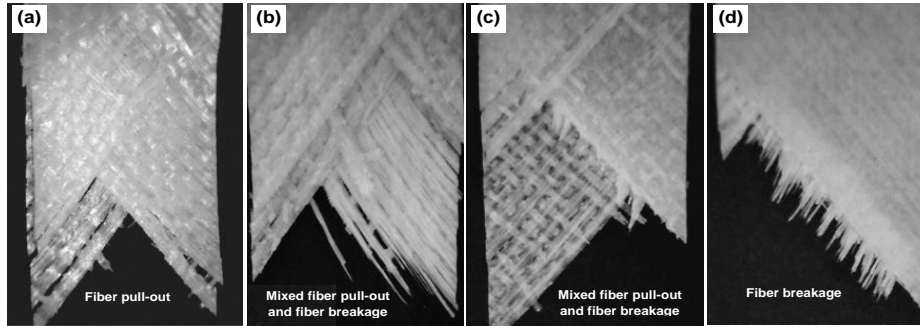


Fig. 2.19. Fatigue fracture surface, (a) $\sigma_{\max} = 68$ MPa (Conf-0.1-68-c), (b) $\sigma_{\max} = 58$ MPa (Conf-0.1-58-c), (c) $\sigma_{\max} = 53$ MPa (Conf-0.1-53-c), and (d) $\sigma_{\max} = 49$ MPa (Conf-0.1-49-a).

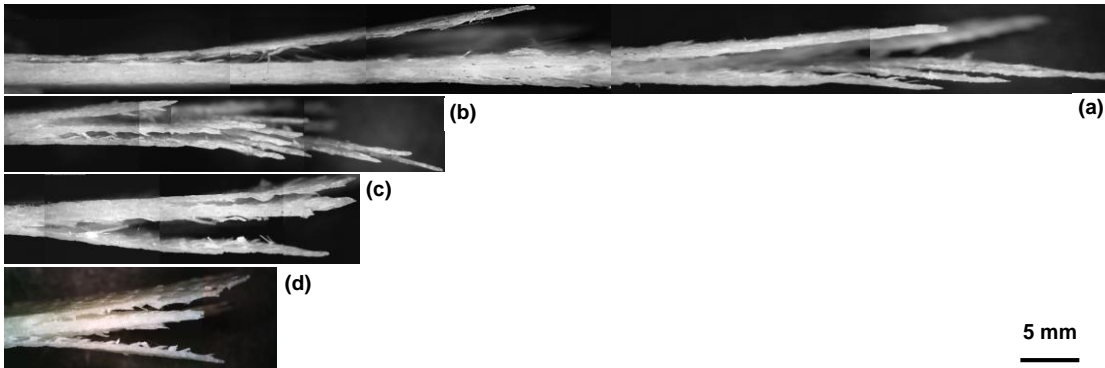


Fig. 2.20. Lateral depiction of fracture surface, (a) $\sigma_{\max} = 68$ MPa (Conf-0.1-68-c), (b) $\sigma_{\max} = 58$ MPa (Conf-0.1-58-c), (c) $\sigma_{\max} = 53$ MPa (Conf-0.1-53-c), and (d) $\sigma_{\max} = 49$ MPa (Conf-0.1-49-a)

2.4. Discussion

The two S-N curve parameters (Eq. 2.2) are compared with those from existing data for angle-ply laminates from the literature in Table 2.3. It is seen that the slopes of the S-N curves are comparable with other angle-ply GFRP and CFRP laminates, while the value of σ_0 depends on the material, being higher for carbon, and lower for glass-fiber composites. The examined GFRP laminates exhibited very consistent fatigue behavior, with similar or even lower scatter that typical of one order of magnitude exhibited by composite laminates [11,30,31].

Table 2.3. Fatigue parameters for different ± 45 glass/epoxy and carbon/epoxy laminates

Material	σ_0	$1/k$	Ref.
Glass/epoxy (± 45)_{2s}	103.09	-0.0596	This work
Double bias (± 45) glass type L/epoxy	184	-0.0740	36
Double bias (± 45) M – glass FRP	216	-0.0880	36
Glass FRP (± 45)	118	-0.0620	36
GFRP (± 45)	95	-0.0500	36
S2/5208 glass–epoxy (± 45)	132	-0.0560	50
Glass–epoxy (± 45) _{2s}	161	-0.0690	51
Carbon (T800H)/epoxy(± 45) _{3s}	250	-0.0580	52
Carbon (HTA,12K)/epoxy(± 45) _{2s}	234	-0.0510	53

At high stress levels, the observed hotspots and low light transmission indicated that damage was localized and unevenly distributed (Fig. 2.14a). High stress levels caused more damage, however localized around one hotspot, a critical area of the specimen where failure finally occurs. The consequence of the significant deterioration of the stress transfer efficiency of the matrix and the interface at the concentrated damage zone was the observed failure mode with excessive fiber pull-out, which led to the greater delamination sizes and large matrix and interface cracks. By decreasing the fatigue stress level, as shown in Fig. 2.14b, the damage distribution became more uniform and less severe, which caused mixed-mode failure with fiber pull-out and fiber breakage, as shown in Figs. 2.19 and 2.20. The almost uniform damage distribution allowed the matrix and interface at the hotspot to transfer stresses to the fibers that eventually failed.

At high stress levels, due to the severity of damage, the stiffness dropped at a high rate; however, gradual and well-distributed damage growth at low stress levels caused the fatigue stiffness to decrease at a lower rate at the same (early) age (Fig. 2.12). Taking into consideration the whole fatigue

life of specimens (Fig. 2.11) revealed that with decreasing stress levels, the material failed at a lower fatigue stiffness. This showed that by decreasing the stress levels, the capacity of the material to withstand damage was enhanced. In addition, stiffness degradation was not affected by the matrix softening as a result of self-generated temperature, as mentioned above.

From the optical measurements it is deduced that the amount of reflectance is a function of the stress level; therefore, according to this technique, and the assumption that reflectance can be interpreted as damage in the specimen volume, more damage was accumulated throughout the specimen at higher stress levels (Fig. 2.18), which is in contradiction to the stiffness degradation results (Fig. 2.11). Therefore, this method does not seem appropriate for capturing all the damage that has occurred, especially at low stress levels. Small cracks across the beam of light may not reflect the light, particularly when they close after load removal.

In comparison to lower fatigue stress levels, it was observed that the average cyclic strain increased more significantly at higher stress levels, with the number of cycles, mainly due to the viscoelastic deformation of the polymeric matrix. Nevertheless, the formation of large diagonal cracks (along the fibers) and a significant necking very close to failure for higher stress levels can contribute to a significant increase of the average cyclic strain.

An increase of the stress-strain hysteresis loop area with number of cycles and loading was observed for all studied cases, which is attributed to the following two reasons. Friction due to the slip in damaged regions is the main cause of the increased energy dissipation [35]. The magnitude of friction depends on the area of unbound regions (crack size), which is bigger as the number of cycles increases and at higher stress levels. In addition, thermal energy dissipation, which again originates from the internal friction between the created cracks, was greater with an increasing number of cycles and at higher stress levels. An increase of energy dissipation with the number of cycles in laminate composites including angle-ply composites has been reported by other researchers [14,33,46]. Other works show that the hysteresis area decreases with fatigue life, e.g., Launay et al [47] and Kharrazi and Sarkani [46], however this decrease is related to changes in the material, e.g. hardening of the thermoplastic matrix in [47] and flaw blunting and other local stress concentration relief effects mentioned in [46]. Although the amount of energy dissipation per cycle is smaller at lower stress levels, due to the longer fatigue life, the total dissipated energy (TDE) is greater as shown in Fig. 2.10.

2.5. Conclusions

The fatigue behavior of $(\pm 45)_{2s}$ glass/epoxy composite laminates has been experimentally investigated in this work. Different mechanical, thermal, and optical measurements were used for the observation

of the fatigue damage process and quantification of the damage caused due to loading at different stress levels. The following conclusions can be drawn:

- The different stress levels led to different damage distributions as shown by the optical measurements, digital photos and temperature measurements during fatigue loading. At higher stress levels the damage was severe and localized and caused the failure of these specimens at shorter lifetimes; however, by decreasing the fatigue stress level, more uniform and less severe damage distribution was observed throughout the specimen volume, which resulted in the longer fatigue life.
- Due to the formation of severe damage in the matrix and interface at high stress levels, the stress was not transferred to the fibers, which caused the failure by fiber pull-out. However, by decreasing the fatigue stress level, the damage distribution became more uniform and less severe, which led to failure through mixed fiber pull-out and fiber breakage at intermediate stress levels, and extensive fiber breakage at lower stress levels.
- With an increasing number of cycles, the fatigue stiffness dropped at a higher rate at higher stress levels than at lower ones at the same age due to the localized and intense damage growth. The fatigue stiffness at failure, however, decreased more at lower stress levels than at higher ones, which was attributed to the material's higher capacity to withstand damage.
- The increase of dissipated energy with the number of cycles and fatigue stress level was observed. This was mainly attributed to more friction in the area of unbounded regions as a result of damage growth. In addition, thermal energy dissipation, which again originates from internal friction, became greater with an increased number of cycles and fatigue stress level.
- It was observed that with decreasing fatigue stress levels, the magnitude of the total energy dissipation (TDE) significantly increased. This is because the specimens tested under lower cyclic stresses underwent significantly larger numbers of fatigue cycles, which dissipated more energy during their lifetime.

References:

- [1] Harris, B. (Ed.). (2003). *Fatigue in composites: science and technology of the fatigue response of fibre-reinforced plastics*. Woodhead Publishing.
- [2] Reifsnider, K. L., & Talug, A. (1980). Analysis of fatigue damage in composite laminates. *International Journal of Fatigue*, 2(1), 3-11.

- [3] Talreja, R. (1981). Fatigue of composite materials: damage mechanisms and fatigue-life diagrams. *Proceedings of the Royal Society of London A: Mathematical, Physical and Engineering Sciences*, 378(1775), 461-475.
- [4] Zhang, Y., Vassilopoulos, A. P., & Keller, T. (2008). Stiffness degradation and fatigue life prediction of adhesively-bonded joints for fiber-reinforced polymer composites. *International Journal of Fatigue*, 30(10-11), 1813-1820.
- [5] Philippidis, T. P., & Vassilopoulos, A. P. (1999). Fatigue of composite laminates under off-axis loading. *International Journal of fatigue*, 21(3), 253-262.
- [6] Daniels, C. A. (1989). *Polymers: structure and properties*. CRC Press.
- [7] Reifsnider, K. L., Schulte, K., & Duke, J. C. (1983). Long-term fatigue behavior of composite materials. In *Long-term behavior of composites*. ASTM International.
- [8] Varvani-Farahani, A., & Shirazi, A. (2007). A fatigue damage model for (0/90) FRP composites based on stiffness degradation of 0 and 90 composite plies. *Journal of Reinforced Plastics and Composites*, 26(13), 1319-1336.
- [9] Ramakrishnan, V., & Jayaraman, N. (1993). Mechanistically based fatigue-damage evolution model for brittle matrix fibre-reinforced composites. *Journal of materials science*, 28(20), 5592-5602.
- [10] Varvani-Farahani, A., Haftchenari, H., & Panbechi, M. (2007). An energy-based fatigue damage parameter for off-axis unidirectional FRP composites. *Composite Structures*, 79(3), 381-389.
- [11] Petermann, J., & Schulte, K. (2002). The effects of creep and fatigue stress ratio on the long-term behaviour of angle-ply CFRP. *Composite Structures*, 57(1-4), 205-210.
- [12] Movahedirad, A., Keller, T., & Vassilopoulos, A. (2016). Creep-fatigue interaction in composite materials, *17th European Conference on Composite Materials*.
- [13] Philippidis, T. P., & Vassilopoulos, A. P. (2004). Life prediction methodology for GFRP laminates under spectrum loading. *Composites Part A: applied science and manufacturing*, 35(6), 657-666.
- [14] Vassilopoulos, A. P., & Keller, T. (2011). *Fatigue of fiber-reinforced composites*. Springer Science & Business Media.
- [15] Samborsky, D. D., Mandell, J. F., & Miller, D. A. (2013). Creep/fatigue behavior of resin infused biaxial glass fabric laminates. In *AIAA SDM Conference, Wind Energy Session, Boston, MA, USA* (pp. 1-15).
- [16] Ziemian, C. W., Ziemian, R. D., & Haile, K. V. (2016). Characterization of stiffness degradation caused by fatigue damage of additive manufactured parts. *Materials & Design*, 109, 209-218.
- [17] Peng, T., Liu, Y., Saxena, A., & Goebel, K. (2015). In-situ fatigue life prognosis for composite laminates based on stiffness degradation. *Composite Structures*, 132, 155-165.

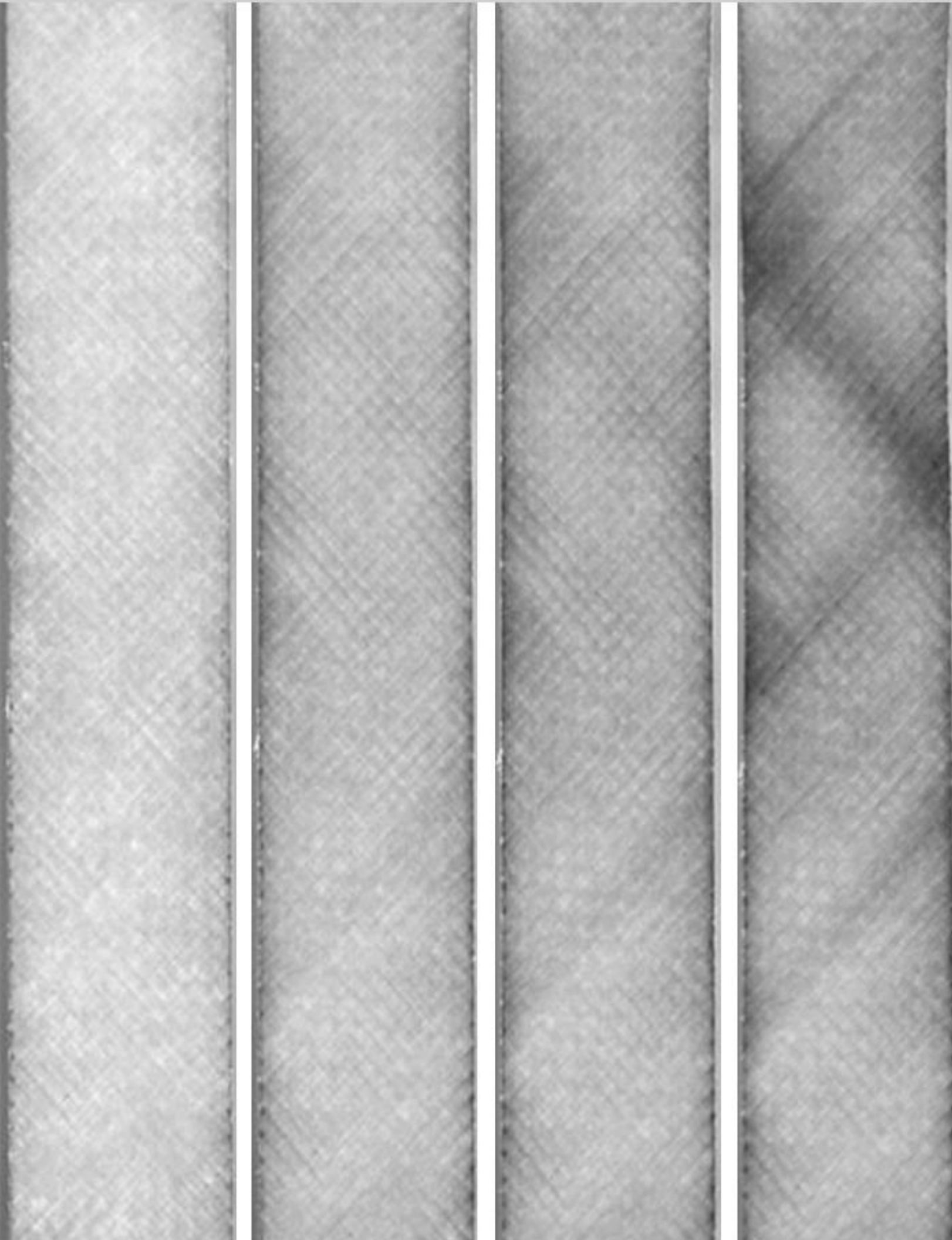
- [18] Vieille, B., & Albouy, W. (2015). Fatigue damage accumulation in notched woven-ply thermoplastic and thermoset laminates at high-temperature: influence of matrix ductility and fatigue life prediction. *International Journal of Fatigue*, 80, 1-9.
- [19] Benaarbia, A., Chrysochoos, A., & Robert, G. (2015). Thermomechanical behavior of PA6. 6 composites subjected to low cycle fatigue. *Composites Part B: Engineering*, 76, 52-64.
- [20] Naderi, M., & Khonsari, M. M. (2013). On the role of damage energy in the fatigue degradation characterization of a composite laminate. *Composites Part B: Engineering*, 45(1), 528-537.
- [21] Kalogiannakis, G., Van Hemelrijck, D., & Van Assche, G. (2004). Measurements of thermal properties of carbon/epoxy and glass/epoxy using modulated temperature differential scanning calorimetry. *Journal of composite materials*, 38(2), 163-175.
- [22] Steinberger, R., Leitão, T. V., Ladstätter, E., Pinter, G., Billinger, W., & Lang, R. W. (2006). Infrared thermographic techniques for non-destructive damage characterization of carbon fibre reinforced polymers during tensile fatigue testing. *International Journal of Fatigue*, 28(10), 1340-1347.
- [23] Katunin, A., & Fidali, M. (2012). Self-heating of polymeric laminated composite plates under the resonant vibrations: Theoretical and experimental study. *Polymer Composites*, 33(1), 138-146.
- [24] Herman, W. A., Hertzberg, R. W., & Manson, J. A. (1990). The influence of loading history on fatigue in engineering plastics. *Journal of Materials Science*, 25(1), 434-440.
- [25] Naderi, M., Kahirdeh, A., & Khonsari, M. M. (2012). Dissipated thermal energy and damage evolution of glass/epoxy using infrared thermography and acoustic emission. *Composites Part B: Engineering*, 43(3), 1613-1620.
- [26] Lampman, S. Characterization and failure analysis of plastics. *ASM International*, 2003.
- [27] Gao, Z., Niu X., Zhou W., Gogotsi Yu., Chudnovsky A., and Stivala S.S., Effect of Oxidation in Crack Growth Process in Polybutylene Tubing in Potable Water Application ." *ANTEC 2001, conference proceedings, Dallas, Texas, May 6-10* (2001).
- [28] Korkiakoski, S., Brøndsted, P., Sarlin, E., & Saarela, O. (2016). Influence of specimen type and reinforcement on measured tension–tension fatigue life of unidirectional GFRP laminates. *International Journal of Fatigue*, 85, 114-129.
- [29] Adam, T. J., & Horst, P. (2017). Fatigue damage and fatigue limits of a GFRP angle-ply laminate tested under very high cycle fatigue loading. *International Journal of Fatigue*, 99, 202-214.
- [30] Brunbauer, J., & Pinter, G. (2015). Fatigue life prediction of carbon fibre reinforced laminates by using cycle-dependent classical laminate theory. *Composites Part B: Engineering*, 70, 167-174.

- [31] Mandell, J. F., Ashwill, T. D., Wilson, T. J., Sears, A. T., Agastra, P., Laird, D. L., and Samborsky, D. Analysis of SNL/MSU/DOE fatigue database trends for wind turbine blade materials. No. SAND2010-7052. *Sandia National Laboratories*, 2010.
- [32] Savvilitidou, M., Keller, T., & Vassilopoulos, A. P. (2017). Fatigue performance of a cold-curing structural epoxy adhesive subjected to moist environments. *International Journal of Fatigue*, 103, 405-414.
- [33] Meneghetti, G., Ricotta, M., Lucchetta, G., & Carmignato, S. (2014). An hysteresis energy-based synthesis of fully reversed axial fatigue behaviour of different polypropylene composites. *Composites Part B: Engineering*, 65, 17-25.
- [34] Sobieraj, M. C., Murphy, J. E., Brinkman, J. G., Kurtz, S. M., & Rimnac, C. M. (2010). Notched fatigue behavior of PEEK. *Biomaterials*, 31(35), 9156-9162.
- [35] Chandra, R., Singh, S. P., & Gupta, K. (1999). Damping studies in fiber-reinforced composites—a review. *Composite structures*, 46(1), 41-51.
- [36] Patil, S. P., Markert, B., & Gräter, F. (2014). Rate-dependent behavior of the amorphous phase of spider dragline silk. *Biophysical journal*, 106(11), 2511-2518.
- [37] Blanter, M. S., Golovin, I. S., Neuhauser, H., and Sinning, H. R. "Internal friction in metallic materials." A Handbook. *Springer Verlag* (2007): 540.
- [38] Plumtree, A., Melo, M., & Dahl, J. (2010). Damage evolution in a $[\pm 45]$ 2S CFRP laminate under block loading conditions. *International Journal of Fatigue*, 32(1), 139-145.
- [39] Kawai, M., & Taniguchi, T. (2006). Off-axis fatigue behavior of plain weave carbon/epoxy fabric laminates at room and high temperatures and its mechanical modeling. *Composites Part A: Applied Science and Manufacturing*, 37(2), 243-256.
- [40] Van Paepegem, W., De Baere, I., & Degrieck, J. (2006). Modelling the nonlinear shear stress–strain response of glass fibre-reinforced composites. Part I: experimental results. *Composites science and technology*, 66(10), 1455-1464.
- [41] ASTM D3039/D3039M-14 Standard Test Method for Tensile Properties of Polymer Matrix Composite Materials. *ASTM International*, 2014.
- [42] ASTM, D7791–17. Standard Test Method for Uniaxial Fatigue Properties of Plastics. *ASTM International*; 2017.
- [43] ASTM, D3171–99. Standard Test Methods for Constituent Content of Composite Materials. *ASTM International*, 2002.
- [44] Cutler M. L., "Reflection of light from multi-layer films," bachelor thesis, Massachusetts Institute of Technology (1939).

- [45] ISO-6721-11 Plastics - determination of dynamic mechanical properties - part 11: glass transition temperature. *ISO International Standard*, 2012.
- [46] Kharrazi, M. R., & Sarkani, S. (2001). Frequency-dependent fatigue damage accumulation in fiber-reinforced plastics. *Journal of composite materials*, 35(21), 1924-1953.
- [47] Launay, A., Maitournam, M. H., Marco, Y., & Raoult, I. (2013). Multiaxial fatigue models for short glass fiber reinforced polyamide—Part I: Nonlinear anisotropic constitutive behavior for cyclic response. *International Journal of Fatigue*, 47, 382-389.

Contributions:

A.Vahid Movahedi-Rad conceived, designed and performed the experimental campaign under the supervision of Dr. Anastasios Vassilopoulos and Prof. Thomas Keller. The analysis of the results was carried out by A.Vahid Movahedi-Rad in collaboration with Dr. Anastasios Vassilopoulos and Prof. Thomas Keller.



Chapter 3



Stress ratio effect on fatigue behavior

3.1. Introduction

It is widely accepted that fatigue is one of the most common failure types, especially in load-transferring parts of structures operating in the open air. The structural integrity of such components is vital for design purposes and therefore researchers have devoted great efforts to understand their fatigue behavior ^[1,2,3,4,5]. Fiber-reinforced polymer (FRP) composites operating in open-air applications are subjected to different irregular loading profiles of a stochastic nature, comprising variable amplitude, and interrupted loading spectra ^[6,7,8]. Nevertheless, since it is impossible to experimentally investigate the fatigue behavior of each material of interest under all possible loading conditions, standard continuous fatigue experiments are performed in laboratories under different stress ratios in order to characterize the fatigue performance of each material for structural design purposes ^[3].

During fatigue loading, the mechanical properties of specimens are degraded as a result of the activation of various damage mechanisms, including fiber breakage and matrix cracking, debonding, transverse-ply cracking, and delamination ^[9,10]. Therefore, several parameters, such as stress level, loading frequency, stress ratio ($R=\sigma_{min}/\sigma_{max}$), and material type, must be considered in order to appropriately design a fatigue-testing program. It has been well documented that stress level significantly affects the fatigue life of composites ^[10,11,12,13,14,15]. Moreover, it was recently shown that the different stress levels in constant amplitude fatigue experiments could cause different damage

distributions in the specimen volume, and result in different stiffness degradation levels, hysteresis loop areas, and final fracture surfaces ^[10]. Any frequency increase has been shown to improve the fatigue life of several material systems as long as this increased frequency did not produce significant self-generated temperature increases that softened the matrix and decreased the fatigue life ^[16,17,18,19,20]. The stress ratio also exerts a considerable effect on fatigue behavior, which is mainly attributed to the interaction between the time- and cyclic-dependent mechanical properties, since laminated composites creep under fatigue mean stress even at room temperature ^[10,26,27,28,29,30,31]. Under $R=1$, a specimen is loaded in pure creep. As the stress ratio decreases (in tensile-tensile fatigue), the stress amplitude increases, which leads to fewer cyclic creep effects and greater fatigue damage, and finally under $R=-1$ the specimen undergoes only fatigue damage ^[35,36]. In continuous fatigue, the interaction between the cyclic creep and fatigue damage has mainly been studied by monitoring the evolution of the fatigue hysteresis loops. In this case, the shift of the fatigue hysteresis loops represents the cyclic creep effects and the degradation of fatigue stiffness, which is the slope of the hysteresis loops, represents the damage effect ^[26,32,33,34]. The interaction degree between the cyclic creep and fatigue damage and dominance of one over the other also depends strongly on the material type. In matrix-dominated composites, the viscoelastic deformation is very significant, which leads to greater cyclic creep effects than in fiber-dominated composites.

To simulate the stress ratio effect on fatigue life, theoretical models, the so-called constant life diagrams (CLDs), were established ^[3,21,22,23,24,25]. A comparison of the simulation capabilities of the most commonly used models for composite materials was presented in ^[23].

Previous investigations of angle-ply laminated composites under tension-tension fatigue are limited to stress ratios of 0.1, or 0, while little information regarding the evolution of fatigue-related mechanical properties (e.g. fatigue strength and stiffness) and response (e.g. dissipated energy, cyclic creep strain) is available at other stress ratios ^[2,10,13,15,30,37,38,39]. Moreover, the majority of the works dealing with fatigue under higher stress ratios mainly focused on the development of relevant fatigue life prediction methodologies, and not on the thorough investigation of the effects of the R -ratio on the damage accumulation and cyclic- and time-dependent mechanical properties ^[1,12,21,22,27,40].

The aim of this work is to investigate the stress ratio effect on the fatigue behavior of matrix-dominated laminated composites in which the stress ratio effect on fatigue behavior is considerable. To achieve this objective, a dedicated experimental program was conducted to investigate the behavior of $\pm 45^\circ$ angle-ply GFRP composite laminates at a stress level of $R=0.5$. The variation of the fatigue stiffness, hysteresis loop areas, and cyclic creep was monitored by measuring the load and displacement in each fatigue cycle. In addition, the evolution of the fatigue damage and specimen surface temperature was recorded during the cyclic loading. The results were then compared to

previous fatigue results obtained under $R=0.1$ ^[10] and the effect of the R -ratio has been thoroughly discussed.

3.2. Experimental procedure

3.2.1 Material and specimen preparation

Unidirectional E-glass fiber fabrics (EC 9-68) with an area density of 425 gr/m^2 and layer thickness of 0.45 mm were used. These fabrics comprise a finish-bonding agent, which provides better adhesion to the matrix. The low viscosity resin, Biresin® CR83, mixed with the hardener Sika CH83-2 in a ratio of 3:1, was used for the impregnation of the fabrics. The fabrication was carried out on a plastic substrate, which was coated with a release agent to prevent the resin from bonding to the surface after fabrication. Laminates of $500 \times 500 \times 2.25 \text{ mm}^3$ and stacking sequence of $[\pm 45]_{2s}$ were fabricated by vacuum-assisted hand lay-up, using a vacuum pump with pressure of 0.9 bar . Each laminate was placed in vacuum for 24 hours under laboratory conditions ($22 \pm 2^\circ\text{C}$, $40 \pm 10\% \text{ RH}$), and subsequently placed in an oven at 70°C for eight hours to complete the curing process. The achieved fiber content was 62% determined by burn-off experiments as described in ASTM D 3171-99 ^[41]. Rectangular specimens with the dimensions of $250 \times 25 \times 2.3 \text{ mm}^3$ (length \times width \times thickness), according to ASTM D3039 ^[42], were cut from the laminates with a water-jet and two aluminum tabs with dimensions of $45 \times 25 \times 4 \text{ mm}^3$ were glued to each specimen end using an cyanoacrylate glue for gripping.

3.2.2 Experimental set-up and instrumentation

All fatigue experiments were carried out according to ASTM D7791-12 ^[43] on an MTS Landmark servo-hydraulic loading machine, calibrated to a load capacity of 25 kN with $\pm 0.5\%$ of applied force accuracy. The cyclic loading was performed in the stress range of $58 \text{ MPa} - 78 \text{ MPa}$ to achieve failure at between 10^3 and 10^7 fatigue cycles. Four specimens were examined at each of the five selected stress levels. Details of the experimental results are presented in Table 3.1. A loading rate of 30.5 kN/s was used for all tests. Different frequencies were selected to keep the loading rate constant for all stress levels. The experimental matrix in detail is presented in Table 3.1. All experiments were performed in an environmental chamber regulated to a constant temperature of 20°C . Two fans were used to circulate the air inside the chamber and cool the specimens.

Different instrumentation was used to monitor the mechanical, thermal, and optical changes in the material during and after the fatigue process. During the fatigue experiments, the machine's displacement, load, and number of cycles were recorded. The variation of the longitudinal strains was

measured by a high-resolution video-extensometer (a Point Grey Grasshopper3 camera with a resolution of 1936×1216 Mpixels and a Fujinon HF35SA-1 35mm F/1.4 lens) with a frequency of acquisition of 160 fps. Depending on the stress level, between 17 and 23 load and displacement measurements were recorded in each fatigue cycle. The video-extensometer measured the relative position of two lines marked on the specimen surface and calculated the corresponding strain values. An LED white light with negligible heat emission was projected onto the sample surface to enhance measurement accuracy. To record the evolution of the specimen surface temperature during the fatigue experiments, an infrared (IR) thermal camera with an accuracy of 0.1°C and optical resolution of 160×120 pixels was also employed. The fabricated material was semi-transparent and the formation and accumulation of the fatigue damage decreased specimen translucency ^[6,10]. Therefore, to detect the damage development in the specimens at a macroscale level, photographs were taken at regular intervals (depending on the life expectancy) with a digital camera with maximum aperture f/2.8 and focal length range of 24–70mm zoom range during loading. A bright white light source was positioned behind the specimens to assist this procedure.

Table 3.1. Fatigue experimental results

No.	Code	σ_{\max} (MPa)	Frequency (Hz)	N_f
1	Conf -0.5-78-a	78.0	6.8	20505
2	Conf -0.5-78-b	78.0	6.8	5206
3	Conf -0.5-78-c	78.0	6.8	1767
4	Conf -0.5-78-d	78.0	6.8	1471
5	Conf -0.5-72-a	72.0	7.4	60130
6	Conf -0.5-72-b	72.0	7.4	61616
7	Conf -0.5-72-c	72.0	7.4	36435
8	Conf -0.5-72-d	72.0	7.4	6513
9	Conf -0.5-68-a	68.0	7.8	5436
10	Conf -0.5-68-b	68.0	7.8	112681
11	Conf -0.5-68-c	68.0	7.8	119132
12	Conf -0.5-68-d	68.0	7.8	16642
13	Conf -0.5-64-a	64.2	8.4	76431
14	Conf -0.5-64-b	64.2	8.4	228923
15	Conf -0.5-64-c	64.2	8.4	345818
16	Conf -0.5-64-d	64.2	8.4	108719
17	Conf -0.5-58-a	58.2	9.1	2110761
18	Conf -0.5-58-b	58.2	9.1	295972
19	Conf -0.5-58-c	58.2	9.1	645568
20	Conf -0.5-58-d	58.2	9.1	5245384

3.3. Experimental results and discussion

3.3.1. Fatigue life

The fatigue data are presented in Fig. 3.1, where the maximum stress level, σ_{\max} , is plotted versus the number of cycles to failure, N_f . The fatigue behavior was modeled by a single power law equation as follows [44]:

$$\sigma_{\max} = \sigma_0 N_f^{-\frac{1}{k}} \quad (3.1)$$

in which σ_0 , the y-intercept, and $1/k$, the slope of the S-N curve, are model parameters that were derived by linear regression analysis of the experimental data, and their estimated values are given in Table 3.2.

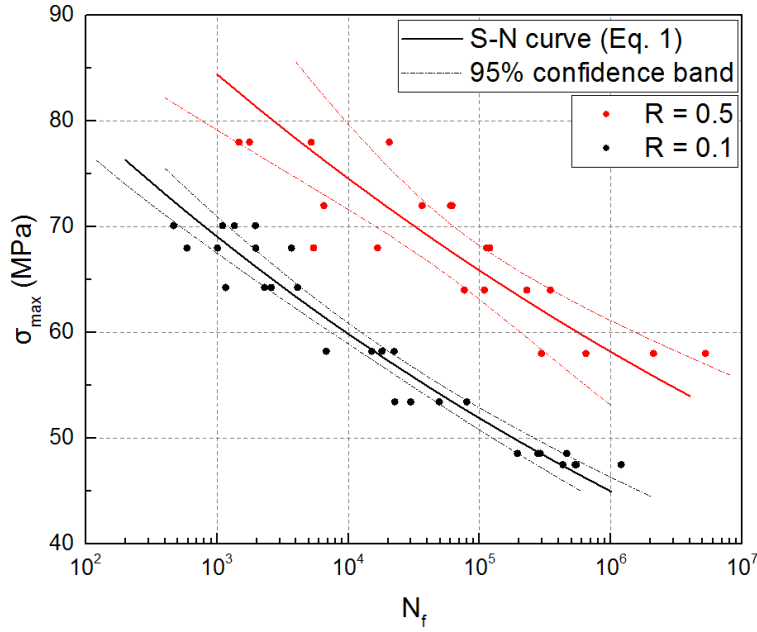


Fig. 3.1. Comparison of S-N curves under different R -ratios.

Table 3.2. Fatigue parameters for continuous loading patterns under stress ratios of 0.1 and 0.5

Stress ratio	σ_0	$1/k$	$\hat{\sigma}^2$
$R=0.1$	106.09	0.0622	0.025
$R=0.5$	122.54	0.0540	0.137

3.3.2 Specimen translucency and self-generated temperature

Figs. 3.2a and 3.2b show the evolution of specimen translucency at different percentages of specimen fatigue life for high and low cyclic loads. During the cyclic loading, the formation of any form of cracks in the matrix and fiber matrix debonding, when the crack surface was perpendicular to the beam of light, caused light scattering and changed the specimen translucency^[10]. Therefore, darker regions in the photos correspond to decreased light transmittance due to greater damage formation. As shown for both cases, damage gradually appeared along the fibers as the number of cycles increased, at around 45° with respect to the specimen longitudinal axis, which was thus attributed mainly to interface debonding. In addition, at higher stress levels, a necking of the concentrated damage zone was formed as can be seen in Fig. 3.2a (the initial specimen dimensions are indicated by red dashed lines) and gradually became greater.

The magnitude and distribution of the self-generated temperature across the surface of specimens at two stress levels of $\sigma_{\max}=78$ MPa (high stress level) and $\sigma_{\max}=64$ (low stress level) are shown in Figs. 3.3a and 3.3b, respectively. At high stress levels, during the early stages of the fatigue life, a uniform distribution of surface temperature was observed and as the number of cycles increased, the self-generated temperature increased while its uniformity across the specimen surface was maintained (in the represented temperature scale of 10-30°C). During the final cycles of the fatigue experiment, an oval-shaped hotspot started to appear (see Fig. 3.3a, after 99% of fatigue life) oriented in the direction of the fiber bundles, and fatigue failure occurred at the location of the hotspot. These temperature increases were attributed to internal friction in the damaged zones. Lower temperatures were measured at low stress levels, also uniformly distributed across the specimen surface during loading, until only a few cycles before failure, when a hot spot formed.

Figs. 3.4a and 3.4b show the evolution of the maximum and average surface temperatures of specimens at each stress level. At high stress levels, the self-generated temperature increased gradually as the number of cycles increased. However, at low and intermediate stress levels, the self-generated temperature initially increased and then stabilized until the last cycles of the fatigue experiment. Finally, fatigue failure occurred with a sudden increase of temperature. The highest maximum temperature was less than 30°C, remained clearly below $T_{g,onset}$ (78°C) measured by DMA^[10], and the material thus remained in the glassy state.

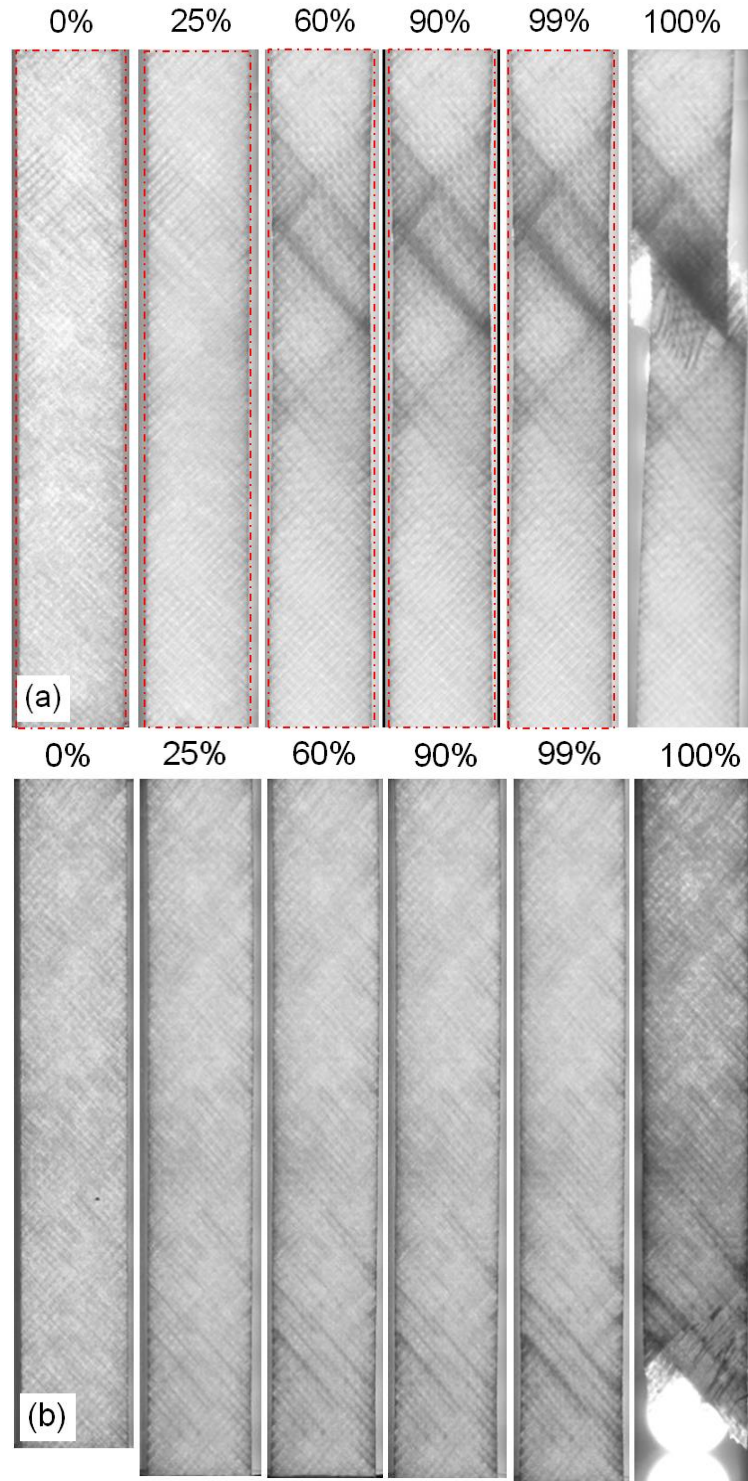


Fig. 3.2. Light transmittance at different percentages of fatigue life, at (a) $\sigma_{\max}=78$ MPa (Conf-0.5-78-b), and (b) $\sigma_{\max}=58$ MPa (Conf-0.5-58-d).

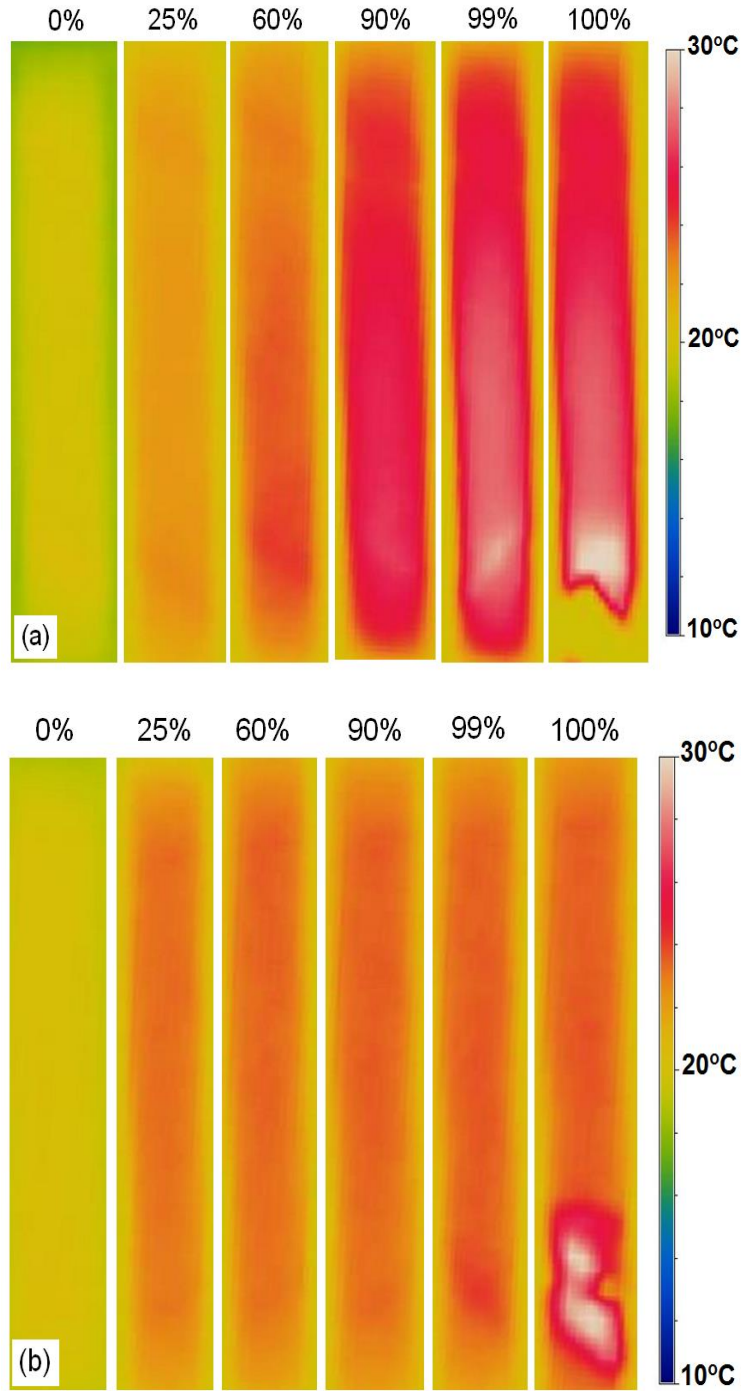


Fig. 3.3. Self-generated temperature at different percentages of fatigue life, at (a) $\sigma_{\max}=78$ MPa (Conf-0.5-78-d), and (b) $\sigma_{\max}=64$ MPa (Conf-0.5-64-d).

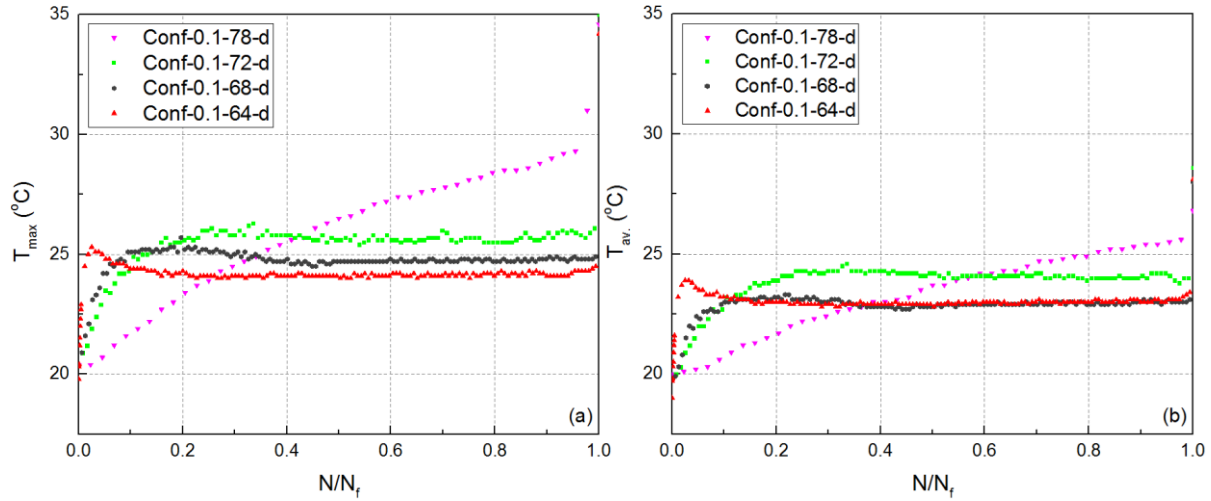


Fig. 3.4. Variation of (a) maximum, and (b) average self-generated temperature versus normalized number of cycles at different stress levels.

3.3.3 Stress-strain loops and fatigue stiffness

The evolution of the typical hysteresis loops during fatigue life at high, $\sigma_{\max}=78$ MPa, and low, $\sigma_{\max}=58$ MPa, stress levels is shown in Fig. 3.5. The number of loading cycles at which the first and the last hysteresis loops were recorded are indicated for both stress levels. To identify the amount of cyclic creep at different stress levels, the variation of the average strain (average of maximum and minimum strains in one cycle) versus the normalized number of cycles is shown in Fig. 3.6 for selected specimens at each stress level. Cyclic creep was mainly due to the increased viscoelastic deformation of the polymeric matrix [26]. Another reason for the occurrence of cyclic creep is the permanent strain due to fatigue damage accumulation. All curves showed a rapid increase with decreasing rate at the early stage of loading, followed by a steady state evolution prior to an increase before failure. As expected, the specimens loaded at higher stress levels exhibited greater cyclic creep. Fig. 7 shows part of a specimen at the different percentages of fatigue life at the high stress level. In Fig. 3.7a, the dashed line indicates the initial position of a selected fiber bundle before starting the experiment. This showed that fiber realignment was not uniform along the specimen but was more evident at the concentrated damage zones, as a result of the cyclic creep; the new fiber orientation indicated with solid lines in Figs. 3.7b-d gradually changed with the number of cycles up to specimen failure.

The average realignment angle, $\Delta\theta_{av}$, was obtained from the measurements of the longitudinal and traverse strains. Fig. 8 shows schematically the realignment of the fiber angle in a specimen as a result of longitudinal (Δa) and traverse (Δb) deformations. The average realignment angle was calculated as:

$$\Delta\theta_{av} = \arctan\left(\frac{1+\varepsilon_x}{1-\varepsilon_y}\right) - 45 \quad (3.2)$$

where ε_x , ε_y are the longitudinal and traverse strains, respectively as measured. The evolution of the calculated average realignment angle versus the normalized number of cycles is shown in Fig. 3.9 at different stress levels and was inversely proportional to the evolution of the longitudinal cyclic creep (Fig. 3.6).

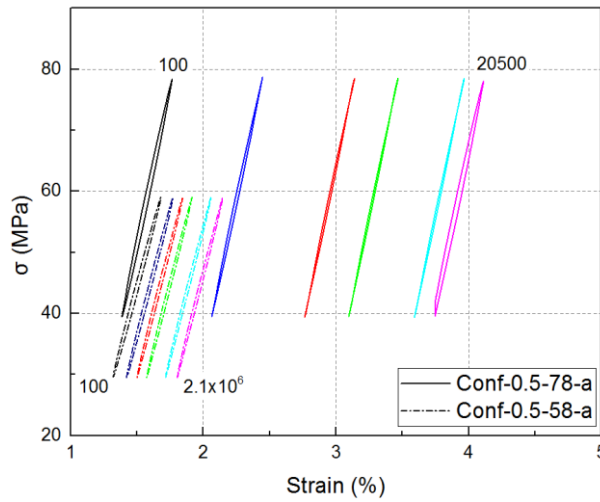


Fig. 3.5. Variation of hysteresis loops under cyclic loading at stress levels of $\sigma_{\max}=78$ MPa (Conf-0.5-78-a) and $\sigma_{\max}=58$ MPa (Conf-0.5-58-a).

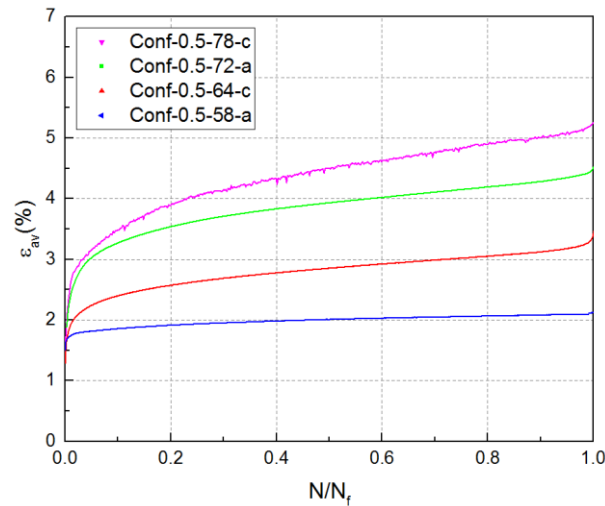


Fig. 3.6. Cyclic creep versus normalized number of cycles at different stress levels.

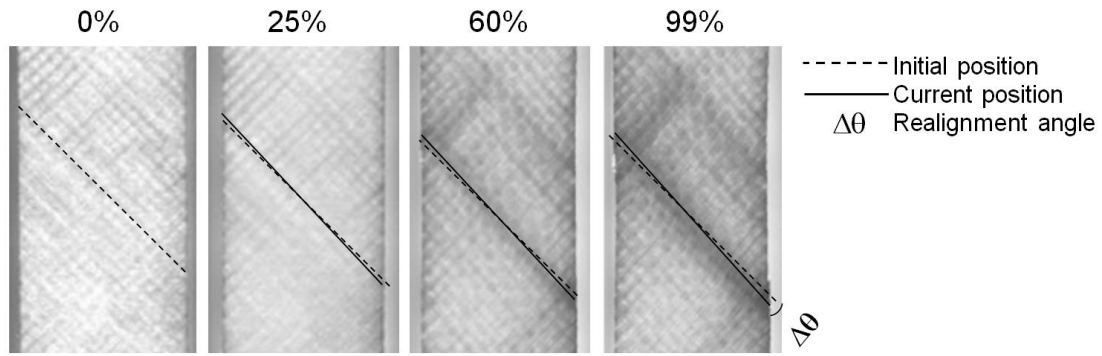


Fig. 3.7. Realignment of glass fiber bundles;(a) 0%, (b) 25%, (c) 60%, and (d) 99% of fatigue life (Conf-0.5-78-b).

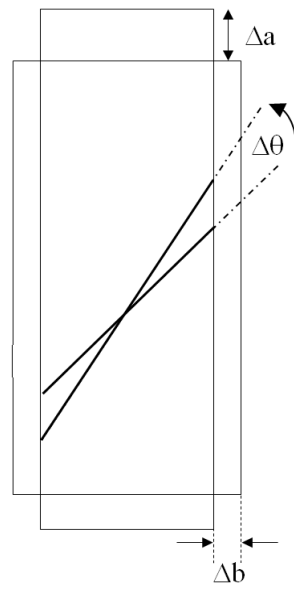


Fig. 3.8. Schematic representation of realignment angle.

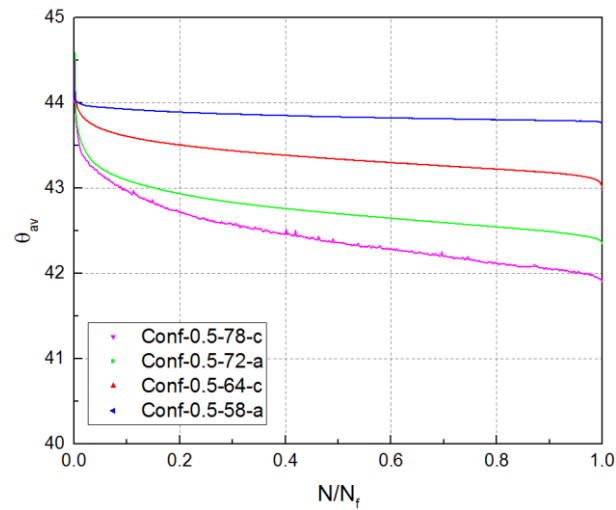


Fig. 3.9. Average realignment of fibers at different percentages of fatigue life.

The fatigue stiffness, E_N , with respect to the stiffness of the first cycle, E_I , is plotted against the normalized fatigue life for different stress levels in Fig. 3.10. The evolution of fatigue stiffness was a function of the applied stress level as a result of two opposing mechanisms. On the one hand, as the number of cycles increased, the damage accumulated in the volume of the material and reduced the fatigue stiffness (Fig. 3.2). On the other hand, the material was stiffened mainly as a result of cyclic creep, which caused the fiber realignment toward the loading direction (Fig. 3.9). A similar enhancement of fatigue stiffness was also observed in the same specimens when they were subjected to a creep-fatigue loading pattern [7]. Another reason for the increasing fatigue stiffness was attributed to the increasing internal stress of the polymeric matrix, again due to cyclic creep. An enhancement of fatigue stiffness due to increasing internal stress was also observed in an epoxy adhesive during cyclic loading at high stress levels [34]. At the low stress level, the stiffness evolution gradually decreased during the first 15% of specimen fatigue life followed by a steady state decrease up to specimen failure. This observation was in agreement with the behavior exhibited by most common (FRP) composite systems in the literature, e.g., [10,45,46,47]. However, at high stress levels, the fatigue stiffness increased at the beginning of the experiments due to the fiber realignment, while gradually, as damage accumulated in the specimen, it reached a constant value for most of the specimen fatigue life, before decreasing again prior to failure. At $\sigma_{\max}=64$ MPa, fatigue stiffness was almost constant up to the 90% of the specimen lifetime as a result of a balance between the stiffening and degradation during the cyclic loading, and then dropped prior to failure due to the prevailing specimen damage. Similarly, almost constant fatigue stiffness during the fatigue experiments was also observed in $(\pm 45)_{2S}$ angle-ply laminates of carbon/epoxy under $R=0.5$; however, no explanation for this behavior was given [26].

The variation of the hysteresis loop area per cycle versus the normalized number of cycles is shown for selected specimens at each stress level in Fig. 3.11. The hysteresis loop area represents the energy dissipated per cycle mainly due to the internal friction, which increases as the damage area grows [6,48]. On the other hand, the increase of fatigue stiffness reduces the internal friction, and consequently the amount of energy dissipated decreases [7]. At high and intermediate stress levels and at the beginning of the experiments, due to the rapidly increasing cyclic creep and resulting stiffening effect, the hysteresis loop area decreased. Subsequently, the area remained the same, due to the balance between the fatigue damage growth and the stiffening effect of fiber realignment, until close to the end of the fatigue life, when the damage became highly concentrated and the amount of internal friction became greater, resulting to a hysteresis loop area increase. At the low stress level, since the damage was not as severe and concentrated, and the mean stress level was low and did not lead to any significant stiffening effect, the hysteresis loop area remained almost constant during the entire lifetime.

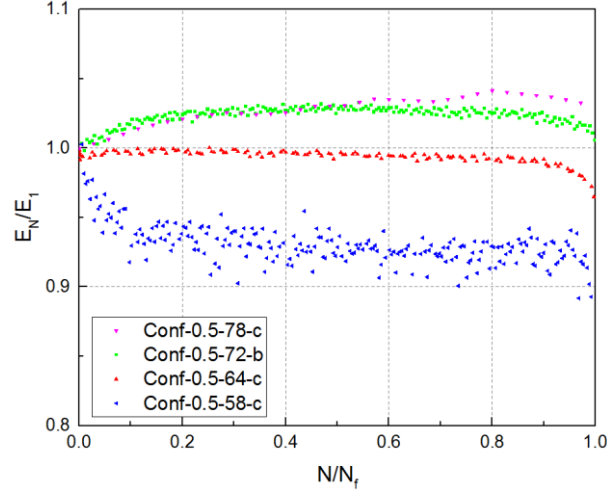


Fig. 3.10. Variation of normalized fatigue stiffness versus normalized number of cycles at different stress levels.

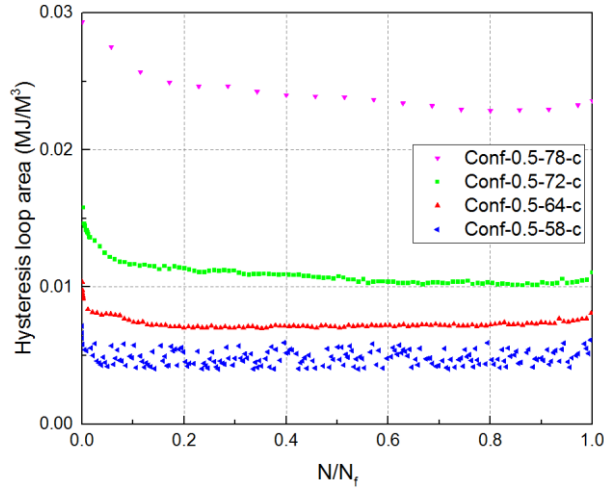


Fig. 3.11. Hysteresis area per cycle versus normalized number of cycles at different stress levels.

3.4. Effect of stress ratio

The S-N curve obtained from the fatigue experiments under the stress ratio of 0.5 together with the 95% confidence bounds are compared to those derived from experiments under $R=0.1$ ^[10] in Fig. 3.1. The fatigue life of specimens under $R=0.5$ was longer than that of specimens under $R=0.1$ at the same σ_{\max} . The estimated values of the model parameters are given in Table 3.2; as shown, the slope of the S-N curve was steeper under the stress ratio of 0.1. It can also be seen that the fatigue data under

$R=0.5$ exhibited greater scatter, with a variance of twice the normal distribution, $\hat{\sigma}^2$, calculated according to ^[49] and also tabulated in Table 3.2. In laminated composites, preexisting defects can vary from specimen to specimen, and fatigue damage initiates at these locations. At low stress amplitudes ($R=0.5$), damage formation and accumulation were highly dependent on the differences in preexisting defects, which led to lower repeatability in the fatigue results ^[50]. In addition, when the stress ratio changed from 0.1 to 0.5, the loading pattern became more complex since the creep effect became more prevalent, causing more scattered results.

A comparison of the specimen translucency in Fig. 3.2 with that in ^[10] indicated that under the stress ratio of 0.5, more uniform damage distribution was formed along the specimens than in those under the stress ratio of 0.1. Under the higher stress ratio, when damage initiated, it propagated at a lower rate due to the smaller stress amplitude, which led to more uniform damage distribution. The self-generated surface temperature measurements shown in Fig. 3.3 support this. The temperature across the specimen surface remained even throughout the fatigue experiment, and hot spots were present only during the last 10% of fatigue life, in contrast to specimens loaded continuously under $R=0.1$ ^[10] where hot spots could be observed from the early stages of the fatigue experiment ^[10]. At constant σ_{\max} , a greater cyclic stress amplitude under $R=0.1$ caused the formation of dominant cracks in the specimen volume creating concentrated damage zones. Nevertheless, under $R=0.5$, the cyclic stress amplitude was much lower, insufficient to create dominant cracks, and therefore fatigue damage was evenly distributed in the specimen volume throughout the fatigue lifetime, which finally led to longer fatigue life.

The evolution of the cyclic creep with the number of cycles under the two studied stress ratios is compared in Fig. 3.12 for the two stress levels of $\sigma_{\max}=68$ MPa and $\sigma_{\max}=58$ MPa. As the stress ratio increased, at the same σ_{\max} , the mean stress became greater and the stress amplitude decreased. Therefore, in the experiment with $R=0.5$, the cyclic creep mainly increased because of the viscoelastic strain; however, in the case of $R=0.1$, the cyclic creep was governed by the permanent strain. According to Fig. 3.12, the cyclic creep initially increased very rapidly in the experiment with $R=0.5$ and almost 70% of the cyclic creep of the specimens was achieved in the first 20% of the fatigue life, which was due to the high viscoelastic deformation. However, the strain of specimens loaded under $R=0.1$ increased uniformly as the number of cycles increased because of gradual damage formation and accumulation. Although the initial two stages of the cyclic creep curves under different stress ratios increased at different rates, the strains at failure were comparable. In addition, Fig. 3.12 shows that the difference between the observed cyclic creep became lesser at the lower stress level. The evolution of the failure strains versus σ_{\max} is shown in Fig. 3.13. A direct relationship between the

failure strain and stress level can be observed for both stress ratios. In addition, it can be seen that independent of stress levels, the failure strains were comparable at other stress levels.

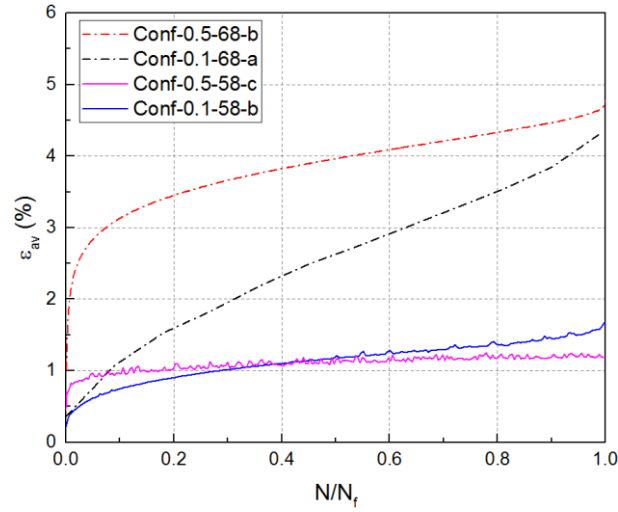


Fig. 3.12. Cyclic creep versus normalized number of cycles loaded under different stress ratios and at different stress levels.

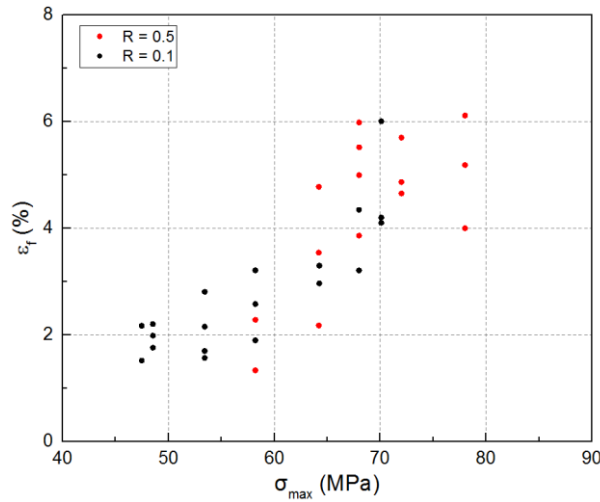


Fig. 3.13. Failure strain under different stress ratios and at different stress levels.

The variation of the average normalized fatigue stiffness (E_N / E_I) versus normalized fatigue life is shown in Fig. 3.14 for the high and low stress levels under both $R=0.1$ and $R=0.5$. At $\sigma_{\max}=68$ MPa and $R=0.1$, the normalized fatigue stiffness continuously decreased, initially at a high rate (during the first 10-15% of the lifetime), and subsequently at a lower, steady state rate up to specimen failure. The

stiffness evolution was different for those specimens loaded under $R=0.5$, for which, as explained above, the stiffness increased due to the fiber realignment until sufficient damage developed. The continuous decreasing of the normalized fatigue stiffness under $R=0.1$ was attributed to the greater stress amplitude and lower mean stress than under $R=0.5$, causing more fatigue damage and less stiffening effect. At lower stress levels (e.g., $\sigma_{\max}=58$ MPa), for both stress ratios, fatigue stiffness decreased as the number of cycles increased. At this stress level, the stiffening effect was not sufficiently high to compensate the degradation effect of fatigue damage.

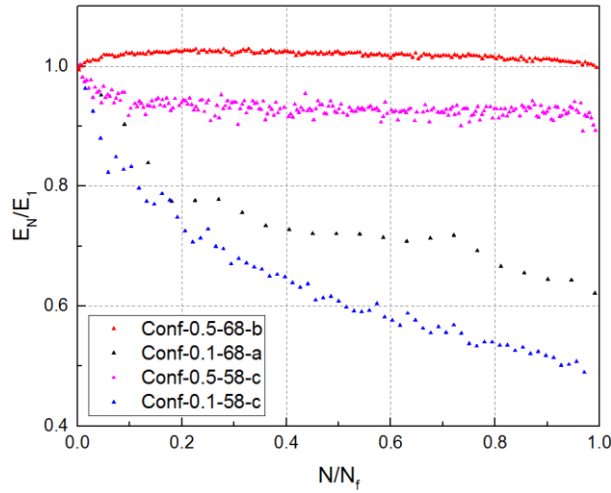


Fig. 3.14. Normalized fatigue stiffness versus normalized number of cycles loaded under different stress ratios and at different stress levels.

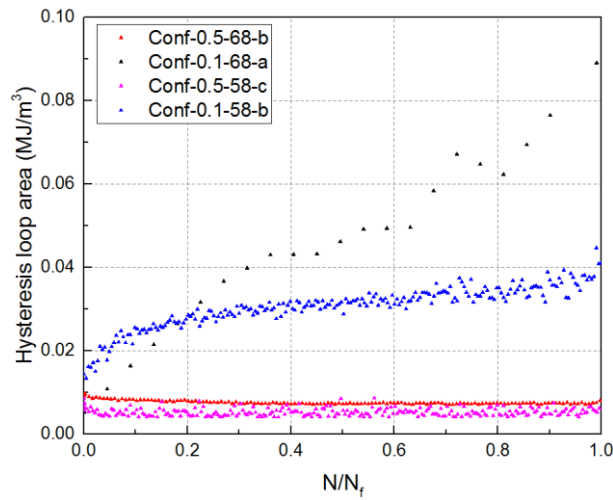


Fig. 3.15. Hysteresis loop area versus normalized number of cycles loaded under different stress ratios and at different stress levels.

The same comparison of the different stress ratios is shown for the evolution of the hysteresis loop areas in Fig. 3.15. Under the stress ratio of 0.1, when the number of cycles increased, the hysteresis loop area continuously increased. By increasing the stress ratio from 0.1 to 0.5, the magnitude of the hysteresis loop area decreased considerably mainly because of the smaller stress amplitude and less damage accumulation, which finally led to lower internal friction. Additionally, under the stress ratio of 0.5, the mean stress was greater than that at the same stress levels under $R=0.1$, causing more fiber realignment and more specimen stiffening, which again decreased the hysteresis loop area.

3.5. Conclusions

In this work, to determine the stress ratio effect on the fatigue behavior of angle-ply laminated composites, the mechanical, thermal, and optical properties of $(\pm 45)_{2s}$ glass/epoxy composite under two stress ratios of 0.5 and 0.1 were compared at different stress levels. The following conclusions can be drawn:

- By increasing the stress ratio from 0.1 to 0.5, the fatigue life was enhanced at constant σ_{\max} , and the slope of the S-N curve decreased with more scattered fatigue results.
- The different stress ratios led to different damage distributions, as shown by the specimen translucency during the fatigue loading. In the experiments conducted under the stress ratio of 0.5, damage was uniformly distributed along the specimens, while under the stress ratio of 0.1, it was severe and localized, which caused higher self-generated temperatures, and failure of these specimens at shorter lifetimes.
- The cyclic creep increased due to the viscoelastic deformation and the permanent strain accumulation in a ternary form. Under $R=0.5$, the cyclic creep mainly increased because of the viscoelastic deformation in the primary stage; however, under $R=0.1$, the cyclic creep principally grew as a result of the gradual increase of permanent strain in the steady state stage. Nevertheless, in both cases, the failure strains were comparable.
- The fatigue stiffness evolution during fatigue life was influenced by two opposing mechanisms; fatigue damage that degraded stiffness and a stiffening effect caused mainly by the fiber realignment due to cyclic creep. Under $R=0.5$ and at high stress levels, fiber realignment and the corresponding stiffening effect were significant, which enhanced the fatigue stiffness at the beginning of the fatigue experiments. However, the two mechanisms subsequently became balanced as the number of cycles

increased, and finally, the predominant damage growth decreased the fatigue stiffness. At the low stress level, the stiffening effect was not pronounced and therefore the fatigue stiffness monotonically decreased. When the stress ratio was decreased from 0.5 to 0.1, more severe damage zones and less stiffening effect caused the continuous decrease of fatigue stiffness at all stress levels.

- The variation of the hysteresis loop area during fatigue life was influenced by the same two opposing mechanisms; fatigue damage growth, which increased the internal friction, and the stiffening effect, which decreased the internal friction. Under $R=0.5$ and at high and intermediate stress levels, after a primary stage where the dominant stiffening effect decreased the hysteresis loop area, the damage growth and specimen stiffening became balanced for the greater part of the specimen fatigue life, which resulted in a constant hysteresis loop area. At the end of fatigue life, when the damage growth effect dominated, the hysteresis loop area slightly increased. However, under the stress ratio of 0.1, the hysteresis loop area continuously increased at all examined stress levels.

References

- [1] Philippidis, T. P., & Vassilopoulos, A. P. (2004). Life prediction methodology for GFRP laminates under spectrum loading. *Composites Part A: applied science and manufacturing*, 35(6), 657-666.
- [2] Plumtree, A., Melo, M., & Dahl, J. (2010). Damage evolution in a $[\pm 45]$ 2S CFRP laminate under block loading conditions. *International Journal of Fatigue*, 32(1), 139-145.
- [3] Shahverdi, M., Vassilopoulos, A. P., & Keller, T. (2012). Experimental investigation of R-ratio effects on fatigue crack growth of adhesively-bonded pultruded GFRP DCB joints under CA loading. *Composites Part A: Applied Science and Manufacturing*, 43(10), 1689-1697.
- [4] Mandell, J. F., Samborsky, D. D., Miller, D. A., Agastra, P., & Sears, A. T. (2016). *Analysis of SNL/MSU/DOE Fatigue Database Trends for Wind Turbine Blade Materials 2010-2015*(No. SAND2016-1441). Sandia National Lab.(SNL-NM), Albuquerque, NM (United States).
- [5] Pelaseyed, S. S., Mashayekhi, F., & Movahedi-Rad, A. (2015). Investigation of the shaft failure connected to extruder. *Journal of Failure Analysis and Prevention*, 15(6), 775-781.
- [6] Movahedi-Rad, A. V., Keller, T., & Vassilopoulos, A. P. (2018). Interrupted tension-tension fatigue behavior of angle-ply GFRP composite laminates. *International Journal of Fatigue*, 113, 377-388.

- [7] Movahedi-Rad, A. V., Keller, T., & Vassilopoulos, A. P. (2018). Creep effects on tension-tension fatigue behavior of angle-ply GFRP composite laminates. *International Journal of Fatigue*. Accepted for publication in *International Journal of Fatigue*.
- [8] Vassilopoulos, A. P., & Keller, T. (2011). *Fatigue of fiber-reinforced composites*. Springer Science & Business Media.
- [9] Reifsnider, K. L., & Talug, A. (1980). Analysis of fatigue damage in composite laminates. *International Journal of Fatigue*, 2(1), 3-11.
- [10] Movahedi-Rad, A. V., Keller, T., & Vassilopoulos, A. P. (2018). Fatigue damage in angle-ply GFRP laminates under tension-tension fatigue. *International Journal of Fatigue*, 109, 60-69.
- [11] Salkind, M. J. (1972). Fatigue of composites. In *Composite Materials: Testing and Design (Second Conference)*. ASTM International.
- [12] Rotem, A. (1991). The fatigue behavior of composite laminates under various mean stresses. *Composite structures*, 17(2), 113-126.
- [13] Kawai, M. (2004). A phenomenological model for off-axis fatigue behavior of unidirectional polymer matrix composites under different stress ratios. *Composites Part A: applied science and manufacturing*, 35(7-8), 955-963.
- [14] Kawai, M., & Kato, K. (2006). Effects of R-ratio on the off-axis fatigue behavior of unidirectional hybrid GFRP/Al laminates at room temperature. *International journal of fatigue*, 28(10), 1226-1238.
- [15] Brunbauer, J., & Pinter, G. (2015). Effects of mean stress and fibre volume content on the fatigue-induced damage mechanisms in CFRP. *International Journal of Fatigue*, 75, 28-38.
- [16] Sun, C. T., & Chan, W. S. (1979). Frequency effect on the fatigue life of a laminated composite. In *Composite materials: testing and design (fifth conference)*. ASTM International.
- [17] Sun, C. T., & Chim, E. S. (1981). Fatigue retardation due to creep in a fibrous composite. In *Fatigue of Fibrous Composite Materials*. ASTM International.
- [18] Perreux, D., & Joseph, E. (1997). The effect of frequency on the fatigue performance of filament-wound pipes under biaxial loading: experimental results and damage model. *Composites science and technology*, 57(3), 353-364.
- [19] Barron, V., Buggy, M., & McKenna, N. H. (2001). Frequency effects on the fatigue behaviour on carbon fibre reinforced polymer laminates. *Journal of materials science*, 36(7), 1755-1761.
- [20] Philippidis, T. P., & Vassilopoulos, A. P. (2003). Fatigue strength of composites under variable plane stress. In *Fatigue in Composites* (pp. 504-525).
- [21] El Kadi, H., & Ellyin, F. (1994). Effect of stress ratio on the fatigue of unidirectional glass fibre/epoxy composite laminae. *Composites*, 25(10), 917-924.

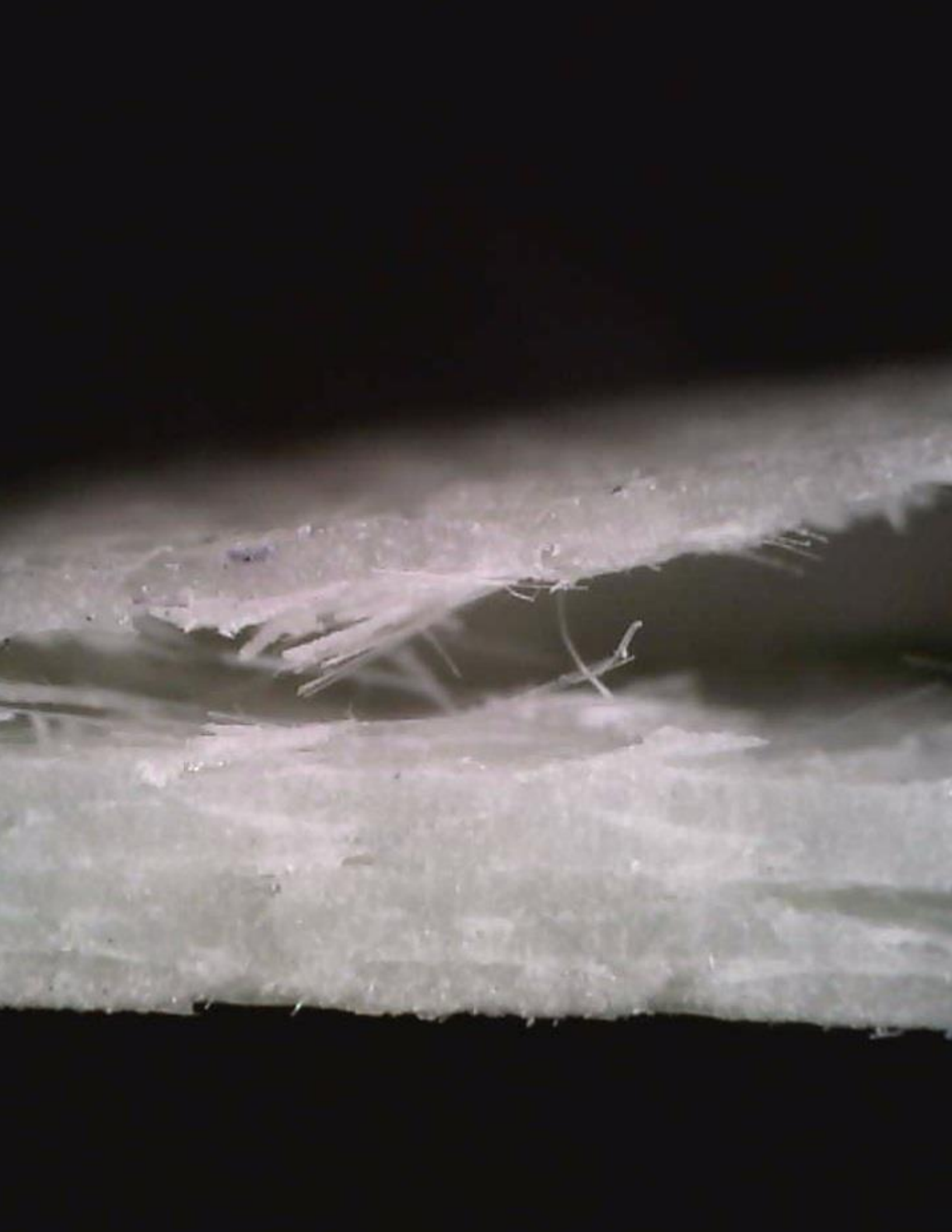
- [22] Epaarachchi, J. A., & Clausen, P. D. (2003). An empirical model for fatigue behavior prediction of glass fibre-reinforced plastic composites for various stress ratios and test frequencies. *Composites Part A: Applied science and manufacturing*, 34(4), 313-326.
- [23] Vassilopoulos, A. P., Manshadi, B. D., & Keller, T. (2010). Influence of the constant life diagram formulation on the fatigue life prediction of composite materials. *International journal of fatigue*, 32(4), 659-669.
- [24] Andersons, J., & Paramonov, Y. (2011). Applicability of empirical models for evaluation of stress ratio effect on the durability of fiber-reinforced creep rupture-susceptible composites. *Journal of materials science*, 46(6), 1705-1713.
- [25] Huh, Y. H., Lee, J. H., Kim, D. J., & Lee, Y. S. (2012). Effect of stress ratio on fatigue life of GFRP composites for WT blade. *Journal of mechanical science and technology*, 26(7), 2117-2120.
- [26] Petermann, J., & Schulte, K. (2002). The effects of creep and fatigue stress ratio on the long-term behaviour of angle-ply CFRP. *Composite Structures*, 57(1-4), 205-210.
- [27] Miyano, Y., Nakada, M., McMurray, M. K., & Muki, R. (1997). Prediction of flexural fatigue strength of CRFP composites under arbitrary frequency, stress ratio and temperature. *Journal of Composite Materials*, 31(6), 619-638.
- [28] Guedes, R. M. (2007). Durability of polymer matrix composites: Viscoelastic effect on static and fatigue loading. *Composites Science and Technology*, 67(11-12), 2574-2583.
- [29] Mallick, P. K., & Zhou, Y. (2004). Effect of mean stress on the stress-controlled fatigue of a short E-glass fiber reinforced polyamide-6, 6. *International journal of fatigue*, 26(9), 941-946.
- [30] Vieille, B., Albouy, W., & Taleb, L. (2014). About the creep-fatigue interaction on the fatigue behaviour of off-axis woven-ply thermoplastic laminates at temperatures higher than T_g. *Composites Part B: Engineering*, 58, 478-486.
- [31] Sayyidmousavi, A., Bougherara, H., & Fawaz, Z. (2015). The role of viscoelasticity on the fatigue of angle-ply polymer matrix composites at high and room temperatures-a micromechanical approach. *Applied Composite Materials*, 22(3), 307-321.
- [32] Vinogradov, A. M., & Schumacher, S. (2001). Cyclic creep of polymers and polymer-matrix composites. *Mechanics of composite materials*, 37(1), 29-34.
- [33] Stelzer, S., Ucsnik, S., & Pinter, G. (2015). Fatigue behaviour of composite-composite joints reinforced with cold metal transfer welded pins. *International Journal of Fatigue*, 81, 37-47.
- [34] Savvilitidou, M., Keller, T., & Vassilopoulos, A. P. (2017). Fatigue performance of a cold-curing structural epoxy adhesive subjected to moist environments. *International Journal of Fatigue*, 103, 405-414.

- [35] Raghavan, J., & Meshii, M. (1997). Creep rupture of polymer composites. *Composites Science and Technology*, 57(4), 375-388.
- [36] Enyama, J., McMurry, M.K., Nakada M., & Miyano Y. (1993). Effects of stress ratio on flexural fatigue behavior of a satin woven CFRP laminate. In *Proc. 3rd Japan SAMPE* (Vol. 2, pp. 2418-2421).
- [37] Zhang, Y., Vassilopoulos, A. P., & Keller, T. (2008). Stiffness degradation and fatigue life prediction of adhesively-bonded joints for fiber-reinforced polymer composites. *International Journal of Fatigue*, 30(10-11), 1813-1820.
- [38] Ma, Y., Zhang, Y., Sugahara, T., Jin, S., Yang, Y., & Hamada, H. (2016). Off-axis tensile fatigue assessment based on residual strength for the unidirectional 45 carbon fiber-reinforced composite at room temperature. *Composites Part A: Applied Science and Manufacturing*, 90, 711-723.
- [39] Ziemian, C. W., Ziemian, R. D., & Haile, K. V. (2016). Characterization of stiffness degradation caused by fatigue damage of additive manufactured parts. *Materials & Design*, 109, 209-218.
- [40] Fawaz, Z., & Ellyin, F. (1994). Fatigue failure model for fibre-reinforced materials under general loading conditions. *Journal of Composite Materials*, 28(15), 1432-1451.
- [41] ASTM, D3171–99, (2002). *Standard test methods for constituent content of composite materials*. ASTM International.
- [42] ASTM D3039/D3039M-14, (2014). *Standard Test Method for Tensile Properties of Polymer Matrix Composite Materials*. ASTM International.
- [43] ASTM, D7791–17, (2017). *Standard Test Method for Uniaxial Fatigue Properties of Plastics*. ASTM International.
- [44] Sarfaraz, R., Vassilopoulos, A. P., & Keller, T. (2012). A hybrid S–N formulation for fatigue life modeling of composite materials and structures. *Composites Part A: Applied Science and Manufacturing*, 43(3), 445-453.
- [45] Reifsnider, K. L., Schulte, K., & Duke, J. C. (1983). Long-term fatigue behavior of composite materials. In *Long-term behavior of composites*. ASTM International.
- [46] Philippidis, T. P., & Vassilopoulos, A. P. (1999). Fatigue of composite laminates under off-axis loading. *International Journal of fatigue*, 21(3), 253-262.
- [47] Mivehchi, H., & Varvani-Farahani, A. (2010). The effect of temperature on fatigue strength and cumulative fatigue damage of FRP composites. *Procedia Engineering*, 2(1), 2011-2020.
- [48] Chandra, R., Singh, S. P., & Gupta, K. (1999). Damping studies in fiber-reinforced composites—a review. *Composite structures*, 46(1), 41-51.
- [49] ASTM E739-91. (1995). Statistical analysis of linear or linearized stress-life (S-N) and strain-life (ϵ -N) fatigue data. *Annual Book of ASTM Standards*, 3.

[50] Schijve, J. (2001). *Fatigue of structures and materials*. Springer Science & Business Media.

Contributions:

A.Vahid Movahedi-Rad conceived, designed and performed the experimental campaign under the supervision of Dr. Anastasios Vassilopoulos and Prof. Thomas Keller. The analysis of the results was carried out by A.Vahid Movahedi-Rad in collaboration with Dr. Anastasios Vassilopoulos and Prof. Thomas Keller.



Chapter 4



Creep-fatigue behavior

4.1. Introduction

Fiber-reinforced polymer (FRP) composites used in engineering structures in several domains, such as wind energy, bridges, automotive, etc., exhibit behavior that is sensitive to the loading pattern due to their cyclic- and time-dependent mechanical properties ^[1,2,3,4,5]. The cyclic-dependent or time-independent mechanical properties such as fatigue stiffness and hysteresis loop are mainly attributed to high frequency fatigue experiments at zero mean stress level in which the time-dependent deformation of material does not have to be considered. However, the time-dependent mechanical properties are related to the rheological deformation of the material when it is subjected to an external load ^[6]. Cyclic-dependent and time-dependent phenomena can interact during fatigue loading, and the degree of their interactions and dominance of one over the other depend on the loading spectrum and material type ^[2,3,4,5,7]. Creep and fatigue have long been recognized as critical mechanisms for the reliability of composites ^[8]. A significant amount of information has meanwhile been acquired regarding the pure creep ^[9,10], the pure fatigue ^[9,10,11], as well as (although this was not always the objective) the combined creep-fatigue behavior ^[3,10,12,13] of polymer matrix composite materials.

The degradation of the cyclic-dependent mechanical properties of laminated composites occurs via several damage mechanisms, such as matrix cracking, debonding, delamination, transverse-ply cracking, and fiber failure, that are activated, either independently or synergistically, during fatigue loading [5,14,15]. The predominance of one or another of the aforementioned damage mechanisms is dependent on both material variables and loading conditions as described in [14]. Laminated composites are susceptible to creep, even at room temperature, due to the viscoelastic nature of their polymeric matrix. At temperatures below the resin's glass transition temperature (T_g), creep is governed by viscoelastic deformation, which may cause crazing of the resin because of its lower ductility, fiber straightening in tension and fiber buckling in compression, delamination at the matrix/fiber interface, fiber breakage, and finally complete failure [16]. Apart from the typical creep deformation, it has been well documented that laminated composites cyclically creep under fatigue mean stresses [4,5,15].

The creep-fatigue behavior of composite materials and structures can be investigated by monitoring the evolution of fatigue hysteresis loops in which their shift indicates cyclic creep effect and the degradation of the fatigue stiffness represents the damage effect. Fatigue stiffness is the slope of each stress-strain hysteresis loop as explicitly described in [15]. Another approach assumes both creep and fatigue effects sequentially by subjecting the component to a loading profile – usually a trapezoidal waveform – with a measurable time under load, while “pure creep” or “pure fatigue” loading are considered as special loading profile cases [9,10,13,17]. Pure creep is considered to be a time-dependent phenomenon that can be investigated by loading the material under static fatigue conditions, i.e. under stress ratio, $R=\sigma_{min}/\sigma_{max}$, equal to 1. Pure fatigue is considered as the cyclic loading at the stress ratio of -1 where the mean cyclic stress is zero [18,19]. In some models, tensile fatigue with zero minimum level ($R=0$) is also assumed as pure fatigue [2,4], although this profile includes a certain amount of constant (mean) cyclic stress during loading. Nevertheless, in many applications, a structural component is subjected to loading profiles that are neither pure creep, nor pure fatigue, but comprise elements of both forms of loading [3,10,16,20].

There is little information in the literature regarding the effect of creep on the fatigue life of composites because of the complexity of such effects and the difficulty involved in clearly separating the two phenomena. Several works exist regarding the frequency effects on the fatigue life of composite materials, see e.g. [21,22,23,24,25], which investigate the effect of creep indirectly however. It is documented that any frequency increase improves the fatigue life of several material systems, since the time under load (cyclic creep) decreases [26,27,28]. However, this only remains true as long as the increased frequency does not result in loading rates sufficiently high to produce considerable temperature increases that soften the matrix and decrease the fatigue life [24]. Fewer works investigate the creep-fatigue interaction in composite materials however, e.g., [7,9,14,26,29], all agreeing that creep

and fatigue are mutually influencing phenomena ^[7]. For example, Vieille et al. ^[7] showed that fatigue life could be extended with prior creep depending on loading conditions in a woven-ply thermoplastic laminate at temperatures higher than T_g . Similarly, in angle-ply thermoset graphite/epoxy composites, it was also shown that sustained periods of static loads have significant retardation effects on damage propagation and therefore extended fatigue life ^[26]. In unidirectional thermoset carbon/epoxy laminates however, it was observed that the repetitive interruption of fatigue loading at σ_{max} reduced fatigue life ^[32]. It is thus commonly accepted that to a great extent, creep plays a significant role in high-cycle fatigue regimes, especially at low frequencies, when the time under load is increased ^[17,26]. In such cases, creep is dominant, and time-dependent failure occurs, while the failure is mainly cycle-dominated at high-cycle fatigue regimes under high frequencies ^[29,30].

Although creep and fatigue coincide in any fatigue loading profile, the physics of damage are different for cyclic creep and fatigue, since both phenomena involve different types of damage mechanisms and processes ^[16,31]. Very limited experimental evidence exists on this topic, since creep and fatigue effects on damage development are usually not decomposed and their joint effect on fatigue life is investigated ^[7,26,32]. According to the available literature, in some cases, the effect of creep on fatigue life appears to be beneficial ^[7,14,26], while in others it is shown that creep can act synergistically with fatigue mechanisms to accelerate damage accumulation ^[9,29]. Therefore, it is not yet clear under which conditions - for example the applied stress level and hold time - creep has a positive, negative, or neutral effect on fatigue life. In addition, to the best of the authors' knowledge, the creep effect on the evolution of fatigue damage during cyclic loading and the effect of fatigue damage on creep behavior during the interruption have not yet been clearly discussed. Furthermore, for the study of creep-fatigue behavior, neither continuous fatigue nor trapezoidal waveform represents a realistic scenario for the description of the “creep-fatigue loading”.

The objective of this work is to investigate the creep-fatigue interaction effects on the fatigue and creep behavior of $\pm 45^\circ$ angle-ply GFRP laminates at different stress levels and hold times by monitoring the evolution of the mechanical, thermal, and optical properties of the material as well as the failure modes. A more realistic loading pattern was selected in which constant amplitude fatigue experiments intermitted by constant loads for 2h and 48h hold times, at the maximum cyclic load, were performed. The material performance was continuously monitored via measurement of the stress-strain and the self-generated temperature developments during the experiments. The evolution of the damage and the developed failure modes were also recorded by monitoring the variation of the material's transparency during the loading and studying the fracture surfaces. In addition to the fatigue experiments, pure creep experiments were performed on the same material system to facilitate the analysis of the results and provide useful material for the discussion on the creep-fatigue interaction.

The experimental results of this work were compared to relevant fatigue data previously obtained from continuous constant amplitude fatigue experiments by the authors ^[15].

4.2. Experimental procedure

4.2.1 Material and specimen preparation

In order to highlight the creep effects on the tension-tension fatigue behavior of laminated composites, angle-ply glass/epoxy specimens with $[\pm 45]_{2s}$ layout were selected. The average dimensions of the specimens were $250.0 \times 25.0 \times 2.3 \text{ mm}^3$ (length \times width \times thickness) according to ASTM D3039 ^[33]. Unidirectional E-glass fiber fabrics (EC 9-68) with an area density of 425 gr/m^2 and layer thickness of 0.45 mm were used. These fabrics comprised a finish bonding agent, which provided better adhesion to the matrix. The low viscosity resin, Biresin® CR83, mixed with the hardener Sika CH83-2, in a ratio of 3:1 was used for impregnation of the fabrics. Laminates of dimensions $500 \times 500 \times 2.3 \text{ mm}^3$ were fabricated by vacuum assisted hand lay-up, using a vacuum pump with a pressure of 0.9 bar. The fabrication was performed on a plastic substrate, which was coated with a release agent to prevent resin from bonding to the surface after fabrication. Each laminate was kept in a vacuum bag for 24 hours under laboratory conditions ($22 \pm 2^\circ\text{C}$, $40 \pm 10\% \text{ RH}$), and subsequently placed in an oven at 70°C for eight hours to complete the curing process. The achieved fiber content was 62% by volume as determined according to burn-off experiments as described in ASTM D 3171-99 ^[34]. Specimens were then cut from the laminates using a water-jet cutting machine and two aluminum tabs with dimensions of $45 \times 25 \times 4 \text{ mm}^3$ were glued to each specimen end with a cyanoacrylate glue for gripping purposes.

4.2.2 Experimental set-up and instrumentation

4.2.2.1 Pure creep

The creep experiments were performed using in-house designed and fabricated creep frames, schematically shown in Fig. 4.1. The creep load was applied by hanging different weights from the lever arm (point A in Fig. 4.1a), in order to derive creep stresses of between 49-70 MPa, the same range as the maximum cyclic stresses developed during the fatigue experiments (see below). The measurement of the longitudinal creep displacement was performed by two vertical displacement transducers (LVDTs) with a measurement accuracy of 0.02 mm, attached on both sides of the specimens as shown in Fig. 4.1b. A small difference in the LVDT results due to specimen warping during installation in the fixture and initial loading was observed, however it was less than 2% and remained constant until the end of each experiment. Therefore, the average displacement was

used for the analysis. The experimental matrix is shown in Table 4.1, with the specimen denomination “creep” denoting pure creep experiment, followed by the stress level.

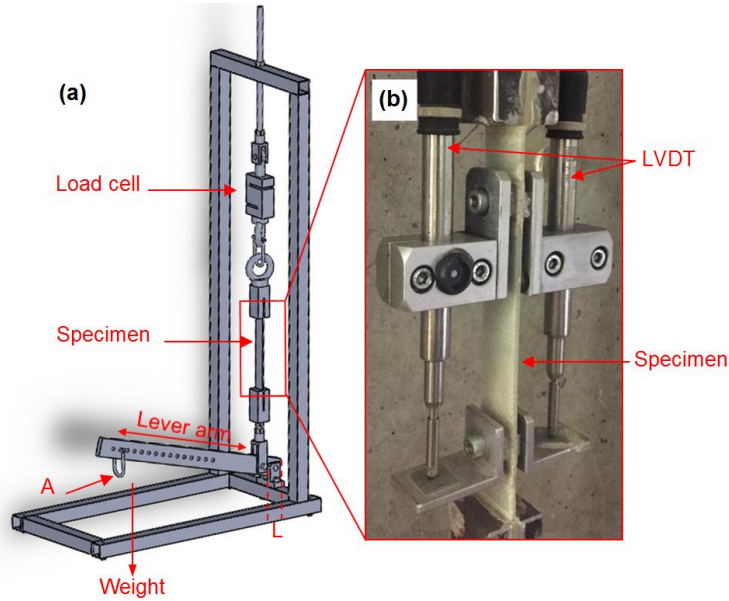


Fig. 4.1. Creep experimental set-up.

Table 4.1. Overview of creep experiments and results

No	Code	σ_0 (MPa)	t_f (h)
1	Creep-70	70.0	213.5
2	Creep-68	68.0	322.6
3	Creep-64	64.2	507.4
4	Creep-58	58.2	1007.9
5	Creep-53	53.4	15768.0
6	Creep-49	48.6	17500(On going)

4.2.2.2 Creep-fatigue

All interrupted fatigue experiments were carried out on an Instron 8800 hydraulic universal testing rig of 100-kN capacity with accuracy of ± 0.2 kN. Fig. 4.2 shows a schematic representation of the applied loading profile, comprising repetitive loading blocks of constant amplitude and hold times up to specimen failure. For each experiment, the load was increased until the mean value was reached in 60 seconds. Subsequently, sinusoidal constant amplitude fatigue loading was applied for a predetermined number of cycles, i.e. 20% of the average continuous fatigue life, obtained for the same stress levels in [15]. The cyclic loading was performed in the range of maximum stress levels of 47 – 70 MPa based on

ASTM D7791-12 ^[35]. In order to examine the effect of short and long hold times on the fatigue behavior, 2h or 48h were selected as schematically shown in Fig. 4.2. The duration of 20% of the fatigue life in each loading block, as well as the hold time, were selected to obtain a reasonable number of interruptions and total duration of the fatigue experiments. The stress ratio, $R=\sigma_{min}/\sigma_{max}$, was kept constant to 0.1 to apply tensile cyclic loads to the specimens. A loading rate, \dot{F} , of 30.5 kN/s was used for all experiments. This loading rate was derived after preliminary experiments to avoid excessive temperature increases during fatigue loading ^[15]. Different frequencies were thus obtained to keep the loading rate constant for all stress levels. Four specimens were examined at each of the seven selected stress levels for the case of the 2h hold time, and two specimens per stress level when the hold time was set to 48h. The experimental matrix is shown in Table 4.2. The specimens are denominated as follows: the first term, “Cref”, denotes creep-fatigue, the second term refers to the stress ratio, the third term indicates the maximum fatigue stress, the fourth term the duration of the hold time (2h or 48h), while the last letter denotes the specimen identification number for each parameter combination. All experiments were performed in an environmental chamber regulated to a constant temperature of 20°C. Two fans were used to circulate the air inside the chamber and cool the specimens.

Different instrumentation was used to monitor the mechanical, thermal, and optical changes in the specimens during and after the fatigue process. During the fatigue experiments, the machine’s displacement, load and number of cycles were recorded at a frequency depending on the stress levels, i.e. from once per 10 cycles at high stress levels to once per 1000 cycles at low stress levels. The variation of the longitudinal strain was measured by a high-resolution video-extensometer (a Point Grey - Grasshopper3 camera with a resolution of 1936×1216 pixels and a Fujinon HF35SA-1 35 mm F/1.4 lens) with a frequency of acquisition of 160 fps. The video-extensometer measured the changes of position of two lines at an average distance of 13 cm apart marked on the specimens’ surfaces. A LED white light with negligible heat emission was projected onto the sample surface to enhance measurement accuracy. Approximately twenty-five load and displacement measurements were recorded per cycle to estimate the strain fluctuations, fatigue stiffness, and hysteresis loops throughout the fatigue life of all the examined specimens. To record the evolution of the specimens’ surface temperature during the fatigue experiments, an infrared (IR) thermal camera with an accuracy of 0.1°C and optical resolution of 160×120 pixels was also employed, starting 1 cm away from each grip as described in ^[15]. In order to detect the damage development at a macro-scale level, photographs of the translucent specimens were taken at regular intervals (depending on life expectancy) with a digital camera with maximum aperture f/2.8 and focal length range of 24–70 mm. Damage in the material volume was attributed to changes in the reflectance, which indicated new interfaces in the path of the penetrated light ^[15]. A bright white light source was positioned behind the specimens to assist this

procedure. After failure, the failure surfaces were examined using a digital handheld Dino-Lite microscope, AD7013MZT, with magnification of 20x and resolution of 2592×1944 pixels, and photos were taken of all specimens.

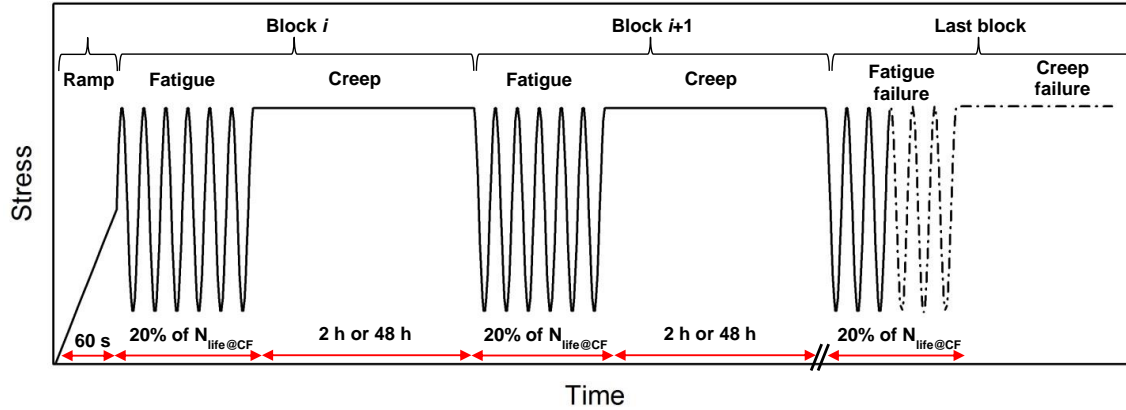


Fig. 4.2. Schematic representation of loading pattern in interrupted fatigue experiments.

4.3. Experimental results and discussion

4.3.1 Pure creep experiments

The evolution of the creep strain, ε , as a function of time is shown in Fig. 4.3a. Typical creep curves were obtained for all stress levels: An elastic strain, followed by a primary creep stage characterized by a rapid initial strain increase, although with a decreasing trend, subsequently followed by a steady state stage with minimum strain rate. The strain increased drastically towards failure. The time to failure for each specimen is shown in Table 4.1. The isochrone stress-strain curves are plotted in Fig. 4.3b by determining the strain values at different stress levels at a constant time. As can be observed from the isochrone curves, the material exhibited a non-linear viscoelastic behavior in which the degree of nonlinearity increased with stress level.

The evolution of the creep strain at $\sigma_{\max} = 70$ MPa and corresponding specimen translucency are shown in Fig. 4.4. No damage was visually observed in the specimen during the primary creep; however, at the beginning of steady state region, damage gradually appeared at different locations along the fibers and propagated uniformly throughout the specimen volume. Creep failure occurred at the third stage after concentrated damage development.

Table 4.2. Overview of interrupted fatigue experiments and main results

No	Code	σ_{\max} (MPa)	Frequency (Hz)	N_{Block}	$t_{\text{Creep}}(\text{h})$	N_f	n_b	Failure
1	Cref-0.1-70-2-a	70.0	3.95	230	2	1840	8	Creep
2	Cref-0.1-70-2-b	70.0	3.95	230	2	1150	5	Creep
3	Cref-0.1-70-2-c	70.0	3.95	230	2	1150	5	Creep
4	Cref-0.1-70-2-d	70.0	3.95	230	2	1150	5	Creep
5	Cref-0.1-70-48-a	70.0	3.95	230	48	230	1	Creep
6	Cref-0.1-70-48-b	70.0	3.95	230	48	230	1	Creep
7	Cref-0.1-68-2-a	68.0	4.35	365	2	6126	16	Fatigue
8	Cref-0.1-68-2-b	68.0	4.35	365	2	2655	7	Fatigue
9	Cref-0.1-68-2-c	68.0	4.35	365	2	2732	7	Fatigue
10	Cref-0.1-68-2-d	68.0	4.35	365	2	1460	4	Creep
11	Cref-0.1-68-48-a	68.0	4.35	365	48	1825	5	Creep
12	Cref-0.1-68-48-b	68.0	4.35	365	48	730	2	Creep
13	Cref-0.1-64-2-a	64.2	4.68	500	2	2500	5	Creep
14	Cref-0.1-64-2-b	64.2	4.68	500	2	4220	8	Fatigue
15	Cref-0.1-64-2-c	64.2	4.68	500	2	5731	11	Fatigue
16	Cref-0.1-64-2-d	64.2	4.68	500	2	4000	8	Creep
17	Cref-0.1-64-48-a	64.2	4.68	500	48	2000	4	Creep
18	Cref-0.1-64-48-b	64.2	4.68	500	48	1000	2	Creep
19	Cref-0.1-58-2-a	58.2	5.06	3100	2	14527	4	Fatigue
20	Cref-0.1-58-2-b	58.2	5.06	3100	2	43023	13	Fatigue
21	Cref-0.1-58-2-c	58.2	5.06	3100	2	25466	8	Fatigue
22	Cref-0.1-58-2-d	58.2	5.06	3100	2	15959	5	Fatigue
23	Cref-0.1-58-48-a	58.2	5.06	3100	48	10589	3	Fatigue
24	Cref-0.1-58-48-b	58.2	5.06	3100	48	24385	7	Fatigue
25	Cref-0.1-53-2-a	53.4	5.53	9000	2	42815	4	Fatigue
26	Cref-0.1-53-2-b	53.4	5.53	9000	2	87654	9	Fatigue
27	Cref-0.1-53-2-c	53.4	5.53	9000	2	63288	7	Fatigue
28	Cref-0.1-53-2-d	53.4	5.53	9000	2	43277	4	Fatigue
29	Cref-0.1-53-48-a	53.4	5.53	9000	48	74391	8	Fatigue
30	Cref-0.1-53-48-b	53.4	5.53	9000	48	30704	3	Fatigue
31	Cref-0.1-49-2-a	48.6	6.10	64000	2	160255	2	Fatigue
32	Cref-0.1-49-2-b	48.6	6.10	64000	2	917136	14	Fatigue
33	Cref-0.1-49-2-c	48.6	6.10	64000	2	364394	5	Fatigue
34	Cref-0.1-49-2-d	48.6	6.10	64000	2	145809	2	Fatigue
35	Cref-0.1-49-48-a	48.6	6.10	64000	48	153769	2	Fatigue
36	Cref-0.1-49-48-b	48.6	6.10	64000	48	423859	6	Fatigue
37	Cref-0.1-47-2-a	47.4	6.33	146000	2	384689	2	Fatigue
38	Cref-0.1-47-2-b	47.4	6.33	146000	2	319752	2	Fatigue
39	Cref-0.1-47-2-c	47.4	6.33	146000	2	1095359	7	Fatigue
40	Cref-0.1-47-2-d	47.4	6.33	146000	2	350072	2	Fatigue
41	Cref-0.1-47-48-a	47.4	6.33	146000	48	1356496	9	Fatigue
42	Cref-0.1-47-48-b	47.4	6.33	146000	48	362532	2	Fatigue

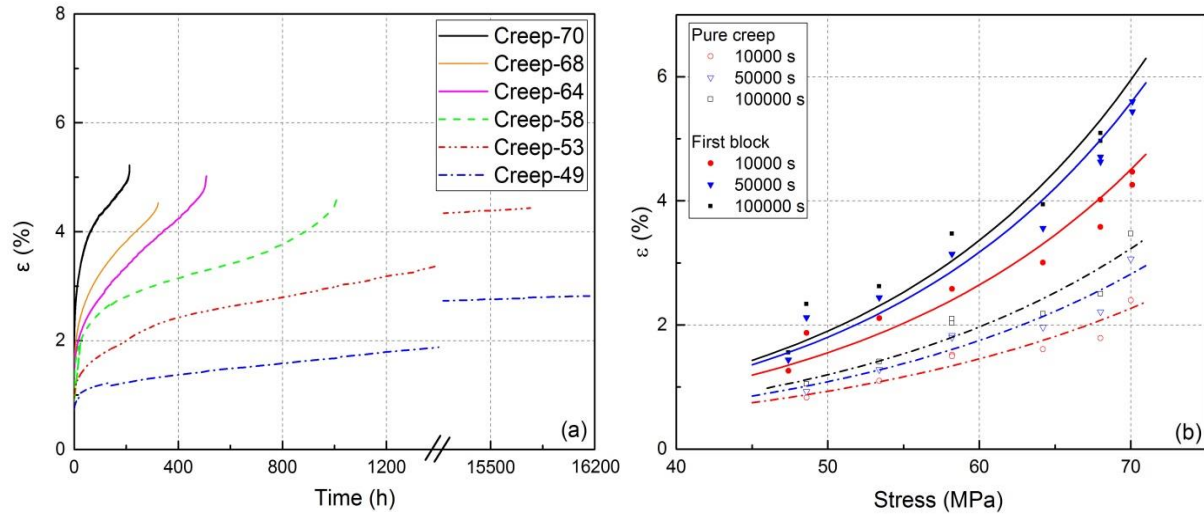


Fig. 4.3. (a) Creep curves at different stress levels, (b) isochrone stress-strain curves at different loading blocks.

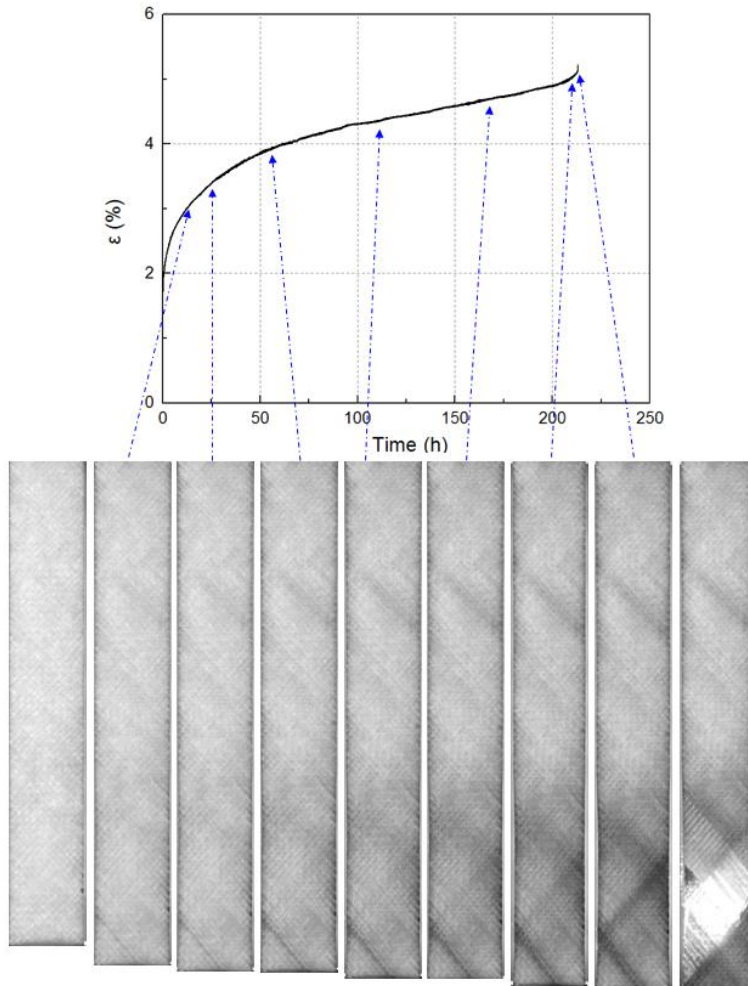


Fig. 4.4. Creep curve at $\sigma_{\max} = 70$ MPa with corresponding representation of light transmittance for different percentages of creep life; (Creep-70).

4.3.2 Creep-fatigue experiments

4.3.2.1 Fatigue life

The fatigue behavior of the specimens loaded under both loading patterns is shown in Fig. 4.5, where the maximum cyclic stress level is plotted against the number of fatigue cycles to failure, N_f . Detailed experimental results are presented in Table 4.3, where N_{Block} denotes the number of fatigue cycles in each loading block, t_{Creep} the applied hold time, N_f the cycles to failure, and n_b the number of completed fatigue loading blocks. The number of cycles to failure was determined by excluding the interruption phase of the loading pattern. All specimens loaded at the highest stress level ($\sigma_{\max} = 70$ MPa), failed during the creep phase of the loading pattern. This changed as the load and hold time were decreased; at σ_{\max} of 68 MPa and 64 MPa with a 2h hold time, failure during the fatigue and creep loading phases was observed. However, the 48h hold time was sufficiently long to cause specimen failure during the creep phase at these stress levels. For stress levels lower than 64 MPa, all failures occurred during the constant amplitude fatigue loading, irrespective of hold time. The regions in the S-N curves in which failure occurred during the creep and fatigue phases are indicated in Fig. 4.5.

The S-N curves of the same specimens under continuous fatigue (without interruptions, denominated ‘‘Conf’’), obtained in [15] are also shown in Fig. 4.5. The fatigue behavior of all loading patterns (Cref and Conf) was simulated by a simple power-law S-N curve equation as follows:

$$\sigma_{\max} = \sigma_0 N_f^{-\frac{1}{k}} \quad (4.1)$$

with the model parameters σ_0 and $1/k$ estimated by linear regression analysis and given in Table 4.3. The resulting curves are also shown in Fig. 4.5. The curve corresponding to the 48h creep load intervals was less steep than the others, due to the creep failure observed at high stress levels. Nevertheless, for shorter creep intervals, the fatigue life improved compared to the continuous fatigue loading. The effect of hold time was less obvious at low stress levels where all loading profiles exhibited a similar lifetime, always taking the experimental scatter into account.

4.3.2.2 Creep strain, hysteresis loops, and stiffness degradation

The evolution of the average cyclic strain with number of cycles is presented in Fig. 4.6, showing a similar trend to the evolution of the pure creep strain with time, presented in Fig. 4.3. The material, during the first loading block of any creep-fatigue experiment, behaved similarly to when loaded under

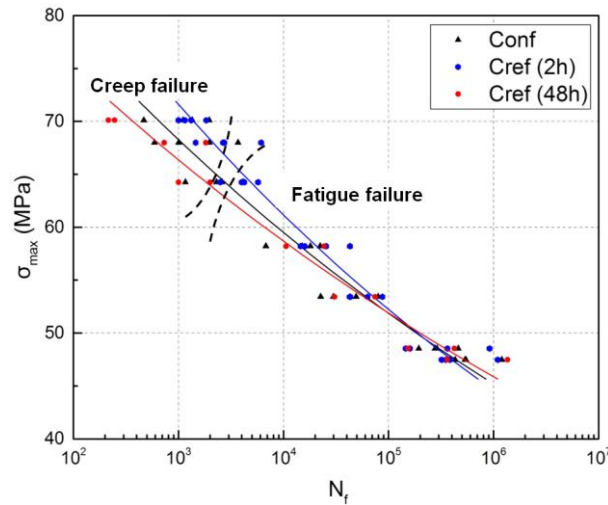


Fig. 4.5. Experimental fatigue data and S-N curves.

Table 4.3. Fatigue parameters for continuous and interrupted loading patterns

Loading pattern	Creep time (h)	σ_0	$1/k$
Continuous loading		106.09	0.0622
Creep-fatigue loading	2	115.01	0.0686
Creep-fatigue loading	48	95.98	0.0534

continuous fatigue profiles. However, it was observed that after the first interruption, depending on the applied stress level and hold time, the creep strain significantly increased during the hold time periods (jumps in the curves), when the material was under constant stress at σ_{\max} . The increase was more obvious for longer hold times and at higher stress levels. In addition, unlike the continuous fatigue where the average cyclic strain monotonically increased, in the creep-fatigue experiments, after the first creep loading and by resuming the cyclic loading, depending on the applied stress level and hold time, three different behaviors of the average cyclic strain were observed - either partially recovered, constant, or increased. These observations were a result of two opposing phenomena. On the one hand, when the loading mode was changed from creep loading (σ_{\max}) to cyclic loading with the average stress lower than σ_{\max} , the specimens recovered and the average cyclic strain decreased. On the other hand, as the number of cycles increased, the specimens crept during the cycles and the average cyclic strain increased. At high stress levels and at the beginning of each loading block, the recovery was more effective than the cyclic creep, which led to a decreasing trend of the average cyclic strain. At

low stress levels and long hold time, due to the balance between recovery and cyclic creep, the observed average cyclic strain was almost constant. However, at low stress levels with short hold time, cyclic creep was dominant and consequently the average cyclic strain increased.

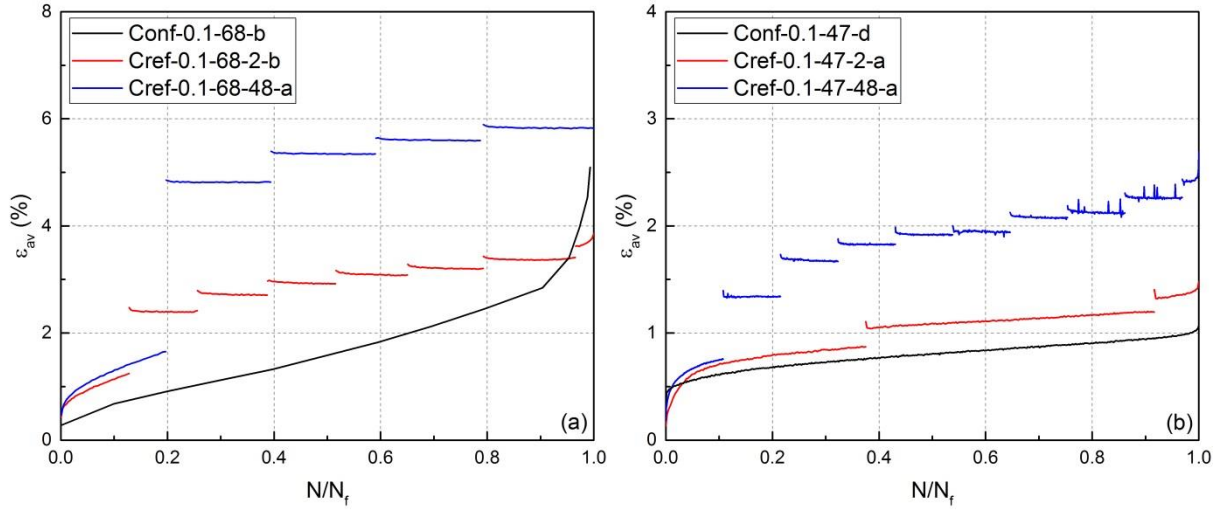


Fig. 4.6. Average cyclic strain versus normalized number of cycles at different loading patterns at two stress levels of (a) $\sigma_{\max} = 68$ MPa, and (b) $\sigma_{\max} = 47$ MPa.

Fig. 4.7 shows the transition from the applied cyclic loading (fatigue part) to the constant stress level (hold time) at $\sigma_{\max} = 70$ MPa. The observed creep curve comprised a rapid increase of creep strain (primary stage), which reached a steady state and continued to increase up to the next loading block. It was observed that the creep behavior in the other loading blocks was similar to the first one; however, the primary stage was shorter. Nevertheless, for this high stress level, even at the 2h hold time, the specimen failed due to creep loading after a sudden creep strain increase (ternary creep curve).

The creep behavior of the specimens during the two hold times is compared to the pure creep behavior at the two stress levels of 64 MPa and 53 MPa in Fig. 4.8. The creep strain rate was faster in creep after fatigue than that recorded during the pure creep experiments, due to the damage accumulated during the fatigue loading blocks, prior to the creep loading. As already mentioned, the isochrone stress-strain curves are shown in Fig. 4.3b for the first loading blocks. Similarly to pure creep, it can be seen that the creep deformation was caused by the non-linear viscoelasticity; with increasing stress level, the degree of nonlinearity increased.

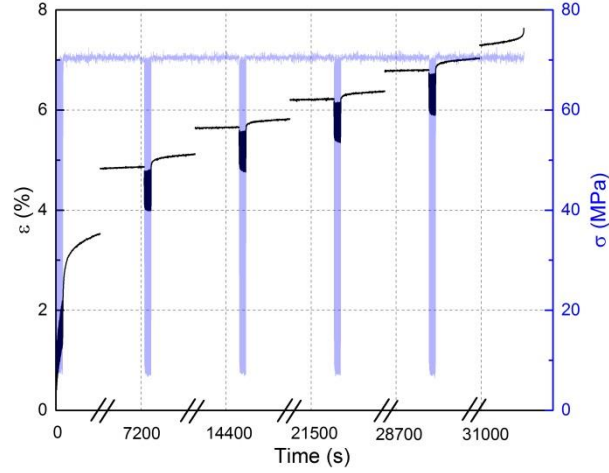


Fig. 4.7. Transition of stress from cyclic loading to constant stress level and corresponding strain response (Cref-0.1-70-2-b).

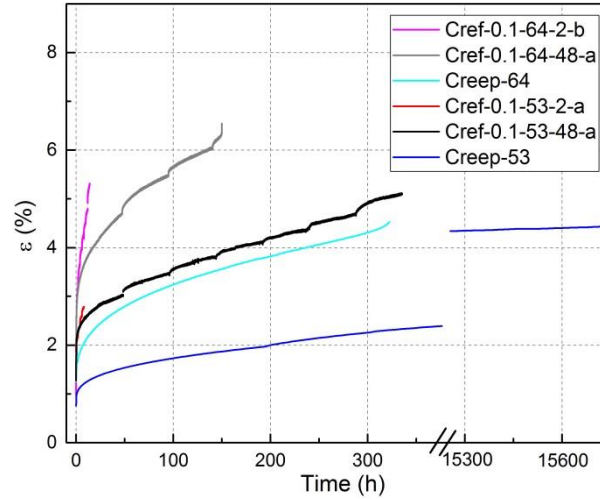


Fig. 4.8. Creep curves at different loading patterns at two different stress levels.

Fig. 4.9 shows part of a specimen surface at the different percentages of the fatigue life at a high stress level. In Fig. 4.9a, the broken line indicates the initial position of a selected fiber bundle before starting the experiment. Fiber realignment was observed after the first loading block, indicated with a solid line in Fig. 4.9b. This fiber realignment gradually increased as the number of loading blocks increased up to specimen failure (Figs. 4.9c and 4.9d). The magnitude of the fiber rotation at the failure point was approximately 5° .

Fig. 4.10 shows the evolution of the normalized fatigue stiffness (E_N/E_I) versus number of cycles at high and low stress levels for all studied loading patterns. Initially, as a result of fatigue matrix damage, the stiffness decreased steeply for all loading patterns [15,36,37,38]. This reduction was more pronounced for lower stress levels due to the higher capacity of the specimen to accumulate damage at

lower stress levels, as explained in [15]. The stiffness of specimens under continuous fatigue loading continued to decrease at a more moderate rate until failure. However, the specimens under creep-fatigue loading patterns were creeping during the hold time (more so at high stress levels and for longer hold times). Under this creep strain, fiber realignment occurred as shown in Fig. 4.9, and the internal stress increased [39]. For this reason the specimens' fatigue stiffness was restored after each fatigue load interruption, but decreased again during the next fatigue loading block. Stiffness restoration, especially after the first fatigue block, was more evident with higher stress levels and longer hold times. On the other hand, at high stress levels and for the longer hold time, creep damage formation shortened the fatigue life (see Fig. 4.5). This phenomenon became more critical at very high stress levels (i.e. 70 MPa), and for the longer hold time, since, as shown in Fig. 4.3b, the materials exhibited a higher degree of nonlinearity.

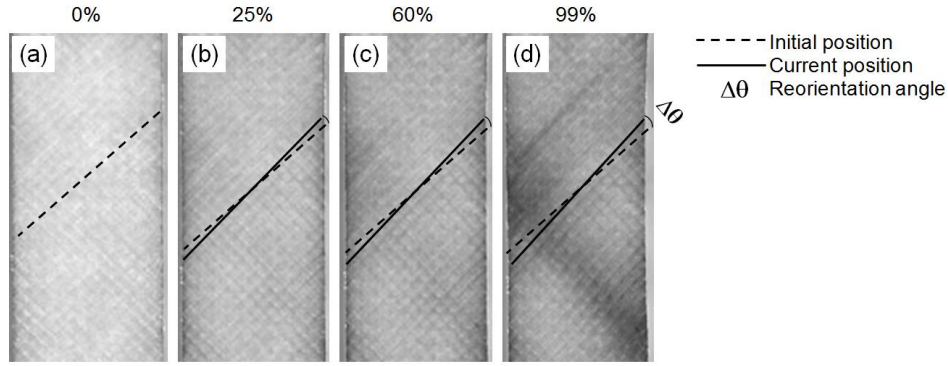


Fig. 4.9. Reorientation of glass fibers at different percentages of fatigue life (Cref-0.1-70-2-d).

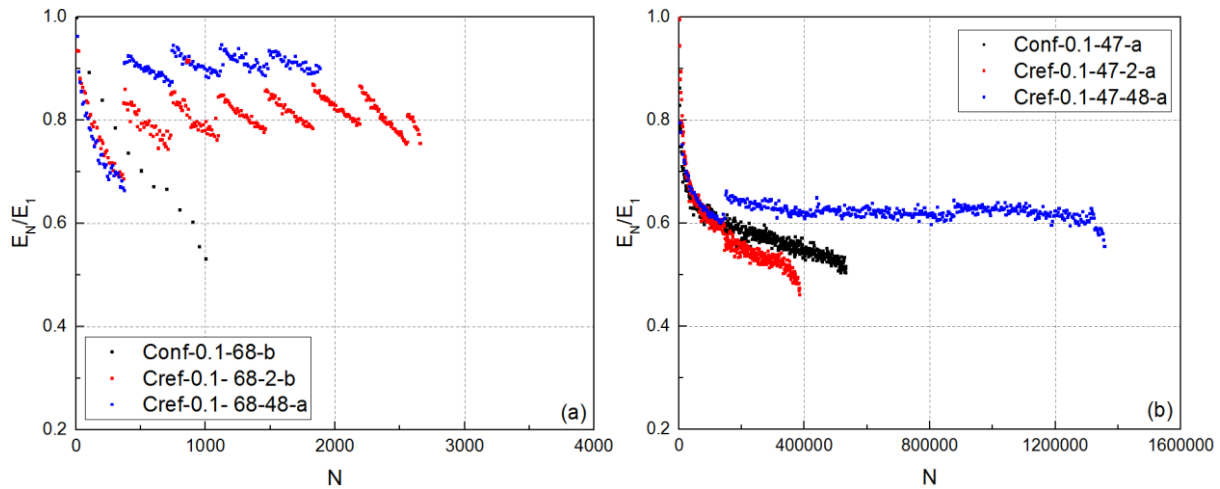


Fig. 4.10. Normalized fatigue stiffness versus number of cycles loaded under different loading patterns at two stress levels (a) $\sigma_{\max} = 68$ MPa, and (b) $\sigma_{\max} = 47$ MPa.

The variation of the hysteresis loop area per cycle versus the number of cycles is shown for selected specimens at high and low stress levels in Fig. 4.11. Internal friction in damaged regions is the main cause of the energy dissipation, and it increases when the areas of unbound regions (e.g. cracks) grow [5,15,40,41]. Additional energy is dissipated due to self-generated temperature as well as the matrix viscoelasticity [41]. The hysteresis loop area of specimens under continuous fatigue loading increased monotonically until specimen failure. However, in creep-fatigue experiments, after each creep loading, the area of the hysteresis loops decreased. This was attributed to the fatigue stiffness restoration, which decreased the cyclic strain amplitude and thus reduced the internal friction. In addition, longer creep time caused higher creep strain and therefore further opening of existing cracks. This was more obvious at high stress levels and the longer hold time. Other reasons for reducing the hysteresis loop area were the lower self-generated temperature (section 4.3.2.3) and higher internal stress compared to the continuous fatigue; however, the effects of these mechanisms were considered negligible. As for the fatigue stiffness, at low stress levels and the short hold time, the trend of the evolution of the hysteresis loop area with number of cycles was the same as that of the specimens loaded continuously until failure. However, when the hold time was increased to 48h, a small decrease in the hysteresis loop area was detected in the first loading block, which was due to the small fatigue stiffness restoration as shown in Fig. 4.10. In addition, by comparing all drops of the hysteresis loop areas after the loading interruption in one experiment, it is seen that the maximum drop occurred in the first loading block because this was where the highest fatigue stiffness restoration occurred.

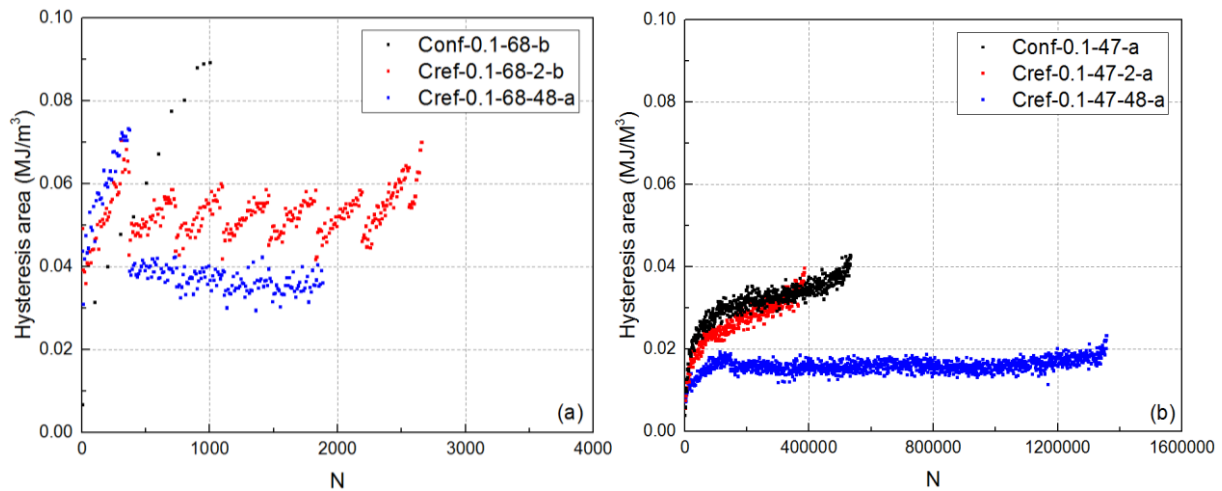


Fig. 4.11. Hysteresis area per cycle versus number of cycles at different stress levels.

4.3.2.3 Damage evolution and self-generated temperature

Figs. 4.12 and 4.13 show the evolution of the specimens' translucency and the corresponding self-generated temperature at different percentages of the specimens' fatigue life for high and low stress levels, respectively. At the high stress level and for the 2h hold time (Fig. 4.12a), up to 25% of fatigue life, no distinguishable damage zone was observable in the specimen and a uniform distribution of surface temperature was measured. As cyclic loading continued, damage gradually appeared along the fibers, at around 45° with respect to the specimen's longitudinal axis. Simultaneously, the distribution of the temperature became slightly uneven, and faint hotspots started appearing in the concentrated damage zone along the fiber direction in which the internal friction was significant. It can be seen that the damage propagated across the specimen volume and several damage zones were formed.

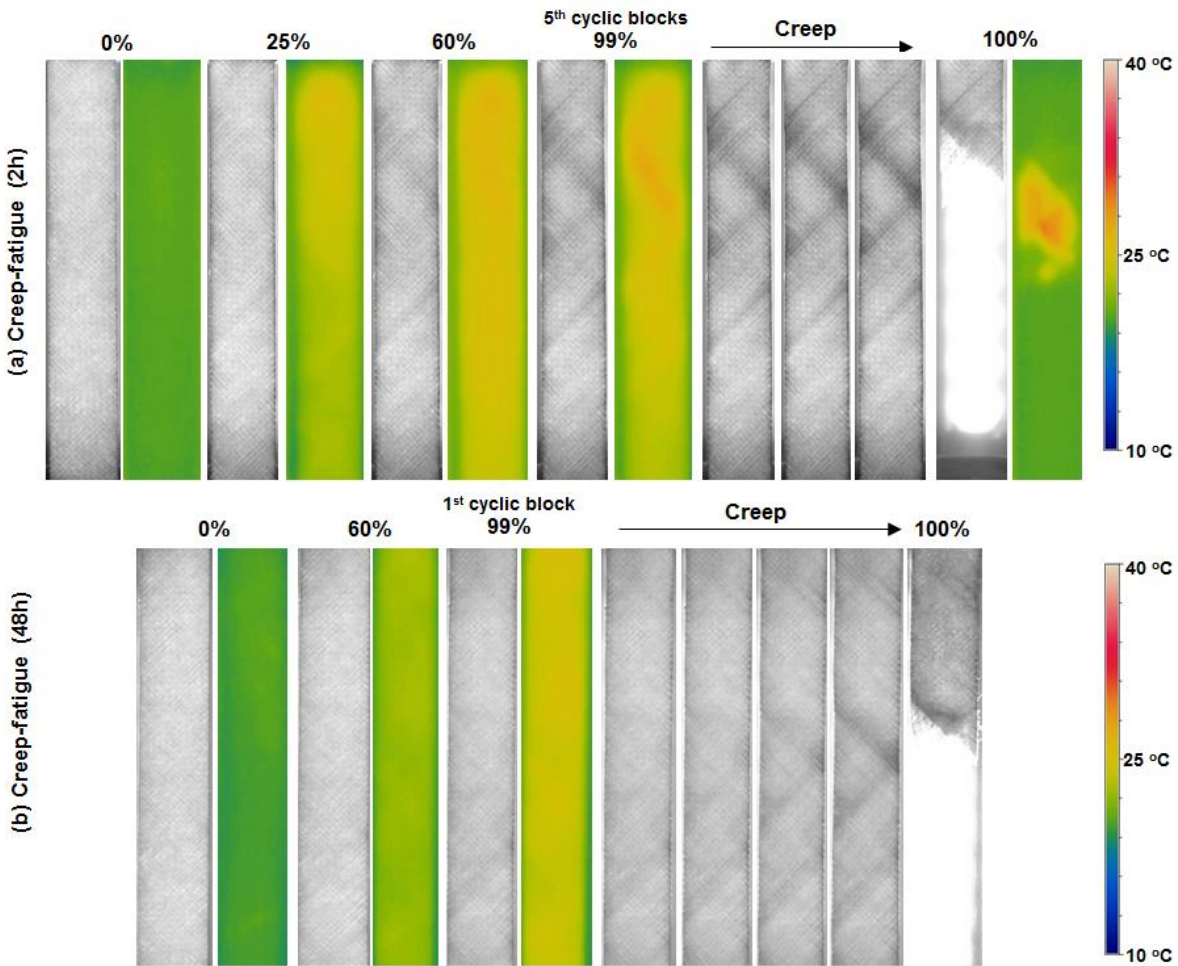


Fig. 4.12. Pairwise representation of light transmittance and self-generated temperature for different percentages of fatigue life at $\sigma_{\text{max}} = 70\text{ MPa}$ (a) $t_{\text{creep}} = 2\text{h}$ (Cref-0.1-70-2-c) and (b) $t_{\text{creep}} = 48\text{h}$ (Cref-0.1-70-48-b).

The damage zones became more evident during the last creep loading period, and finally creep failure occurred at the location of the most severe damage zone with a sudden increase of temperature. When the creep time was increased to 48h (Fig. 4.12b), no specific concentrated damage zone was observed up to the end of the first cyclic loading phase because of the limited number of fatigue cycles. However, during the subsequent creep loading, damage gradually formed and propagated across the specimen volume creating concentrated damage zones, and creep failure finally occurred in the most concentrated damage zone. Specimens loaded under pure creep, exhibited uniformly distributed damage throughout their volume, see Fig. 4.4. Those specimens loaded under continuous fatigue profiles developed more concentrated damage zones as was described in [15]. Specimens loaded under the interrupted creep-fatigue loading showed an intermediate damage state, more similar to pure creep specimens with less damage accumulation [5]. The fiber alignment due to the creep loads at the hold periods reduced local stresses that cause crack initiation as was also described in [26,42,43], lessening the

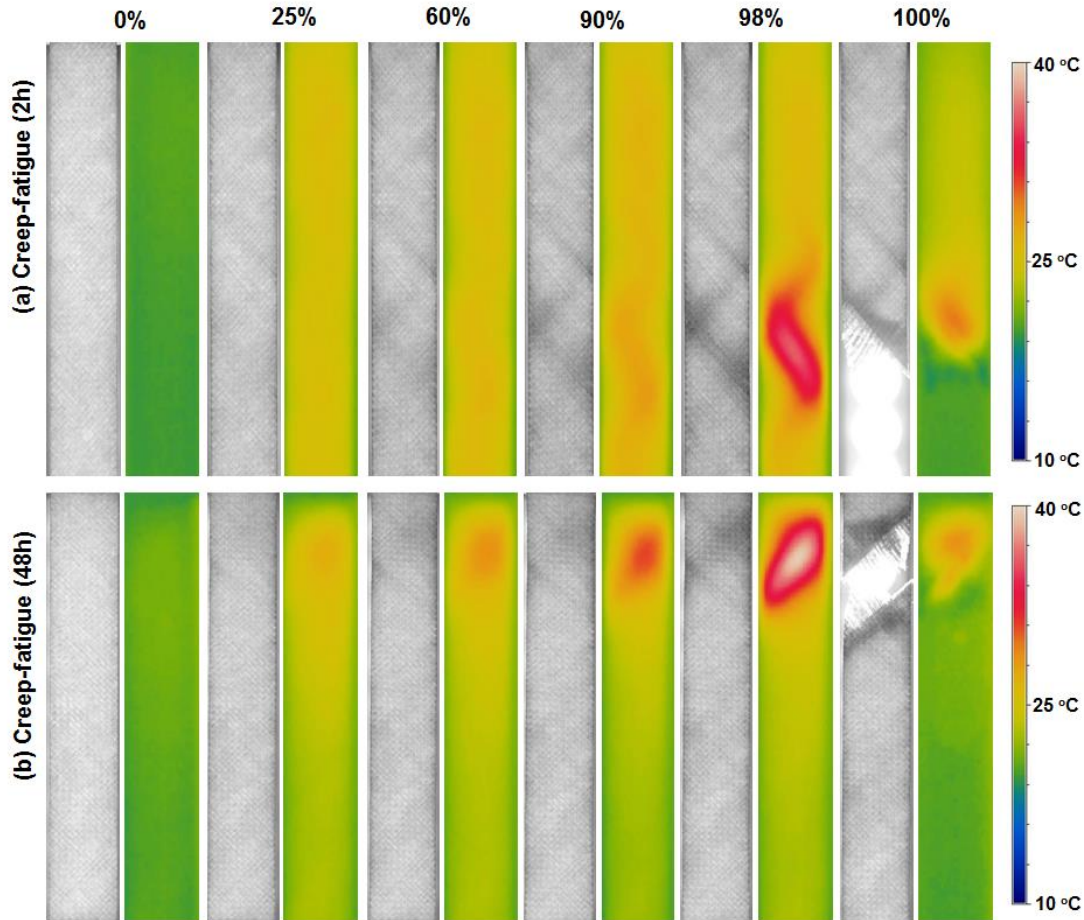


Fig. 4.13. Pairwise representation of light transmittance and self-generated temperature for different percentages of fatigue life at $\sigma_{\max} = 47$ MPa (a) $t_{\text{creep}} = 2$ h (Cref-0.1-47-2-d) and (b) $t_{\text{creep}} = 48$ h (Cref-0.1-47-48-b).

severity of damage zones. At the low stress level (Fig. 4.13), independent of hold time, the damage formed uniformly and propagated across the specimens while a faint hotspot was formed in each specimen in the middle of fatigue life. The comparison of the specimens' translucency between the short and long hold times at this stress level showed that the concentrated damage zone was a little more severe as a result of more applied loading blocks in the loading pattern with the 2h creep time.

The evolution of the maximum surface temperature of selected specimens at high and low stress levels under different loading patterns is shown in Figs. 4.14a and 4.14b, respectively. The evolution of the maximum self-generated temperature under continuous fatigue loading was a ternary type curve, at high and low stress levels. The temperature of specimens under creep-fatigue loading increased similarly to the temperature of specimens under continuous loading until the first interruption; subsequently it dropped during the interruption and increased again when loading was resumed. At the high stress level, since the number of fatigue cycles in each loading block was limited, the specimens' temperature did not increase significantly. In addition, the temperature during the second and all other subsequent loading blocks was lower than the temperature measured during the first loading block because, as discussed above, the internal friction was reduced after each creep loading. As hold time increased, the material also became stiffer, resulting in lower self-generated temperature, as was also validated by the smaller hysteresis area for the longer hold time as presented in Fig. 4.11. The interruptions decreased the self-generated temperature compared to the continuous loading and thus reduced potential material softening. Furthermore, since the temperatures remained clearly below the onset glass transition temperature $T_{g,onset}$ (78 °C) in both cases, the softening effect was considered

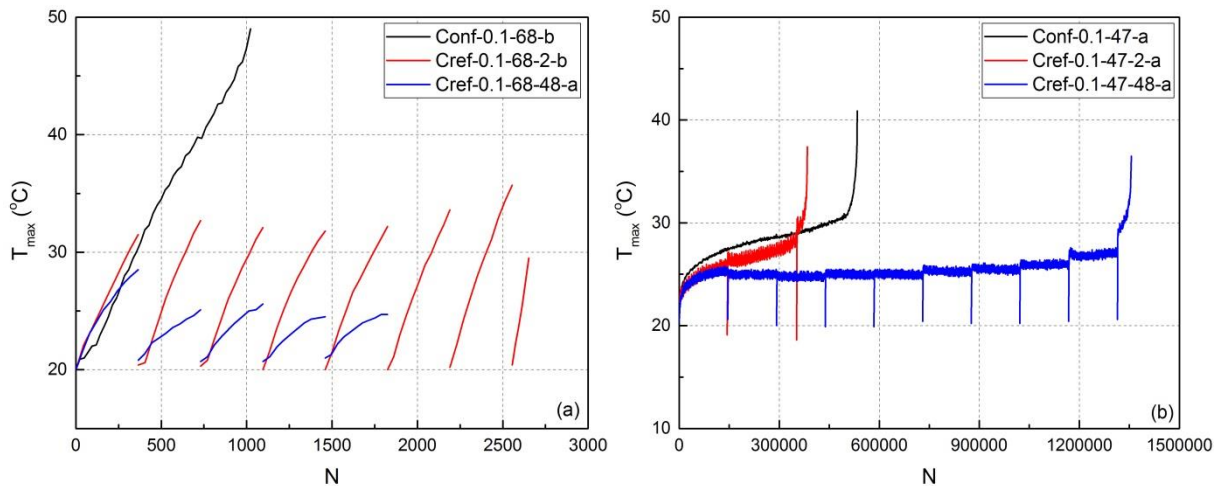


Fig. 4.14. Maximum self-generated temperature versus number of cycles in creep-fatigue experiments (Cref) and continuous fatigue (Conf) at (a) $\sigma_{max} = 68$ MPa, and (a) $\sigma_{max} = 47$ MPa.

minor ^[5]. At the lower stress level, after the initial increase recorded for all loadings, the temperature did reach a steady-state region, except for the last loading block where the temperature continuously increased until specimen failure.

4.3.3 Fracture surfaces and failure mode

The fracture surfaces of specimens loaded under pure creep and creep-fatigue are shown in Fig. 4.15. A main diagonal damage pattern, following the 45° fiber direction, could be noticed. At high stress levels, both for creep and creep-fatigue loading, failure was characterized by extensive fiber pull-out, a consequence of the significant deterioration of the matrix/fiber interfaces, which hindered the transfer of the stresses from the matrix to the fibers at the concentrated damage zones. At moderate and low stress levels, a mixed-mode failure, characterized by fiber pull-out and fiber breakage, was

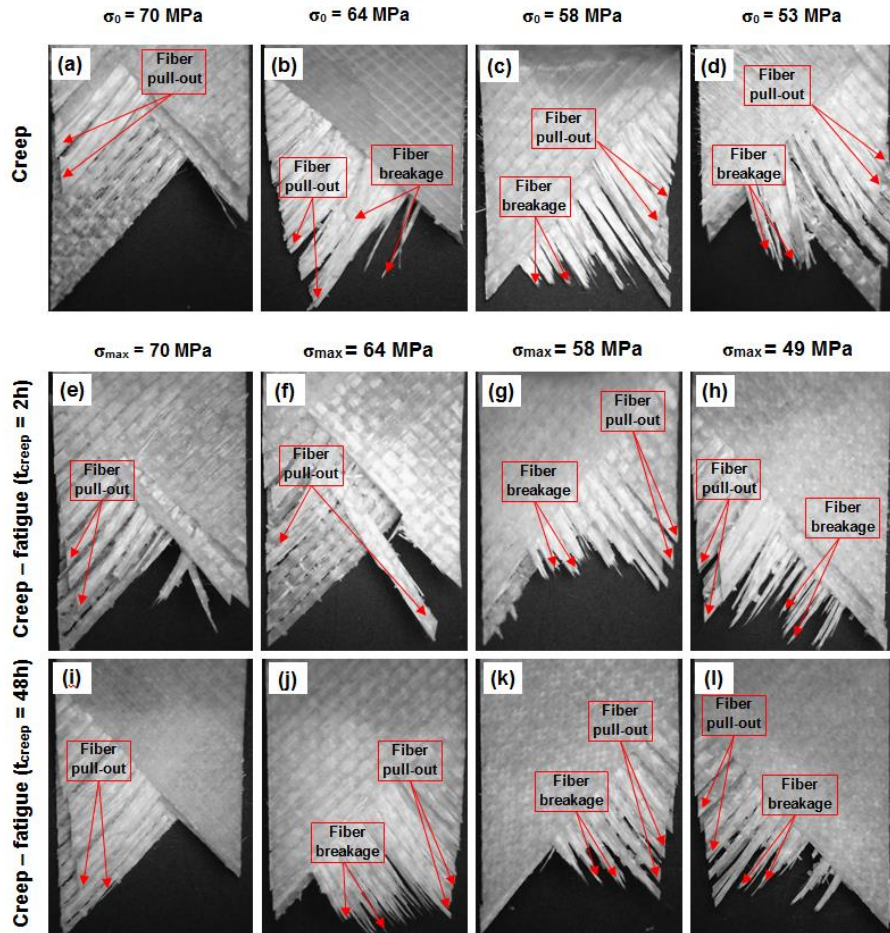


Fig. 4.15. Fracture surfaces under different loading patterns and stress levels, (a) Creep-70, (b) Creep-64, (c) Creep-58, and (d) Creep-53, (e) Cref-0.1-70-2-d, (f) Cref-0.1-64-2-c, (g) Cref-0.1-58-2-c, (h) Cref-0.1-49-2-a, (i) Cref-0.1-70-48-a, (j) Cref-0.1-64-48-a, (k) Cref-0.1-58-48-a, (l) Cref-0.1-49-48-a.

observed with predominant fiber breakage at the lowest stress level, as shown in Figs. 4.15(b-d). The presence of fiber breakage at low stress levels was attributed to the more uniform and less severe damage distribution, which allowed the matrix and interface to transfer stresses to the fibers [5,15]. In the case of mixed-mode failure, the fiber breakage was observed in the central region of the cross-section area, and fiber pull-out occurred near the edges of the specimens. This was attributed to the longer fiber interface at the middle of the specimens being able to transfer more stress to the fibers. Close to the edges, the fibers were more susceptible to pull-out. Therefore, in such cases, specimen geometry may be critical and wider specimens would probably present more fiber breakage.

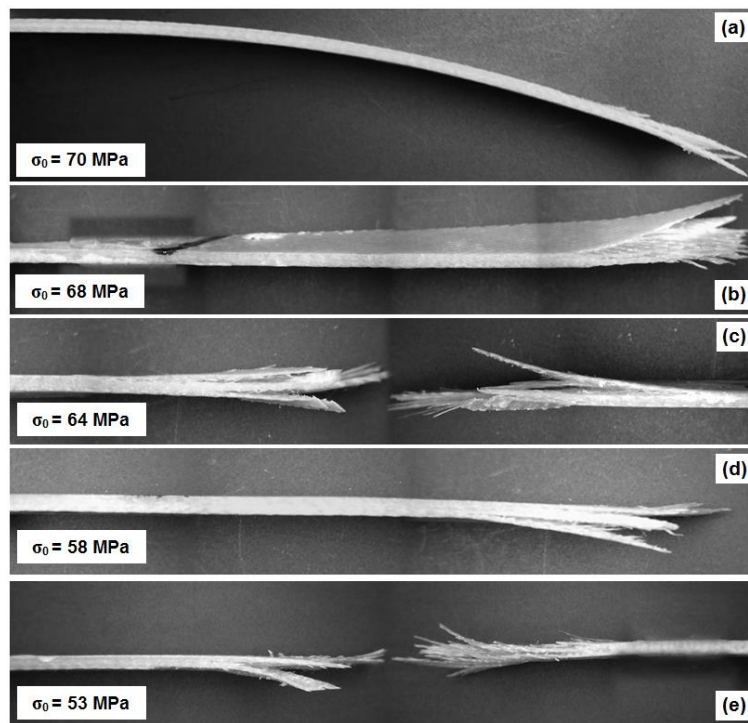


Fig. 4.16. Lateral view of creep failed specimens at different stress levels; (a) Creep-70, (b) Creep-68, (c) Creep-64, and (d) Creep-58, and (e) Creep-53.

The lateral view of the failed creep specimens at different stress levels is shown in Fig. 4.16. Significant out-of-plane deformation (bending and twisting) was observed at high stress levels, as presented in Fig. 4.16a (bending), and 16b (twisting). At different plies of composite, the formed and propagated damage was not uniformly distributed, which affected the recovery of specimens at the moment of failure. As shown in [5], specimen recovery was greater at higher stress and damage levels. Therefore, as a result of non-symmetrical recovery after failure, out-of-plane deformation occurred,

which was greater at higher stress levels. Specimens failed during the creep phase of the creep-fatigue spectrum, see Figs. 4.17a-b, and exhibited similar failure behavior to those loaded under pure creep. Nevertheless, those specimens that failed during the fatigue phase loading did not exhibit any out-of-plane deformation at failure, independent of stress level, as shown in Fig.17c-d.

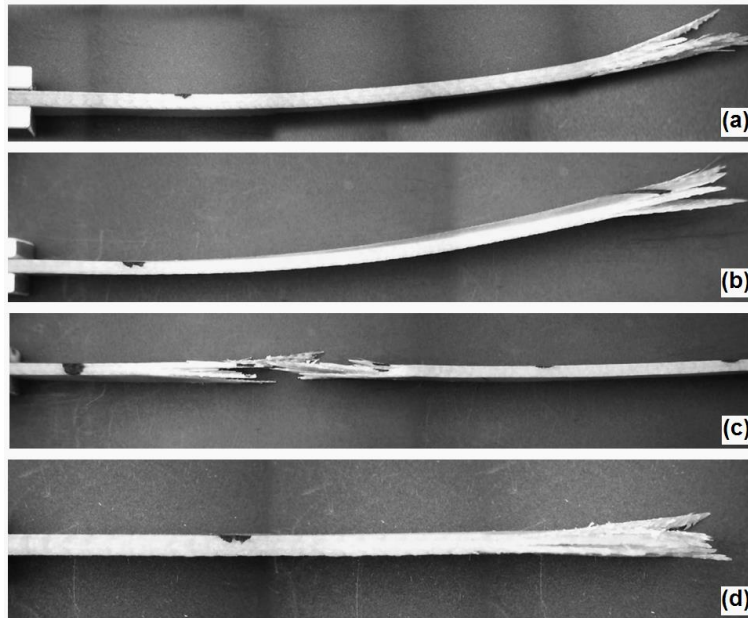


Fig. 4.17. Lateral view of failed specimens at different stress levels, (a) creep failure (Cref-0.1-70-2-a), (b) creep failure (Cref-0.1-68-48-b), (c) fatigue failure (Cref-0.1-68-2-b), and (d) fatigue failure (Cref-0.1-58-2-c).

4.4. Conclusions

The creep-fatigue behavior of angle-ply, $(\pm 45)_{2s}$, glass/epoxy composite laminates has been experimentally investigated in this work. Pure creep and creep-fatigue experiments (constant amplitude fatigue loading regularly interrupted by constant load intervals of 2h or 48h until failure) were performed in order to investigate the effect of creep on the fatigue life and vice versa. The following conclusions were drawn:

- The fatigue life was improved when constant (creep) loads were applied for a short time, 2h in this work. This effect was clear at high stress levels, but not present at low stress levels. This improvement has been attributed to the fiber realignment caused by the creep strain. Nevertheless, longer hold times at high stress levels caused creep failure and therefore premature fatigue failure of the specimens.

- The creep phase of the creep-fatigue loading pattern affected the fatigue stiffness as well as the hysteresis loop area development as the cycles increased. Due to the fiber realignment after each creep phase the fatigue stiffness was restored, and therefore the hysteresis loop area was reduced. This phenomenon was more pronounced after the first creep phase, while fatigue stiffness and hysteresis loop fluctuations were subsequently lower. The phenomenon was more obvious at high stress levels.
- At high stress levels, creep damage started appearing after the primary stage along the fibers, propagated during the steady state, and creep failure occurred at the third stage after concentrated damage development.
- The damage exhibited by the specimens during the cyclic loading phase of the creep-fatigue spectrum accelerated the creep strain development during the hold time; the specimens achieved higher creep strains after fatigue compared to those achieved under pure creep loading. Therefore, at high stress levels specimens were failing at the creep phase following the fatigue loading, although the creep time to failure was much shorter than in the pure creep experiments.
- The fiber alignment led to a reduction of internal friction in the specimens during the fatigue phase. Therefore, the self-generated temperature after the creep phase at high stress levels did not increase to the same magnitude as after the first cyclic loading phase.
- Independent of loading pattern, the fracture of specimens was mainly characterized by fiber pull-out at high stress levels, but by a mixed-mode failure with fiber pull-out and fiber breakage at moderate and lower stress levels. In addition, creep failure at high stress levels caused out-of-plane deformations (bending and twisting) due to the non-uniform damage distribution at different plies, and subsequent non-symmetrical recovery after failure.

References

- [1] Vassilopoulos, A. P., & Keller, T. (2011). *Fatigue of fiber-reinforced composites*. Springer Science & Business Media.
- [2] Miyano, Y., Nakada, M., McMurray, M. K., & Muki, R. (1997). Prediction of flexural fatigue strength of CRFP composites under arbitrary frequency, stress ratio and temperature. *Journal of Composite Materials*, 31(6), 619-638.
- [3] Petermann, J., & Schulte, K. (2002). The effects of creep and fatigue stress ratio on the long-term behaviour of angle-ply CFRP. *Composite Structures*, 57(1-4), 205-210.

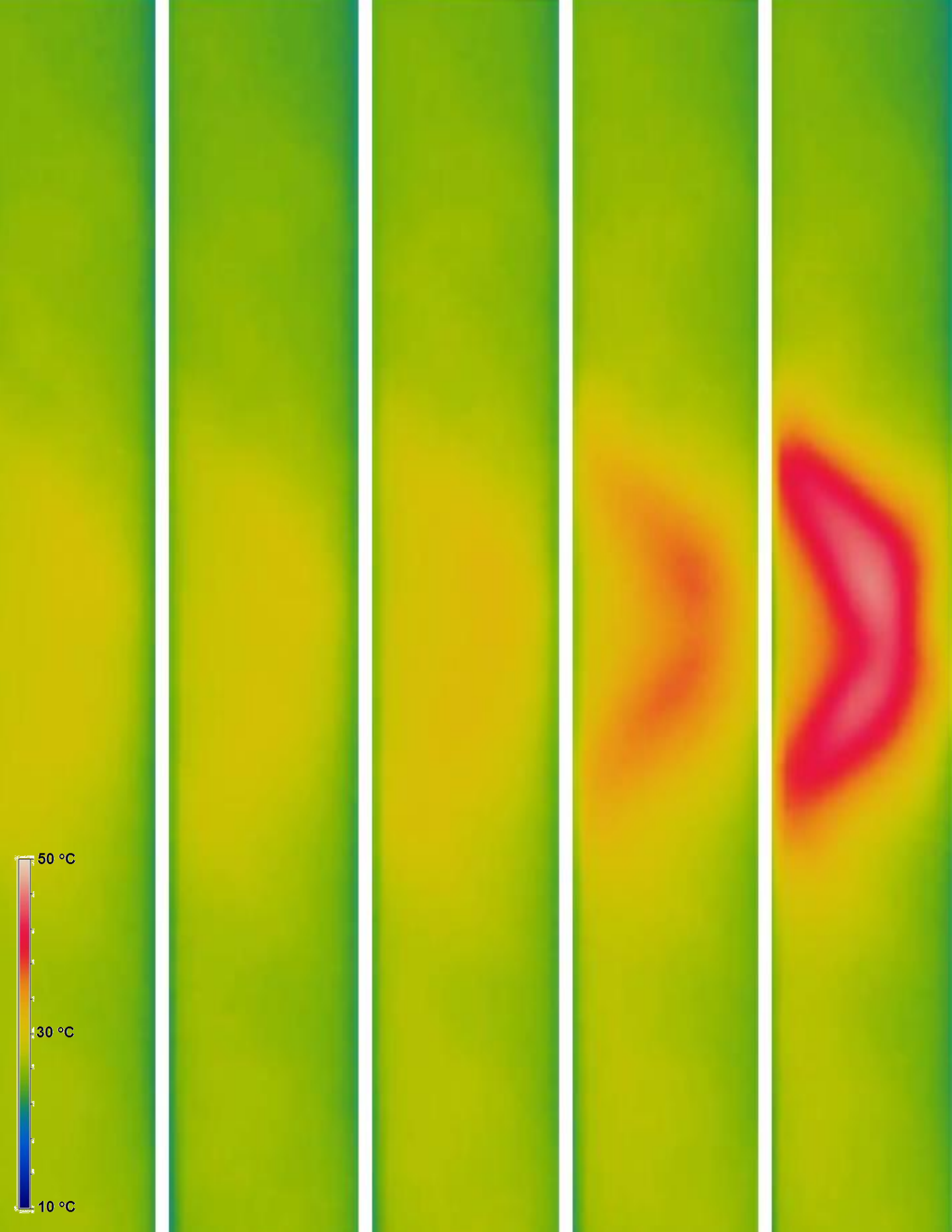
-
- [4] Guedes, R. M. (2007). Durability of polymer matrix composites: Viscoelastic effect on static and fatigue loading. *Composites Science and Technology*, 67(11-12), 2574-2583.
- [5] Movahedi-Rad, A. V., Keller, T., & Vassilopoulos, A. P. (2018). Interrupted tension-tension fatigue behavior of angle-ply GFRP composite laminates. *International Journal of Fatigue*, 113, 377-388.
- [6] Tschoegl, N.W. (1997). Time dependence in material properties: An overview. *Mechanics of Time-Dependent Materials*. 1, 1-31.
- [7] Vieille, B., Albouy, W., & Taleb, L. (2014). About the creep-fatigue interaction on the fatigue behaviour of off-axis woven-ply thermoplastic laminates at temperatures higher than Tg. *Composites Part B: Engineering*, 58, 478-486.
- [8] Hulbert, G. C. (1956). Plastics Structures. *The Aeronautical Journal*, 60(542), 114-120.
- [9] Bowman, J., & Barker, M. B. (1986). A methodology for describing creep-fatigue interactions in thermoplastic components. *Polymer Engineering & Science*, 26(22), 1582-1590.
- [10] Shenoi, R. A., Allen, H. G., & Clark, S. D. (1997). Cyclic creep and creep-fatigue interaction in sandwich beams. *The Journal of Strain Analysis for Engineering Design*, 32(1), 1-18.
- [11] Wong, E. H., & Mai, Y. W. (2014). A unified equation for creep-fatigue. *International Journal of Fatigue*, 68, 186-194.
- [12] Kaminski, M., Laurin, F., Maire, J. F., Rakotoarisoa, C., & Hémon, E. (2015). Fatigue damage modeling of composite structures: the onera viewpoint. *AerospaceLab*, (9), p-1.
- [13] Mandell, J. F., Samborsky, D. D., Miller, D. A., Agastra, P., & Sears, A. T. (2016). *Analysis of SNL/MSU/DOE Fatigue Database Trends for Wind Turbine Blade Materials*. No. SAND2016-1441. Sandia National Lab.(SNL-NM), Albuquerque, NM (United States).
- [14] Reifsnider, K. L., & Talug, A. (1980). Analysis of fatigue damage in composite laminates. *International Journal of Fatigue*, 2(1), 3-11.
- [15] Movahedi-Rad, A. V., Keller, T., & Vassilopoulos, A. P. (2018). Fatigue damage in angle-ply GFRP laminates under tension-tension fatigue. *International Journal of Fatigue*, 109, 60-69.
- [16] Raghavan, J., & Meshii, M. (1997). Creep rupture of polymer composites. *Composites Science and Technology*, 57(4), 375-388.
- [17] Crowther, M. F., Wyatt, R. C., & Phillips, M. G. (1989). Creep-fatigue interactions in glass fibre/polyester composites. *Composites science and technology*, 36(3), 191-210.
- [18] Vassilopoulos, A. P., Manshadi, B. D., & Keller, T. (2010). Influence of the constant life diagram formulation on the fatigue life prediction of composite materials. *International journal of fatigue*, 32(4), 659-669.

- [19] Mallick, P. K., & Zhou, Y. (2004). Effect of mean stress on the stress-controlled fatigue of a short E-glass fiber reinforced polyamide-6, 6. *International journal of fatigue*, 26(9), 941-946.
- [20] Sayyidmousavi, A., Bougherara, H., & Fawaz, Z. (2015). The role of viscoelasticity on the fatigue of angle-ply polymer matrix composites at high and room temperatures-a micromechanical approach. *Applied Composite Materials*, 22(3), 307-321.
- [21] Schapery, R. A. (1975). A theory of crack initiation and growth in viscoelastic media. *International Journal of Fracture*, 11(1), 141-159.
- [22] Mandell, J. F., & Meier, U. (1983). Effects of stress ratio, frequency, and loading time on the tensile fatigue of glass-reinforced epoxy. In *Long-term behavior of composites*. ASTM International.
- [23] Saff, C. R. (1983). Effect of load frequency and lay-up on fatigue life of composites. In *Long-term behavior of composites*. ASTM International.
- [24] Sun, C. T., & Chan, W. S. (1979, January). Frequency effect on the fatigue life of a laminated composite. In *Composite materials: testing and design (fifth conference)*. ASTM International.
- [25] Barron, V., Buggy, M., & McKenna, N. H. (2001). Frequency effects on the fatigue behaviour on carbon fibre reinforced polymer laminates. *Journal of materials science*, 36(7), 1755-1761.
- [26] Sun, C. T., & Chim, E. S. (1981). Fatigue retardation due to creep in a fibrous composite. In *Fatigue of Fibrous Composite Materials*. ASTM International.
- [27] Perreux, D., & Joseph, E. (1997). The effect of frequency on the fatigue performance of filament-wound pipes under biaxial loading: experimental results and damage model. *Composites science and technology*, 57(3), 353-364.
- [28] Philippidis, T. P., & Vassilopoulos, A. P. (2003). Fatigue strength of composites under variable plane stress. In *Fatigue in Composites* (pp. 504-525).
- [29] Harris, B. (1977). Fatigue and accumulation of damage in reinforced plastics. *Composites*, 8(4), 214-220.
- [30] Samborsky, D., Mandell, J. F., & Miller, D. A. (2014). Creep/Fatigue Response of Resin Infused Biaxial Glass Fabric Laminates in Reversed Loading. In *32nd ASME Wind Energy Symposium* (p. 0172).
- [31] Enyama, J. (1993). Effects of stress ratio on flexural fatigue behavior of a satin woven CFRP laminate. In *Proc. 3rd Japan SAMPE* (Vol. 2, pp. 2418-2421).
- [32] Koimtzoglou, C., Dassios, K. G., & Galiotis, C. (2009). Effect of Processing and Loading Conditions upon the Fatigue Behaviour of a Cf/Epoxy Laminate. *Advanced Composites Letters*, 18(3), 95.
- [33] ASTM D3039/D3039M-14 Standard Test Method for Tensile Properties of Polymer Matrix Composite Materials. ASTM International; 2014.

- [34] ASTM, D3171–99. Standard test methods for constituent content of composite materials. ASTM International; 2002.
- [35] ASTM, D7791–17. Standard Test Method for Uniaxial Fatigue Properties of Plastics. ASTM International; 2017.
- [36] Varvani-Farahani, A., & Shirazi, A. (2007). A fatigue damage model for (0/90) FRP composites based on stiffness degradation of 0 and 90 composite plies. *Journal of Reinforced Plastics and Composites*, 26(13), 1319-1336.
- [37] Varvani-Farahani, A., Haftchenari, H., & Panbechi, M. (2007). An energy-based fatigue damage parameter for off-axis unidirectional FRP composites. *Composite Structures*, 79(3), 381-389.
- [38] Ramakrishnan, V., & Jayaraman, N. (1993). Mechanistically based fatigue-damage evolution model for brittle matrix fibre-reinforced composites. *Journal of materials science*, 28(20), 5592-5602.
- [39] Gittus, J. (1975). *Creep, viscoelasticity and creep fracture in solids* (Vol. 49). London: Applied Science Publishers.
- [40] Savvilotidou, M., Keller, T., & Vassilopoulos, A. P. (2017). Fatigue performance of a cold-curing structural epoxy adhesive subjected to moist environments. *International Journal of Fatigue*, 103, 405-414.
- [41] Chandra, R., Singh, S. P., & Gupta, K. (1999). Damping studies in fiber-reinforced composites—a review. *Composite structures*, 46(1), 41-51.
- [42] Reifsnider, K., Case, S., & Duthoit, J. (2000). The mechanics of composite strength evolution. *Composites Science and Technology*, 60(12-13), 2539-2546.
- [43] Imai, Y., Takase, T., & Nakano, K. (1989). Study of fatigue crack growth retardation due to overloads in polymethylmethacrylate. *Journal of materials science*, 24(9), 3289-3294.

Contributions:

A.Vahid Movahedi-Rad conceived, designed and performed the experimental campaign under the supervision of Dr. Anastasios Vassilopoulos and Prof. Thomas Keller. The analysis of the results was carried out by A.Vahid Movahedi-Rad in collaboration with Dr. Anastasios Vassilopoulos and Prof. Thomas Keller.



Chapter 5



Interrupted-fatigue behavior

5.1. Introduction

Engineering structures operating in open-air applications, such as wind turbine rotor blades, airplanes, and bridge decks, are subjected to different irregular loading profiles, in most cases including interrupted loading at high or low stress levels ^[1]. If such structures are composed of fiber-reinforced polymer (FRP) composites, the sensitivity of these materials to these types of loading patterns has to be taken into account due to their cyclic- and time-dependent mechanical properties ^[2,3,4,5].

The degradation of the cyclic-dependent mechanical properties of laminated composites occurs via several damage mechanisms, such as matrix cracking, debonding, delamination, transverse-ply cracking, and fiber failure, that are activated, either independently or synergistically, during fatigue loading. The predominance of one or another of the aforementioned damage mechanisms is dependent on both material variables and loading conditions as described in ^[6,7].

In addition, due to the presence of the viscoelastic polymer matrix in a variety of laminated composites, the time-dependent mechanical properties of the material are also affected during fatigue loading ^[8,9]. The time-dependent material behavior can be studied by observing the creep, recovery, and stress relaxation behaviors of the material ^[8,10].

Cyclic-dependent and time-dependent phenomena usually interact during fatigue loading, and the degree of interaction, but also the dominance of one over the other, depends on the loading spectrum and the material [2,3,4,5,9,10]. For example, it has been shown that viscoelastic materials subjected to fatigue loads with non-zero average strain tend to creep (cyclic creep effect) with the evolution of the fatigue cycles [3,5,9,11]. Although works exist about the effects of the creep-fatigue interaction on the fatigue life of composites, the effects of load interruptions (recovery and relaxation mechanisms) have hardly been investigated. As reported in [1], interruption of fatigue loading of multidirectional $[0/(\pm 45)_2/0]_T$ GFRP laminates at the stress ratio, ($R=\sigma_{\min}/\sigma_{\max}$), of 0.1 and at one particular (relatively high) stress level resulted in a considerable extension of lifetime when the fatigue load was interrupted for specific times. No information regarding the temperature development during the experiments or the percentage of recovery during load interruption is given in this study. Improvement of the measured fatigue life was also reported for engineering polymers, such as epoxy, and polyester, when the fatigue experiments were interrupted periodically as described in [12,13], again without sufficient information about the experimental conditions or any analysis regarding the reasons for this life extension. The literature review showed that the effect of load interruption on the fatigue behavior of composite materials has not been extensively studied. The publications relevant to this topic that are available to the authors of this work, e.g., [1,12,13], clearly indicate a life extension due to the load interruptions, but contain no description of the fatigue damage development and distribution in the material, or the fatigue damaging mechanisms that occur. The previous studies were based on very limited experimental programs, mainly investigating the interrupted fatigue behavior at only one stress level and without giving more information regarding the experimental conditions, monitoring of the specimen temperature evolution, etc. Furthermore, there is no rational discussion regarding the interaction of the mechanisms (damage growth, cyclic creep, recovery, the material's capacity to dissipate energy, etc.) and their influence on fatigue life.

The objective of this work is to investigate the effect of loading interruption on fatigue behavior of GFRP laminates. Constant amplitude fatigue experiments with load interruptions were performed on $\pm 45^\circ$ angle-ply composite laminates at six different stress levels, in order to cover a wide range of fatigue lifetimes. The material behavior was continuously monitored via measurement of the cyclic stress-strain and the self-generated temperature developments during the experiments. The evolution of the fatigue damage and the developed failure modes were also recorded by monitoring the variation of the material's translucency during the cyclic loading and studying, post-mortem, the fracture surfaces. The experimental results of this work were compared to relevant fatigue data from continuous constant amplitude fatigue experiments previously obtained by the authors [9] and the material fatigue behavior in both cases has been thoroughly discussed.

5.2. Experimental procedure

5.2.1 Material and specimen preparation

Rectangular glass/epoxy $[\pm 45]_{2s}$ composite specimens with the average dimensions of $250 \times 25 \times 2.3$ mm³ (length \times width \times thickness) were prepared, according to ASTM D3039 ^[14] as shown in Fig. 5.1. Unidirectional E-glass fiber fabrics (EC 9-68) with the area density of 425 gr/m² and layer thickness of 0.45 mm were used. These fabrics comprise a finish bonding agent, which provides better adhesion to the matrix. The low viscosity resin, Biresin® CR83, mixed with the hardener Sika CH83-2, in a ratio of 3:1 was used for impregnation of the fabrics. The fabrication was performed on a plastic substrate, which was coated with a release agent to prevent resin from bonding to the surface after fabrication. Laminates of dimensions $500 \times 500 \times 2.3$ mm³ and stacking sequence of $[\pm 45]_{2s}$ were fabricated by vacuum assisted hand lay-up, using a vacuum pump with a pressure of 0.9 bar. Each laminate was kept in a vacuum bag for 24 hours under laboratory conditions ($22 \pm 2^\circ\text{C}$, $40 \pm 10\%$ RH), and subsequently placed in an oven at 70°C for eight hours to complete the curing process. The achieved fiber content was 62% by volume as determined according to burn-off experiments as described in ASTM D 3171-99 ^[15]. Specimens were then cut from the laminates using a water-jet cutting machine and two aluminum tabs with dimensions of $45 \times 25 \times 4$ mm³ were glued to each specimen end with a cyanoacrylate glue for gripping purposes (Fig. 5.1).

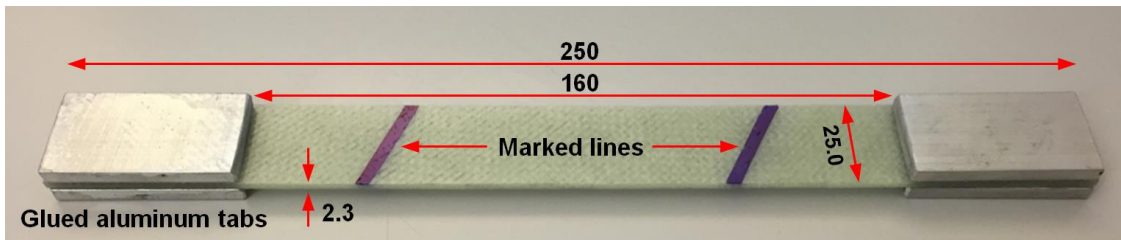


Fig. 5.1. Dimensions (in [mm]) and geometry of fatigue specimen.

5.2.2 Experimental set-up and instrumentation

All interrupted fatigue experiments were carried out on an Instron 8800 hydraulic universal testing rig of 100-kN capacity with accuracy of ± 0.2 kN. Fig. 5.2 shows a schematic representation of the applied loading profile, comprising repetitive loading blocks of constant amplitude up to the specimen's failure. For each experiment, the load was increased until the mean value was reached, after 60 seconds. Subsequently, the constant amplitude fatigue was applied for a predetermined number of cycles (20% of the average continuous fatigue life estimated for the same stress levels in ^[9]), followed

by a zero-load interval lasting for two hours. The duration of 20% of the fatigue life in each loading block was selected in order to obtain a significant number of interruptions in each fatigue experiment and a reasonable duration of the fatigue experiments.

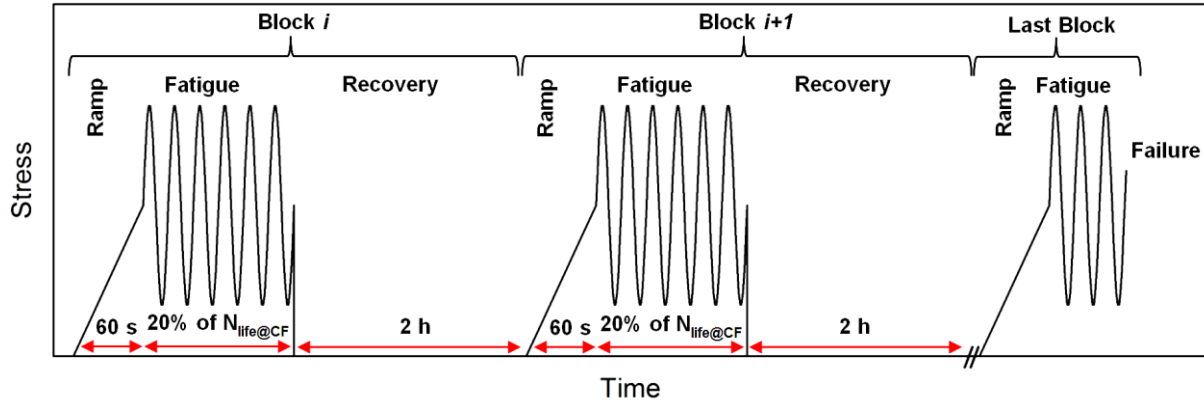


Fig. 5.2. Schematic representation of loading pattern in interrupted fatigue experiments.

The cyclic loading was performed in the range of maximum stress levels of 47 MPa – 68 MPa based on ASTM D7791-12 ^[16], similar to the stress levels selected for the continuous fatigue experiments performed in the previous work by the authors ^[9]. The stress ratio, $R = \sigma_{min}/\sigma_{max}$, was kept constant to 0.1 in order to apply tensile cyclic loads to the specimens. A loading rate, \dot{F} , of 30.5 kN/s was used for all tests. This loading rate was derived after preliminary experimental efforts in order to avoid self-generated temperature increases exceeding the glassy state during the fatigue loading ^[9]. Different frequencies were thus selected in order to keep the loading rate constant for all stress levels. Four specimens were examined at each one of the six selected stress levels. The detailed experimental matrix including the different frequencies is shown in Table 5.1. The specimen denomination is in the following form: the first term is Intf or Conf, which denotes interrupted or continuous fatigue, the second term shows the magnitude of the stress ratio, the third term the maximum fatigue stress, and the last term is the specimen number with the same parameter combination. All experiments were performed in an environmental chamber regulated at a constant temperature of 20°C. Two fans were used to circulate the air inside the chamber and cool the specimen. Moreover, for the stress level of $\sigma_{max} = 53.4$ MPa, ten experiments were performed under both interrupted and continuous loading patterns to allow a statistical analysis and a more detailed comparison of the experimental results. An overview of these additional experiments is given in Table 5.2.

Table 5.1. Overview of interrupted fatigue experiments and main results

No.	Code	σ_{\max} (MPa)	Frequency (Hz)	N_{Block}	N_f	n_b
1	Intf-0.1-68-a	68.0	4.35	365	1205	3
2	Intf-0.1-68-b	68.0	4.35	365	4668	12
3	Intf-0.1-68-c	68.0	4.35	365	3349	9
4	Intf-0.1-68-c	68.0	4.35	365	7085	19
5	Intf-0.1-64-a	64.2	4.68	500	5961	11
6	Intf-0.1-64-b	64.2	4.68	500	3943	7
7	Intf-0.1-64-c	64.2	4.68	500	6225	12
8	Intf-0.1-64-d	64.2	4.68	500	7542	15
9	Intf-0.1-58-a	58.2	5.06	3100	22854	7
10	Intf-0.1-58-b	58.2	5.06	3100	68215	22
11	Intf-0.1-58-c	58.2	5.06	3100	46055	14
12	Intf-0.1-58-d	58.2	5.06	3100	23319	7
13	Intf-0.1-53-a	53.4	5.53	9000	108580	12
14	Intf-0.1-53-b	53.4	5.53	9000	75054	8
15	Intf-0.1-53-c	53.4	5.53	9000	209355	23
16	Intf-0.1-53-d	53.4	5.53	9000	57463	6
17	Intf-0.1-49-a	48.6	6.10	64000	603211	9
18	Intf-0.1-49-b	48.6	6.10	64000	475331	7
19	Intf-0.1-49-c	48.6	6.10	64000	472542	7
20	Intf-0.1-49-d	48.6	6.10	64000	229854	3
21	Intf-0.1-47-a	47.4	6.33	146000	1314482	8
22	Intf-0.1-47-b	47.4	6.33	146000	1360621	9
23	Intf-0.1-47-c	47.4	6.33	146000	521024	3
24	Intf-0.1-47-d	47.4	6.33	146000	469501	3

Table 5.2. Overview of continuous and interrupted fatigue experiments at $\sigma_{\max} = 53.4$ MPa

No.	Code	σ_{\max} (MPa)	Frequency (Hz)	N_f	n_b
1	Conf-0.1-53-a	53.4	5.53	49151	---
2	Conf-0.1-53-b	53.4	5.53	29832	---
3	Conf-0.1-53-c	53.4	5.53	22583	---
4	Conf-0.1-53-d	53.4	5.53	79623	---
5	Conf-0.1-53-e	53.4	5.53	146112	---
6	Conf-0.1-53-f	53.4	5.53	35673	---
7	Conf-0.1-53-g	53.4	5.53	84699	---
8	Conf-0.1-53-h	53.4	5.53	101069	---
9	Conf-0.1-53-i	53.4	5.53	29666	---
10	Conf-0.1-53-j	53.4	5.53	61855	---
11	Intf-0.1-53-d	53.4	5.53	131124	14
12	Intf-0.1-53-e	53.4	5.53	150026	16
13	Intf-0.1-53-f	53.4	5.53	85250	9
14	Intf-0.1-53-g	53.4	5.53	30706	3
15	Intf-0.1-53-h	53.4	5.53	52349	5
16	Intf-0.1-53-i	53.4	5.53	91984	10

In order to monitor the mechanical, thermal, and optical changes in the specimen during and after the fatigue process, different instrumentations were used. During the fatigue experiments, the cross heads displacement, load, and number of cycles were recorded at a frequency depending on the stress levels, i.e. from once per 10 cycles at high stress levels to once per 1000 cycles at low stress levels. The variation of the longitudinal strain was measured by a high-resolution video-extensometer (a Point Grey - Grasshopper3 camera with a resolution of 1936×1216 Mpixels and a Fujinon HF35SA-1 35 mm F/1.4 lens) with a frequency of acquisition of 160 fps. A video-extensometer measured the changes of position of two lines marked on the specimens' surfaces (see Fig. 1) and the corresponding strain values were calculated. A LED white light with negligible heat emission was projected onto the sample surface to enhance measurement accuracy. Approximately twenty-five load and displacement measurements were recorded per cycle to estimate the strain fluctuations, fatigue stiffness, and hysteresis loops throughout the fatigue life of all the examined specimens. The area of the hysteresis loops was further associated to the dissipated energy and thus damage formation [9]. An infrared (IR) thermal camera with an accuracy of 0.1°C, and optical resolution of 160 × 120 pixels was also employed during the fatigue experiments to record the evolution of the specimen's surface temperature during the fatigue experiments. In order to detect the damage development at a macro- scale level, photographs of the translucent specimens were taken at regular intervals (depending on the life expectancy) with a digital camera with maximum aperture f/2.8 and focal length range of 24–70 mm range during loading. Damage in the material volume was attributed to changes in the reflectance, which indicated new interfaces in the path of the transmitted light [9]. A bright white light source was positioned behind the specimens to assist this procedure. After failure, the failure surfaces were observed using a digital handheld Dino-Lite microscope, AD7013MZT, with the magnification of 20x and resolution of 2592×1944 pixels, and photos were taken for all examined specimens.

5.3. Experimental results and discussion

5.3.1 Effect of stress level

The fatigue behavior is shown in Fig. 5.3 (Intf data), where the maximum cyclic stress level, σ_{max} , is plotted versus the number of cycles to failure, N_f . Although different types of mathematical equations can be used for the representation of the fatigue data [17] a simple power-law S-N curve equation has been selected, since it is able to simulate the observed experimental behavior:

$$\sigma_{max} = \sigma_0 N_f^{-\frac{1}{k}} \quad (5.1)$$

σ_0 , $1/k$ are model parameters derived by linear regression analysis of the experimental data; their estimated values are given in Table 5.3. The number of cycles to failure, N_f , as well as number of completed loading blocks up to failure, n_b , are listed in Table 5.1.

The evolution of the hysteresis loops during the fatigue life is shown in Figs. 5.4a and 5.4b for a specimen examined at high, $\sigma_{max}=64$ MPa, and low, $\sigma_{max}=49$ MPa, stress levels. The fatigue stiffness (i.e. the slope of each hysteresis loop as explained in [9]), as well as the hysteretic energy dissipation (the area of each loop), exhibited measureable changes throughout the lifetime. In addition, cyclic creep was observed as the hysteresis loops shifted toward higher strain values during loading.

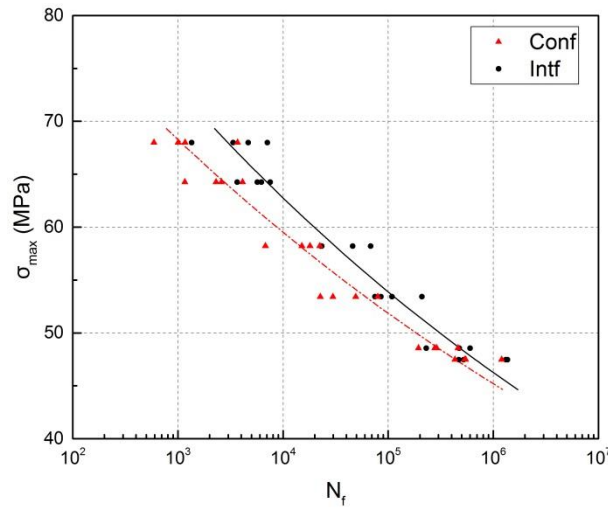


Fig. 5.3. Experimental fatigue data and S-N curves.

Table 5.3. Fatigue parameters for continuous and interrupted loading patterns

Loading pattern	σ_0	$1/k$
Continuous loading	103.09	0.0596
Interrupted loading	115.45	0.0662

The total dissipated energy (TDE) for each specimen until failure, calculated as the integral of all the individual areas of these hysteresis loops throughout the lifetime, is shown in Fig. 5.5. Comparison of the TDE values at different stress levels revealed that the total dissipated energy increased with decreasing stress level, exhibiting a similar trend to that exhibited by the S-N curve. This showed that by decreasing the stress level, the capacity of the specimens to accumulate damage was enhanced.

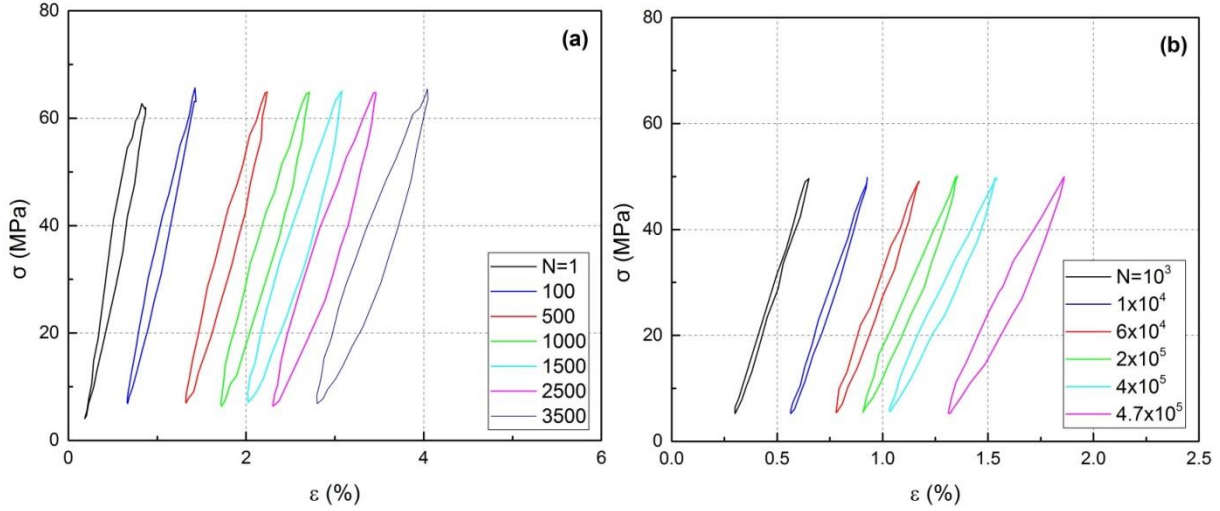


Fig. 5.4. Variation of hysteresis loops under cyclic loading at (a) $\sigma_{\max} = 64$ MPa (Intf-0.1-64-b) and (b) $\sigma_{\max} = 49$ MPa (Intf-0.1-49-b).

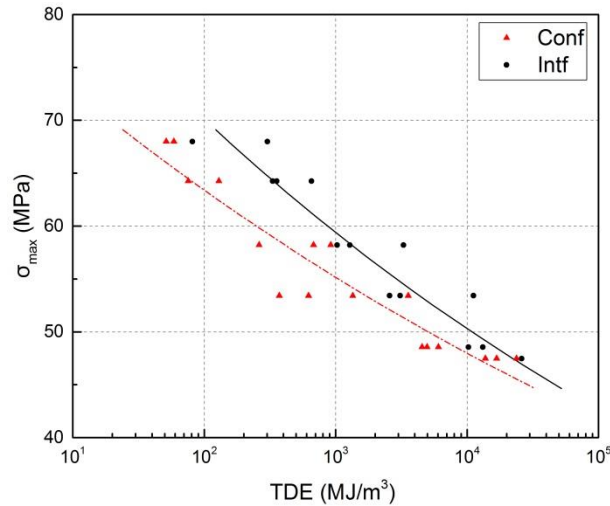


Fig. 5.5. Total dissipated energy (TDE) versus maximum cyclic stress.

The variation of normalized fatigue stiffness (E_N/E_I) versus normalized fatigue life is shown in Fig. 5.6 for different stress levels. At all stress levels, a similar trend of stiffness degradation was observed as a result of damage formation and growth, i.e. an initial steep decrease during the first 10-15% of the lifetime followed by a steady state stiffness decrease up to specimen failure. In addition, the magnitude of stiffness degradation until failure increased with decreasing stress level, again indicating that by decreasing the stress level, the capacity of the specimens to accumulate damage was increased. Further plotting of the normalized fatigue stiffness (E_N/E_I) versus the number of cycles in Fig. 5.7 revealed, however, that the rate of stiffness degradation ($d(E_N/E_I)/dN$) was greater at higher stress levels, indicating faster damage growth with increasing stress level.

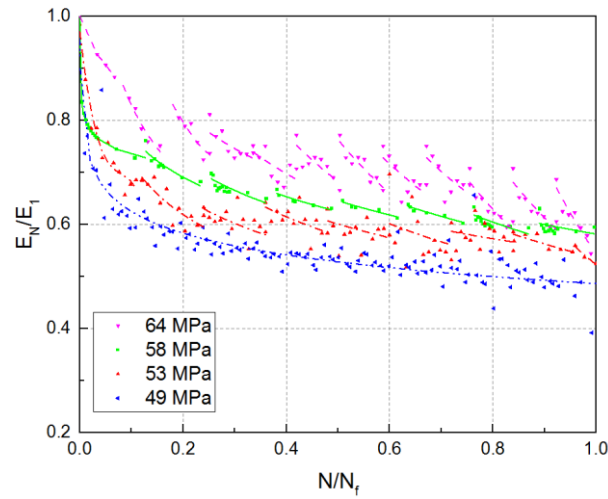


Fig. 5.6. Normalized fatigue stiffness versus normalized number of cycles.

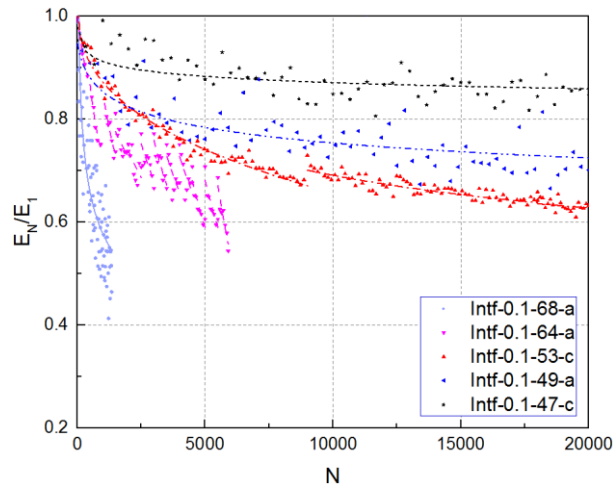


Fig. 5.7. Normalized fatigue stiffness versus number of cycles at different stress levels.

The variation of the hysteresis loop area per cycle versus the normalized number of cycles is shown for selected specimens at each stress level in Fig. 5.8. Generally, the hysteresis area (indicating energy dissipation) increased in three stages with the number of cycles at all stress levels. The values increased rapidly in the first loading block and then reached a steady state, which lasted for 80-90% of the fatigue life and then slightly increased again up to failure. Internal friction in damaged regions was the main cause of this energy dissipation [18]. The magnitude of internal friction depended on the area of unbound regions (e.g. cracks) and thus damage, which therefore grew with an increasing number of cycles and stress level.

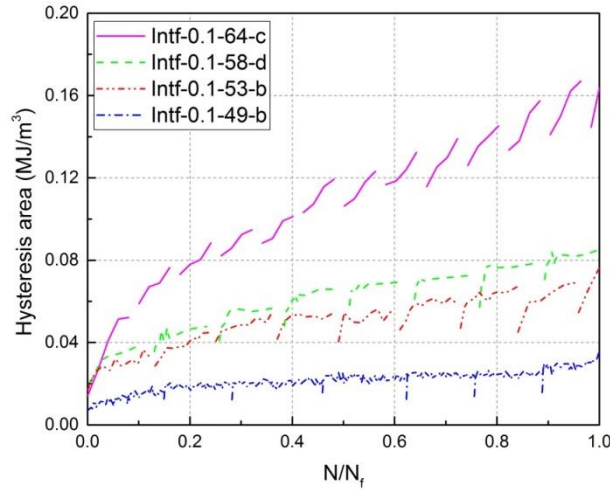


Fig. 5.8. Hysteresis area per cycle versus normalized number of cycles at different stress levels.

Fig. 5.9a and Fig. 5.10a show the evolution of specimen translucency at different percentages of specimen fatigue life for high and low cyclic loads. During the cyclic loading, the formation of any form of cracks in the matrix and fiber matrix debonding, mainly when the crack surface was perpendicular to the beam of light, caused light scattering and changed the specimen translucency [9]. Therefore, darker regions in the photos correspond to decreased light transmittance due to greater damage formation. As shown for both cases, with an increasing number of cycles, damage gradually appeared along the fibers, at around 45° with respect to the specimen longitudinal axis, which was thus attributed to matrix/fiber interface debonding. Damage was more concentrated in the specimen loaded at higher cyclic loads while it was more evenly distributed throughout the specimen volume for lower stress levels. In all cases, failure with minor necking occurred in the region where significant damage was observed.

The magnitude and distribution of the self-generated temperature across the surface of the same specimens are also shown in Figs. 5.9a and 5.10a, respectively. During the early stages of the fatigue life, a uniform distribution of surface temperature was observed. However, by increasing the number of cycles, the distribution of the temperature became more uneven, and hotspots, i.e. regions of high temperature concentrations, started appearing, which had an oval shape oriented in the fiber direction. Such hotspots were more obvious and significantly more intense for specimens at high stress levels and formed in the same regions where the light transmission was reduced. These temperature increases were attributed to internal friction in damaged zones and thus confirmed the interpretations derived so far. Figs. 5.11a and 5.11b further show the evolution of the average and maximum (hotspot) surface temperatures of selected specimens from each stress level. The average temperature exhibited a

globally two-stage increasing trend while the increase of the maximum temperature was in three stages similar to the hysteresis area increase in Fig. 5.8. Both temperatures increased with increasing stress level. The highest maximum temperature was 47°C, which remained clearly below $T_{g,onset}$ (78°C) measured by DMA [9], and the material thus remained in the glassy state.

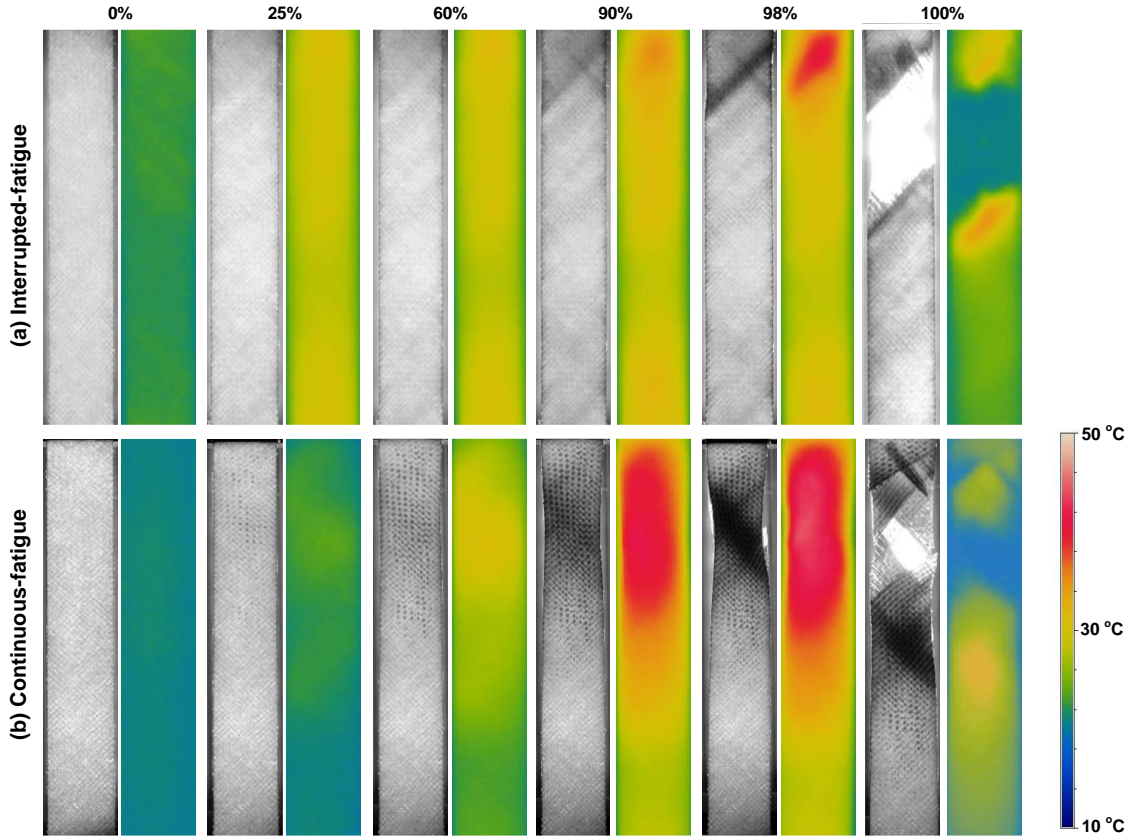


Fig. 5.9. Pairwise representation of light transmittance and self-generated temperature for different percentages of fatigue life in (a) interrupted (Intf-0.1-68-d) and (b) continuous fatigue loading (Conf-0.1-68-c) patterns at $\sigma_{max} = 68$ MPa.

To identify the amount of cyclic creep at different stress levels, the variation of average strain (average of maximum and minimum strains in one cycle) versus the normalized number of cycles is shown in Fig. 5.12 for selected specimens. Independent of stress level, all graphs showed an increasing trend when the number of cycles increased and exhibited three regions. The first region was at the early stage of cyclic loading in which the cyclic creep rate decreased rapidly with the number of cycles. A region of steady increase followed before the rate increased rapidly in the third region up to failure. The last region, however, was less pronounced at lower stress levels. Specimens loaded at higher

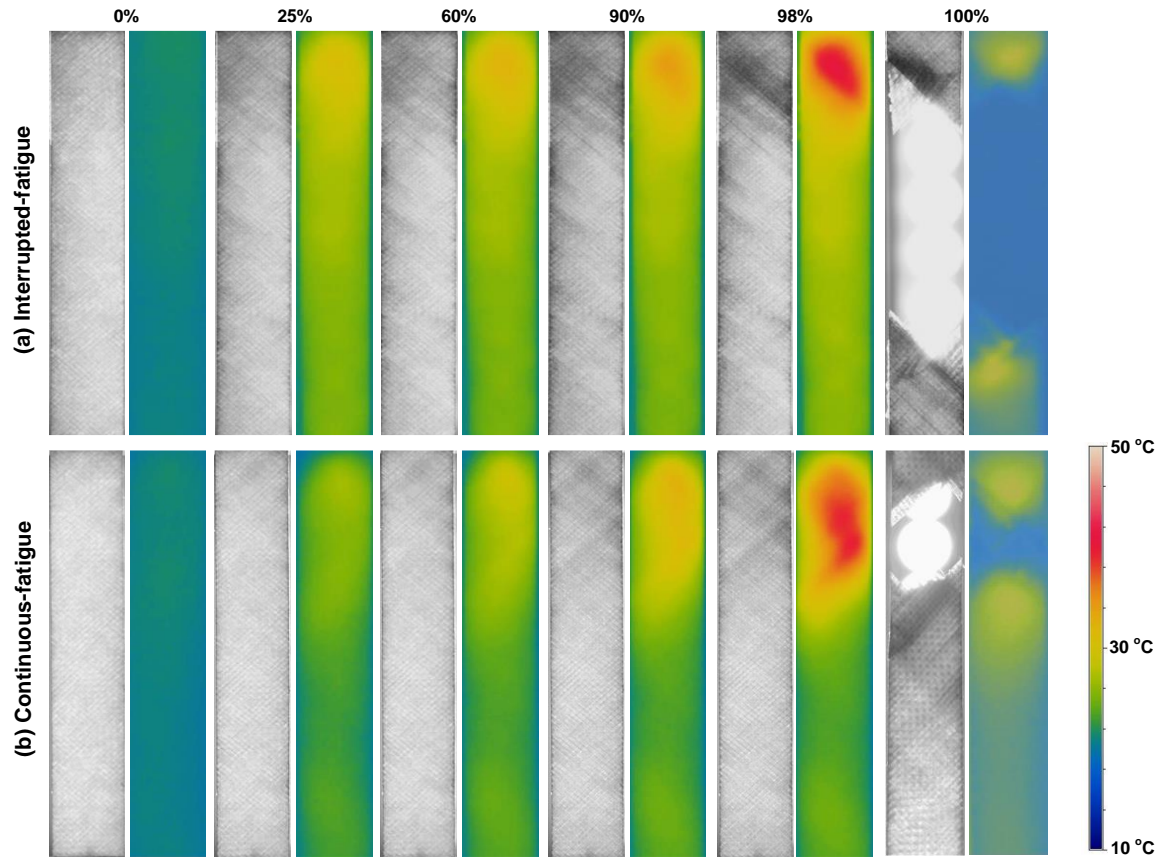


Fig. 5.10. Pairwise representation of light transmittance and self-generated temperature for different percentages of fatigue life in (a) interrupted (Conf-0.1-47-a) and (b) continuous loading patterns (Conf-0.1-47-c) at $\sigma_{\max} = 47$ MPa.

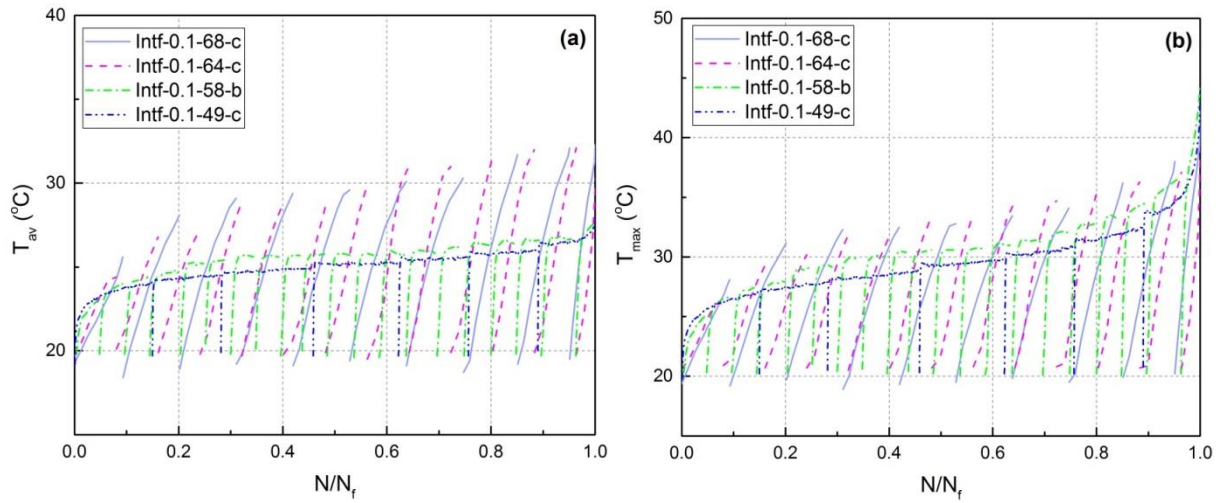


Fig. 5.11. Temperature versus normalized number of cycles at different stress levels, (a) average and (b) maximum temperature.

stress levels exhibited higher cyclic creep, which was mainly due to the increased viscoelastic deformation of the polymeric matrix. In addition, the formation of diagonal cracks (along the fibers) and necking very close to failure for higher stress levels may have contributed to an increase of the average cyclic strain.

The fatigue fracture surfaces of selected specimens examined at different stress levels are shown in Fig. 5.13. For all cases, a diagonal damage pattern, following the 45° fiber direction, was observed. For higher stress levels, Fig. 5.13a, the failure was characterized by extensive fiber pull-out, a consequence of the significant deterioration of the matrix/fiber interfaces, which hindered the transfer of the stresses from the matrix to the fibers at the concentrated damage zones. By decreasing the fatigue stress level, a mixed-mode failure with fiber pull-out and fiber breakage was observed with predominant fiber breakage at the lowest stress level, as shown in Figs. 5.13b-d. The presence of fiber breakage at low stress levels was attributed to the more uniform and less severe damage distribution, which allowed the matrix and interface to transfer stresses to the fibers.

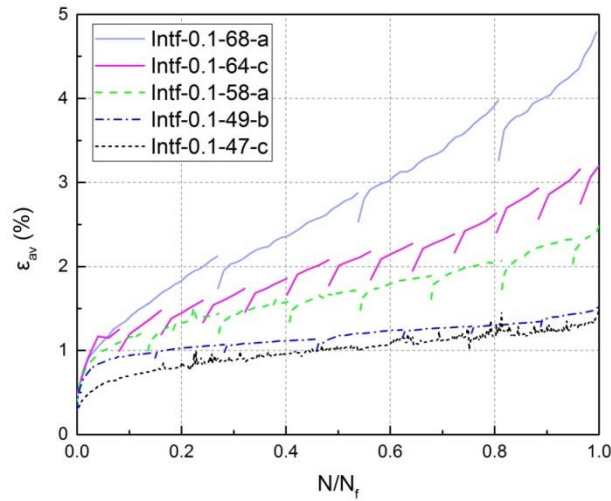


Fig. 5.12. Average cyclic strain versus normalized number of cycles at different stress levels

5.3.2. Effect of interruption

A closer look at the stiffness degradation curves in Fig. 5.6 revealed that the fatigue stiffness was partially restored after each loading interruption; the restoring effect however decreased with decreasing stress level. This restoring of material stiffness was attributed to the recovery of the time-dependent stiffness component of the viscoelastic polymeric matrix [8].

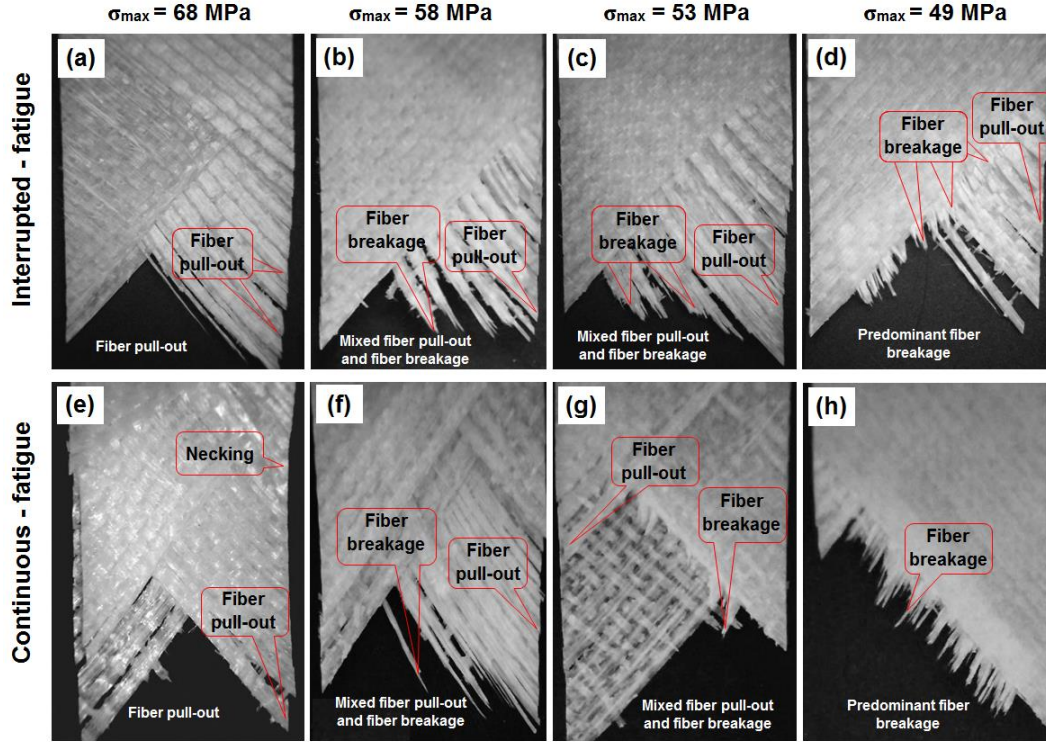


Fig. 5.13. Fatigue fracture surfaces under different loading patterns and stress levels, (a) Intf-0.1-68-a, (b) Intf-0.1-58-a, (c) Intf-0.1-53-c, and (d) Intf-0.1-49-c, (e) Conf-0.1-68-c, (f) Conf-0.1-58-c, (g) Conf-0.1-53-c, and (h) Conf-0.1-49-a.

Similar to the stiffness, each curve of the hysteresis area in Fig. 5.8 was composed of small segments attributed to each loading block; they exhibited initial increase and then a steady-state stage. After interruption, the next segment started at a lower level, i.e. less energy was dissipated in the first cycle after interruption than in the last cycle before interruption. The above-mentioned material stiffening, which decreased the amount of internal friction and delayed damage formation due to increased fracture toughness [19,20], was the cause of the lower amount of dissipated energy at the beginning of each loading block. With an increasing number of cycles, damage formation resumed and friction and therefore the hysteresis area increased.

The effect of interruption could also be retraced in the temperature curves in Fig. 5.11. In all curves, due to the interruption of the cyclic loading, the average and maximum temperatures dropped and increased again when the loading was restored in the next loading block. At high stress levels, where the number of fatigue cycles in each loading block was limited, the specimen's average and maximum surface temperatures increased, without reaching a steady-state region. The rate of temperature rise (dT/dN) increased with the number of loading blocks. Nevertheless, at intermediate and lower stress

levels, after the initial increase recorded for all loading blocks, the temperature did reach a steady-state region, except for the last loading block where the temperature continuously increased until the specimen's failure.

Fig. 5.14a shows the transition from the applied cyclic loading pattern to the interruption at zero-stress level, and from there to reloading and applying cyclic stress at $\sigma_{max}=58$ MPa (cycles are shown with 100-cycle intervals); the corresponding strains are shown in Fig. 5.14b. While the cyclic stress instantly dropped to zero, the strain showed a time-dependent decrease. It is well documented that specimen recovery as a result of the viscoelastic nature of the polymeric matrix is responsible for the observed time-dependent decrease of the specimen strain [8]. In the next loading block, the strain of the fatigue cycles only gradually increased, again due to the viscoelastic behavior; i.e. in the first 600 cycles the strain was lower than in the last cycles of the previous loading block.

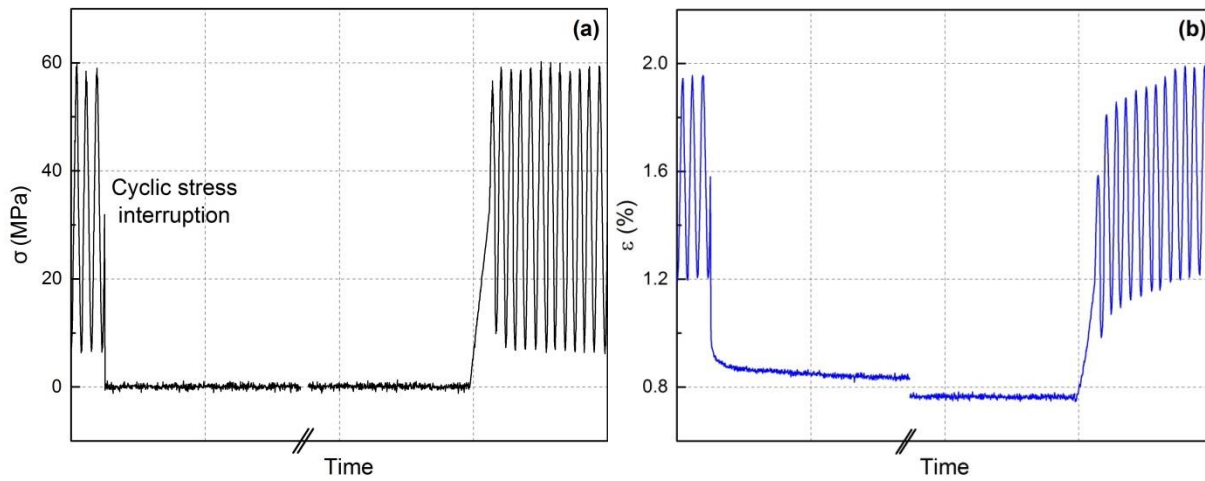


Fig. 5.14. Transition of (a) stress and (b) strain from cyclic loading to interruption at zero stress level in third loading block and passing into fourth loading block (Intf-0.1-58-a).

Fig. 5.15 thus shows, for three loading blocks, how the hysteresis loops were back-shifted on the strain axis from the last cycle after interruption to the first cycle of the subsequent reloading. In addition, it is seen that the hysteresis loops of the first loading cycles were not closed due to the considerable strain at the first cycle caused by the opening of the already existing cracks. The reduction of the average strain, $\Delta\varepsilon_{av}$, as a function of the stress level is shown in Fig. 5.16. The strain reduction increased with the increasing number of cycles and fatigue stress level. The reductions of the average strain after each loading block can also be seen in Fig. 5.12.

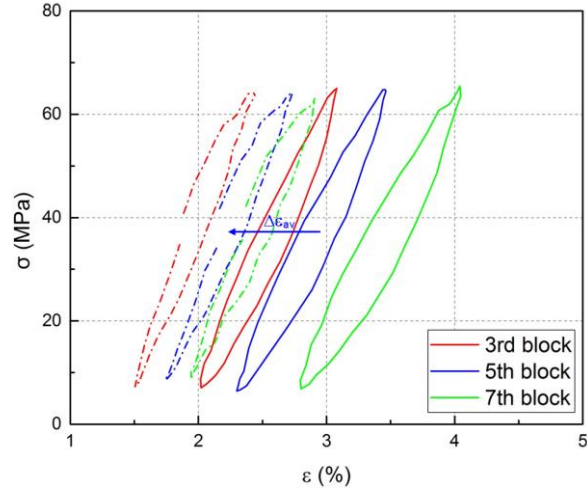


Fig. 5.15. Back-shift of hysteresis loop from last loop before interruption (solid line) to first loop (dashed line) of subsequent reloading (Intf-0.1-64-b).

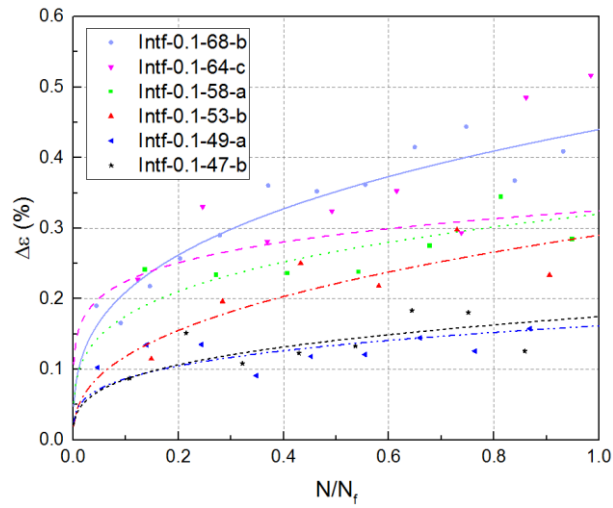


Fig. 5.16. Strain reduction versus normalized number of cycles at different stress levels.

5.4. Comparison to continuous fatigue

5.4.1 Accumulated damage and distribution

The S-N curve obtained from the interrupted fatigue loading is compared to that derived under corresponding continuous fatigue loading ^[9] in Fig. 5.3. The fatigue model parameters, estimated after linear regression analysis of the fatigue results using Eq. 5.1, are also given in Table 5.3. The specimens loaded under the interrupted fatigue pattern sustained significantly more cycles than those loaded continuously until failure. The effect was more pronounced at high stress levels, with lifetime

increases reaching 126% at the level of 68 MPa on average, but lessened at the high cycle regime, showing a 34% average increase at the level of 47 MPa, see Fig. 5.17, where the average lifetime increase ($N_{f,Intf}/N_{f,Conf}$) due to the load interruptions as a function of stress level is shown. From this curve it can also be concluded that the effect of interruption almost disappeared for stress levels lower than 40 MPa. This result may be slightly affected by the fact that at lower stress levels, significantly fewer fatigue blocks were completed, i.e. fewer interruptions occurred on average than at higher stress levels, see Table 5.1.

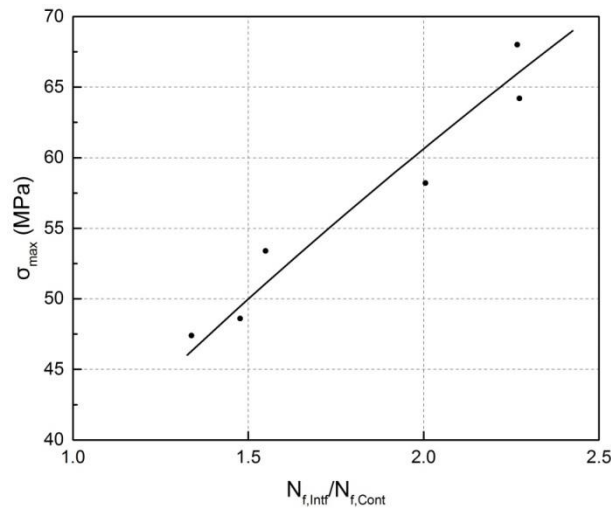


Fig. 5.17. Maximum cyclic stress versus ratio of interrupted-to-continuous fatigue life.

Although the fatigue life increased due to the interruptions, the total dissipated energy (TDE) up to failure in the specimens was significantly higher than under continuous fatigue, as shown in Fig. 5.5, the difference being more pronounced at high than at low stress levels. The specimens under interrupted loading were thus able to accumulate more damage than those loaded continuously.

Fig. 5.18 compares the fatigue stiffness degradation of specimens loaded under continuous and interrupted loading at high stress levels. By applying interrupted loading, the stiffness at failure decreased considerably more than in specimens subjected to continuous loading. This confirmed that the former specimens accumulated much more damage than the latter ones until failure. The rate of stiffness degradation was however lower under interrupted loading. At low stress levels, as shown in Fig. 5.19, the stiffness difference and thus the effect of interruption almost disappeared.

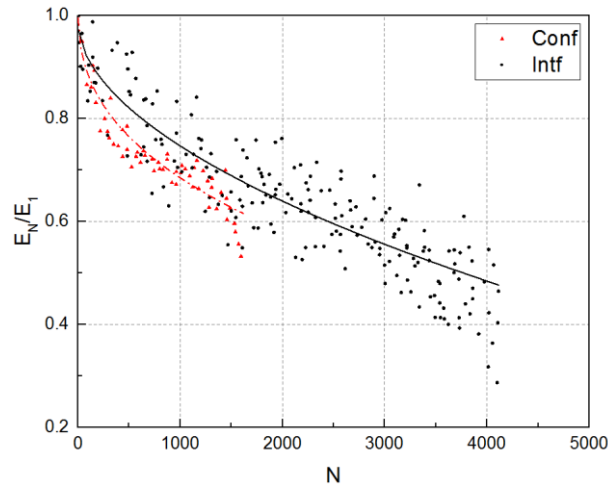


Fig. 5.18. Average normalized fatigue stiffness versus number of cycles loaded under interrupted fatigue (Intf) and continuous fatigue (Conf) at $\sigma_{\max}=68$ MPa.

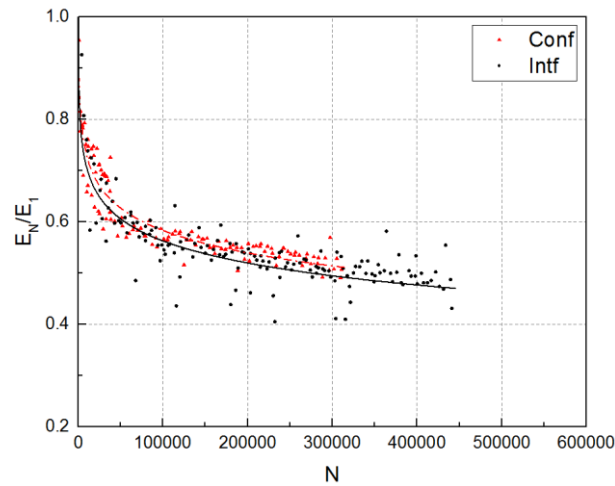


Fig. 5.19. Average normalized fatigue stiffness versus number of cycles loaded under interrupted fatigue (Intf) and continuous fatigue (Conf) at $\sigma_{\max}=49$ MPa.

The same comparison of the different loading patterns is shown for the evolution of the hysteresis loop areas in Fig. 5.20 for high and Fig. 5.21 for low stress levels. At high stress levels, much larger hysteresis loop areas before failure were observed for the specimens under interrupted loading, again indicating far greater energy dissipation and thus damage accumulation. The rate of damage accumulation was however lower under interrupted fatigue loading. At low stress levels, the differences again almost disappeared.

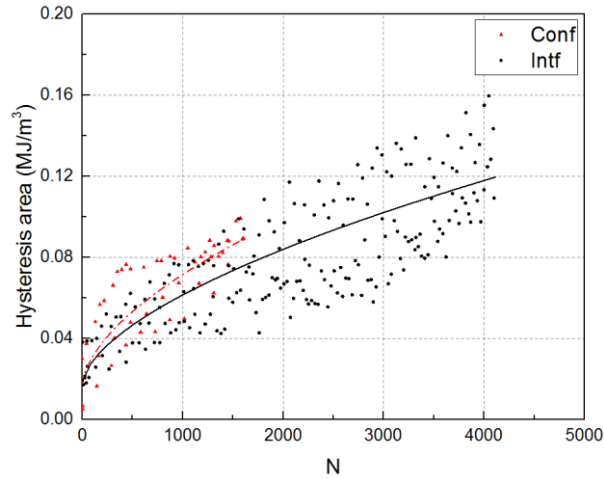


Fig. 5.20. Average hysteresis area per cycle versus number of cycles loaded under interrupted fatigue (Intf) and continuous fatigue (Conf) at $\sigma_{\max}=68$ MPa.

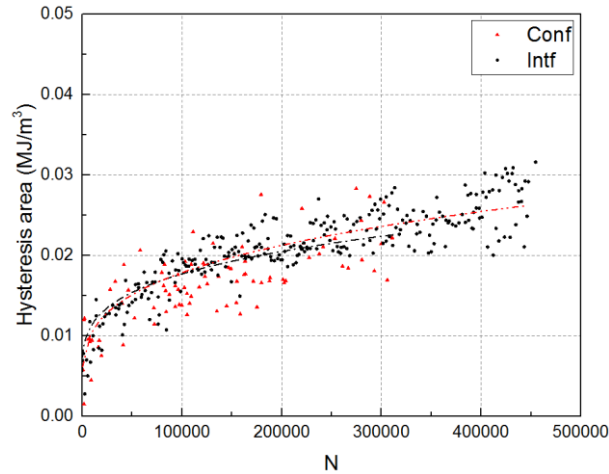


Fig. 5.21. Average hysteresis area per cycle versus number of cycles loaded under interrupted fatigue (Intf) and continuous fatigue (Conf) at $\sigma_{\max}=49$ MPa.

Comparison of the translucency and temperature distributions on the specimens' surfaces in Figs. 5.9 and 5.10 for high and low stress levels respectively revealed, at high stress levels, much more uniform distributions along the specimens under interrupted loading as they approached failure compared to continuous loading, while at low stress levels the differences between interrupted and continuous loading were small. At high stress levels, damage was thus much more evenly distributed along the specimen under interrupted loading, while it was more concentrated, at the subsequent failure location, under continuous loading. This damage distribution throughout the whole specimen volume now

explains why much more damage could be accumulated up to failure under interrupted loading, as described above.

5.4.2 Damage retardation and distribution mechanisms

The enhancement of fatigue life in the specimens loaded under interrupted fatigue loading was attributed to basically two crack-growth retardation mechanisms, which retarded or even arrested crack growth and led to the observed better damage distribution and thus longer fatigue life. Both mechanisms were based on the viscoelastic nature of the matrix. In the first mechanism, the repeated material stiffening at the beginning of each loading block with respect to the previous loading block increased the material fracture toughness (as already mentioned above), which temporarily retarded the crack growth. Material stiffening increased with increasing stress level, which thus caused more crack growth delay at higher stress levels. This mechanism explained the general damage formation delay under interrupted fatigue loading, but not the better distribution across the specimen volume caused by the latter.

In the second mechanism, unloading the damaged viscoelastic matrix led to crack blunting, i.e. the local stress intensity in the craze zone at the crack tip was significantly reduced and did not increase again at the same rate as the reloading and thus delayed the crack growth in the following cycles [21,22,23,24]. This delay further enabled the initiation and growth of new cracks at other locations and thus led to the observed distribution of damage throughout the whole specimen volume. Crack blunting and the resulting damage growth delay and better distribution of damage increased with increasing stress level [21]. In addition, as shown in Fig. 5.22, the interruptions also decreased the self-generated temperature compared to the continuous loading and thus reduced potential material softening, which would have affected the fatigue life. However, since temperatures remained clearly below the glass transition temperature in both cases, this effect was considered minor.

These two crack-growth retardation mechanisms, i.e. repeated material stiffening and crack blunting, thus explained the significant delay in stiffness degradation and damage accumulation shown in Figs. 5.18 and 5.20 at the same number of cycles and the subsequent increased damage accumulation capacity in specimens subjected to interrupted loading and therefore their longer life. The effect of the mechanisms was much greater at high stress levels and almost disappeared at low stress levels. The failure modes did not exhibit any significant differences, as shown in Fig. 5.13; only the necking was more pronounced under continuous fatigue loading.

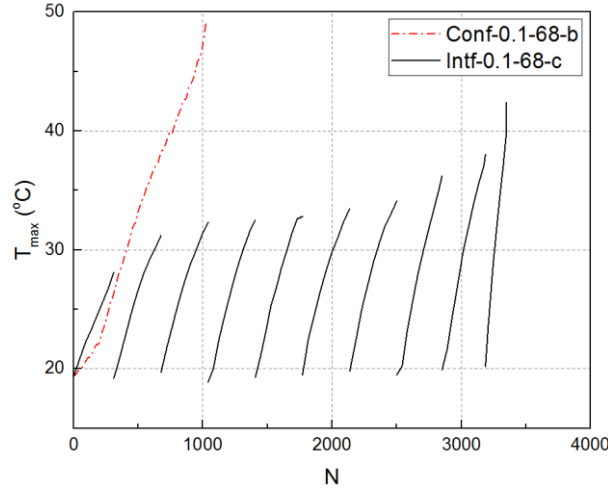


Fig. 5.22. Maximum self-generated temperature versus number of cycles loaded under interrupted fatigue (Intf) and continuous fatigue (Conf) at $\sigma_{\max}=68$ MPa.

5.4.3 Reliability analysis

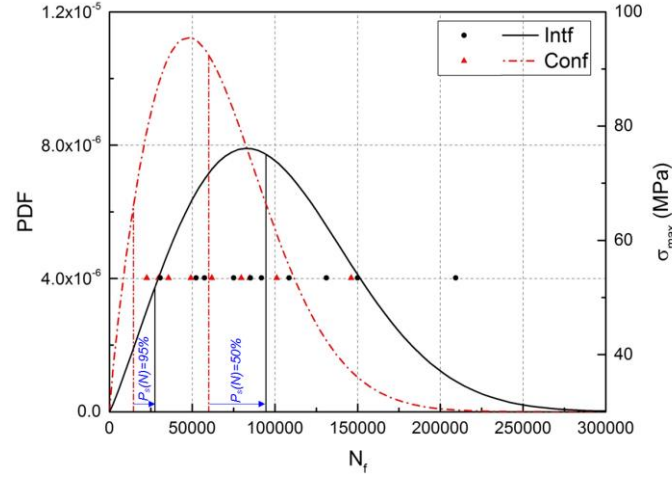
As mentioned in Section 2.2, 10 additional experiments were performed at an intermediate stress level (53 MPa) under each interrupted and continuous loading pattern, see [Tables 5.1](#) and [5.2](#). The aim was to calculate the probability of the fatigue failure and perform reliability studies to investigate the effect of loading interruption on fatigue life for design purposes. The probability of fatigue failure is derived from the probability density function (PDF) ^[1]. To calculate the PDF it is assumed that the data of each loading pattern follow a two-parameter Weibull distribution with a survival probability of $P_s(N)$:

$$P_s(N) = \exp\left(-\left(\frac{N_f}{N_0}\right)^{\alpha_f}\right) \quad (5.2)$$

The scale (N_0) and shape parameters (α_f) for the two distributions were estimated with Maximum Likelihood Estimators (MLEs) and the results are given in [Table 5.4](#). The PDFs of the Weibull distributions describing both sets of data are presented in [Fig. 5.23](#), showing an increase of around 58% of the fatigue life of the interrupted compared to the continuous pattern for 50% reliability. However, when the comparison was based on the characteristic number of cycles (for 95% reliability) the difference increased to 89%. The enhancement of fatigue life by applying an interrupted loading pattern indicates that fatigue design allowables, as determined to date, are conservative if values for continuous patterns are used in cases of interrupted patterns.

Table 5.4. Scale and shape parameters of Weibull distribution at σ_{\max} 53.4 MPa

	Continuous loading	Interrupted loading
N_0	72616	112473
α_f	1.84	2.11

**Fig. 5.23.** Probability density function versus fatigue life and corresponding Weibull distribution for specimens loaded under interrupted fatigue (Intf), and continuous fatigue (Conf) at $\sigma_{\max} = 53$ MPa.

5.5. Conclusions

The tensile-tensile interrupted fatigue behavior of angle-ply, $(\pm 45)_{2s}$, glass/epoxy composite laminates has been experimentally investigated in this work. Different mechanical, thermal, and optical measurements were performed for the study of the specimens' fatigue behavior at different stress levels. The experimental results were compared to those obtained by continuously loading the same type of specimens until failure [9]. The following conclusions were drawn:

- The average strain decreased and fatigue stiffness was partially restored after each loading interruption due to the recovery of the time-dependent stiffness component of the viscoelastic polymeric matrix. The material stiffening and associated increase of fracture toughness also decreased the amount of energy dissipation at the beginning of each loading block. These effects of interruption were dependent on the stress level and almost disappeared at low levels.
- The specimens loaded under interrupted fatigue had longer fatigue lives than those continuously loaded at the same cyclic stress levels. The enhancement of fatigue life increased at higher stress levels. The enhancement of fatigue life was attributed to the repeated material

stiffening at the beginning of each loading block, which delayed crack growth. In addition, the occurrence of crack blunting led to further damage growth delay and better distribution of damage throughout the specimen volume.

- By applying an interrupted fatigue loading pattern, the rate of stiffness degradation and energy dissipation per cycle decreased due to the delayed damage growth. In addition, more uniform damage growth throughout the specimen increased the specimen's capacity to accumulate damage, which led to lower stiffness at failure, greater energy dissipation per cycle at failure and higher total dissipated energy (TDE). However, the effect of loading interruption on the fatigue behavior became negligible at low stress levels.
- Under both loading patterns, due to the formation of severe concentrated damage at high stress levels, the stress was not transferred to the fibers, which caused failure by fiber pull-out. Furthermore, unlike the specimens subjected to interrupted fatigue loading, in specimens loaded continuously, due to the larger concentrated damage zone and fiber realignment toward the loading direction, failure occurred with considerable necking. At low stress levels, the damage distribution became more uniform under both loading patterns, which led to failure with predominant fiber breakage under both loading patterns.
- The results obtained suggest that fatigue design allowables, if determined based on continuous fatigue, are conservative in the case of interrupted fatigue.
- It is expected that by increasing the interruption time and reducing the number of cycles in each loading block, the specimen fatigue life will be enhanced even further than in this investigation. By increasing the interruption time, more material recovery would occur, leading to more material stiffening and consequently more delayed damage growth in the next loading block.

References

- [1] Vassilopoulos, A. P., & Keller, T. (2011). *Fatigue of fiber-reinforced composites*. Springer Science & Business Media.
- [2] Miyano, Y., Nakada, M., McMurray, M. K., & Muki, R. (1997). Prediction of flexural fatigue strength of CRFP composites under arbitrary frequency, stress ratio and temperature. *Journal of Composite Materials*, 31(6), 619-638.
- [3] Petermann, J., & Schulte, K. (2002). The effects of creep and fatigue stress ratio on the long-term behaviour of angle-ply CFRP. *Composite Structures*, 57(1-4), 205-210.

- [4] Guedes, R. M. (2007). Durability of polymer matrix composites: Viscoelastic effect on static and fatigue loading. *Composites Science and Technology*, 67(11-12), 2574-2583.
- [5] Sayyidmousavi, A., Bougherara, H., & Fawaz, Z. (2015). The role of viscoelasticity on the fatigue of angle-ply polymer matrix composites at high and room temperatures-a micromechanical approach. *Applied Composite Materials*, 22(3), 307-321..
- [6] Reifsnider, K. L., & Talug, A. (1980). Analysis of fatigue damage in composite laminates. *International Journal of Fatigue*, 2(1), 3-11.
- [7] Harris, B. (Ed.). (2003). *Fatigue in composites: science and technology of the fatigue response of fibre-reinforced plastics*. Woodhead Publishing.
- [8] Guedes, R. M. (Ed.). (2010). *Creep and fatigue in polymer matrix composites*. Elsevier.
- [9] Movahedi-Rad, A. V., Keller, T., & Vassilopoulos, A. P. (2018). Fatigue damage in angle-ply GFRP laminates under tension-tension fatigue. *International Journal of Fatigue*, 109, 60-69.
- [10] Vieille, B., Albouy, W., & Taleb, L. (2014). About the creep-fatigue interaction on the fatigue behaviour of off-axis woven-ply thermoplastic laminates at temperatures higher than T_g. *Composites Part B: Engineering*, 58, 478-486.
- [11] Benaarbia, A., Chrysochoos, A., & Robert, G. (2015). Thermomechanical behavior of PA6. 6 composites subjected to low cycle fatigue. *Composites Part B: Engineering*, 76, 52-64.
- [12] Broutman, L. J., & Gaggar, S. K. (1972). Fatigue behavior of epoxy and polyester resins. *International Journal of Polymeric Materials*, 1(4), 295-316.
- [13] Herman, W. A., Hertzberg, R. W., & Manson, J. A. (1990). The influence of loading history on fatigue in engineering plastics. *Journal of Materials Science*, 25(1), 434-440.
- [14] ASTM D3039/D3039M-14 Standard Test Method for Tensile Properties of Polymer Matrix Composite Materials. ASTM International; 2014.
- [15] ASTM, D3171–99. Standard test methods for constituent content of composite materials. ASTM International; 2002.
- [16] ASTM, D7791–17. Standard Test Method for Uniaxial Fatigue Properties of Plastics. ASTM International; 2017.
- [17] Sarfaraz, R., Vassilopoulos, A. P., & Keller, T. (2012). A hybrid S–N formulation for fatigue life modeling of composite materials and structures. *Composites Part A: Applied Science and Manufacturing*, 43(3), 445-453.
- [18] Chandra, R., Singh, S. P., & Gupta, K. (1999). Damping studies in fiber-reinforced composites—a review. *Composite structures*, 46(1), 41-51.
- [19] Courtney, T. H. (2005). *Mechanical behavior of materials*. Waveland Press.

- [20] Wei, R. P. (2010). *Fracture mechanics: integration of mechanics, materials science and chemistry*. Cambridge University Press.
- [21] Schapery, R. A. (1975). A theory of crack initiation and growth in viscoelastic media. *International Journal of Fracture*, 11(1), 141-159.
- [22] Fang, Q. Z., Wang, T. J., & Li, H. M. (2008). Overload-induced retardation of fatigue crack growth in polycarbonate. *International Journal of Fatigue*, 30(8), 1419-1429.
- [23] Banasiak, D. H., Grandt Jr, A. F., & Montulli, L. T. (1977). Fatigue crack retardation in polycarbonate. *Journal of Applied Polymer Science*, 21(5), 1297-1309.
- [24] Imai, Y., Takase, T., & Nakano, K. (1989). Study of fatigue crack growth retardation due to overloads in polymethylmethacrylate. *Journal of materials science*, 24(9), 3289-3294.

Contributions:

A.Vahid Movahedi-Rad conceived, designed and performed the experimental campaign under the supervision of Dr. Anastasios Vassilopoulos and Prof. Thomas Keller. The analysis of the results was carried out by A.Vahid Movahedi-Rad in collaboration with Dr. Anastasios Vassilopoulos and Prof. Thomas Keller.

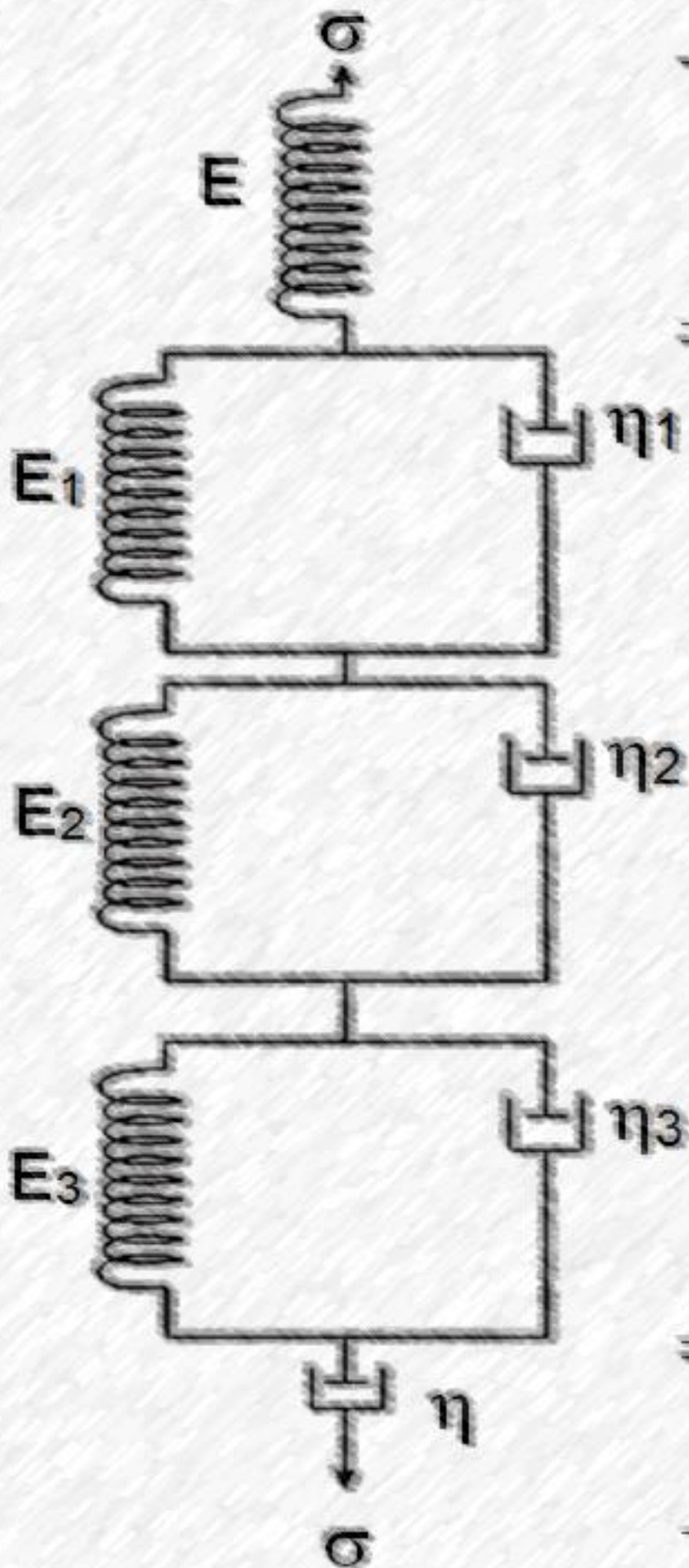
$$\varepsilon(t) = \frac{\sigma(t)}{E}$$

$$\varepsilon(t) = \frac{\sigma(t)}{E_1 + \eta_1 \frac{\partial}{\partial t}}$$

$$\varepsilon(t) = \frac{\sigma(t)}{E_2 + \eta_2 \frac{\partial}{\partial t}}$$

$$\varepsilon(t) = \frac{\sigma(t)}{E_3 + \eta_3 \frac{\partial}{\partial t}}$$

$$\varepsilon(t) = \frac{\sigma(t)}{\eta \frac{\partial}{\partial t}}$$



Chapter 6



Modeling of fatigue behavior

6.1. Introduction

Fiber-reinforced polymer (FRP) composites are used in a wide range of applications such as wind turbine rotor blades, airplanes, and bridge decks and are subjected to different types of loading patterns during operation. The behavior of these materials is sensitive to the loading pattern due to their cyclic- and time-dependent mechanical properties ^[1,2]. The cyclic-dependent mechanical properties, such as fatigue stiffness and hysteresis loop area, are mainly linked to high frequency fatigue experiments at zero mean stress level in which the time-dependent deformation of the material does not have a significant effect. On the other hand, the time-dependent mechanical properties are related to the rheology of the material when it is subjected to a sustained load ^[2,3,4].

Constitutive equations to describe the time-dependent mechanical properties were established based on either physical or phenomenological approaches. Following the physical-based approach, the material behavior is studied on the microscopic scale in order to model, for instance, the uniaxial loading behavior of polymer-based materials including yielding, work-hardening, strain rate and temperature effects ^[5,6]. Hysteresis loops resulting from quasi-static uniaxial tensile loading-unloading cycles of viscoelastic materials were also simulated using a physical-based approach ^[7,8,9,10,11,12,13,14]. This was achieved by modeling the specimen's nonlinear viscoelastic behavior during the loading and unloading phases where the challenge was to model the non-linear unloading phase since the material

behaved differently during loading and unloading. To achieve this, new models, based on different approaches, were developed. For example, Colak ^[13] developed a model to describe the nonlinear rate-dependent loading and nonlinear unloading behavior by introducing a variable into the elastic strain rate relationship. Krasnobrizha et al ^[14] developed a model to describe the evolution of the hysteresis behavior during loading and unloading of laminated composites taking into account the visco-elastoplastic behavior of damaged material.

Phenomenological approaches, studying the material on the macroscale, e.g. ^[15,16,17], were successfully applied to model the laminated composites' creep, recovery, and relaxation in the linear viscoelastic domain amongst other things. Of the different techniques, the Boltzmann superposition formulation is the most commonly used to model the time-dependent behavior of laminated composites in the linear domain ^[18,19,20]. Although linear viscoelastic principles were useful for the description of the long-term properties, they were inadequate in cases where the stress levels applied were so high that non-linear creep was observed ^[15,20,21]. Efforts for modeling the non-linear creep behavior of polymers have concentrated on the modification of the Boltzmann superposition formulation. Schapery ^[22] modified the Boltzmann superposition formulation by adding four time-independent but stress- dependent parameters, which expressed the degree of non-linearity in elastic, viscoelastic and permanent strains. Most constitutive equations used to model cyclic-dependent material behavior were based on phenomenological approaches ^[23,24,25,26,27,28,29,30,31]. Such models describe fatigue damage by using an evolutionary law to simulate the gradual degradation of the specimen's properties. Damage mechanisms are not considered in these methods, although appropriate damage metrics (such as fatigue stiffness, fatigue strengths, residual strength etc.) are used for the assessment of damage. These damage metrics depend on many factors, including the applied cyclic stress, number of fatigue cycles, loading frequency and environmental conditions ^[27].

Most of the models in the literature describe the time- and cyclic-dependent mechanical properties separately. However, the time- and cyclic-dependent mechanical properties of laminated composites usually interact with each other, and the degree of interaction depends on the loading spectrum and the material configuration ^[32,33,34,35,36]. In continuous fatigue, the interaction between the time- and cyclic-dependent mechanical properties was studied by monitoring the evolution of fatigue hysteresis loops ^[33,34,36,37] attributing the shift of the fatigue hysteresis loops to creep effects and the slope of the loops to degradation of the fatigue stiffness due to damage ^[36]. The interaction between the time- and cyclic-dependent mechanical properties was also studied by applying more complicated loading patterns in which continuous-fatigue was interrupted in different ways ^[1,2,34,38]. Interruption of cyclic loading could also change the fatigue life depending on the applied stress level and material type, as presented in ^[1,2]. Vieille et al ^[34] showed that fatigue life could be extended with prior creep in an angle-ply

carbon/PPS thermoplastic composite depending on the loading conditions at temperatures higher than T_g . Similarly, in an angle-ply thermoset graphite/epoxy composite, it was shown that sustained periods of static loads have significant retardation effects on damage propagation and extended fatigue life [38]. Recently, it was shown that the effect of creep on the fatigue life of angle-ply thermoset laminates could be positive or negative depending on the applied stress level and the hold time [2].

According to the aforementioned studies, the time- and cyclic-dependent properties of composite systems affect each other when the mean stress is not zero and therefore both should be considered in the constitutive equation for an appropriate description of the fatigue behavior. Previous works described in the literature modeled the hysteresis loops during quasi-static tensile loading-unloading; however, the modeling of hysteresis loop behavior (including their shifting as a result of creep) during the fatigue loading has not yet been performed. To the authors' best knowledge, models developed to link the time- and cyclic-dependent mechanical properties mainly focused on creep effects in continuous fatigue to improve fatigue life predictions, e.g. in [32,20]. However, a general model to simulate the fatigue behavior (the evolution of fatigue stiffness, hysteresis loops, cyclic creep, $\tan(\delta)$, storage modulus, and loss modulus) of composite materials has not yet been developed.

The objective of the present work is to derive a general constitutive equation to link and simulate the time- and cyclic-dependent mechanical properties of viscoelastic materials. For this purpose, a general constitutive equation was developed and solved for two specific loading patterns of 1) an unloading to zero stress level (recovery solution) and 2) load control cyclic loading (fatigue solution). To implement this equation, a loading pattern comprising a constant amplitude cyclic loading with repetitive interruptions at zero stress level was selected and applied on matrix-dominated $\pm 45^\circ$ angle-ply glass/epoxy composite laminates in which the time-dependent effect was significant. The viscoelastic parameters were estimated by fitting the recovery solution to the experimental recovery curves. The obtained viscoelastic parameters were imported into the fatigue solution to predict the fatigue behavior at different numbers of cycles and stress levels. The accuracy of prediction was evaluated by comparing the results with those obtained from the experiments.

6.2. General constitutive equation

To model the behavior of a viscoelastic material, different configurations of springs and dashpots can be used depending on the material behavior [7,10,11,44]. A linear spring with the elastic modulus E simulates the instantaneous elastic deformation (Eq. 6.1) while a linear dashpot element simulates the viscous deformation (Eq. 6.2) in which the constant η is the viscosity coefficient.

$$\sigma = E\varepsilon \quad (6.1)$$

$$\sigma = \eta \frac{d\varepsilon}{dt} \quad (6.2)$$

The Maxwell unit is a two-element model consisting of a linear spring element and a linear viscous dashpot element connected in series (Eq. 6.3) while the Kelvin unit is when the spring element and dashpot element are connected in parallel (Eq. 6.4).

$$\varepsilon(t) = \left(\frac{1}{E} + \frac{1}{\eta \frac{\partial}{\partial t}} \right) \sigma(t) \quad (6.3)$$

$$\varepsilon(t) = \left(\frac{1}{E_1 + \eta_1 \frac{\partial}{\partial t}} \right) \sigma(t) \quad (6.4)$$

In order to simulate the viscoelastic response of complex material systems under different loading patterns such as creep, relaxation, recovery or cyclic loading, combinations of springs and dashpots in series and/or in parallel configurations can be used. A generally assumed form of a system of springs and dashpots is shown in Fig. 6.1. An independent spring is used to model the elastic strain, while Kelvin units are used to model the viscoelastic strain, and an independent dashpot is used to model the remaining strain after recovery. The corresponding general constitutive equation is shown below.

$$\varepsilon(t) = \left(\frac{1}{E} + \frac{1}{E_1 + \eta_1 \frac{\partial}{\partial t}} + \frac{1}{E_2 + \eta_2 \frac{\partial}{\partial t}} + \cdots + \frac{1}{E_i + \eta_i \frac{\partial}{\partial t}} + \frac{1}{\eta \frac{\partial}{\partial t}} \right) \sigma(t) \quad (6.5)$$

This general constitutive equation can be solved for different loading patterns, e.g. 1) for stress unloading from a mean to a zero stress level (a recovery solution), and 2) for load-control sinusoidal cyclic loading (a fatigue solution), as demonstrated using interrupted fatigue experiments, which comprised phases of cyclic loading and repetitive loading interruptions. The specimen recovery behavior during the loading interruptions was modeled using the recovery solution, and correspondingly, the evolution of the viscoelastic parameters was quantified as the number of loading blocks increased. The fatigue behavior at different numbers of cycles was then predicted by importing the estimated viscoelastic parameters into the fatigue solution. The flowchart of the different modeling stages is shown in Fig. 6.2.

6.3. Recovery solution and application

6.3.1 Experimental investigation and recovery results

Interrupted fatigue tensile experiments were performed on rectangular fully-cured glass/epoxy $[\pm 45]_2$ s specimens with dimensions of $250 \times 25 \times 2.3 \text{ mm}^3$ (length \times width \times thickness) and a fiber content of 62%

by volume. Fig. 6.3 shows a schematic representation of the applied loading profile, comprising

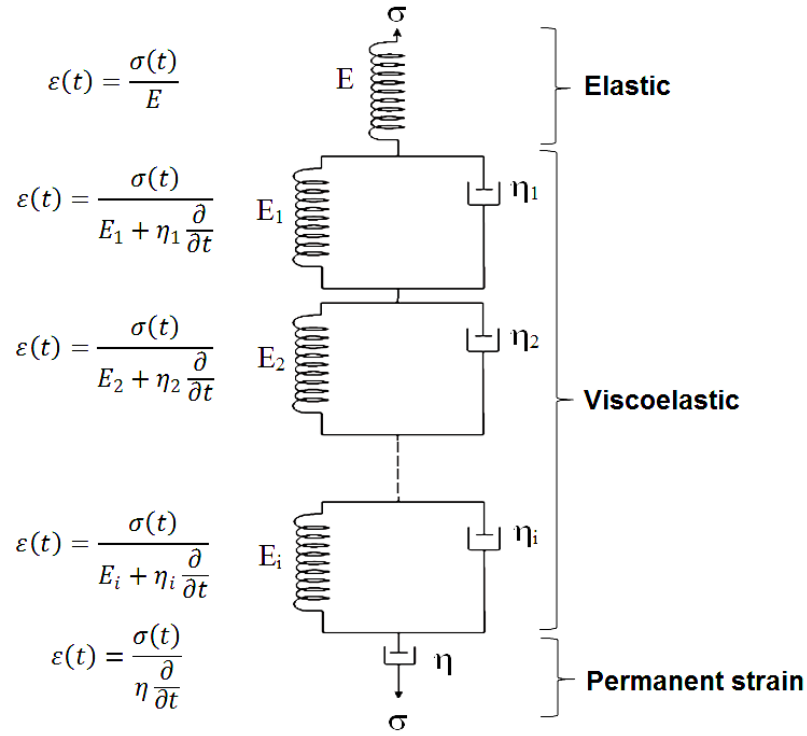


Fig. 6.1. Basis of constitutive equation to describe behavior of viscoelastic materials.

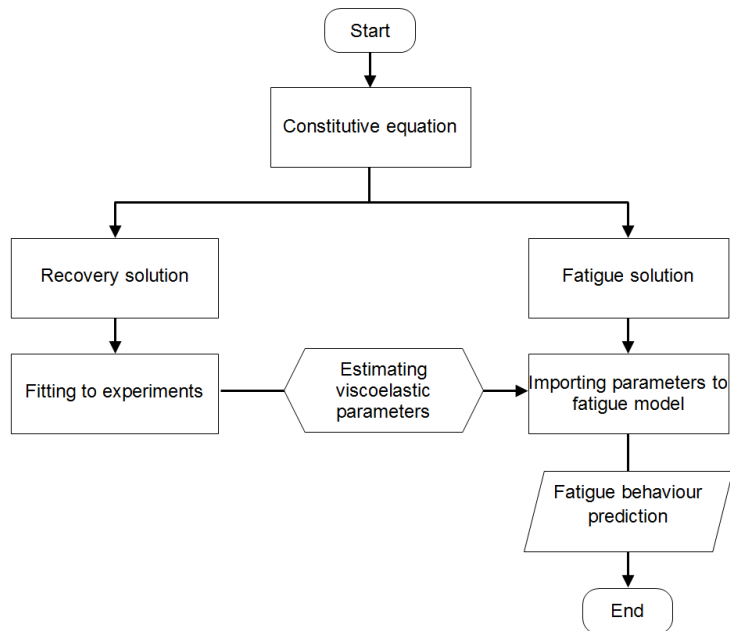


Fig. 6.2. Flowchart of implementation of constitutive equation.

repetitive loading blocks of constant amplitude interrupted by unloading periods up to specimen failure. For each experiment, the load was increased until the mean value was reached, after 60 s. Subsequently, the constant amplitude fatigue was applied for a predetermined number of cycles (20% of the average continuous fatigue life), followed by a zero-load interval lasting two hours. The cyclic loading was performed in the range of maximum stress levels of 47 MPa–68 MPa. The stress ratio, $R = \sigma_{\min}/\sigma_{\max}$, was kept constant at 0.1 and a constant loading rate of 30.5 kN/s was used; the frequencies thus varied. The details of the fabrication process, experimental set-up and instrumentation are given in [1].

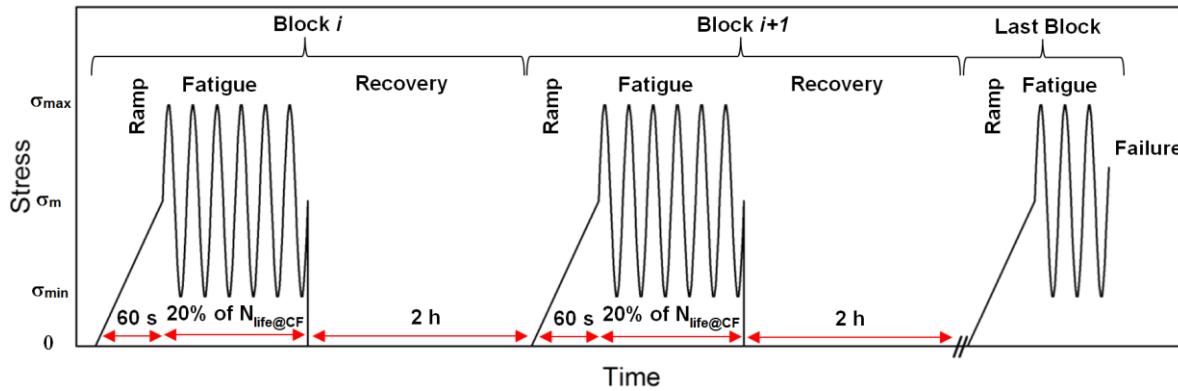


Fig. 6.3. Schematic representation of loading pattern in interrupted fatigue experiments.

Fig. 6.4 shows the strain response at the end of a cyclic loading and after the load removal of a selected specimen during one of the loading interruptions. While the cyclic stress instantly decreased to zero, the strain showed a gradual decrease, i.e. first a very sudden elastic strain reduction at the moment of unloading, followed by a viscoelastic strain reduction down to a remaining unrecovered strain after 2 h. It is well documented that specimen recovery, as a result of the viscoelastic nature of the polymeric matrix, is responsible for the observed time-dependent decrease of strain [20]. It was shown that the viscoelastic recovery could be described as a three-stage time-dependent strain reduction. Stage I represented a rapid specimen viscoelastic recovery after the elastic strain reduction, and Stage III illustrated the long-term recovery behavior of the specimen in which the strain changed very slowly. Between these two stages, there was a transition region (Stage II), which linked the former and the latter. The remaining strain after a 2-h recovery was attributed to the unrecovered viscoelastic strain and also the accumulated permanent strain due to the fatigue damage.

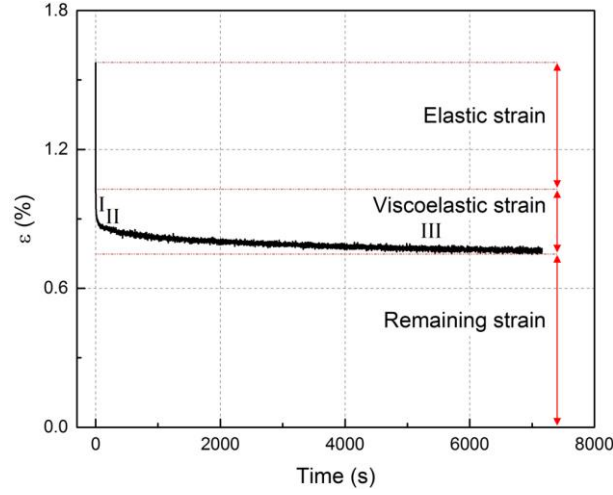


Fig. 6.4. Elastic, three-stage viscoelastic recovery, and remaining strains of specimen Intf-0.1-58-a after third loading block.

6.3.2 Recovery solution

The elastic and remaining strains can be calculated by Eq. 6.6, based on the Maxwell unit, and the viscoelastic strain can be calculated by the Kelvin units, Eq. 6.7 [20,45].

$$\varepsilon_{Maxwell}(t) = \frac{\sigma_m}{E} + \frac{\sigma_m}{\eta}(t_1 - t_0) \quad (6.6)$$

$$\varepsilon_{Kelvin}(t) = \frac{\sigma_m}{E_i} (1 - e^{-\lambda_i(t-t_1)}) \quad (6.7)$$

where the mean stress is symbolized with σ_m , and λ is equal to E/η in the Kelvin unit, t_0 is the point at which the specimen was subjected to the cyclic loading, and t_1 is the stress removal time. The total strain after the load removal is the sum of all the aforementioned strain components of elastic strain, three stages of viscoelastic strain, and remaining strain (see Fig. 6.4) and is calculated by Eq. 6.8:

$$\varepsilon(t) = \underbrace{\frac{\sigma_m}{E}}_{\text{Elastic strain}} + \underbrace{\frac{\sigma_m}{E_1}(1 - e^{-\lambda_1(t-t_1)})}_{\text{Time-dependent recovery, Stage I}} + \underbrace{\frac{\sigma_m}{E_2}(1 - e^{-\lambda_2(t-t_1)})}_{\text{Time-dependent recovery, Stage II}} + \underbrace{\frac{\sigma_m}{E_3}(1 - e^{-\lambda_3(t-t_1)})}_{\text{Time-dependent recovery, Stage III}} + \underbrace{\frac{\sigma_m}{\eta}(t_1 - t_0)}_{\text{Remaining strain}} \quad (6.8)$$

Viscoelastic strain

The viscoelastic parameters related to the independent spring and dashpot elements (E and η) are estimated directly by measuring the elastic and remaining strains. The parameters of the viscoelastic

terms of Eq. 6.8 are calibrated using the experimental data in the three regions of the viscoelastic part of the recovery curves. The corroboration process was carried out using the Orthogonal Distance Regression (ODR) iteration algorithm ^[46], and a Chi-Square tolerance value of 10^{-9} was reached in all cases.

6.3.3 Estimation of viscoelastic parameters

Figs. 6.5a and 6.5b show the recovery curves as the number of loading blocks increased at stress levels of 58 MPa and 49 MPa, respectively. The recovery behavior was simulated using Eq. 6.8, as described above. The obtained recovery curves closely followed the experimental curves. The resulting viscoelastic parameters related to the elastic, viscoelastic, and remaining strains and those of three more stress levels are shown in Fig. 6.6. Each recovery curve is represented by one data point. The behavior of each viscoelastic parameter (VP) could be simulated by power law equations of the type $VP = \alpha N^\beta$ in which α and β are fitting parameters. All parameters, except η , gradually decreased with the number of cycles. An initial steep decrease during the first 10–15% of the lifetime was followed by a steady-state decreasing trend. Furthermore, with increasing stress levels, the values of the parameters generally decreased, except for E_2 and η_2 , where no clear trend could be recognized, which was attributed to the fact that the second stage of recovery was a transition stage from short- to long-term recovery. The decreasing trends of the viscoelastic parameters were attributed to the fatigue damage accumulation as shown in ^[1].

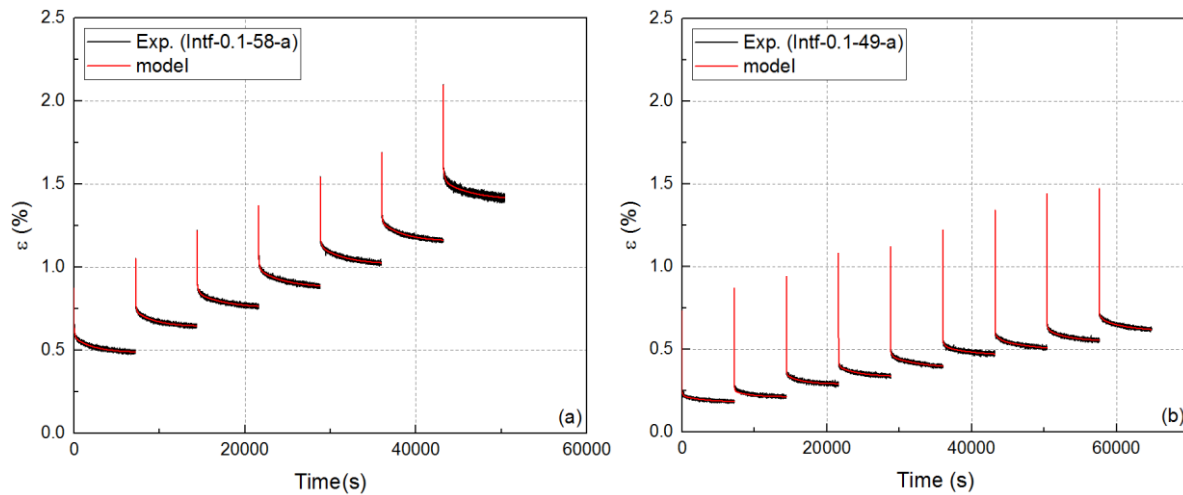


Fig. 6.5. Experimental and modeled recovery curves for different loading blocks and stress levels, (a) Intf-0.1-58-a, and (b) Intf-0.1-49-a.

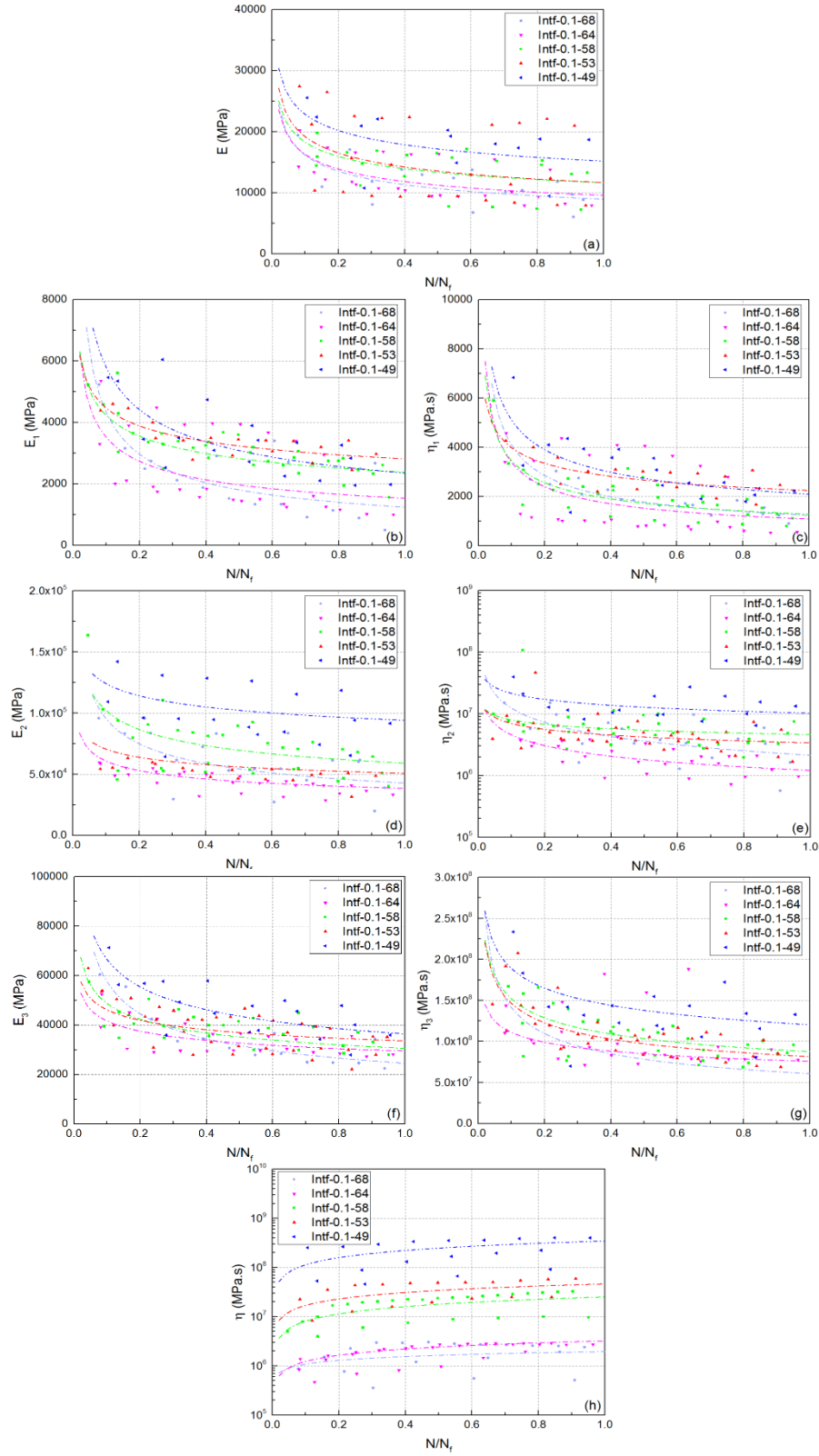


Fig. 6.6. Variation of viscoelastic parameters (a) E , (b) E_1 , (c) η_1 , (d) E_2 , (e) η_2 , (f) E_3 , (g) η_3 , and (h) η versus normalized number of cycles at different stress levels.

In addition, according to ^[2], creep at these stress levels was non-linear, which contributed to the change in the viscoelastic parameters. Unlike the other parameters, the evolution of η , attributed to the remaining strain, showed a growing trend, which was attributed to the decreasing rate of remaining strain (Eq. 6.8), which subsequently became constant as the number of blocks increased.

6.4. Fatigue solution, application and validation

6.4.1 Fatigue solution

The sinusoidal cyclic stress with a stress amplitude, σ_a , and a given fatigue frequency, f , was applied according to the following relationship:

$$\sigma(t) = \sigma_m + \sigma_a \sin(\omega t) \quad (6.9)$$

where ω is equal to $2\pi f$. By substituting the cyclic stress equation (Eq. 6.9) in the general constitutive equation (Eq. 6.5), the fatigue strain can be calculated as follows (see Annex I):

$$\varepsilon(t) = \varepsilon_c(t) + \varepsilon_a \sin(\omega t - \delta) \quad (6.10)$$

where $\varepsilon_c(t)$ is the average cyclic strain, $\varepsilon_a(t)$ the strain amplitude, and δ the phase-lag. The strain calculated by Eq. 6.10, which is similar to the equation of applied stress (Eq. 6.9) except that the phase-lag, δ , appears in the sinus term. The terms introduced in Eq. 6.9 and Eq. 10 are schematically shown in Fig. 6.7. The corresponding equations for the calculation of $\varepsilon_c(t)$, $\varepsilon_a(t)$, and δ are shown in Eqs. 11-13, respectively (see Annex I).

$$\varepsilon_c(t) = \underbrace{\frac{\sigma_m}{E}}_{\text{Elastic strain}} + \underbrace{\sum_{i=1}^{i=3} \frac{\sigma_m}{E_i} (1 - e^{-\lambda_i(t-t_0)})}_{\text{Viscoelastic strain}} + \underbrace{\frac{\sigma_m}{\eta} (t - t_0)}_{\text{Permanent strain}} \quad (6.11)$$

$$\varepsilon_a = \sigma_a \sqrt{\left(\sum_{i=1}^{i=3} \frac{1}{\eta_i} \frac{\lambda_i}{\lambda_i^2 + \omega^2} + \frac{1}{E} \right)^2 + \left(\sum_{i=1}^{i=3} \frac{1}{\eta_i} \frac{\omega}{\lambda_i^2 + \omega^2} + \frac{1}{\eta \omega} \right)^2} \quad (6.12)$$

$$\delta = \tan^{-1} \left(\frac{\sum_{i=1}^{i=3} \frac{\omega}{\eta_i (\lambda_i^2 + \omega^2)} + \frac{1}{\eta \omega}}{\sum_{i=1}^{i=3} \frac{\lambda_i}{\eta_i (\lambda_i^2 + \omega^2)} + \frac{1}{E}} \right) \quad (6.13)$$

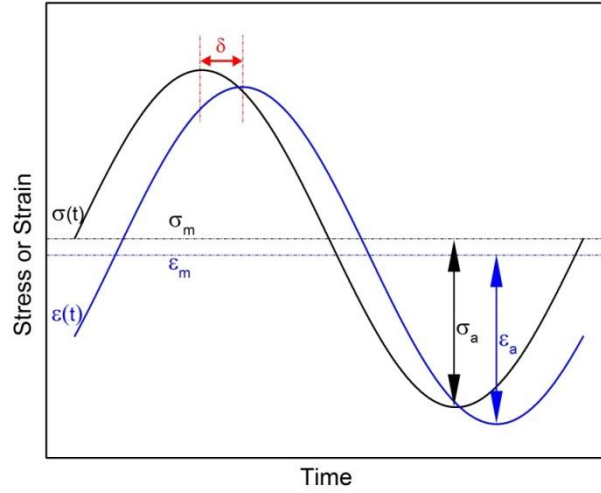


Fig. 6.7. Applied sinusoidal stress and strain response in viscoelastic material.

6.4.2 Validation of implemented solutions

In each experiment, the fatigue strain was simulated by importing the estimated viscoelastic parameters into Eqs. 11-13 to calculate the cyclic creep strain, cyclic strain amplitude, and phase-lag, respectively. The hysteresis loops were simulated by plotting the applied cyclic stress (Eq. 6.9) against the fatigue strain (Eq. 6.10) for each cycle. The detailed evaluation of the obtained results was carried out by comparing the hysteresis loop area, fatigue stiffness, and average cyclic strain with the experimental results obtained from the cyclic phase of the loading pattern (see Fig. 6.3) at the different numbers of cycles and stress levels.

The experimental fatigue hysteresis loops at 64 MPa and 49 MPa are indicated by dots in Fig. 6.8a and Fig. 6.9b, respectively. The hysteresis loop area, fatigue stiffness, and average cyclic strain exhibited measureable changes as the number of fatigue cycles increased for both high and low cyclic stresses. The predicted hysteresis loops are also indicated in Fig. 6.8a and Fig. 6.8b by solid lines. The experimental and predicted hysteresis loop areas, fatigue stiffnesses and average cyclic strains are compared in detail in Figs. 6.9-6.11.

The variations of the experimental and predicted hysteresis loop areas per cycle versus the normalized number of cycles are shown in Fig. 6.9 at high and low stress levels. The hysteresis area increased gradually with the number of cycles. At the high stress level, the experimental and predicted curves compared well. At the low stress level, the predicted curve however slightly underestimated the experimental results, which showed that the fatigue solution using the estimated viscoelastic parameters from the recovery curve could not fully simulate the hysteresis loop area.

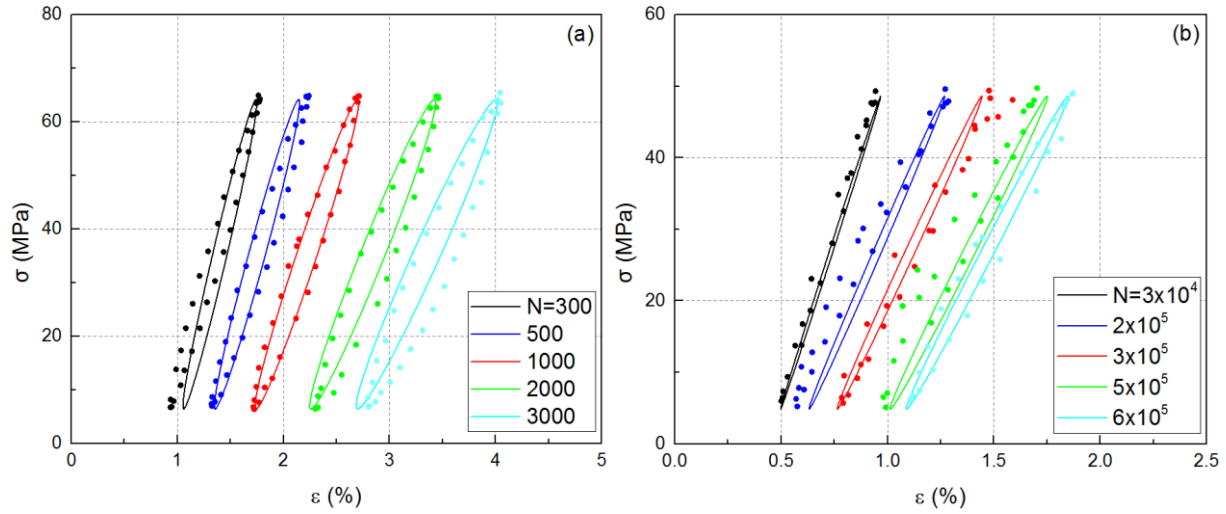


Fig. 6.8. Experimental (dots) and predicted fatigue (solid line) hysteresis loops at different number of cycles (N) at two stress levels, (a) Intf-0.1-64-b, and (b) Intf-0.1-49-a.

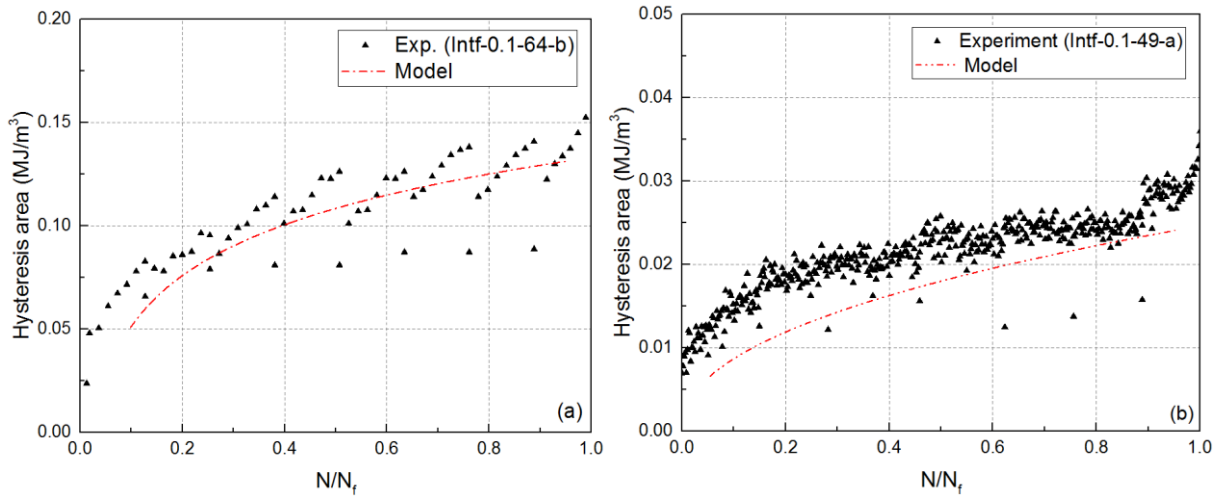


Fig. 6.9. Hysteresis loop area versus normalized number of cycles at different stress levels (a) Intf-0.1-64-b, and (b) Intf-0.1-49-a.

The variation of the experimental and predicted fatigue stiffness versus the normalized fatigue life is shown in Fig. 6.10 for high and low stress levels. In both cases, an initial steep decrease during the first 10–15% of the lifetime, followed by a steady-state stiffness decrease up to specimen failure, was observed. Experimental and predicted results compared well at both stress levels, with the exception of the initial stage at the high stress level, where the former were slightly overestimated.

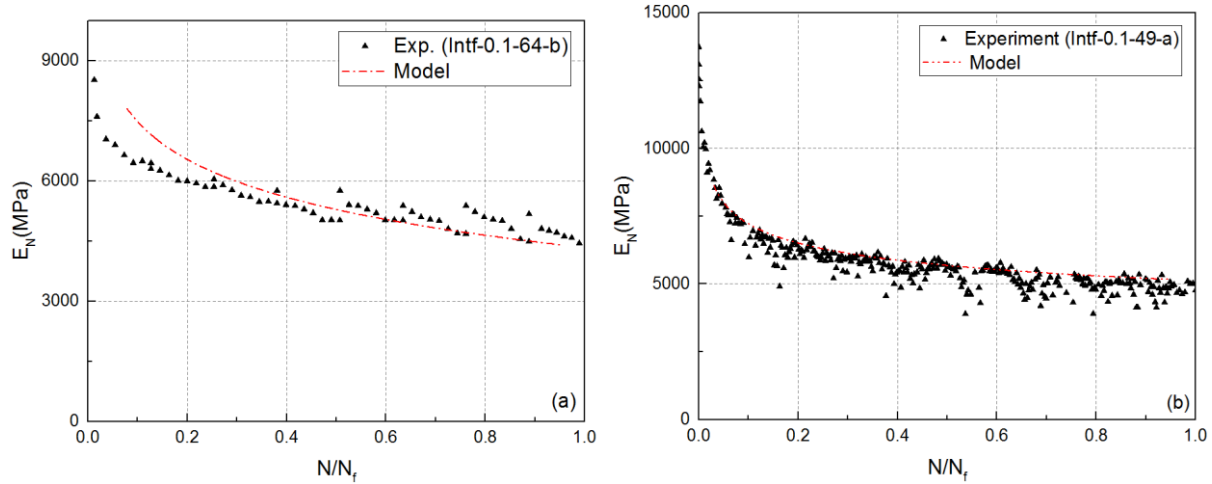


Fig. 6.10. Fatigue stiffness versus normalized number of cycles at different stress levels (a) Intf-0.1-64-b, and (b) Intf-0.1-49-a.

The variation of the average cyclic strain (average of maximum and minimum strains in one cycle) versus the normalized number of cycles is shown in Fig. 6.11. Independent of the stress level, the strains showed an increasing trend in the form of a ternary curve. The first region was at the early stage of cyclic loading in which the average cyclic creep strain rapidly increased, however at a decreasing rate. During the second stage, the average cyclic strain increased at a steady rate, while, finally, a rapid increase was observed prior to failure. At the beginning of each loading block, a gradual increasing of the cyclic strain was observed due to specimen recovery during the cyclic stress interruption at zero stress level ^[1]. The predicted average cyclic strains versus number of cycles are also indicated in Fig. 6.11 by green curves. The fatigue solution predicted well the general trend of the average cyclic strain as well as the initial increase in each loading block at both stress levels.

In addition to the average cyclic strain, the evolution of the strain components, i.e., the elastic, viscoelastic, and remaining strains were also obtained and are shown in Fig. 6.11. As the number of cycles increased, all strain components increased as a result of the fatigue damage formation and accumulation. The rate of increase of the different strain components varied between the two stress levels. The remaining strain was observed to increase more rapidly than the elastic and viscoelastic strain components and was the main reason for the growth of the cyclic strain. Additionally, viscoelastic strains were composed of small segments attributed to each loading block; they exhibited an initial increase and then a steady-state stage.

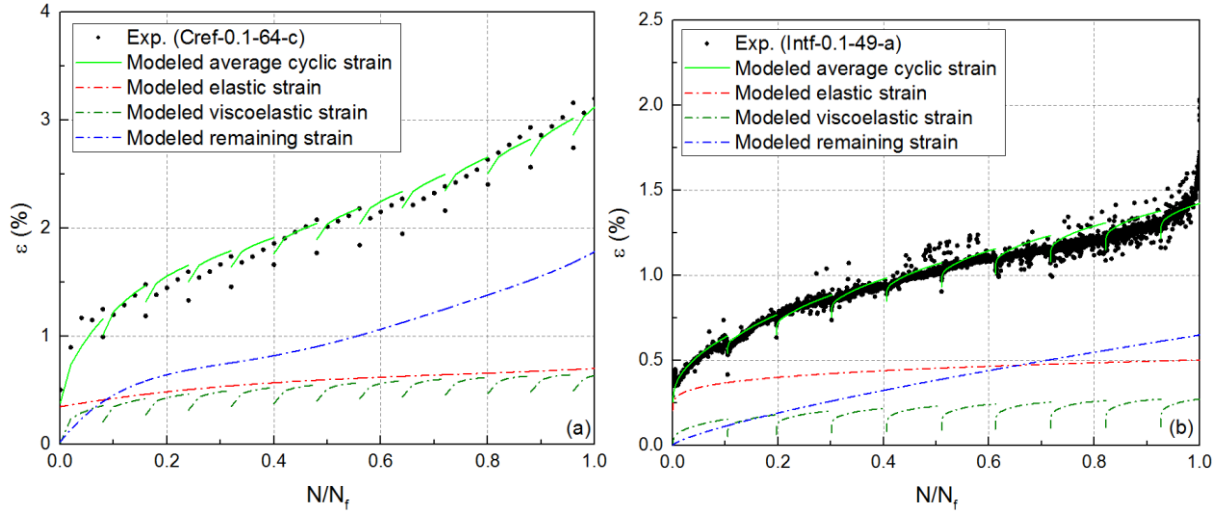


Fig. 6.11. Evolution of average cyclic, elastic, viscoelastic, and remaining strain at different stress levels (a) Intf-0.1-64-c, and (b) Intf-0.1-49-a.

The storage and loss moduli of viscoelastic materials measure the stored energy, representing the elastic portion, and the dissipated energy, representing the viscous portion ^[47]. The derived constitutive equation is also capable of simulating the evolution of the storage and loss moduli and $\tan(\delta)$ with the number of cycles.

$\tan(\delta)$ derived from experiments at each cycle was calculated using the following equation, as derived in ^[48]:

$$\sin(\delta) = \frac{Ew}{\pi\sigma_a^2} \quad (6.14)$$

where w is the hysteresis loop area of cycle N . E and w were obtained from the experiments at the applied stress amplitude σ_a . The magnitude of the storage and loss moduli in each cycle was then determined by solving the two following equations:

$$\tan(\delta) = \frac{E''}{E'} \quad (6.15)$$

$$E = \sqrt{E'^2 + E''^2} \quad (6.16)$$

where E' and E'' are the storage modulus and loss modulus, respectively. The evolution of the resulting experimental storage modulus, loss modulus, and $\tan(\delta)$ are shown in Fig. 6.12 for high and low stress levels, respectively. Accordingly, as the number of cycles increased, the storage modulus decreased, whereas loss modulus and $\tan(\delta)$ gradually increased. As shown in ^[1], damage gradually formed and propagated as the number of cycles increased, which reduced the storage modulus, while it

also caused more dissipation of energy due to the internal friction that augmented the magnitudes of the loss modulus and $\tan(\delta)$.

Based on the evolution of the viscoelastic parameters estimated at different numbers of cycles (Fig. 6.6), the storage and loss moduli as well as $\tan(\delta)$ were simulated according to Eq. 6.17, Eq. 6.18, and Eq. 6.13 respectively. The mathematical derivation of these equations is given in Annex II. The comparison of the predicted and experimentally derived storage modulus showed good agreement; however, the loss modulus and $\tan(\delta)$ were generally slightly underestimated. The lack of accuracy in predicting the loss modulus and $\tan(\delta)$ confirmed that the fatigue solution could not fully simulate the amount of energy dissipated at low stress levels.

$$E' = \frac{\sum_{i=1}^{i=3} \frac{\lambda_i}{\eta_i(\lambda_i^2 + \omega^2)} + \frac{1}{E}}{(\sum_{i=1}^{i=3} \frac{\lambda_i}{\eta_i(\lambda_i^2 + \omega^2)} + \frac{1}{E})^2 + (\sum_{i=1}^{i=3} \frac{\omega}{\eta_i(\lambda_i^2 + \omega^2)} + \frac{1}{\eta\omega})^2} \quad (6.17)$$

$$E'' = \frac{\sum_{i=1}^{i=3} \frac{\omega}{\eta_i(\lambda_i^2 + \omega^2)} + \frac{1}{\eta\omega}}{(\sum_{i=1}^{i=3} \frac{\lambda_i}{\eta_i(\lambda_i^2 + \omega^2)} + \frac{1}{E})^2 + (\sum_{i=1}^{i=3} \frac{\omega}{\eta_i(\lambda_i^2 + \omega^2)} + \frac{1}{\eta\omega})^2} \quad (6.18)$$

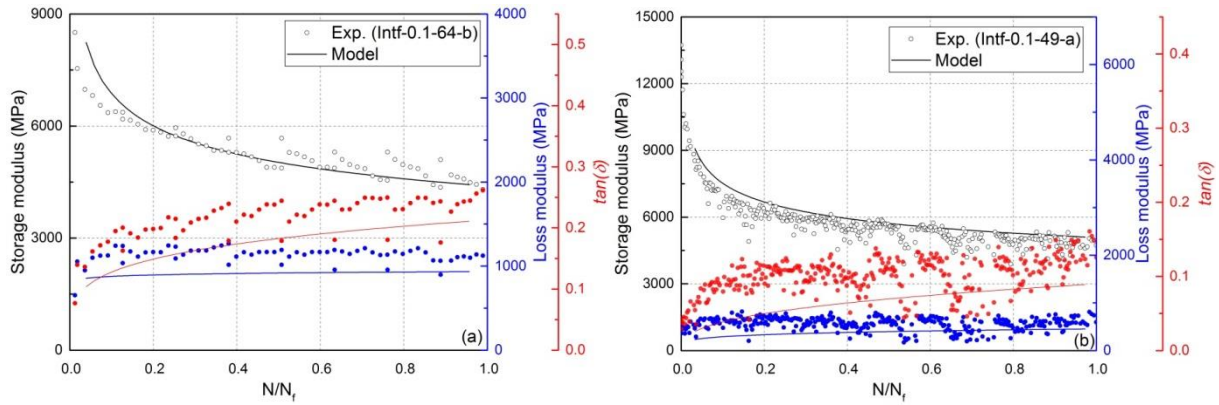


Fig. 6.12. Variation of storage modulus, loss modulus, and $\tan(\delta)$ during fatigue loading at different stress levels (a) Intf-0.1-64-b, and (b) Intf-0.1-49-a.

6.5. Conclusions

A general constitutive equation was derived to consider the interaction of the time- and cyclic-dependent mechanical properties of viscoelastic materials, and solved for two specific loading patterns, 1) stress unloading from mean to zero stress level (recovery solution), and 2) load control sinusoidal loading (fatigue solution). To implement and validate these solutions, a loading pattern

comprising a constant amplitude cyclic loading with repetitive interruptions was selected and applied to $\pm 45^\circ$ angle-ply glass/epoxy composite laminates. The evolution of the viscoelastic parameters was estimated at different percentages of fatigue life by adjusting the recovery solution to the experiments. In order to evaluate the accuracy of the constitutive equation implemented, the predictions of the fatigue solution were then compared with the experimental results in cyclic phases of the loading pattern. The following conclusions were drawn:

- As the number of cycles increased, the viscoelastic parameters decreased due to damage accumulation, except that corresponding to the remaining deformation that increased, as a result of the decreasing rate of the remaining strain.
- With the viscoelastic parameters calibrated, the predicted results of the fatigue solution could simulate the fatigue hysteresis loops, fatigue stiffness, and cyclic creep. All were in good agreement with the results of the experiments with the exception of the hysteresis loop area which was slightly underestimated at low stress levels.
- The fatigue solution enabled the average cyclic strain to be decomposed into the elastic, viscoelastic, and remaining strain components. As the number of cycles increased, all strain components increased as a result of fatigue damage formation and accumulation. It was observed that the elastic and viscoelastic strains increased gradually while the remaining strain increased more rapidly and was the main reason for the growth of the cyclic strain.
- The proposed constitutive equation was also able to predict the evolution of the storage modulus well while the predicted loss modulus and $\tan(\delta)$ were only slightly underestimated. It was observed that, as the number of cycles increased, the storage modulus decreased, while both the loss modulus and $\tan(\delta)$ increased.
- The proposed governing equation is applicable in cases where cyclic loading is interrupted for a sufficient length of time. Additionally, the constitutive equation is useable when there is an interaction between time- and cyclic-mechanical properties, and therefore it may not be used in fiber-dominated composites with negligible time-dependent mechanical properties.

References:

[1] Movahedi-Rad, A. V., Keller, T., & Vassilopoulos, A. P. (2018). Interrupted tension-tension fatigue behavior of angle-ply GFRP composite laminates. *International Journal of Fatigue*, 113, 377-388.

- [2] Movahedi-Rad, A. V., Keller, T., & Vassilopoulos, A. P. (2019). Creep effects on tension-tension fatigue behavior of angle-ply GFRP composite laminates. *International Journal of Fatigue*, 123, 144-156.
- [3] Tschoegl, N. W. (1998). Time-dependence in materials. In *Progress and Trends in Rheology V* (pp. 1-3). Steinkopff, Heidelberg.
- [4] Mallick, P. K., & Zhou, Y. (2004). Effect of mean stress on the stress-controlled fatigue of a short E-glass fiber reinforced polyamide-6, 6. *International journal of fatigue*, 26(9), 941-946.
- [5] Haward, R. N., & Thackray, G. 1. (1968). The use of a mathematical model to describe isothermal stress-strain curves in glassy thermoplastics. *Proc. R. Soc. Lond. A*, 302(1471), 453-472.
- [6] Boyce, M. C., Parks, D. M., & Argon, A. S. (1988). Large inelastic deformation of glassy polymers. Part I: rate dependent constitutive model. *Mechanics of Materials*, 7(1), 15-33.
- [7] Hizoum, K., Rémond, Y., Bahlouli, N., Oshmyan, V., Patlazhan, S., & Ahzi, S. (2006). Non linear strain rate dependency and unloading behavior of semi-crystalline polymers. *Oil & Gas Science and Technology-Revue de l'IFP*, 61(6), 743-749.
- [8] Yakimets, I., Lai, D., & Guigon, M. (2007). Model to predict the viscoelastic response of a semi-crystalline polymer under complex cyclic mechanical loading and unloading conditions. *Mechanics of Time-Dependent Materials*, 11(1), 47-60.
- [9] Drozdov, A. D. (2009). Constitutive model for cyclic deformation of perfluoroelastomers. *Mechanics of Time-Dependent Materials*, 13(3), 275-299.
- [10] Ayoub, G., Zaïri, F., Naït-Abdelaziz, M., & Gloaguen, J. M. (2010). Modelling large deformation behaviour under loading–unloading of semicrystalline polymers: application to a high density polyethylene. *International Journal of Plasticity*, 26(3), 329-347.
- [11] Vandenbroucke, A., Laurent, H., Hocine, N. A., & Rio, G. (2010). A Hyperelasto-Visco-Hysteresis model for an elastomeric behaviour: experimental and numerical investigations. *Computational Materials Science*, 48(3), 495-503.
- [12] Drozdov, A. D. (2012). Cyclic viscoelastoplasticity of polypropylene/nanoclay hybrids. *Computational Materials Science*, 53(1), 396-408.
- [13] Colak, O. U. (2005). Modeling deformation behavior of polymers with viscoplasticity theory based on overstress. *International Journal of Plasticity*, 21(1), 145-160.
- [14] Krasnobrizha, A., Rozycki, P., Cosson, P., & Gornet, L. (2015, July). Modelling the hysteresis composite behavior using an elasto-plasto-damage model with fractional derivatives. In *20th International Conference on Composite Materials-ICCM20*.

- [15] Schapery, R. A. (1984). Correspondence principles and a generalized J integral for large deformation and fracture analysis of viscoelastic media. *International journal of fracture*, 25(3), 195-223.
- [16] Zhang, C., & Moore, I. D. (1997). Nonlinear mechanical response of high density polyethylene. Part II: Uniaxial constitutive modeling. *Polymer Engineering & Science*, 37(2), 414-420.
- [17] Khan, A., & Zhang, H. (2001). Finite deformation of a polymer: experiments and modeling. *International Journal of Plasticity*, 17(9), 1167-1188.
- [18] Flügge, W., *Viscoelasticity*. Blaisdell, Waltham, MA, 1964.
- [19] Ferry, J. D., *Viscoelastic Properties of Polymers*, 3rd edn. John Wiley and Sons, New York, 1980.
- [20] Guedes, Rui Miranda, ed. *Creep and fatigue in polymer matrix composites*. Elsevier, 2010.
- [21] Schapery, R. A. (1969). On the characterization of nonlinear viscoelastic materials. *Polymer Engineering & Science*, 9(4), 295-310.
- [22] Zaoutsos, S. P., Papanicolaou, G. C., & Cardon, A. H. (1998). On the non-linear viscoelastic behaviour of polymer-matrix composites. *Composites Science and Technology*, 58(6), 883-889.
- [23] Whitworth, H. A. (1997). A stiffness degradation model for composite laminates under fatigue loading. *Composite structures*, 40(2), 95-101.
- [24] Machado, R. D., Abdalla Filho, J. E., & da Silva, M. P. (2008). Stiffness loss of laminated composite plates with distributed damage by the modified local Green's function method. *Composite Structures*, 84(3), 220-227.
- [25] Wu, F., & Yao, W. (2010). A fatigue damage model of composite materials. *International Journal of Fatigue*, 32(1), 134-138.
- [26] Zhang, Y., Vassilopoulos, A. P., & Keller, T. (2010). Fracture of adhesively-bonded pultruded GFRP joints under constant amplitude fatigue loading. *International Journal of Fatigue*, 32(7), 979-987.
- [27] Vassilopoulos AP, Keller T. *Fatigue of fiber-reinforced composites*. Springer Science & Business Media, 2011.
- [28] Sarfaraz, R., Vassilopoulos, A. P., & Keller, T. (2011). Experimental investigation of the fatigue behavior of adhesively-bonded pultruded GFRP joints under different load ratios. *International Journal of Fatigue*, 33(11), 1451-1460.
- [29] Shahverdi, M., Vassilopoulos, A. P., & Keller, T. (2012). A total fatigue life model for the prediction of the R-ratio effects on fatigue crack growth of adhesively-bonded pultruded GFRP DCB joints. *Composites Part A: Applied Science and Manufacturing*, 43(10), 1783-1790.

- [30] Kennedy, C. R., Brádaigh, C. M. Ó., & Leen, S. B. (2013). A multiaxial fatigue damage model for fibre reinforced polymer composites. *Composite Structures*, 106, 201-210.
- [31] Mohammadi, B., Fazlali, B., & Salimi-Majd, D. (2017). Development of a continuum damage model for fatigue life prediction of laminated composites. *Composites Part A: Applied Science and Manufacturing*, 93, 163-176.
- [32] Miyano, Y., Nakada, M., McMurray, M. K., & Muki, R. (1997). Prediction of flexural fatigue strength of CRFP composites under arbitrary frequency, stress ratio and temperature. *Journal of Composite Materials*, 31(6), 619-638.
- [33] Petermann, J., & Schulte, K. (2002). The effects of creep and fatigue stress ratio on the long-term behaviour of angle-ply CFRP. *Composite Structures*, 57(1-4), 205-210.
- [34] Vieille, B., Albouy, W., & Taleb, L. (2014). About the creep-fatigue interaction on the fatigue behaviour of off-axis woven-ply thermoplastic laminates at temperatures higher than T_g. *Composites Part B: Engineering*, 58, 478-486.
- [35] Sayyidmousavi, A., Bougherara, H., & Fawaz, Z. (2015). The role of viscoelasticity on the fatigue of angle-ply polymer matrix composites at high and room temperatures-a micromechanical approach. *Applied Composite Materials*, 22(3), 307-321.
- [36] Movahedi-Rad, A. V., Keller, T., & Vassilopoulos, A. P. (2018). Fatigue damage in angle-ply GFRP laminates under tension-tension fatigue. *International Journal of Fatigue*, 109, 60-69.
- [37] Savvilotidou, M., Keller, T., & Vassilopoulos, A. P. (2017). Fatigue performance of a cold-curing structural epoxy adhesive subjected to moist environments. *International Journal of Fatigue*, 103, 405-414.
- [38] Sun, C. T., & Chim, E. S. (1981). Fatigue retardation due to creep in a fibrous composite. In *Fatigue of Fibrous Composite Materials*. ASTM International.
- [39] ASTM, D3171–99. *Standard test methods for constituent content of composite materials*. ASTM International; 2002.
- [40] ASTM D3039/D3039M-14 *Standard Test Method for Tensile Properties of Polymer Matrix Composite Materials*. ASTM International; 2014.
- [41] ASTM, D7791–17. *Standard Test Method for Uniaxial Fatigue Properties of Plastics*. ASTM International; 2017.
- [42] Krause O, Philippidis TP. General test specification Optimat report: OB_TC_R015 available on line from <https://www.wmc.eu/public_docs/10157_005.pdf>.
- [43] Kawai, M., & Masuko, Y. (2004). Creep behavior of unidirectional and angle-ply T800H/3631 laminates at high temperature and simulations using a phenomenological viscoplasticity model. *Composites Science and Technology*, 64(15), 2373-2384.

- [44] Ascione, L., Berardi, V. P., & D'Aponte, A. (2011). A viscoelastic constitutive law for FRP materials. *International Journal for Computational Methods in Engineering Science and Mechanics*, 12(5), 225-232.
- [45] Xu, Y. (2009). Creep behavior of natural fiber reinforced polymer composites.
- [46] Boggs, P. T., & Rogers, J. E. (1990). Orthogonal distance regression. *Contemporary Mathematics*, 112, 183-194.
- [47] Chawla, K. K., & Meyers, M. A. (1999). *Mechanical behavior of materials* (p. 217). Upper Saddle River: Prentice Hall.
- [48] Brinson, H. F., & Brinson, L. C. (2008). Polymer engineering science and viscoelasticity. *New York: Springer*, 66, 79.

Annex I:

The applied loading pattern in sinusoidal cyclic loading is;

$$\sigma(t) = \sigma_m + \sigma_a \sin(\omega t) \quad (\text{I-1})$$

The response of Maxwell and Kelvin units to this loading pattern is as follows:

Solution for one Maxwell unit:

The constitutive equation for a Maxwell unit consisting of a series of a spring and a dashpot is:

$$\sigma(t) + \frac{\eta}{E} \dot{\sigma}(t) = \eta \dot{\varepsilon}(t) \quad (\text{I-2})$$

By inserting [Eq. I-1](#) into [Eq. I-2](#) and rearranging, the following equation is obtained:

$$\varepsilon(t) = \frac{\sigma_m}{\eta} t + \frac{\sigma_a}{\eta \omega} \cos(\omega t) - \frac{\sigma_a}{E} \sin(\omega t) + C_1 \quad (\text{I-3})$$

Solution for one Kelvin unit:

The constitutive equation for a Kelvin unit consisting of a parallel pair of a spring and a dashpot is:

$$\sigma(t) = E\varepsilon(t) + \eta \dot{\varepsilon}(t) \quad (\text{I-4})$$

By inserting [Eq. I-1](#) into [Eq. I-4](#) and rearranging, the obtained equation is:

$$\dot{\varepsilon}(t) + \lambda \varepsilon(t) = \frac{\sigma_m}{\eta} + \frac{\sigma_a}{\eta} \sin(\omega t) \quad (\text{I-5})$$

By multiplying the integral factor of $e^{\lambda t}$ to both sides of [Eq. I-5](#), rearranging, and integrating the resulting equation, the following relationship is obtained:

$$\varepsilon(t)e^{\lambda t} = \frac{\sigma_m}{\eta \lambda} e^{\lambda t} + \frac{\sigma_a}{\eta} \int e^{\lambda t} \sin(\omega t) dt \quad (\text{I-6})$$

By using the theorem of partial integration twice, the following relationship results:

$$\varepsilon(t) = \frac{\sigma_m}{E} + C_2 \frac{\sigma_m}{\eta} e^{\lambda t} + \left(\frac{\sigma_a}{\eta_i} \frac{\lambda}{\lambda^2 + \omega^2} \sin(\omega t) - \frac{\sigma_a}{\eta} \frac{\omega}{\lambda^2 + \omega^2} \cos(\omega t) \right) \quad (\text{I-7})$$

Solution for one Maxwell and three Kelvin units:

The general solution for one Maxwell and three Kelvin units is the summation of Eq. I-3 and Eq. I-7 as follows:

$$\varepsilon(t) = \frac{\sigma_m}{E} + \sum_{i=1}^3 \frac{\sigma_m}{E_i} \left(1 - e^{-\frac{E_i}{\eta_i}(t-t_0)} \right) + \frac{\sigma_m}{\eta} (t - t_0) + \sum_{i=1}^3 \left(\frac{\sigma_a}{\eta_i} \frac{\lambda_i}{\lambda_i^2 + \omega^2} + \frac{\sigma_a}{E} \right) \sin(\omega t) - \left(\frac{\sigma_a}{\eta_i} \frac{\omega}{\lambda_i^2 + \omega^2} + \frac{\sigma_a}{\eta \omega} \right) \cos(\omega t) \quad (\text{I-8})$$

which can also be written as:

$$\begin{aligned} \varepsilon(t) = & \frac{\sigma_m}{E} + \sum_{i=1}^3 \frac{\sigma_m}{E_i} \left(1 - e^{-\frac{E_i}{\eta_i}(t-t_0)} \right) + \frac{\sigma_m}{\eta} (t - t_0) + \\ & \sigma_a \sqrt{\left(\sum_{i=1}^3 \frac{1}{\eta_i} \frac{\lambda}{\lambda_i^2 + \omega^2} + \frac{1}{E} \right)^2 + \left(\sum_{i=1}^3 \frac{1}{\eta_i} \frac{\omega}{\lambda_i^2 + \omega^2} + \frac{1}{\eta \omega} \right)^2} \sin \left(\omega t + \tan^{-1} \left(\frac{\sum_{i=1}^3 \frac{\omega}{\eta_i(\lambda_i^2 + \omega^2)} + \frac{1}{\eta \omega}}{\sum_{i=1}^3 \frac{\lambda}{\eta_i(\lambda_i^2 + \omega^2)} + \frac{1}{E}} \right) \right) \end{aligned} \quad (\text{I-9})$$

The previous equation can be simplified to the following form:

$$\varepsilon(t) = \varepsilon_c(t) + \varepsilon_a \sin(\omega t - \delta) \quad (\text{I-10})$$

where

$$\varepsilon_c(t) = \frac{\sigma_m}{E} + \sum_{i=1}^3 \frac{\sigma_m}{E_i} \left(1 - e^{-\lambda_i(t-t_0)} \right) + \frac{\sigma_m}{\eta} (t - t_0) \quad (\text{I-11})$$

$$\varepsilon_a = \sigma_a \sqrt{\left(\sum_{i=1}^3 \frac{1}{\eta_i} \frac{\lambda_i}{\lambda_i^2 + \omega^2} + \frac{1}{E} \right)^2 + \left(\sum_{i=1}^3 \frac{1}{\eta_i} \frac{\omega}{\lambda_i^2 + \omega^2} + \frac{1}{\eta \omega} \right)^2} \quad (\text{I-12})$$

$$\delta = \tan^{-1} \left(\frac{\sum_{i=1}^3 \frac{\omega}{\eta_i(\lambda_i^2 + \omega^2)} + \frac{1}{\eta \omega}}{\sum_{i=1}^3 \frac{\lambda_i}{\eta_i(\lambda_i^2 + \omega^2)} + \frac{1}{E}} \right) \quad (\text{I-13})$$

Annex II:

The evolution of the storage and loss moduli during the fatigue loading can be calculated as follows.

By considering:

$$b = \sum_{i=1}^{i=3} \frac{1}{\eta_i} \frac{\omega}{\lambda_i^2 + \omega^2} + \frac{1}{\eta\omega} \quad (\text{II-1})$$

$$a = \sum_{i=1}^{i=3} \frac{1}{\eta_i} \frac{\lambda}{\lambda_i^2 + \omega^2} + \frac{1}{E} \quad (\text{II-2})$$

the following equations are valid:

$$E^* = \sqrt{E'^2 + E''^2} = \frac{1}{\sqrt{a^2 + b^2}} \quad (\text{II-3})$$

$$\tan(\delta) = \frac{E''}{E'} = \frac{b}{a} \quad (\text{II-4})$$

By considering both [Eq. II-3](#) and [Eq. II-4](#), the magnitude of storage and loss moduli were calculated according to [Eq. II-5](#) and [Eq. II-6](#);

$$E' = \frac{a}{a^2 + b^2} \quad (\text{II-5})$$

$$E'' = \frac{b}{a^2 + b^2} \quad (\text{II-6})$$

Contributions:

A.Vahid Movahedi-Rad conceived, designed and performed the experimental campaign under the supervision of Dr. Anastasios Vassilopoulos and Prof. Thomas Keller. The analysis of the results was carried out by A.Vahid Movahedi-Rad in collaboration with Dr. Anastasios Vassilopoulos and Prof. Thomas Keller.



Chapter 7



Conclusions and future work

7.1. Conclusions

- The effect of loading pattern on the fatigue behavior of $(\pm 45)_{2s}$ glass/epoxy composite laminates at different stress levels has been investigated in this thesis. Different mechanical, thermal, and optical measurements were used for the observation of the fatigue damage process and quantification of the damage caused due to loading at different stress levels. It was observed that the loading pattern affected the fatigue behavior of the studied specimens especially at intermediate and high stress levels. A summary of the most significant results obtained during the work carried out for this thesis is given below. Different loading patterns were applied to the specimens by changing the cyclic stress levels and stress ratio as well as interrupting the cyclic loading at different stress levels and different hold times. As the cyclic stress levels decreased, the fatigue life increased under all loading patterns. Increasing the stress ratio from 0.1 to 0.5 at constant σ_{\max} increased fatigue life. The interruption of cyclic loading could either increase or decrease the number of cycles to failure depending on the stress level and hold time. The interruption at σ_{\max} (creep) at a short hold-time of 2 h resulted in fatigue life enhancement at intermediate and high stress levels. Longer hold times at high stress levels caused creep failure and therefore premature fatigue failure of the specimens. The specimens loaded under interrupted fatigue at zero stress level had longer fatigue lives than

those continuously loaded at the same cyclic stress levels. The enhancement of fatigue life was considerable at higher stress levels and almost disappeared at low stress levels.

- Under all loading patterns, as the number of cycles increased, damage started appearing on the specimen surface as revealed by digital photos. Generally, at higher stress levels, the damage was severe and localized; however, by decreasing the fatigue stress level, more uniform and less severe damage distribution was observed throughout the specimen volume. In addition, the interruption of cyclic loading also made the damage distribution more uniform and reduced the severity of the concentrated damage zone formed.
- The specimens generated temperature during the cyclic loading, mainly due to the internal friction in the damaged regions. The evolution of the self-generated temperature was measured using an IR thermal camera. In continuous fatigue, the self-generated temperature continuously increased and the temperature distribution became non-uniform across the specimen surface, due to the formation of concentrated damage zones. However, the self-generated temperature was lower at lower stress levels and the higher stress ratio due to the smaller stress amplitude. When the cyclic loading was interrupted, the self-generated temperature dropped and increased again when the loading was restored in the next loading block. The specimen stiffening after the creep phase in the creep-fatigue experiments led to a reduction of internal friction and self-generated temperature in the specimens during the fatigue phase.
- The degree of severity of the concentrated damage zone determined the shape of the final fracture surface. At high stress levels under all loading patterns, due to the formation of severe concentrated damage, the stress was not transferred to the fibers, and therefore fiber pull-out was observed. In this case, in severely concentrated damage zones, due to the fiber realignment toward the loading direction, failure occurred with considerable necking. At low stress levels, the damage distribution became more uniform under all loading patterns, which led to a mixed-mode failure with fiber pull-out and fiber breakage.
- Typical fatigue stiffness reduction was observed as a result of damage formation and accumulation in the specimens loaded under continuous fatigue at $R=0.1$. At the same time, the hysteresis loop area continuously increased with the number of cycles under the same loading pattern, which was mainly attributed to more internal friction as a result of damage growth. The loading pattern could change the structure of the studied composite by considerably realigning its fiber direction toward the loading direction. Fiber realignment was observed in the creep phase of the creep-fatigue loading pattern, and also in continuous fatigue at $R=0.5$ at high and intermediate stress levels, which led to increasing fatigue stiffness and

decreasing hysteresis loop area. Similar enhancement of fatigue stiffness and reduction of hysteresis loop area also occurred due to the recovery of the viscoelastic matrix in the interrupted fatigue experiments at high and intermediate stress levels.

- The formed and accumulated fatigue damage affected the time-dependent mechanical properties of the studied material as was revealed by monitoring its recovery and creep behavior in interrupted fatigue and creep-fatigue experiments. The accumulated fatigue damage accelerated the creep strain development and increased the viscoelastic recovery.
- A model was developed to simulate the recovery behavior of angle-ply laminated composites in order to predict their cyclic-dependent mechanical properties. A general constitutive equation was proposed and solved for the loading conditions of recovery and load-control cyclic loading. The recovery equation parameters were calibrated using the experimental recovery curves to estimate the viscoelastic parameters, and these parameters were used to predict the fatigue stiffness, hysteresis loop area, cyclic creep, storage and loss moduli, as well as $Tan(\delta)$.
- Typical ternary curves were observed when the specimen was loaded under the continuous fatigue loading pattern. According to the developed model, the first stage of cyclic creep was mainly attributed to the rapid increase of the viscoelastic and permanent strain; however, in the region with the steady strain increase, the cyclic creep was governed by permanent strain. The average cyclic strain increased rapidly in the initial stage of the continuous fatigue experiments at $R=0.5$ while at $R=0.1$, it gradually increased in the steady state stage. Interrupting the loading pattern also changed the evolution of the average cyclic strain. In the creep-fatigue experiments, after the first interruption, depending on the applied stress level and hold time, three different behaviors of the average cyclic strain were observed - either partially recovered, constant, or increased. These observations were due to two opposing phenomena of specimen recovery from creep loading (σ_{max}) to cyclic loading with the average stress lower than σ_{max} and the specimens creeping during the cyclic loading. It was observed that in the interrupted fatigue experiments, during each interruption the strain decreased due to specimen recovery, which led to the lower average cyclic strain in the following loading block; however, again it gradually increased as the number of cycles increased.

7.2 Original contributions

The original contributions of this thesis are the following:

- The effect of loading pattern on the fatigue behavior of $(\pm 45)_{2S}$ angle-ply glass/epoxy composite laminates was experimentally investigated at different stress levels to cover a wide range of fatigue lives. Rectangular specimens were subjected to continuous fatigue with the stress ratio of 0.1 and 0.5, creep-fatigue experiments with hold times of 2 h and 48 h, and interrupted fatigue at zero stress level for 2 h. In addition, pure creep experiments at different stress levels were performed.
- The evolution of cyclic creep, fatigue stiffness, and hysteresis loop area were recorded in each experiment and the effect of the applied stress level was investigated.
- The damage progression under the different loading patterns was monitored and the final fracture surfaces were studied at different stress levels.
- The magnitude and distribution of the self-generated temperature were monitored under different loading patterns and the effect of stress levels was investigated.
- The effect of fatigue damage on creep behavior was identified by comparing specimen creep behavior in the creep-fatigue experiments with pure creep at the same stress level.
- The effect of fatigue damage on the recovery behavior in the interrupted fatigue experiments was investigated by measuring the strain reduction as the number of blocks and stress levels increased.
- A model based on the theory of viscoelasticity was developed to simulate the recovery behavior of angle-ply laminated composites in order to predict their cyclic-dependent mechanical properties.

7.3 Recommendations for future work

Research topics for future investigations to develop the current work are presented in the following.

7.3.1 Study the effect of loading pattern on other types of composite

The effect of loading pattern on laminated composites composed of different resins and with stacking sequences is not yet clear. Generally speaking, the sensitivity of composites to the type of loading pattern depends on the matrix viscoelastic/plastic properties and damage growth mechanism. Resin properties are a function of the resin type (thermoset or thermoplastic), its curing degree, and environmental conditions (temperature and humidity) while damage growth mechanisms mainly

depend on composite stacking sequence and fiber/resin properties. For example, when the matrix is highly viscoelastic in an angle-ply composite, the fiber reorientation occurs more during the cyclic loading, which leads to a greater stiffening effect. In addition, the crack blunting effect and matrix recovery are more significant, which can lead to greater sensitivity of material fatigue behavior to the applied loading pattern.

7.3.2 Study the effect of loading pattern in compressive-compressive fatigue loading

Composite materials behave differently under tension and compression, since different mechanisms are developed under these loading patterns. When tensile loads are applied, fatigue failure is mainly fiber-dominated, whereas under compression the role of such factors as matrix, fiber misalignment, and material defects is more pronounced, which could change the sensitivity of the material fatigue behavior to the applied loading pattern.

7.3.3 Study the temperature and moisture effect on the sensitivity of laminated composites to the applied loading pattern

Since GFRP composites are used in outdoor applications, the effect of moisture and temperature on fatigue behavior under different loading patterns will be important. It is expected that the moisture diffuses inside the polymeric material and changes its viscoelastic behavior through the plasticization process ^[1]. In addition, as shown in Fig. 2.3, the mechanical properties start changing at temperatures above 40°C, which is a typical temperature during the summer in many places. Therefore, the fatigue behavior of these materials and the effect of loading pattern on this fatigue behavior at elevated temperatures and different percentages of humidity need to be studied.

7.3.4 Finite element analysis of the crack tip in viscoelastic materials

As discussed in Chapter 5, unloading the damaged viscoelastic matrix led to crack blunting in which the local stress intensity in the craze zone at the crack tip was significantly reduced. Upon reloading, the local stress intensity did not increase again at the same rate as the previous loading block, which thus delayed the crack growth in the following cycles. Similar observations were also reported in the literature ^[2,3,4,5]. This phenomenon can be studied using finite element analysis to model the stress intensity factor at the crack tip in viscoelastic media during loading and unloading.

7.3.5 Study the effect of loading pattern on repeatability of fatigue results

As shown in Chapter 6 and also [6], interrupting the continuous fatigue increased the fatigue life scatter. However, the effect of other loading patterns on the fatigue life scatter has not yet been studied in the literature and this could be a topic for future works.

7.3.6 Study the evolution of inter-lamina stress during cyclic loading

In Chapter 2, it was shown that the different stress levels led to different delamination sizes. The delamination size depends on the magnitude of the internal stress during the fatigue experiments and the layout of the composite [7]. The inter-lamina stresses in the laminate composite with free edges in the plane stress state can be determined indirectly by calculating two shear interlaminar stresses (τ_{zx} and τ_{yz}) and one normal out-of-plane stress (σ_z) based on the equilibrium equations as explained in [7]. However, the evolution of interlaminar stress during fatigue loading has not yet been studied. For the composite studied in this thesis with the $(\pm 45)_{2s}$ layout, the distribution of F_{zx} interlaminar stress is shown in Fig. 7.1. It can be seen that the calculated pattern of the interlaminar stress level is similar to the observed fracture surface shown in Fig. 7.2.

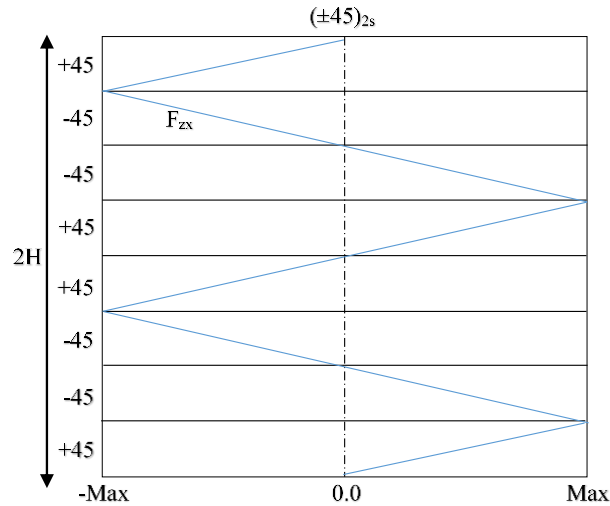


Fig. 7.1. Distribution of F_{zx} interlaminar stress in $(\pm 45)_{2s}$.



Fig. 7.2. Fatigue fracture surface of glass/epoxy composite with $(\pm 45)_{2s}$ layout.

References

- [1] Savvilotidou, M., Keller, T., & Vassilopoulos, A. P. (2017). Fatigue performance of a cold-curing structural epoxy adhesive subjected to moist environments. *International Journal of Fatigue*, 103, 405-414.
- [2] Schapery, R. A. (1975). A theory of crack initiation and growth in viscoelastic media. *International Journal of Fracture*, 11(1), 141-159.
- [3] Mandell, J. F., & Meier, U. (1983). Effects of stress ratio, frequency, and loading time on the tensile fatigue of glass-reinforced epoxy. In *Long-term behavior of composites*. ASTM International.
- [4] Saff, C. R. (1983). Effect of load frequency and lay-up on fatigue life of composites. In *Long-term behavior of composites*. ASTM International.
- [5] Sun, C. T., & Chan, W. S. (1979, January). Frequency effect on the fatigue life of a laminated composite. In *Composite materials: testing and design (fifth conference)*. ASTM International.
- [6] A.P. Vassilopoulos, T.P. Philippidis, Effect of interrupted cyclic loading on fatigue life of composites, Comp 03, 5th international symposium on advanced composites, Advances in composite technology, Corfu imperial Hotel, Corfu, Greece, 5-7 May 2003.
- [7] Herakovich, C. T. (1998). Mechanics of fibrous composites.

Annexes



Annex A: Continuous-fatigue ($R=0.1$)

Annex B: Continuous-fatigue ($R=0.5$)

Annex C: Creep-fatigue

Annex D: Interrupted-fatigue

Annex E: DSC results

Annex F: Localized measurements of strain in creep-fatigue experiments

Annex G: Study the effect of damage on viscoelasticity by using DMA

Annex H: Experimental study of crack blunting effect in viscoelastic media

Annex A: Continuous-fatigue ($R=0.1$)



A.1 Introduction

Annex A presents supplementary results from the experiments conducted on the continuous fatigue at the stress ratio of 0.1, which was described in Chapter 2.

No.	Code	f (Hz)	N_f
1	Conf-0.1-68-a	4.35	1,969

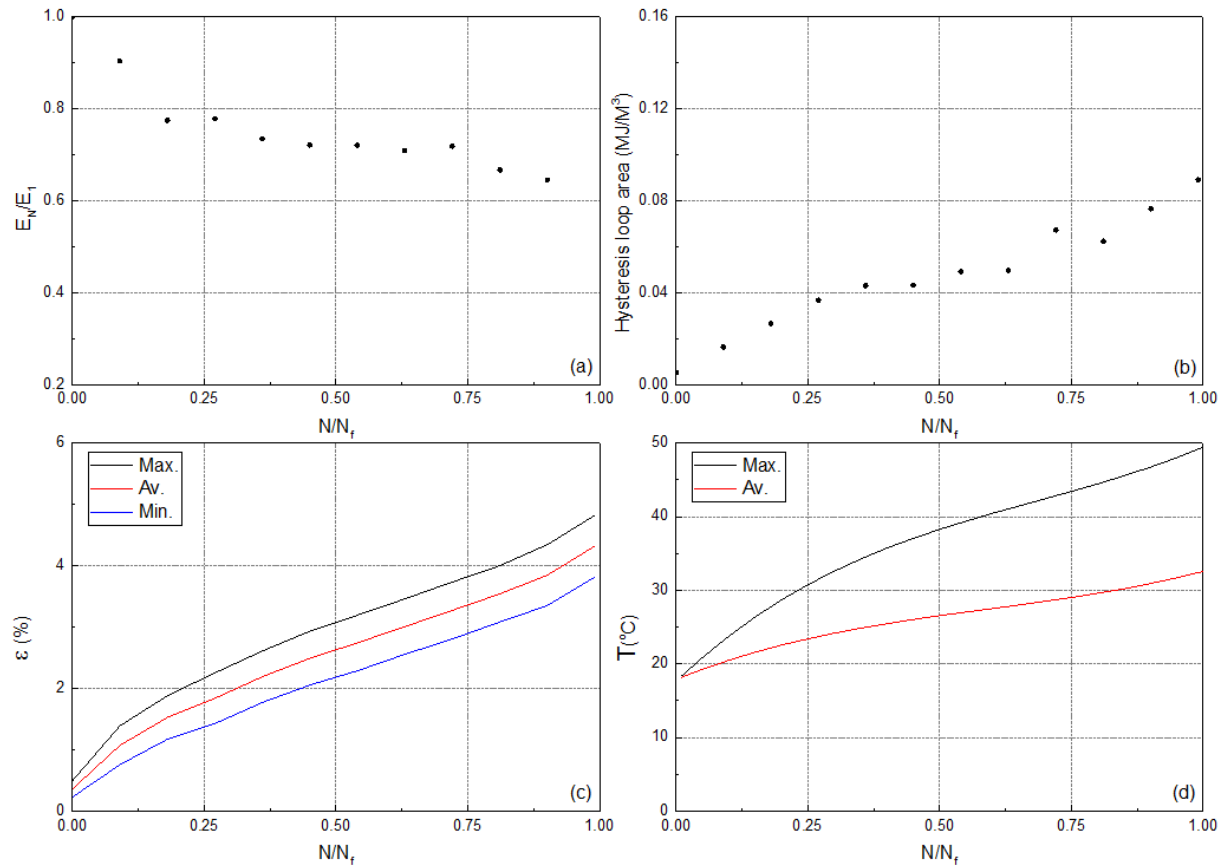


Fig. 1. Variation of (a) normalized fatigue stiffness, (b) hysteresis area, (c) maximum, average, and minimum cyclic strain, and (d) maximum and average self-generated temperature versus normalized number of cycles.

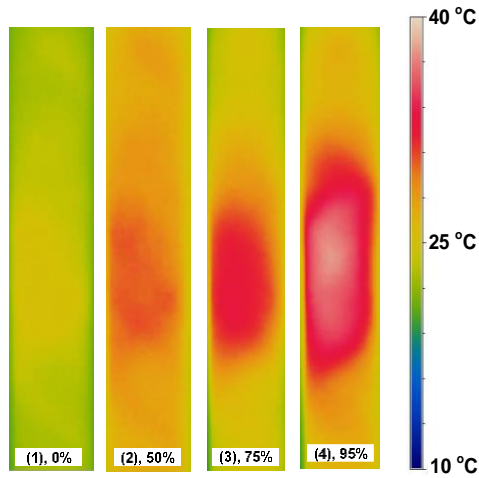


Fig. 2. Representation of the self-generated temperature in different percentages of fatigue life.

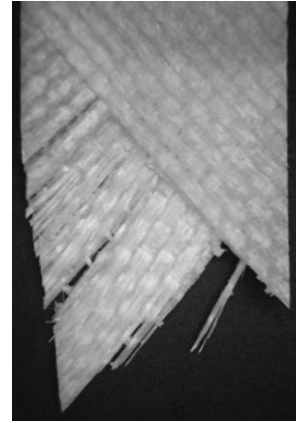


Fig. 3. Fatigue fracture surface.

No.	Code	f (Hz)	N_f
2	Conf-0.1-68-b	4.35	1,007

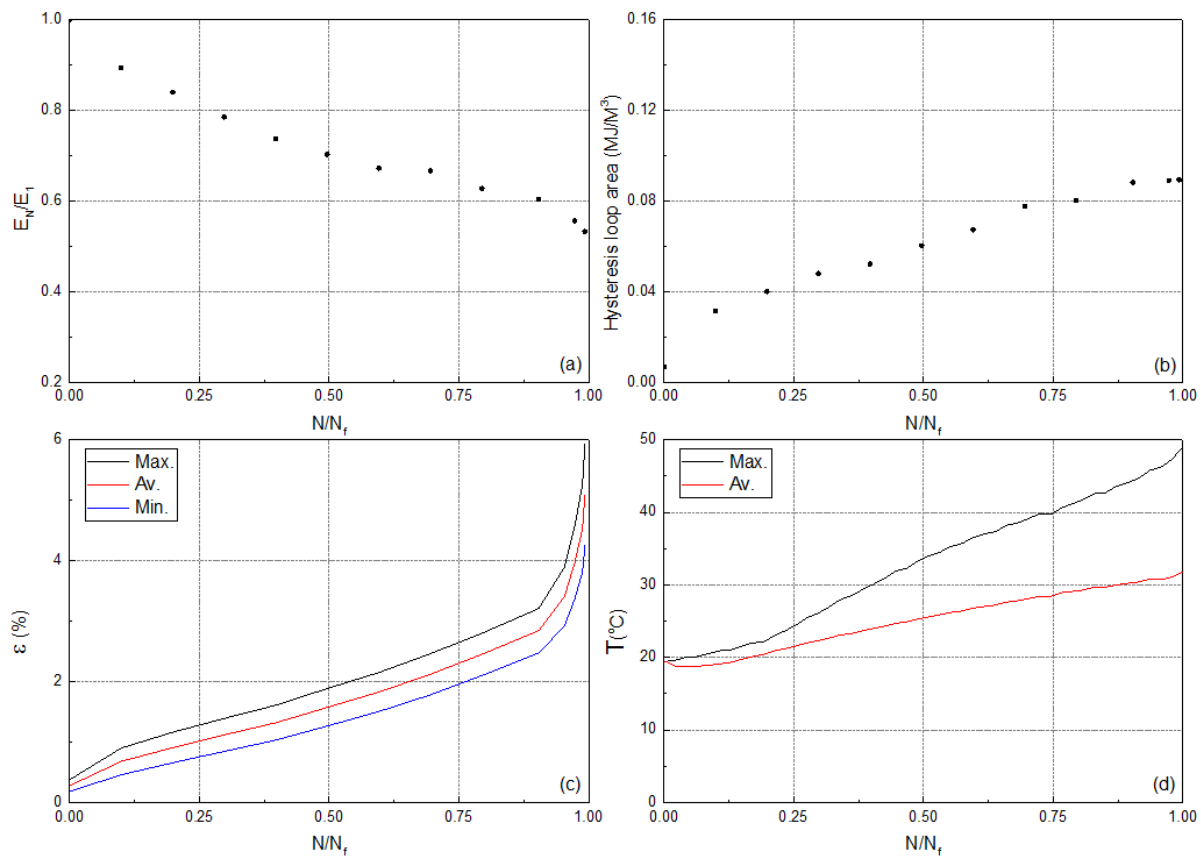


Fig. 1. Variation of (a) normalized fatigue stiffness, (b) hysteresis area, (c) maximum, average, and minimum cyclic strain, and (d) maximum and average self-generated temperature versus normalized number of cycles.

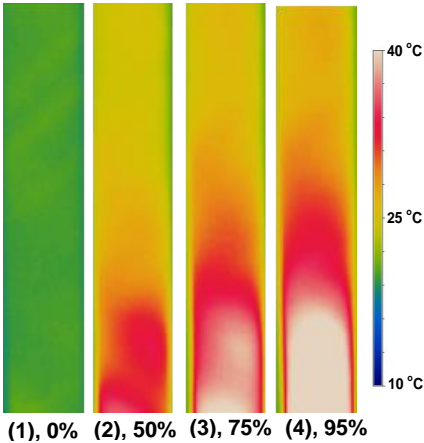


Fig. 2. Representation of the self-generated temperature in different percentages of fatigue life.

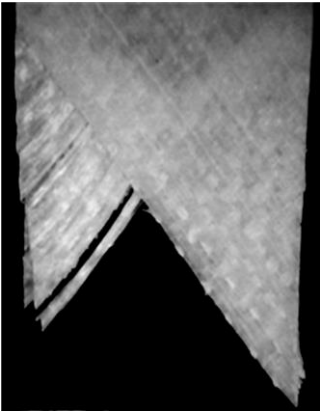


Fig. 3. Fatigue fracture surface.

No.	Code	f (Hz)	N_f
3	Conf-0.1-68-c	4.35	591

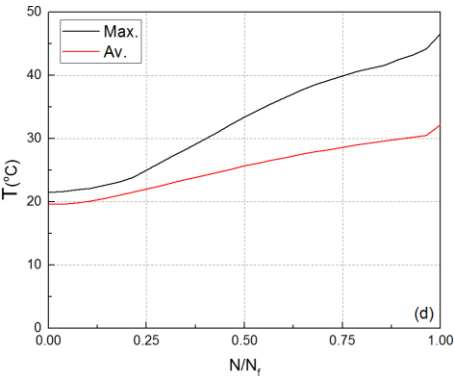


Fig. 1. Variation of maximum and average self-generated temperature.

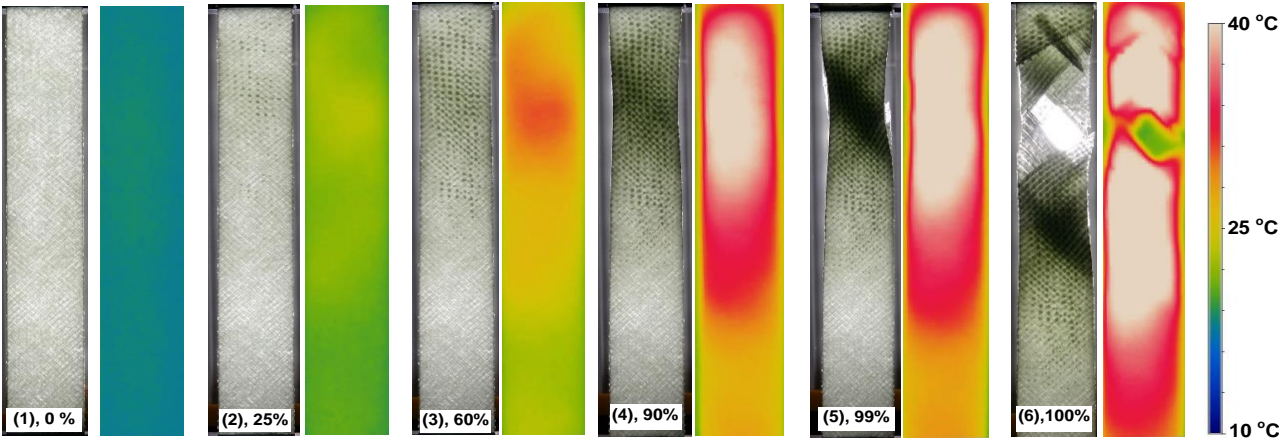


Fig. 2. Pairwise representation of light transmittance and the self-generated temperature in different percentages of fatigue life.

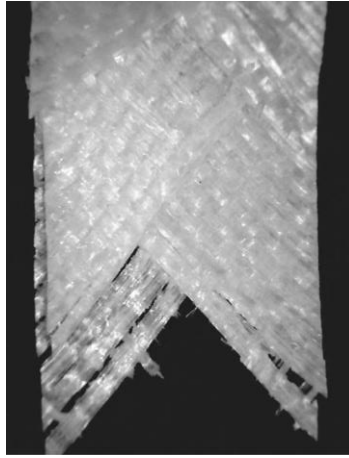


Fig. 3. Fatigue fracture surface.

No.	Code	f (Hz)	N_f
4	Conf-0.1-68-d	4.35	3689

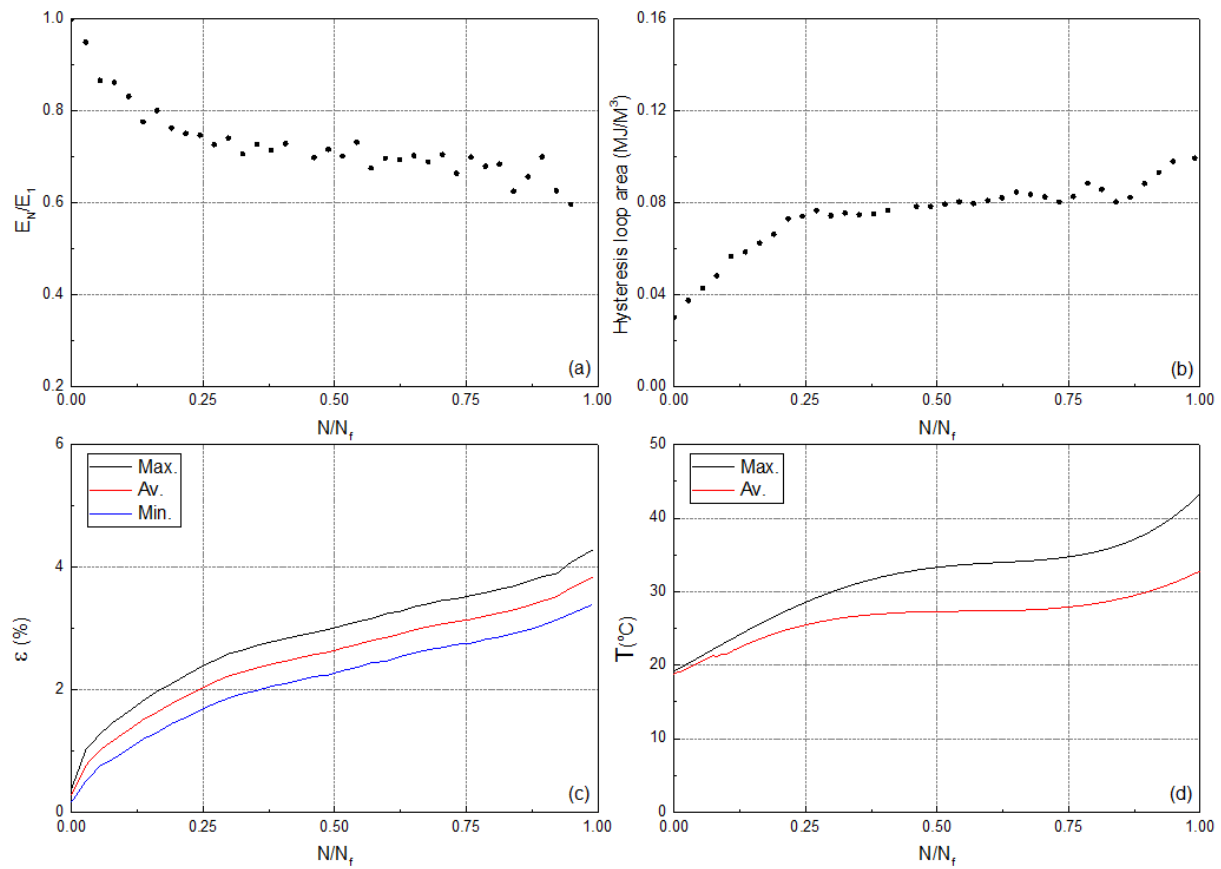


Fig. 1. Variation of (a) normalized fatigue stiffness, (b) hysteresis area, (c) maximum, average, and minimum cyclic strain, and (d) maximum and average self-generated temperature versus normalized number of cycles.

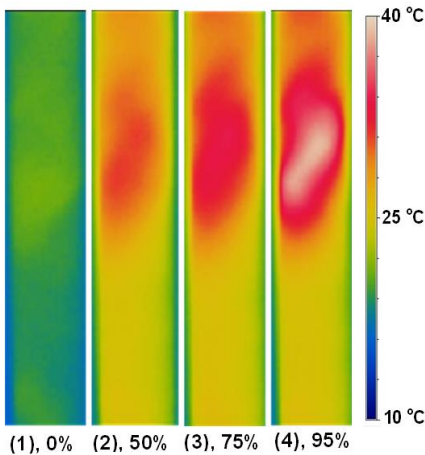


Fig. 2. Representation of the self-generated temperature in different percentages of fatigue life.

No.	Code	f (Hz)	N_f
5	Conf-0.1-64-a	4.68	2,593

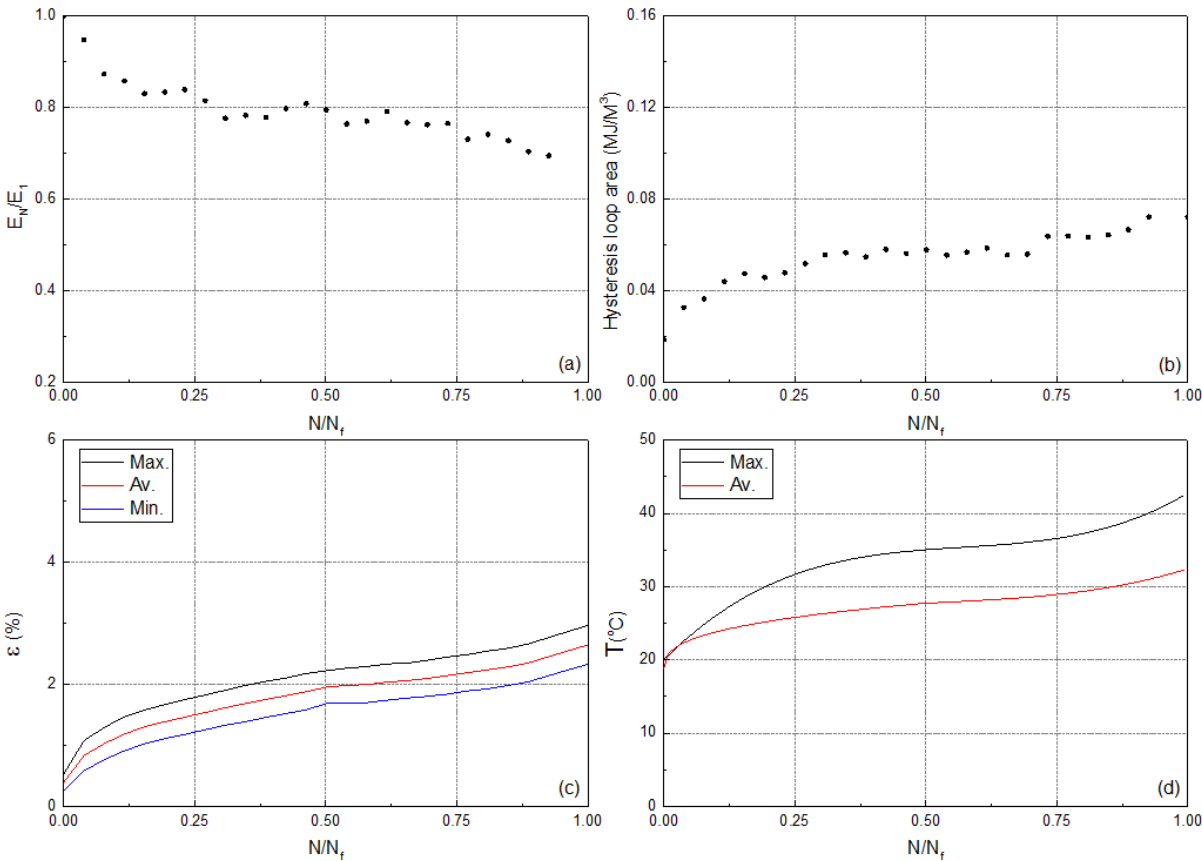


Fig. 1. Variation of (a) normalized fatigue stiffness, (b) hysteresis area, (c) maximum, average, and minimum cyclic strain, and (d) maximum and average self-generated temperature versus normalized number of cycles.

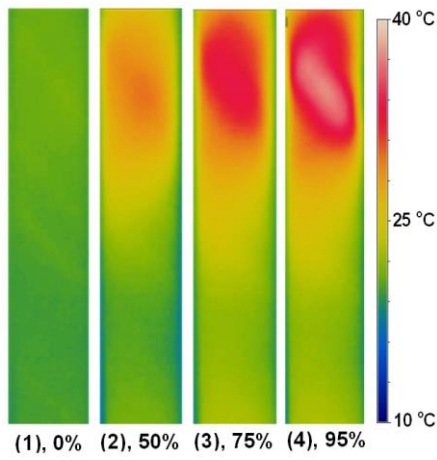


Fig. 2. Representation of the self-generated temperature in different percentages of fatigue life.

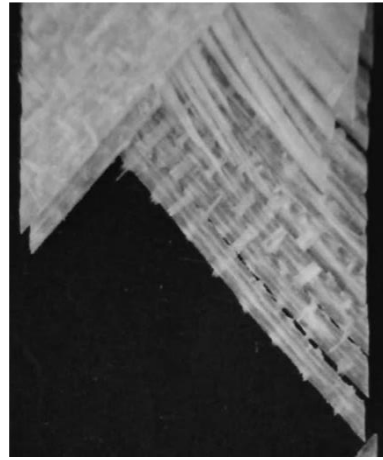


Fig. 3. Fatigue fracture surface.

No.	Code	f (Hz)	N_f
6	Conf-0.1-64-b	4.68	2,304

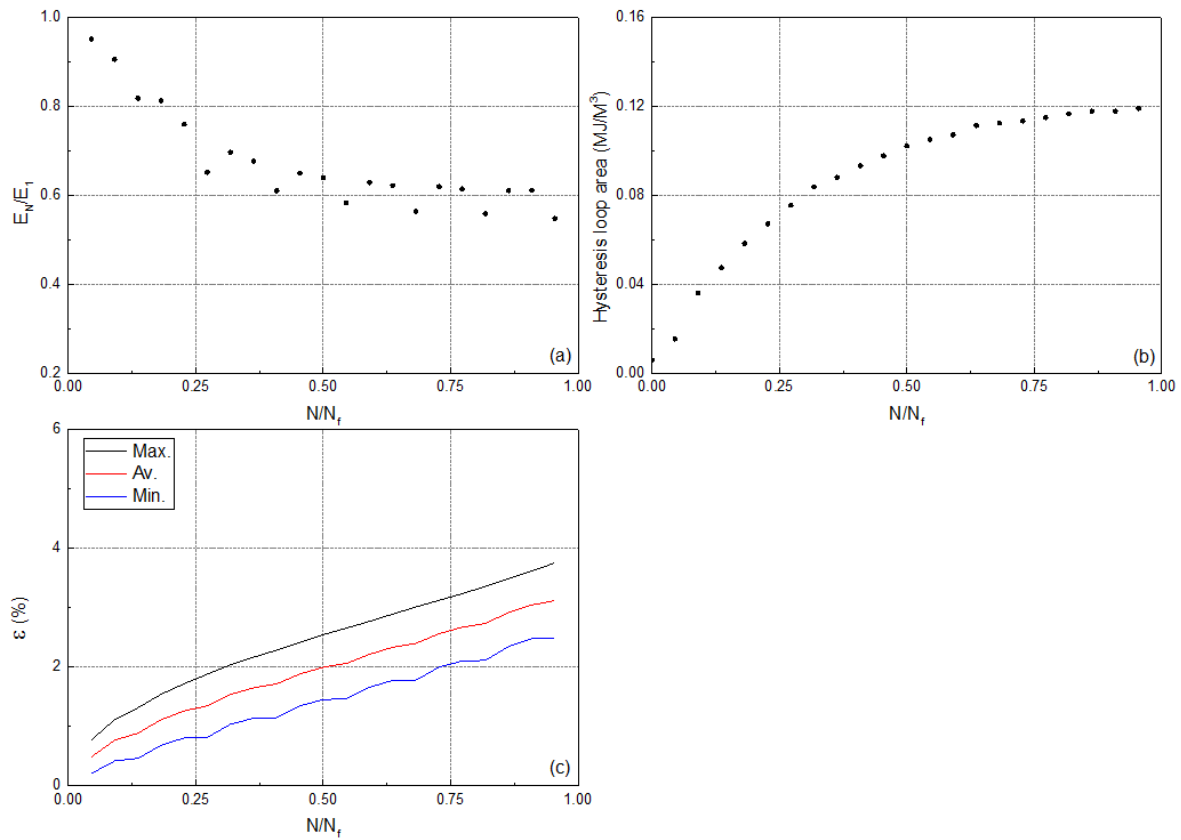


Fig. 1. Variation of (a) normalized fatigue stiffness, (b) hysteresis area, and (c) maximum, average, and minimum cyclic strain versus normalized number of cycles.

No.	Code	f (Hz)	N_f
7	Conf-0.1-64-c	4.68	1,161

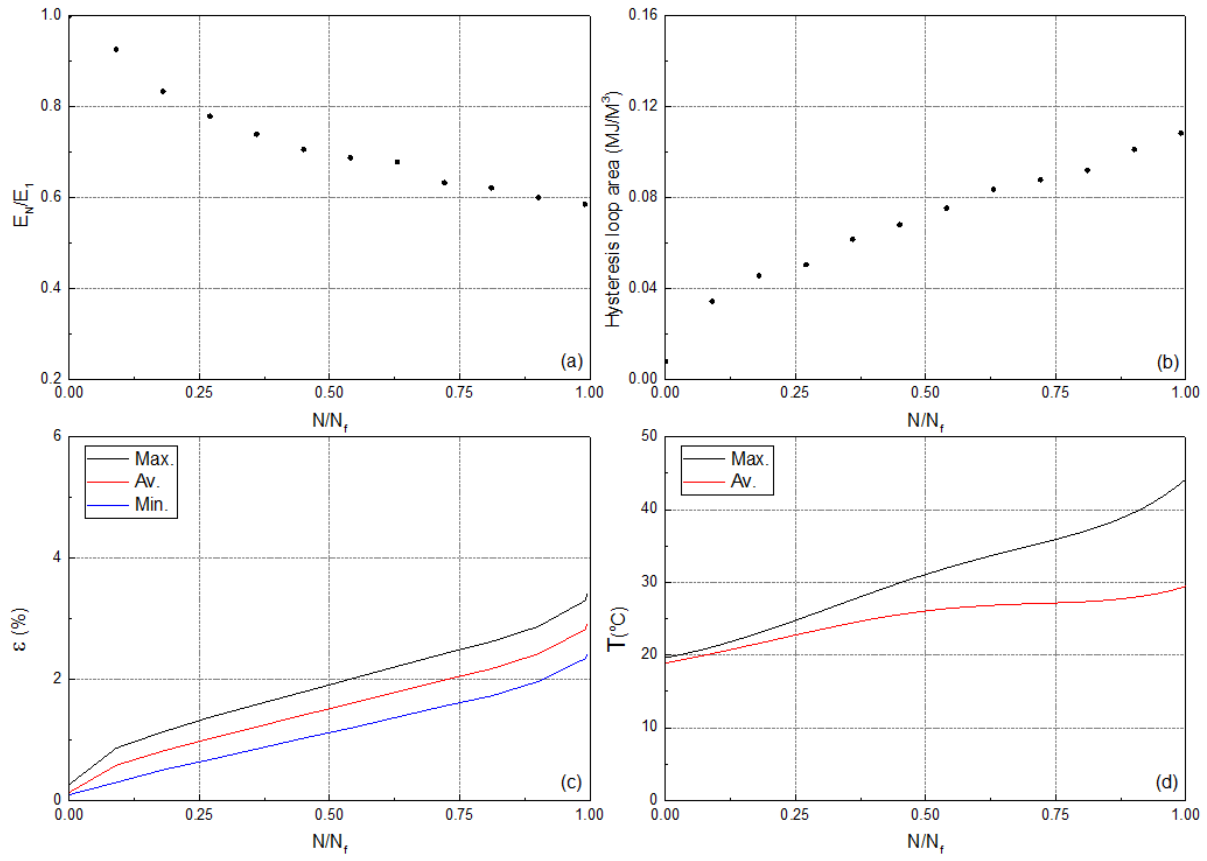


Fig. 1. Variation of (a) normalized fatigue stiffness, (b) hysteresis area, (c) maximum, average, and minimum cyclic strain, and (d) maximum and average self-generated temperature versus normalized number of cycles.

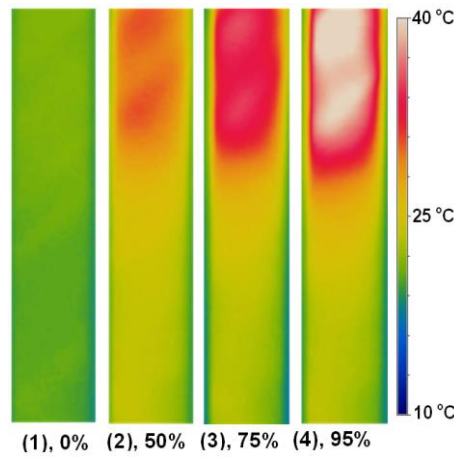


Fig. 2. Representation of the self-generated temperature in different percentages of fatigue life.

No.	Code	f (Hz)	N_f
8	Conf-0.1-64-d	4.68	4112

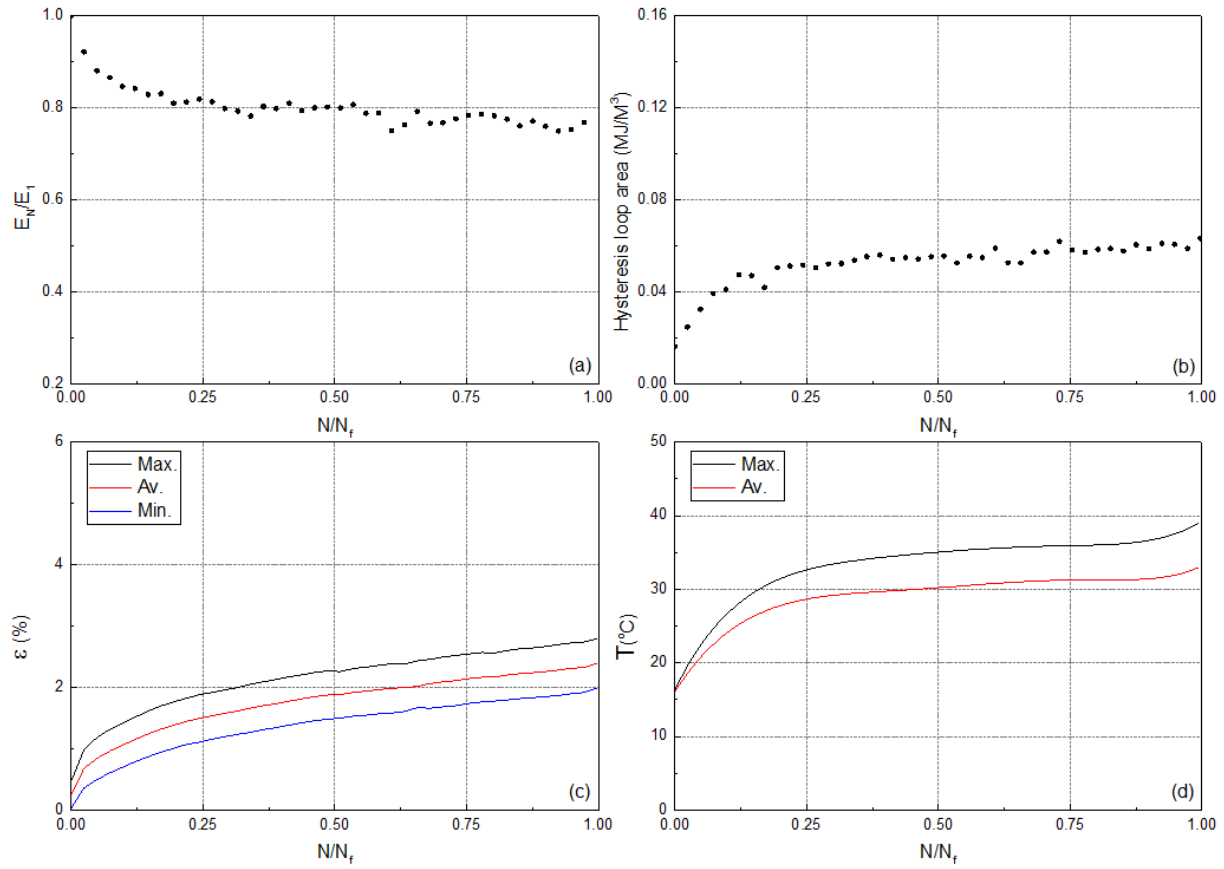


Fig. 1. Variation of (a) normalized fatigue stiffness, (b) hysteresis area, (c) maximum, average, and minimum cyclic strain, and (d) maximum and average self-generated temperature versus normalized number of cycles.

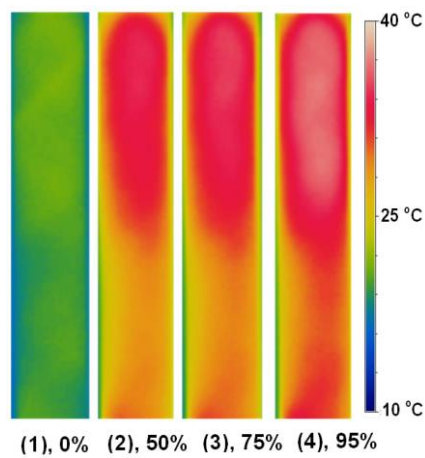


Fig. 2. Representation of the self-generated temperature in different percentages of fatigue life.

No.	Code	f (Hz)	N_f
9	Conf-0.1-58-a	5.06	6,785

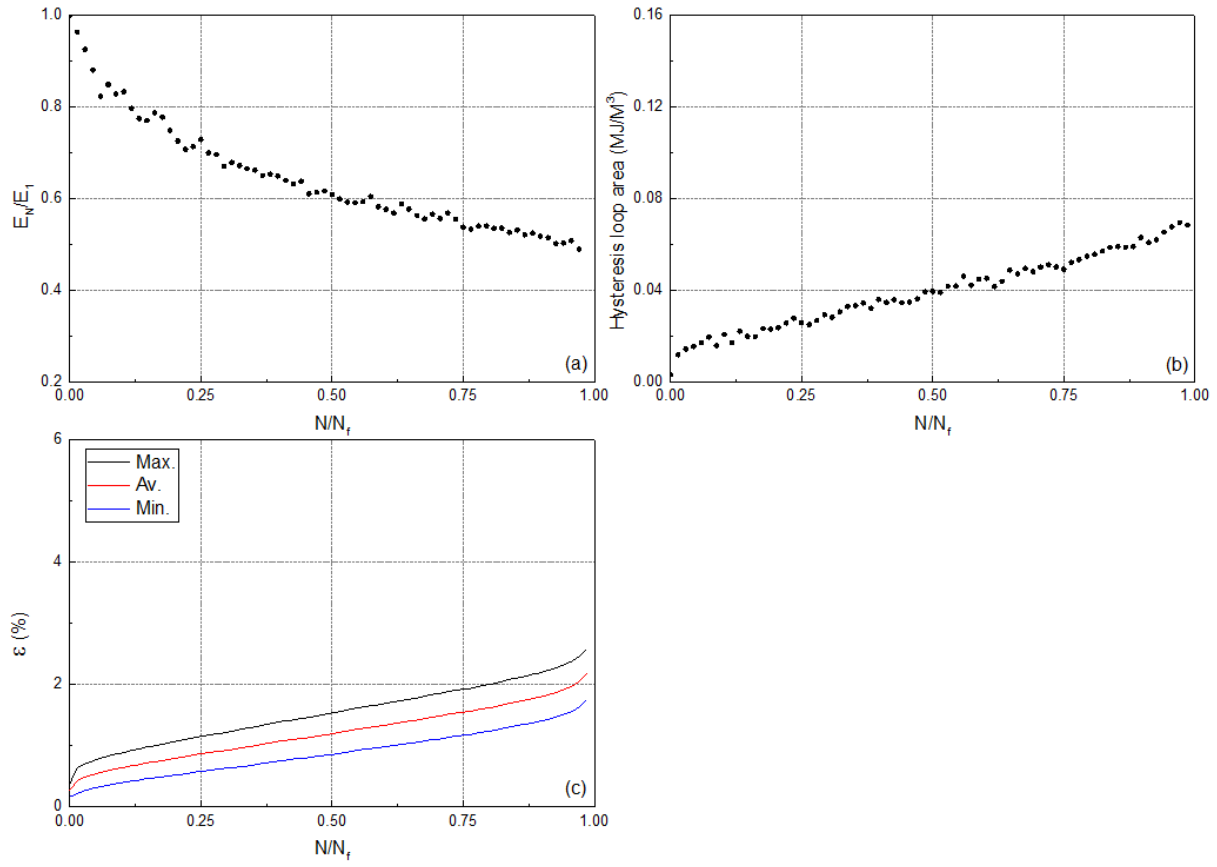


Fig. 1. Variation of (a) normalized fatigue stiffness, (b) hysteresis area, and (c) maximum, average, and minimum cyclic strain versus normalized number of cycles.

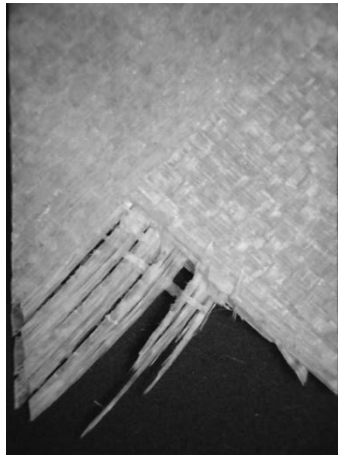


Fig. 2. Fatigue fracture surface.

No.	Code	f (Hz)	N_f
10	Conf-0.1-58-b	5.06	22,321

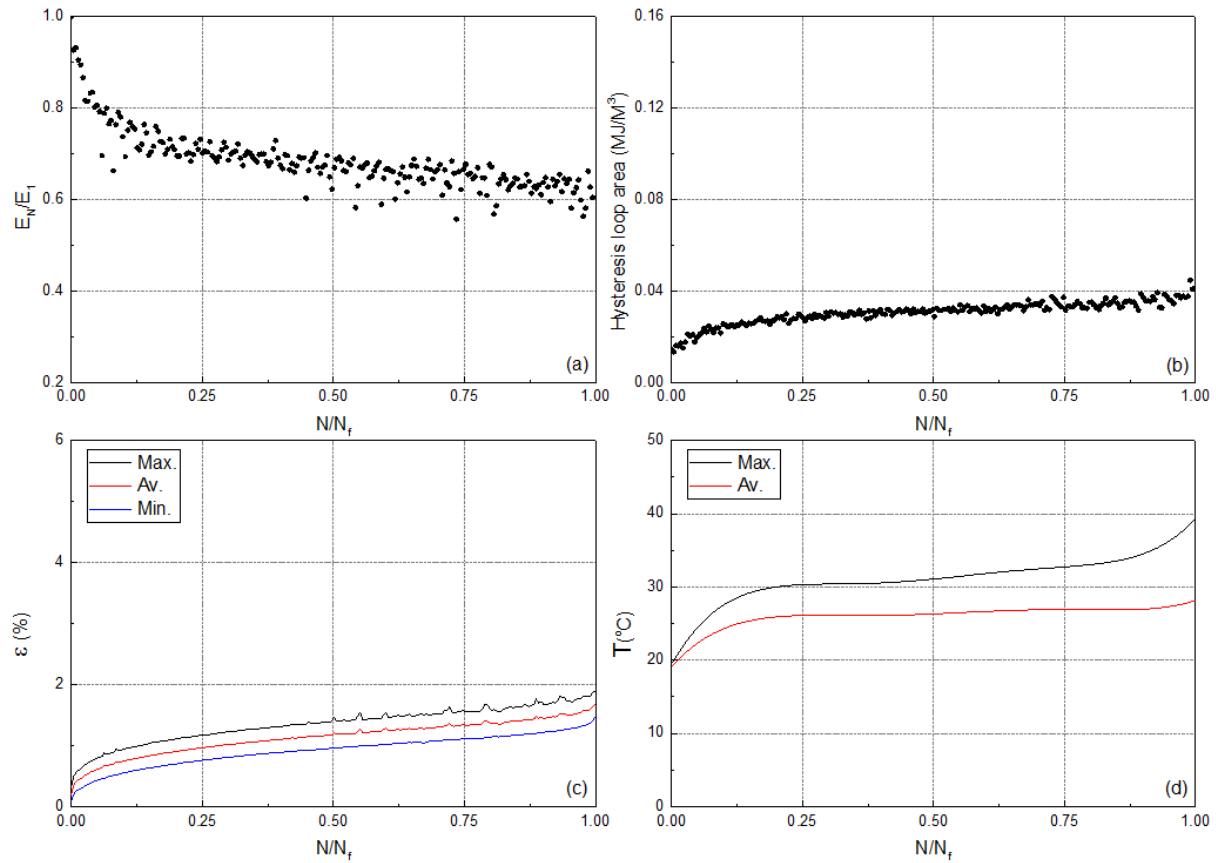


Fig. 1. Variation of (a) normalized fatigue stiffness, (b) hysteresis area, (c) maximum, average, and minimum cyclic strain, and (d) maximum and average self-generated temperature versus normalized number of cycles.

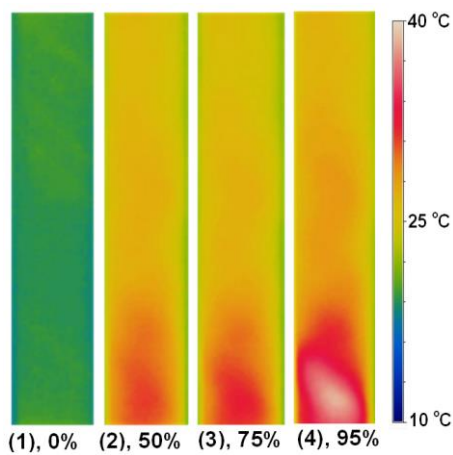


Fig. 2. Representation of the self-generated temperature in different percentages of fatigue life.

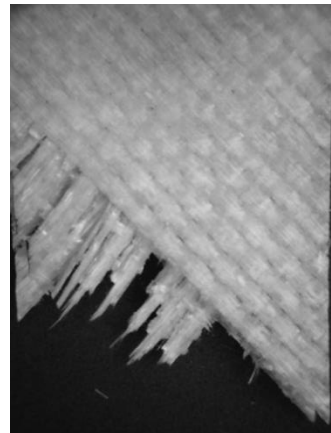


Fig. 3. Fatigue fracture surface.

No.	Code	f (Hz)	N_f
11	Conf-0.1-58-c	5.06	18,028

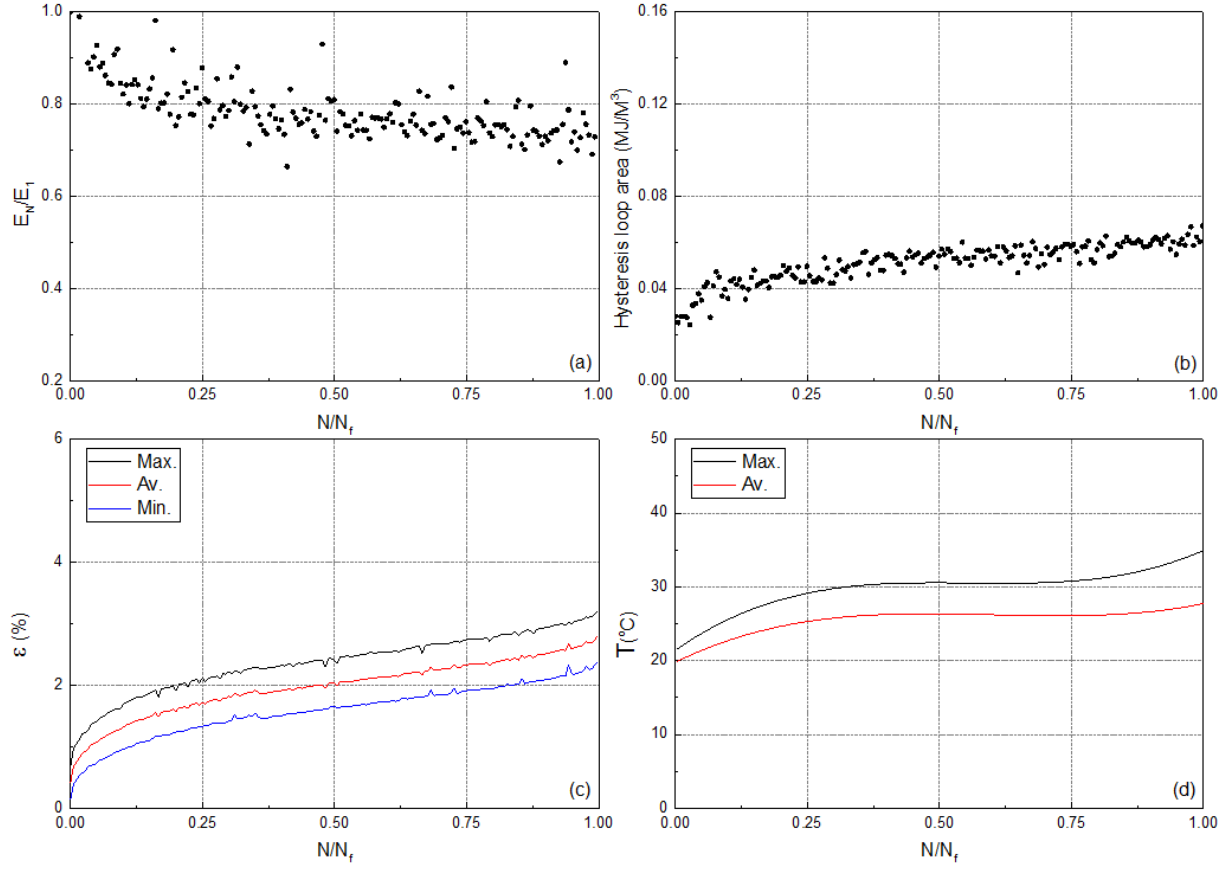


Fig. 1. Variation of (a) normalized fatigue stiffness, (b) hysteresis area, (c) maximum, average, and minimum cyclic strain, and (d) maximum and average self-generated temperature versus normalized number of cycles.

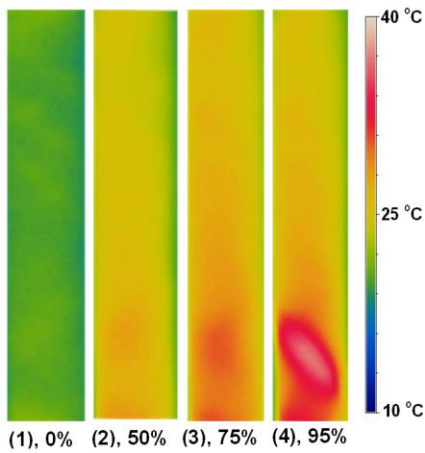


Fig. 2. Representation of the self-generated temperature in different percentages of fatigue life.

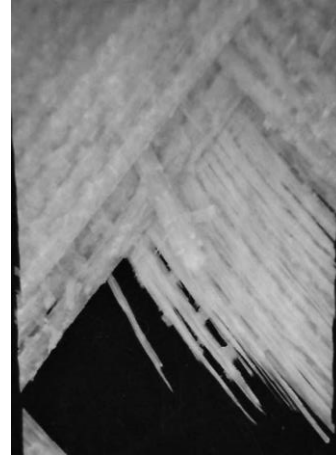


Fig. 3. Fatigue fracture surface.

No.	Code	f (Hz)	N_f
12	Conf-0.1-58-d	5.06	15,063

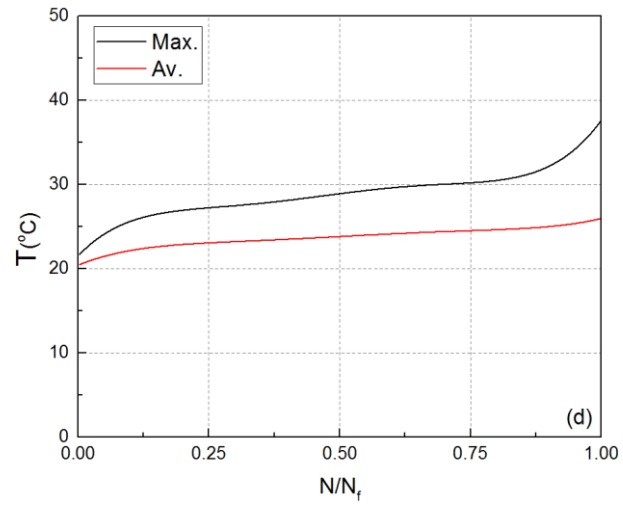


Fig. 1. Variation of maximum and average self-generated temperature.

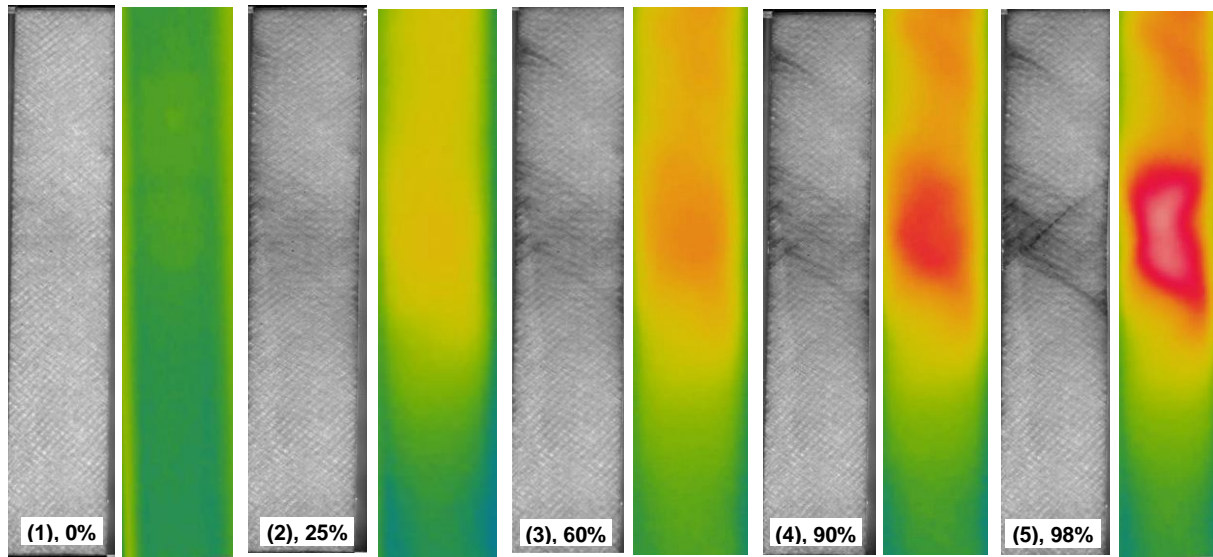


Fig. 2. Pairwise representation of light transmittance and the self-generated temperature in different percentages of fatigue life.

No.	Code	f (Hz)	N_f
13	Conf-0.1-53-a	5.53	49,151

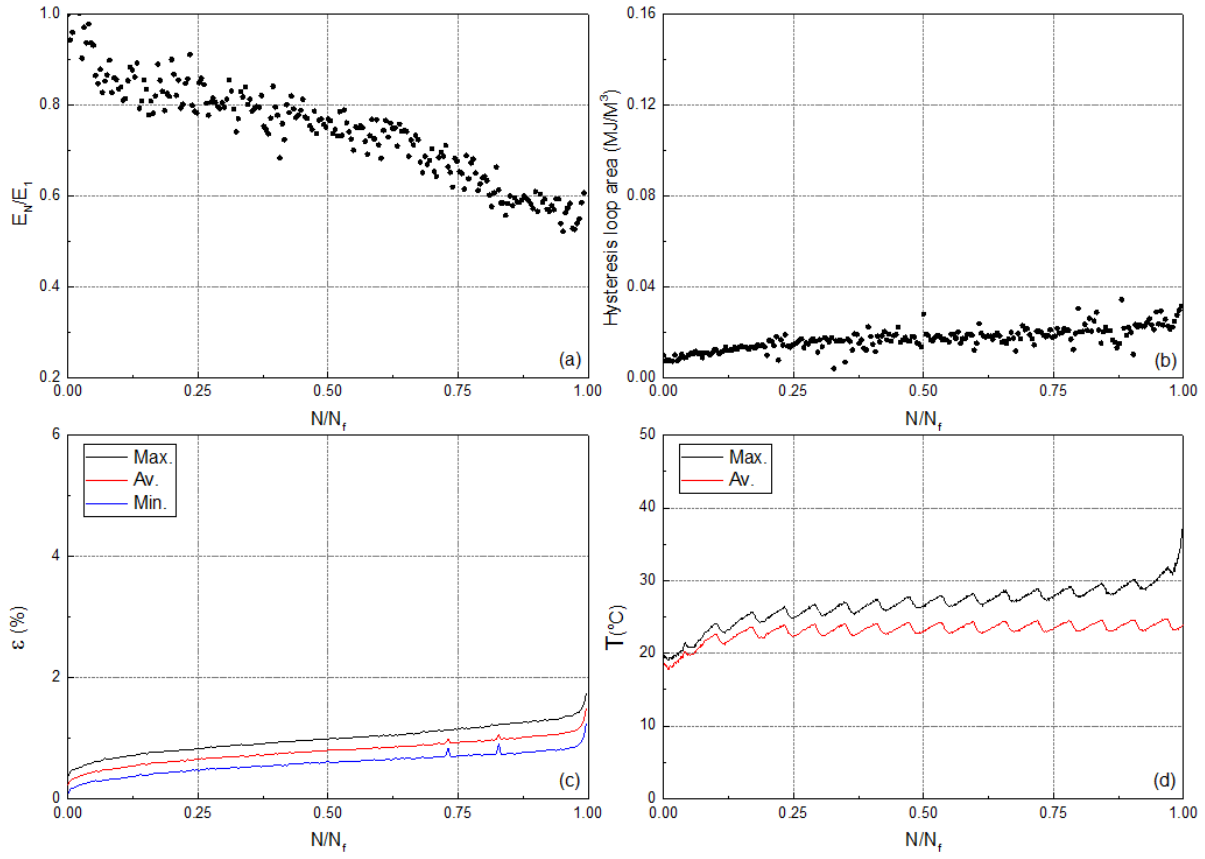


Fig. 1. Variation of (a) normalized fatigue stiffness, (b) hysteresis area, (c) maximum, average, and minimum cyclic strain, and (d) maximum and average self-generated temperature versus normalized number of cycles.

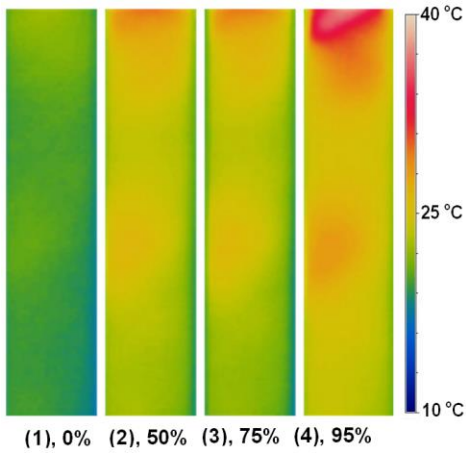


Fig. 2. Representation of the self-generated temperature in different percentages of fatigue life.



Fig. 3. Fatigue fracture surface.

No.	Code	f (Hz)	N_f
14	Conf-0.1-53-b	5.53	29,832

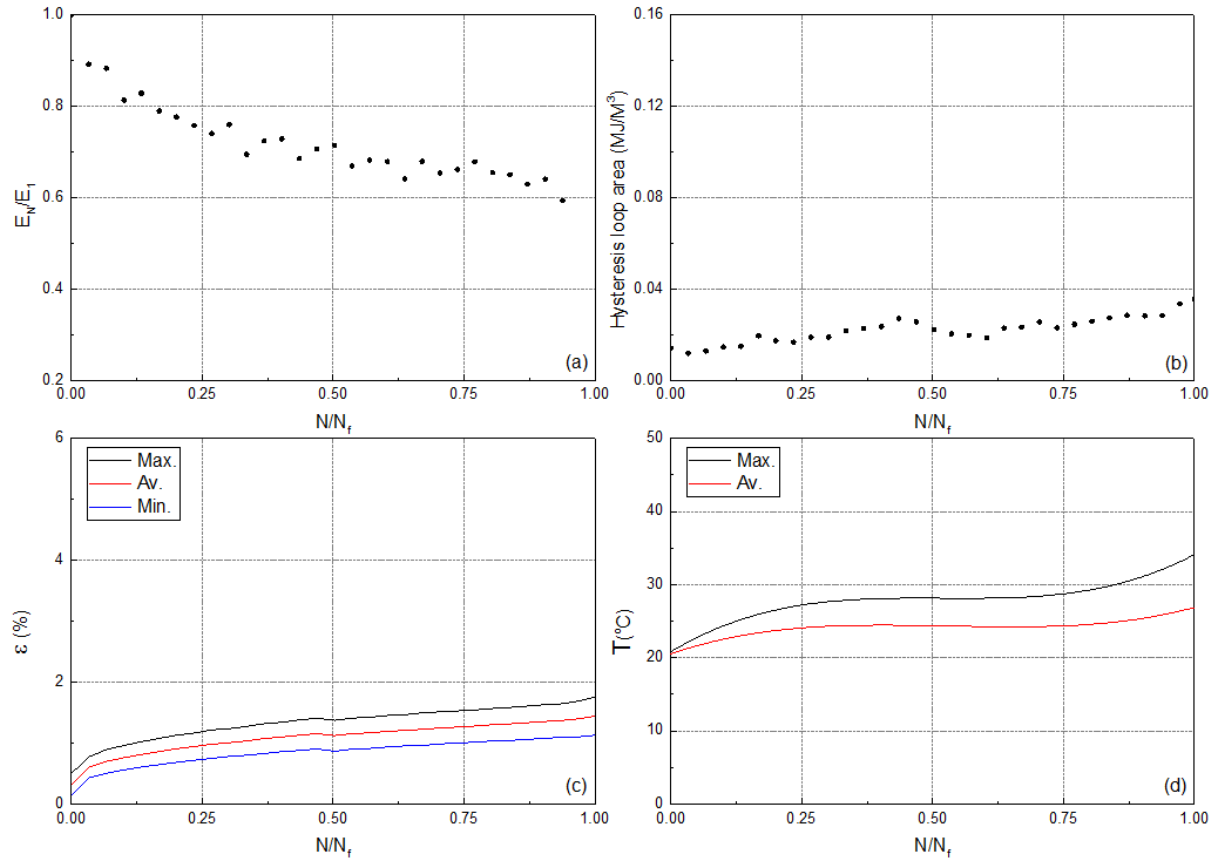


Fig. 1. Variation of (a) normalized fatigue stiffness, (b) hysteresis area, (c) maximum, average, and minimum cyclic strain, and (d) maximum and average self-generated temperature versus normalized number of cycles.

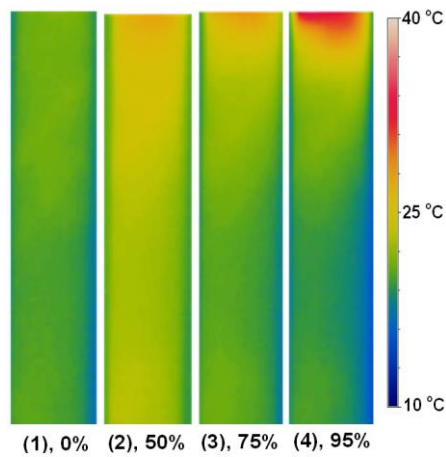


Fig. 2. Representation of the self-generated temperature in different percentages of fatigue life.

No.	Code	f (Hz)	N_f
15	Conf-0.1-53-c	5.53	22,583

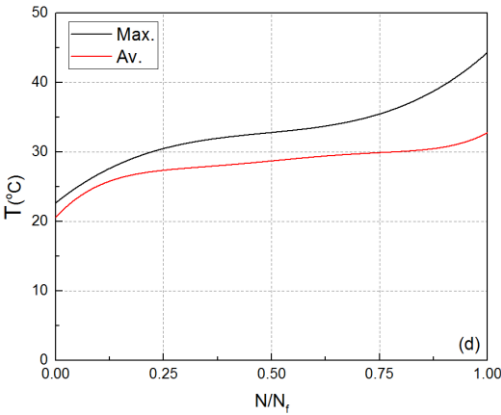


Fig. 1. Variation of maximum and average self-generated temperature.

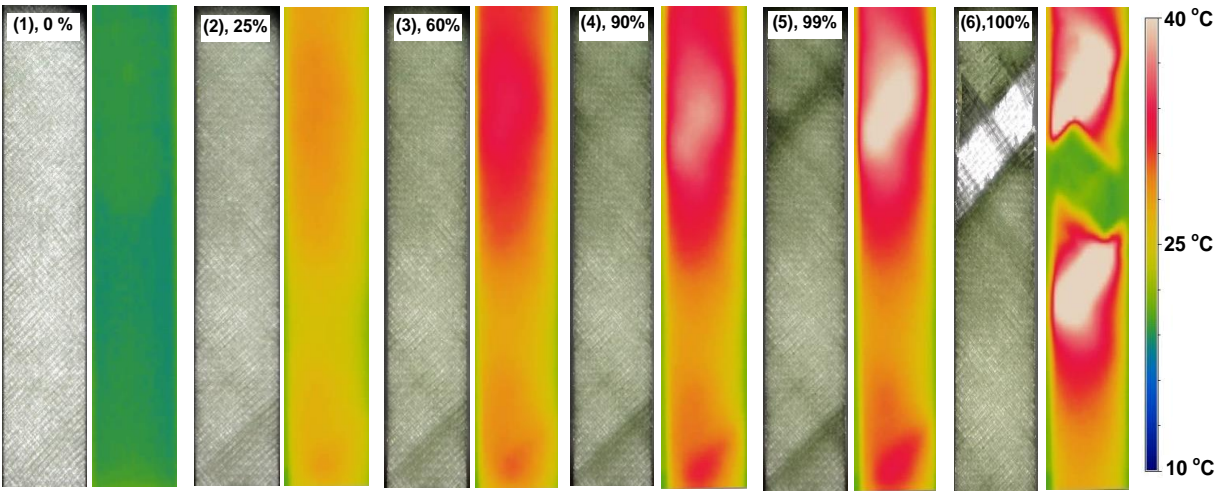


Fig. 2. Pairwise representation of light transmittance and the self-generated temperature in different percentages of fatigue life.

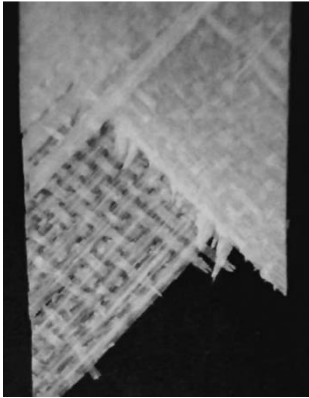


Fig. 3. Fatigue fracture surface.

No.	Code	f (Hz)	N_f
16	Conf-0.1-53-d	5.53	79,623

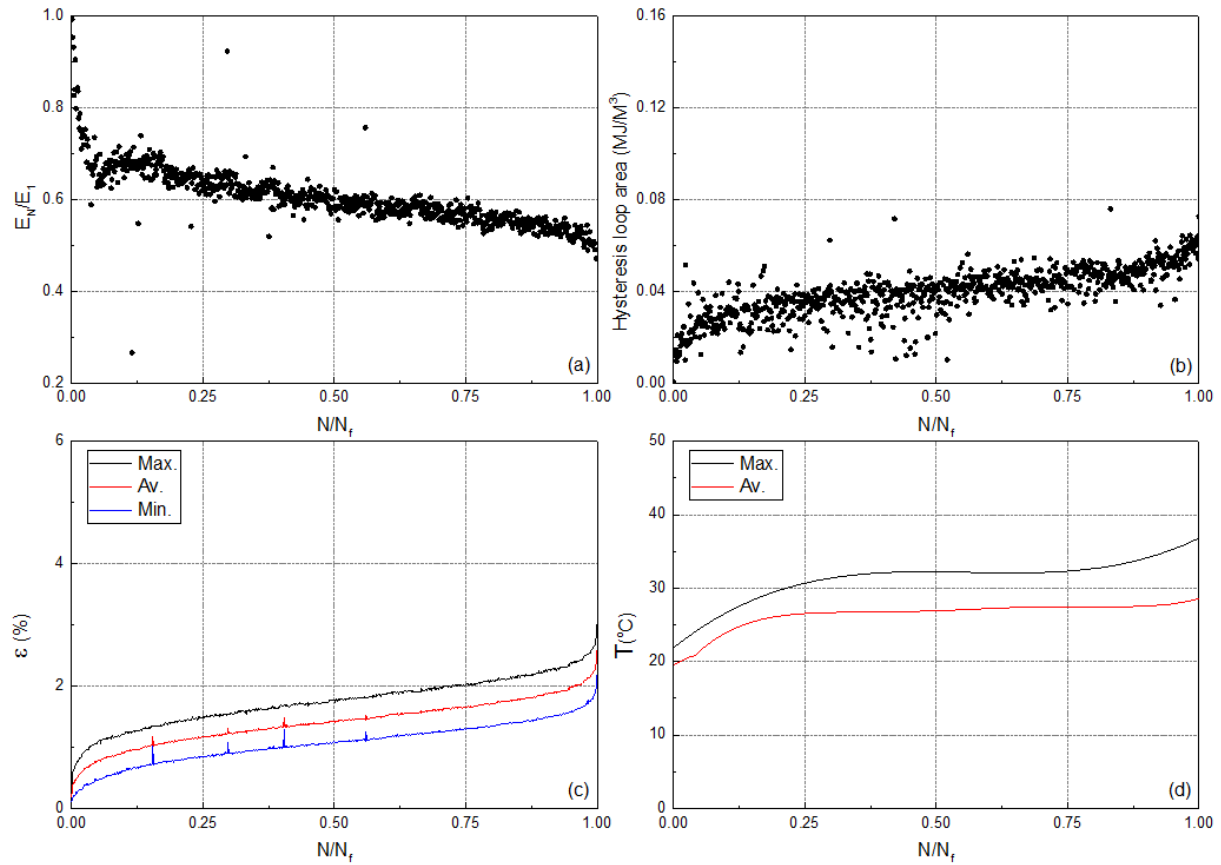


Fig. 1. Variation of (a) normalized fatigue stiffness, (b) hysteresis area, (c) maximum, average, and minimum cyclic strain, and (d) maximum and average self-generated temperature versus normalized number of cycles.

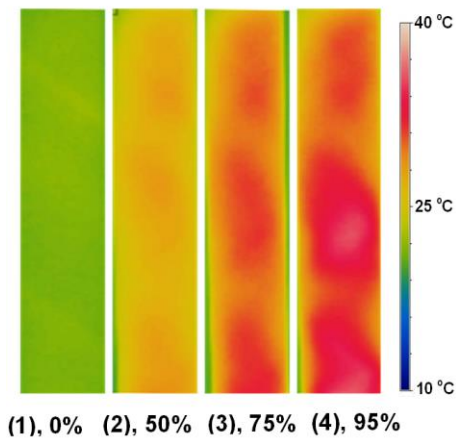


Fig. 2. Representation of the self-generated temperature in different percentages of fatigue life.

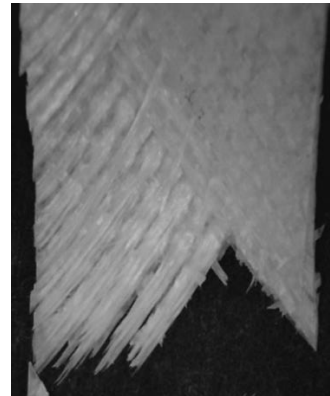


Fig. 3. Fatigue fracture surface.

No.	Code	f (Hz)	N_f
17	Conf-0.1-49-a	6.10	289,050

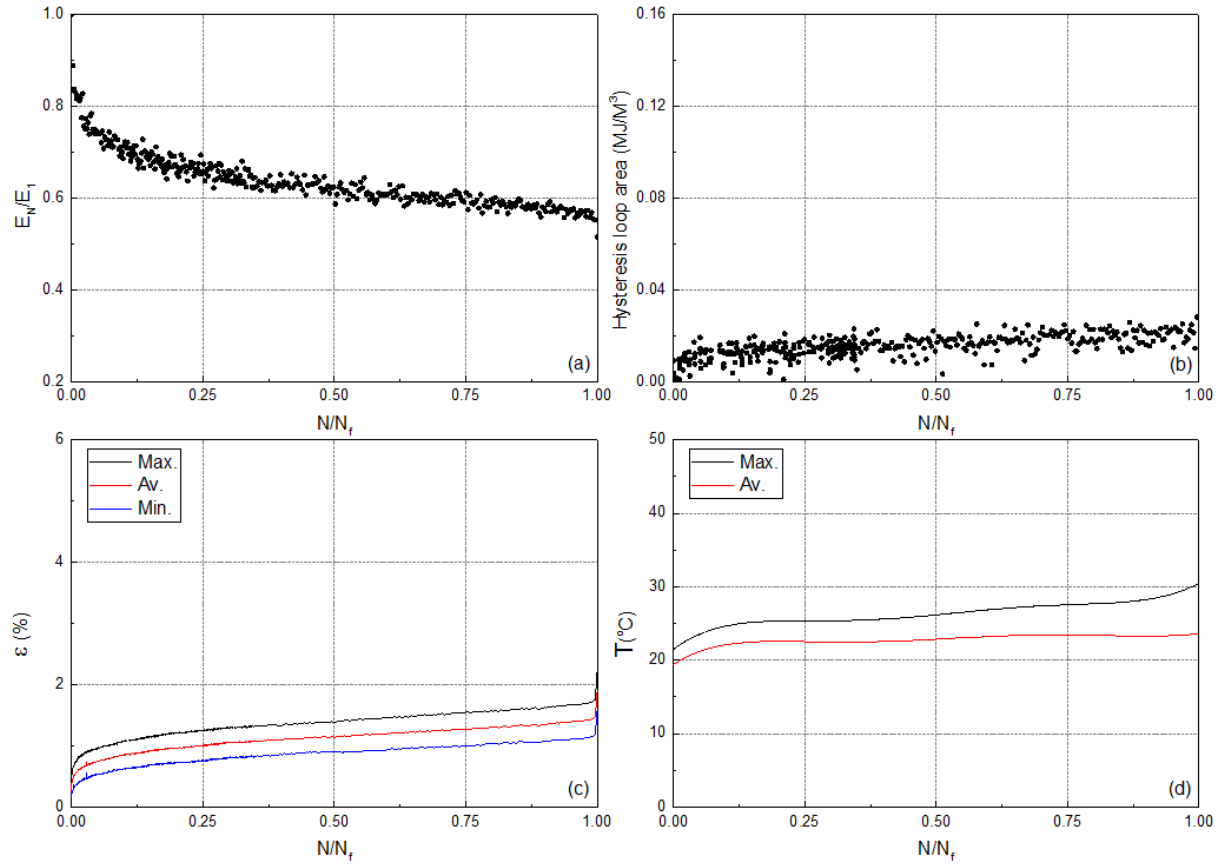


Fig. 1. Variation of (a) normalized fatigue stiffness, (b) hysteresis area, (c) maximum, average, and minimum cyclic strain, and (d) maximum and average self-generated temperature versus normalized number of cycles.

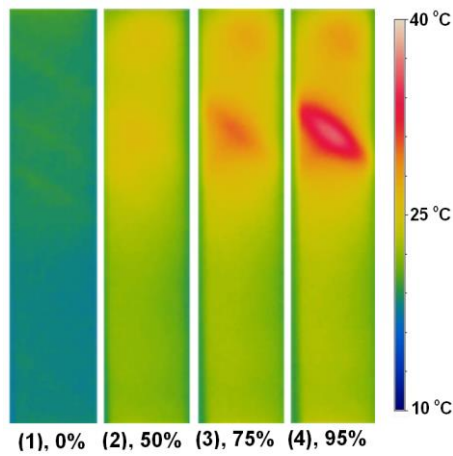


Fig. 2. Representation of the self-generated temperature in different percentages of fatigue life.

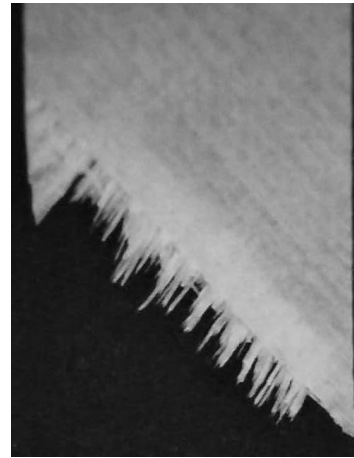


Fig. 3. Fatigue fracture surface.

No.	Code	f (Hz)	N_f
18	Conf-0.1-49-b	6.10	194,115

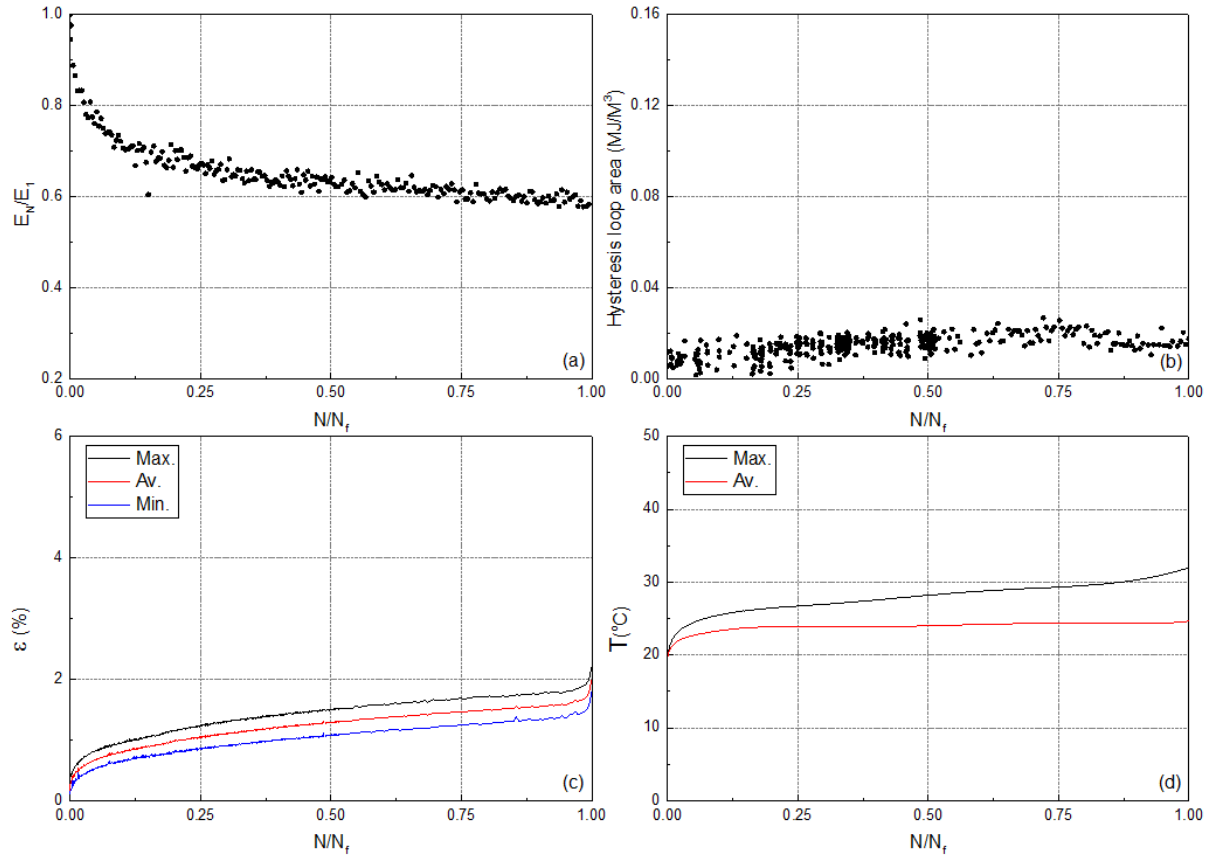


Fig. 1. Variation of (a) normalized fatigue stiffness, (b) hysteresis area, (c) maximum, average, and minimum cyclic strain, and (d) maximum and average self-generated temperature versus normalized number of cycles.

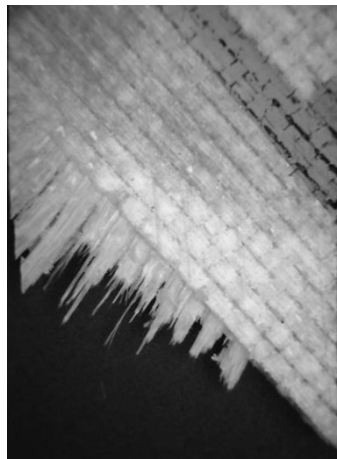


Fig. 2. Fatigue fracture surface.

No.	Code	f (Hz)	N_f
19	Conf-0.1-49-c	6.10	460,664

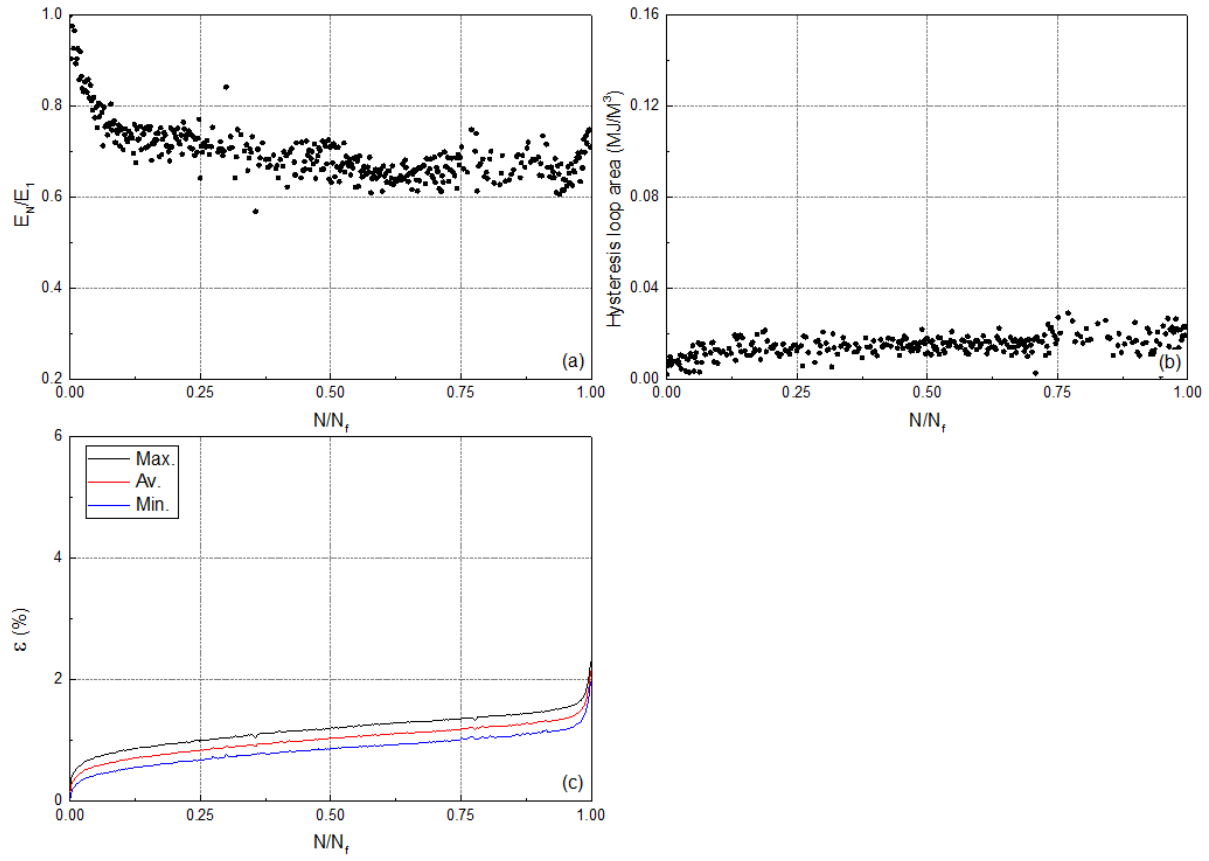


Fig. 1. Variation of (a) normalized fatigue stiffness, (b) hysteresis area, and (c) maximum, average, and minimum cyclic strain versus normalized number of cycles.

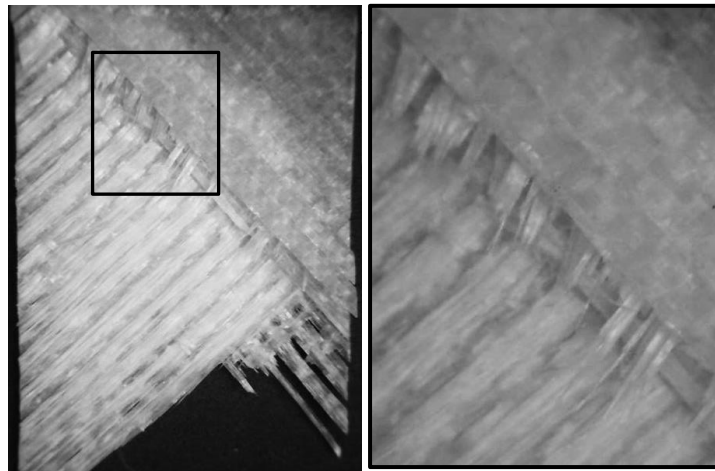


Fig. 2. Fatigue fracture surface at two magnifications.

No.	Code	f (Hz)	N_f
20	Conf-0.1-49-d	6.10	277,227

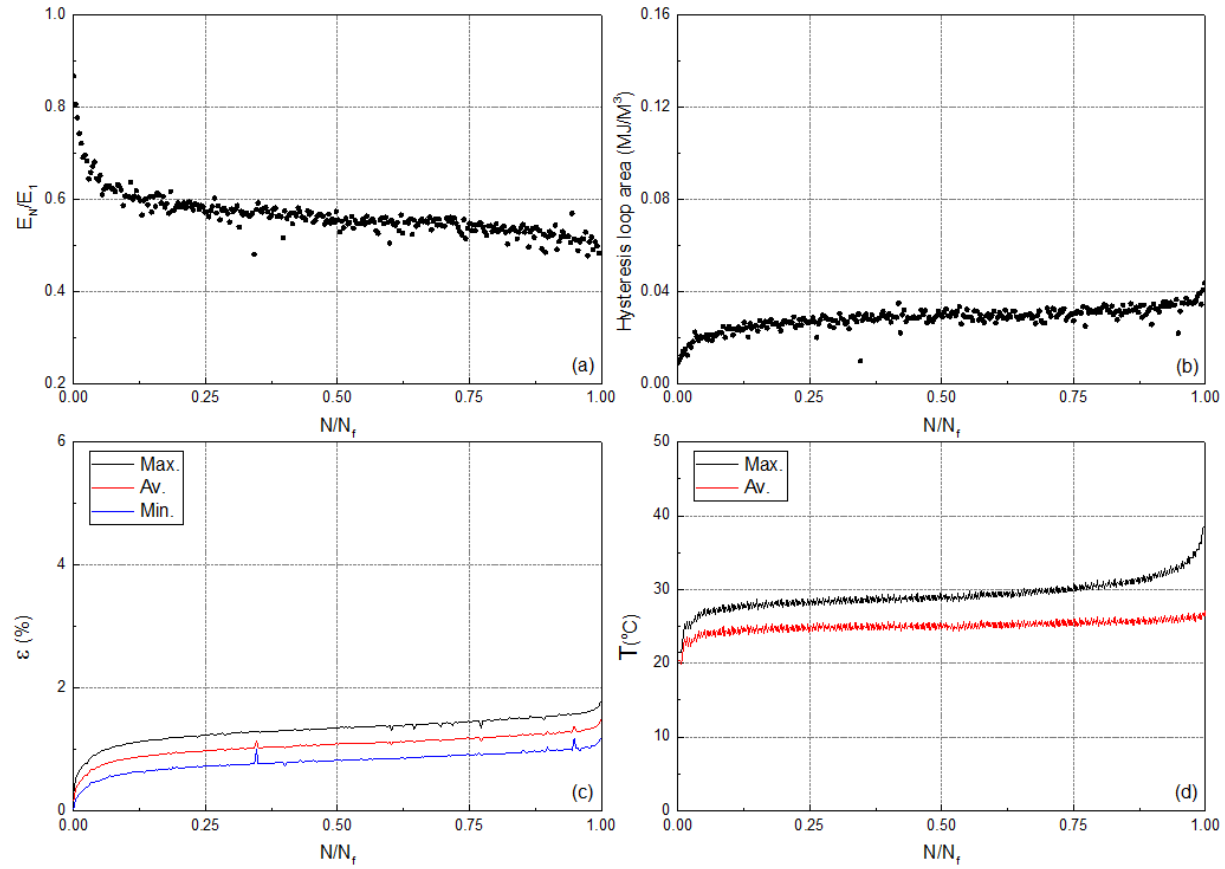


Fig. 1. Variation of (a) normalized fatigue stiffness, (b) hysteresis area, (c) maximum, average, and minimum cyclic strain, and (d) maximum and average self-generated temperature versus normalized number of cycles.

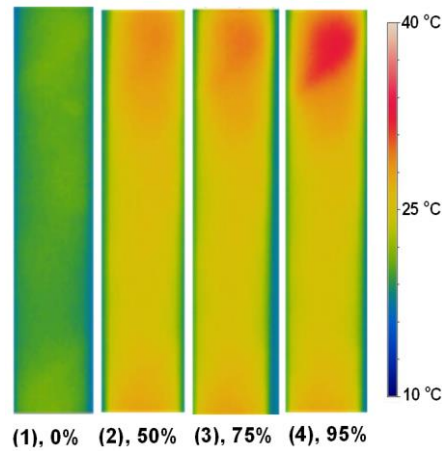


Fig. 2. Representation of the self-generated temperature in different percentages of fatigue life.

No.	Code	f (Hz)	N_f
21	Conf-0.1-47-a	6.33	533,634

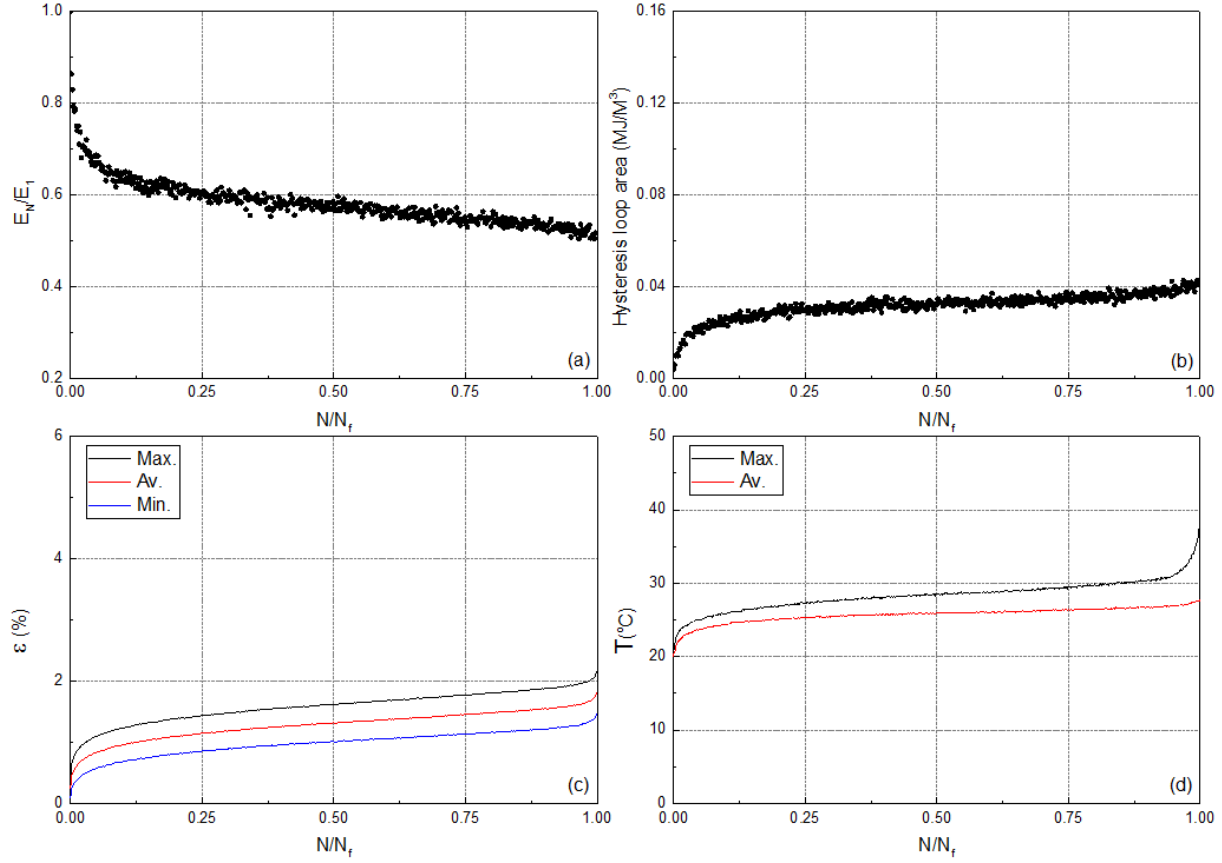


Fig. 1. Variation of (a) normalized fatigue stiffness, (b) hysteresis area, (c) maximum, average, and minimum cyclic strain, and (d) maximum and average self-generated temperature versus normalized number of cycles.

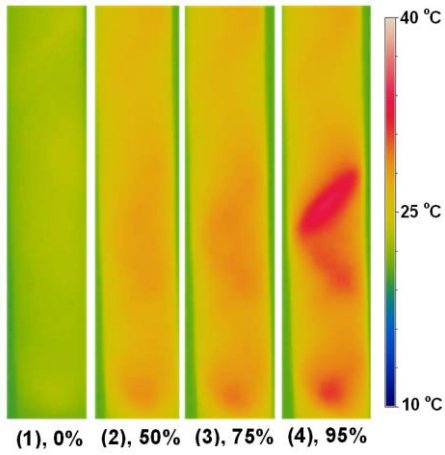


Fig. 2. Representation of the self-generated temperature in different percentages of fatigue life.

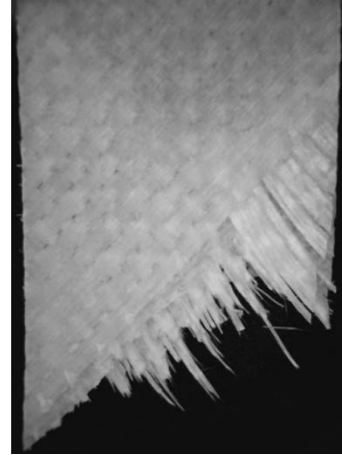


Fig. 3. Fatigue fracture surface.

No.	Code	f (Hz)	N_f
22	Conf-0.1-47-b	6.33	1,198,627

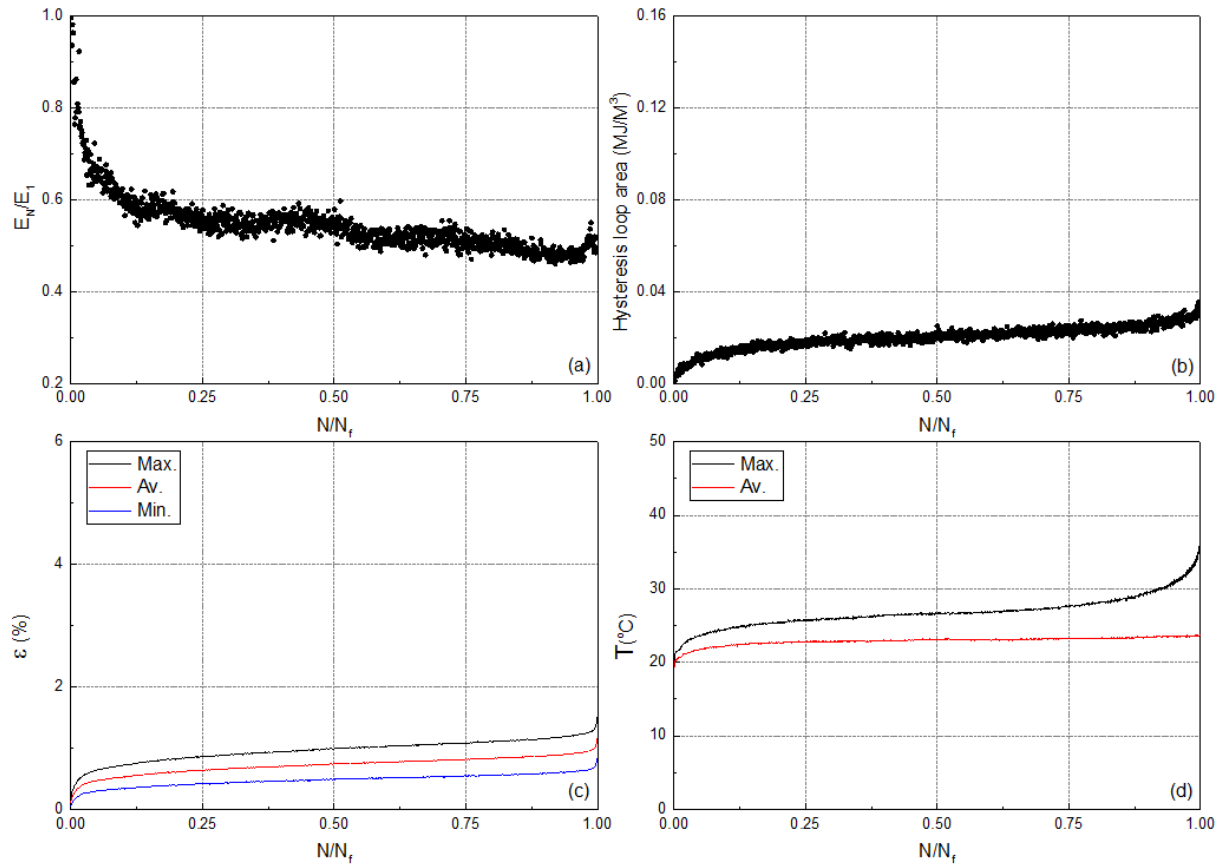


Fig. 1. Variation of (a) normalized fatigue stiffness, (b) hysteresis area, (c) maximum, average, and minimum cyclic strain, and (d) maximum and average self-generated temperature versus normalized number of cycles.

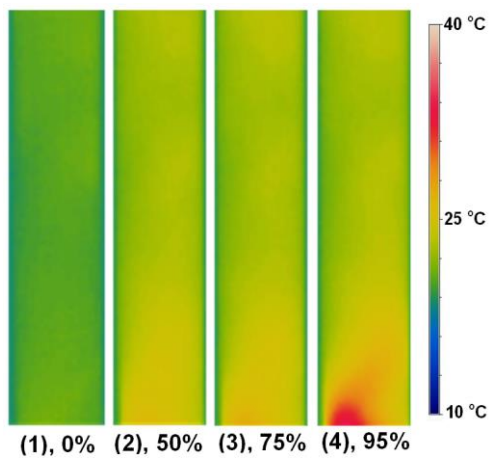


Fig. 2. Representation of the self-generated temperature in different percentages of fatigue life.

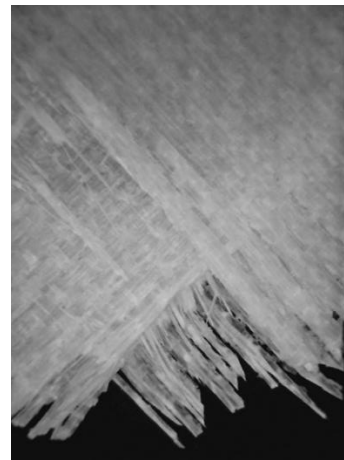


Fig. 3. Fatigue fracture surface.

No.	Code	f (Hz)	N_f
23	Conf-0.1-47-c	6.33	430,211

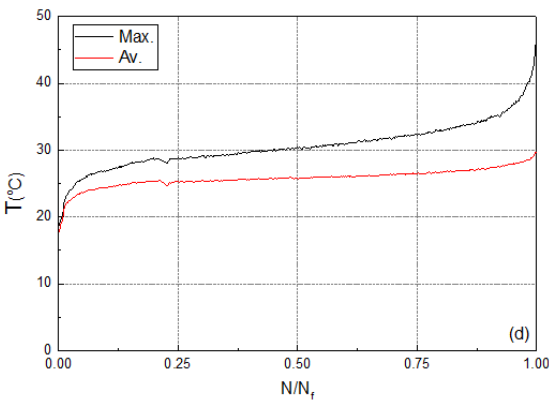


Fig. 1. Variation of maximum and average self-generated temperature.

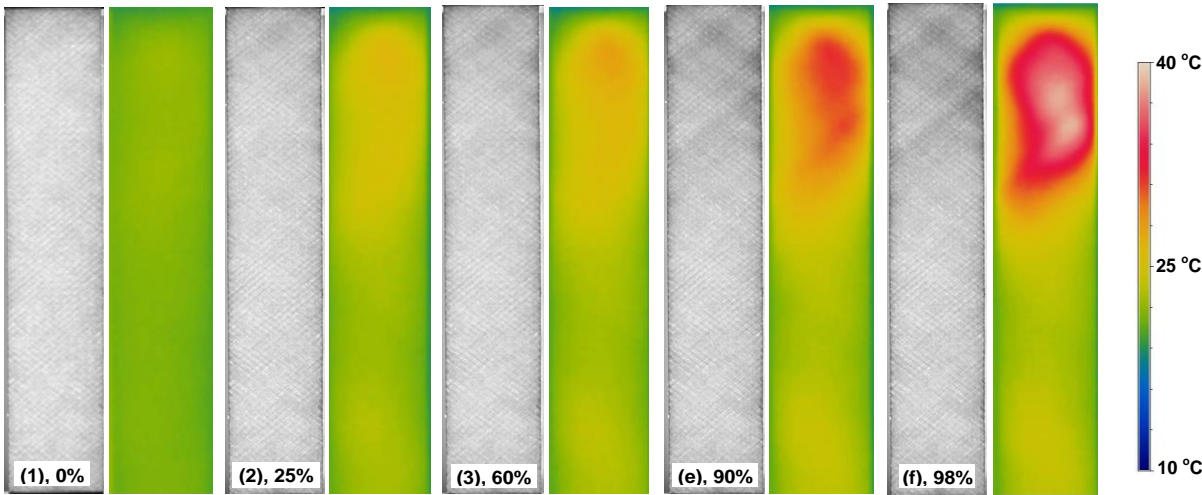


Fig. 2. Pairwise representation of light transmittance and the self-generated temperature in different percentages of fatigue life.

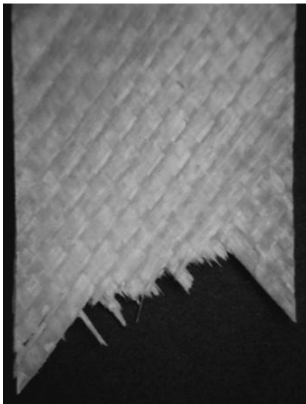


Fig. 3. Fatigue fracture surface.

No.	Code	f (Hz)	N_f
24	Conf-0.1-47-d	6.33	545,689

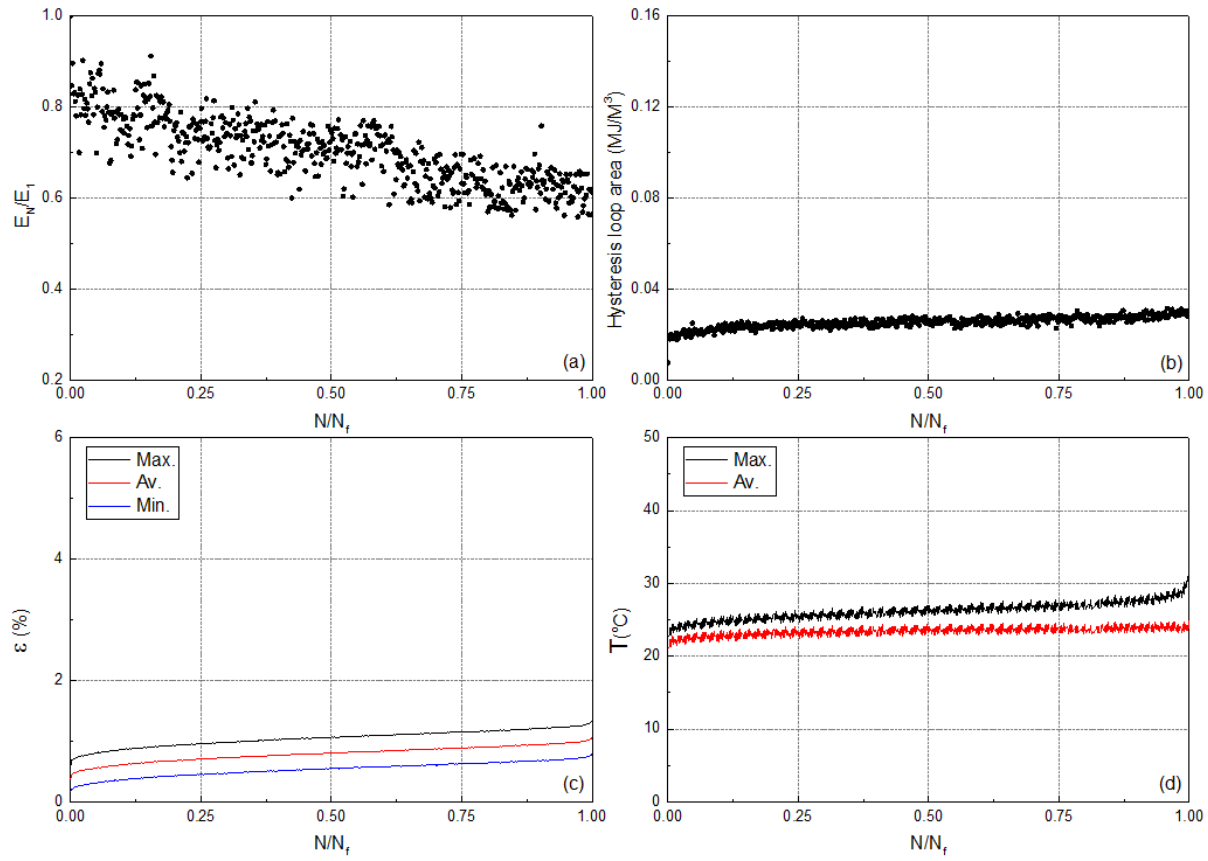


Fig. 1. Variation of (a) normalized fatigue stiffness, (b) hysteresis area, (c) maximum, average, and minimum cyclic strain, and (d) maximum and average self-generated temperature versus normalized number of cycles.

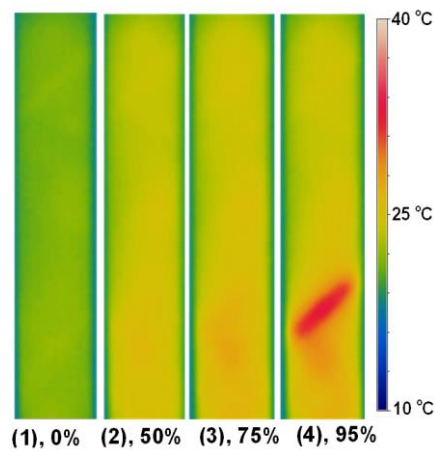


Fig. 2. Representation of the self-generated temperature in different percentages of fatigue life.

Annex B: Continuous-fatigue ($R=0.5$)



B.1 Introduction

Annex B presents supplementary results from the experiments conducted on the continuous fatigue at the stress ratio of 0.5, which was described in Chapter 3.

No.	Code	f (Hz)	N_f
1	Conf-0.5-78-a	6.8	20,505

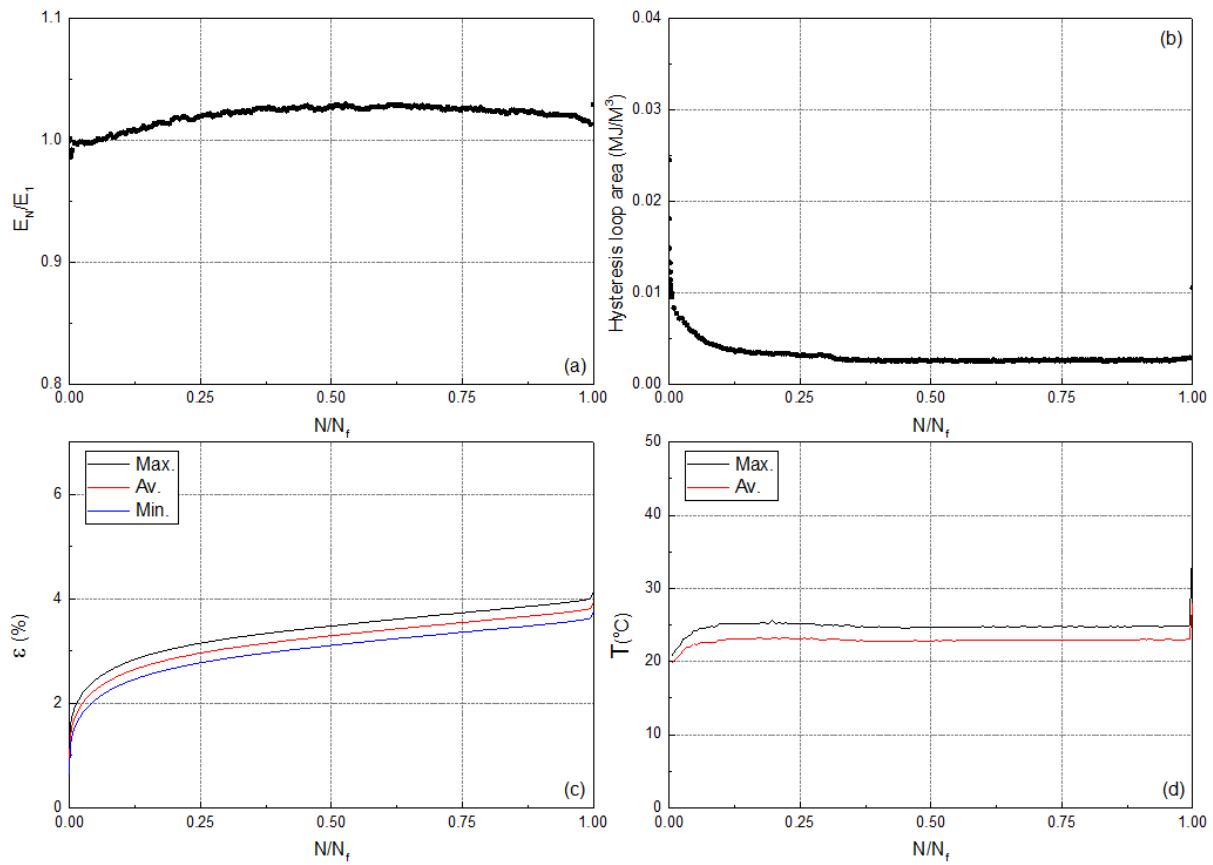


Fig. 1. Variation of (a) normalized fatigue stiffness, (b) hysteresis area, (c) maximum, average, and minimum cyclic strain, and (d) maximum and average self-generated temperature versus normalized number of cycles.

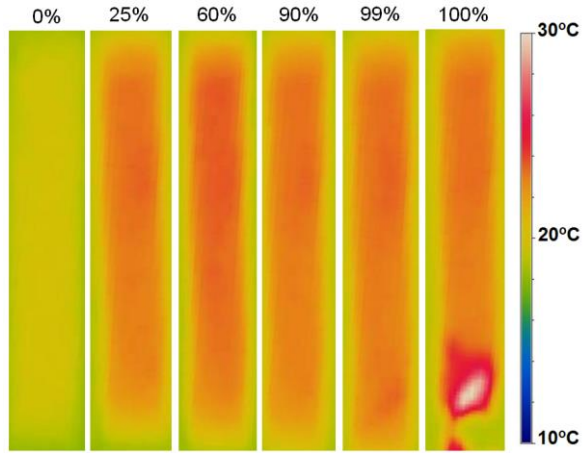


Fig. 2. Representation of the self-generated temperature in different percentages of fatigue life.

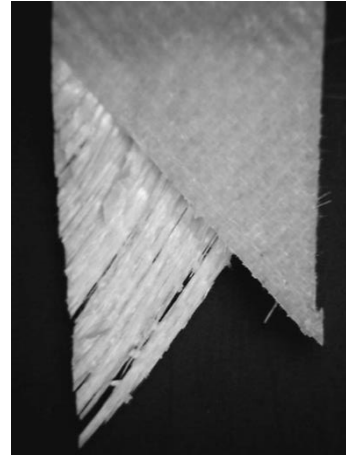


Fig. 3. Fatigue fracture surface.

No.	Code	f (Hz)	N_f
2	Conf-0.5-78-b	6.8	5,206

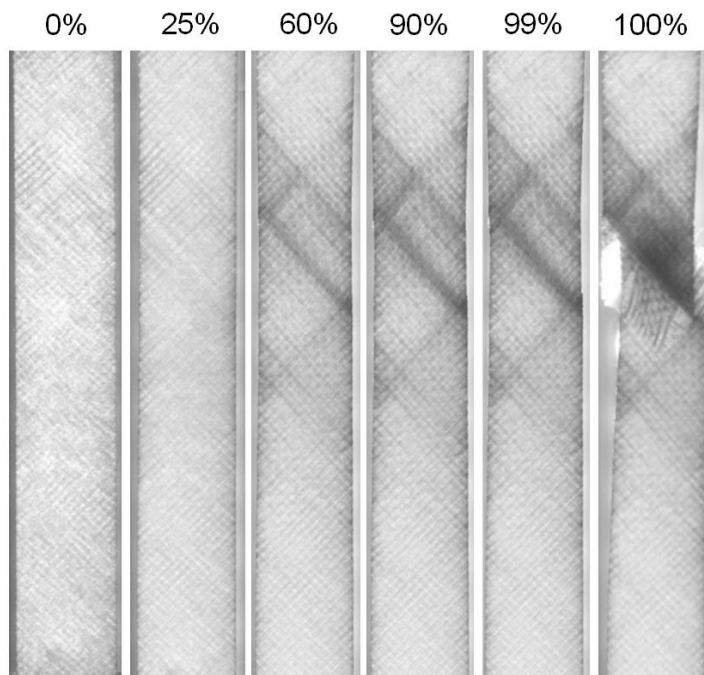


Fig. 1. Light transmittance in different percentages of fatigue life.

No.	Code	f (Hz)	N_f
3	Conf-0.5-78-c	6.8	1,767

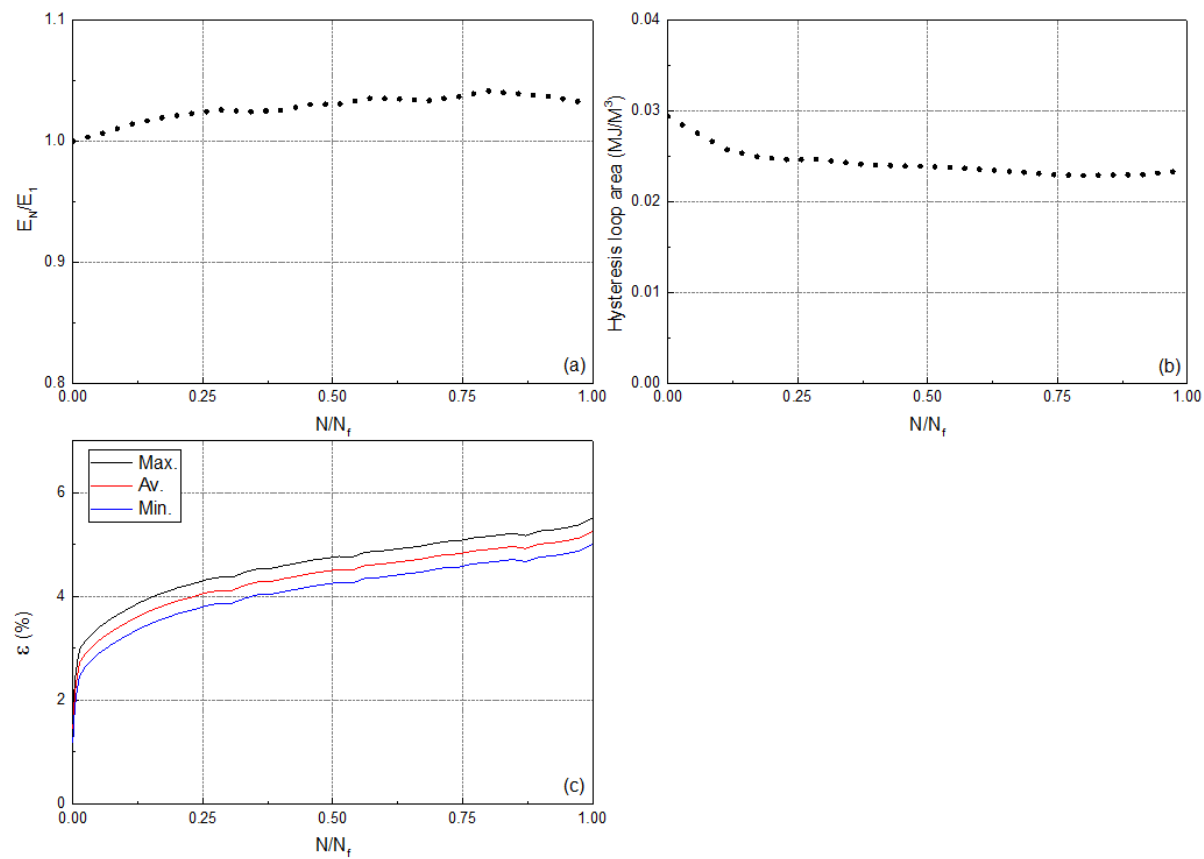


Fig. 1. Variation of (a) normalized fatigue stiffness, (b) hysteresis area, and (c) maximum, average, and minimum cyclic strain versus normalized number of cycles.

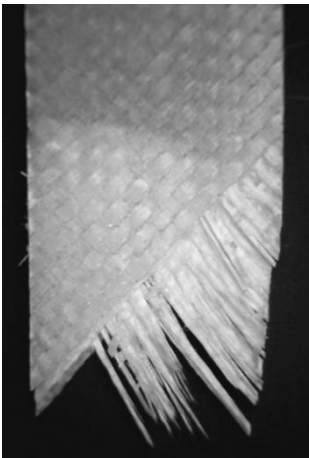


Fig. 2. Fatigue fracture surface.

No.	Code	f (Hz)	N_f
4	Conf-0.5-78-d	6.8	1,471

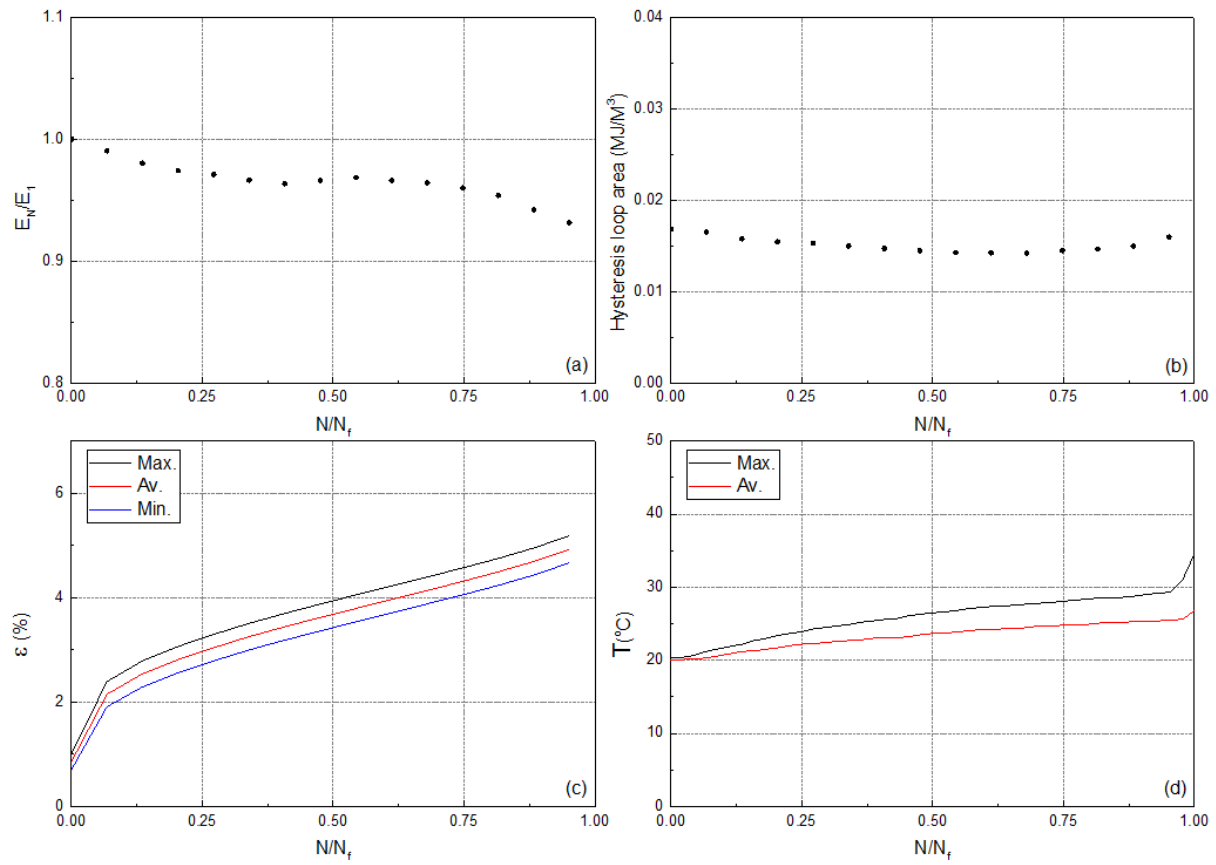


Fig. 1. Variation of (a) normalized fatigue stiffness, (b) hysteresis area, (c) maximum, average, and minimum cyclic strain, and (d) maximum and average self-generated temperature versus normalized number of cycles.

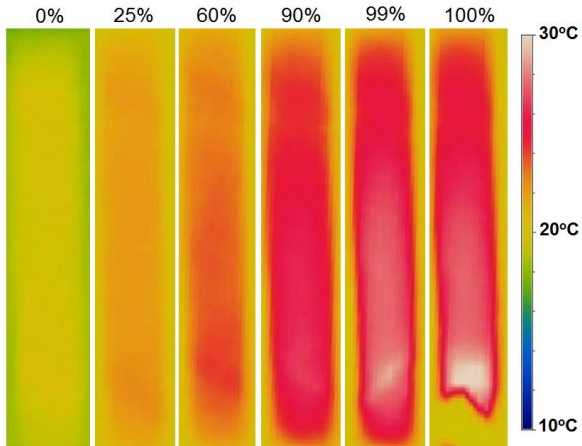


Fig. 2. Representation of the self-generated temperature in different percentages of fatigue life.

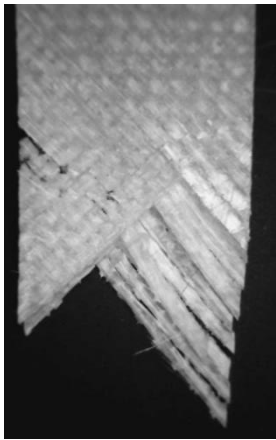


Fig. 3. Fatigue fracture surface.

No.	Code	f (Hz)	N_f
5	Conf-0.5-72-a	7.4	60,130

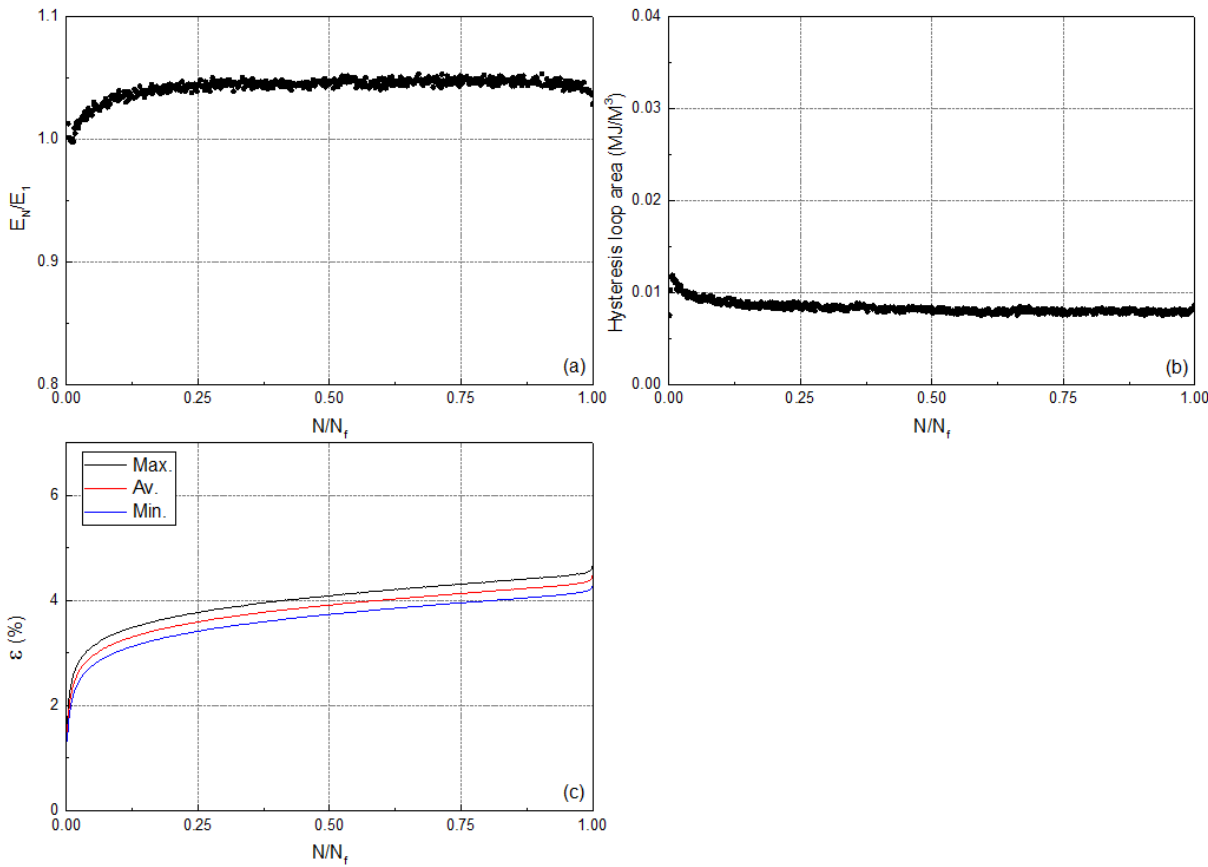


Fig. 1. Variation of (a) normalized fatigue stiffness, (b) hysteresis area, and (c) maximum, average, and minimum cyclic strain versus normalized number of cycles.

No.	Code	f (Hz)	N_f
6	Conf-0.5-72-b	7.4	61,616

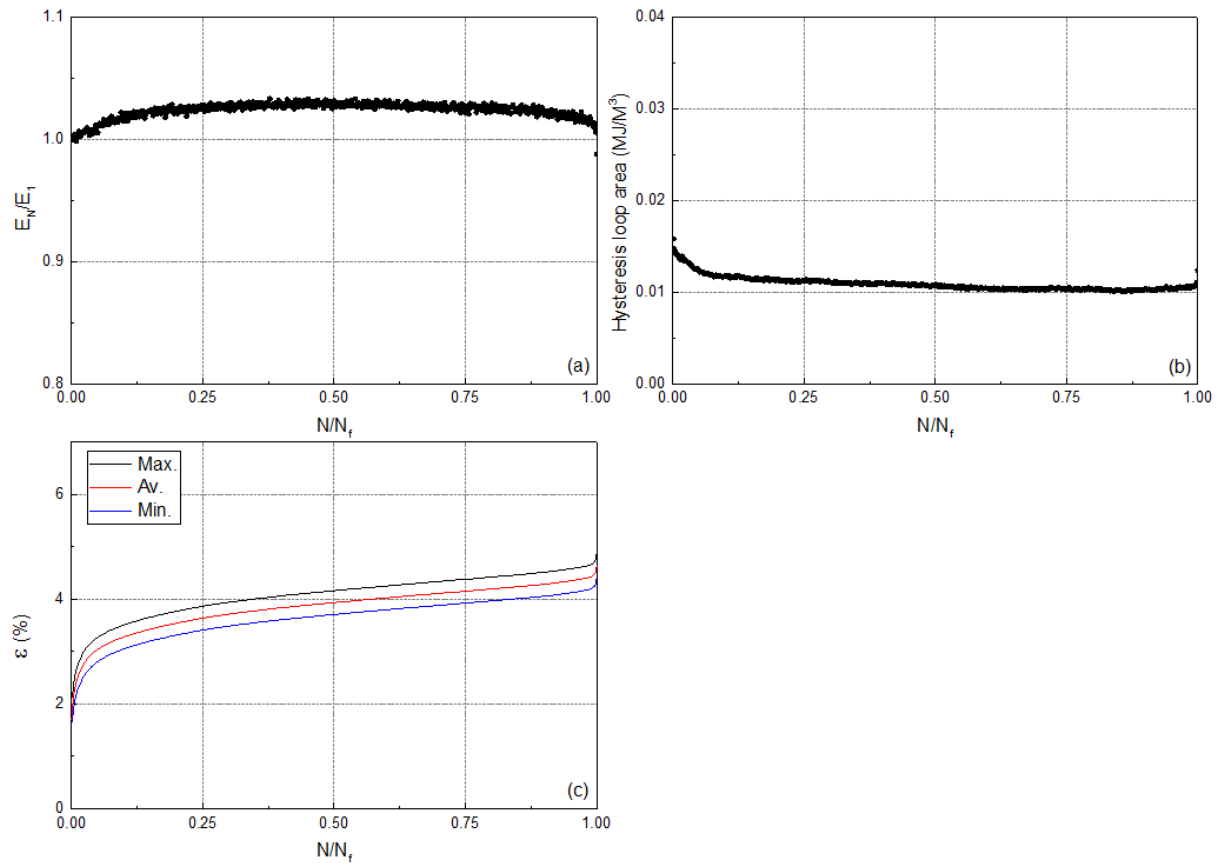


Fig. 1. Variation of (a) normalized fatigue stiffness, (b) hysteresis area, and (c) maximum, average, and minimum cyclic strain, versus normalized number of cycles.

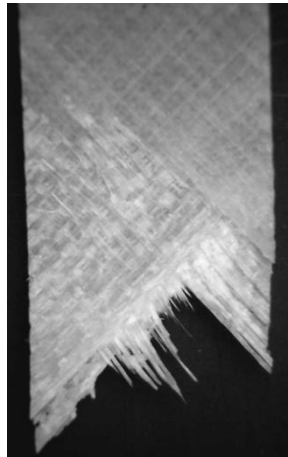


Fig. 2. Fatigue fracture surface.

No.	Code	f (Hz)	N_f
7	Conf-0.5-72-c	7.4	36,435

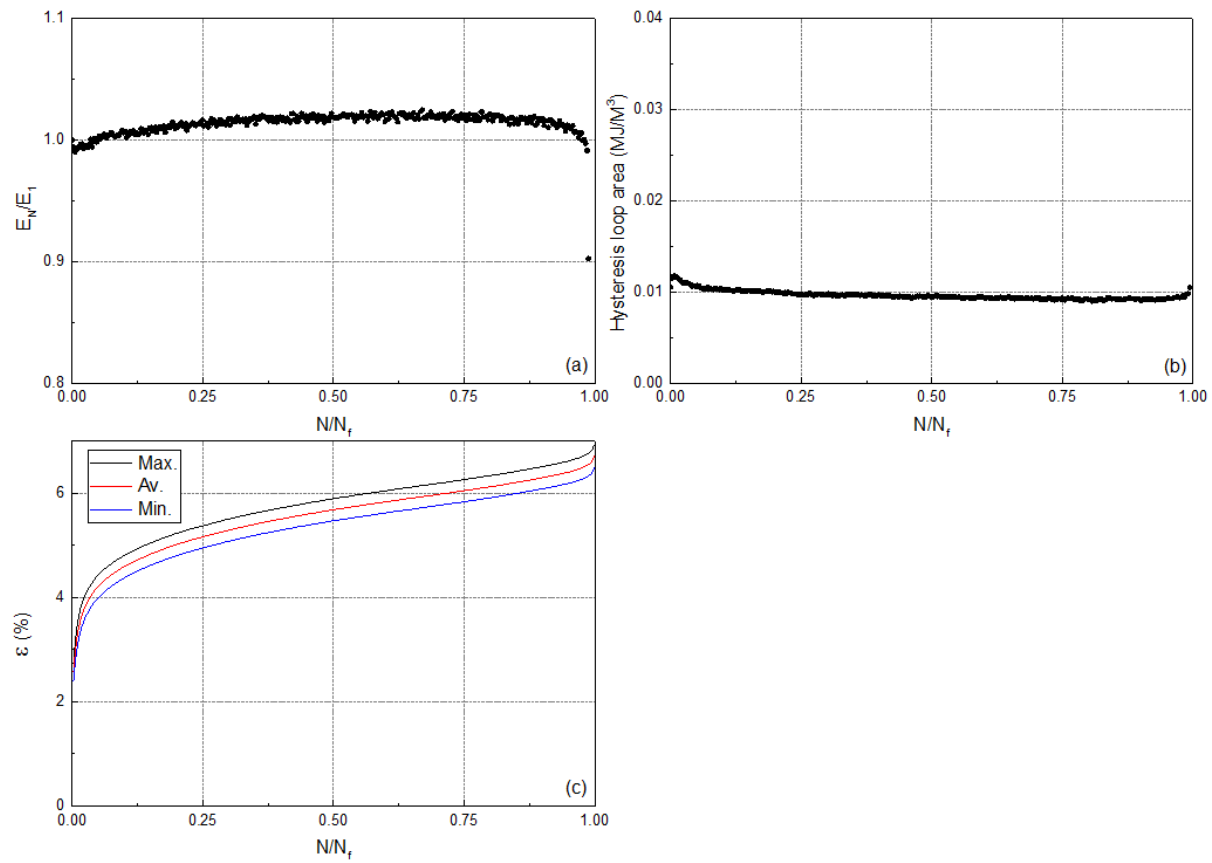


Fig. 1. Variation of (a) normalized fatigue stiffness, (b) hysteresis area, and (c) maximum, average, and minimum cyclic strain versus normalized number of cycles.

No.	Code	f (Hz)	N_f
8	Conf-0.5-72-d	7.4	6,513

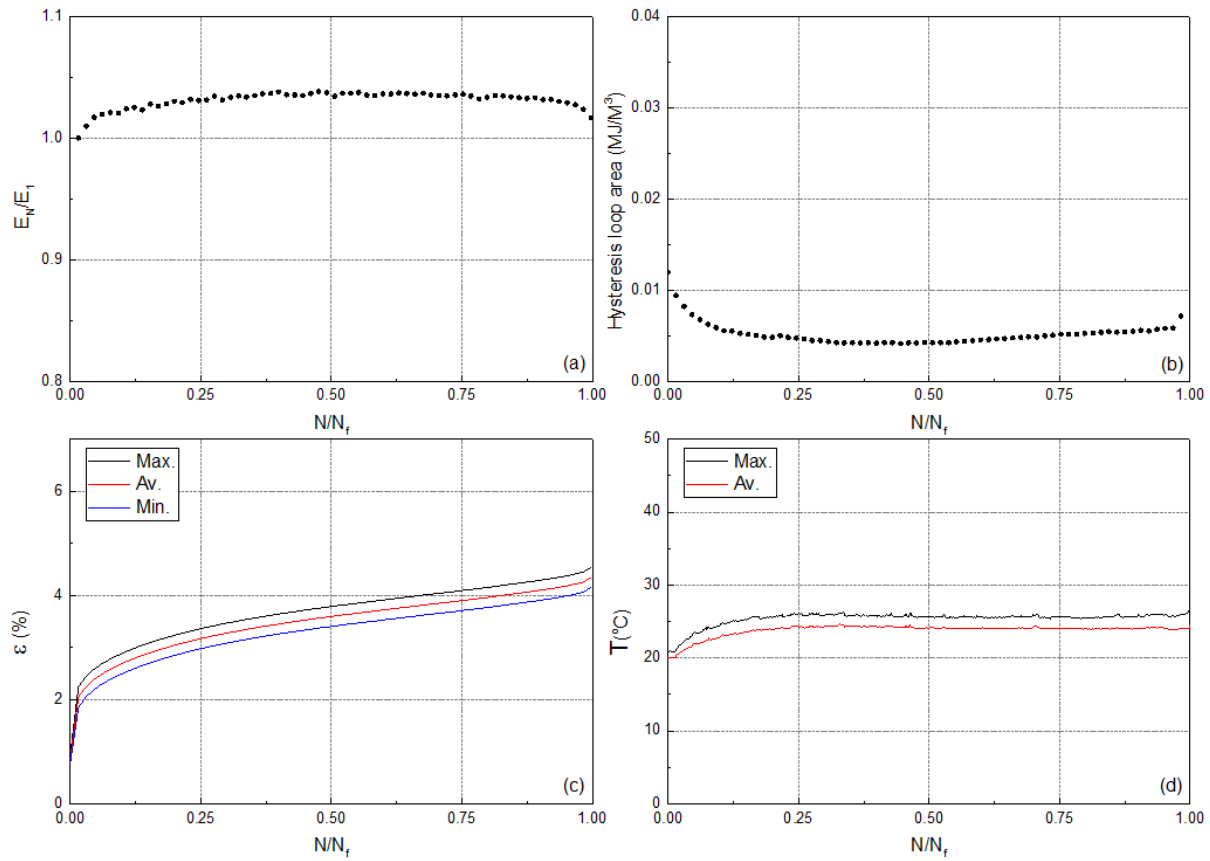


Fig. 1. Variation of (a) normalized fatigue stiffness, (b) hysteresis area, (c) maximum, average, and minimum cyclic strain, and (d) maximum and average self-generated temperature versus normalized number of cycles.

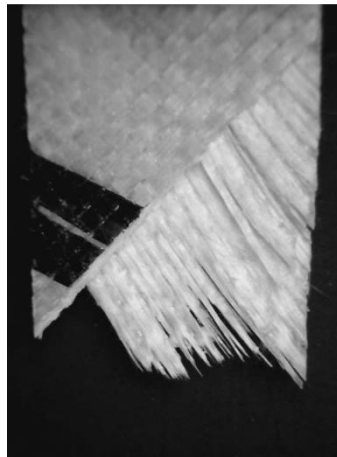


Fig. 2. Fatigue fracture surface.

No.	Code	f (Hz)	N_f
9	Conf-0.5-68-a	7.8	5,436

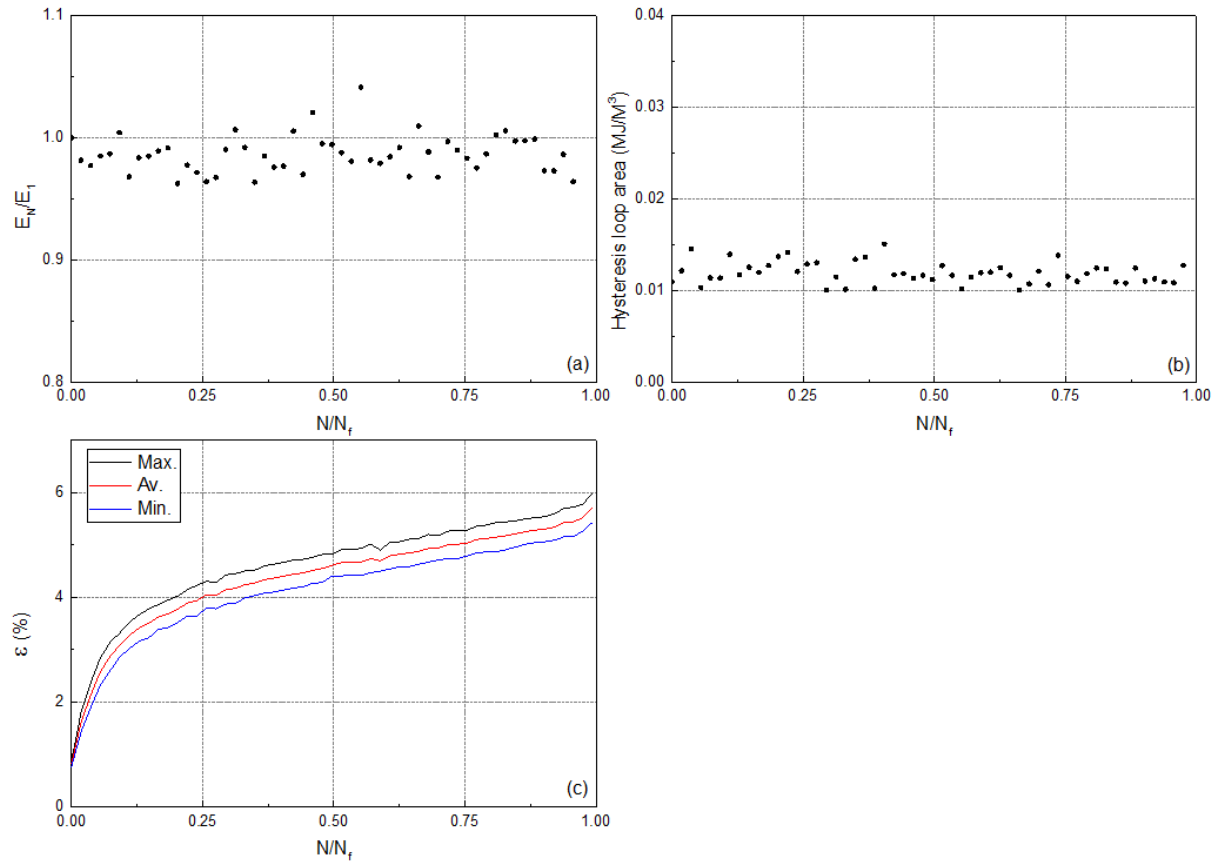


Fig. 1. Variation of (a) normalized fatigue stiffness, (b) hysteresis area, and (c) maximum, average, and minimum cyclic strain versus normalized number of cycles.

No.	Code	f (Hz)	N_f
10	Conf-0.5-68-b	7.8	112,681

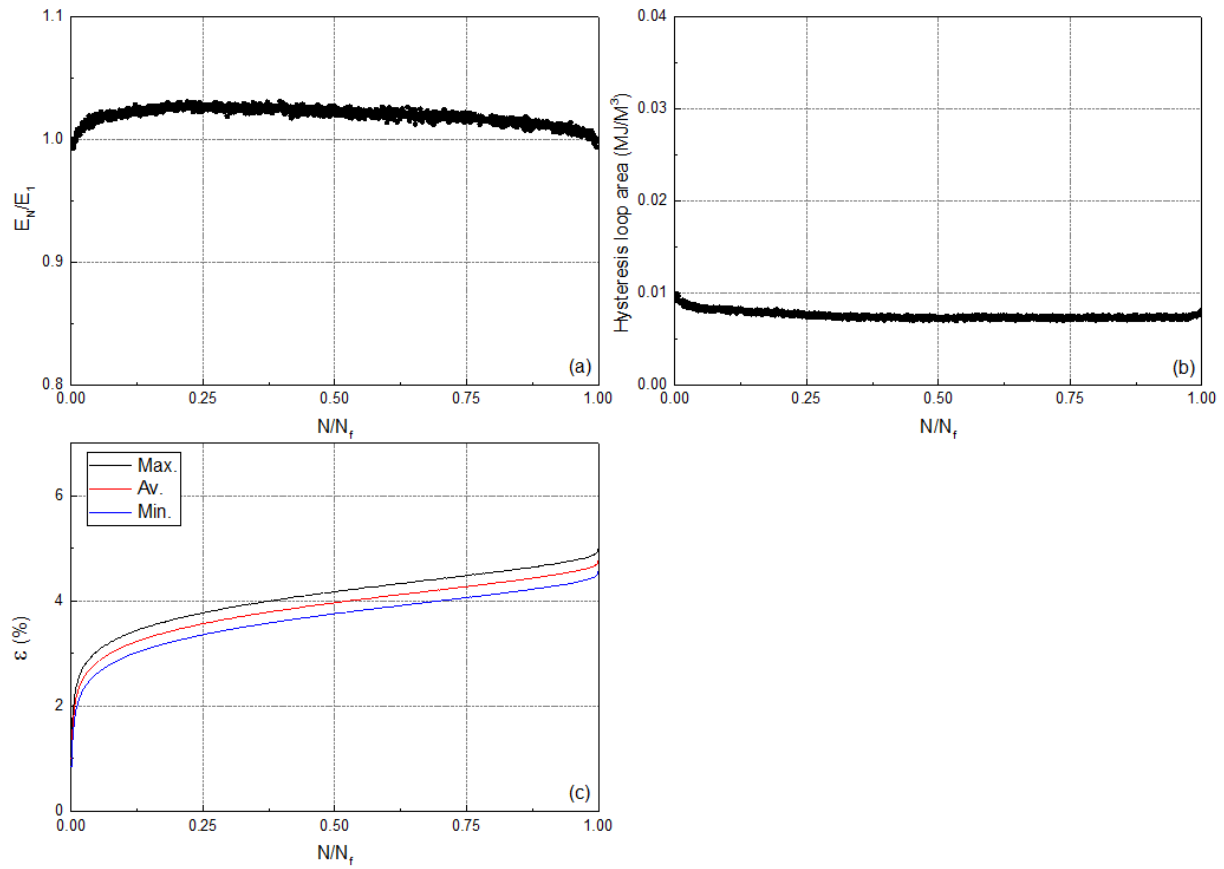


Fig. 1. Variation of (a) normalized fatigue stiffness, (b) hysteresis area, and (c) maximum, average, and minimum cyclic strain versus normalized number of cycles.

No.	Code	f (Hz)	N_f
11	Conf-0.5-68-c	7.8	119,132

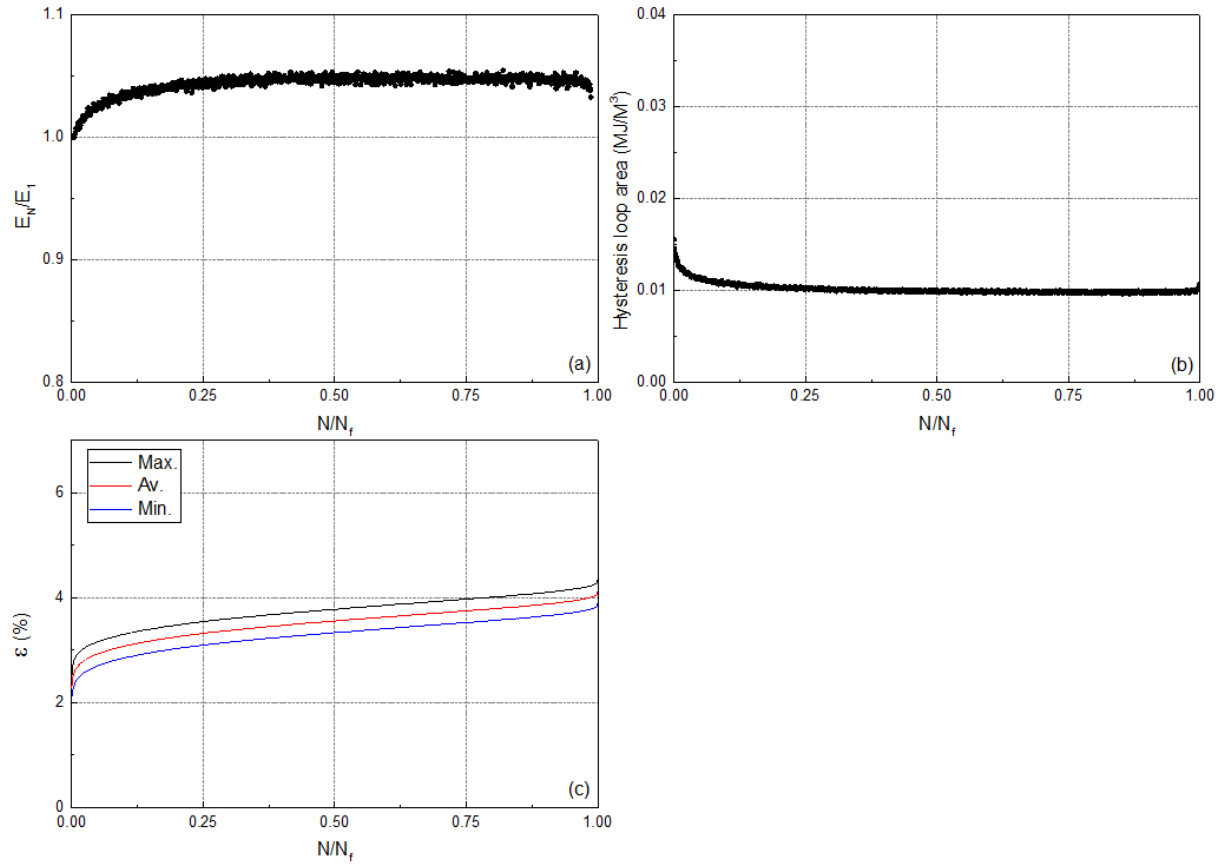


Fig. 1. Variation of (a) normalized fatigue stiffness, (b) hysteresis area, and (c) maximum, average, and minimum cyclic strain versus normalized number of cycles.

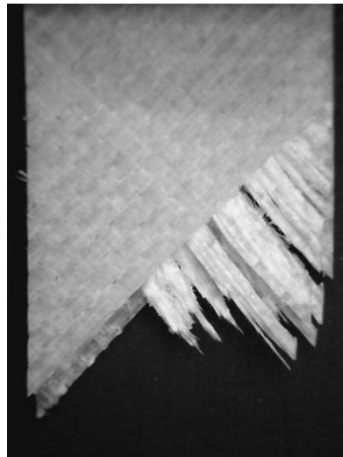


Fig. 2. Fatigue fracture surface.

No.	Code	f (Hz)	N_f
12	Conf-0.5-68-d	7.8	16,642

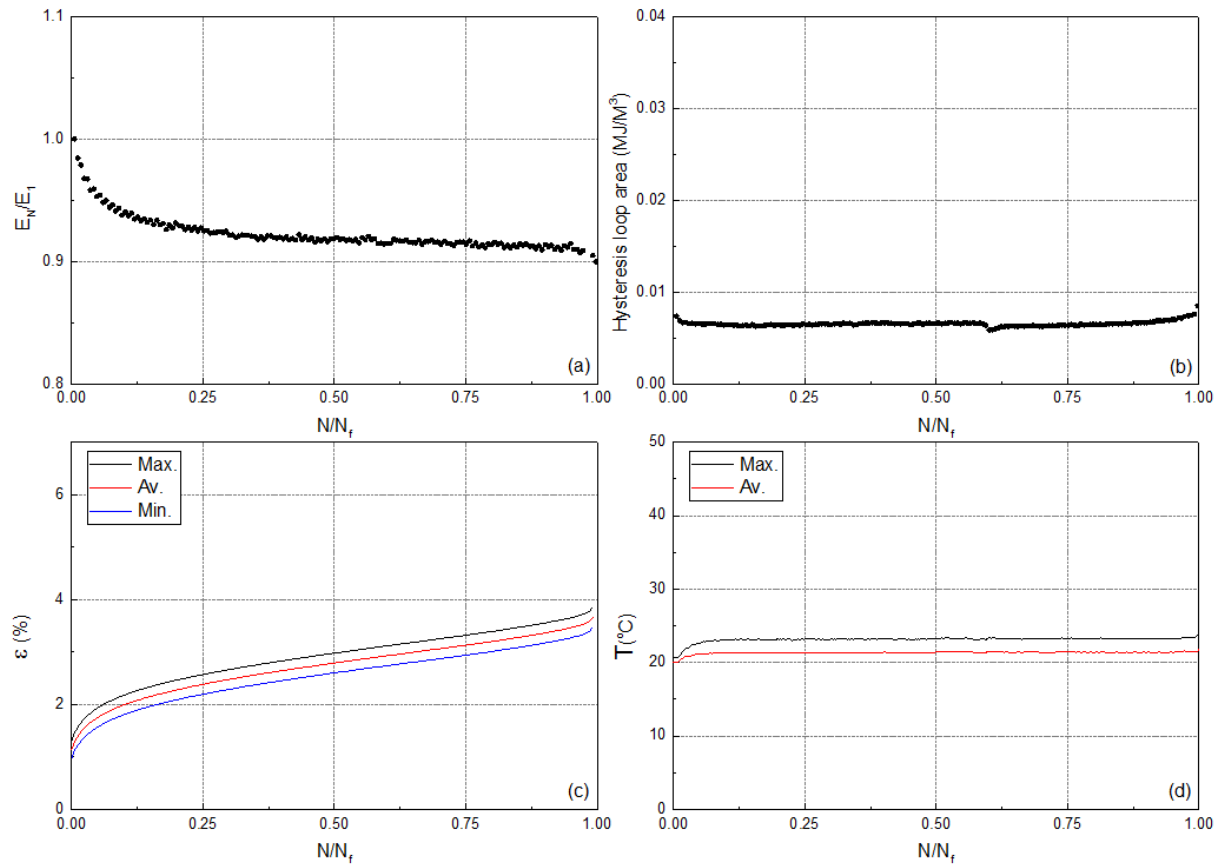


Fig. 1. Variation of (a) normalized fatigue stiffness, (b) hysteresis area, (c) maximum, average, and minimum cyclic strain, and (d) maximum and average self-generated temperature versus normalized number of cycles.

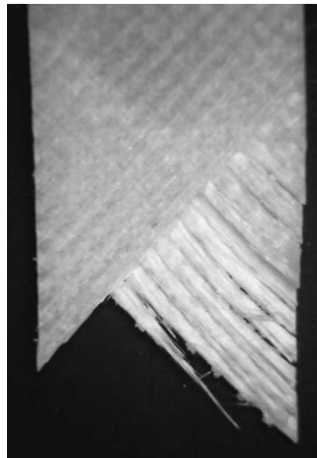


Fig. 2. Fatigue fracture surface.

No.	Code	f (Hz)	N_f
13	Conf-0.5-64-a	8.4	76,431

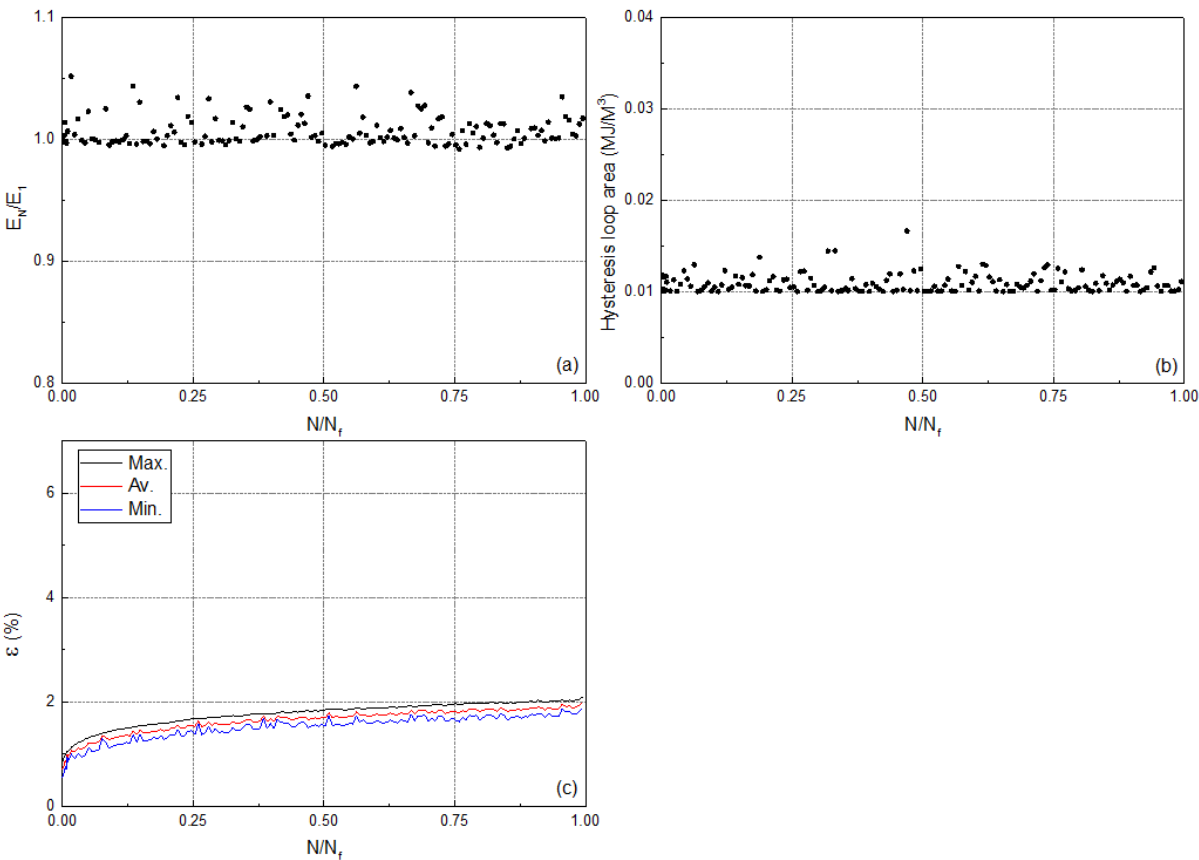


Fig. 1. Variation of (a) normalized fatigue stiffness, (b) hysteresis area, and (c) maximum, average, and minimum cyclic strain versus normalized number of cycles.

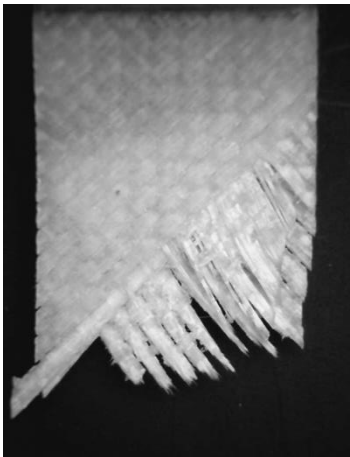


Fig. 2. Fatigue fracture surface.

No.	Code	f (Hz)	N_f
14	Conf-0.5-64-b	8.4	228,923

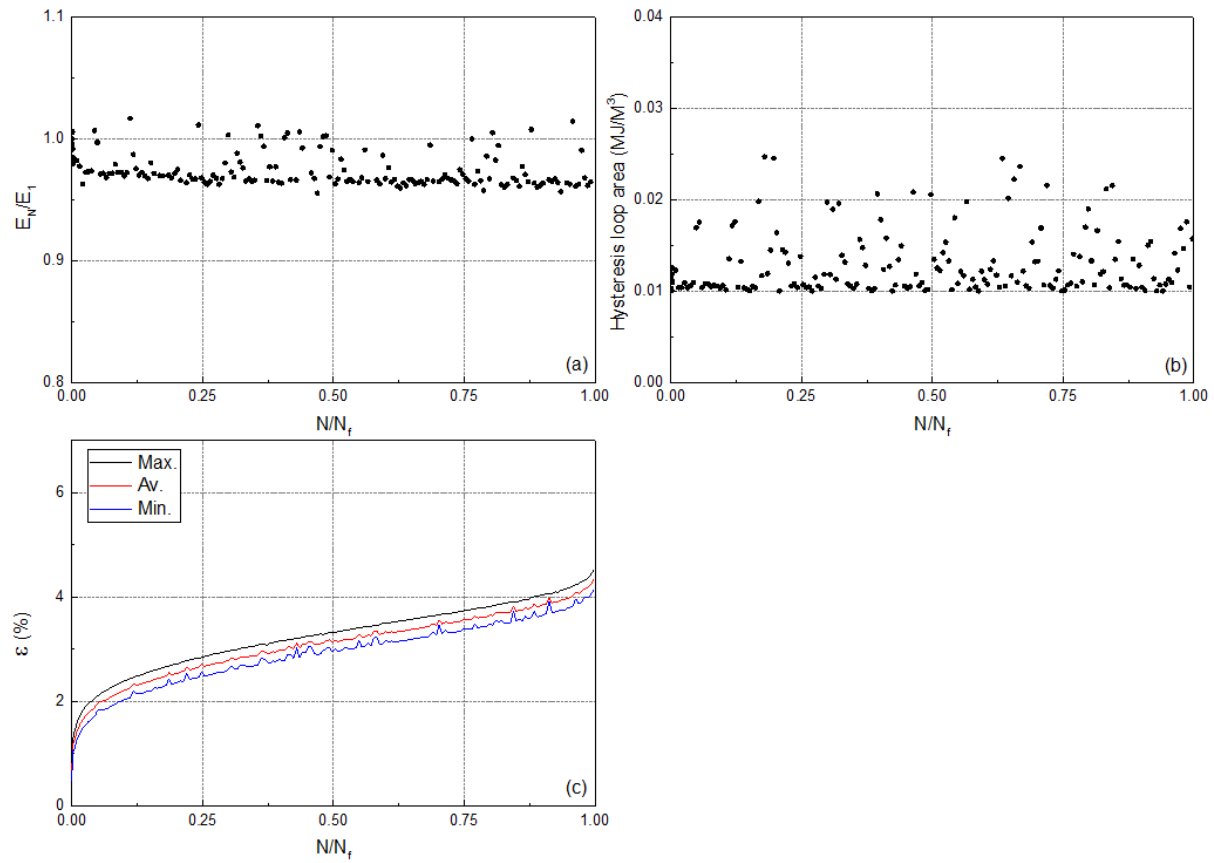


Fig. 1. Variation of (a) normalized fatigue stiffness, (b) hysteresis area, and (c) maximum, average, and minimum cyclic strain versus normalized number of cycles.

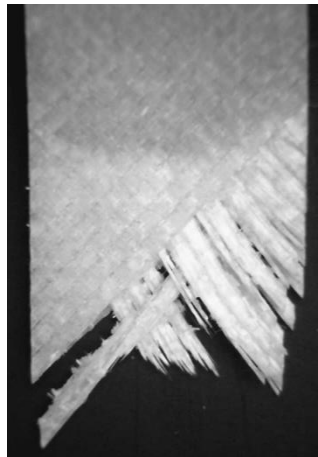


Fig. 2. Fatigue fracture surface.

No.	Code	f (Hz)	N_f
15	Conf-0.5-64-c	8.4	345,818

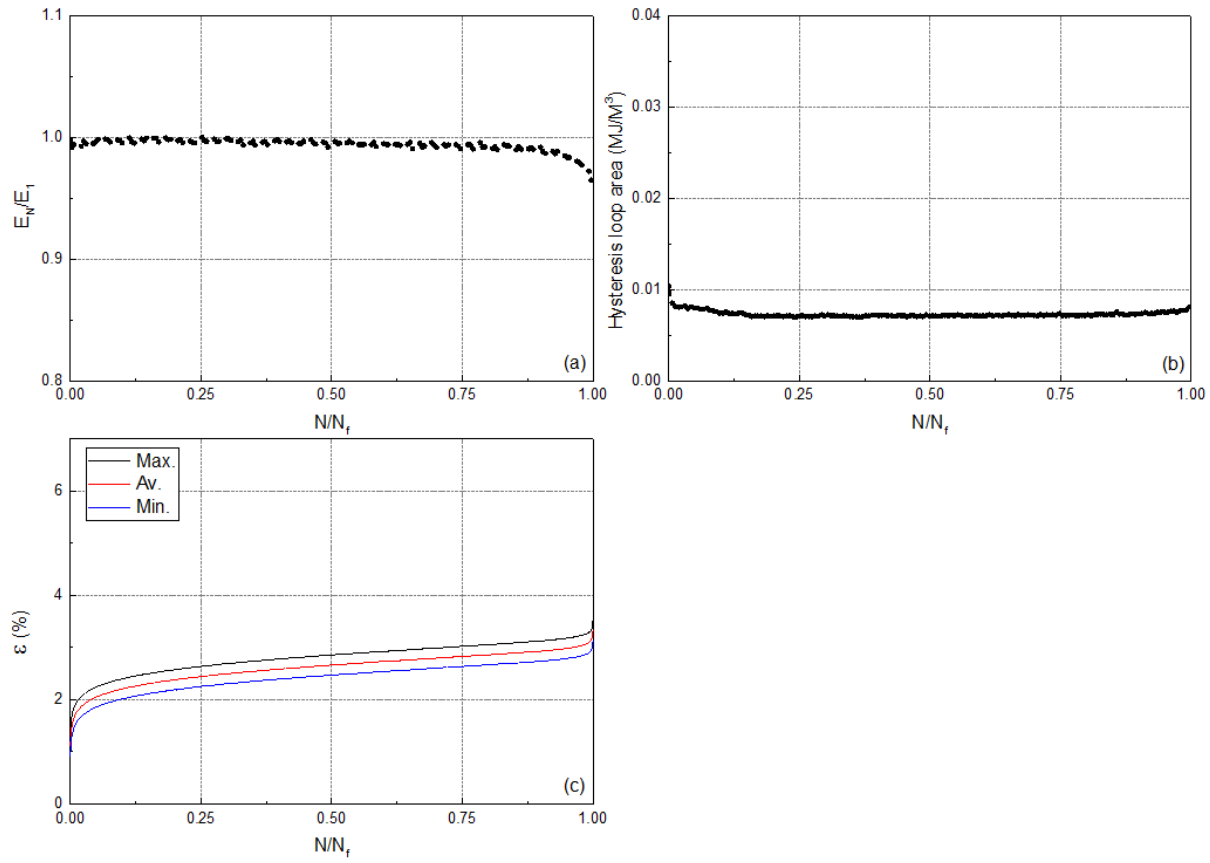


Fig. 1. Variation of (a) normalized fatigue stiffness, (b) hysteresis area, and (c) maximum, average, and minimum cyclic strain versus normalized number of cycles.

No.	Code	f (Hz)	N_f
16	Conf-0.5-64-d	8.4	108,719

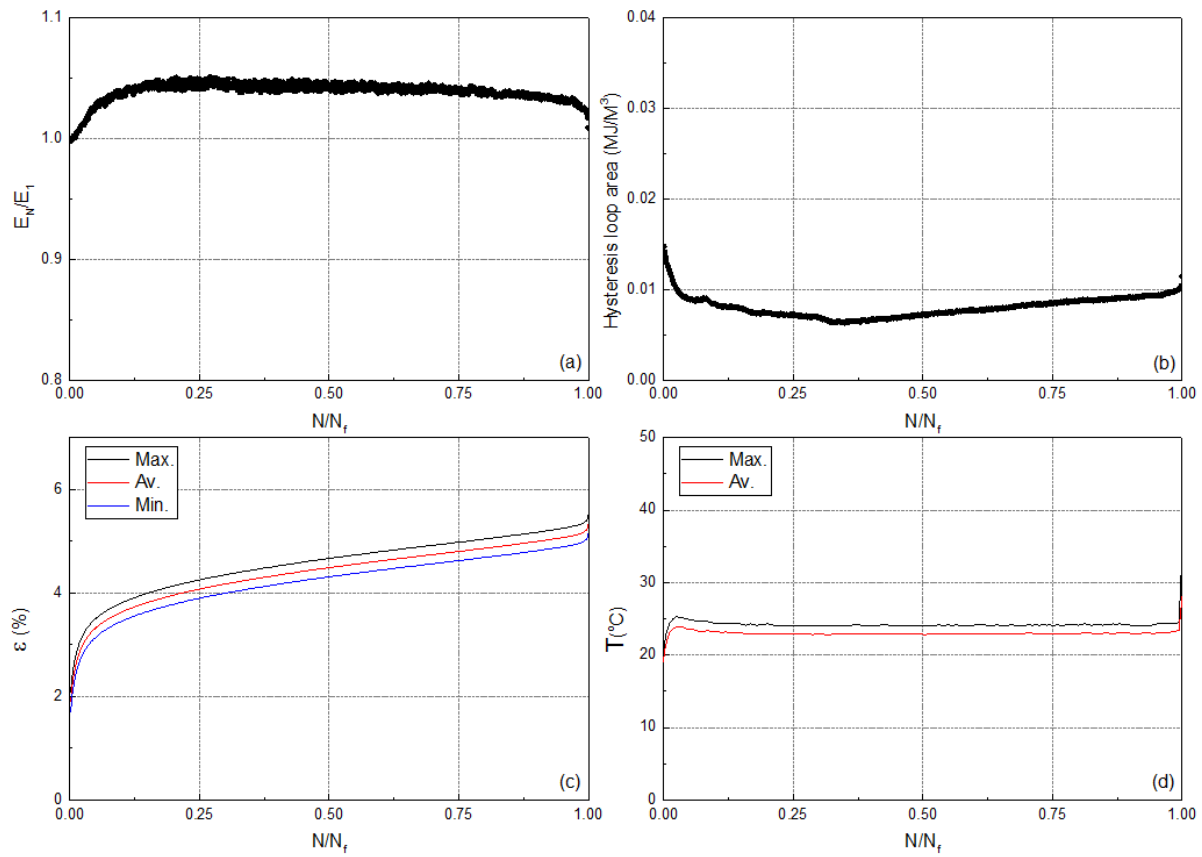


Fig. 1. Variation of (a) normalized fatigue stiffness, (b) hysteresis area, (c) maximum, average, and minimum cyclic strain, and (d) maximum and average self-generated temperature versus normalized number of cycles.

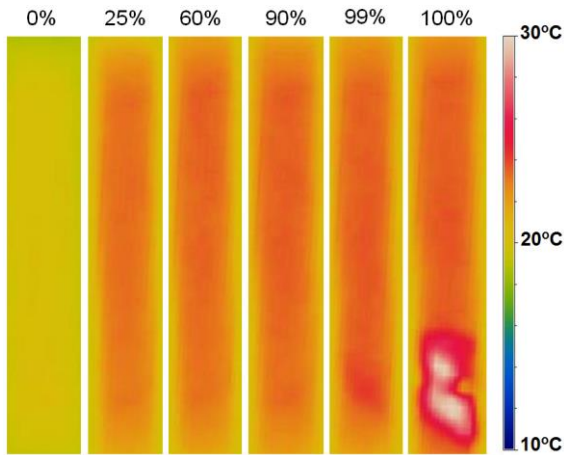


Fig. 2. Representation of the self-generated temperature in different percentages of fatigue life.

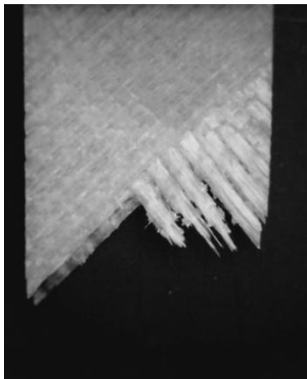


Fig. 3. Fatigue fracture surface.

No.	Code	f (Hz)	N_f
17	Conf-0.5-58-a	9.1	2,110,761

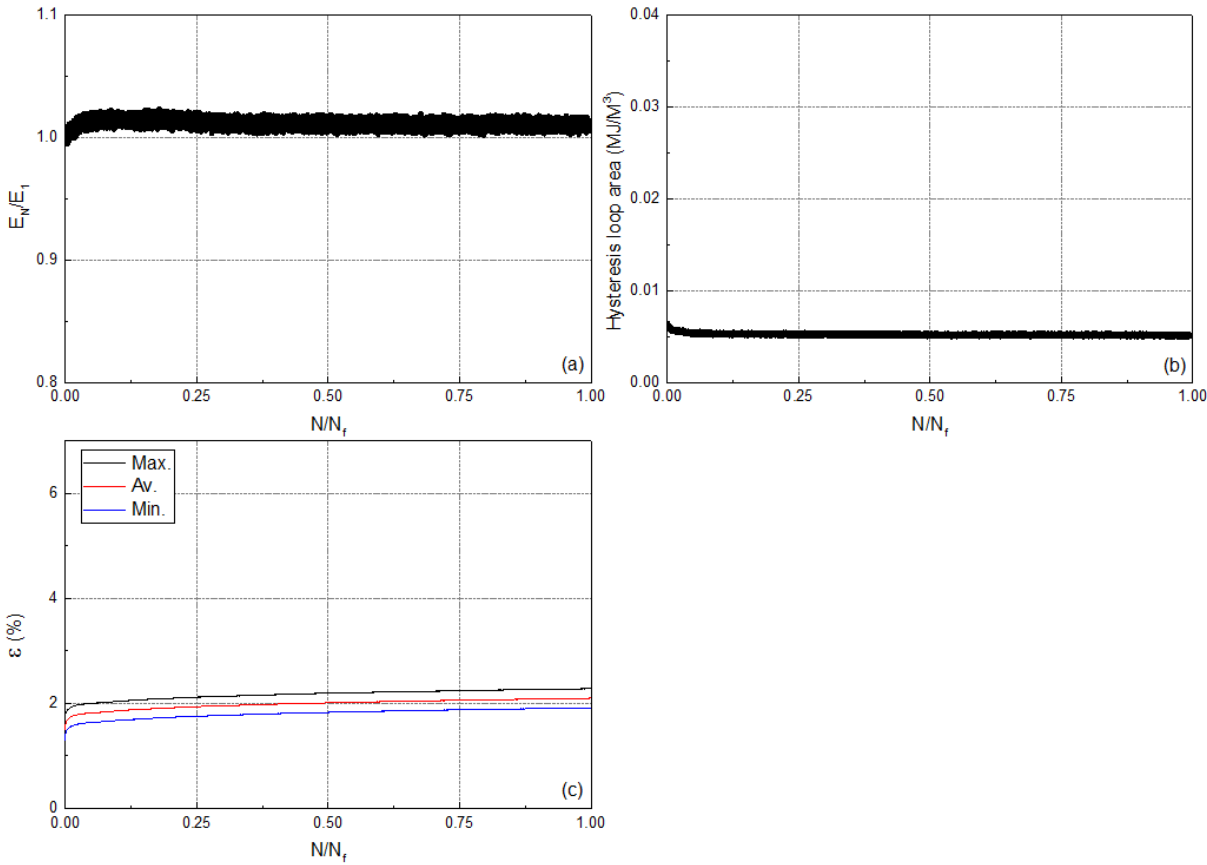


Fig. 1. Variation of (a) normalized fatigue stiffness, (b) hysteresis area, and (c) maximum, average, and minimum cyclic strain versus normalized number of cycles.

No.	Code	f (Hz)	N_f
18	Conf-0.5-58-b	9.1	295,972

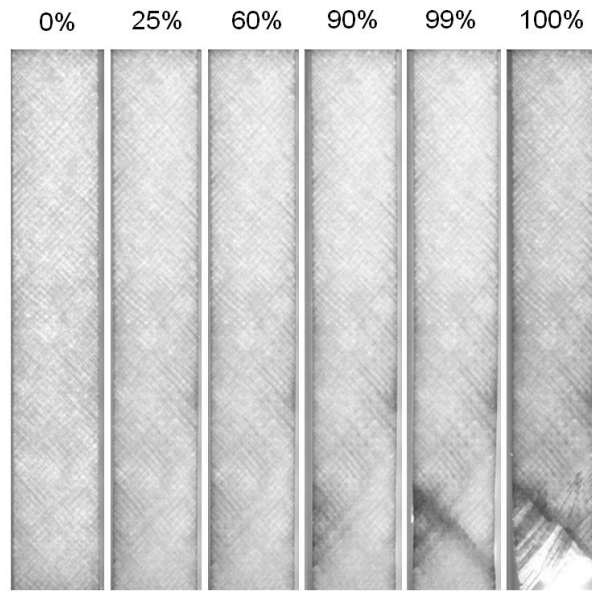


Fig. 1. Light transmittance in different percentages of fatigue life.



Fig. 2. Fatigue fracture surface.

No.	Code	f (Hz)	N_f
19	Conf-0.5-58-c	9.1	645,568

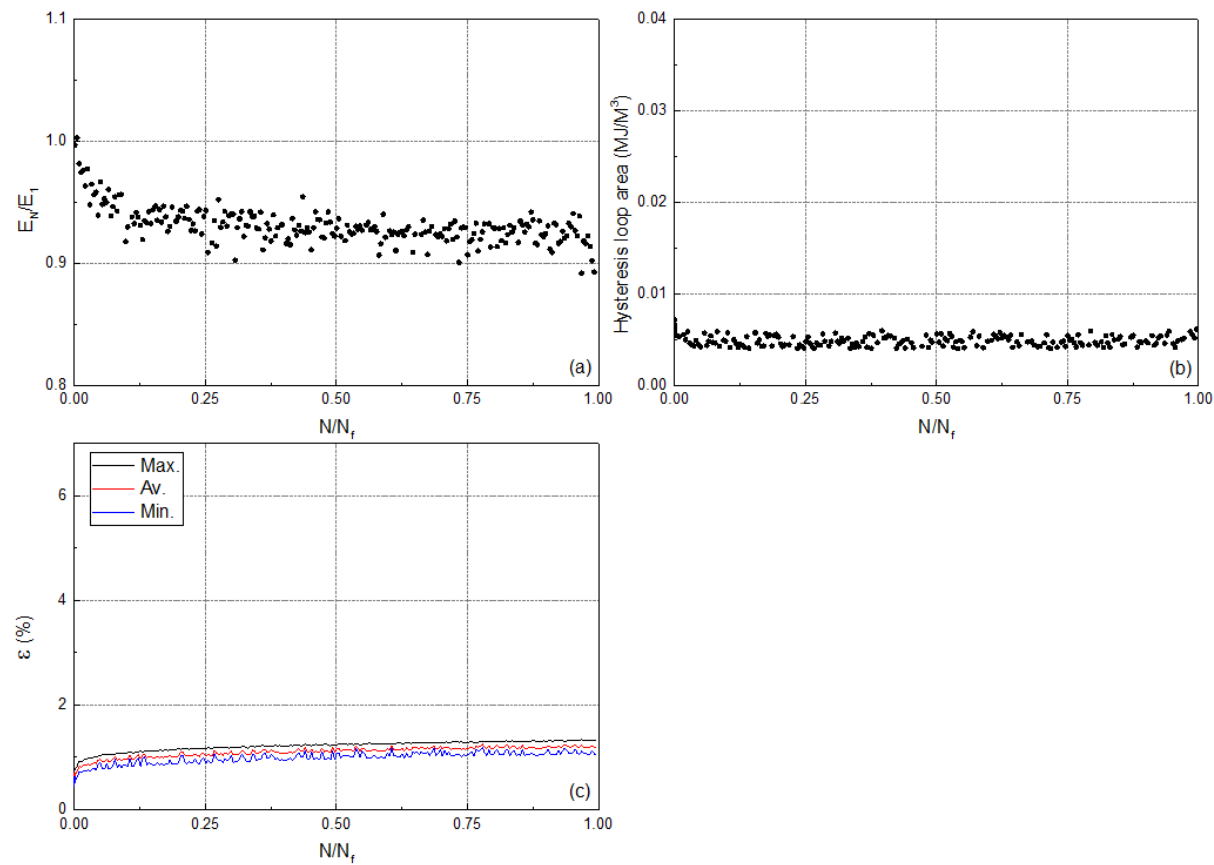


Fig. 1. Variation of (a) normalized fatigue stiffness, (b) hysteresis area, and (c) maximum, average, and minimum cyclic strain versus normalized number of cycles.

No.	Code	f (Hz)	N_f
20	Conf-0.5-58-d	9.1	5,245,384

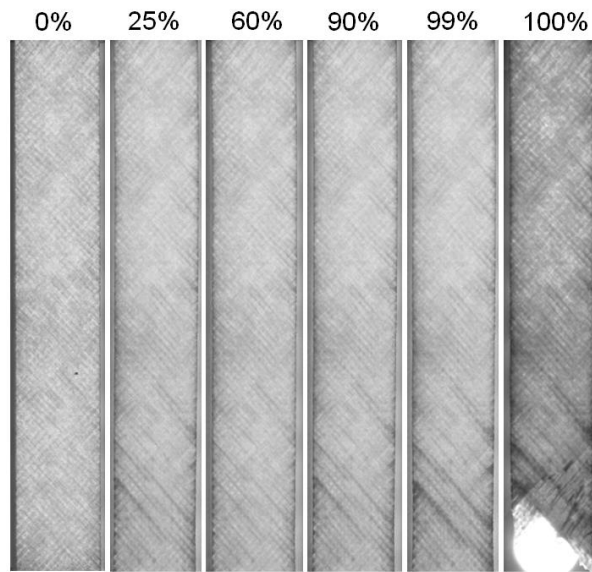


Fig. 1. Light transmittance in different percentages of fatigue life.

Annex C: Creep-fatigue



C.1 Introduction

Annex C presents supplementary results from the creep-fatigue experiments, which was described in Chapter 4.

No.	Code	f (Hz)	N_f
1	Cref-0.1-70-2-a	3.95	1840

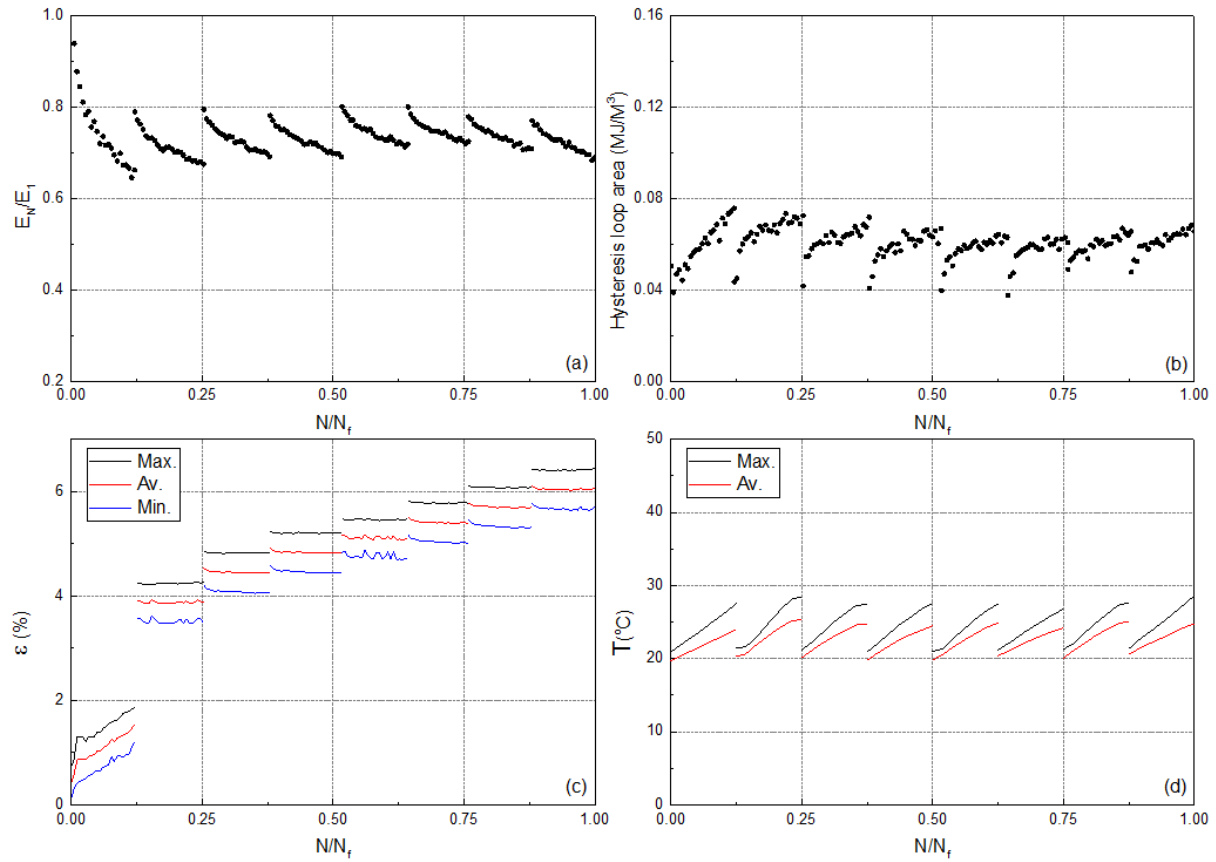


Fig. 1. Variation of (a) normalized fatigue stiffness, (b) hysteresis area, (c) maximum, average, and minimum cyclic strain, and (d) maximum and average self-generated temperature versus normalized number of cycles.

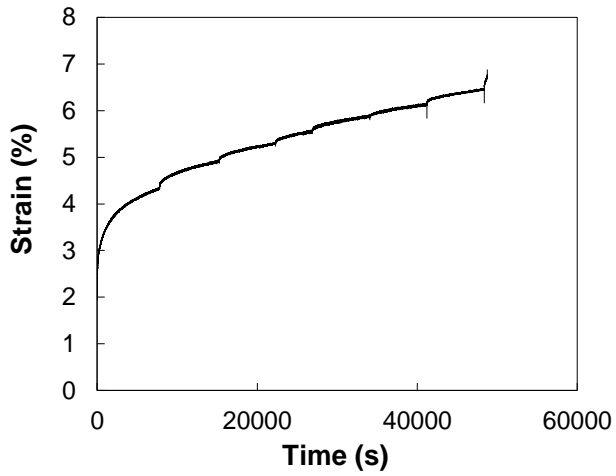


Fig. 2. Creep curves during the interruptions.

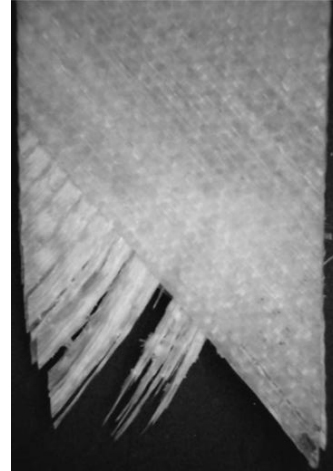


Fig. 3. Fatigue fracture surface.

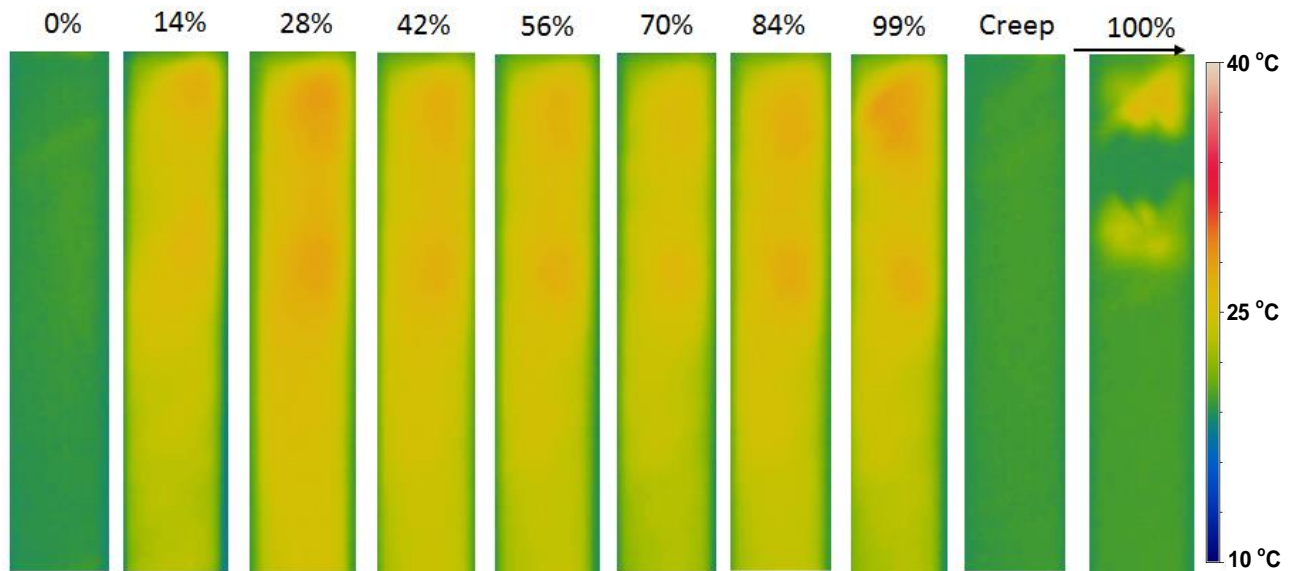


Fig. 4. Representation of the self-generated temperature in different percentages of fatigue life.

No.	Code	f (Hz)	N_f
2	Cref-0.1-70-2-b	3.95	1150

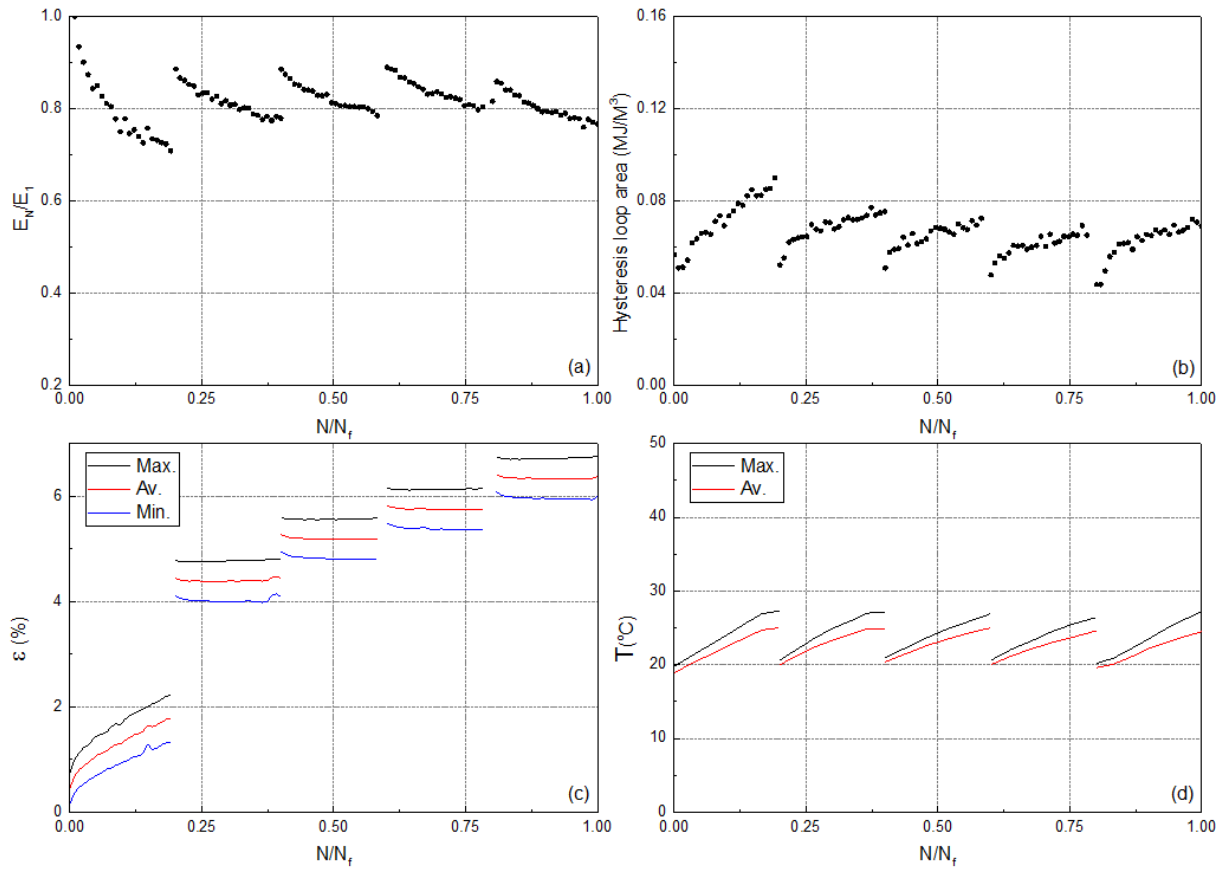


Fig. 1. Variation of (a) normalized fatigue stiffness, (b) hysteresis area, (c) maximum, average, and minimum cyclic strain, and (d) maximum and average self-generated temperature versus normalized number of cycles.

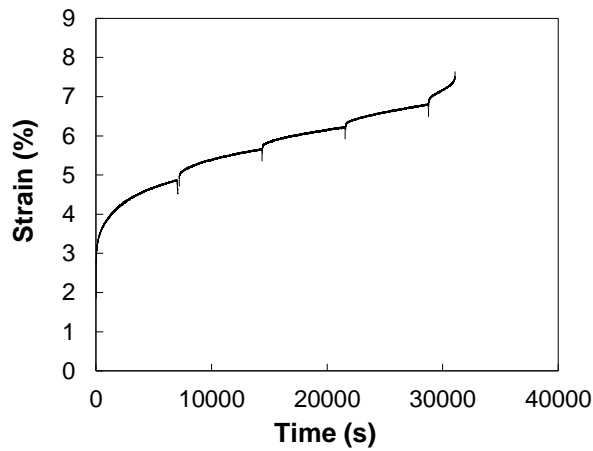


Fig. 2. Creep curves during the interruptions.

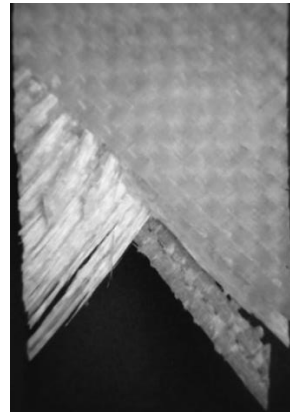


Fig. 3. Fatigue fracture surface.

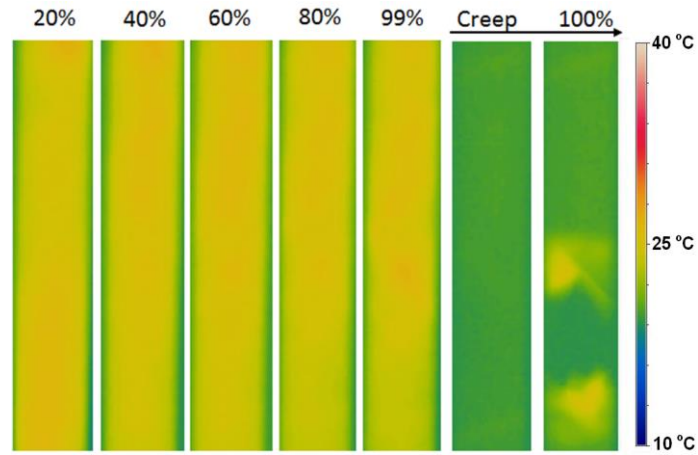


Fig. 4. Representation of the self-generated temperature in different percentages of fatigue life.

No.	Code	f (Hz)	N_f
3	Cref-0.1-70-2-c	3.95	1150

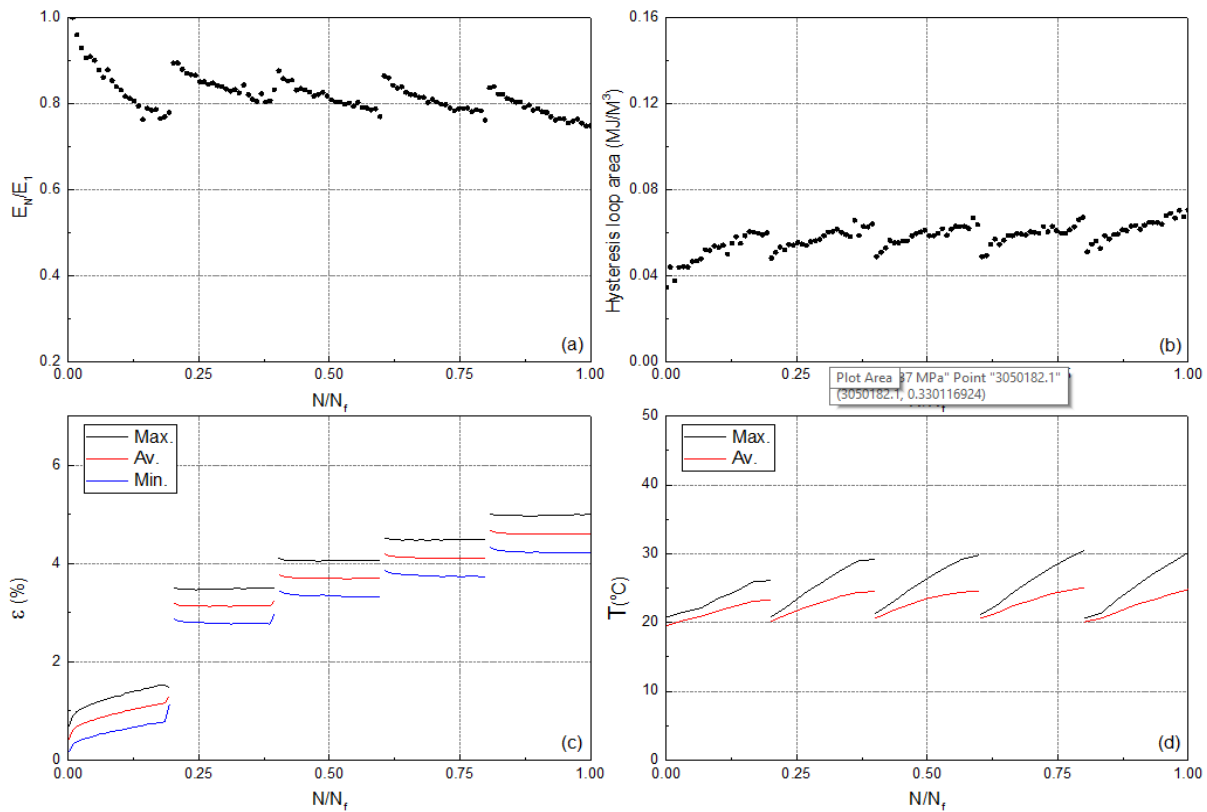


Fig. 1. Variation of (a) normalized fatigue stiffness, (b) hysteresis area, (c) maximum, average, and minimum cyclic strain, and (d) maximum and average self-generated temperature versus normalized number of cycles.

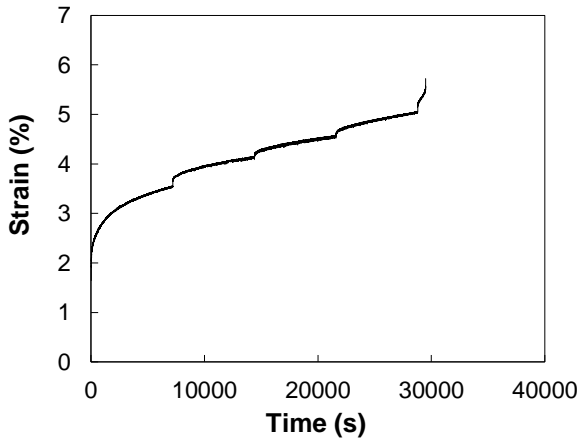


Fig. 2. Creep curves during the interruptions.

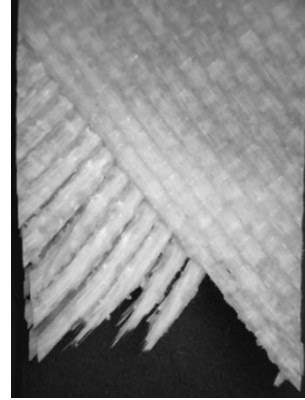


Fig. 3. Fatigue fracture surface.

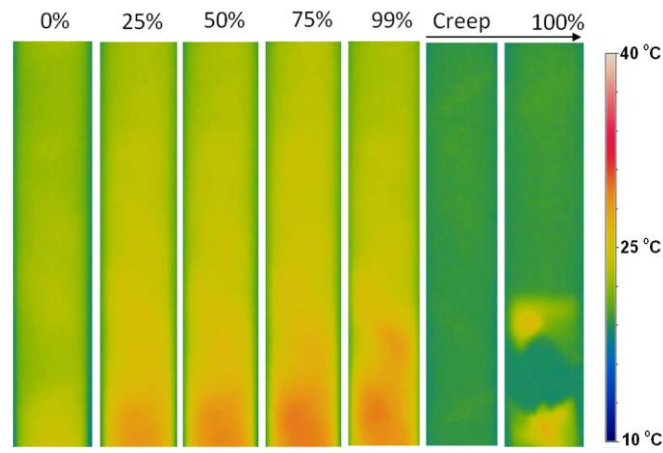


Fig. 4. Representation of the self-generated temperature in different percentages of fatigue life.

No.	Code	f (Hz)	N_f
4	Cref -0.1-70-2-d	3.95	1150

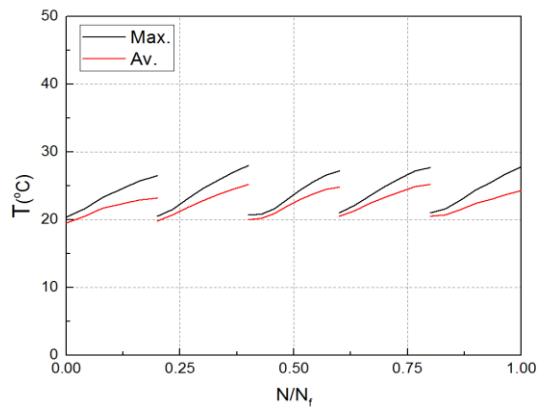


Fig. 1. Variation of maximum and average self-generated temperature.

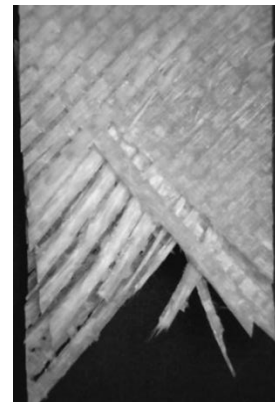


Fig. 2. Fatigue fracture surface.

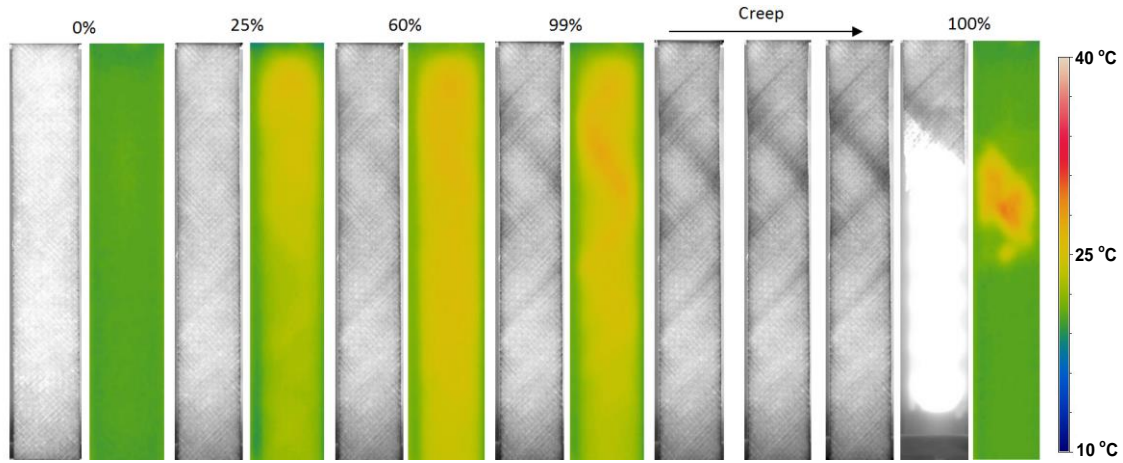


Fig. 3. Pairwise representation of light transmittance and self-generated temperature for different percentages of fatigue life.

No.	Code	f (Hz)	N_f
5	Cref-0.1-70-48-a	3.95	230

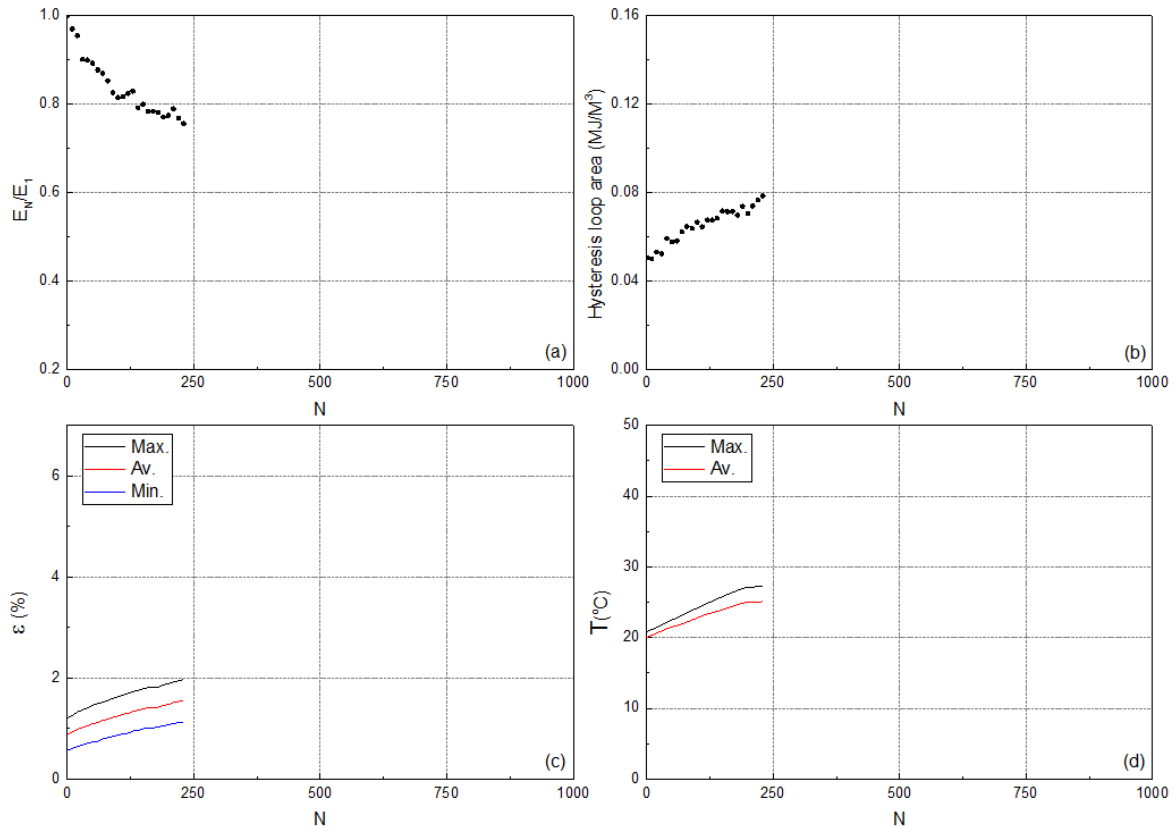


Fig. 1. Variation of (a) normalized fatigue stiffness, (b) hysteresis area, (c) maximum, average, and minimum cyclic strain, and (d) maximum and average self-generated temperature versus normalized number of cycles.

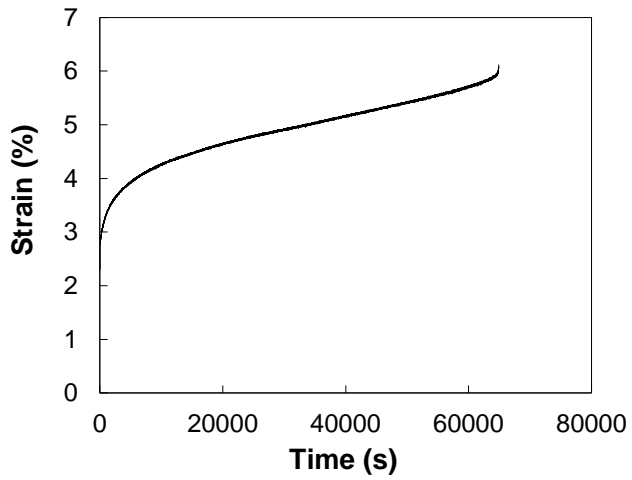


Fig. 2. Creep curves during the interruption.

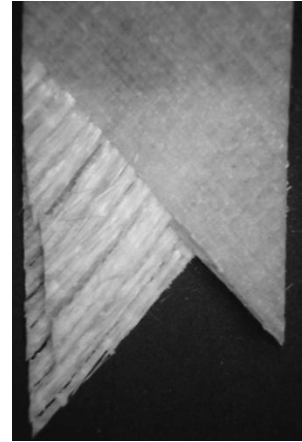


Fig. 3. Fatigue fracture surface.

No.	Code	f (Hz)	N_f
6	Cref-0.1-70-48-b	3.95	230

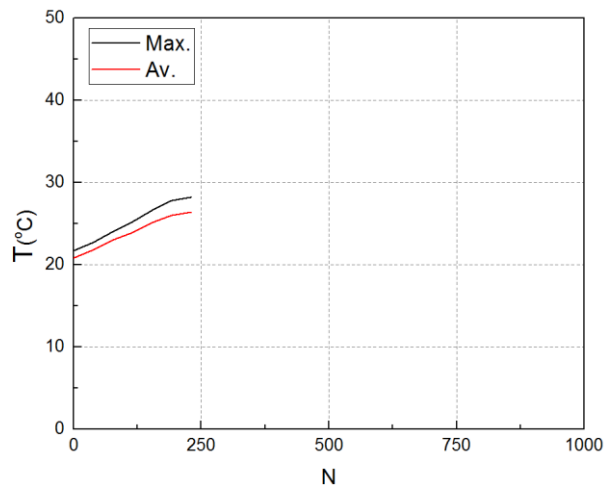


Fig. 1. Creep curves during the interruptions.

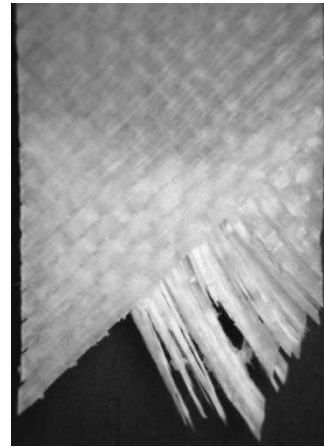


Fig. 2. Fatigue fracture surface.

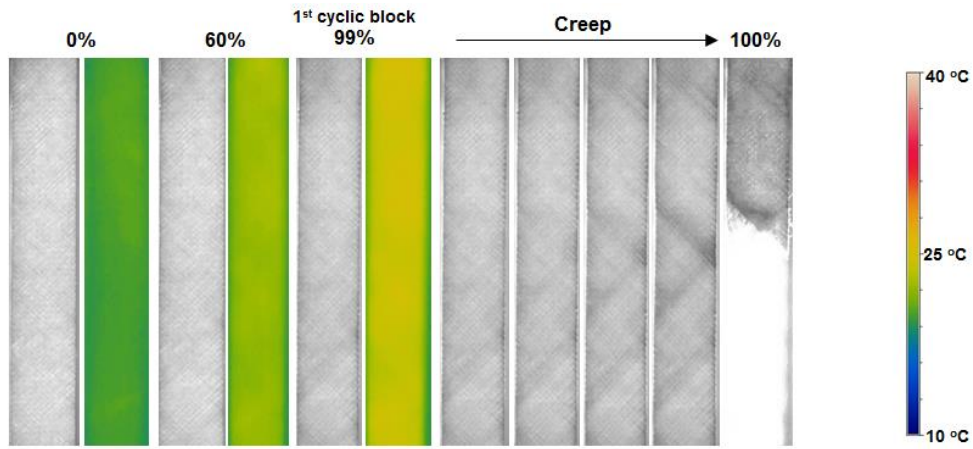


Fig. 3. Pairwise representation of light transmittance and self-generated temperature for different percentages of fatigue life.

No.	Code	f (Hz)	N_f
7	Cref-0.1-68-2-a	4.35	6126

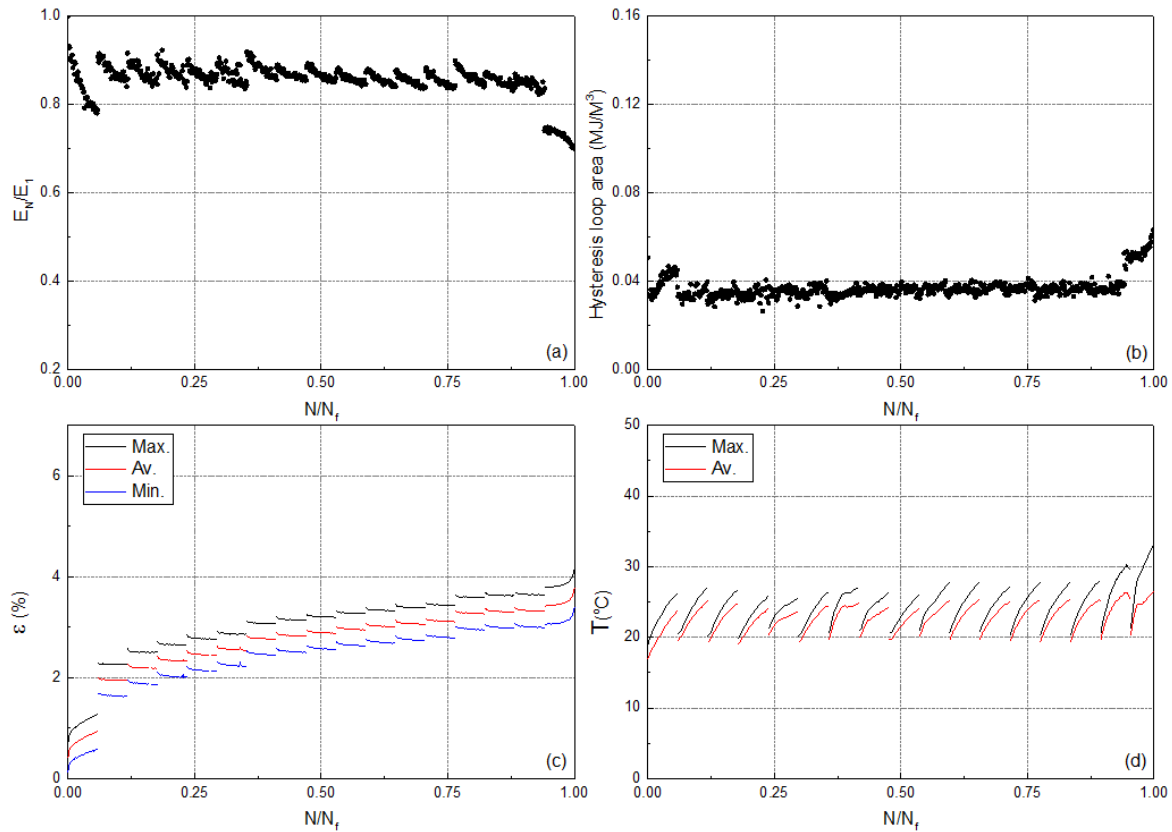


Fig. 1. Variation of (a) normalized fatigue stiffness, (b) hysteresis area, (c) maximum, average, and minimum cyclic strain, and (d) maximum and average self-generated temperature versus normalized number of cycles.

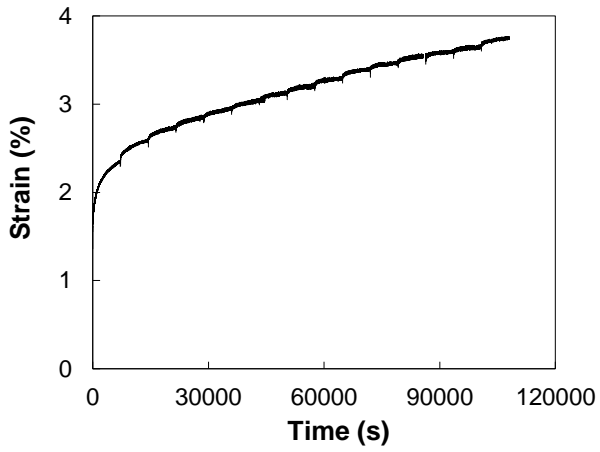


Fig. 2. Creep curves during the interruption.

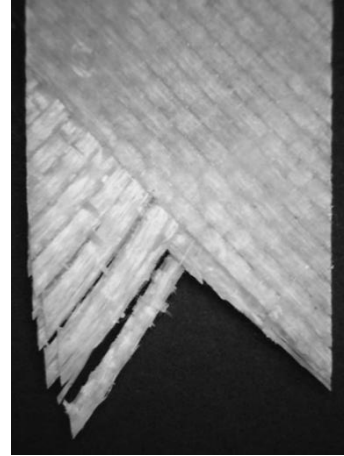


Fig. 3. Fatigue fracture surface.

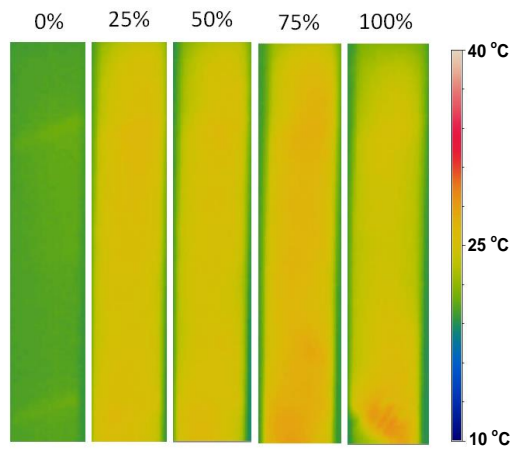


Fig. 4. Representation of the self-generated temperature in different percentages of fatigue life.

No.	Code	f (Hz)	N_f
8	Cref -0.1-68-2-b	4.35	2655

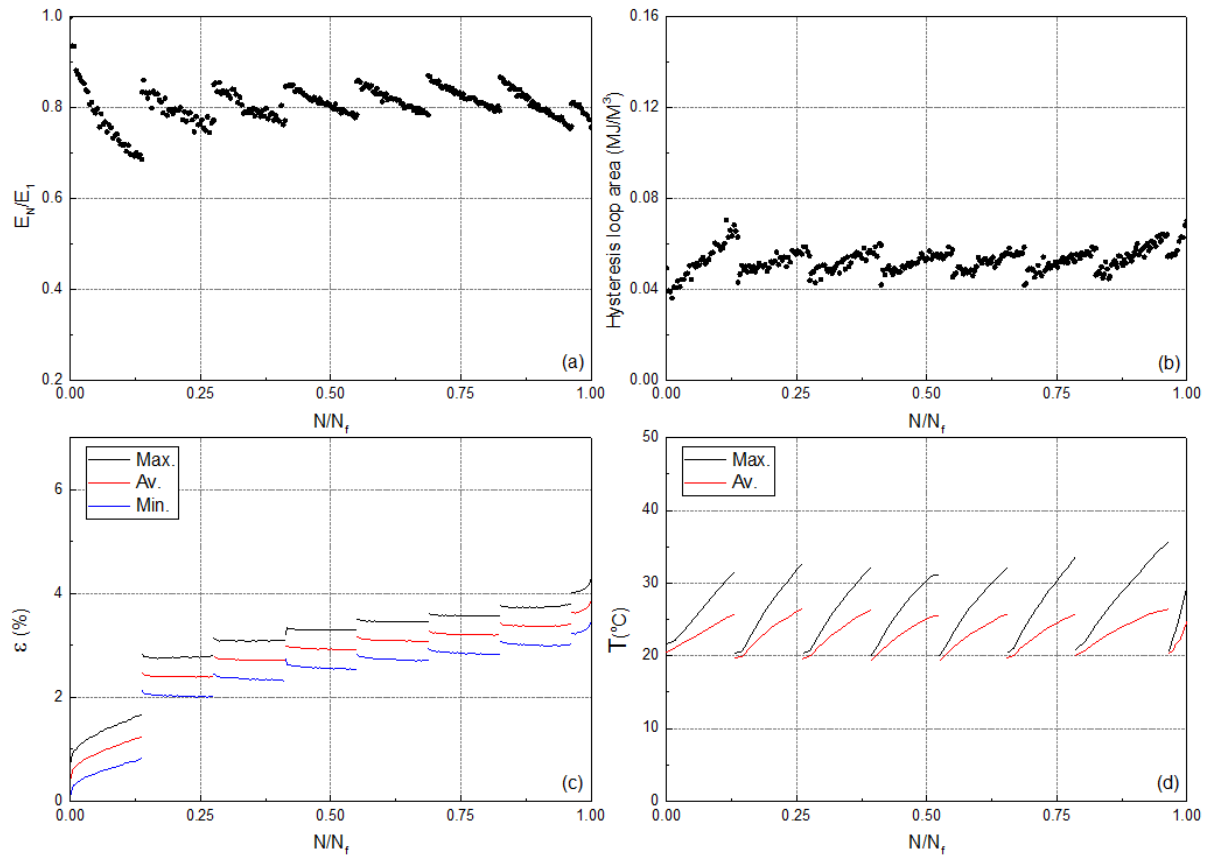


Fig. 1. Variation of (a) normalized fatigue stiffness, (b) hysteresis area, (c) maximum, average, and minimum cyclic strain, and (d) maximum and average self-generated temperature versus normalized number of cycles.

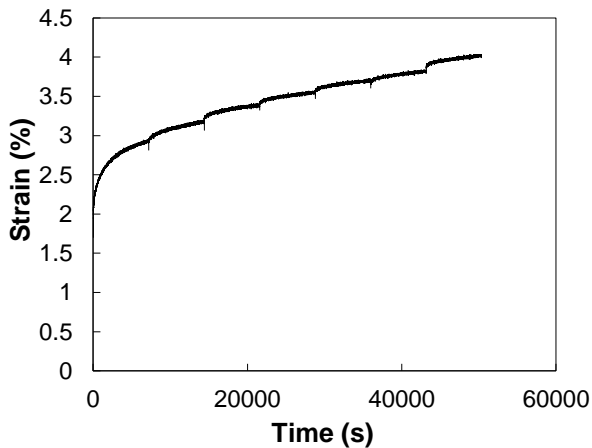


Fig. 2. Creep curves during the interruption.

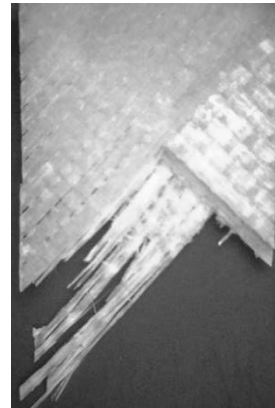


Fig. 3. Fatigue fracture surface.

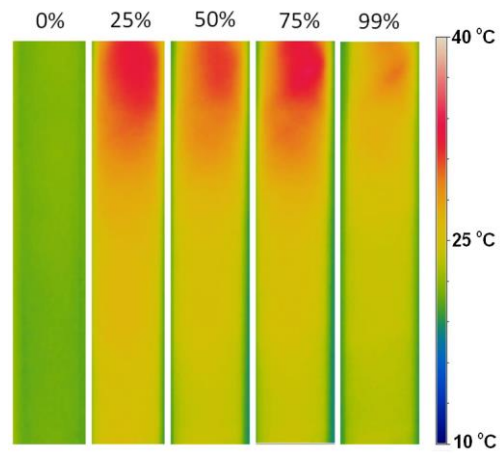


Fig. 4. Representation of the self-generated temperature in different percentages of fatigue life.

No.	Code	f (Hz)	N_f
9	Cref -0.1-68-2-c	4.35	2732

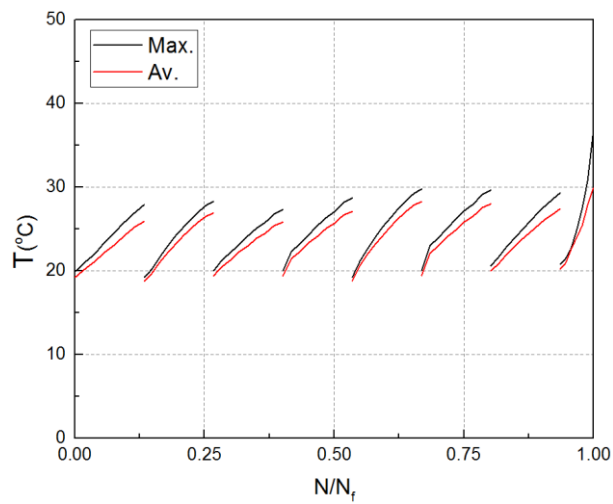


Fig. 1. Variation of maximum and average self-generated temperature.

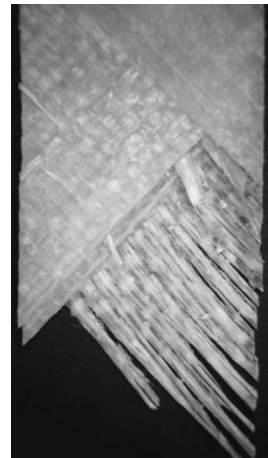


Fig. 2. Fatigue fracture surface.

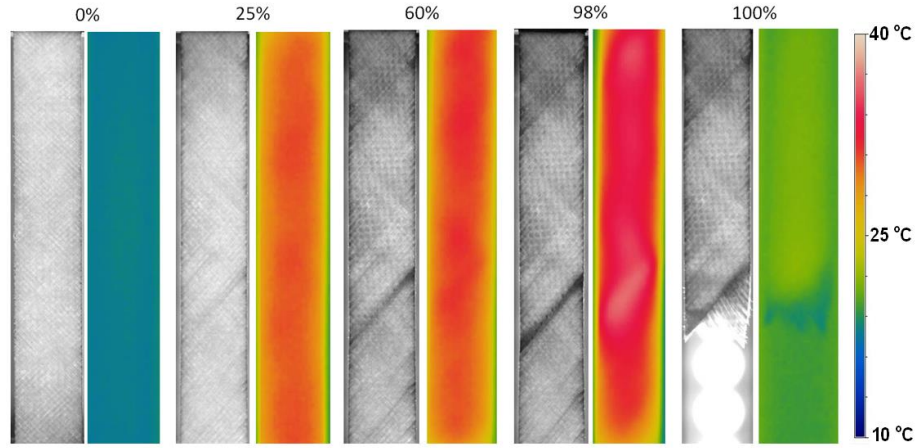


Fig. 3. Pairwise representation of light transmittance and self-generated temperature for different percentages of fatigue life.

No.	Code	f (Hz)	N_f
10	Cref-0.1-68-2-d	4.35	1460

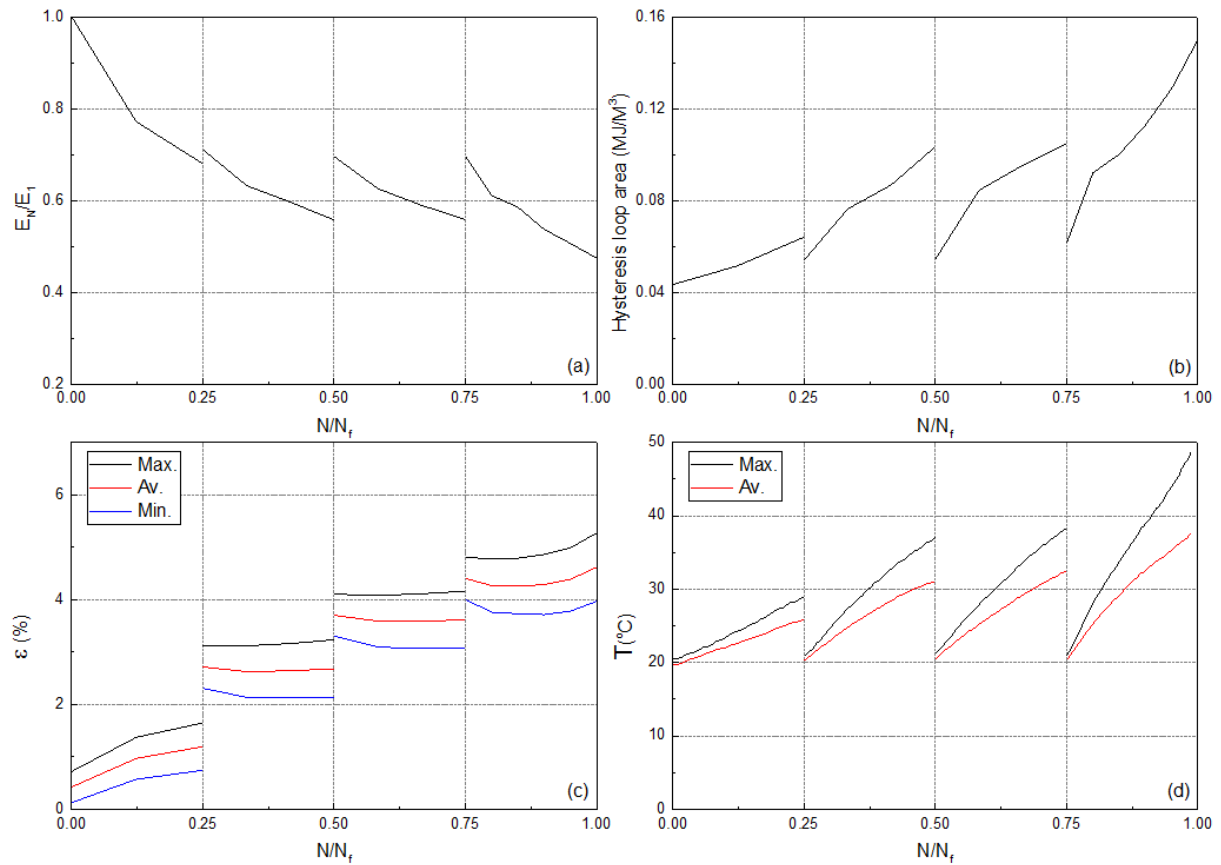


Fig. 1. Variation of (a) normalized fatigue stiffness, (b) hysteresis area, (c) maximum, average, and minimum cyclic strain, and (d) maximum and average self-generated temperature versus normalized number of cycles.

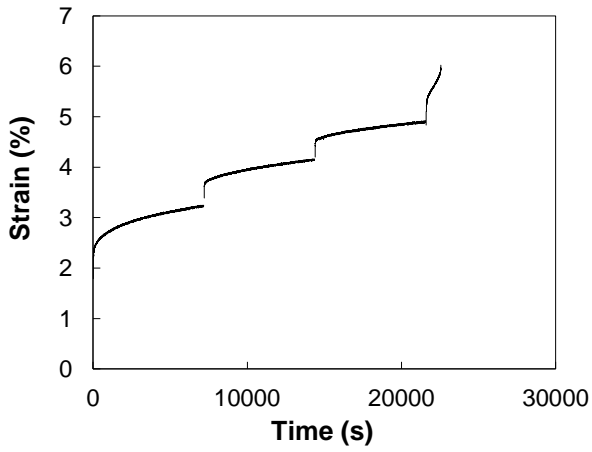


Fig. 2. Creep curves during the interruption.

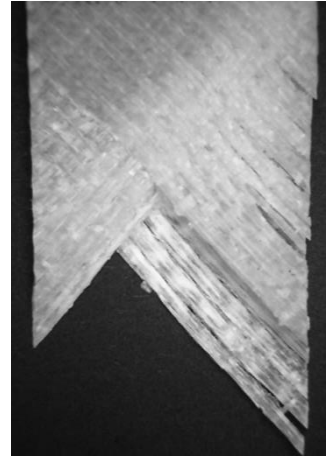


Fig. 3. Fatigue fracture surface.

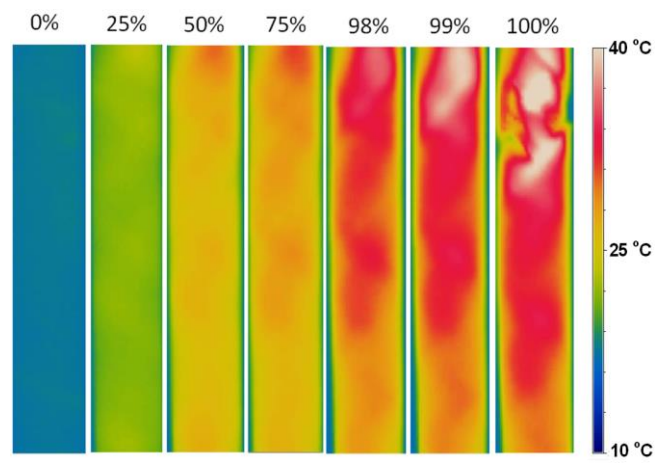


Fig. 4. Representation of the self-generated temperature in different percentages of fatigue life.

No.	Code	f (Hz)	N_f
11	Cref-0.1-68-48-a	4.35	1825

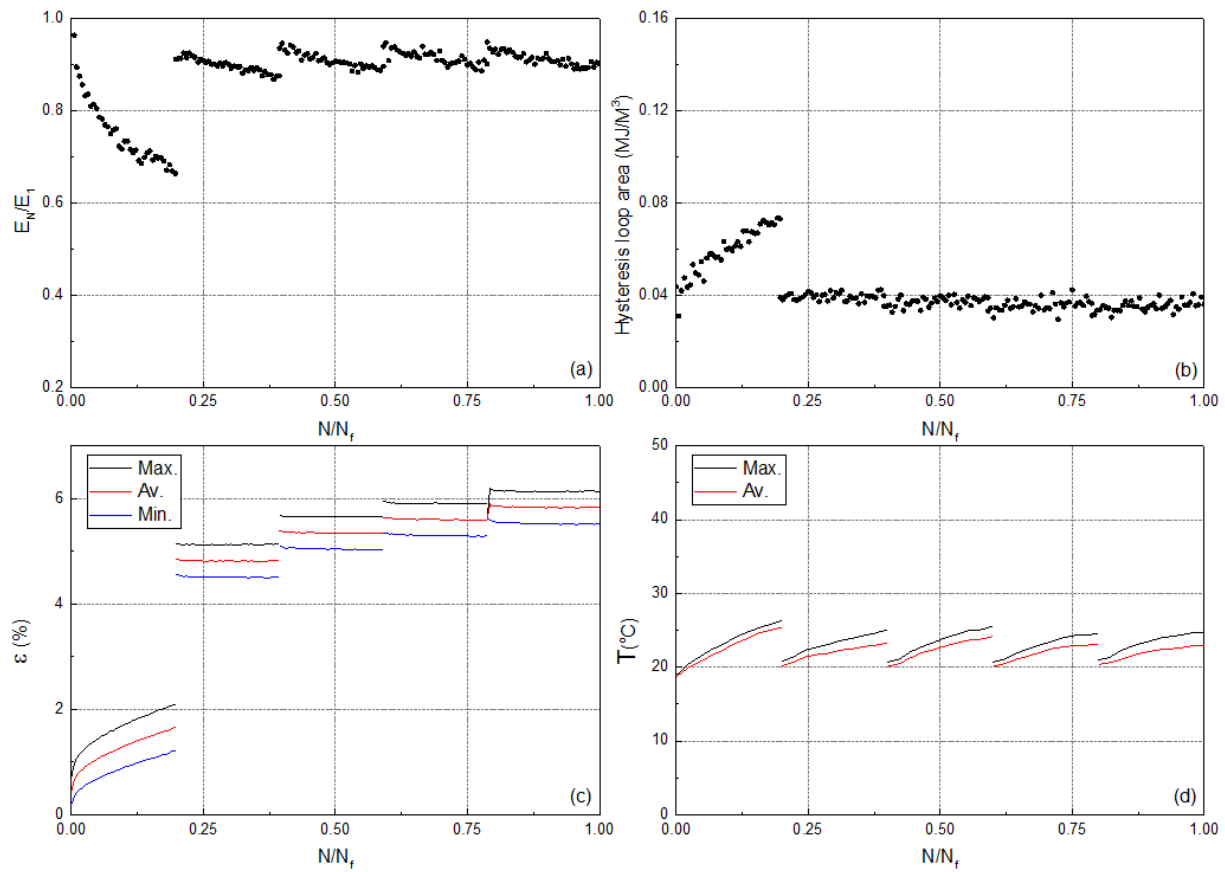


Fig. 1. Variation of (a) normalized fatigue stiffness, (b) hysteresis area, (c) maximum, average, and minimum cyclic strain, and (d) maximum and average self-generated temperature versus normalized number of cycles.

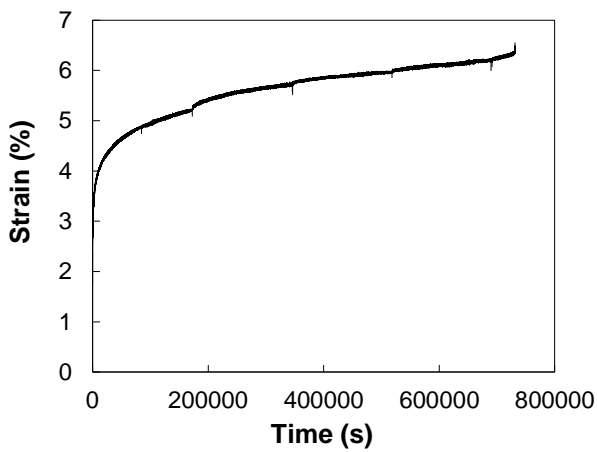


Fig. 2. Creep curves during the interruption.

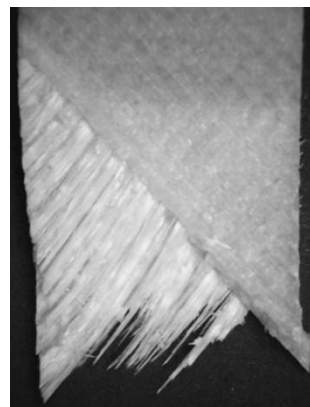


Fig. 3. Fatigue fracture surface.

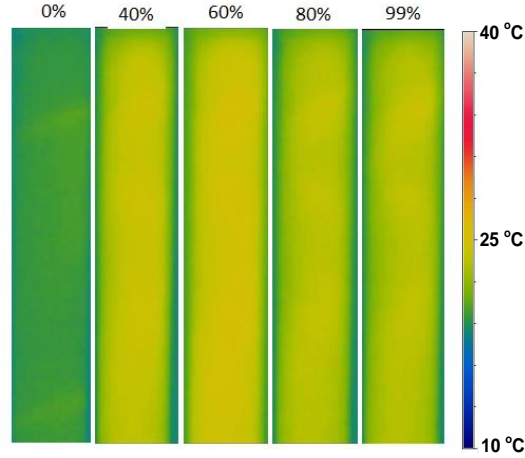


Fig. 4. Representation of the self-generated temperature in different percentages of fatigue life.

No.	Code	f (Hz)	N_f
12	Cref-0.1-68-48-b	4.35	730

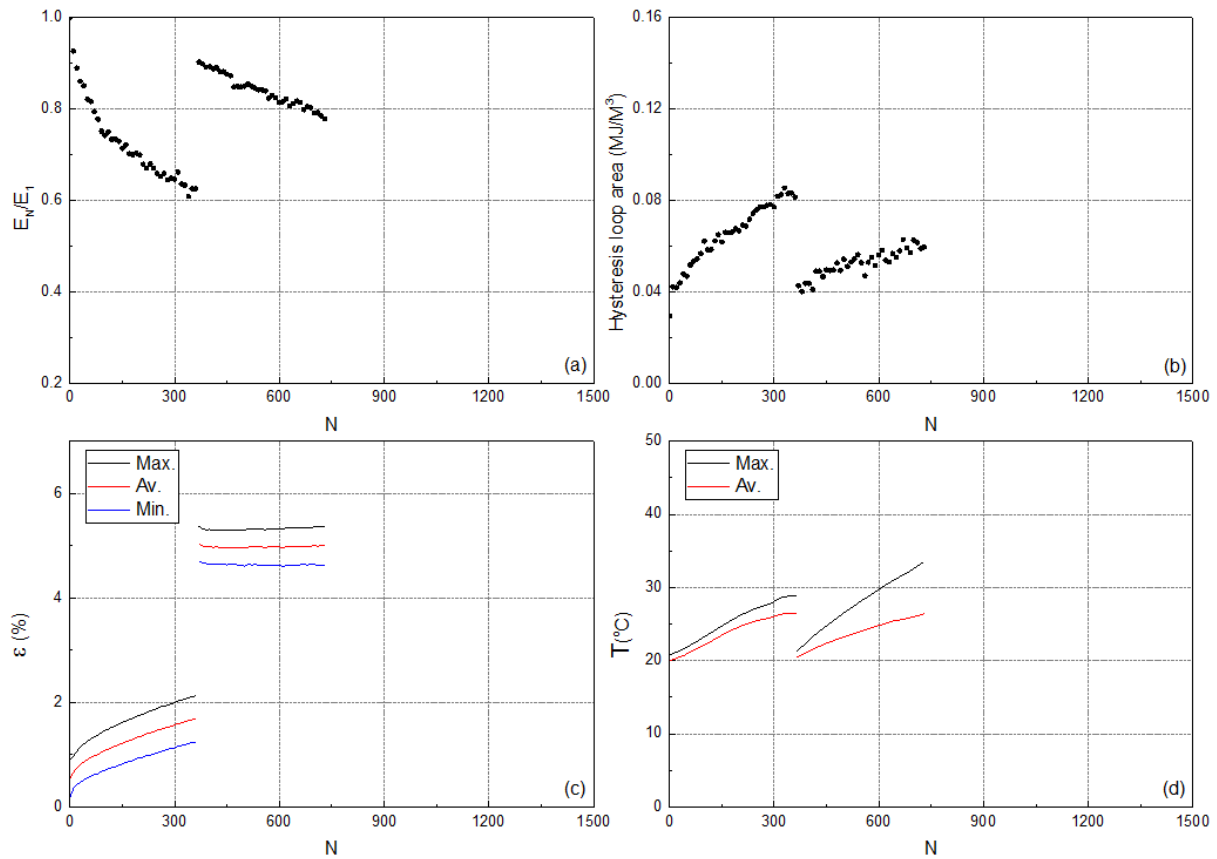


Fig. 1. Variation of (a) normalized fatigue stiffness, (b) hysteresis area, (c) maximum, average, and minimum cyclic strain, and (d) maximum and average self-generated temperature versus normalized number of cycles.

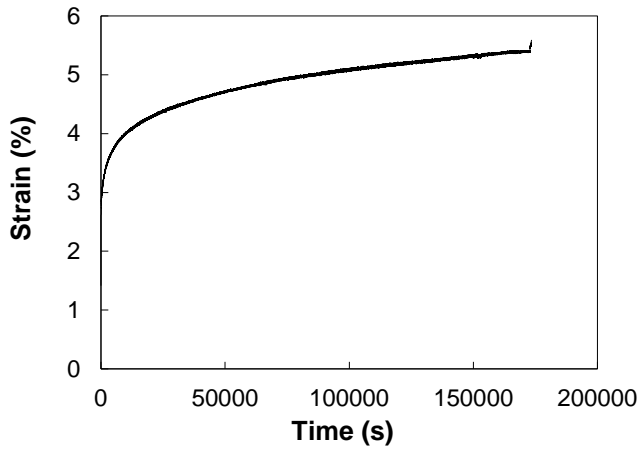


Fig. 2. Creep curves during the interruption.

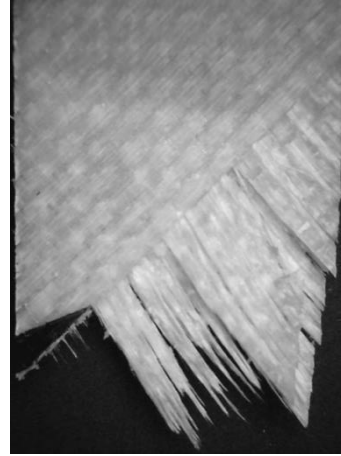


Fig. 3. Fatigue fracture surface.

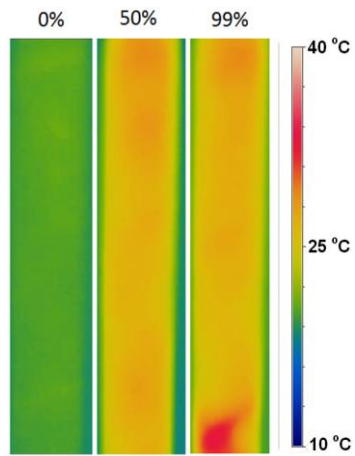


Fig. 4. Representation of the self-generated temperature in different percentages of fatigue life.

No.	Code	f (Hz)	N_f
13	Cref-0.1-64-2-a	4.68	2500

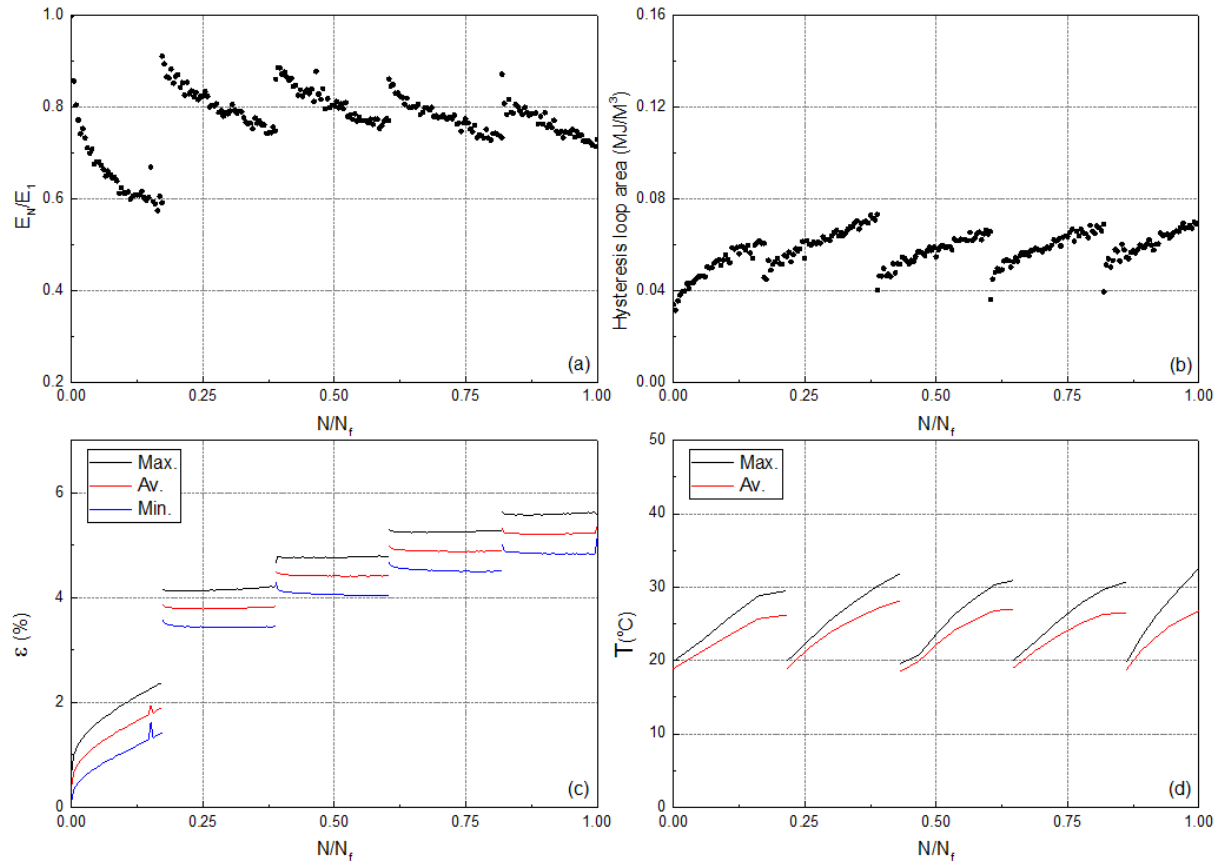


Fig. 1. Variation of (a) normalized fatigue stiffness, (b) hysteresis area, (c) maximum, average, and minimum cyclic strain, and (d) maximum and average self-generated temperature versus normalized number of cycles.

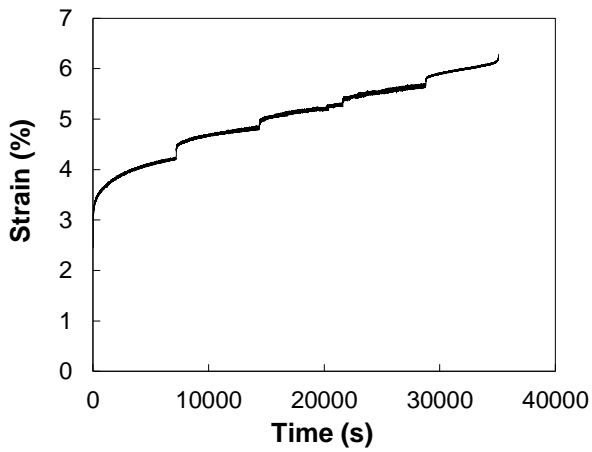


Fig. 2. Creep curves during the interruption.

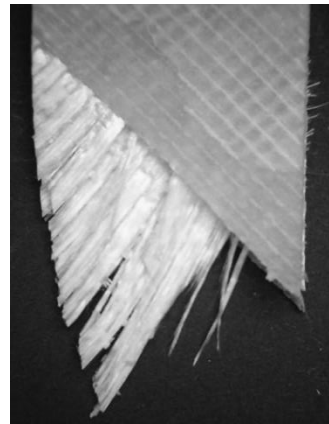


Fig. 3. Fatigue fracture surface.

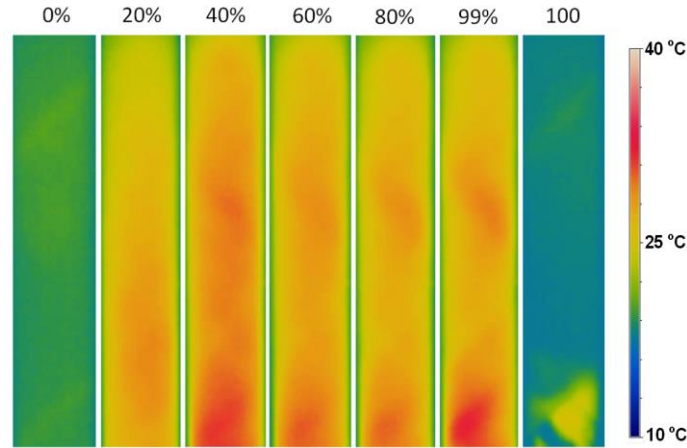


Fig. 4. Representation of the self-generated temperature in different percentages of fatigue life.

No.	Code	f (Hz)	N_f
14	Cref-0.1-64-2-b	4.68	3988

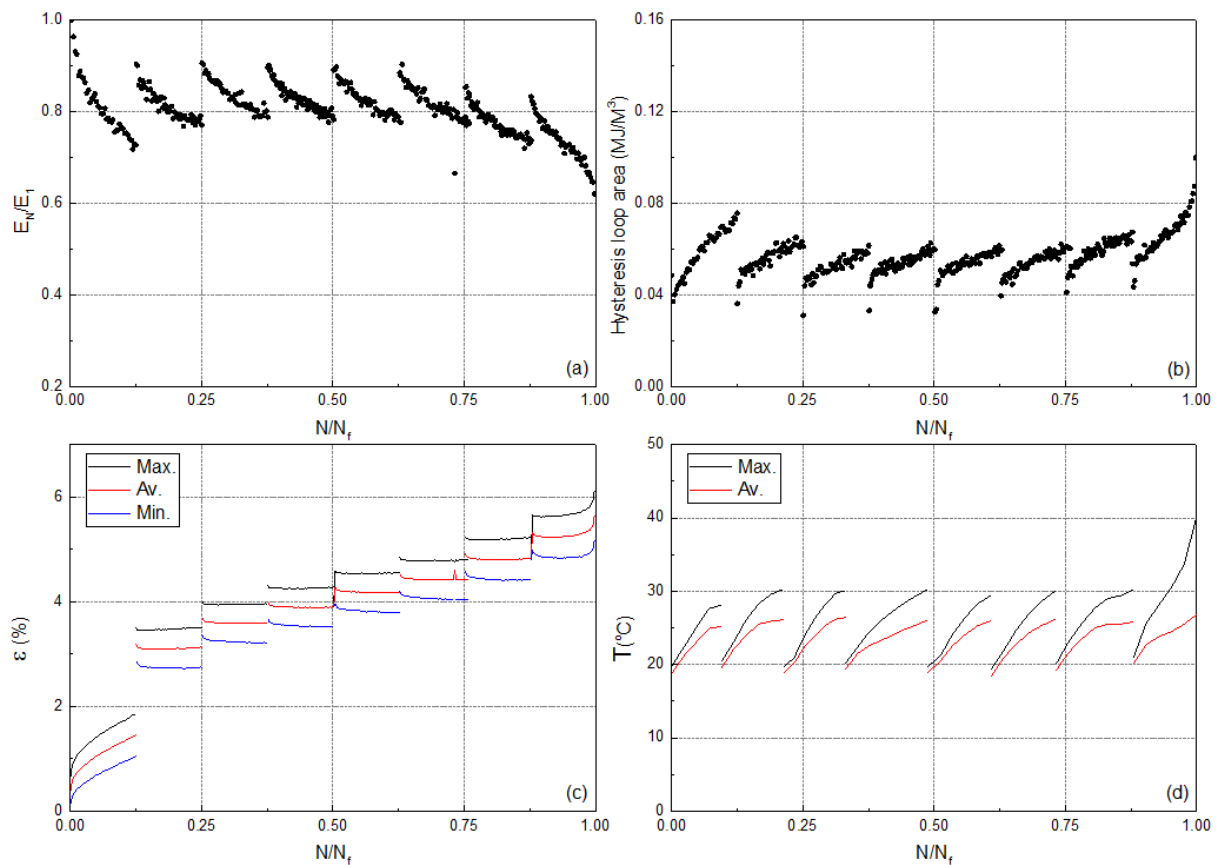


Fig. 1. Variation of (a) normalized fatigue stiffness, (b) hysteresis area, (c) maximum, average, and minimum cyclic strain, and (d) maximum and average self-generated temperature versus normalized number of cycles.

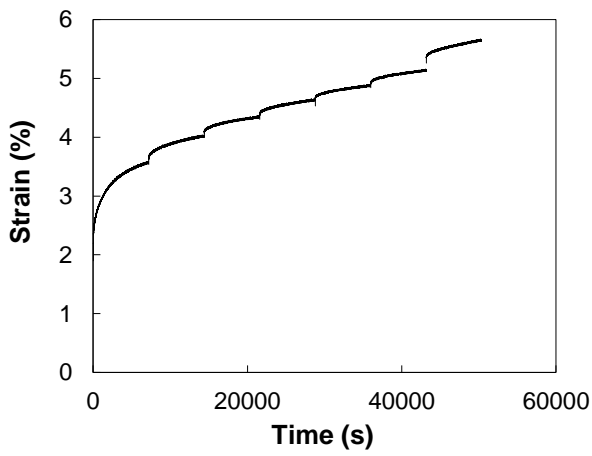


Fig. 2. Creep curves during the interruption.

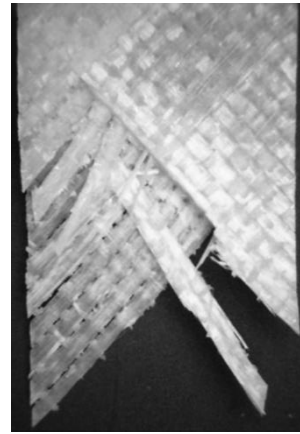


Fig. 3. Fatigue fracture surface.

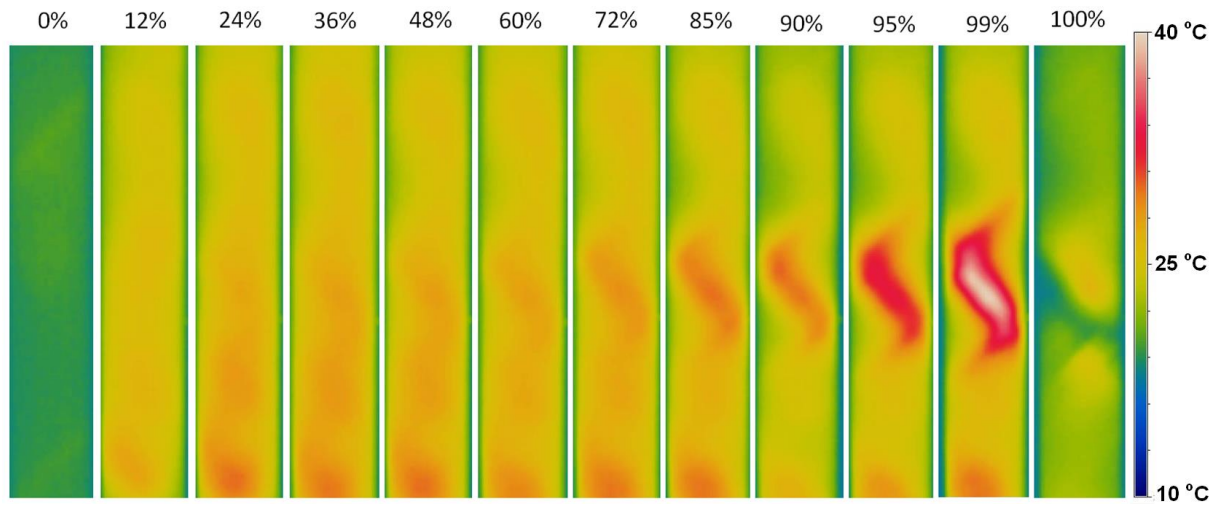


Fig. 4. Representation of the self-generated temperature in different percentages of fatigue life.

No.	Code	f (Hz)	N_f
15	Cref-0.1-64-2-c	4.68	5731

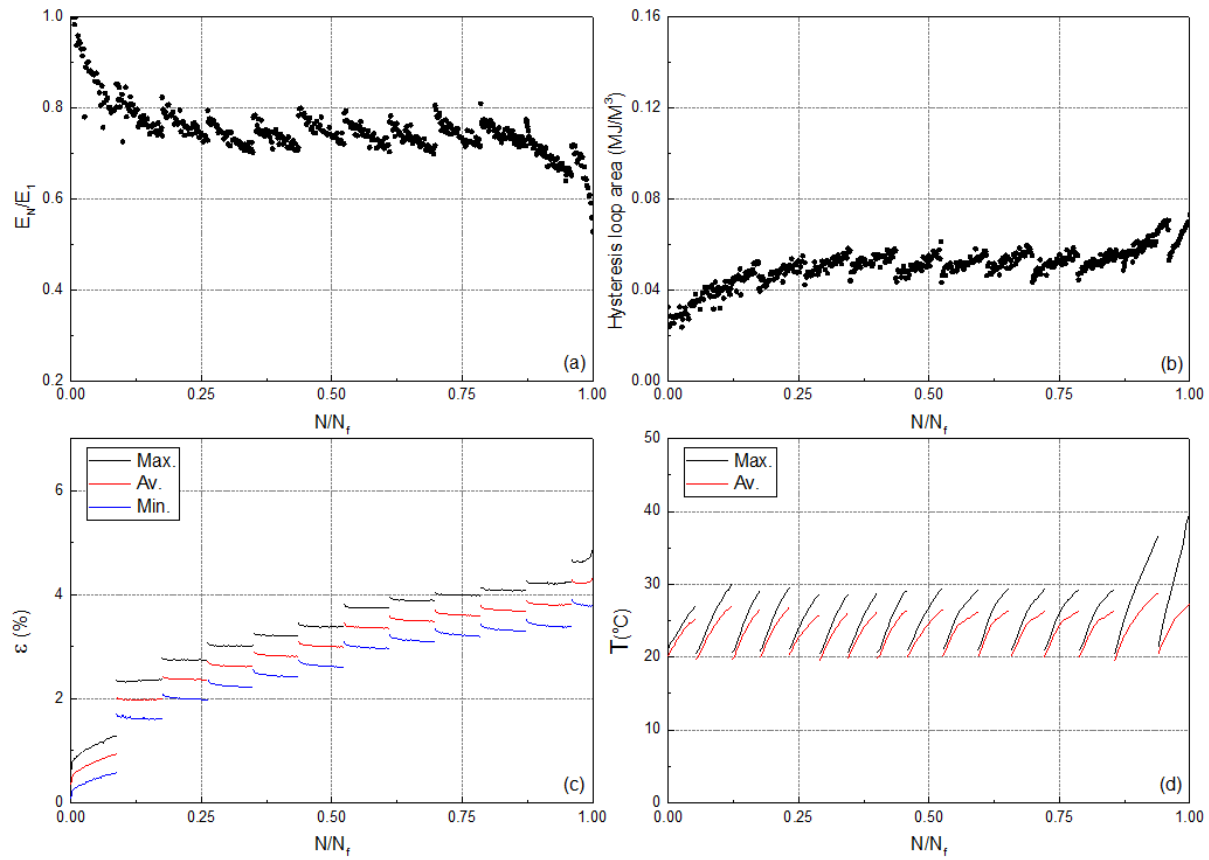


Fig. 1. Variation of (a) normalized fatigue stiffness, (b) hysteresis area, (c) maximum, average, and minimum cyclic strain, and (d) maximum and average self-generated temperature versus normalized number of cycles.

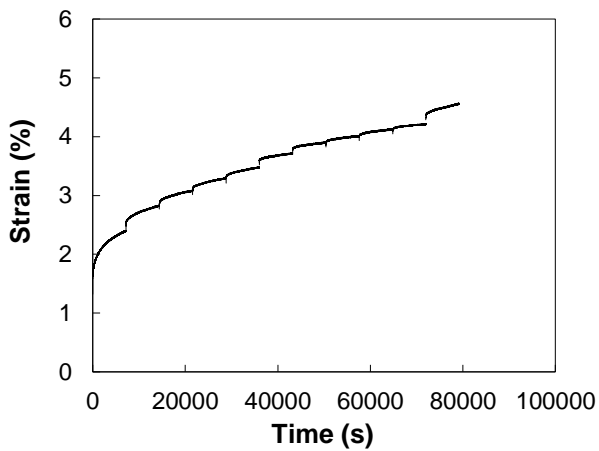


Fig. 2. Creep curves during the interruption.

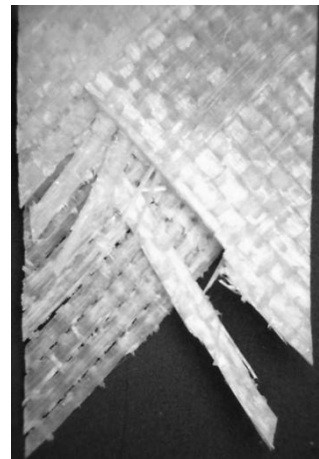


Fig. 3. Fatigue fracture surface.

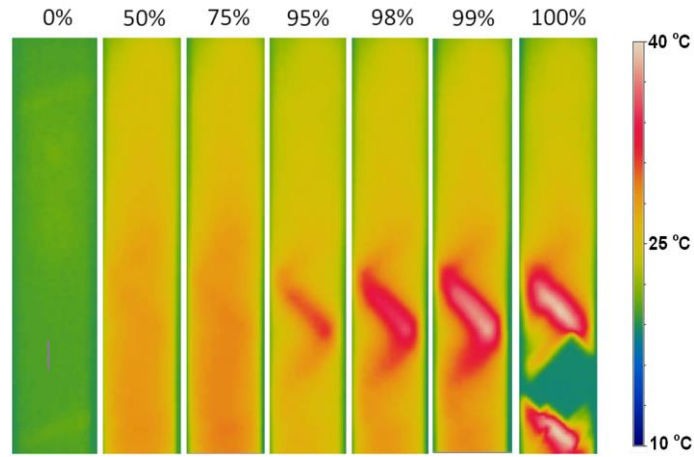


Fig. 4. Representation of the self-generated temperature in different percentages of fatigue life.

No.	Code	f (Hz)	N_f
16	Cref-0.1-64-2-d	4.68	4000

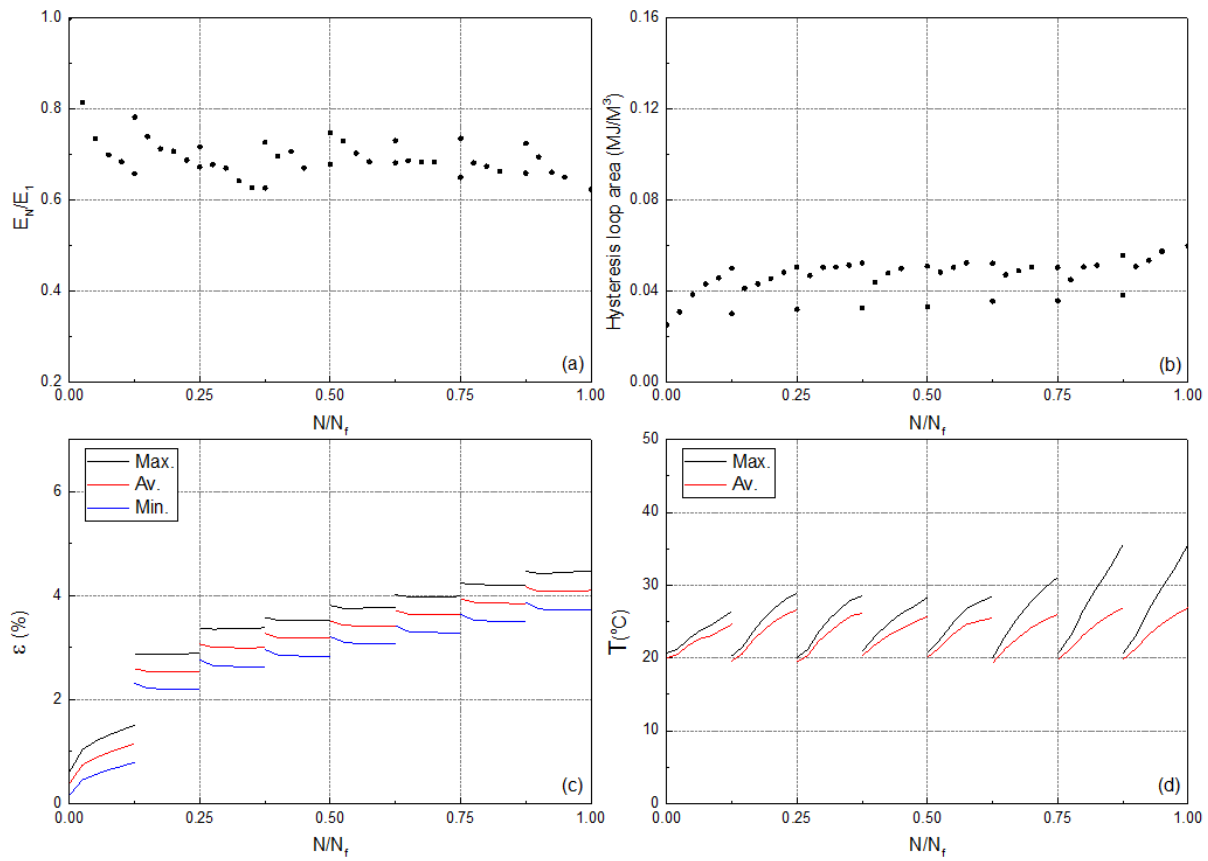


Fig. 1. Variation of (a) normalized fatigue stiffness, (b) hysteresis area, (c) maximum, average, and minimum cyclic strain, and (d) maximum and average self-generated temperature versus normalized number of cycles.

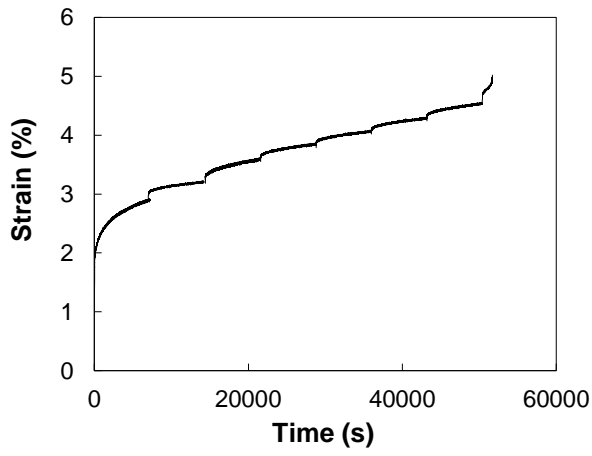


Fig. 2. Creep curves during the interruption.

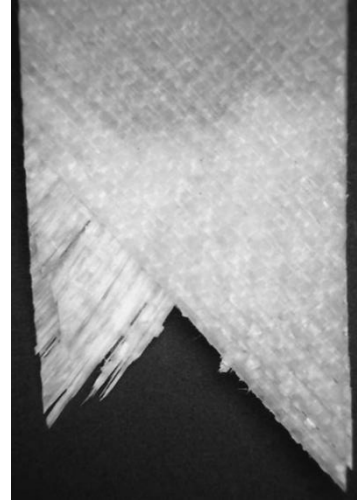


Fig. 3. Fatigue fracture surface.

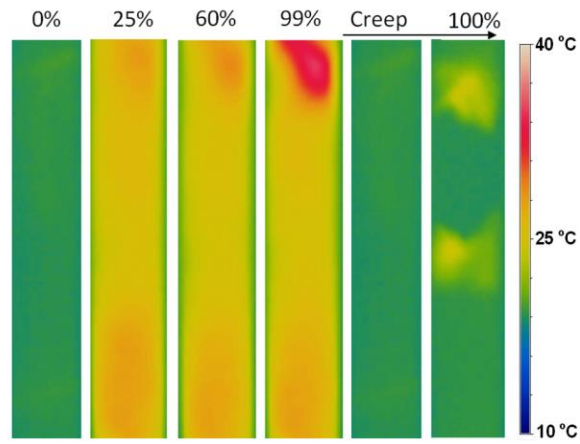


Fig. 4. Representation of the self-generated temperature in different percentages of fatigue life.

No.	Code	f (Hz)	N_f
17	Cref-0.1-64-48-a	4.68	2000

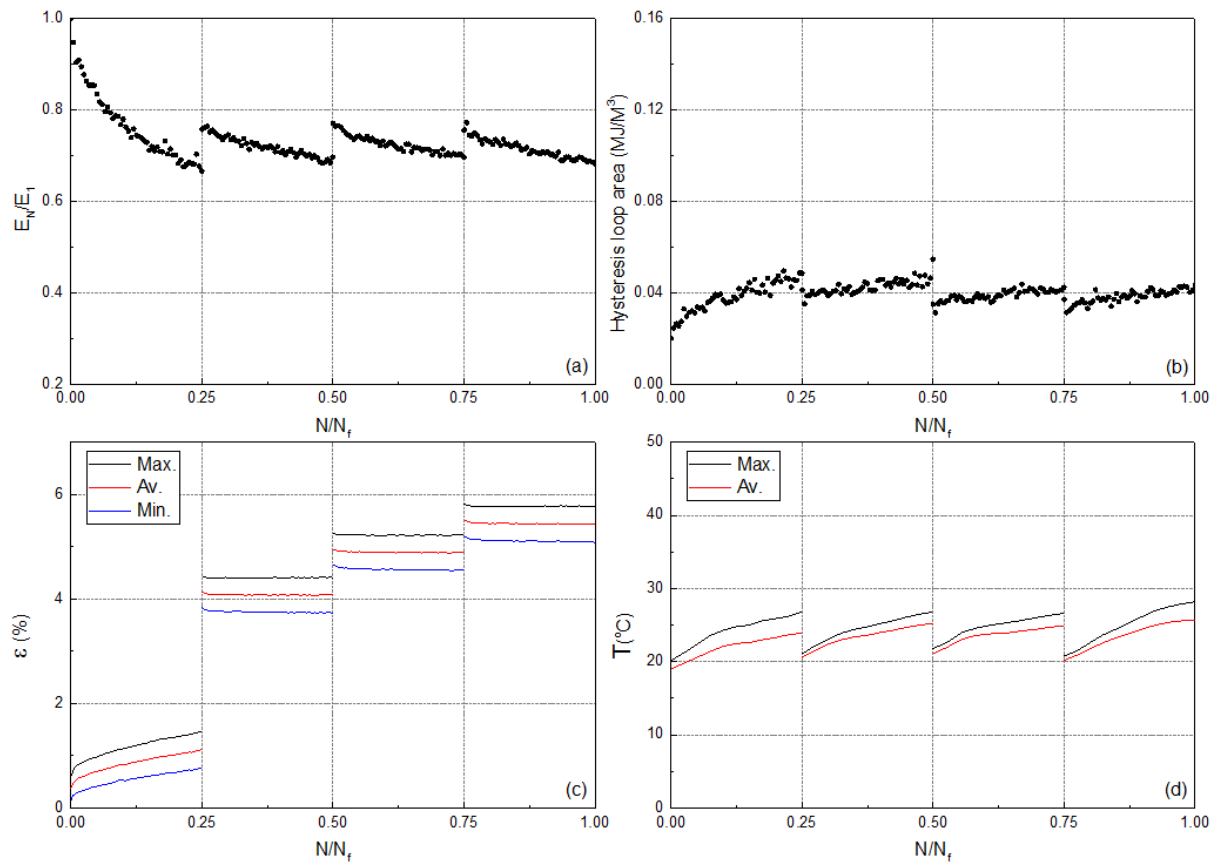


Fig. 1. Variation of (a) normalized fatigue stiffness, (b) hysteresis area, (c) maximum, average, and minimum cyclic strain, and (d) maximum and average self-generated temperature versus normalized number of cycles.

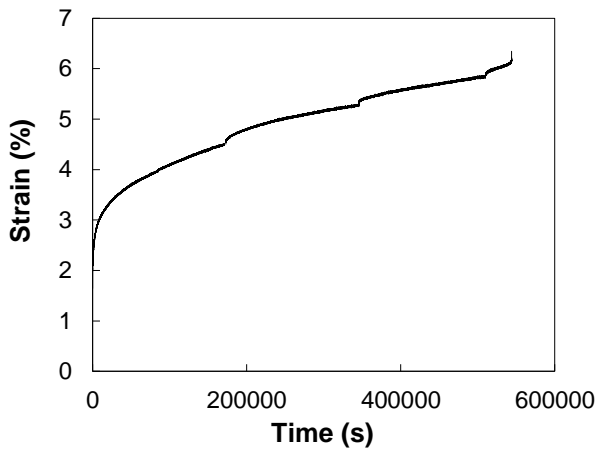


Fig. 2. Creep curves during the interruption.

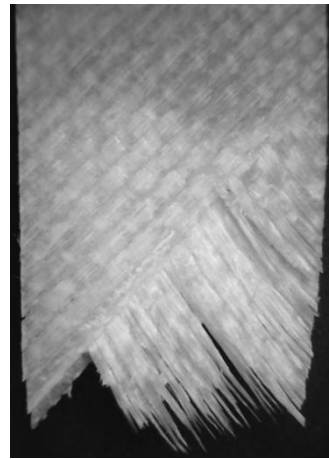


Fig. 3. Fatigue fracture surface.

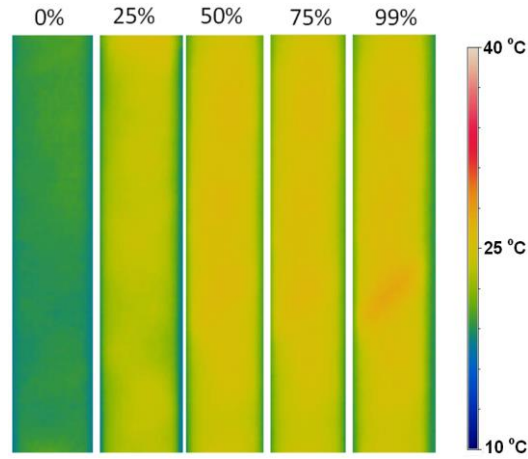


Fig. 4. Representation of the self-generated temperature in different percentages of fatigue life.

No.	Code	f (Hz)	N_f
18	Cref-0.1-64-48-b	4.68	1000

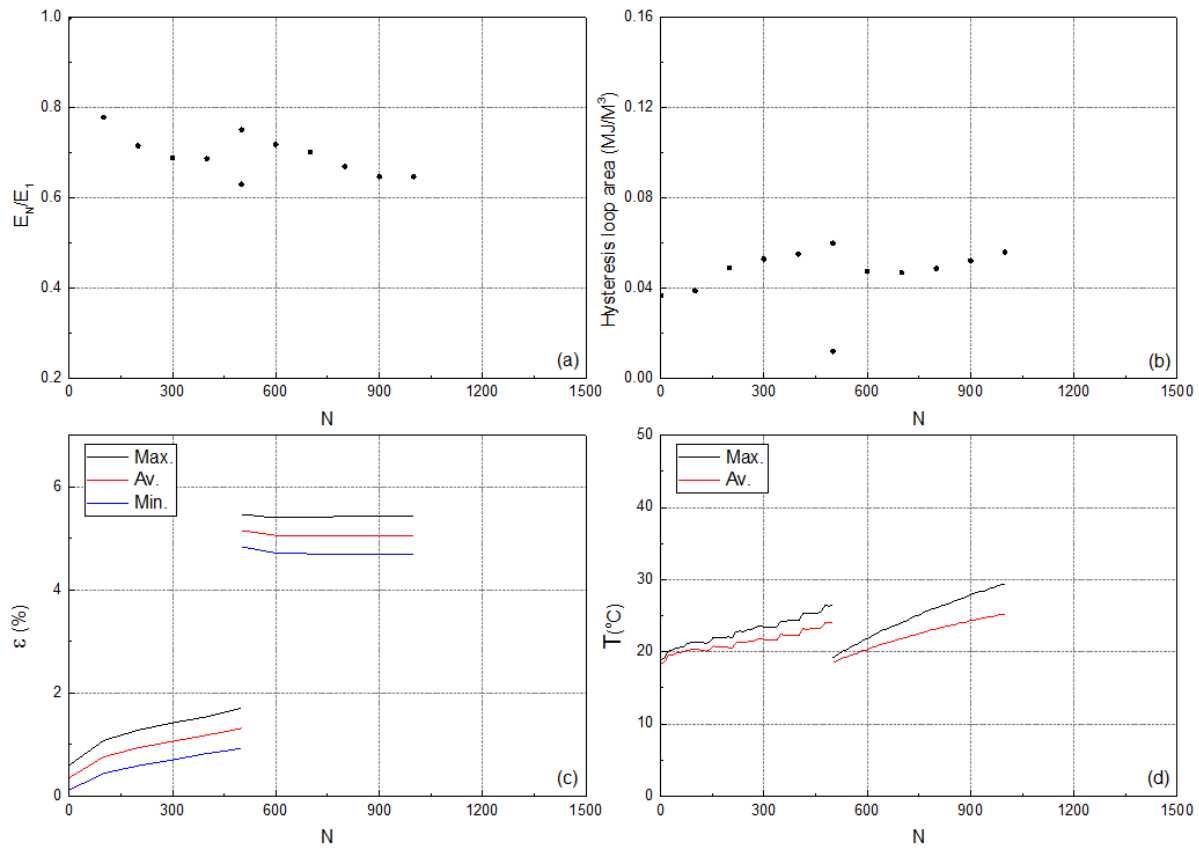


Fig. 1. Variation of (a) normalized fatigue stiffness, (b) hysteresis area, (c) maximum, average, and minimum cyclic strain, and (d) maximum and average self-generated temperature versus normalized number of cycles.

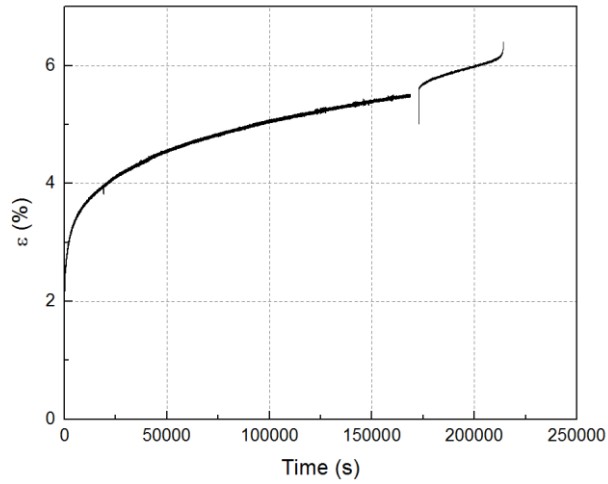


Fig. 2. Creep curves during the interruption.

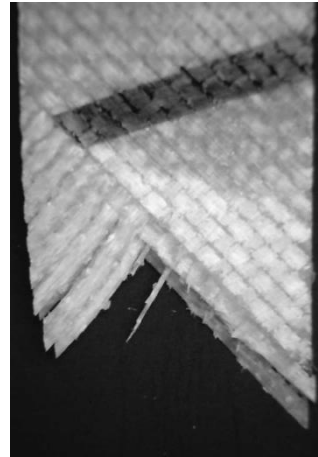


Fig. 3. Fatigue fracture surface.

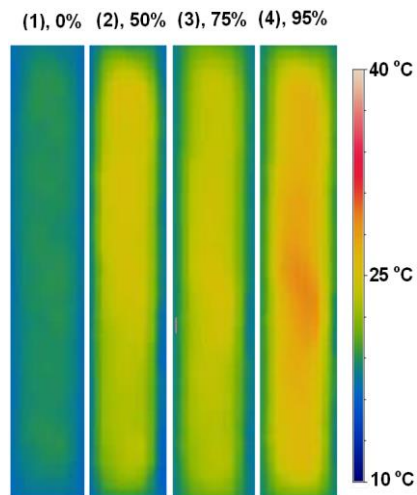


Fig. 4. Representation of the self-generated temperature in different percentages of fatigue life.

No.	Code	f (Hz)	N_f
19	Cref-0.1-58-2-a	5.06	14527

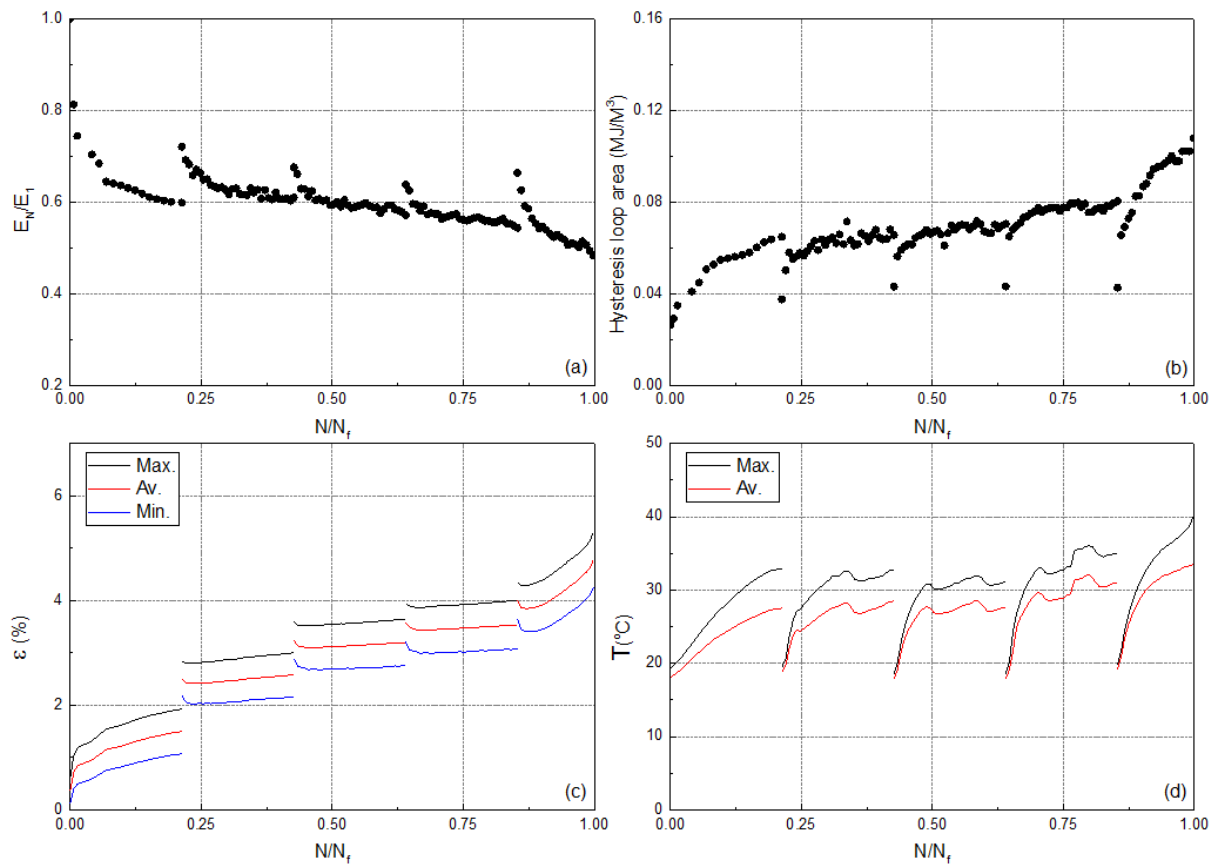


Fig. 1. Variation of (a) normalized fatigue stiffness, (b) hysteresis area, (c) maximum, average, and minimum cyclic strain, and (d) maximum and average self-generated temperature versus normalized number of cycles.

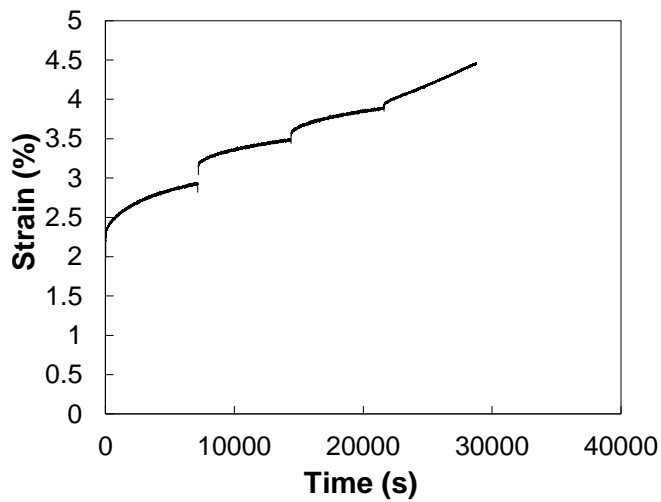


Fig. 2. Creep curves during the interruption.

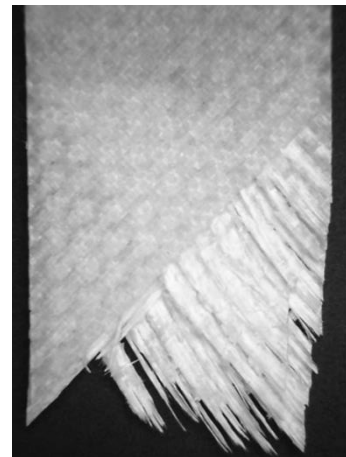


Fig. 3. Fatigue fracture surface.

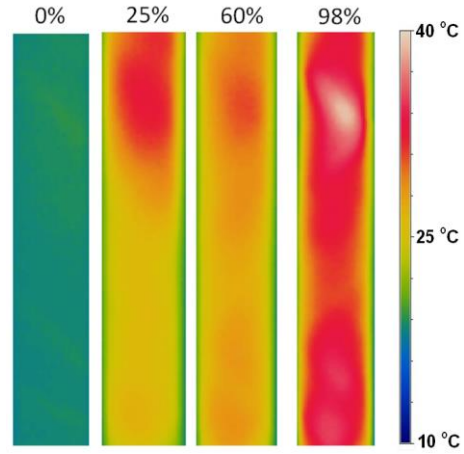


Fig. 4. Representation of the self-generated temperature in different percentages of fatigue life.

No.	Code	f (Hz)	N_f
20	Cref -0.1-58-2-b	5.06	52337

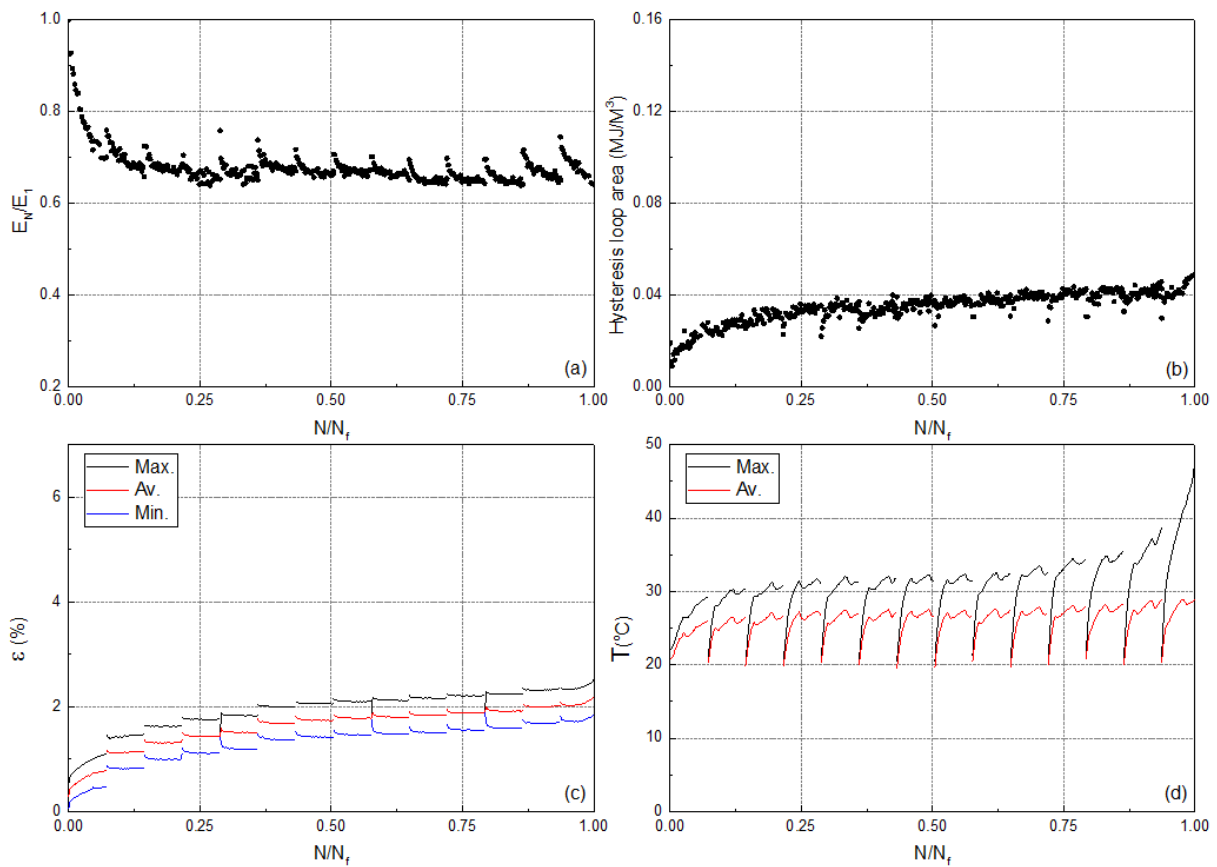


Fig. 1. Variation of (a) normalized fatigue stiffness, (b) hysteresis area, (c) maximum, average, and minimum cyclic strain, and (d) maximum and average self-generated temperature versus normalized number of cycles.

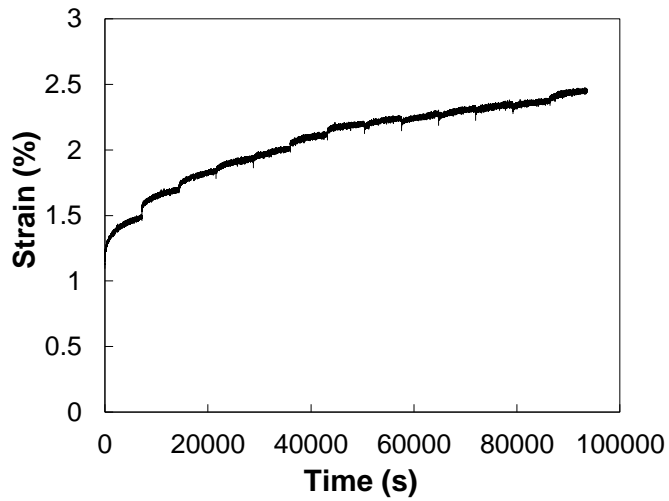


Fig. 2. Creep curves during the interruption.

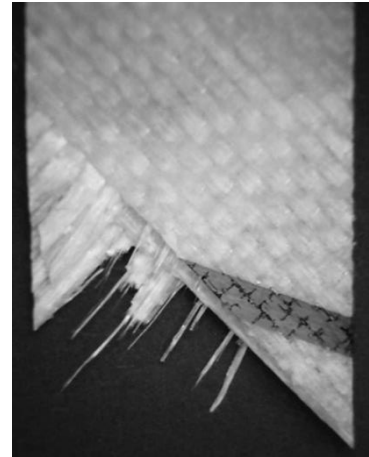


Fig. 3. Fatigue fracture surface.

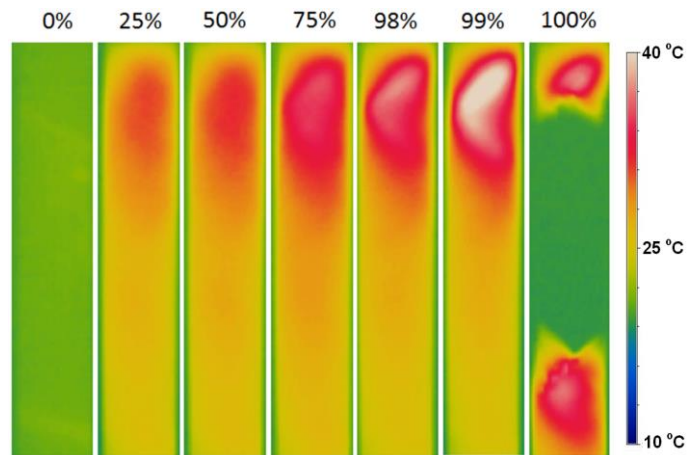


Fig. 4. Representation of the self-generated temperature in different percentages of fatigue life.

No.	Code	f (Hz)	N_f
21	Cref-0.1-58-2-c	5.06	25466

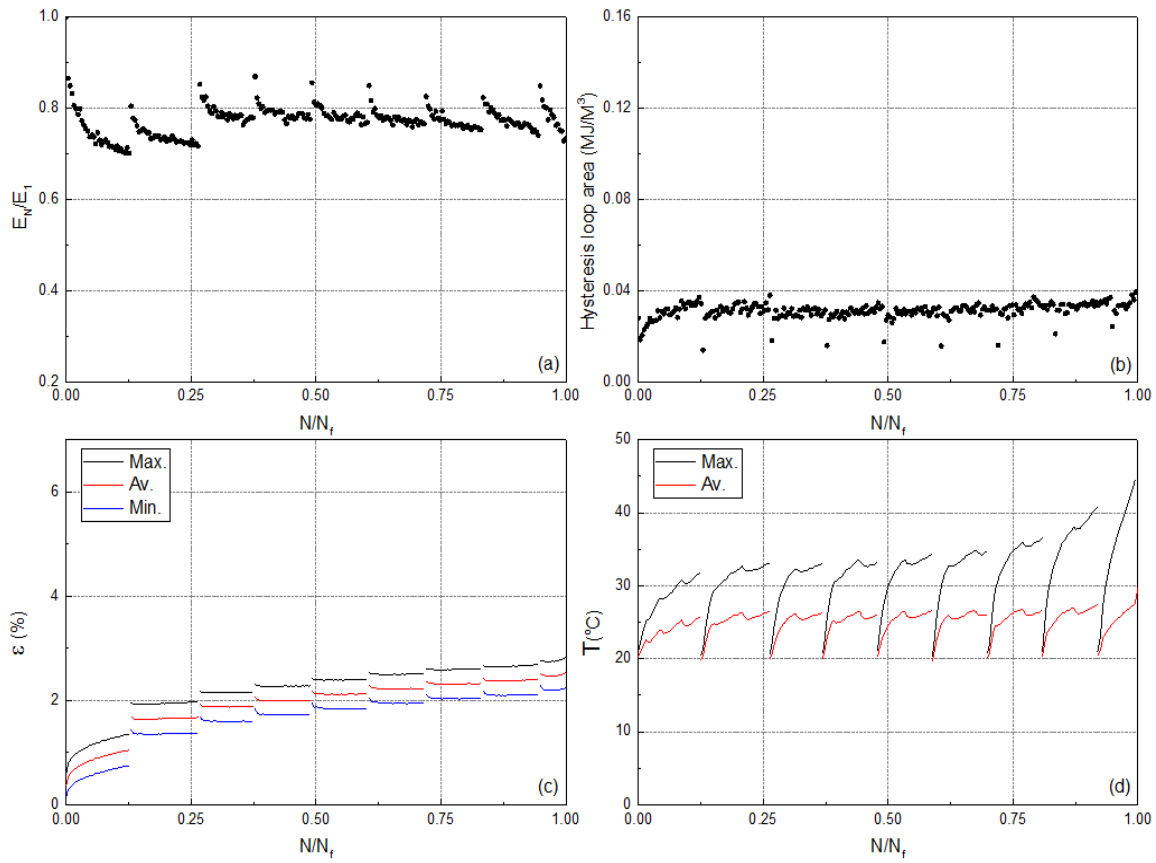


Fig. 1. Variation of (a) normalized fatigue stiffness, (b) hysteresis area, (c) maximum, average, and minimum cyclic strain, and (d) maximum and average self-generated temperature versus normalized number of cycles.

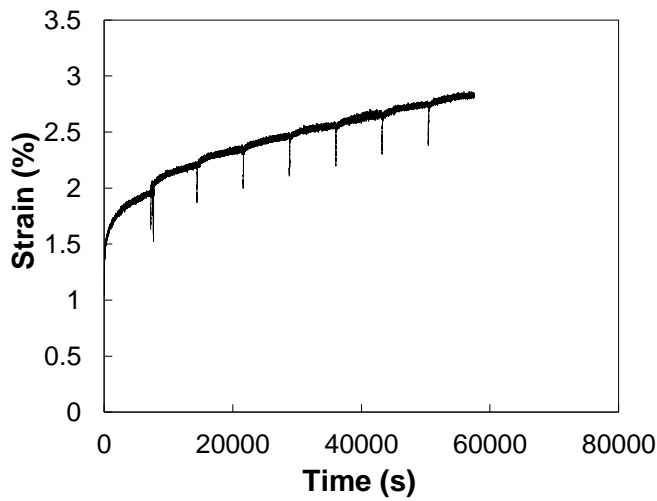


Fig. 2. Creep curves during the interruption.

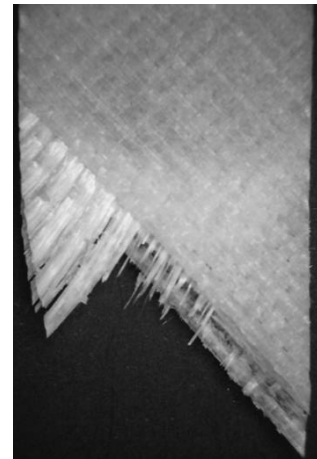


Fig. 3. Fatigue fracture surface.

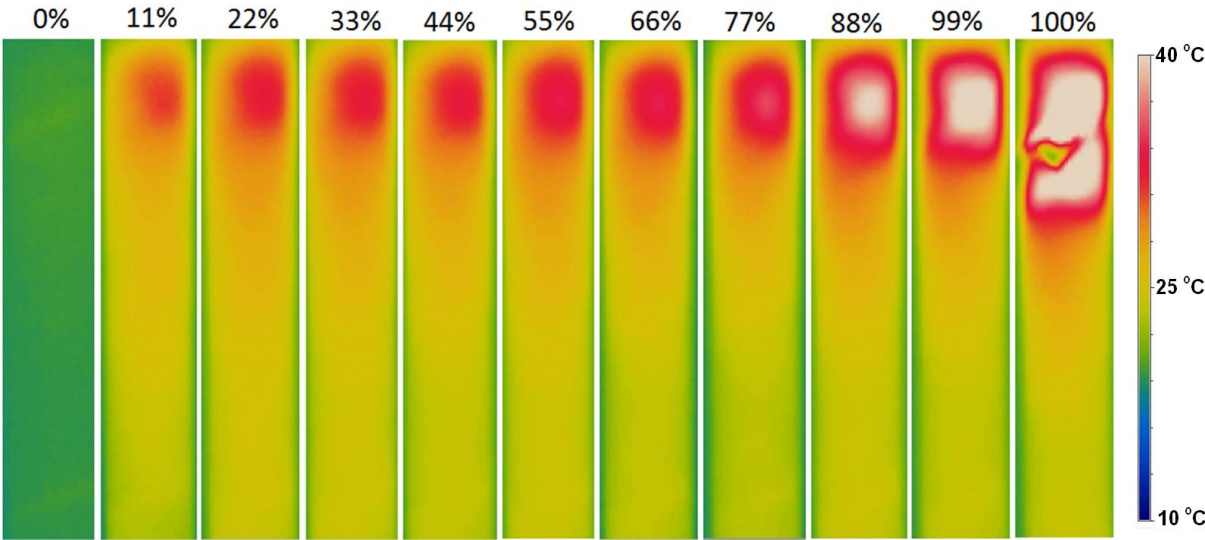


Fig. 4. Variation of maximum and average self-generated temperature.

No.	Code	f (Hz)	N_f
22	Cref -0.1-58-2-d	5.06	15559

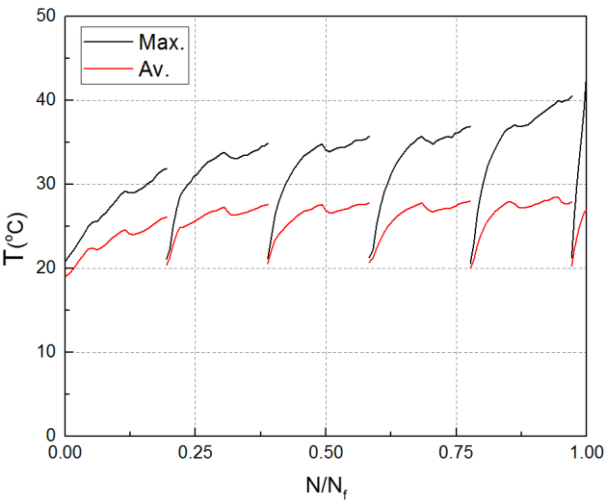


Fig. 1. Variation of maximum and average self-generated temperature.

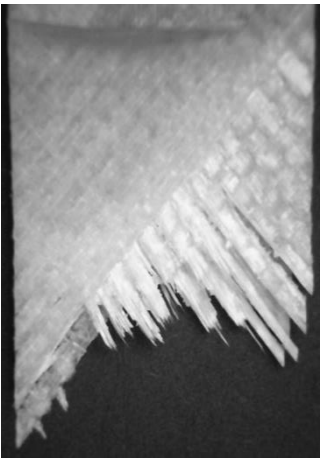


Fig. 2. Fatigue fracture surface.

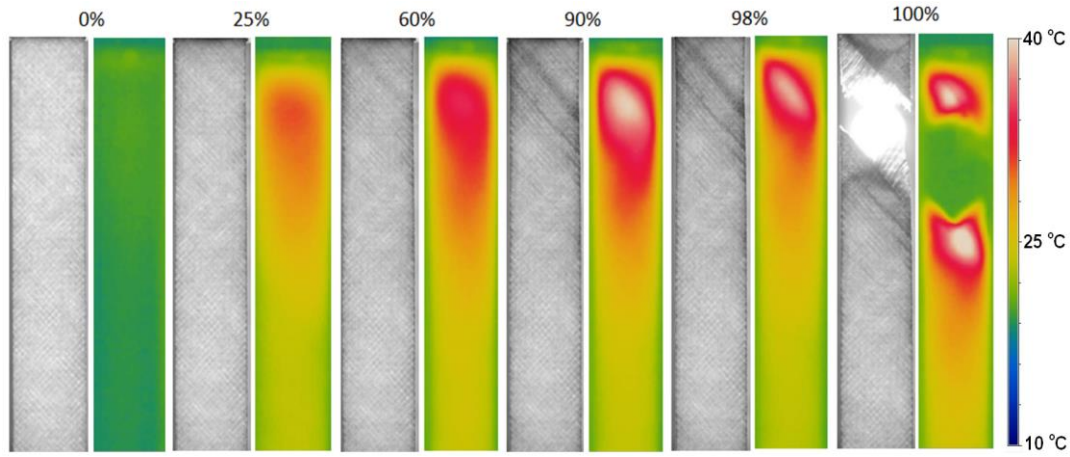


Fig. 3. Pairwise representation of light transmittance and the self-generated temperature in different percentages of fatigue life.

No.	Code	f (Hz)	N_f
23	Cref-0.1-58-48-a	5.06	10589

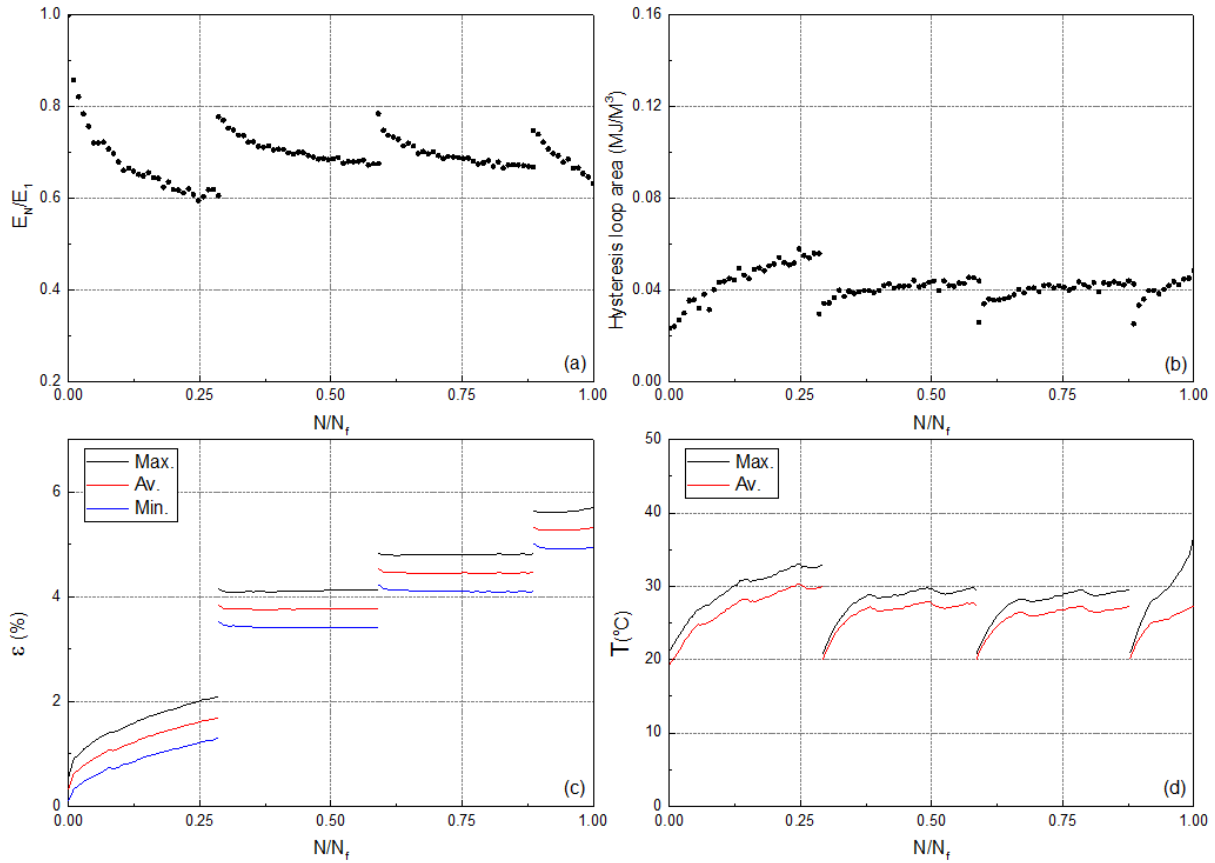


Fig. 1. Variation of (a) normalized fatigue stiffness, (b) hysteresis area, (c) maximum, average, and minimum cyclic strain, and (d) maximum and average self-generated temperature versus normalized number of cycles.

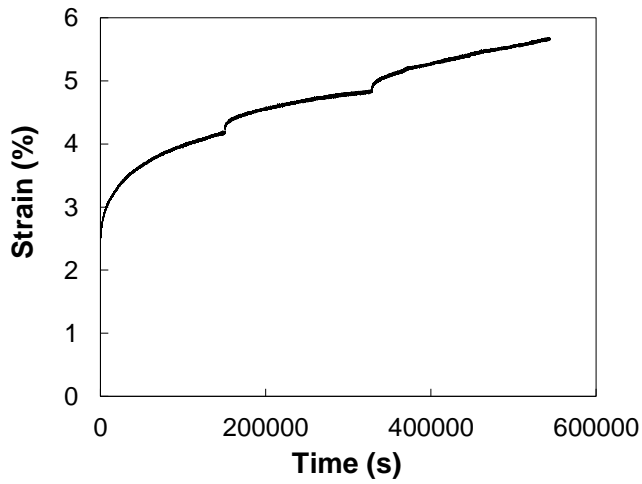


Fig. 2. Creep curves during the interruption.

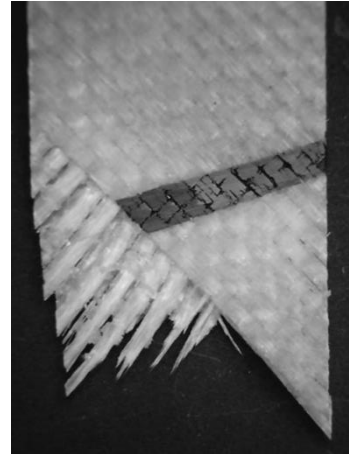


Fig. 3. Fatigue fracture surface.

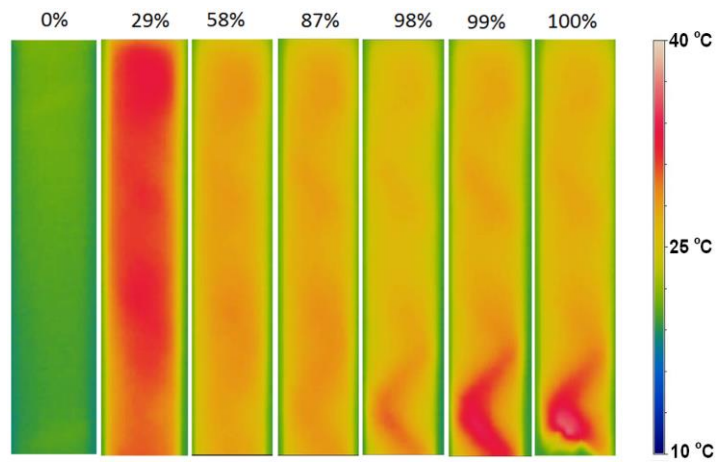


Fig. 4. Representation of the self-generated temperature in different percentages of fatigue life.

No.	Code	f (Hz)	N_f
24	Cref-0.1-58-48-b	5.06	24385

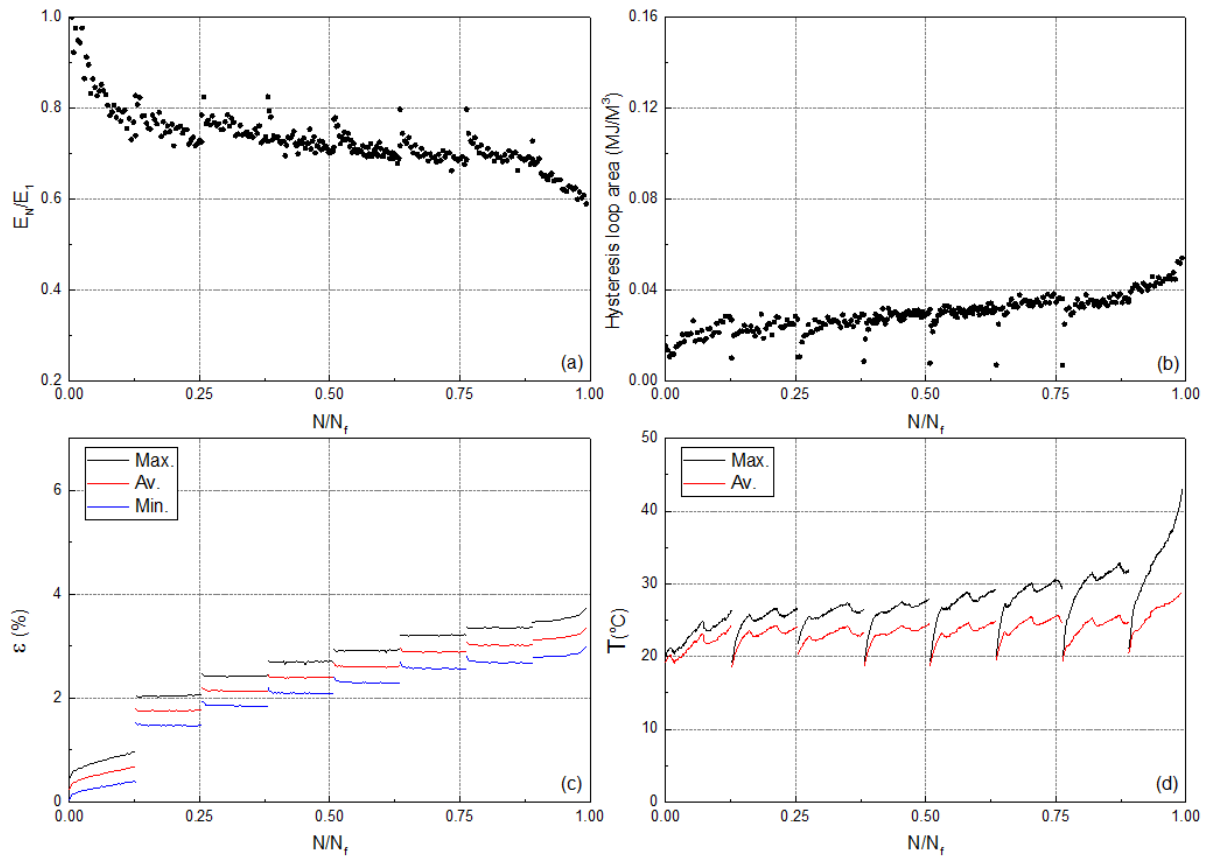


Fig. 1. Variation of (a) normalized fatigue stiffness, (b) hysteresis area, (c) maximum, average, and minimum cyclic strain, and (d) maximum and average self-generated temperature versus normalized number of cycles.

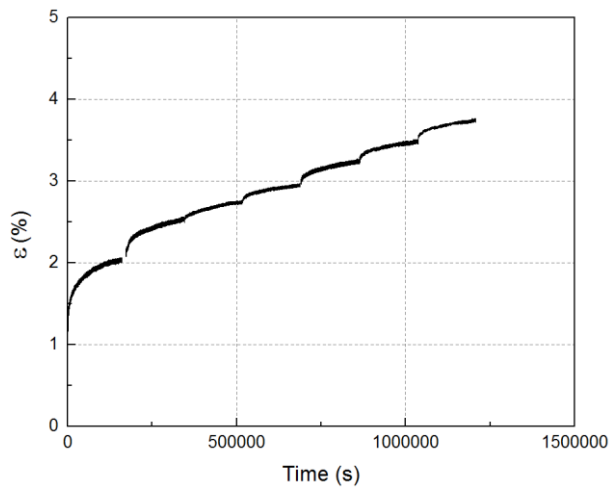


Fig. 2. Creep curves during the interruption.

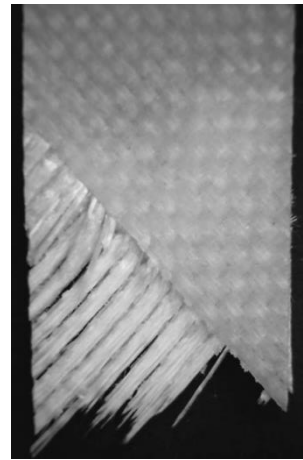


Fig. 3. Fatigue fracture surface.

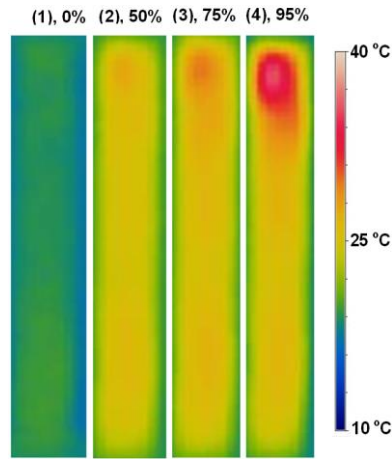


Fig. 4. Representation of the self-generated temperature in different percentages of fatigue life.

No.	Code	f (Hz)	N_f
25	Cref-0.1-53-2-a	5.53	42815

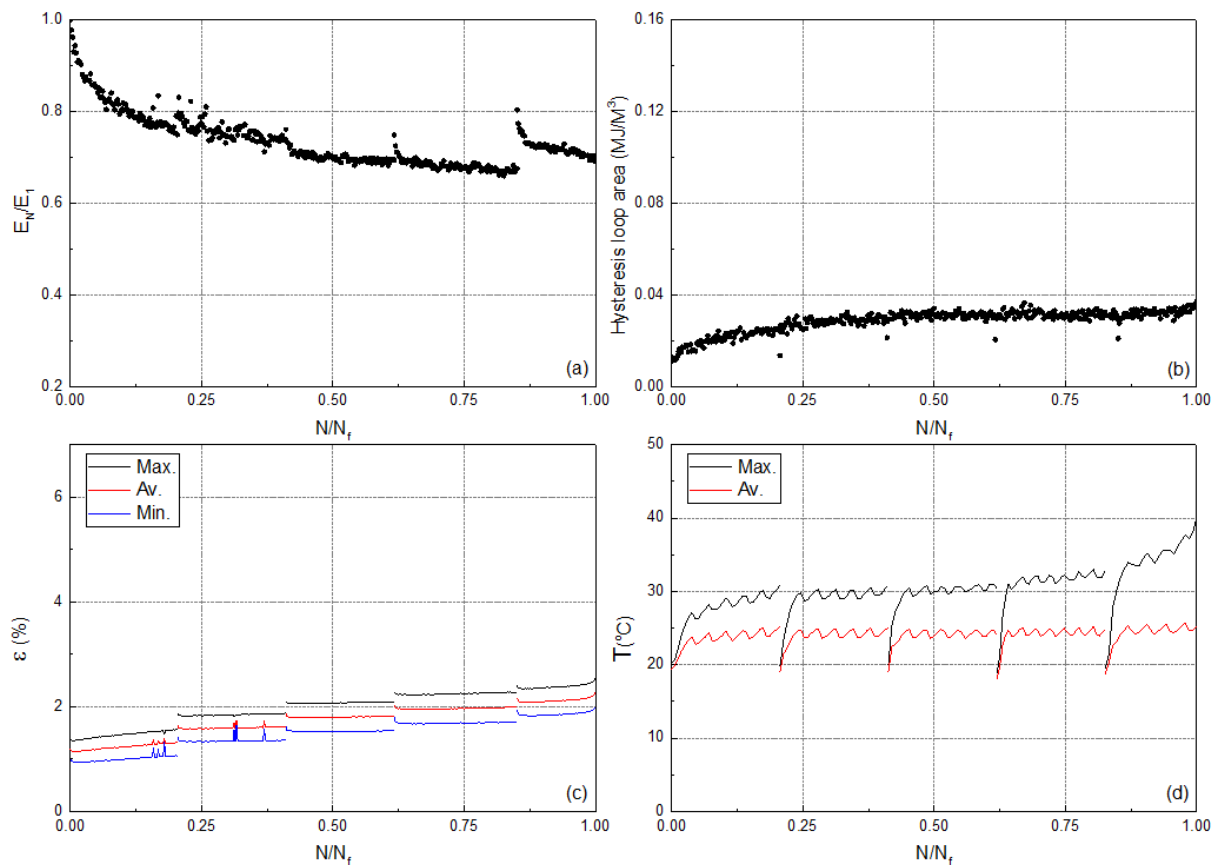


Fig. 1. Variation of (a) normalized fatigue stiffness, (b) hysteresis area, (c) maximum, average, and minimum cyclic strain, and (d) maximum and average self-generated temperature versus normalized number of cycles.

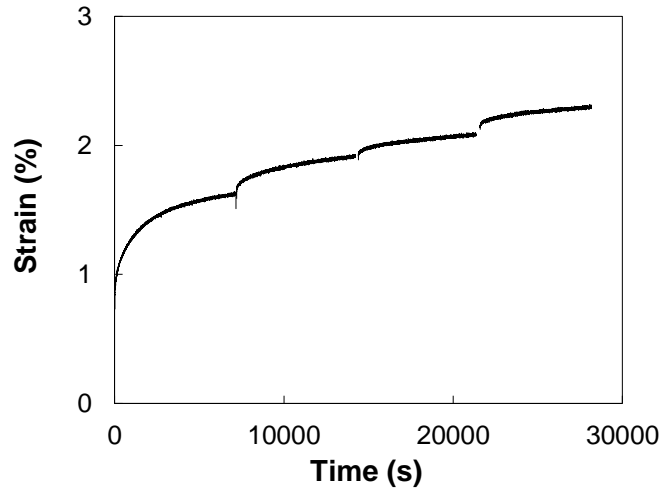


Fig. 2. Creep curves during the interruption.

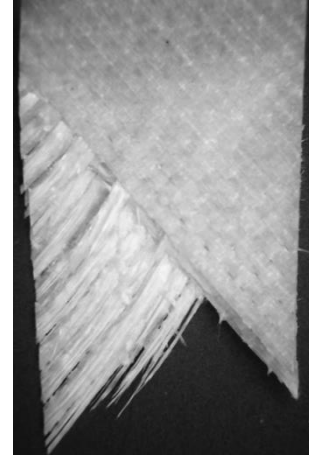


Fig. 3. Fatigue fracture surface.

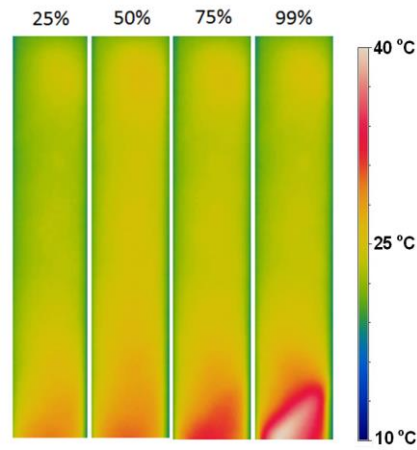


Fig. 4. Representation of the self-generated temperature in different percentages of fatigue life.

No.	Code	f (Hz)	N_f
26	Cref-0.1-53-2-b	6.10	87654

No.	Code	f (Hz)	N_f
27	Cref-0.1-53-2-c	6.10	63288

No.	Code	f (Hz)	N_f
28	Cref-0.1-53-2-d	5.53	43277

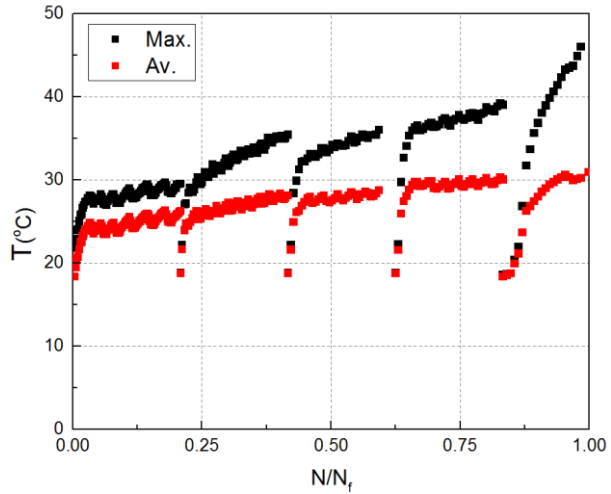


Fig. 1. Variation of maximum and average self-generated temperature.

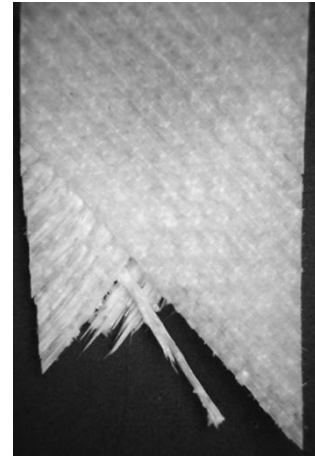


Fig. 2. Fatigue fracture surface.

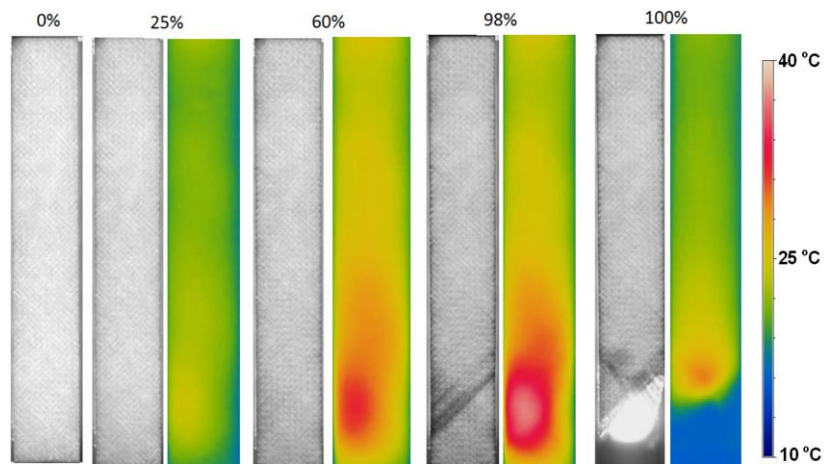


Fig. 3. Pairwise representation of light transmittance and the self-generated temperature in different percentages of fatigue life.

No	Code	f (Hz)	N_f
29	Cref-0.1-53-48-a	5.53	74391

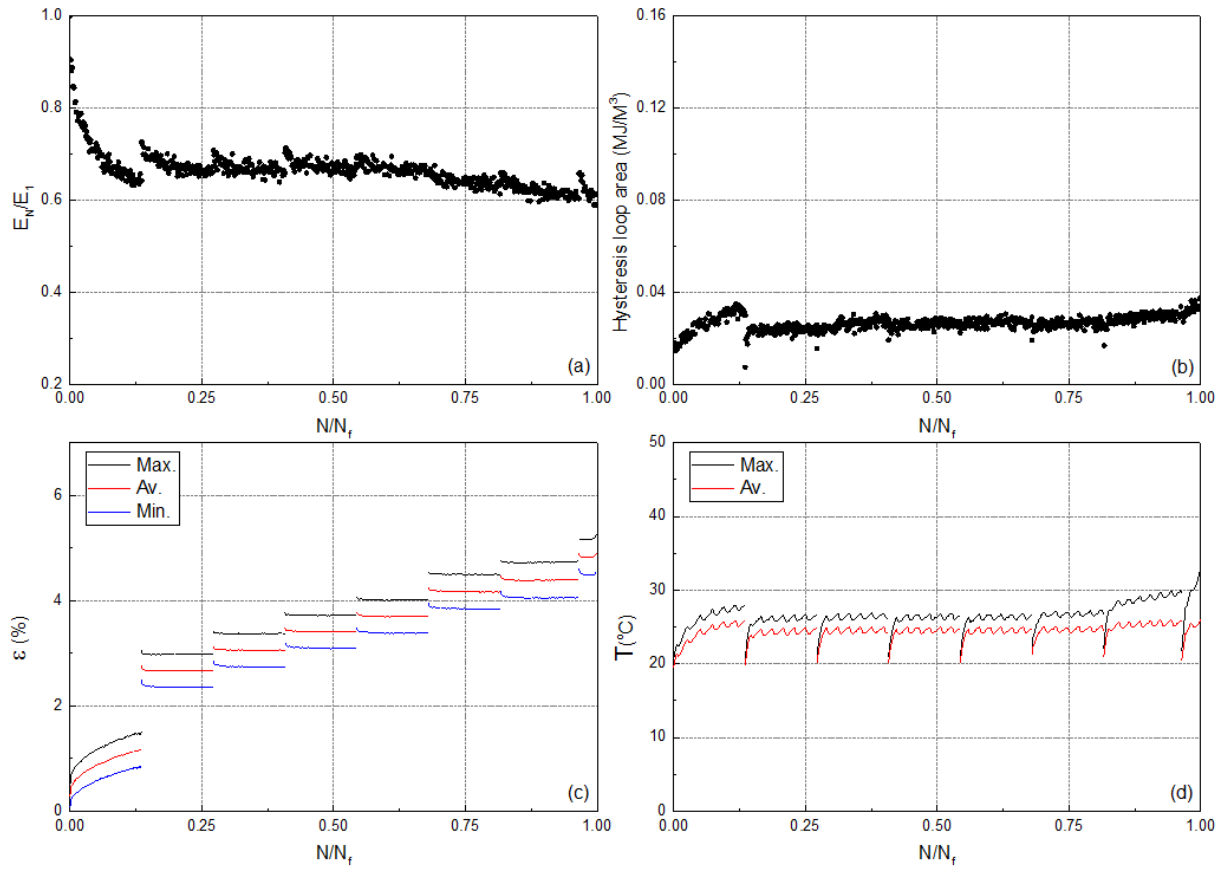


Fig. 1. Variation of (a) normalized fatigue stiffness, (b) hysteresis area, (c) maximum, average, and minimum cyclic strain, and (d) maximum and average self-generated temperature versus normalized number of cycles.

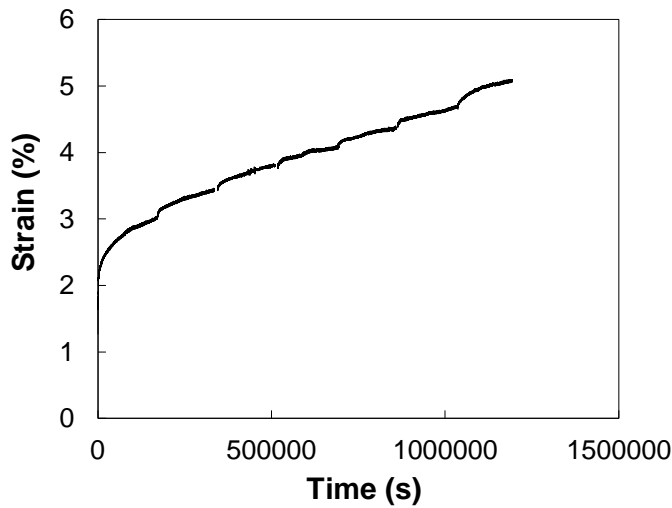


Fig. 2. Creep curves during the interruptions.



Fig. 3. Fatigue fracture surface.

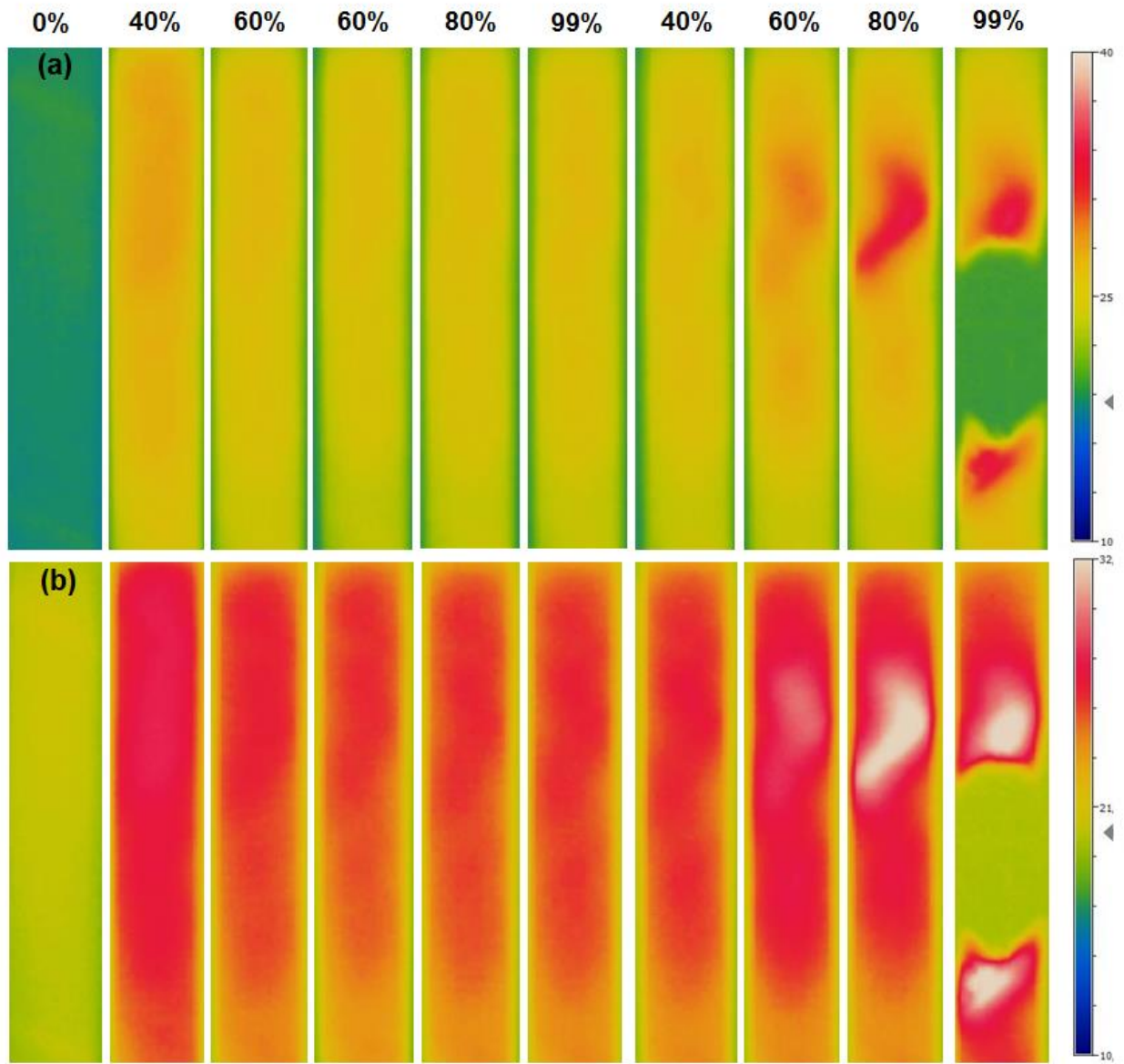


Fig. 4. Representation of the self-generated temperature in different percentages of fatigue life at two temperature scales of (a) 10-40 °C, and (b) 10-32 °C.

No	Code	f (Hz)	N_f
30	Cref-0.1-53-48-b	5.53	30704

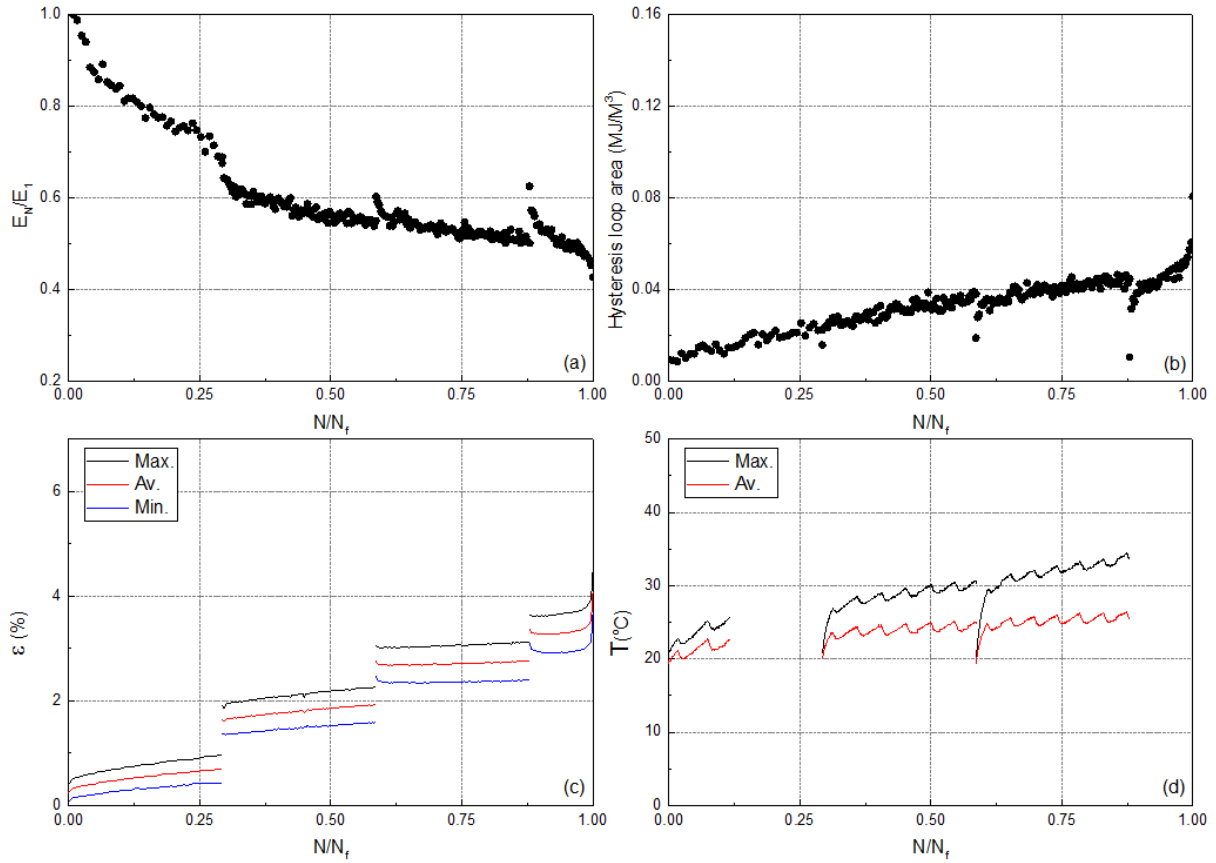


Fig. 1. Variation of (a) normalized fatigue stiffness, (b) hysteresis area, (c) maximum, average, and minimum cyclic strain, and (d) maximum and average self-generated temperature versus normalized number of cycles.

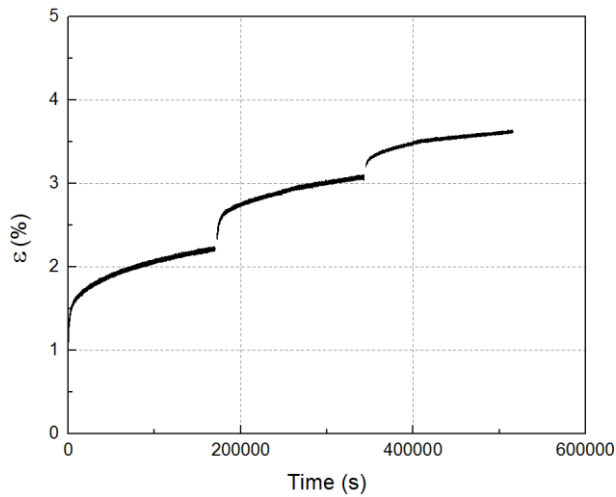


Fig. 2. Creep curves during the interruptions.

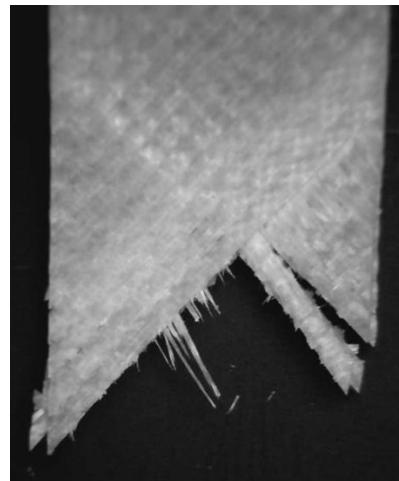


Fig. 3. Fatigue fracture surface.

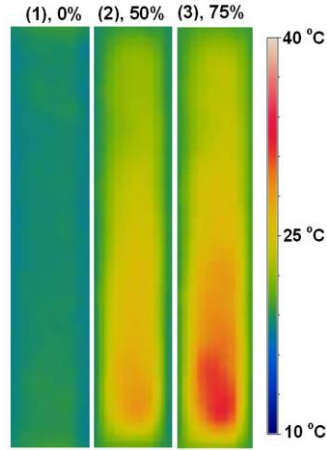


Fig. 4. Representation of the self-generated temperature in different percentages of fatigue life.

No.	Code	f (Hz)	N_f
31	Cref-0.1-49-2-a	6.10	160255

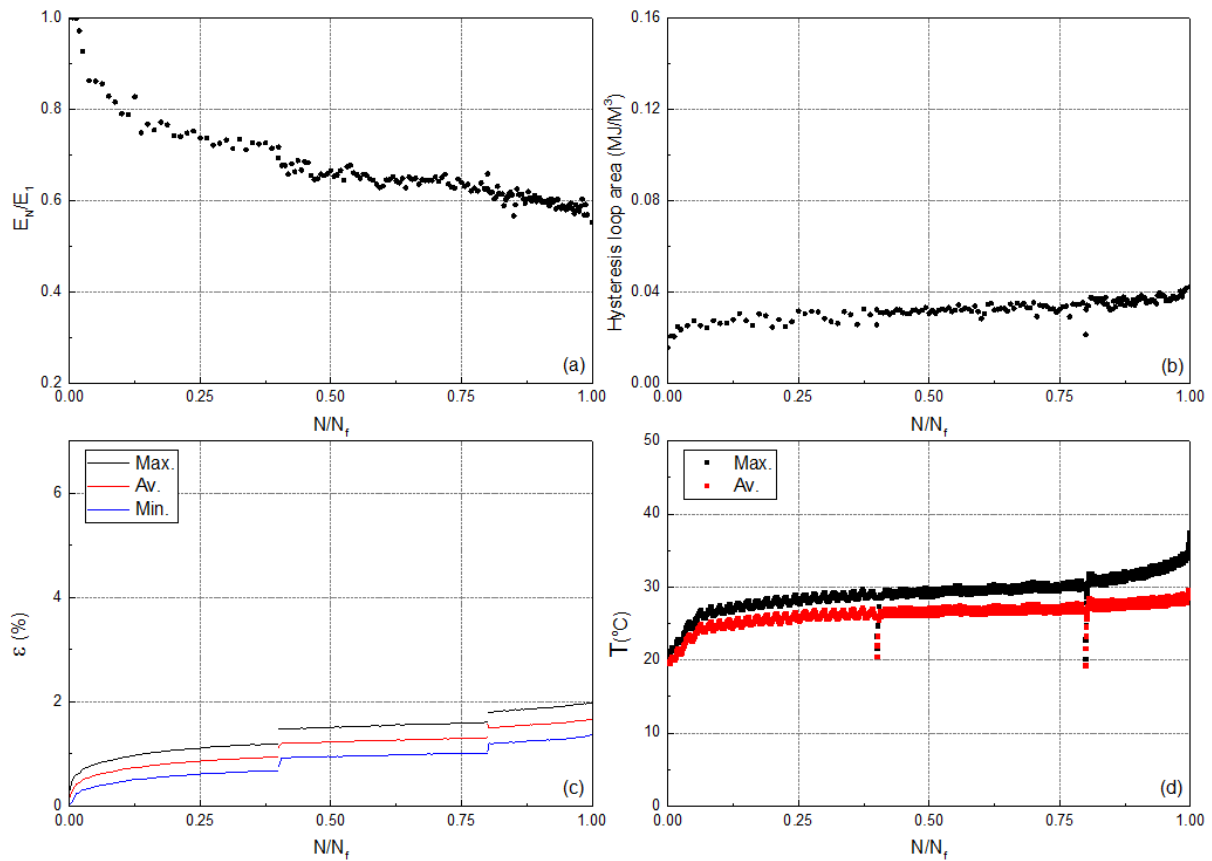


Fig. 1. Variation of (a) normalized fatigue stiffness, (b) hysteresis area, (c) maximum, average, and minimum cyclic strain, and (d) maximum and average self-generated temperature versus normalized number of cycles.

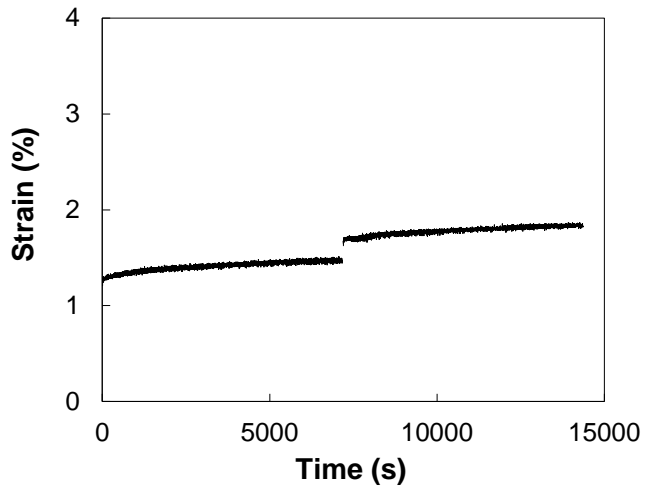


Fig. 2. Creep curves during the interruptions.

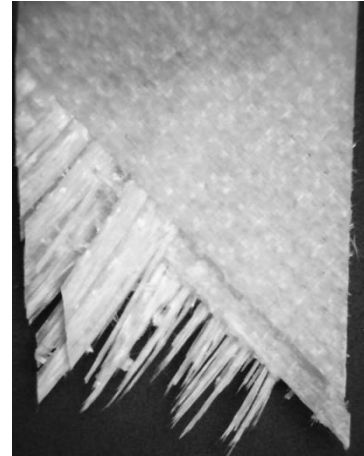


Fig. 3. Fatigue fracture surface.

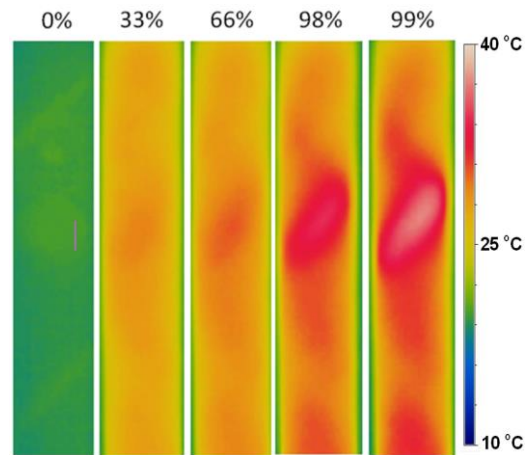


Fig. 4. Representation of the self-generated temperature in different percentages of fatigue life.

No.	Code	f (Hz)	N_f
32	Cref-0.1-49-2-b	6.10	917136

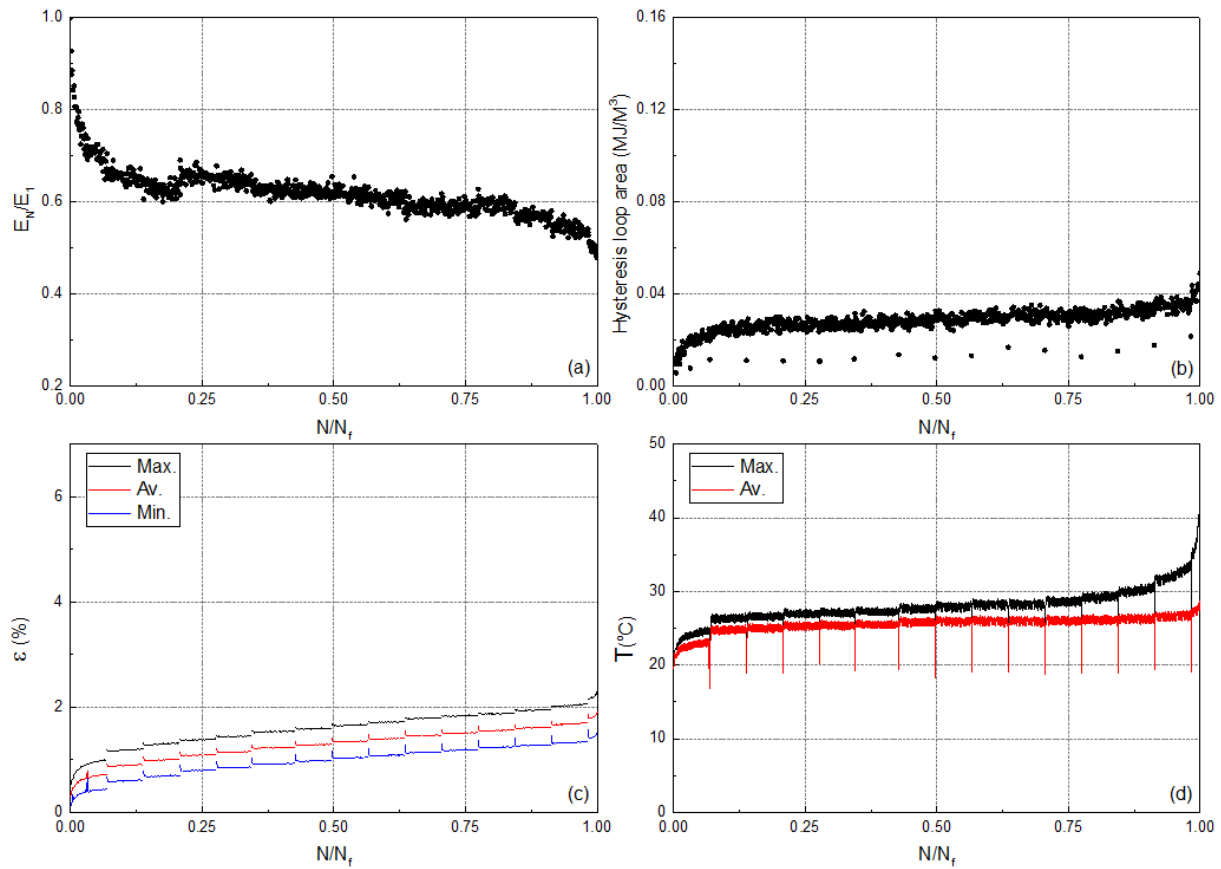


Fig. 1. Variation of (a) normalized fatigue stiffness, (b) hysteresis area, (c) maximum, average, and minimum cyclic strain, and (d) maximum and average self-generated temperature versus normalized number of cycles.

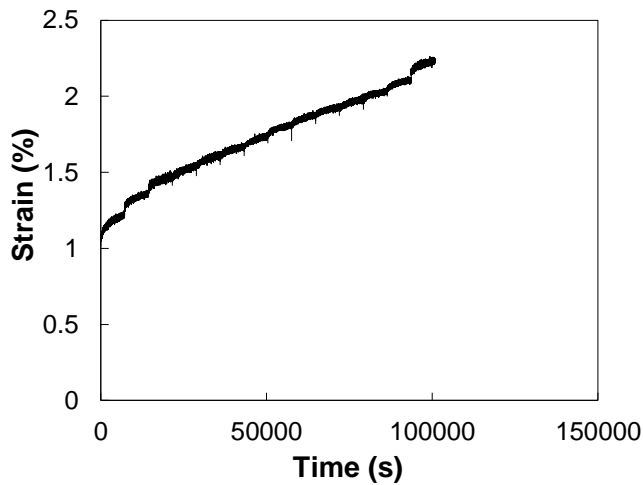


Fig. 2. Creep curves during the interruptions.

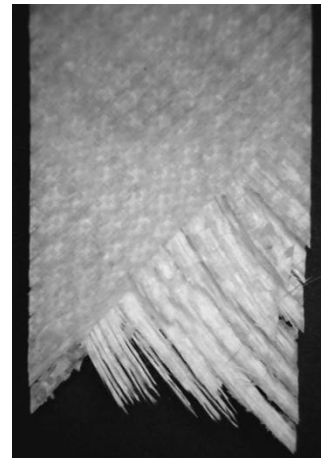


Fig. 3. Fatigue fracture surface.

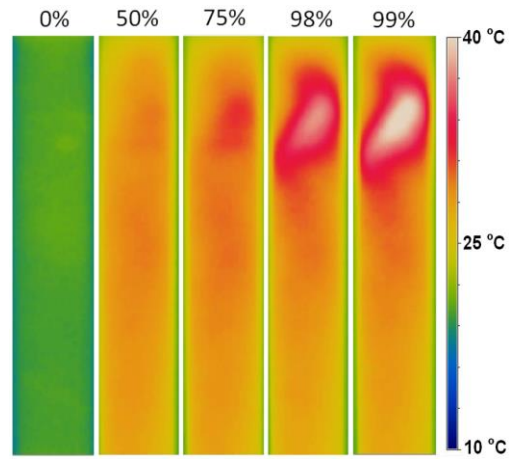


Fig. 4. Representation of the self-generated temperature in different percentages of fatigue life.

No.	Code	f (Hz)	N_f
33	Cref-0.1-49-2-c	6.10	364394

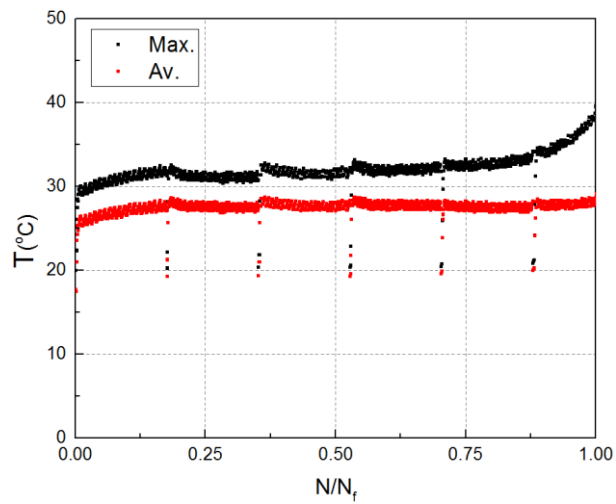


Fig. 1. Variation of maximum and average self-generated temperature.

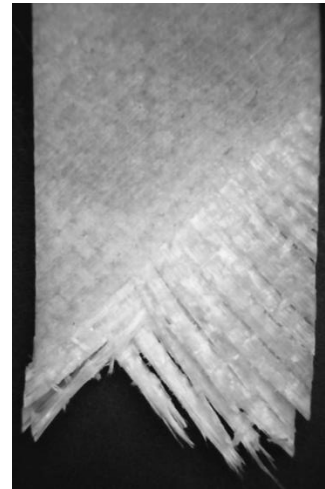


Fig. 2. Fatigue fracture surface.

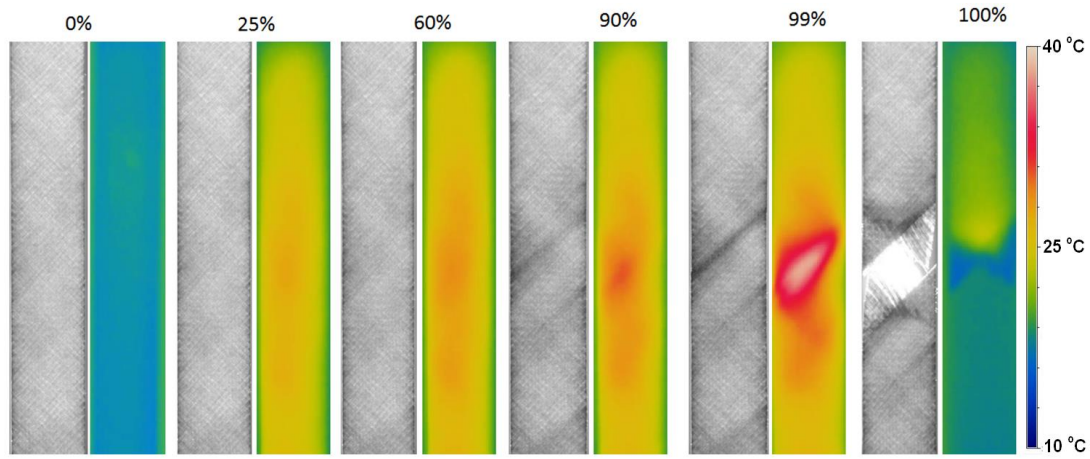


Fig. 2. Pairwise representation of light transmittance and the self-generated temperature in different percentages of fatigue life.

No.	Code	f (Hz)	N_f
34	Cref-0.1-49-2-d	6.10	145809

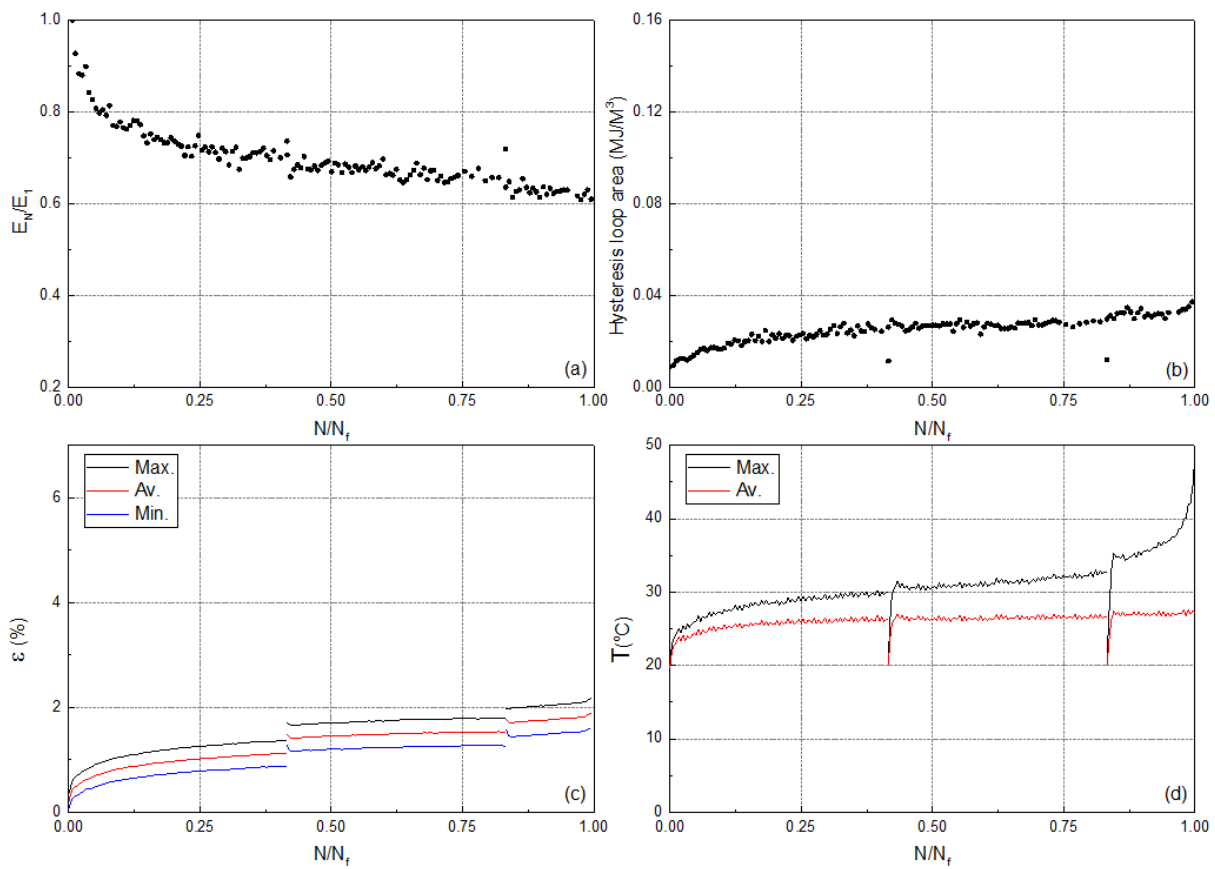


Fig. 1. Variation of (a) normalized fatigue stiffness, (b) hysteresis area, (c) maximum, average, and minimum cyclic strain, and (d) maximum and average self-generated temperature versus normalized number of cycles.

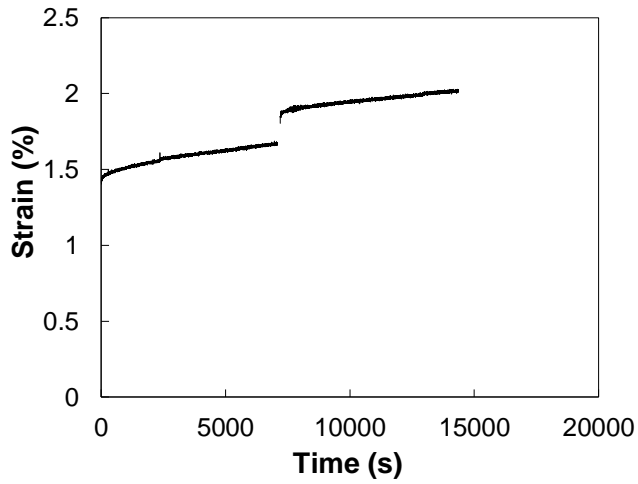


Fig. 2. Creep curves during the interruptions.

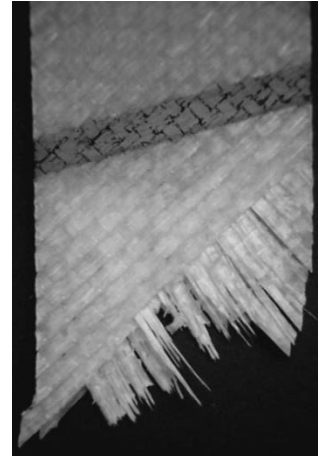


Fig. 3. Fatigue fracture surface.

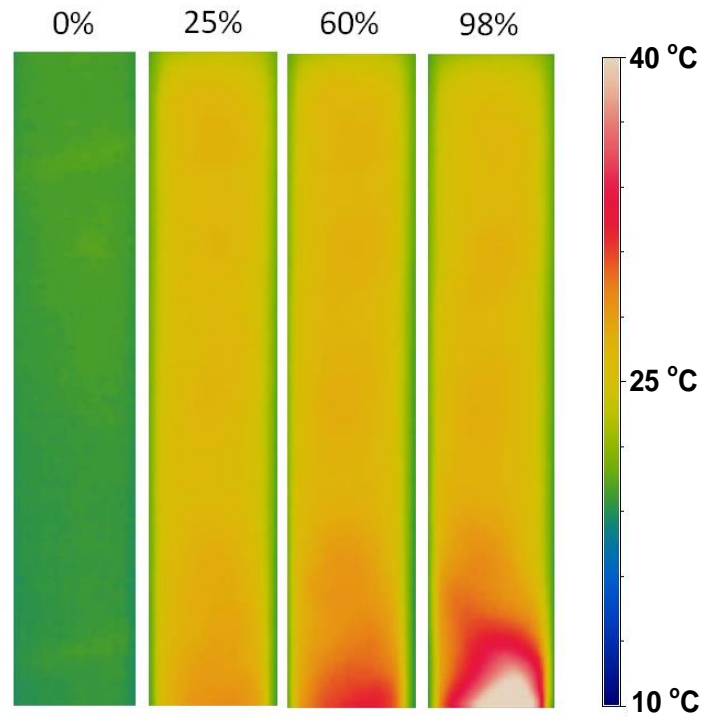


Fig. 4. Pairwise representation of light transmittance and the self-generated temperature in different percentages of fatigue life.

No.	Code	f (Hz)	N_f
35	Cref-0.1-49-48-a	5.53	153769

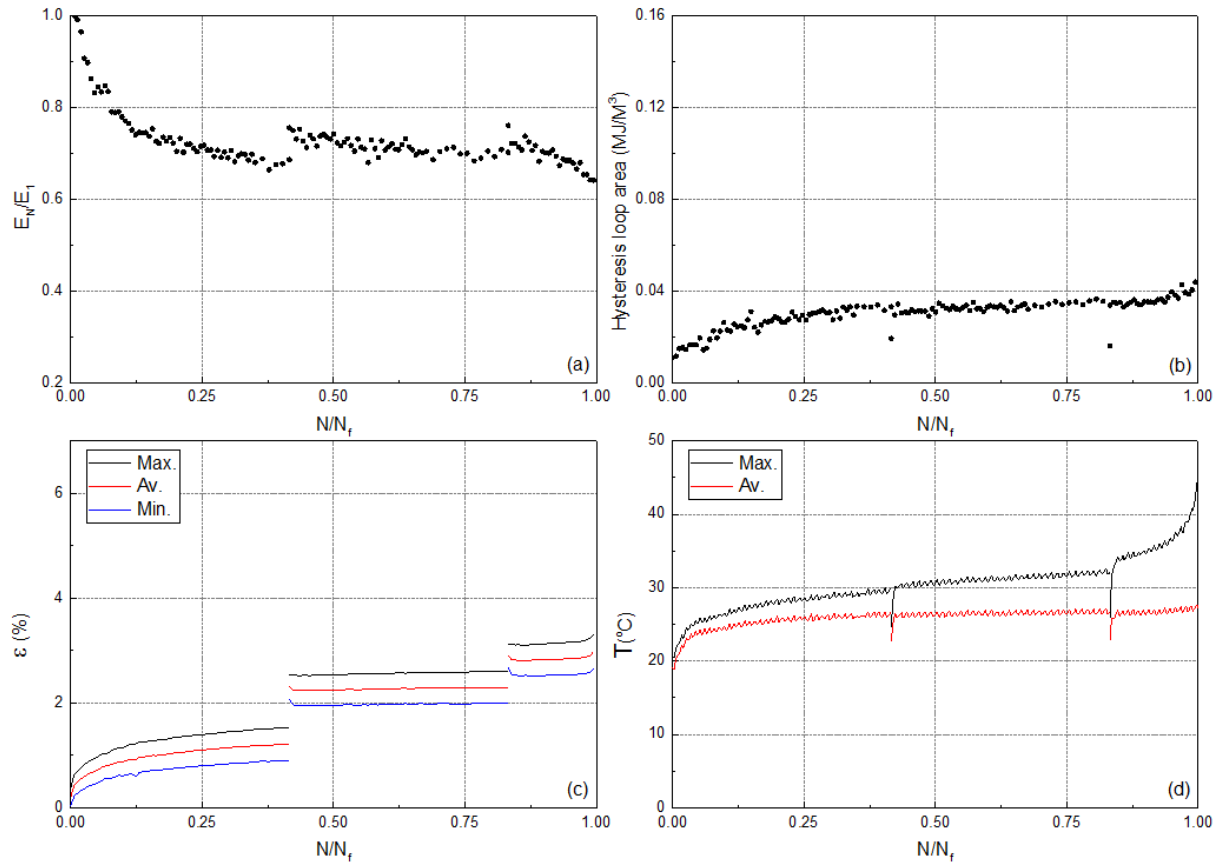


Fig. 1. Variation of (a) normalized fatigue stiffness, (b) hysteresis area, (c) maximum, average, and minimum cyclic strain, and (d) maximum and average self-generated temperature versus normalized number of cycles.

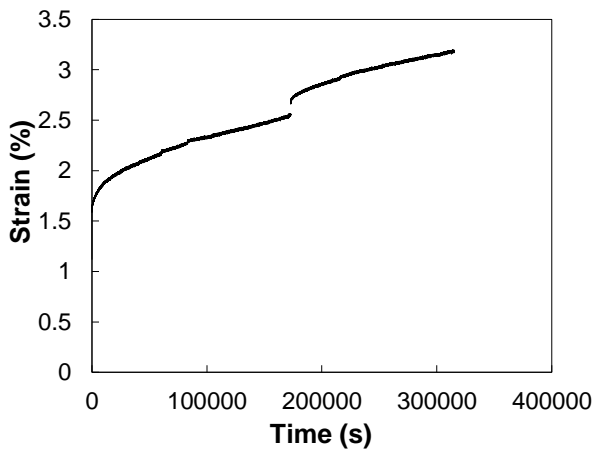


Fig. 2. Creep curves during the interruptions.

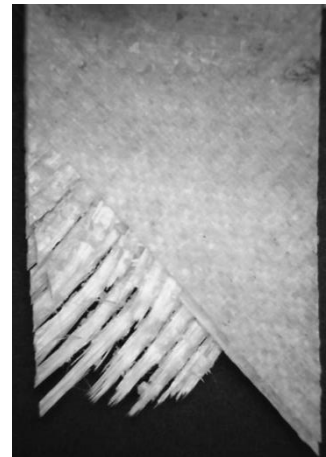


Fig. 3. Fatigue fracture surface.

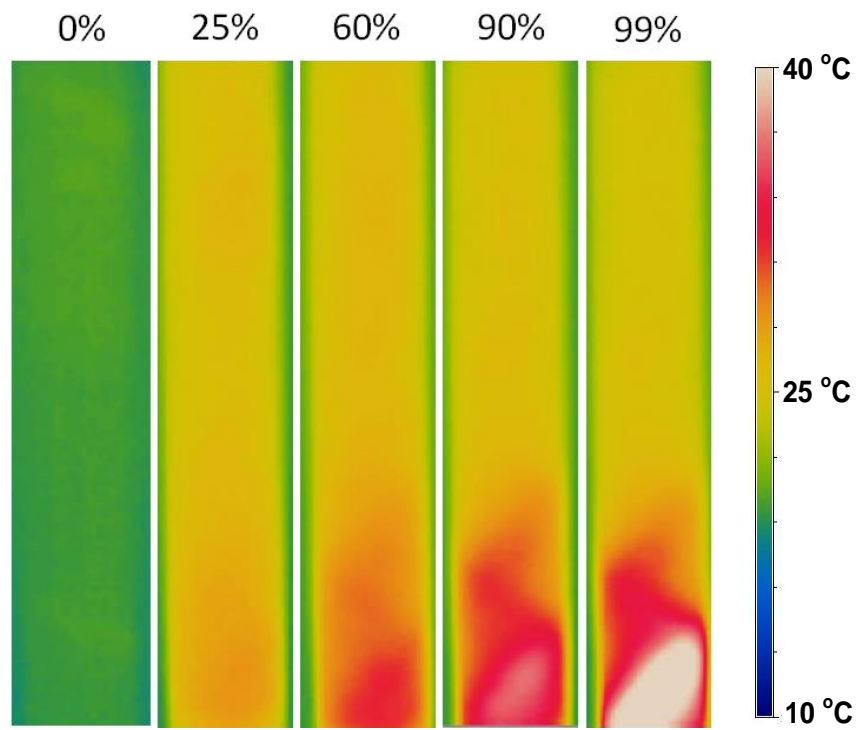


Fig. 4. Pairwise representation of light transmittance and the self-generated temperature in different percentages of fatigue life.

No.	<i>Code</i>	f (Hz)	N_f
36	Cref-0.1-49-48-b	5.53	423859

No.	Code	f (Hz)	N_f
37	Cref-0.1-47-2-a	6.33	384689

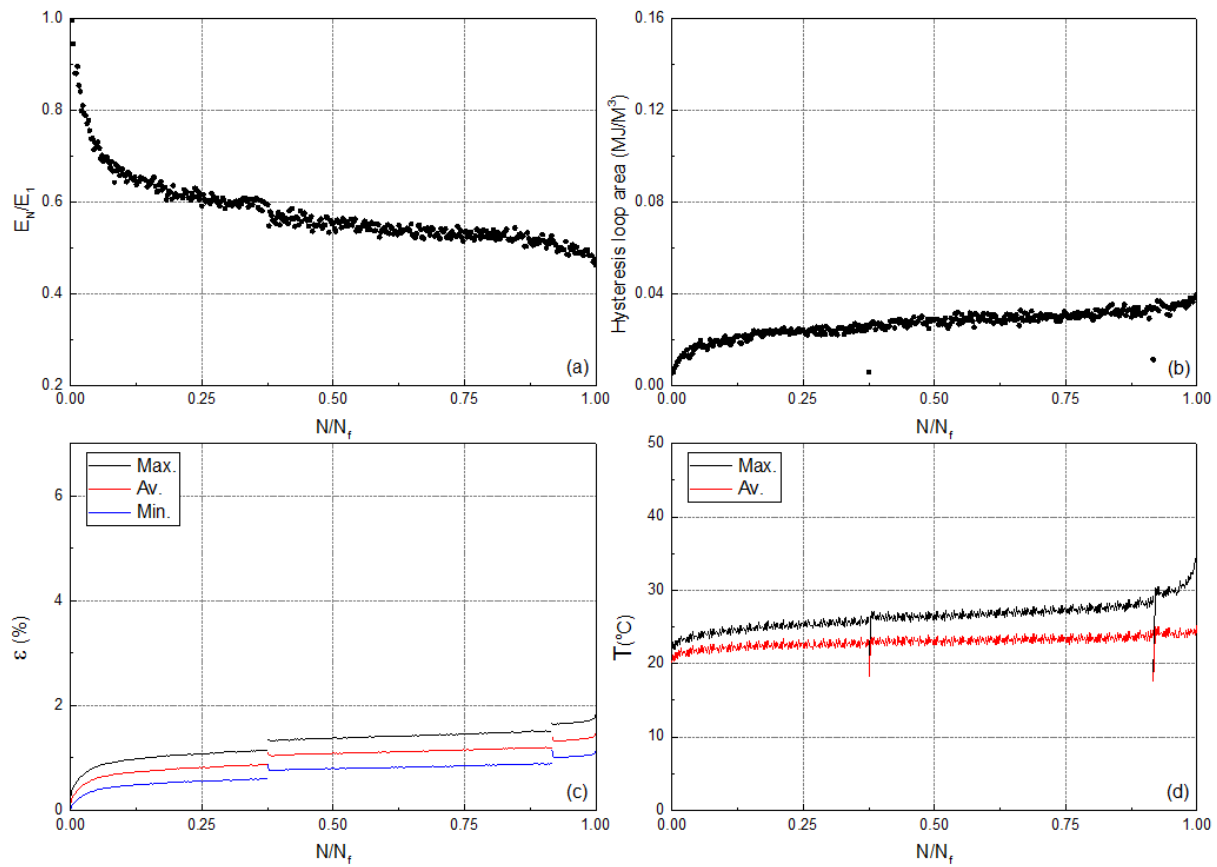


Fig. 1. Variation of (a) normalized fatigue stiffness, (b) hysteresis area, (c) maximum, average, and minimum cyclic strain, and (d) maximum and average self-generated temperature versus normalized number of cycles.

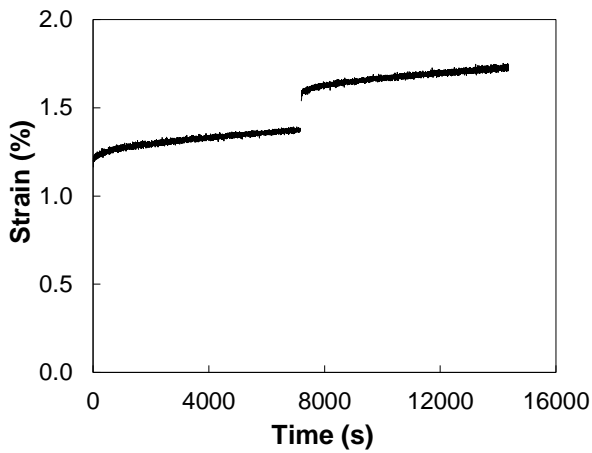


Fig. 2. Creep curves during the interruptions.

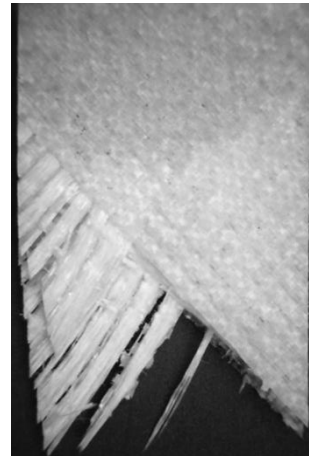


Fig. 3. Fatigue fracture surface.

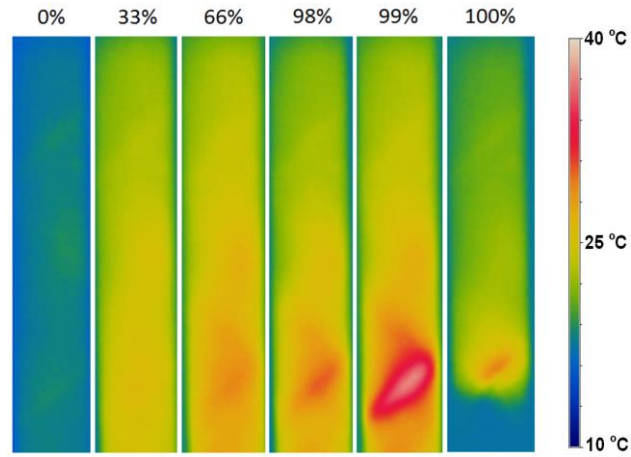


Fig. 4. Pairwise representation of light transmittance and the self-generated temperature in different percentages of fatigue life.

No.	Code	f (Hz)	N_f
38	Cref-0.1-47-2-b	6.33	319752

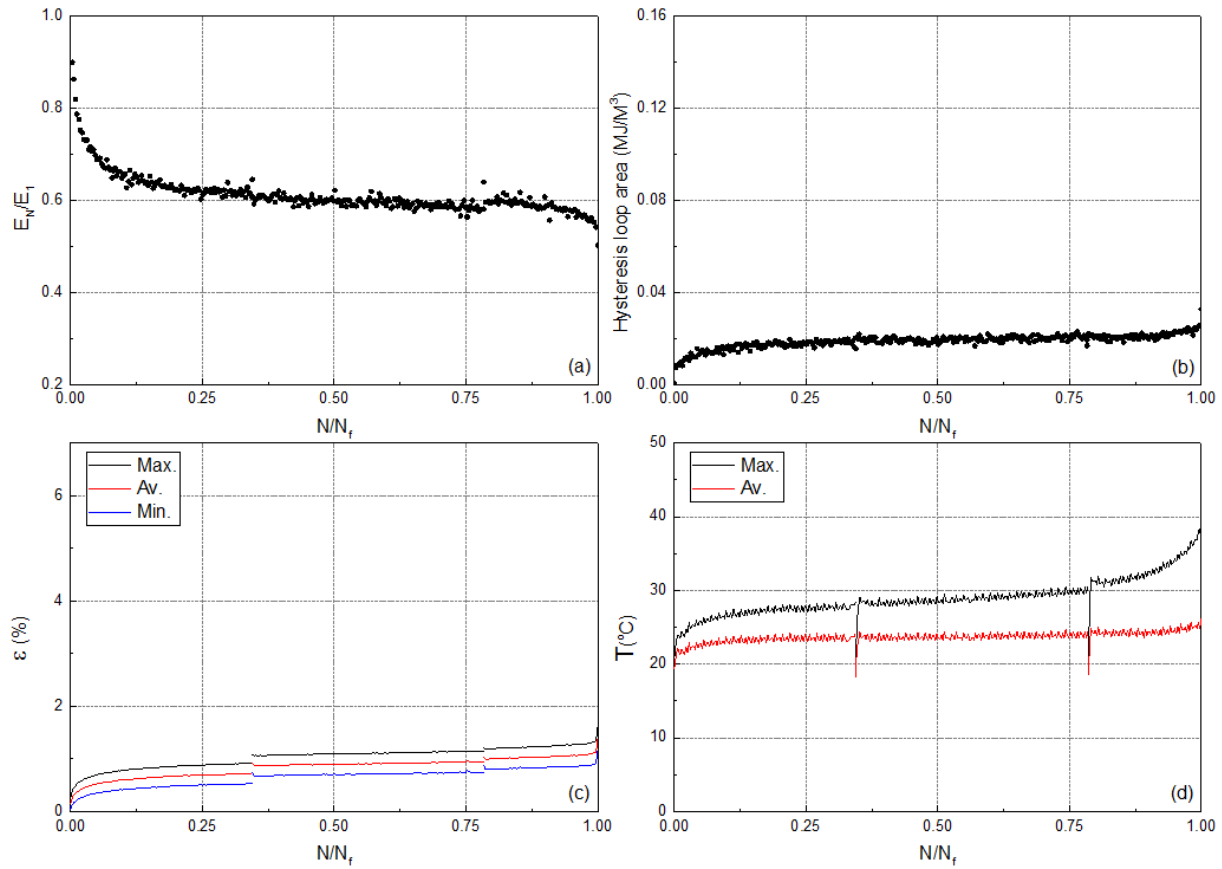


Fig. 1. Variation of (a) normalized fatigue stiffness, (b) hysteresis area, (c) maximum, average, and minimum cyclic strain, and (d) maximum and average self-generated temperature versus normalized number of cycles.

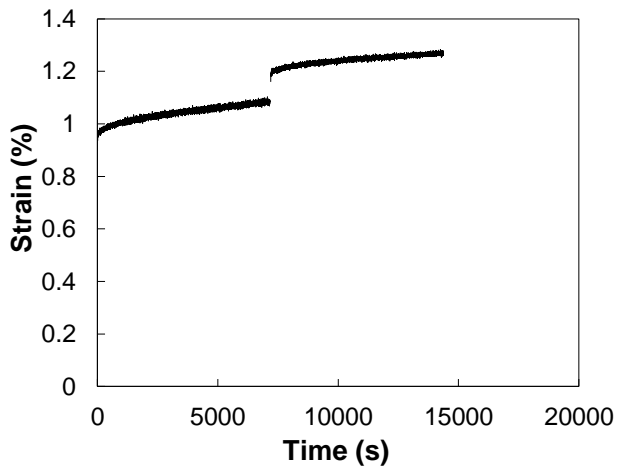


Fig. 2. Creep curves during the interruptions.

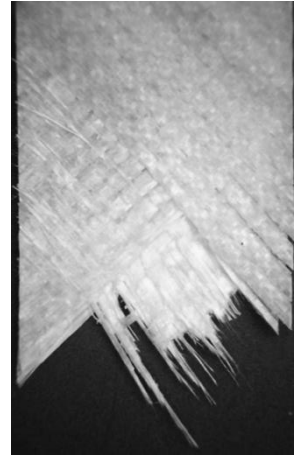


Fig. 3. Fatigue fracture surface.

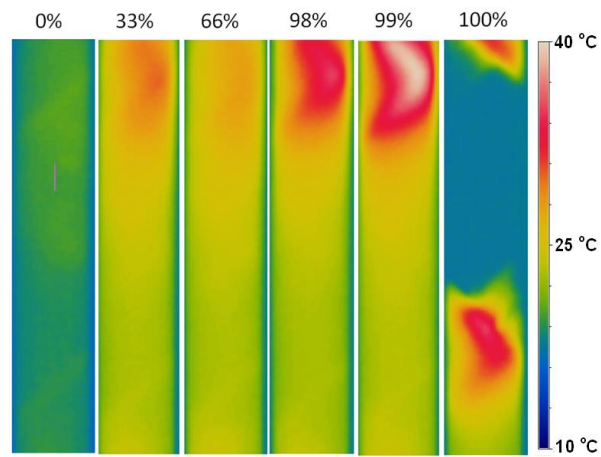


Fig. 4. Representation of the self-generated temperature in different percentages of fatigue life.

No.	Code	f (Hz)	N_f
39	Cref-0.1-47-2-c	6.33	1095359

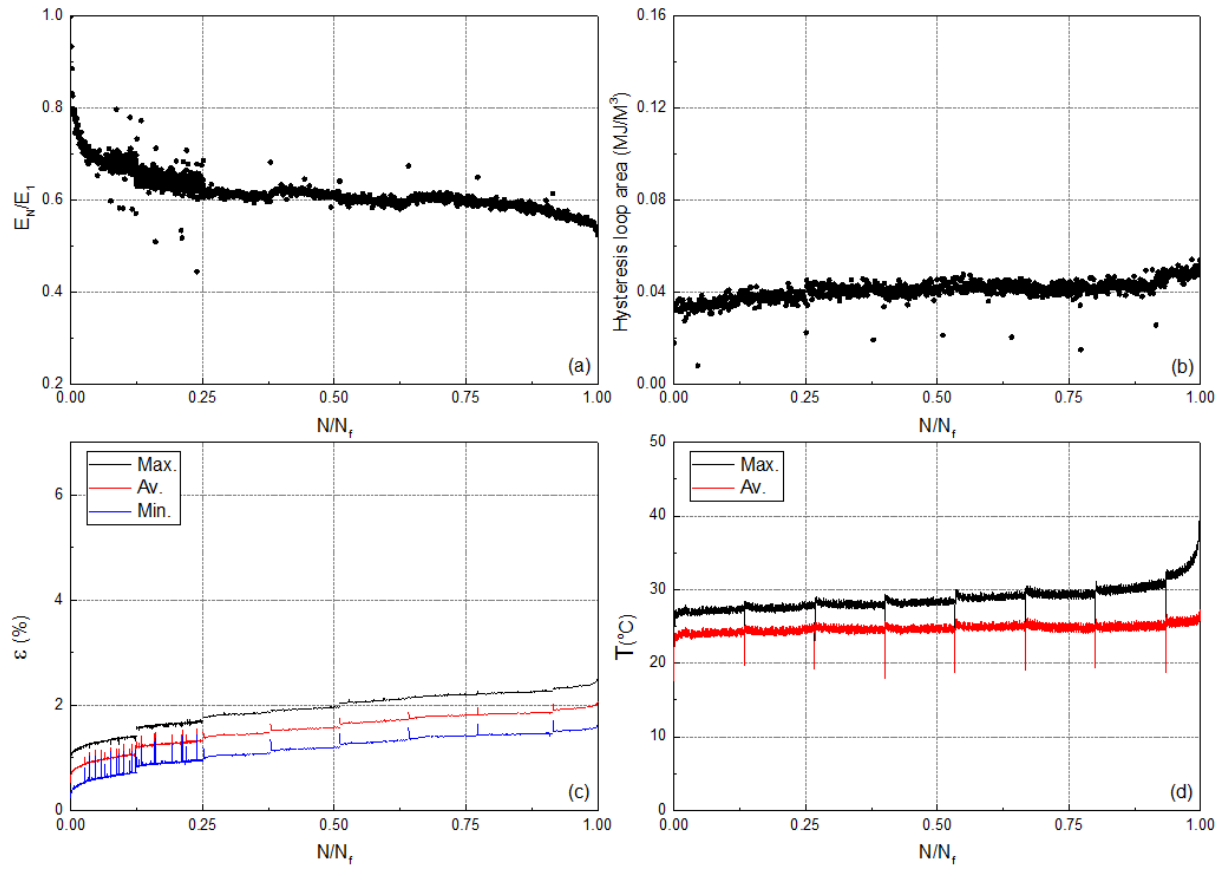


Fig. 1. Variation of (a) normalized fatigue stiffness, (b) hysteresis area, (c) maximum, average, and minimum cyclic strain, and (d) maximum and average self-generated temperature versus normalized number of cycles.

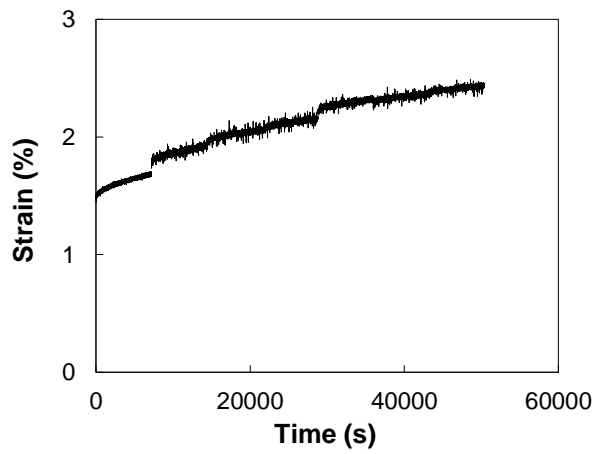


Fig. 2. Creep curves during the interruptions.

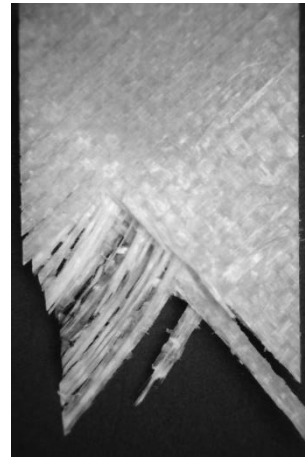


Fig. 3. Fatigue fracture surface.

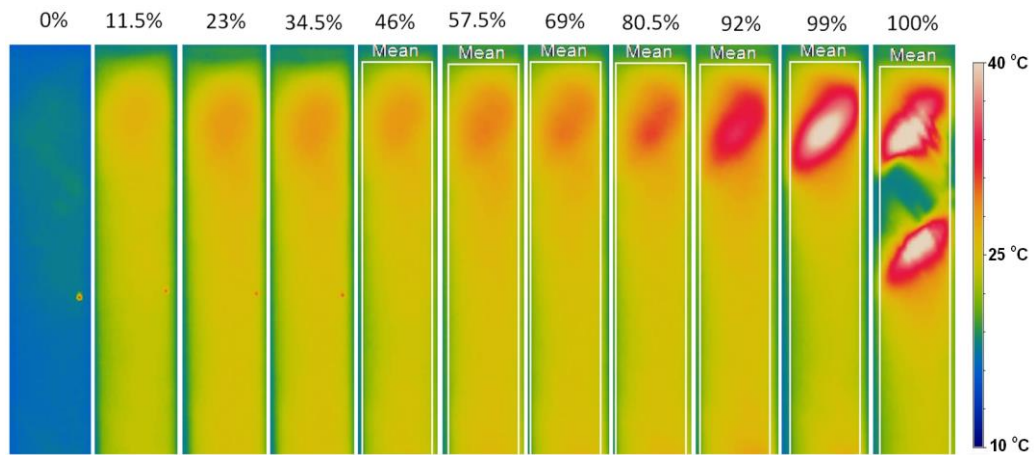


Fig. 4. Representation of the self-generated temperature in different percentages of fatigue life.

No.	Code	f (Hz)	N_f
40	Cref-0.1-47-2-d	6.33	350072

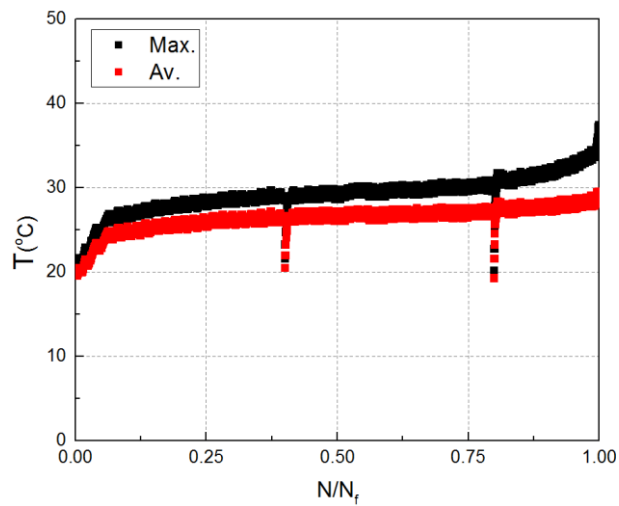


Fig. 1. Variation of maximum and average self-generated temperature.

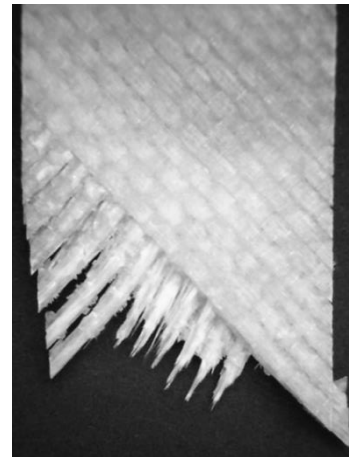


Fig. 2. Fatigue fracture surface.

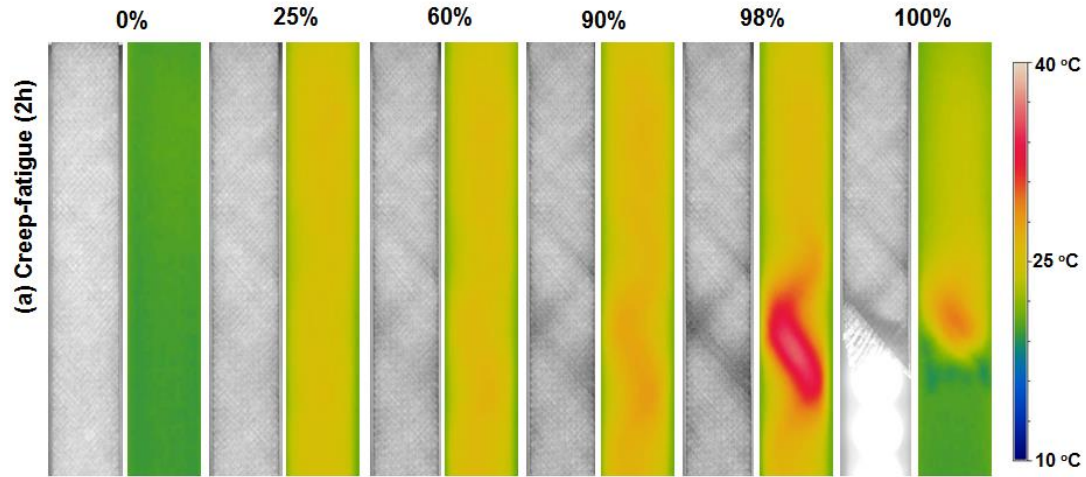


Fig. 3. Pairwise representation of light transmittance and the self-generated temperature in different percentages of fatigue life.

No.	Code	f (Hz)	N_f
41	Cref-0.1-47-48-a	6.33	1356496

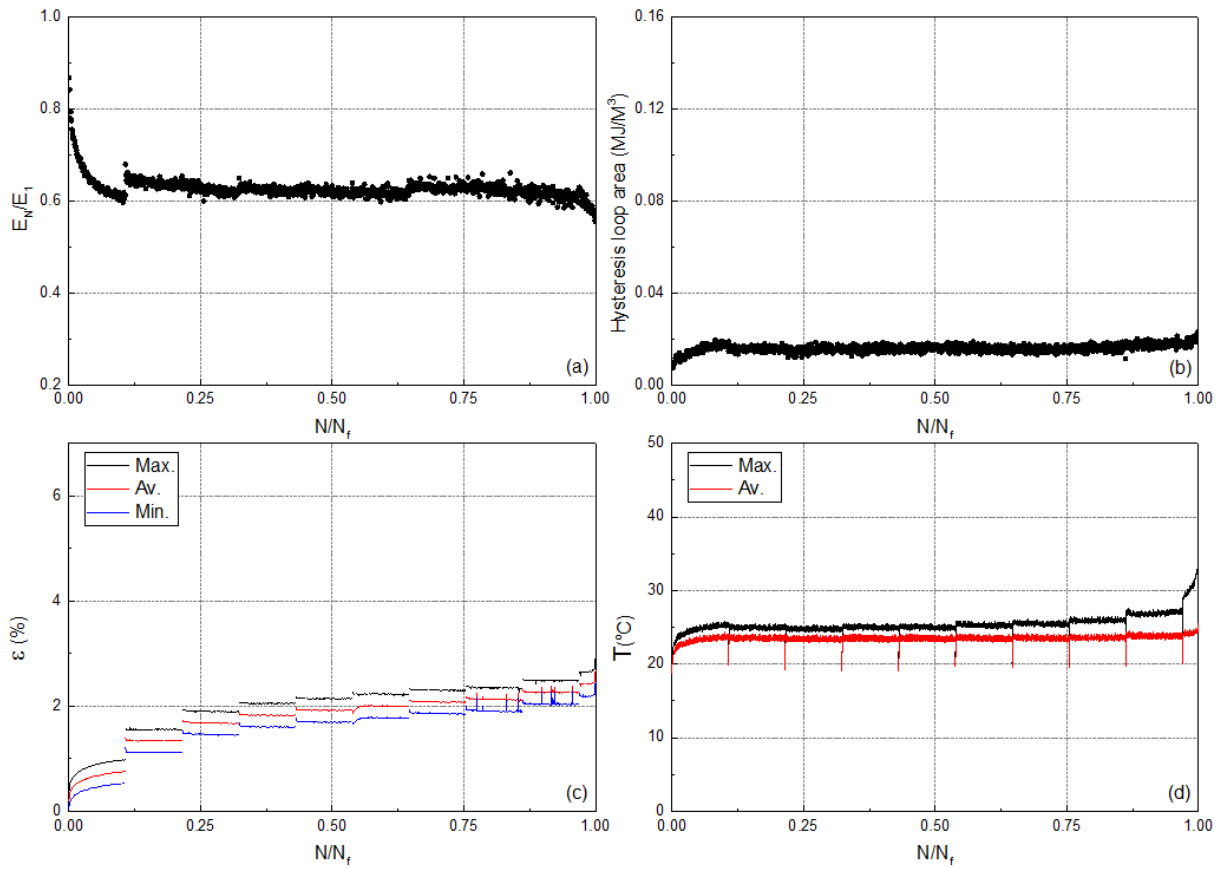


Fig. 1. Variation of (a) normalized fatigue stiffness, (b) hysteresis area, (c) maximum, average, and minimum cyclic strain, and (d) maximum and average self-generated temperature versus normalized number of cycles.

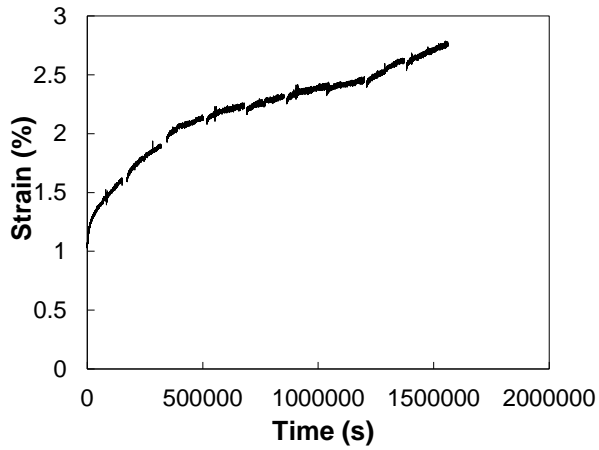


Fig. 2. Creep curves during the interruptions.

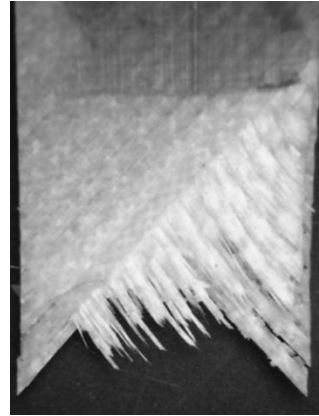


Fig. 3. Fatigue fracture surface.

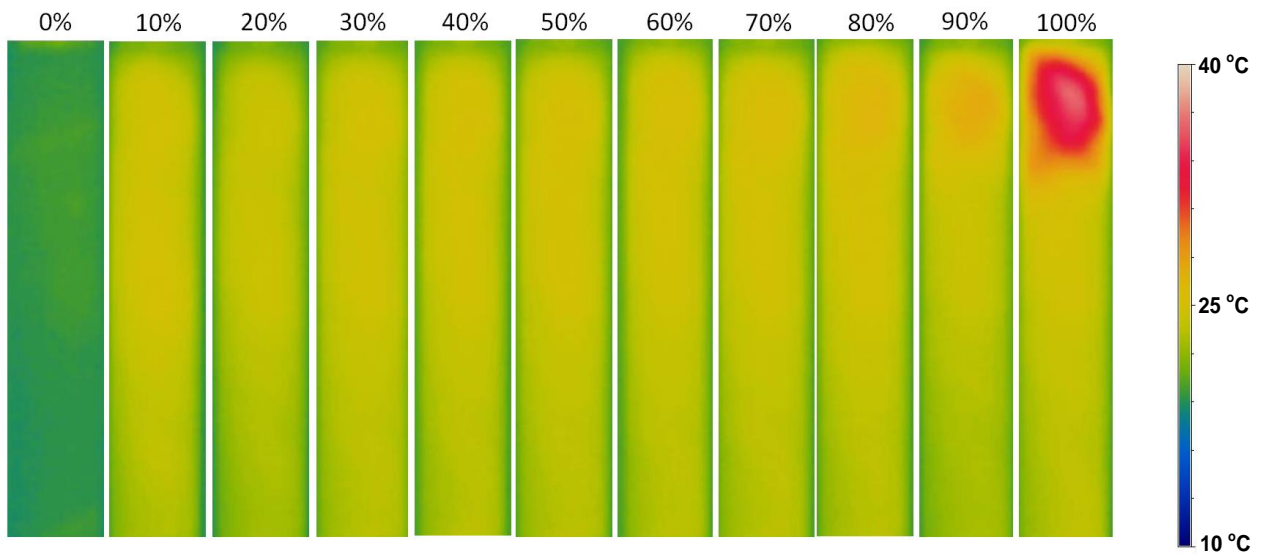


Fig. 4. Representation of the self-generated temperature in different percentages of fatigue life.

No.	Code	f (Hz)	N_f
42	Cref-0.1-47-48-b	6.33	362532

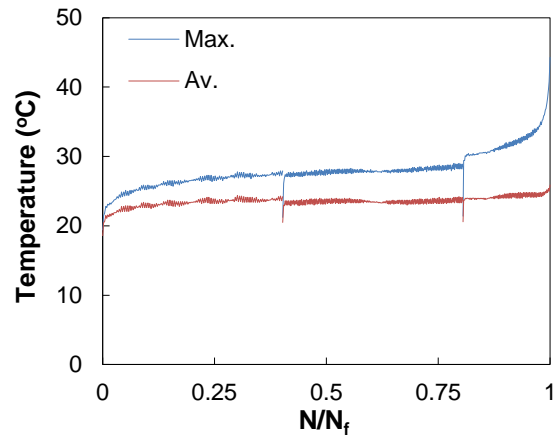


Fig. 1. Variation of maximum and average self-generated temperature.

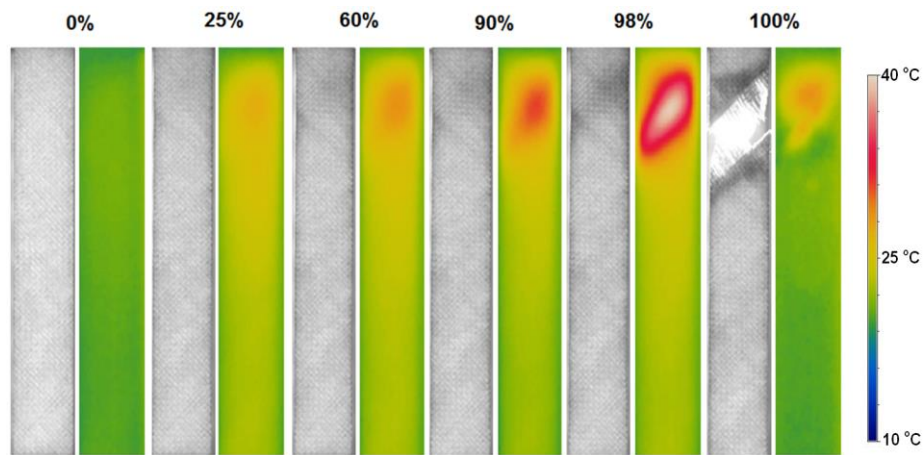


Fig. 2. Pairwise representation of light transmittance and the self-generated temperature in different percentages of fatigue life.

Annex D: Interrupted-fatigue



D.1 Introduction

Annex D presents supplementary results from the interrupted fatigue experiments, which was described in Chapter 5.

No.	Code	f (Hz)	N_f
1	Intf-0.1-68-a	3.95	1205

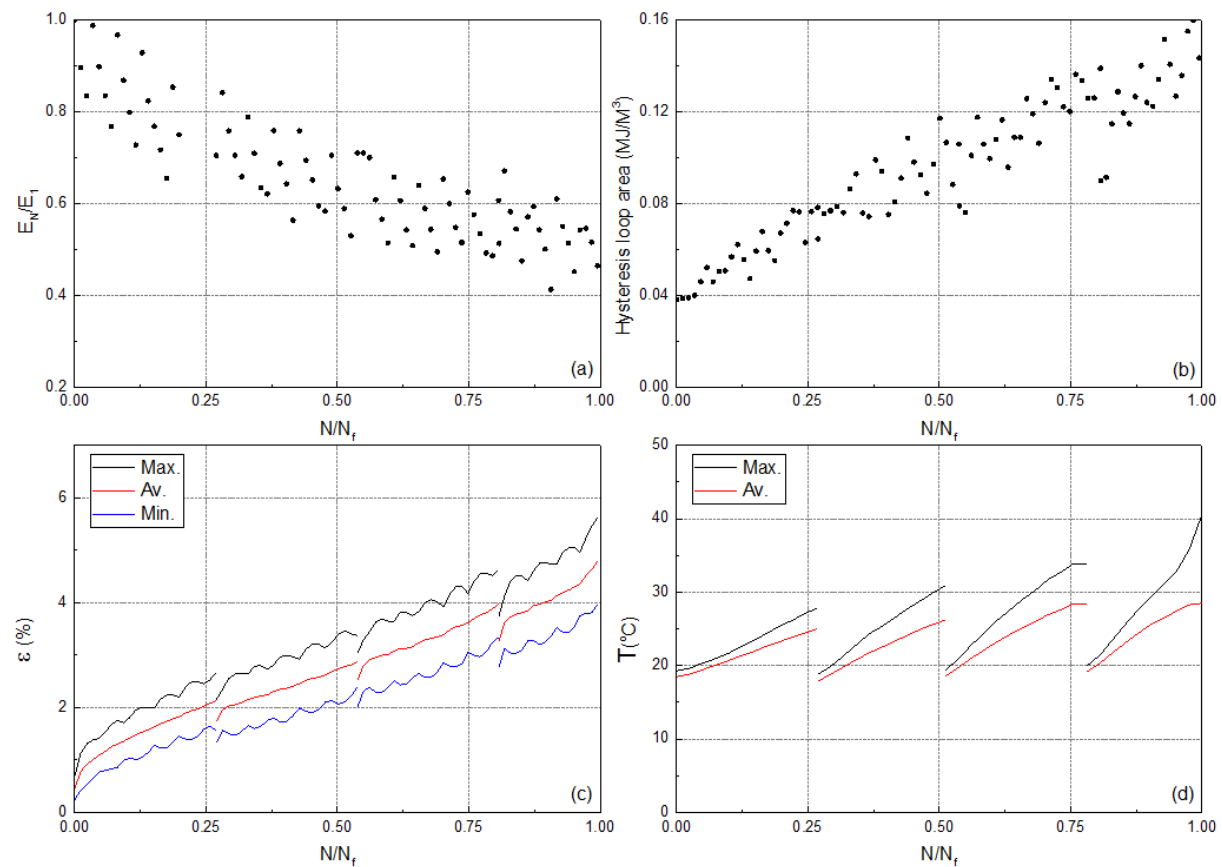


Fig. 1. Variation of (a) normalized fatigue stiffness, (b) hysteresis area, (c) maximum, average, and minimum cyclic strain, and (d) maximum and average self-generated temperature versus normalized number of cycles.

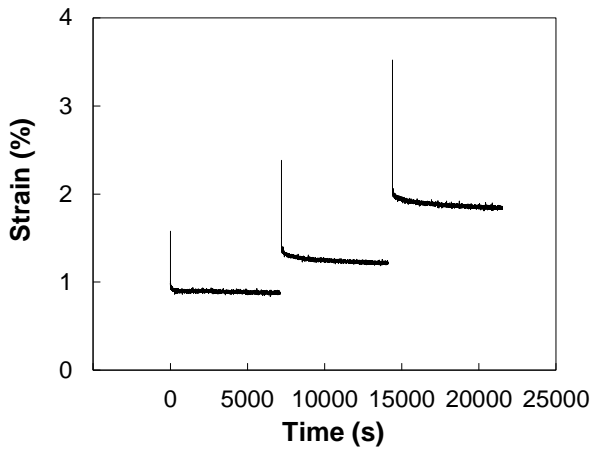


Fig. 2. Recovery curves during the interruptions.

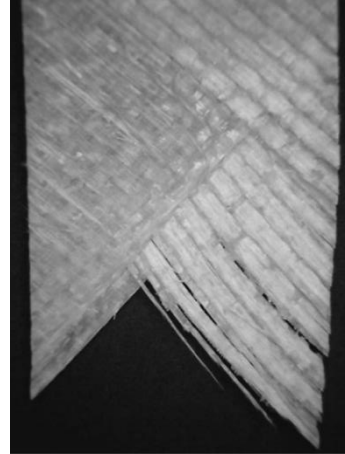


Fig. 3. Fatigue fracture surface.

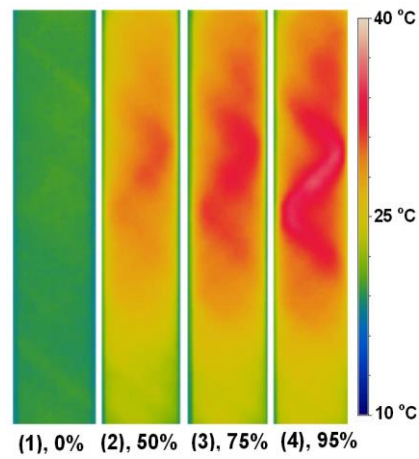


Fig. 4. Representation of the self-generated temperature in different percentages of fatigue life.

No.	Code	f (Hz)	N_f
2	Intf-0.1-68-b	4.35	4,668

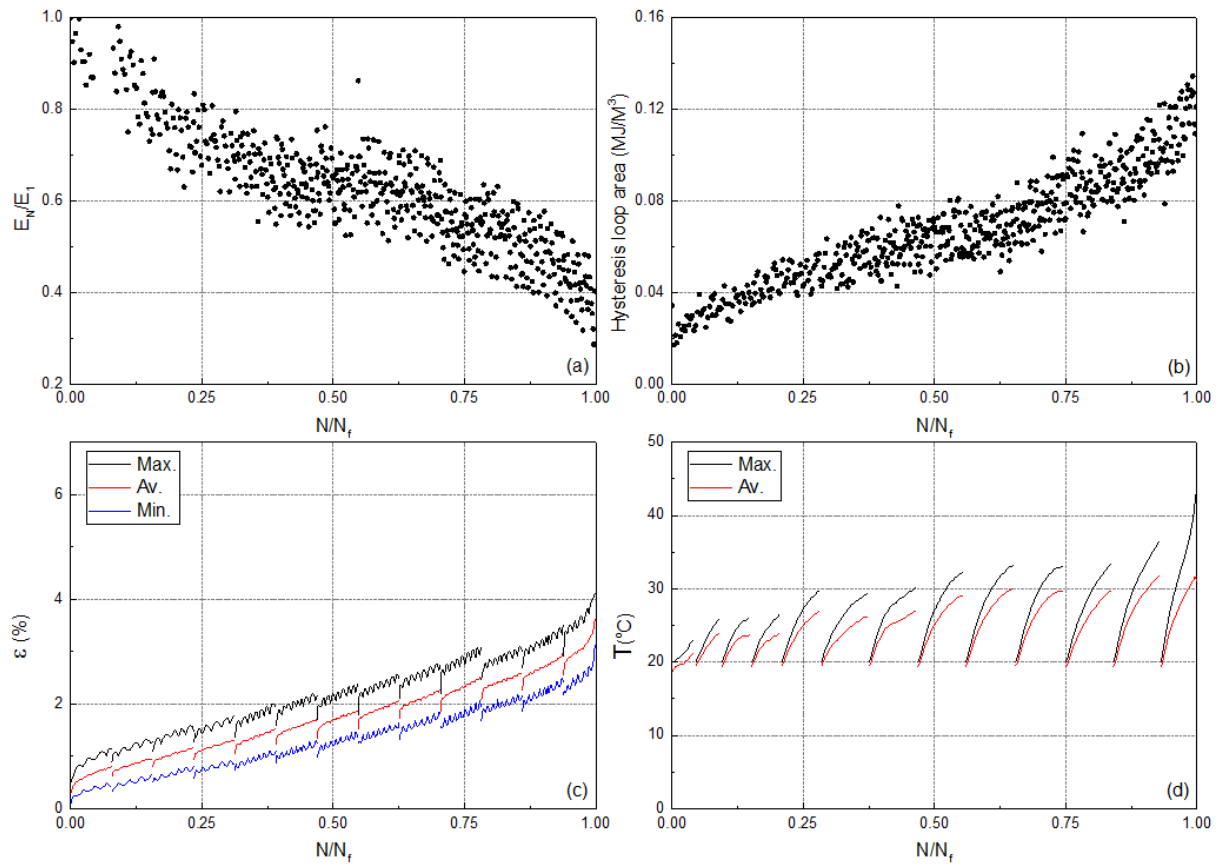


Fig. 1. Variation of (a) normalized fatigue stiffness, (b) hysteresis area, (c) maximum, average, and minimum cyclic strain, and (d) maximum and average self-generated temperature versus normalized number of cycles.

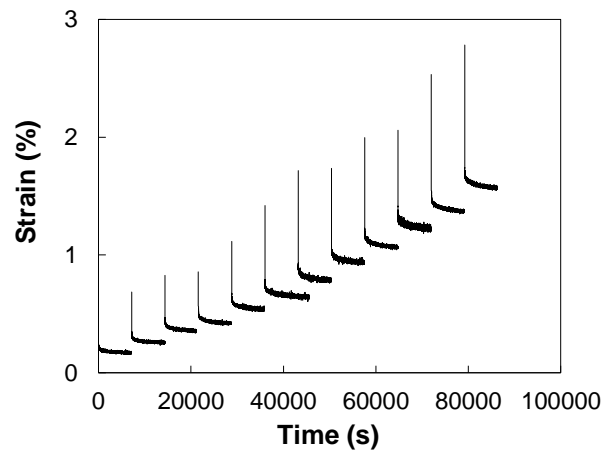


Fig. 2. Recovery curves during the interruptions.

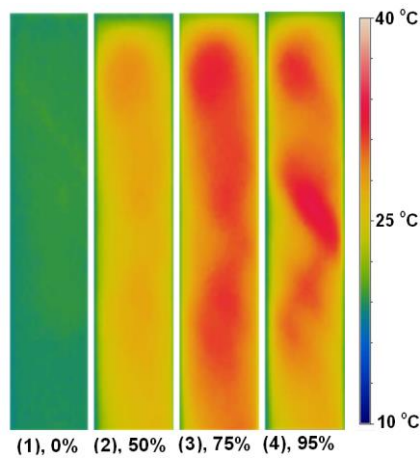


Fig. 3. Representation of the self-generated temperature in different percentages of fatigue life.

No.	Code	f (Hz)	N_f
3	Intf-0.1-68-c	4.35	3,349

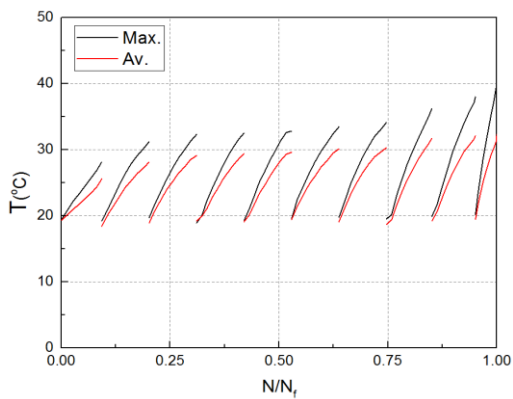


Fig. 1. Variation of maximum and average self-generated temperature.

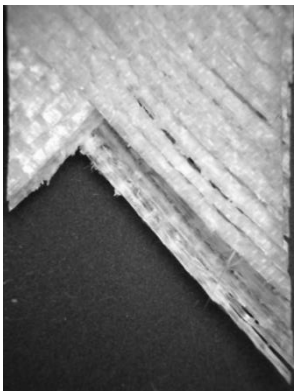


Fig. 2. Fatigue fracture surface.

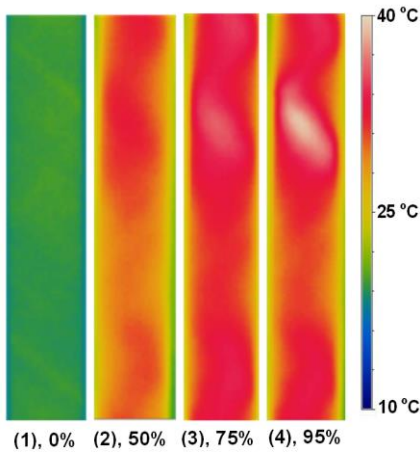


Fig. 3. Representation of the self-generated temperature in different percentages of fatigue life.

No.	Code	f (Hz)	N_f
4	Intf-0.1-68-d	4.35	7,085

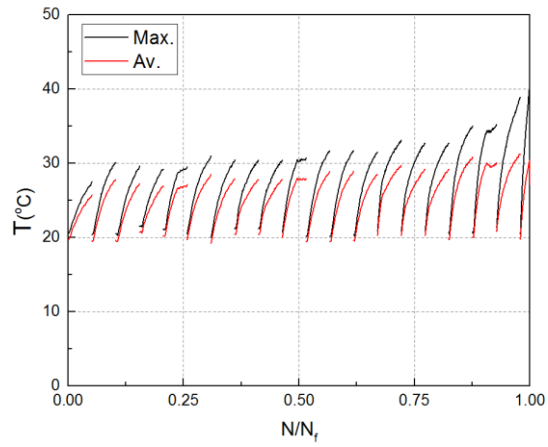


Fig. 1. Variation of maximum and average self-generated temperature.

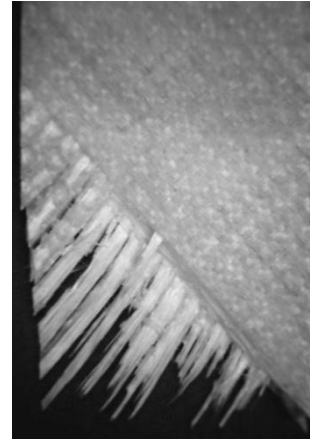


Fig. 2. Fatigue fracture surface.

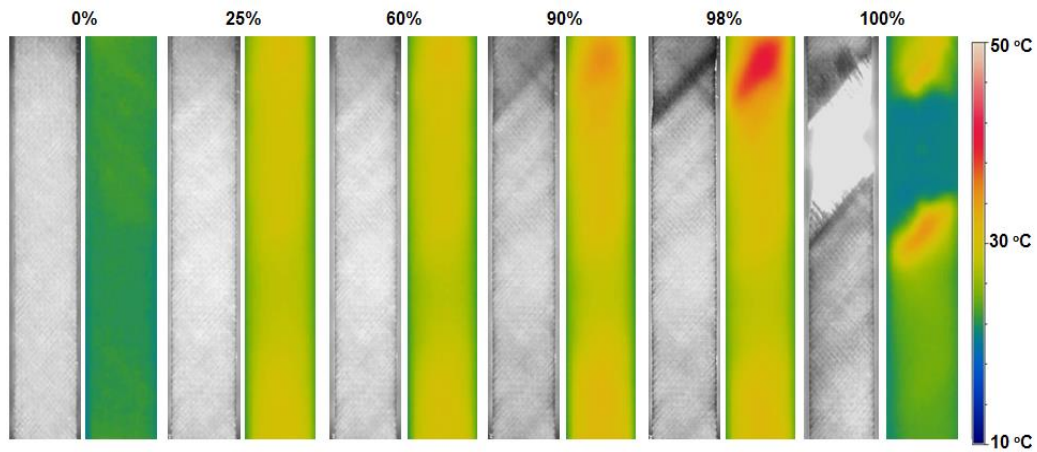


Fig. 3. Pairwise representation of light transmittance and the self-generated temperature in different percentages of fatigue life.

No.	Code	f (Hz)	N_f
5	Intf-0.1-64-a	4.68	5,961

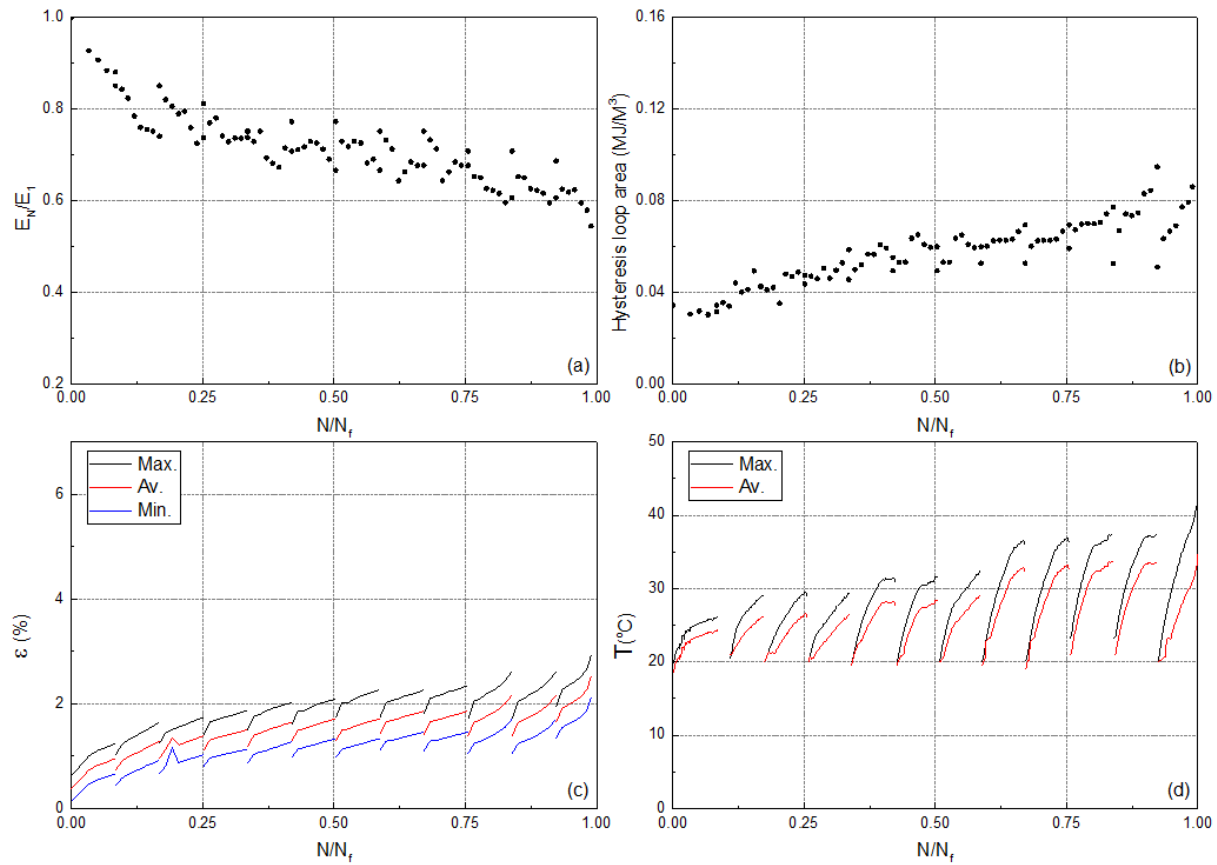


Fig. 1. Variation of (a) normalized fatigue stiffness, (b) hysteresis area, (c) maximum, average, and minimum cyclic strain, and (d) maximum and average self-generated temperature versus normalized number of cycles.

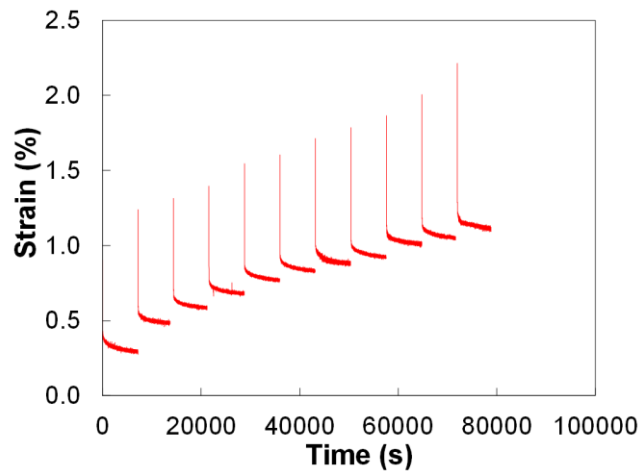


Fig. 2. Recovery curves during the interruptions.

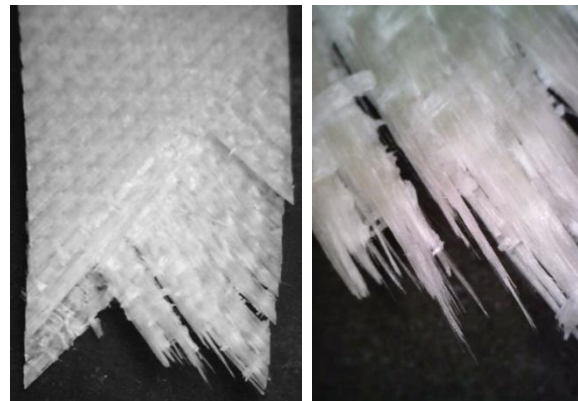


Fig. 3. Fatigue fracture surface.

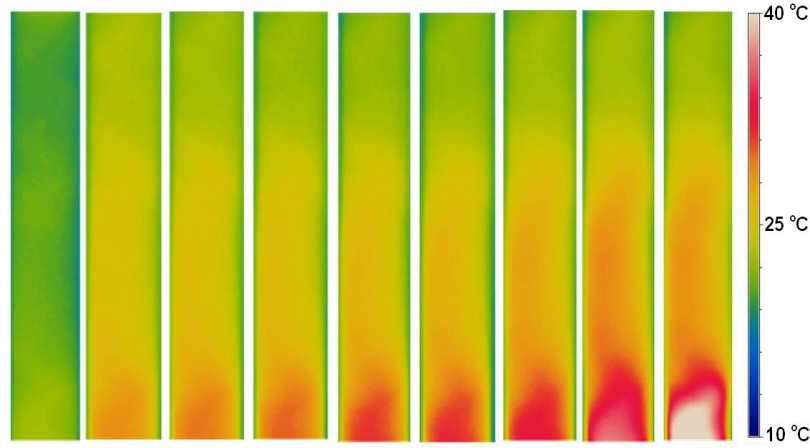


Fig. 4. Representation of the self-generated temperature in different percentages of fatigue life.

No.	Code	f (Hz)	N_f
6	Intf-0.1-64-b	4.68	3,943

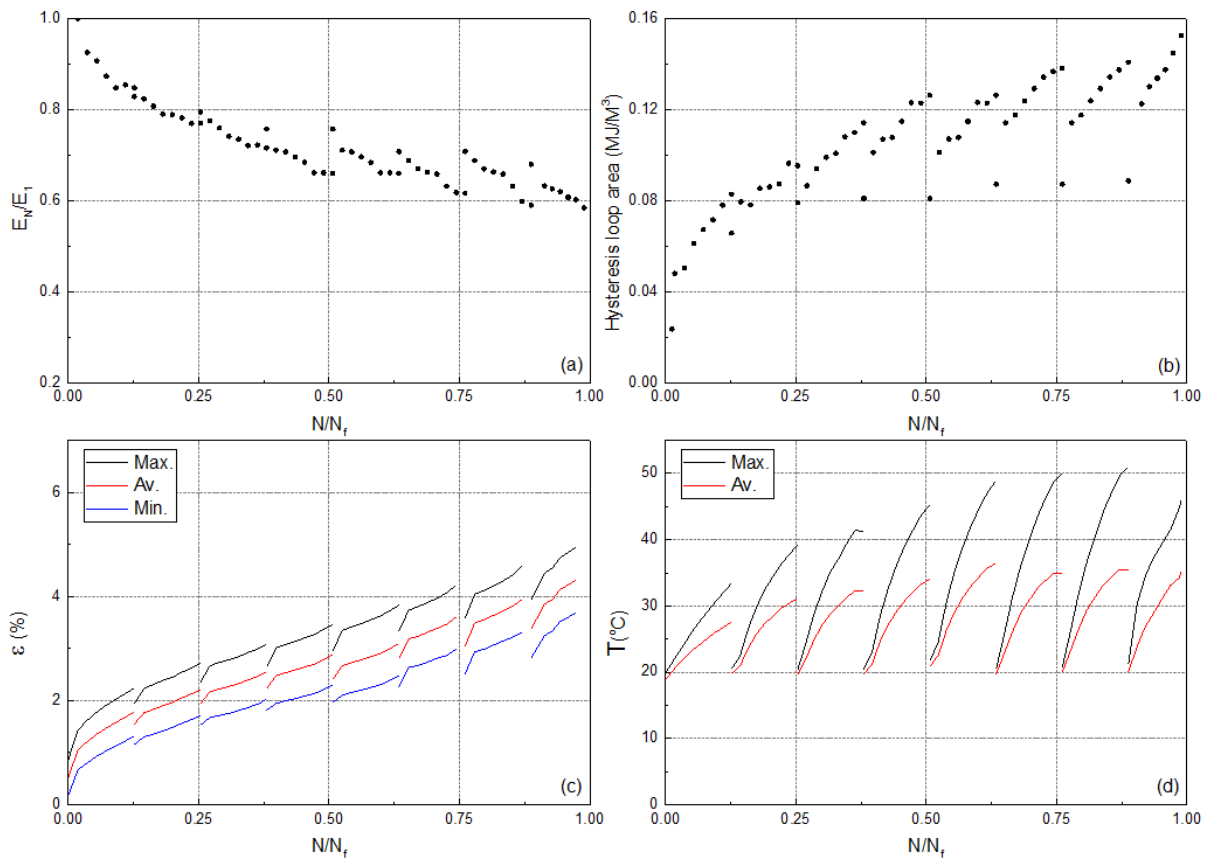


Fig. 1. Variation of (a) normalized fatigue stiffness, (b) hysteresis area, (c) maximum, average, and minimum cyclic strain, and (d) maximum and average self-generated temperature versus normalized number of cycles.

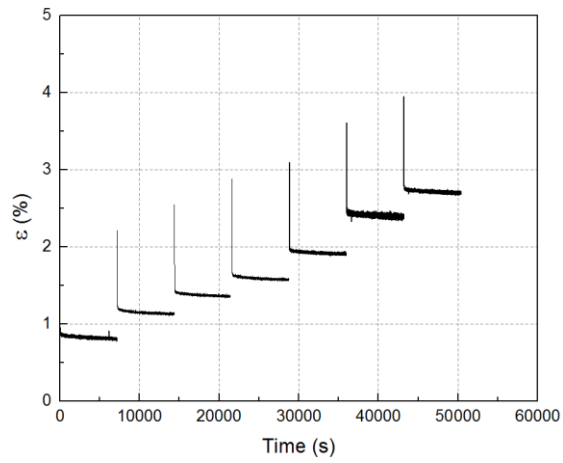


Fig. 2. Recovery curves during the interruptions.

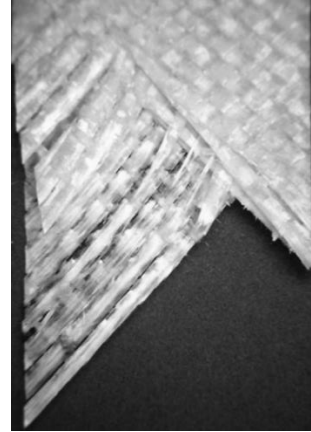


Fig. 3. Fatigue fracture surface.

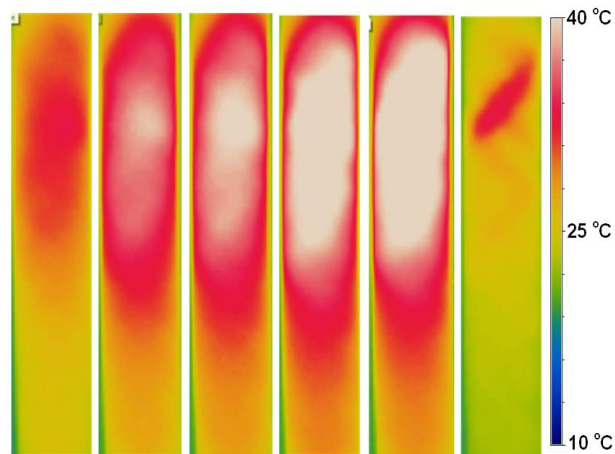


Fig. 4. Representation of the self-generated temperature in different percentages of fatigue life.

No.	Code	f (Hz)	N_f
7	Intf-0.1-64-c	4.68	6,225

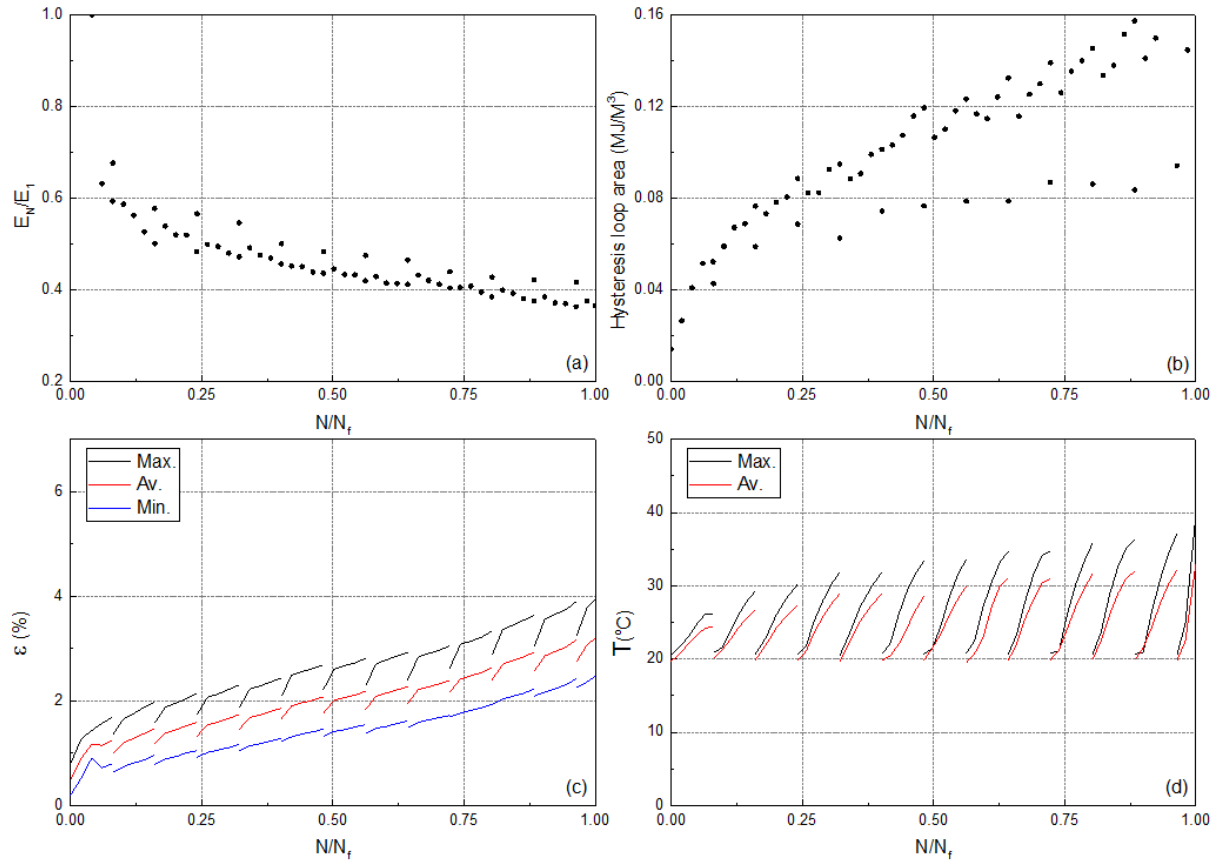


Fig. 1. Variation of (a) normalized fatigue stiffness, (b) hysteresis area, (c) maximum, average, and minimum cyclic strain, and (d) maximum and average self-generated temperature versus normalized number of cycles.

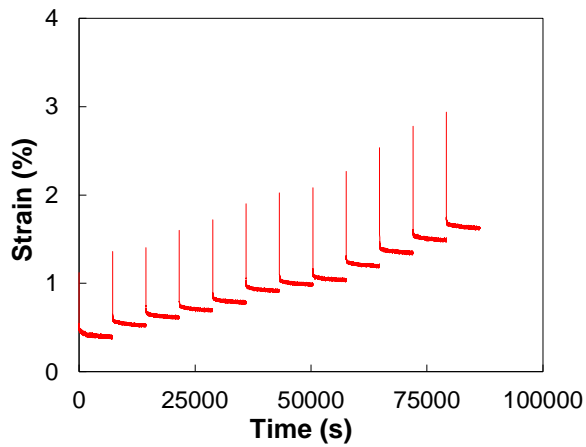


Fig. 2. Recovery curves during the interruptions.

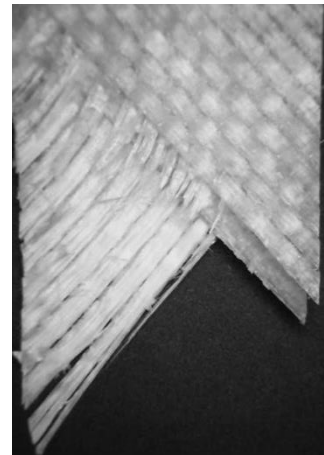


Fig. 3. Fatigue fracture surface.

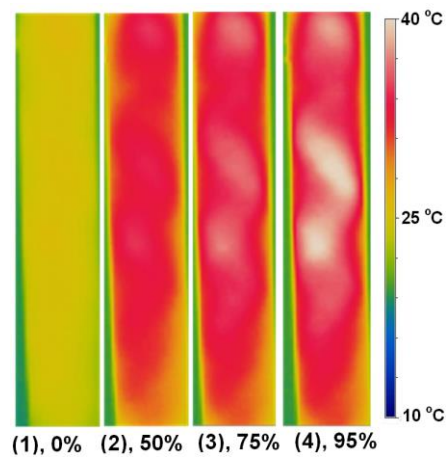


Fig. 4. Representation of the self-generated temperature in different percentages of fatigue life.

No.	Code	f (Hz)	N_f
8	Intf-0.1-64-d	4.68	7,542

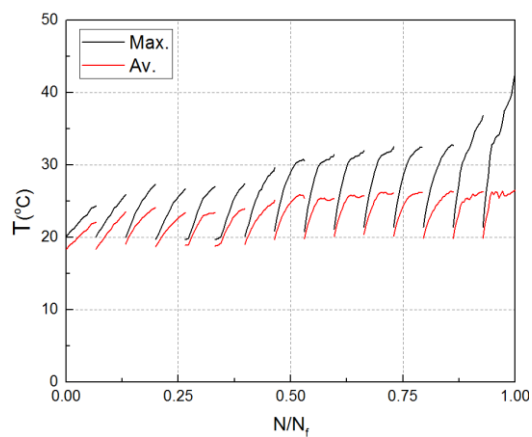


Fig. 1. Variation of maximum and average self-generated temperature.

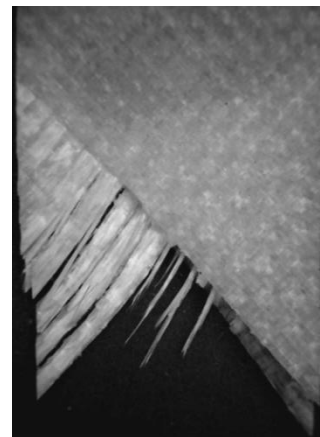


Fig. 2. Fatigue fracture surface.

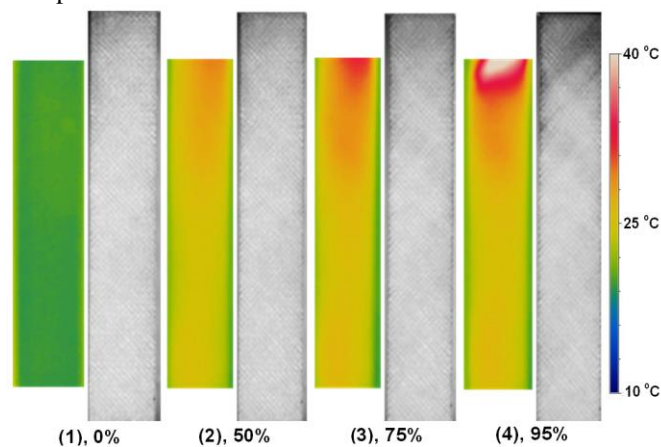


Fig. 3. Pairwise representation of light transmittance and the self-generated temperature in different percentages of fatigue life.

No.	Code	f (Hz)	N_f
9	Intf-0.1-58-a	5.06	22,854

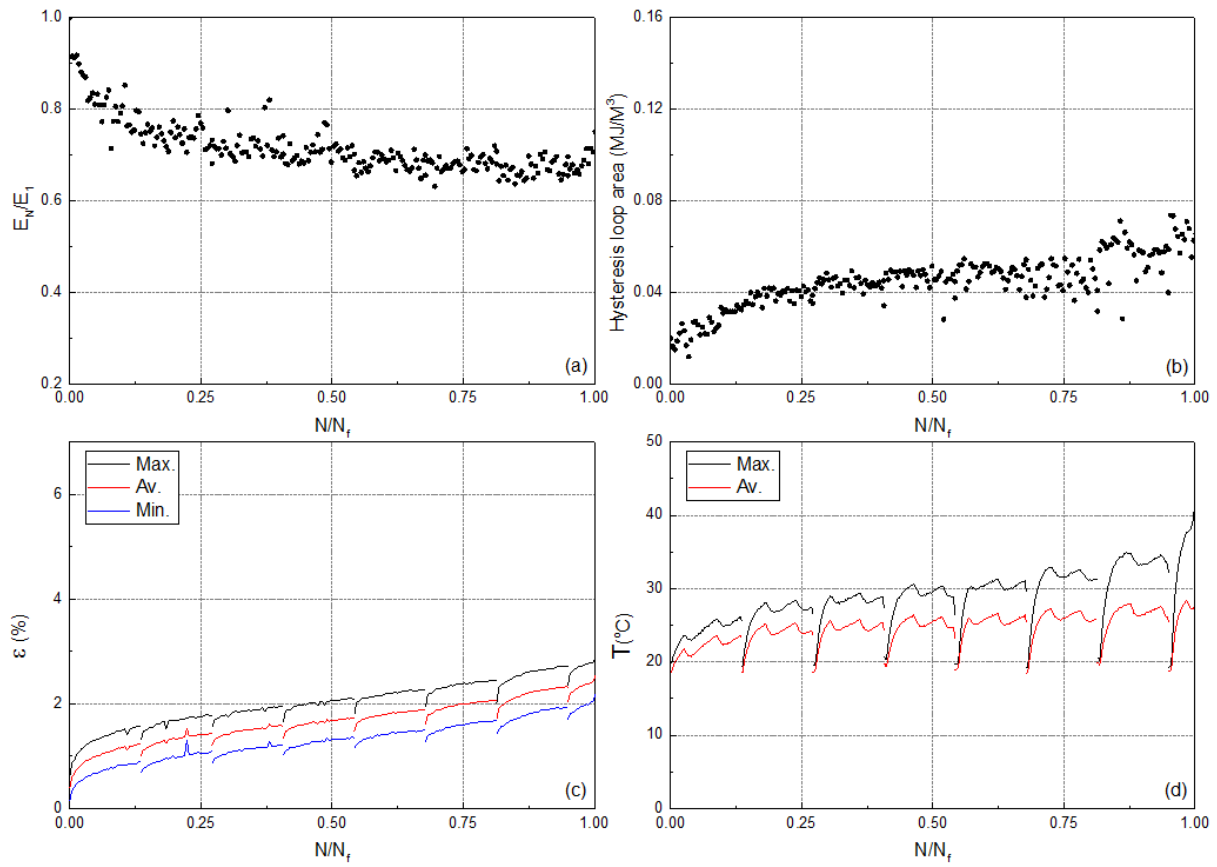


Fig. 1. Variation of (a) normalized fatigue stiffness, (b) hysteresis area, (c) maximum, average, and minimum cyclic strain, and (d) maximum and average self-generated temperature versus normalized number of cycles.

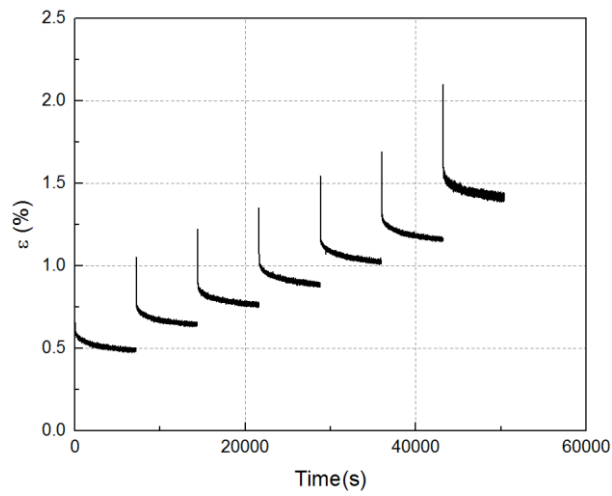


Fig. 2. Recovery curves during the interruptions.

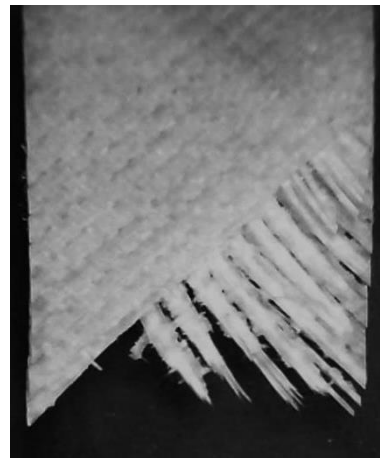


Fig. 3. Fatigue fracture surface.

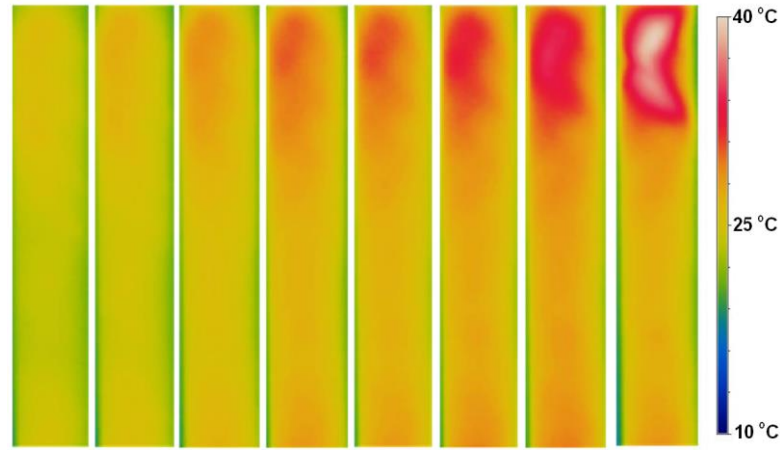


Fig. 4. Variation of maximum and average self-generated temperature.

No.	Code	f (Hz)	N_f
10	Intf-0.1-58-b	5.06	68,215

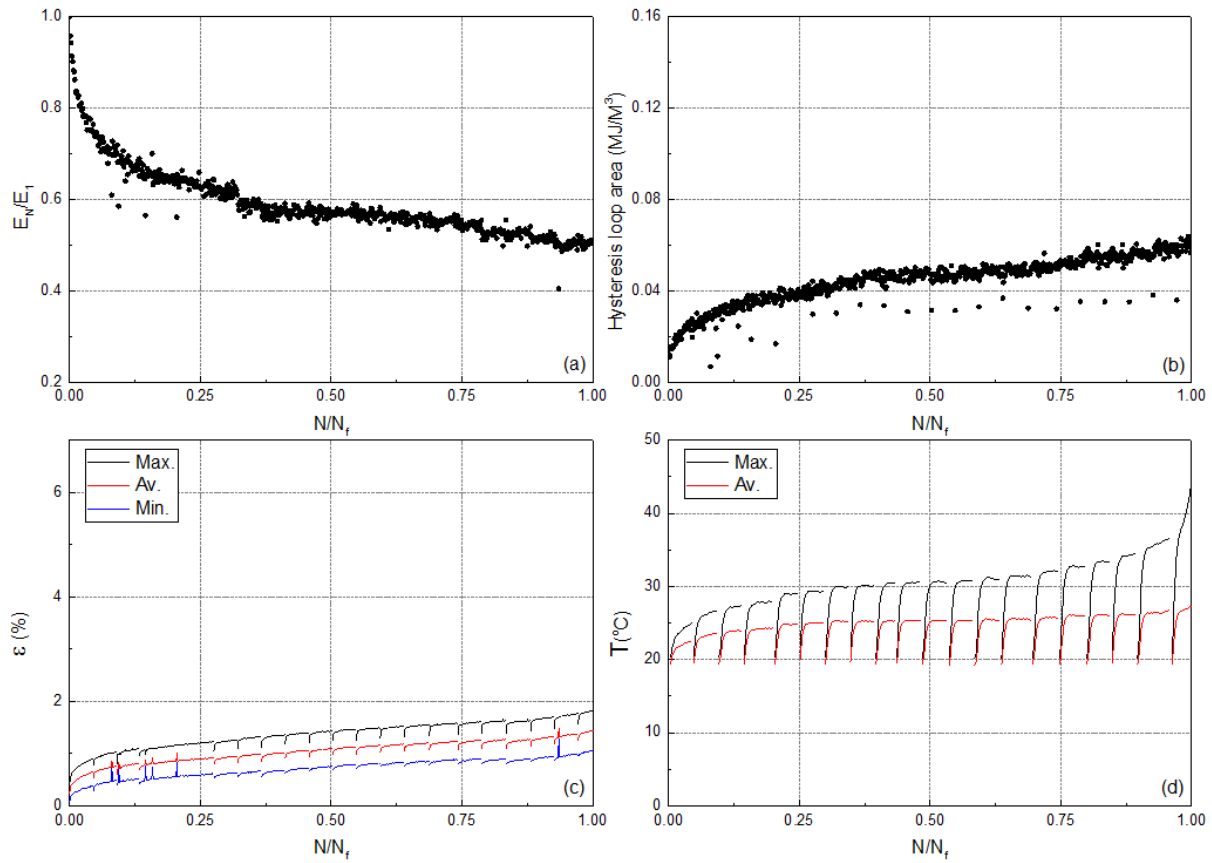


Fig. 1. Variation of (a) normalized fatigue stiffness, (b) hysteresis area, (c) maximum, average, and minimum cyclic strain, and (d) maximum and average self-generated temperature versus normalized number of cycles.

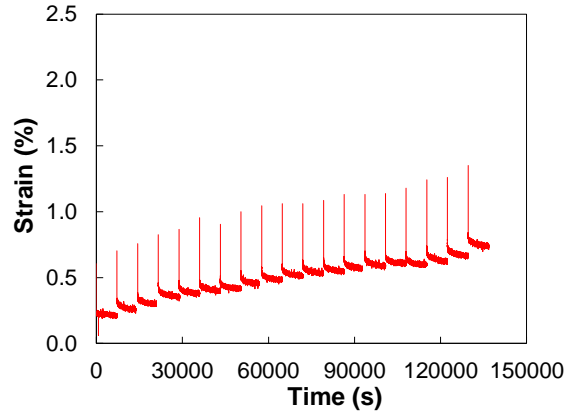


Fig. 2. Recovery curves during the interruptions.

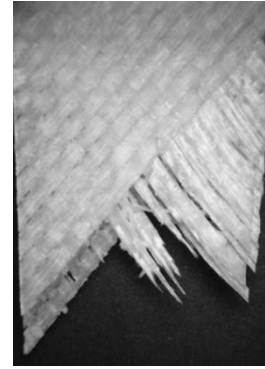


Fig. 3. Fatigue fracture surface.

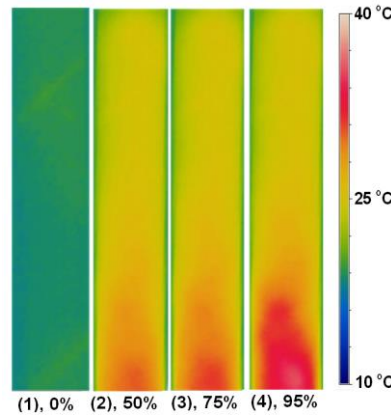


Fig. 4. Representation of the self-generated temperature in different percentages of fatigue life.

No.	Code	f (Hz)	N_f
11	Intf-0.1-58-c	5.06	46,055

No.	Code	f (Hz)	N_f
12	Intf-0.1-58-d	5.06	23,319

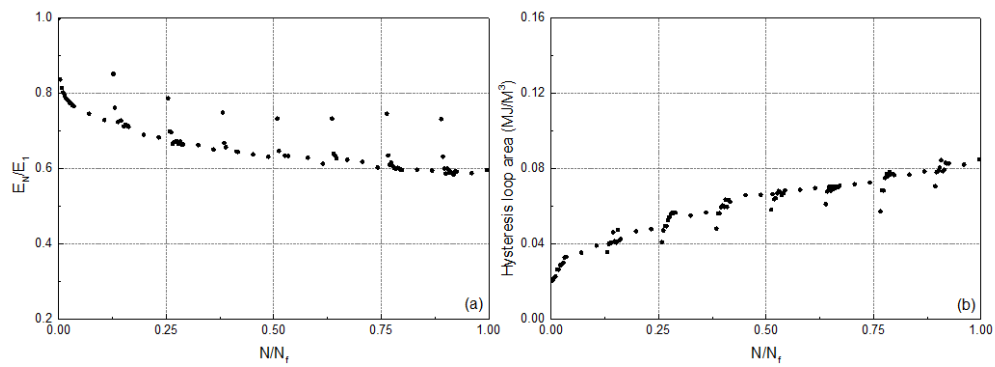


Fig. 1. Variation of (a) normalized fatigue stiffness and (b) hysteresis area versus normalized number of cycles.

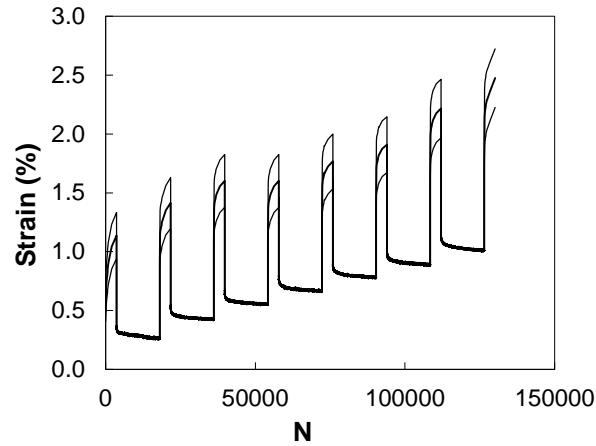


Fig. 2. Co-representation of maximum, average, and minimum fatigue strain followed by recovery strain.

No.	Code	f (Hz)	N_f
13	Intf-0.1-53-a	5.53	108,580

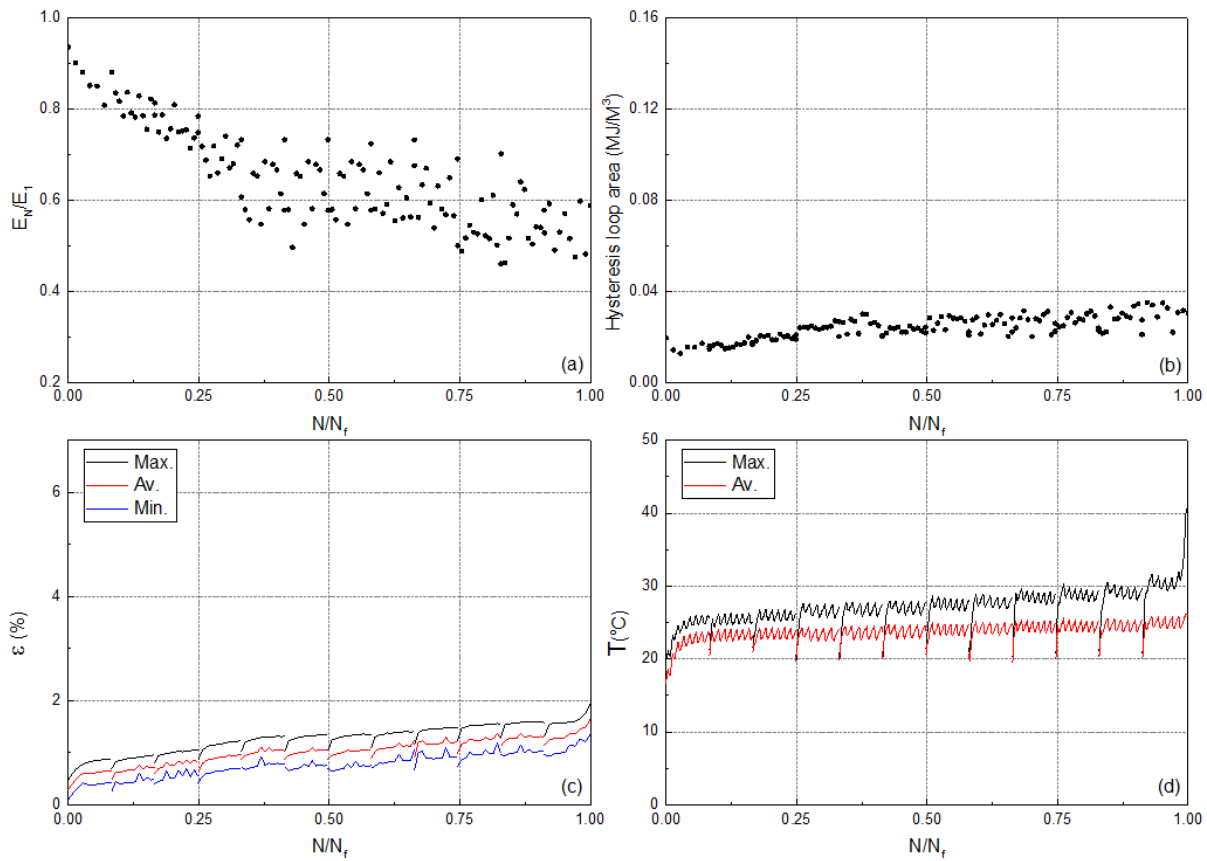


Fig. 1. Variation of (a) normalized fatigue stiffness, (b) hysteresis area, (c) maximum, average, and minimum cyclic strain, and (d) maximum and average self-generated temperature versus normalized number of cycles.

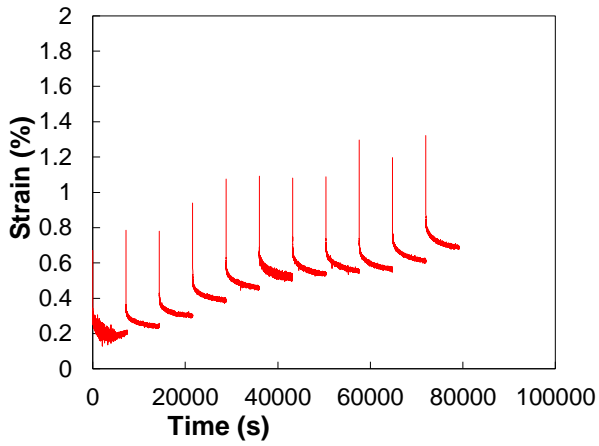


Fig. 2. Recovery curves during the interruptions.

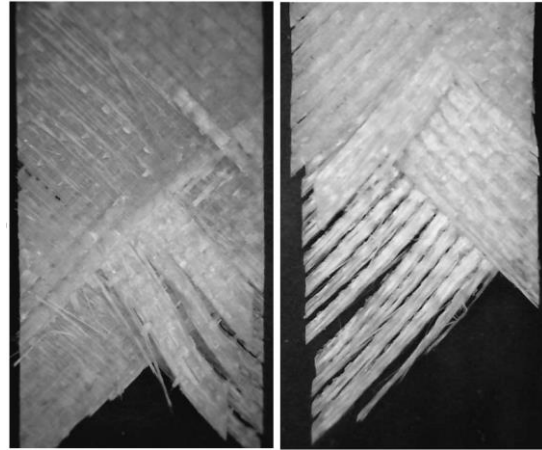


Fig. 3. Fatigue fracture surface.

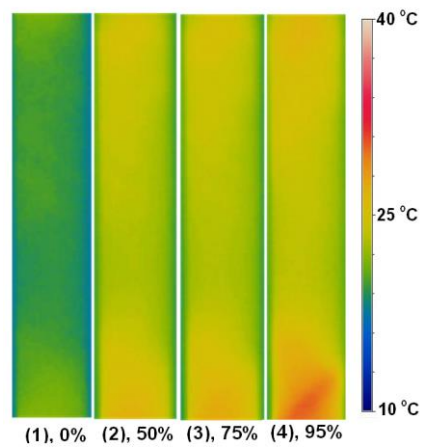


Fig. 4. Representation of the self-generated temperature in different percentages of fatigue life.

No.	Code	f (Hz)	N_f
14	Intf-0.1-53-b	5.53	75,054

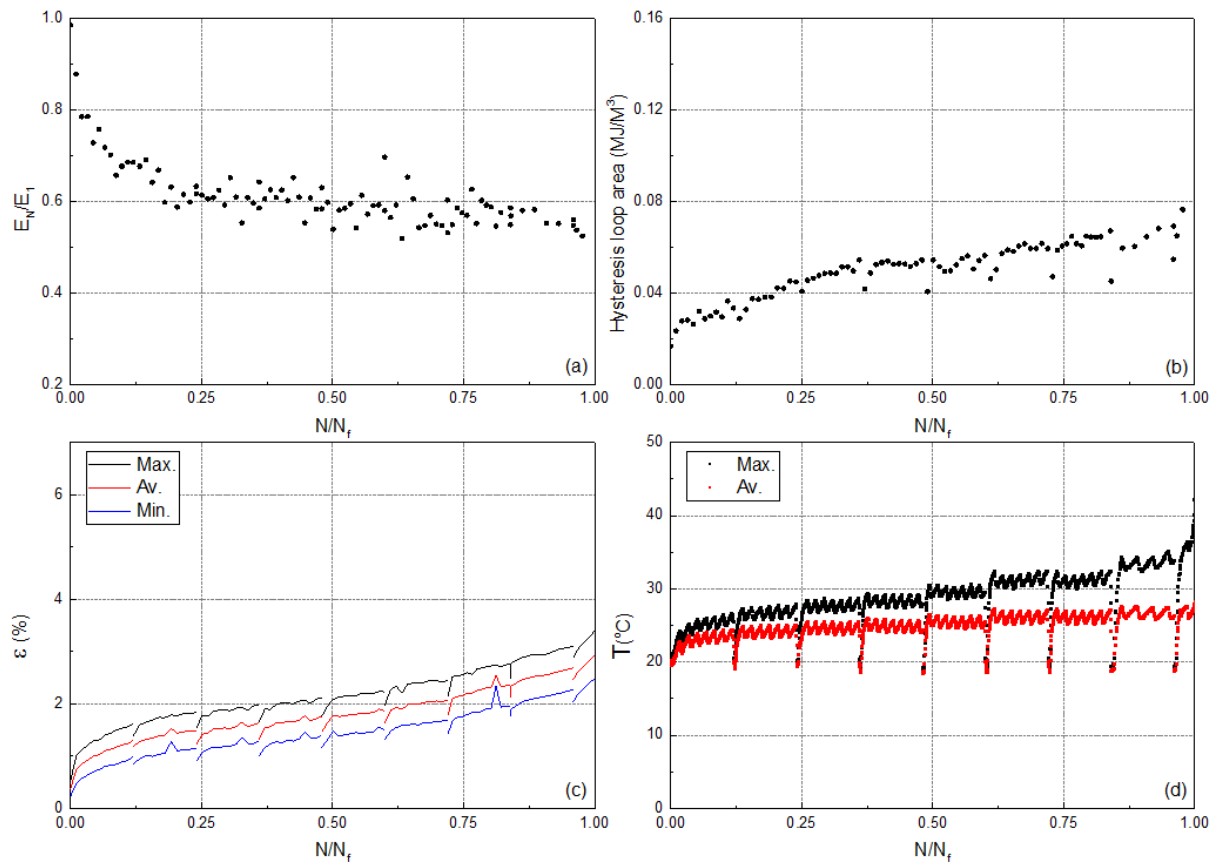


Fig. 1. Variation of (a) normalized fatigue stiffness, (b) hysteresis area, (c) maximum, average, and minimum cyclic strain, and (d) maximum and average self-generated temperature versus normalized number of cycles.

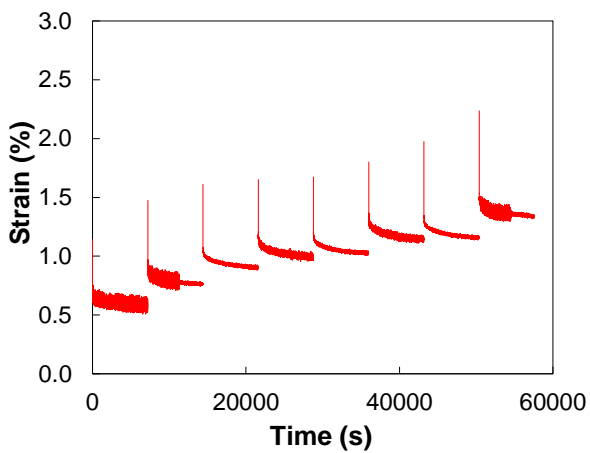


Fig. 2. Recovery curves during the interruptions.



Fig. 3. Fatigue fracture surface.

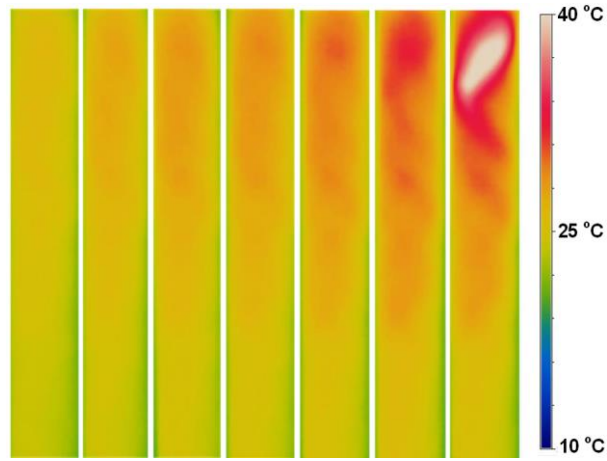


Fig. 4. Representation of the self-generated temperature in different percentages of fatigue life.

No.	Code	f (Hz)	N_f
15	Inf-0.1-53-c	5.53	209,355

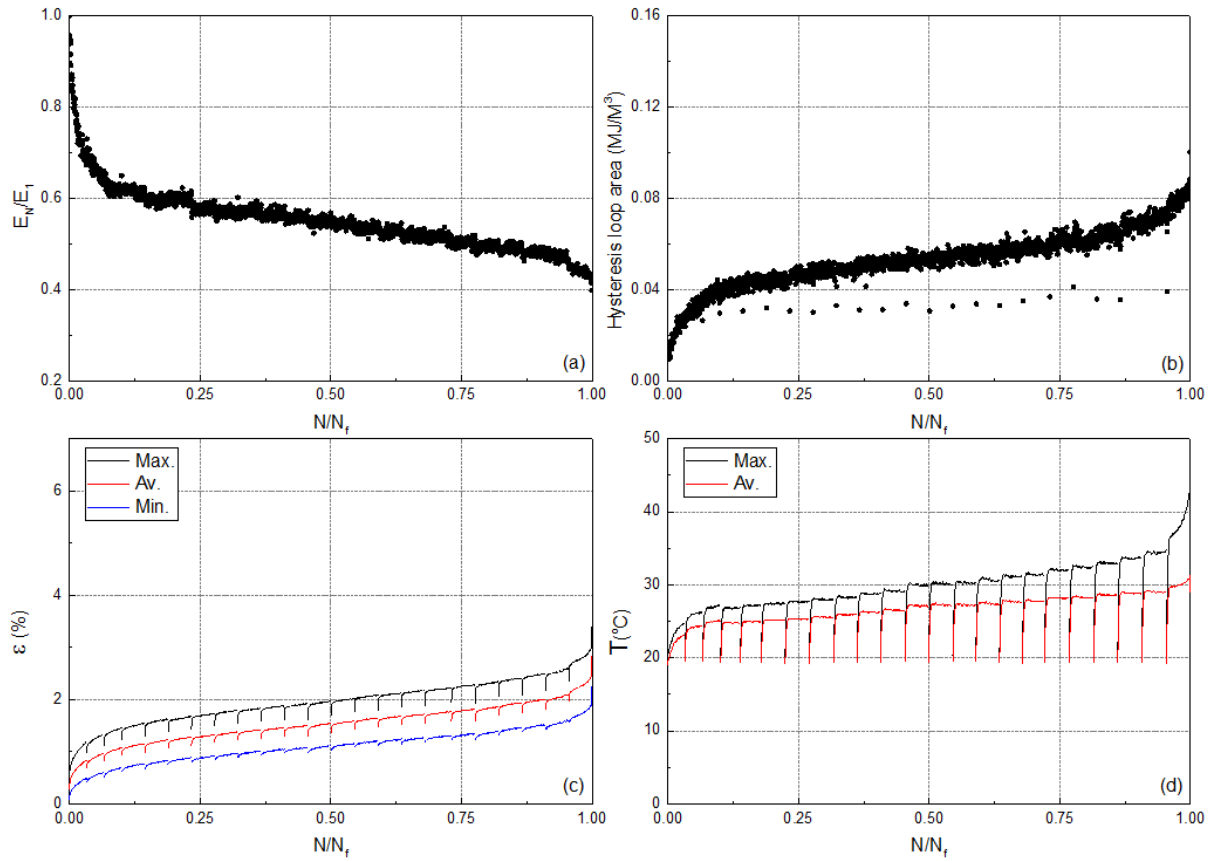


Fig. 1. Variation of (a) normalized fatigue stiffness, (b) hysteresis area, (c) maximum, average, and minimum cyclic strain, and (d) maximum and average self-generated temperature versus normalized number of cycles.

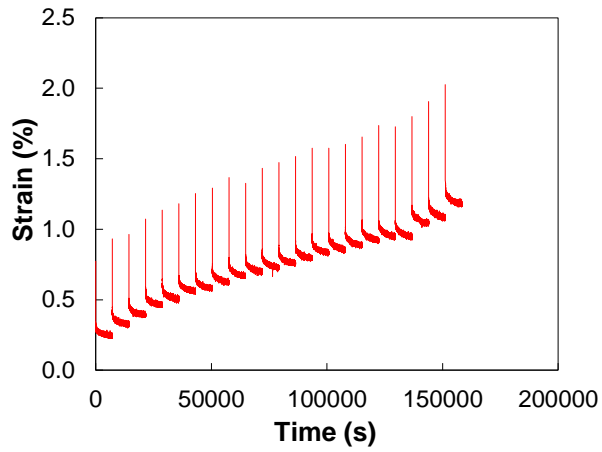


Fig. 2. Recovery curves during the interruptions.

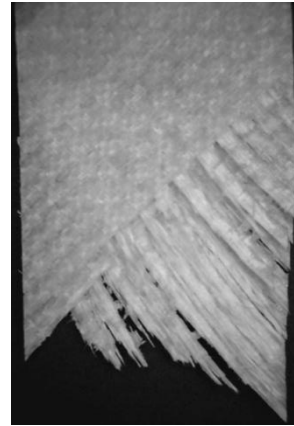


Fig. 3. Fatigue fracture surface.

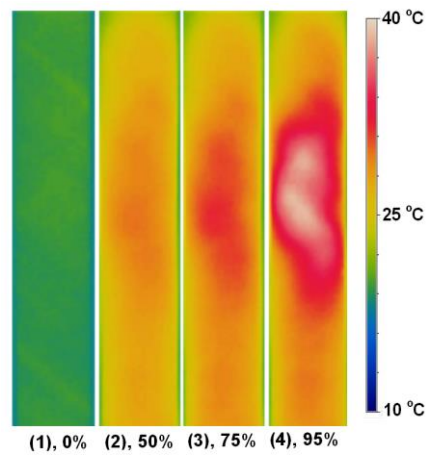


Fig. 4. Representation of the self-generated temperature in different percentages of fatigue life.

No.	Code	f (Hz)	N_f
16	Inf-0.1-53-d	5.53	57,463

No.	Code	f (Hz)	N_f
17	Intf-0.1-49-a	6.10	603,211

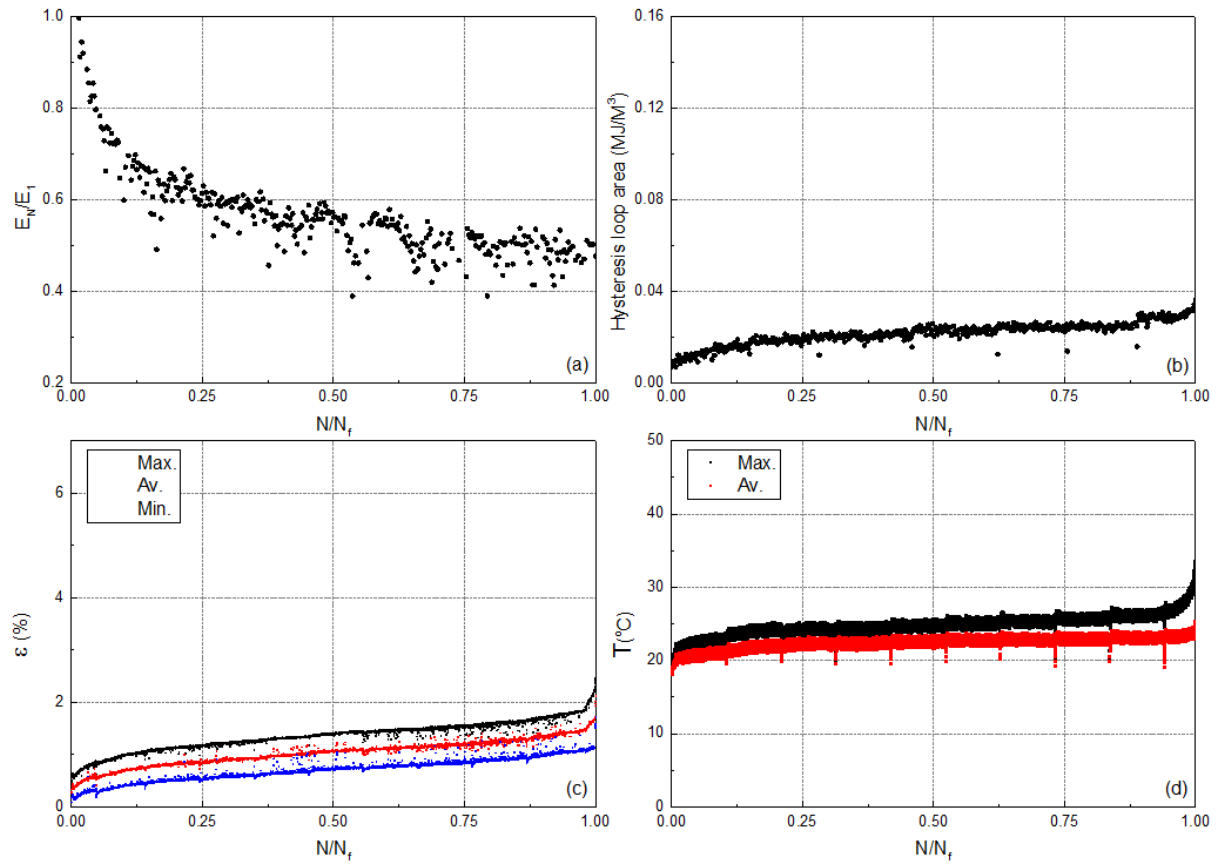


Fig. 1. Variation of (a) normalized fatigue stiffness, (b) hysteresis area, (c) maximum, average, and minimum cyclic strain, and (d) maximum and average self-generated temperature versus normalized number of cycles.

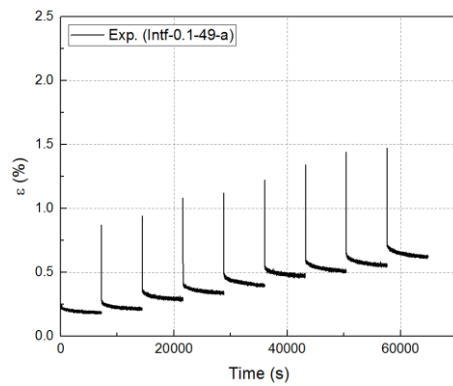


Fig. 2. Recovery curves during the interruptions.

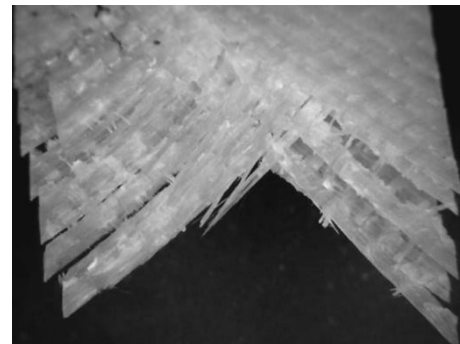


Fig. 3. Fatigue fracture surface.

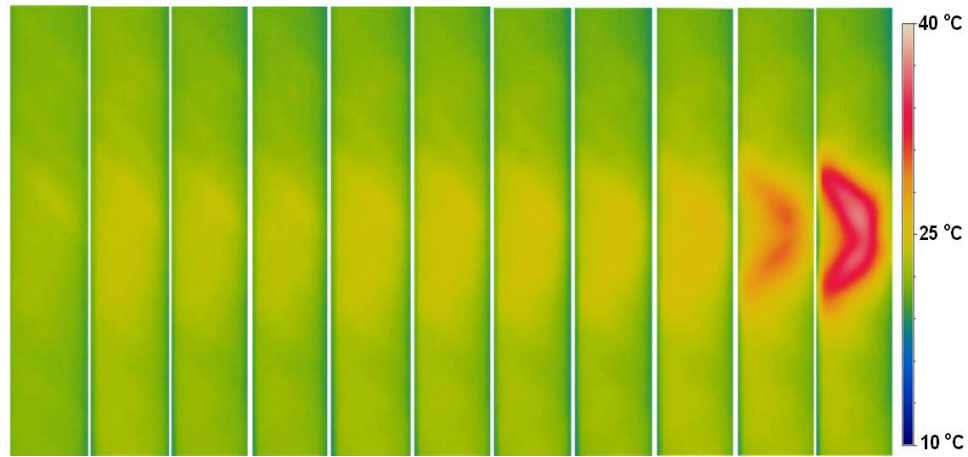


Fig. 4. Representation of the self-generated temperature in different percentages of fatigue life.

No.	Code	f (Hz)	N_f
18	Intf-0.1-49-b	6.10	475,331

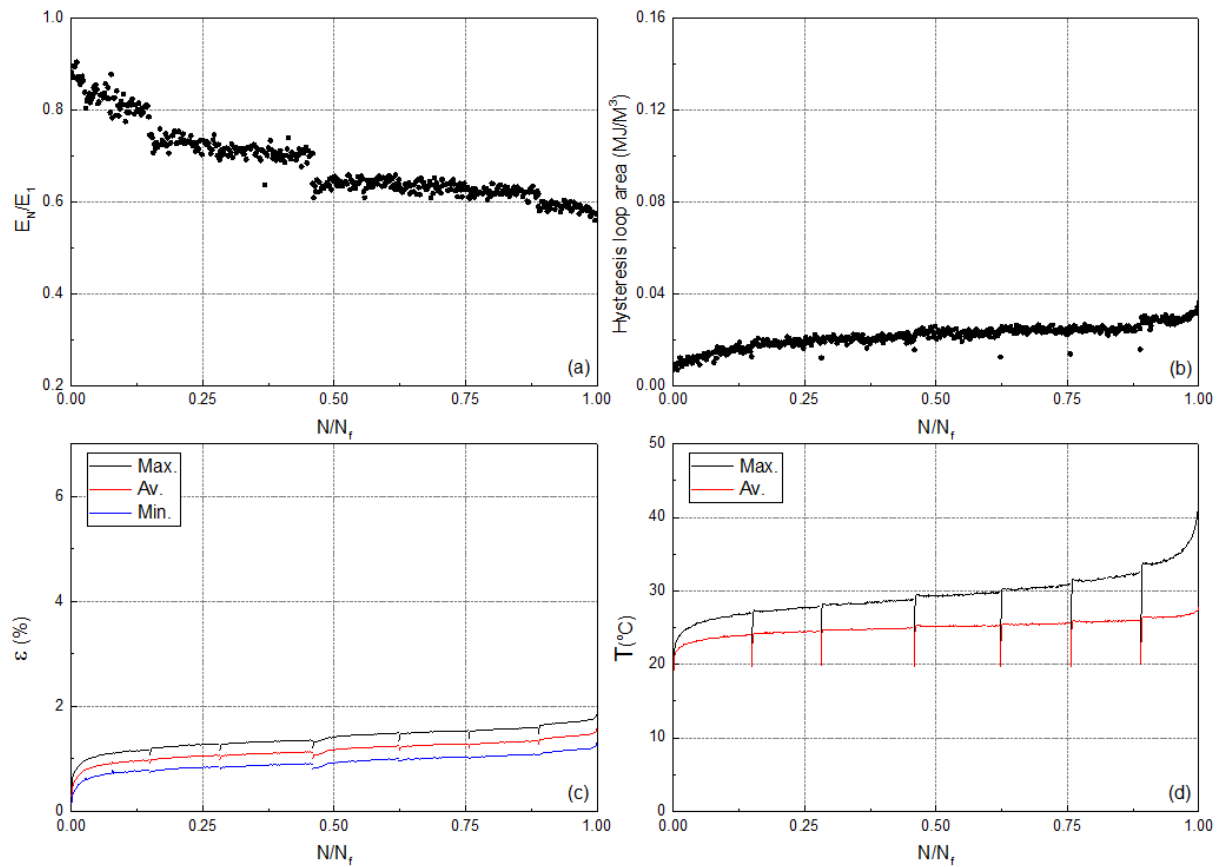


Fig. 1. Variation of (a) normalized fatigue stiffness, (b) hysteresis area, (c) maximum, average, and minimum cyclic strain, and (d) maximum and average self-generated temperature versus normalized number of cycles.

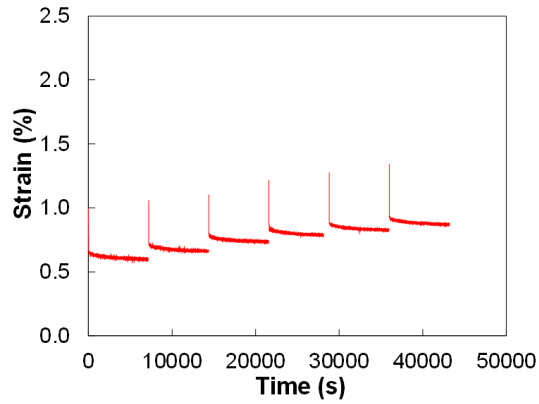


Fig. 2. Recovery curves during the interruptions.

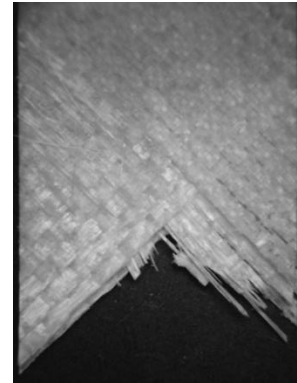


Fig. 3. Fatigue fracture surface.

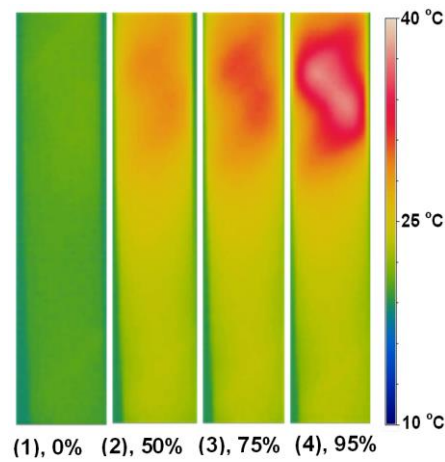


Fig. 4. Representation of the self-generated temperature in different percentages of fatigue life.

No.	Code	f (Hz)	N_f
19	Intf-0.1-49-c	6.10	472,542

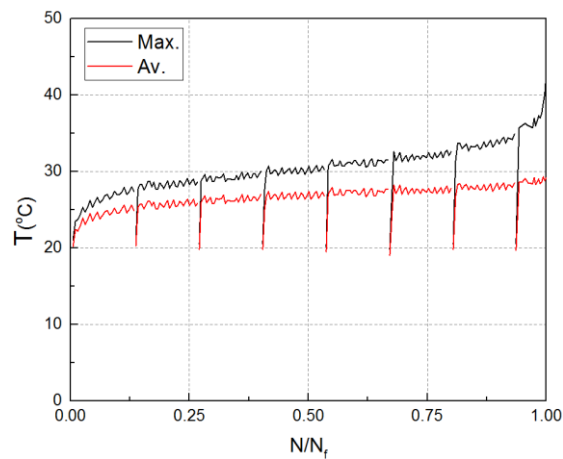


Fig. 1. Variation of maximum and average self-generated temperature.

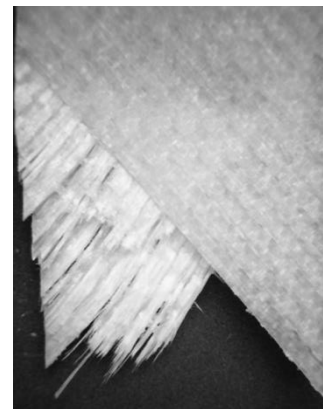


Fig. 2. Fatigue fracture surface.

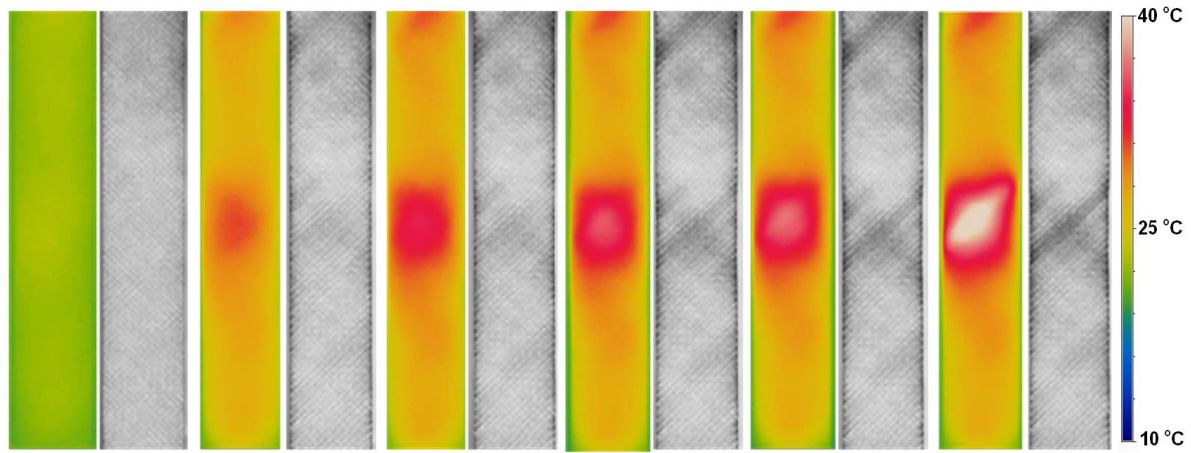


Fig. 3. Pairwise representation of light transmittance and the self-generated temperature in different percentages of fatigue life.

No.	Code	f (Hz)	N_f
20	Intf-0.1-49-d	6.10	229,854

No.	Code	f (Hz)	N_f
21	Conf-0.1-47-a	6.33	1,314,482

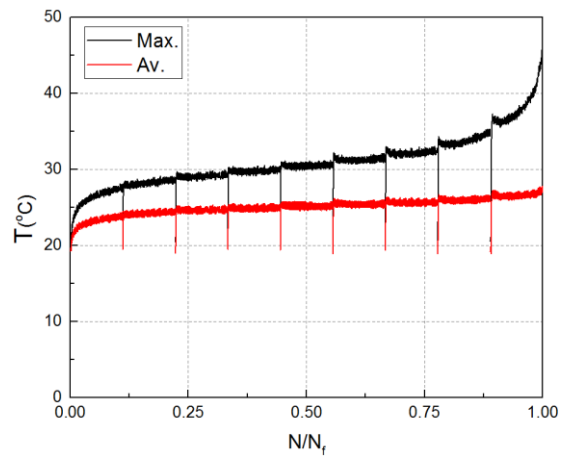


Fig. 1. Variation of maximum and average self-generated temperature.

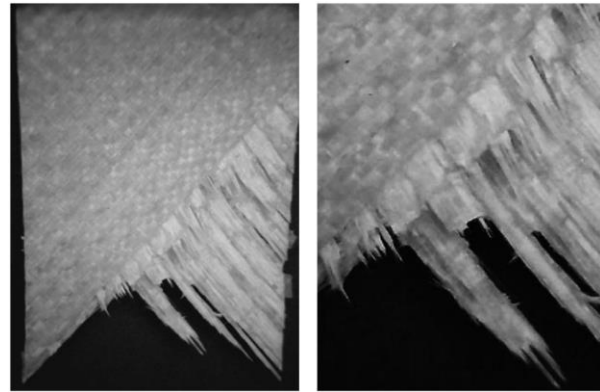


Fig. 2. Fatigue fracture surface.

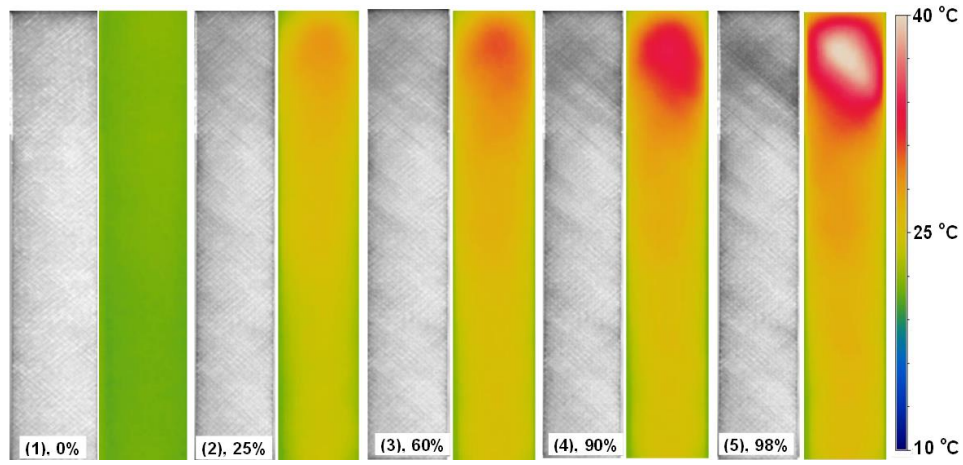


Fig. 3. Pairwise representation of light transmittance and the self-generated temperature in different percentages of fatigue life.

No.	Code	f (Hz)	N_f
22	Conf-0.1-47-b	6.33	1,360,621

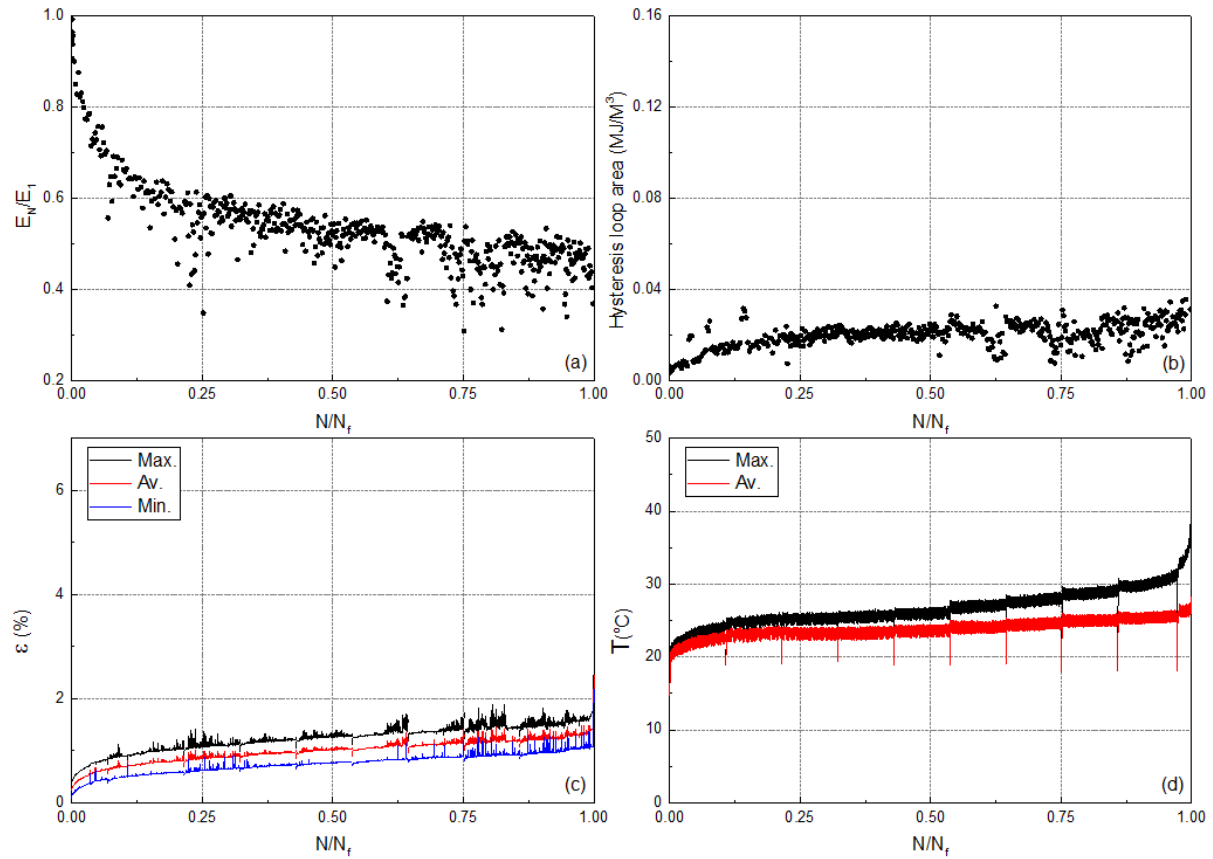


Fig. 1. Variation of (a) normalized fatigue stiffness, (b) hysteresis area, (c) maximum, average, and minimum cyclic strain, and (d) maximum and average self-generated temperature versus normalized number of cycles.

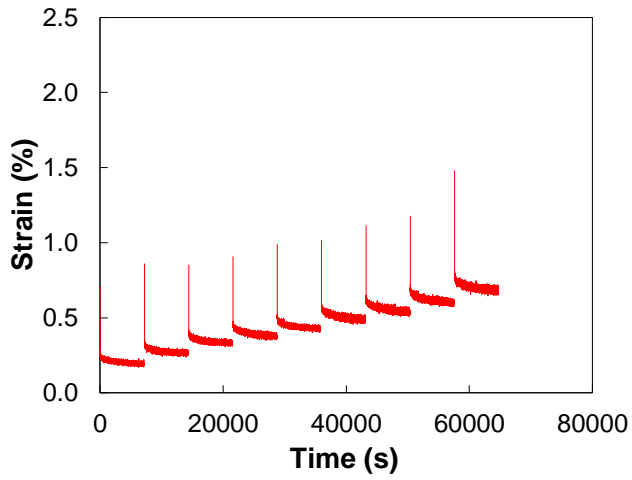


Fig. 2. Recovery curves during the interruptions.



Fig. 3. Fatigue fracture surface.

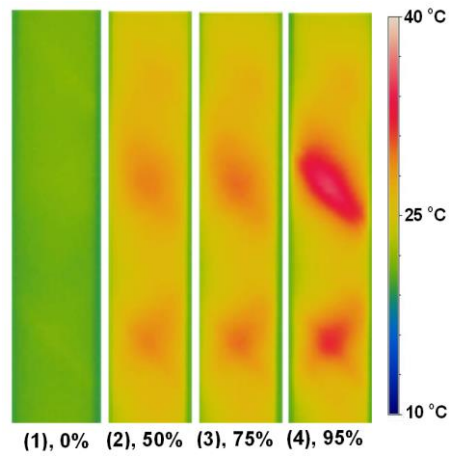


Fig. 4. Representation of the self-generated temperature in different percentages of fatigue life.

No.	Code	f (Hz)	N_f
23	Conf-0.1-47-c	6.33	521,024

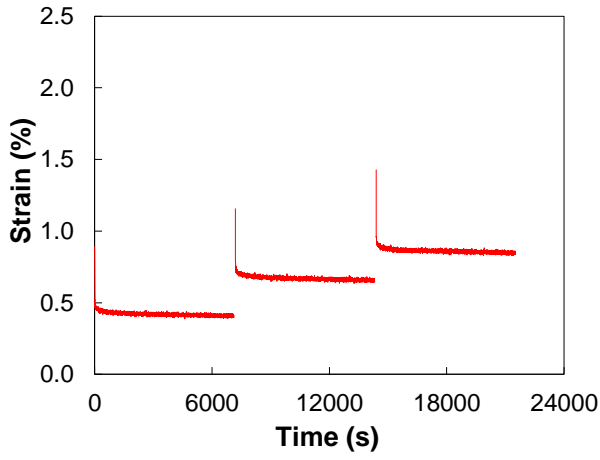


Fig. 1. Recovery curves during the interruptions.

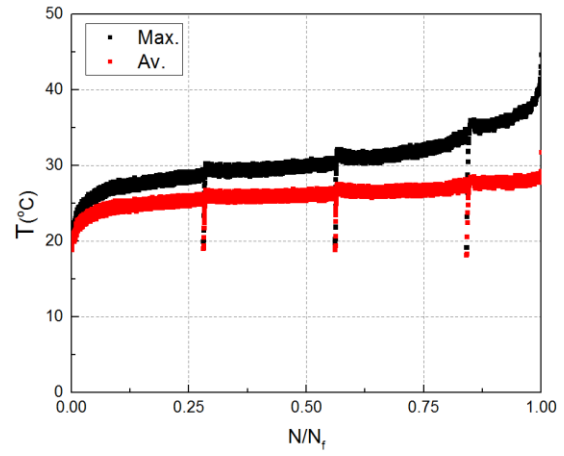


Fig. 2. Variation of maximum and average self-generated temperature.

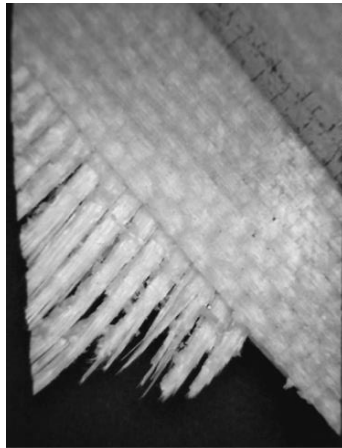


Fig. 3. Fatigue fracture surface.

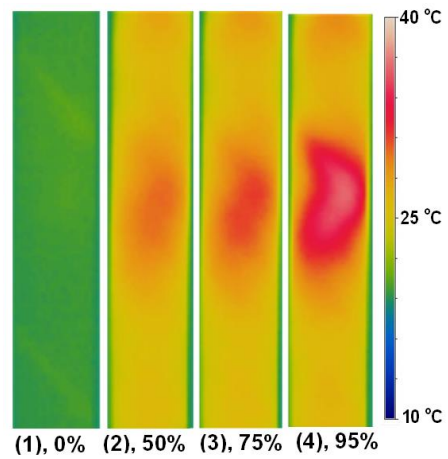


Fig. 4. Representation of the self-generated temperature in different percentages of fatigue life.

No.	Code	f (Hz)	N_f
24	Conf-0.1-47-d	6.33	469,501

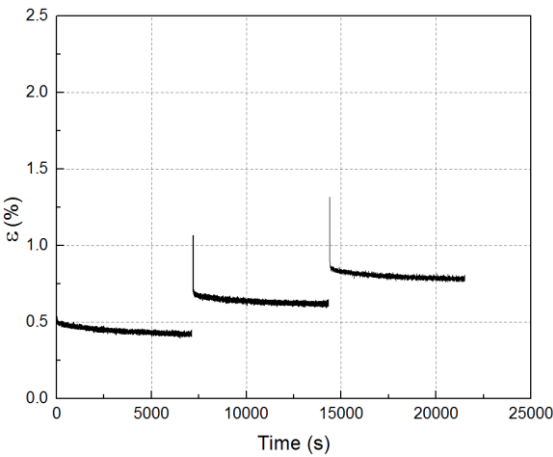


Fig. 1. Recovery curves during the interruptions.

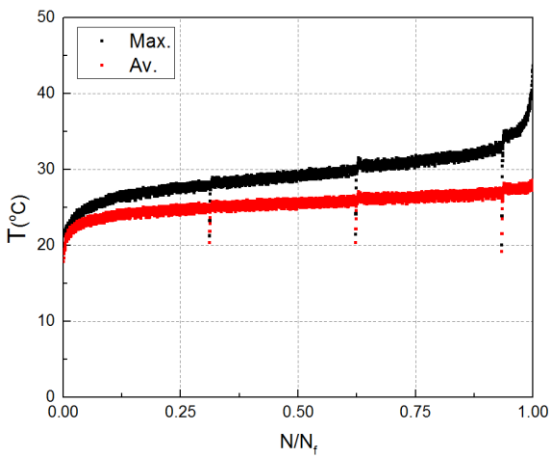


Fig. 2. Variation of maximum and average self-generated temperature.

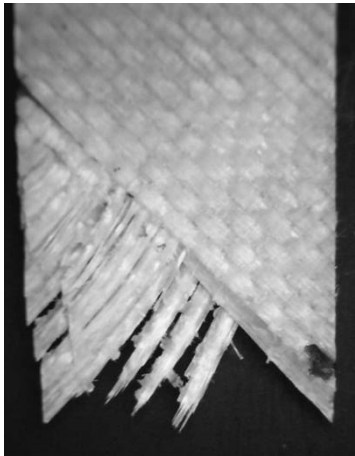


Fig. 3. Fatigue fracture surface.

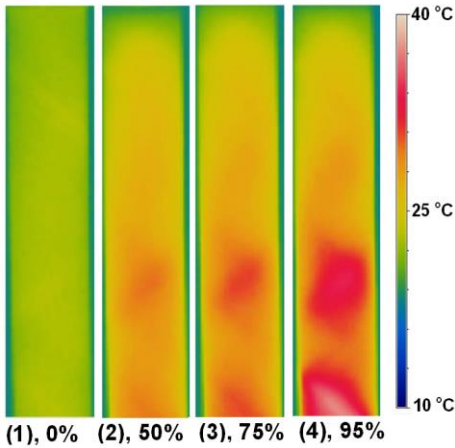


Fig. 4. Representation of the self-generated temperature in different percentages of fatigue life.

Annex E: DSC results



The glass transition temperature (T_g) and curing degree can be obtained by Differential Scanning Calorimetry (DSC) ^[1]. The thermal regime used is shown in Fig. E.1 in which, initially, temperature was reduced from laboratory temperature to 0°C after which it increased at the rate of 10°C/min up to 300°C under a nitrogen atmosphere. Subsequently, the temperature decreased again down to 0°C.

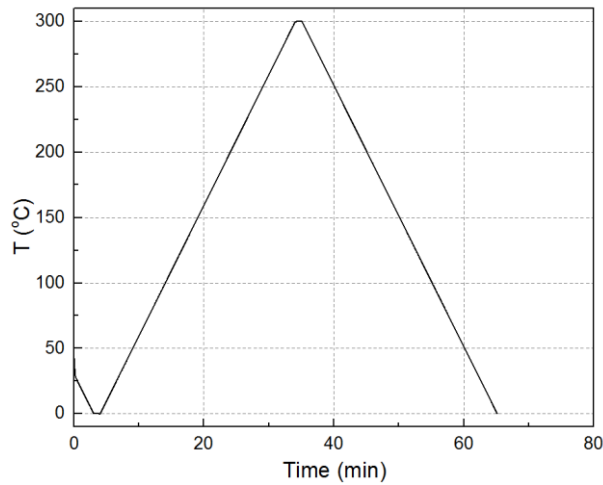


Fig. E.1. Applied thermal regime in DSC experiments.

After the laminate fabrication, small pieces were cut and placed in the oven for curing at a constant temperature of 70°C. Different times of 8 h, 40 h, and 100 h were selected and the obtained results are presented in Fig. E.2. It can be seen that as the temperature increased in all cases, the heat flow also increased and at around the temperature of 100°C, the area of the endothermic peak of the glass transition region, which is attributed to the enthalpy relaxation, was observed. It can be noted that no exothermic peak area of the residual heat related to the cross-linking reaction was observed, which proved that the specimens were in a fully cured condition after 8 h of curing.

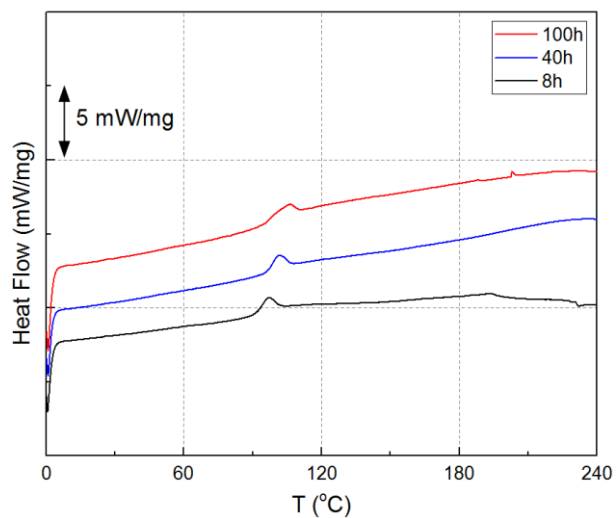


Fig. E.2. DSC response at different curing times.

Reference:

- [1] Barral, L., Cano, J., Lopez, J., Lopez-Bueno, I., Nogueira, P., Abad, M. J., & Ramirez, C. (2000). Physical aging of a tetrafunctional/phenol novolac epoxy mixture cured with diamine. DSC and DMA measurements. *Journal of thermal analysis and calorimetry*, 60(2), 391-399.

Annex F: Localized measurements of strain in creep-fatigue experiment



As shown in Chapters 2-5, damage distribution was not uniform across the specimen surface. To investigate the effect of the mentioned non-uniform localized damage distribution on creep behavior, localized strains were measured during the creep-fatigue experiment with 2-h hold time. Fig. F.1 shows the specimen on which four lines were marked and three strain measurements were recorded. The experimental design and corresponding loading pattern in the creep-fatigue experiment were fully explained in Chapter 4.

Fig. F.2 shows the average self-generated temperature of localized zones for the specimen loaded under $\sigma_{\max}=68$ MPa. It can be seen that as the number of cycles increased, the average temperature obtained from Measurement 1 was the highest, which indicated that the damage level was greater in this zone. However, the lowest self-generated temperature was obtained from Measurement 3, proving that the damage level was lowest in this zone.

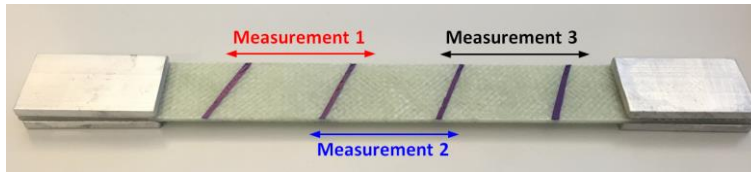


Fig. F.1. Representation of three localized strain measurements.

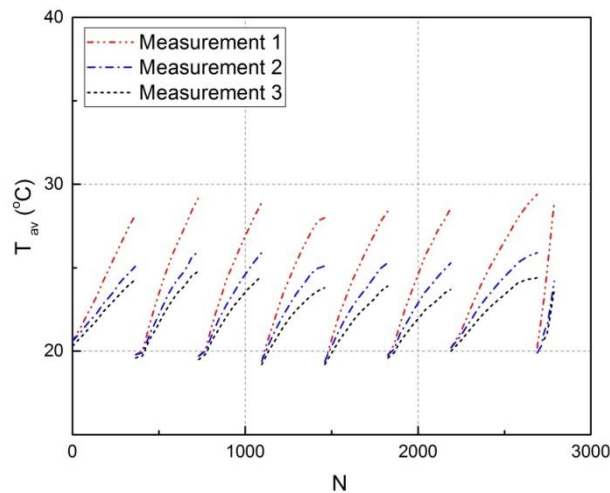


Fig. F.2. Evolution of average temperature in areas defined in Fig. F.1.

In fully cured thermoset polymers, the molecular chains were cross linked, however the applied deformation enhanced the mobility of the materials, enabling the structure to accommodate the strain; although their mobility in the case of greater deformation was limited ^[2,3]. The greater deformation at higher stress levels or longer creep times in tension creep was made possible via the crazing formation. In addition, when the specimen was damaged, as a result of local stresses in the vicinity of the craze, the molecular chains became even more mobilized, which led to more viscoelastic deformation ^[4]. The evolution of the strain measurements in defined zones during the creep phase of the loading pattern are shown in Fig. F.3. The obtained results indicated that the creep behavior was a function of the damage level, and the creep strain obtained from Measurement 1, which was the region with the greatest amount of damage, was the largest. However, in Measurement 3, which corresponded to the zone with the least amount of damage, the magnitude of creep strain was the lowest. Therefore, it was concluded that the accumulated damage facilitated viscoelastic deformation.

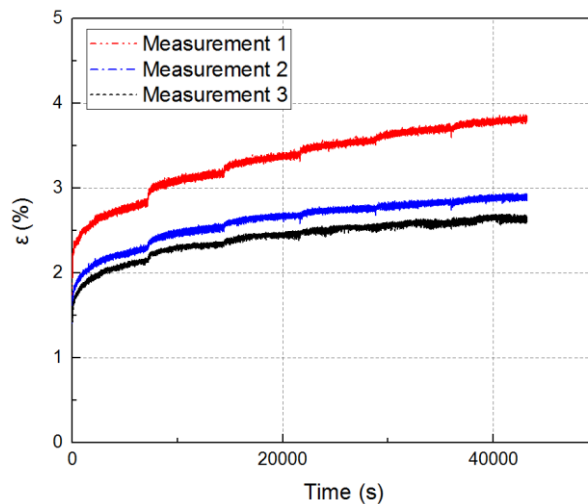


Fig. F.3. Evolution of strain in defined areas in Fig. F.1.

References:

- [1] Caruthers, J. M., Adolf, D. B., Chambers, R. S., & Shrikhande, P. (2004). A thermodynamically consistent, nonlinear viscoelastic approach for modeling glassy polymers. *Polymer*, 45(13), 4577-4597.
- [2] Odegard, G. M., and A. Bandyopadhyay. "Physical aging of epoxy polymers and their composites." *Journal of Polymer Science Part B: Polymer Physics* 49.24 (2011): 1695-1716.
- [3] Berger, L. L., & Kramer, E. J. (1987). Chain disentanglement during high-temperature crazing of polystyrene. *Macromolecules*, 20(8), 1980-1985.

Annex G: Study the effect of damage on viscoelasticity using DMA



Single cantilever Dynamic Mechanical Analysis (DMA) was used to obtain the temperature-dependent viscoelastic properties i.e. storage and loss modulus, and the glass transition temperature. To study the effect of damage on the viscoelastic behavior, DMA experiments were first conducted on the virgin specimen and the results obtained were considered as the reference values. A continuous fatigue experiment with $\sigma_{\max}=68$ MPa was then conducted and after failure, specimens were cut at different distances from the fracture surface. Fig. G.1 shows the IR thermal image shortly before the fatigue failure, and the locations from which the DMA specimens were cut. Different self-generated temperatures implied different damage levels. Therefore, it was considered that the specimens, depending on their distance from the fracture surface, had undergone a different degree of damage.

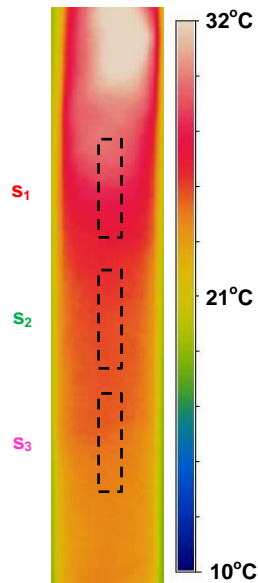


Fig. G.1. (a) An infrared (IR) thermal image with regions selected for three DMA experiments.

Fig. G.2 shows the evolution of the storage modulus against temperature in virgin and damaged specimens. In the glassy state, the storage modulus was higher in the virgin specimen and as the damage level increased, the storage modulus dropped further as indicated in the figure. As the temperature increased, the differences between the specimens with the different damage levels became fewer. It was observed that, at the end of the glass transition region at temperatures higher than 100°C as well as in the rubbery region, the magnitude of the storage modulus became independent of the damage level.

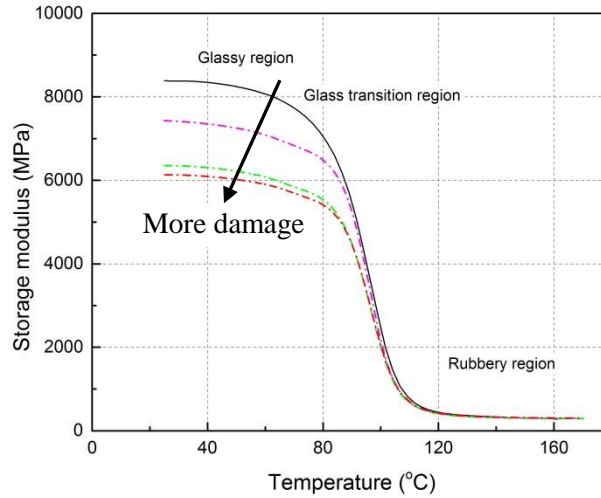


Fig. G.2. Evolution of storage modulus versus temperature in virgin and damaged specimens.

The evolution of the loss modulus and $\tan(\delta)$ versus temperature is shown in Fig. G.3 and Fig. G.4, respectively. Comparison of these two figures shows that the loss modulus and $\tan(\delta)$ behaved very similarly. In the glassy state, comparison of the loss modulus of the virgin and damaged specimens showed that the higher damage level led to a greater loss modulus in the glassy state. However, as the temperature increased beyond the loss modulus peak at 95°C, which was attributed to the T_g temperature, the difference between the curves gradually lessened and totally disappeared in the rubbery state.

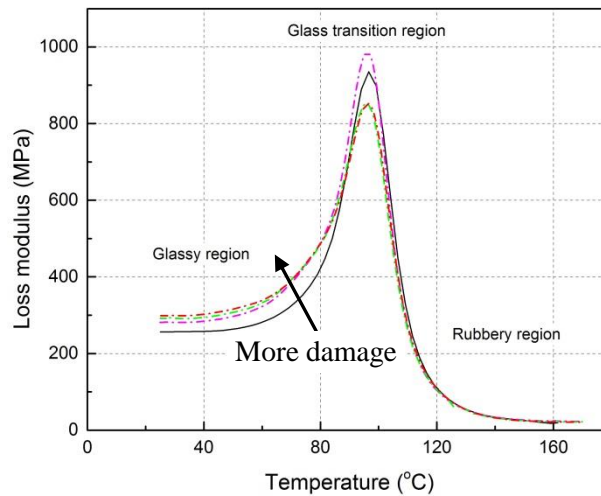


Fig. G.3. Evolution of loss modulus versus temperature in virgin and damaged specimens.

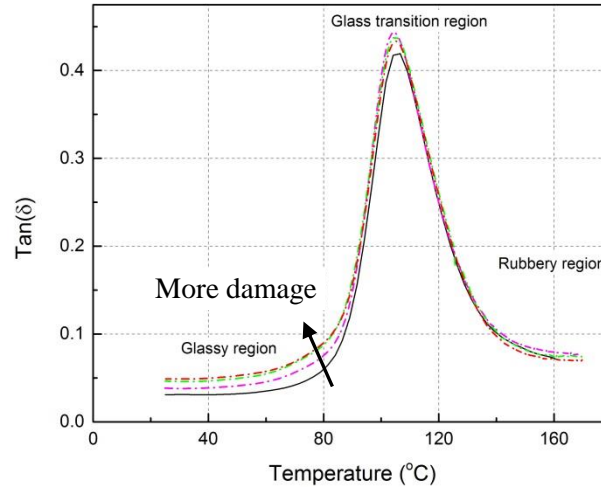


Fig. G.4. Evolution of $\tan(\delta)$ versus temperature in virgin and damaged specimens.

The variation of the T_g temperature according to different definitions is shown in Fig. G.5. It was observed that according to all definitions, the damage level did not change the T_g temperature. T_g values based on the definition of the storage and loss moduli curves were similar; however, T_g values according to the definition in the $\tan(\delta)$ graph were greater. In addition, it was observed that the $T_{g,\text{onset}}$ increased when the damage level increased.

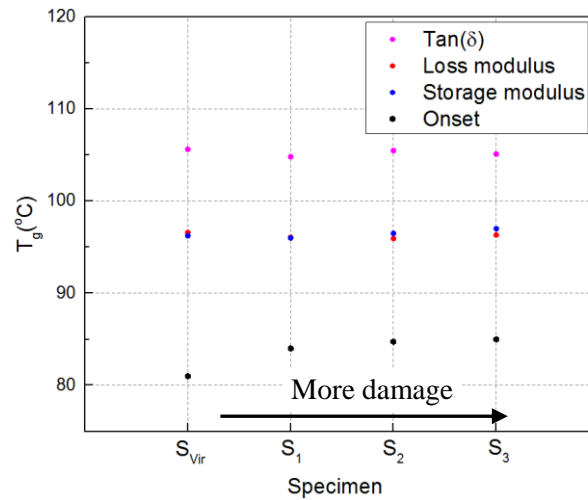


Fig. G.5. Evolution of T_g temperature in virgin and damaged specimens with different definitions.

Annex H: Experimental study of crack blunting effect in viscoelastic media



The crack in viscoelastic media has been of great interest due to the formation of crazes and the complexity in the stress state ^[5]. Fig. H.1 shows a schematic representation of a notched crack and two possible regions *A* and *B* for studying the crack behavior in viscoelastic media. Element *A* symbolized a craze zone at the crack tip with a higher stress intensity factor and *B* signified a region with much less damage and a lower stress intensity factor. As asserted in Chapter 5, by unloading the stress level from σ_m to zero level in the damaged viscoelastic matrix, the local stress intensity in the craze zone at the crack tip significantly decreased and did not increase again at the same rate in the following loading block.

In order to experimentally examine the crack-blunting effect in viscoelastic materials, the interrupted-fatigue experiments were carried out, as explained in Chapter 5. The cyclic creep of specimens during the reloading phase was compared at different damage and stress levels but a similar number of cycles per block and frequency. The first specimen was cyclically loaded at a high stress level ($\sigma_{\max}=68$ MPa) to model the higher damage level and stress intensity factor (point *A*). While in the second specimen, the damage level and stress level were lower ($\sigma_{\max}=47$ MPa) and were used to simulate the damage and stress state in a region distant from the crack tip (point *B*). In both specimens, the number of cycles per block was 365 and the applied frequency was 4.35 Hz.

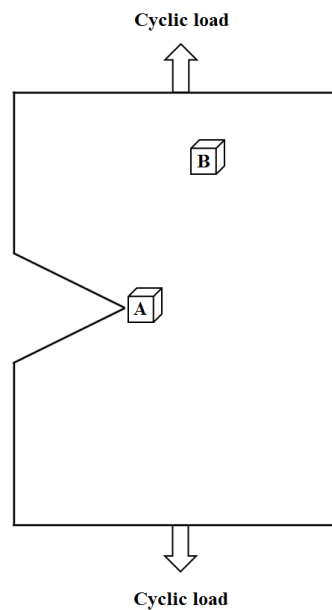


Fig. H.1. Schematic representation of two possible studied locations.

Fig. H.2 shows the evolution of the cyclic strain at high and low stress levels for three loading blocks. In both stress levels, after loading interruption and in the next loading block, the average cyclic strain was lower than the previous loading block due to specimen recovery as a result of the viscoelastic nature of the polymeric matrix. Again in the new loading block, as the number of cycles increased, the average cyclic strain gradually increased. However, the number of cycles required to attain the strain level of the previous loading block was not the same at low and high stress levels. At the low stress level, the number of cycles was lower than 50; however the strain level took longer to reach the same level as that in the previous loading block at the high stress level. This observation explained the concept of crack blunting in which the local stress intensity in the craze zone at the crack tip significantly decreased and did not increase again at the same rate upon reloading and thus delayed crack growth in the following cycles.

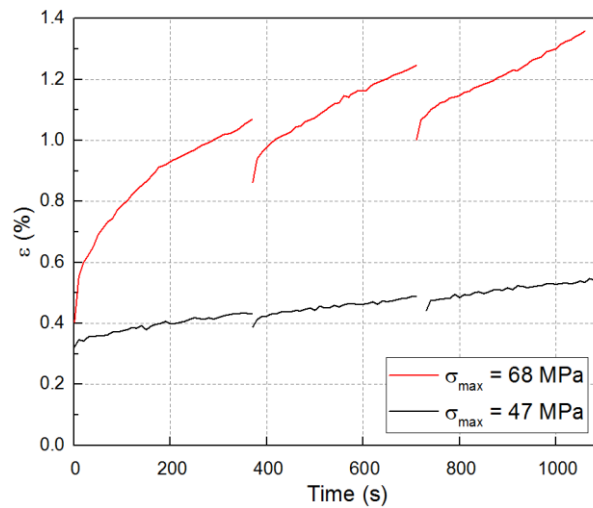


Fig. H.2. Evolution of cyclic creep at high and low stress levels.

Reference:

- [1] Imai, Y., Takase, T., & Nakano, K. (1989). Study of fatigue crack growth retardation due to overloads in polymethylmethacrylate. *Journal of materials science*, 24(9), 3289-3294.

Curriculum Vitae



A. Vahid Movahedi-Rad

Email: movahedirad@gmail.com

LinkedIn address: <https://www.linkedin.com/in/a-vahid-movahedi-rad/>

Google scholar: <https://scholar.google.com/citations?user=xI405PUAAAAJ&hl=en>

Address: Av. de l'Eglise-Anglaise 12, 1006 Lausanne, Switzerland

Cell: +41 78 907 98 28

Professional Profile

- ❖ Materials scientist specialized in manufacturing, characterization, and mechanics of polymers, composites, and metallic materials
- ❖ Experimental design and analytical analysis
- ❖ Identification of material processing-structure-property relationships
- ❖ Project supervisor and teaching assistant

Education

Ph.D. in Materials Science and Engineering (2015 – 2019)

École polytechnique fédérale de Lausanne (EPFL), Lausanne, Switzerland

M.Sc. in Materials Science and Metallurgy, Material Selection and Characterization (2011 – 2013)

University of Tehran, Tehran, Iran

B.Sc. in Materials Science and Metallurgy (2007 – 2011)

University of Tehran, Tehran, Iran

Working Experience

Research and teacher assistant (Mar. 2015 – Mar. 2019)

Composite Construction Laboratory (CCLAB), EPFL, Lausanne, Switzerland

Project: Load history effects in fatigue behavior of fiber-reinforced polymer (FRP) composites

Laboratory: Composite Construction Laboratory (CCLAB)

Supervisor: Dr. Vassilopoulos Anastasios, Professor Thomas Keller

Responsibilities:

- Experimental and analytical research on mechanics of polymer matrix composite materials
- Maintenance of laboratory equipment and instrumentation
- Writing project reports, technical papers and documentation of tests results
- Fulfillment of engineering administrative tasks (logistics, orders, quotations, seminars)
- Research-oriented project management

Output:

- Design of composite structures
- Development of experimental designs to evaluate the mechanical, thermal, and optical properties of laminated composites
- Investigation of the damage mechanisms in laminated composites
- Development of a modeling methodology to simulate the fatigue behavior of laminated composites using viscoelastic theory

Failure analysis engineer (Feb. 2014 – Oct. 2014)

Razi Metallurgical Research Center (RMRC), Tehran, Iran

Responsibilities:

- Determination of the root cause failure of industrial components

- Performance of life assessment analysis
- Material selection

Output:

- Performance failure analysis on the steel tubes, shafts, and welded joints
- Determination hot-oxidation behavior of stainless steels

Research assistant (Jul. 2011 – Jan. 2014)

Formability Laboratory, University of Tehran, Tehran, Iran

Project: Mechanical properties and creep behavior of Mg-Gd-Y-Zr and Mg-Gd-Y-Zr-Ag alloys.

Laboratory: Formability Laboratory

Supervisor: Professor Reza Mahmudi

Output:

- Microstructural characterizations of as-cast, heat-treated, and hot-extruded Mg alloys
- Improvement of the mechanical properties and creep resistance of Mg-Al and Mg-Gd alloys by:
 - Modifying the chemical composition
 - Performing heat treatment (T6)
 - Performing hot deformation
- Determination of the textural behavior of hot-extruded Mg-Gd alloys
- Enhancement of the superplasticity of Mg-Gd alloys

Project Co-supervision

- Eurocode establishment, Determination of curing degree of fiber-reinforced polymer (FRP) structures using Dynamic Mechanical Analysis (DMA), (2018), Master Project, EPFL, Composite Construction Laboratory (CCLAB), Lausanne, Switzerland
- Design of a fiberglass skateboard, (2017), Master Project, EPFL, Composite Construction Laboratory (CCLAB), Lausanne, Switzerland
- Study of the microstructural and mechanical properties of as-cast Al-Zn alloys, (2014), Bachelor Project, University of Tehran, Formability Laboratory, Tehran, Iran

Management and Organizational Experience

- **Business concept course (Feb. 2018 – Jun. 2018):**
Commission for Technology and Innovation (CTI), EPFL, Lausanne, Switzerland
- **Science communication course (Jul. 2018)**
Imperial College London, London, UK
- **A member of Organization committee in 12th International Conference on Sandwich Structures (ICSS) (August, 2018),** EPFL, Lausanne, Switzerland

Publications

Journal papers

Mechanical properties and fatigue behavior of polymer matrix composites

- A.Vahid Movahedi-Rad, Thomas Keller, Anastasios P. Vassilopoulos, Interrupted tension-tension fatigue behavior of angle-ply GFRP composite laminates, International Journal of Fatigue, 113 (2018) 337-388.
- A.Vahid Movahedi-Rad, Thomas Keller, Anastasios P. Vassilopoulos, Fatigue damage in angle-ply GFRP laminates under tension-tension fatigue, International Journal of Fatigue, 109 (2018) 60-69.

- A.Vahid Movahedi-Rad, Thomas Keller, Anastasios P. Vassilopoulos, Creep effects on the tension-tension fatigue behavior of angle-ply GFRP composite laminates, *International Journal of Fatigue*, 123 (2019) 337-388.
- A.Vahid Movahedi-Rad, Thomas Keller, Anastasios P. Vassilopoulos, Modeling of fatigue behavior using viscoelastic theory, submitted.
- A.Vahid Movahedi-Rad, Thomas Keller, Anastasios P. Vassilopoulos, Stress ratio effect on fatigue behavior of angle-ply GFRP laminates, submitted.

Failure Analysis of industrial components

- A. Movahedi-Rad, S.S. Pelaseyed, M. Attarian, R. Shokrallahzadeh “Oxidation behavior of AISI 321, AISI 316, and AISI 409 stainless steels: Kinetic, thermodynamic, and diffusion studies” *Journal of Materials Research*, 31 (2016) 2088-2096.
- A. Movahedi-Rad, S.S. Plasseyed, M. Attarian,” Failure Analysis of Super-heater Tube”. *Engineering Failure Analysis*, 48 (2015) 94-104.
- S. S. Pelaseyed, F. Mashayekhi, A. Movahedi-Rad “Investigation of the Shaft Failure Connected to Extruder” *Journal of Failure Analysis and Prevention*, 15 (2015) 775-781.

Mechanical properties and creep behavior of Magnesium alloys

- A. Movahedi-Rad, R. Mahmudi, G.H. Wu, H.R. Jafari Nodooshan, “Enhanced superplasticity in an extruded high strength Mg–Gd–Y–Zr alloy with Ag addition” *Journal of Alloys and Compounds*, 626 (2015) 309–313.
- A. Movahedi-Rad, R. Mahmudi, “Effect of Ag addition on the elevated-temperature mechanical properties of an extruded high strength Mg–Gd–Y–Zr alloy”, *Materials Science & Engineering A* 614 (2014) 62–66.
- R. Geranmayeh, R. Mahmudi, A. Movahedi-Rad, M. H. Malekshoaraei, “High temperature mechanical properties of AZ61 and AZ61-0.7Si magnesium alloys”, *Kovove Materialy*, 50 (2012) 393-397.

Computational modeling

- A. Movahedi-Rad, R. Alizadeh, “Dependence of strain rate sensitivity on the slip system: A molecular dynamics simulation” *Journal of Materials engineering and performance*, 26 (2017) 5173-5179.
- A. Movahedi-Rad, R. Alizadeh, “Simulating Grain Boundary Energy Using Molecular Dynamics”, *Journal of Modern Physics* 5 (2014) 627–632.

Conference papers

- A.Vahid Movahedi-Rad, Thomas Keller, Anastasios P. Vassilopoulos, “Effect of Loading Pattern on Fatigue Behavior of Laminated Composites” *ICEM18 - 18th International Conference of experimental Mechanics*, Brussels, Belgium, July 2018.
- A.Vahid Movahedi-Rad, Thomas Keller, Anastasios P. Vassilopoulos, “Effects of load interruption on the fatigue life of GFRP composites” *ECCM18 - 18th European Conference on Composite Materials*, Athens, Greece, June 2018.
- A.Vahid Movahedi-Rad, Thomas Keller, Anastasios P. Vassilopoulos, “Creep-fatigue interaction in composite materials” *ECCM17 - 17th European Conference on Composite Materials*, Munich, Germany, June 2016.

Personal Details

- ❖ Date of birth: 11th December 1988
- ❖ Nationality: Iranian
- ❖ Swiss residence
- ❖ Languages: English (Fluent), French (B2), German (B1), Persian (Native language)

